School of Electrical Engineering, Computing and Mathematical Sciences
Department of Physics and Astronomy
Curtin Institute of Radio Astronomy
International Centre for Radio Astronomy Research

The Radio Source Population of Globular Clusters

Vlad Andrei Tudor

This thesis is presented for the Degree of
Doctor of Philosophy
of
Curtin University

July 2018

To the best of my knowledge and belief this thesis contains no material previously published by any other person except where due acknowledgement has been made. This thesis contains no material which has been accepted for the award of any other degree or diploma in any university.

.....
Vlad Tudor
July 22, 2018

Statement of contribution by others

The content of Chapter 3, “Radio survey of globular clusters” is as yet unpublished. It is my own work, excepting the following. Some observations with Australia Telescope Compact Array (ATCA) were carried out by J. C. A. Miller-Jones, T. D. Russell and A. K. Tzioumis. Discussions were contributed to by members of the MAVERIC team – L. Chomiuk, C. O. Heinke, T. J. Maccarone, J. C. A. Miller-Jones, L. Shishkovsky, G. R. Sivakoff, and J. Strader, as well as by my supervisory panel – J. C. A. Miller-Jones, R. M. Plotkin, G. E. Anderson, and R. Soria.

The content of Chapter 4, “Disk–jet coupling in low–luminosity accreting neutron stars”, reproduces the publication with the same title by Tudor et al. (2017). It is my own work, excepting the following. The Swift/XRT analysis for SAX J1808.4–3658 was performed by A. Patruno, for IGR J00291+5934 by T. D. Russell, and for Cen X–4 partly by P. G. Jonker. D. M. Russell, F. Bernardini and F. Lewis provided and performed the analysis for the optical observations of SAX J1808.4–3658.

The content of Chapter 5, “HST spectrum and timing of the ultra-compact X-ray binary candidate 47 Tuc X9”, reproduces the publication with the same title by Tudor et al. (2018). It is my own work, excepting the following. The FUV spectrum was provided by C. Knigge, along with the optical/FUV timing analysis, writing its corresponding sections (Sections 5.1.3 and 5.2.3), and making Figures 5.3 and 5.4. The sections detailing the interpretation of the X-ray spectrum (Section 5.3.6), and the estimated rate of bright black hole ultracompact X-ray binaries (second half of Section 5.3.9) were written by T. Maccarone. The binary simulation (first half of Section 5.3.9) was run by T. Tauris, along with making Figures 5.12 and 5.13. The X-ray data plotted in Figure 5.9 were provided by A. Bahramian, and the optical/X-ray data for V404 Cyg and Cen X–4 were provided by F. Bernardini and D. M. Russell.

(Signature of Candidate)

(Signature of Supervisor)

"Midway upon the journey of our life
I found myself within a forest dark,
For the straightforward pathway had been lost."

Dante Aligheri (Inferno)

Acknowledgements

Firstly, I would like to thank my supervisors James Miller-Jones, Richard Plotkin, Gemma Anderson, Roberto Soria and Peter Curran for their guidance, ideas, knowledge and support. It goes without saying that none of this would have been possible without you. Also, to the administration team at CIRA who make sure everything runs smoothly.

Thank you to my friends at CIRA, particularly Pikky for her cheery disposition, Ronniy for his world view, and Ryan for being the best teammate. Outside of CIRA, Laura Shishkovsky for her life lessons, and Tom Russell for his stories.

I am grateful to my high-school physics teacher Nicoleta Becheanu, who introduced me to astronomy academically.

I thank my family for their support, understanding, and for instilling in me a love of the natural world and the Universe. To my partner Mia, thank you for the excitement, and for being there for me.

I would like to acknowledge the traditional owners of the sites on which ATCA and the Curtin University campus were built, the Gomeroi and the Nyungar people.

Abstract

Globular clusters are dense aggregates of up to a few million stars, gravitationally bound to a region similar in size to the distance between the Sun and the next-nearest star. These high-density environments are conducive to regular interactions between stars, leading to the formation of exotic systems. These include cataclysmic variables (white dwarfs pulling matter from normal stars), X-ray binaries (similar to cataclysmic variables, replacing the white dwarf with a neutron star or black hole) and millisecond pulsars (neutron stars with millisecond spin periods).

Due to source crowding and the relatively large distances (a few kpc) to globular clusters, the study of such objects at optical wavelengths can be difficult. Cataclysmic variables and X-ray binaries are typically discovered in globular clusters as X-ray sources. Similar to the rest of the Galaxy, X-ray binaries in globular clusters are easier to identify during outbursts, when their X-ray luminosity increased by orders of magnitude over their baseline level of emission. None of these X-ray transients have so far been found to host black holes, but theoretical and observational studies suggest black hole X-ray binaries should exist.

The drawbacks of single-wavelength studies extend to interpreting the nature of each object. In X-rays, the spectra of different classes of objects can be alike. To explore the full range of exotic sources in globular clusters, and facilitate their classification, multiple observational techniques must be employed. The magnetic fields and ejecta launched by a few classes of binary systems make them detectable at radio frequencies, albeit with different properties depending on their nature. In particular, black holes are thought to launch more powerful jets than other types of systems. The radio band can therefore be an important window through which exotic objects, including black holes, can be identified in globular clusters.

To uncover the faint population of radio sources within globular clusters, we conducted the Milky-way ATCA and VLA Exploration of Radio-sources in Clusters (MAVERIC) survey, which was carried out with the Australia Telescope Compact Array (ATCA) and the Karl G. Jansky Very Large Array (VLA). The ATCA sample, on which this thesis focuses, was observed at 5.5 and 9 GHz (the most sensitive bands of ATCA), and included 26 nearby ($\lesssim 9$ kpc), massive ($\gtrsim 10^5\ M_\odot$) southern clusters. A few more distant clusters were included as previous studies have suggested they might

host intermediate-mass black holes. After estimating the background source counts, I found that from a total of ∼1300 detected sources across the survey, fewer than ∼70 sources are likely to be part of the globular cluster system. Some globular clusters contain a significant (albeit small) excess of sources above the background. These are likely to be pulsars, neutron star and potentially black hole X-ray binaries. While pulsars are relatively easy to identify based on their steep radio spectra, differentiating between other classes of objects is more difficult.

To assess whether X-ray-faint neutron star X-ray binaries can reach radio luminosities similar to black holes, we carried out observations of four such systems in the Galactic field. We found that neutron stars show a range of behaviours, differing across classes and between systems. Even so, taken as a whole, their population is fainter in the radio band than black holes at a similar X-ray luminosity. Some systems, however, may be indistinguishable from black holes. As such, neutron stars (as both pulsars and X-ray binaries) are likely to constitute the majority of detectable radio sources in globular clusters.

Not all radio sources in globular clusters need to be neutron stars. One of the first black hole candidates identified in the MAVERIC survey was 47 Tuc X9. However, its radio and X-ray luminosities straddle the regions occupied by both neutron stars and black holes. Complementing previous work, we have acquired optical spectra of this system to glean information about its nature. Finding no evidence of hydrogen in its spectrum, we have corroborated the interpretation of a white-dwarf donor. Searching for periodicities in its optical/ultraviolet light curve, we retrieve similar signals to those seen in X-rays. The ∼30 min orbital period indicates the donor star has a mass $M \approx 0.013\,M_{\odot}$. The seven-day superorbital period might be driven by tidal effects or inclination variations induced by a third, unseen companion. At this stage we cannot identify the nature of the primary. The broadband spectrum indicates the system is either a low-inclination black hole system, or a high inclination neutron star system.

Optical/ultraviolet follow-up observations of sources identified in the MAVERIC survey have the potential to reveal previously unknown exotic sources. In addition to X9, I discuss the nature of a few other systems from a multi-wavelength perspective. As radio-selected (rather than X-ray selected) sources, they are likely to different properties from the currently known population of dynamically-formed objects in globular clusters. Such discoveries can help pave the way towards a better understanding of binary black hole formation rates, and binary evolution and interaction with their host cluster.

Abbreviations and acronyms

Acronyms

ACIS *Chandra* Advanced CCD Imaging Spectrometer (Energy range = 0.1–10 keV; Weisskopf et al., 2002)

ADAF advection-dominated accretion flow

AGN active galactic nucleus

AMUSE-Virgo AGN Multiwavelength Survey of Early-type galaxies in the Virgo cluster

AMXP accreting millisecond X-ray pulsar

ARF ancillary response file

ASM *Ariel V* All-Sky X-ray Monitor (Energy range = 3–6 keV; Holt, 1976)

ATCA Australia Telescope Compact Array (Frequency range = 1.1–105 GHz; Wilson et al., 2011)

AU astronomical units

BAT *Swift* Burst Alert Telescope (Energy range = 15–150 keV; Barthelmy et al., 2005)

CASA Common Astronomy Software Application

CCD charge-coupled device

CV cataclysmic variable

DIM disc instability model

EW equivalent width

HMXB high-mass X-ray binary

HRC *Chandra* High-Resolution Camera (Energy range = 0.1–10 keV; Weisskopf et al., 2002)

HST Hubble Space Telescope

ICRF International Celestial Reference Frame

IMBH intermediate-mass black hole

INTEGRAL INTErnational Gamma-Ray Astrophysics Laboratory

IRAF Image Reduction and Analysis Facility

LIGO Laser Interferometer Gravitational-Wave Observatory

LISA Laser Interferometer Space Antenna

LMXB low-mass X-ray binary

MAVERIC Milky-way ATCA and VLA Exploration of Radio-sources in Clusters

MSP millisecond pulsar

ngVLA Next Generation VLA (Frequency range = 1.2–116 GHz Selina et al., 2018)

PCA *RXTE* Proportional Counter Array (Energy range = 2–60 keV; Jahoda et al., 1996)

PSF point spread function

RFI radio-frequency interference

RMF response matrix file

rms root-mean-square

RXTE Rossi X-ray Timing Explorer Mission

SKA Square Kilometre Array (Frequency range = 70 MHz – 30 GHz; Dewdney et al., 2009)

SMBH supermassive black hole

SNR signal-to-noise ratio

STIS *HST* Space Telescope Imaging Spectrograph (Wavelength range = 1150–10000 Å)

tMSP transitional millisecond X-ray pulsar

ULX ultraluminous X-ray source

UV ultraviolet

VLA Very Large Array (Frequency range = 1–50 GHz Perley et al., 2011)

VLBI Very Long Baseline Interferometry

XRT *Swift* X-ray Telescope (Energy range = 0.2–10 keV; Burrows et al., 2005)

XSPEC X-Ray Spectral Fitting Package

Contents

Chapter 1

Introduction

1.1 Compact objects

Most stars in the universe will end their lives as compact objects with extremely high densities. However, the main sequence lifetime of stars with masses below $M < 0.8 M_{\odot}$ is longer than the age of the universe. Depending on the mass of their progenitor stars, compact stellar remnants can be white dwarfs, neutron stars, or black holes. For initial masses in the range $0.5 - 8 M_{\odot}$, the star will shed its outer layers during its red giant phase, exposing its core, which will later become a white dwarf within a short-lived planetary nebula. Neutron stars and black holes form for initial masses above $\gtrsim 8 M_{\odot}$, with stars below $< 20 M_{\odot}$ forming mostly neutron stars, and above $> 20 M_{\odot}$ mostly black holes (Sukhbold et al., 2016). Black holes form when the remnant is too compact for hydrostatic or degeneracy pressures to prevent it from collapsing. When the escape velocity at the surface of the remnant exceeds the speed of light (its radius equal to its Schwarzschild radius, or event horizon), we may never receive any information from such a remnant (Salaris and Cassisi, 2005; Chapter 7).

On average, white dwarfs have radii of $0.01 R_{\odot}$, similar to that of the Earth, and masses of $0.6 M_{\odot}$ (Bergeron et al., 1992). Neutron stars are more massive and compact, with typical masses of $\sim 1.4 M_{\odot}$ and radii of ~ 10 km (Özel et al., 2016), comparable to the size of a city (Figure 1.1). The event horizons of typical stellar-mass black holes have similar sizes to neutron stars, but are a few times more massive, with an average observed mass of $8 M_{\odot}$ (Özel et al., 2010), and some masses exceeding $30 M_{\odot}$ (Belczynski et al., 2010; Abbott et al., 2016). Observationally, confirming an object as a black hole is based on the measurement of its mass. As the most massive neutron stars can only reach masses of $\sim 2.3 M_{\odot}$ (Margalit and Metzger, 2017; Linares et al., 2018), and minimum mass for stellar-mass black holes may be $\sim 4 M_{\odot}$ (Farr et al., 2011), the threshold between a neutron star and black hole is often taken to be $3 M_{\odot}$. Finding the maximum mass achievable by a neutron star is therefore paramount in describing the

fundamental physics that dictate how matter at extreme densities behaves.

The Milky Way contains on the order of $\sim 10^{11}$ stars (Perryman et al., 2001). As most stars end their lives as white dwarfs, around 10% of the Galactic population of stars consists of these degenerate objects (Sion et al., 2009). In contrast, the Galaxy contains on the order of $\sim 10^{9}$ neutron stars (Narayan and Ostriker, 1990; Arnett et al., 1989; Treves et al., 2000; Cappellaro et al., 1997) and $\sim 10^{8}$ black holes (Timmes et al., 1996; Samland, 1998; Agol and Kamionkowski, 2002; Elbert et al., 2018), corresponding to $\sim$1% and $\sim$0.1% of all stars in the Galaxy, respectively.

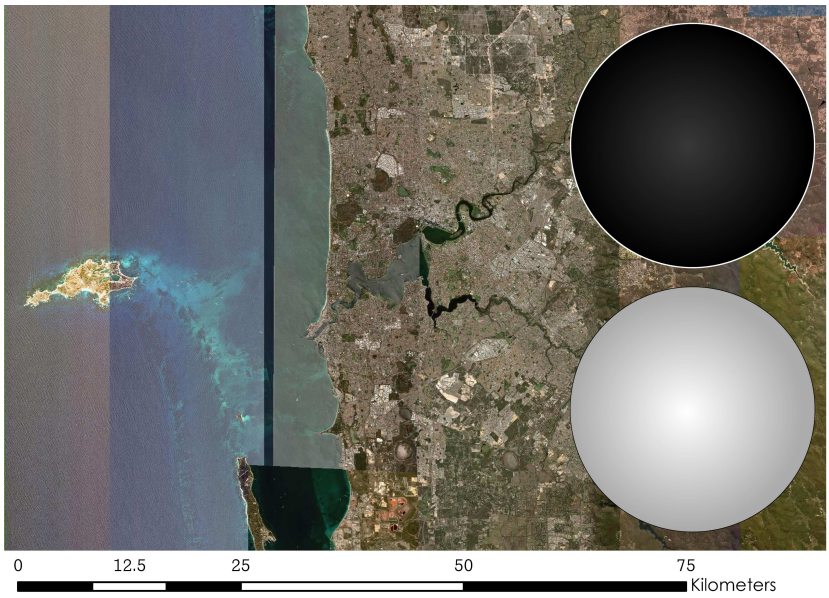

Figure 1.1: The sizes of a typical neutron star ($1.4M_{\odot}$, white) and black hole event horizon ($5M_{\odot}$, black) relative to a city (Perth, Western Australia). Credit: satellite data acquired from DigitalGlobe.

1.2 Accretion

Accretion is the infall of matter onto an astrophysical body, releasing gravitational potential energy. A vast range of astrophysical objects are powered by accretion, ranging from young stellar objects, to gamma-ray bursts, X-ray binaries, and active galactic nuclei (AGN).

The gravitational potential energy released by accretion of a mass m from infinity onto an object of mass M and radius R is given by equation 1.1:

$$\Delta E = GMm/R\,, \tag{1.1}$$

where G is the gravitational constant. Compact objects with large M/R ratios are therefore more efficient accretors, so that for neutron stars and black holes, accretion

is more efficient than nuclear burning. From a mass m of hydrogen, > 10 times more energy can be extracted by accreting it onto a neutron star or black hole, than by converting it to helium through nuclear fusion. Hydrogen fusion in stars can convert 0.7% of rest-mass energy to other forms of energy via the PP chain, and the efficiency of disc accretion onto a maximally-spinning black hole is 42% (Frank et al., 2002, Chapter 6). During accretion, gravitational potential energy is either converted to kinetic energy, or electromagnetic radiation. In the case of neutron stars or white dwarfs, some of the kinetic energy is subsequently converted to electromagnetic radiation when it hits their surface. In contrast, black holes do not have a surface, so kinetic energy and rest mass disappears (is advected) inside the event horizon. All the luminous output from a black hole comes from the accretion flow. Therefore, even if black holes can have higher M/R ratios than neutron stars, they are less efficient at producing a luminous output at low mass accretion rates (Narayan et al., 1996; Garcia et al., 2001). At very high accretion rates, mass inflow is limited by the outward photon pressure, as described by the Eddington luminosity.

1.2.1 The Eddington luminosity

For an object of fixed M/R, the energy output from accretion depends on the mass accretion rate, so that a source becomes more luminous the more mass it accretes. For spherical accretion, as the luminosity increases, the radiation will exert an outward pressure on the inflowing ionized material, in the form of Thompson scattering of free electrons, which are electromagnetically coupled to protons. When radiation pressure equals gravitational pressure, accretion is regulated so it does not get any higher. The limiting luminosity at which this happens is called the Eddington luminosity,

$$L_{\rm Edd} = 1.3 \times 10^{38} \left(\frac{M}{M_\odot} \right) \, {\rm erg \, s^{-1}} , \tag{1.2}$$

where $M_\odot$ is the mass of the Sun. Depending on how luminous an object is, it can be described by the Eddington ratio, which is the fraction of the Eddington luminosity at which it is emitting. Equation 1.2 assumes steady, spherical accretion of hydrogen. For other accretion compositions and especially geometries, the limiting accretion luminosity is only loosely associated with the Eddington luminosity. For example, the recently-discovered ultraluminous X-ray pulsars can exceed this limit (Bachetti et al., 2014). The strong magnetic fields of young pulsars, which can distort the flow of accretion flows, are thought to be involved in this phenomenon (King and Lasota, 2016).

1.2.2 Inflow

As the simplest case of accretion, *spherical accretion* was initially investigated by Hoyle and Lyttleton (1939), when describing what effect the passage of the Sun through the interstellar medium would have on Earth's climate. Later studied by Bondi and Hoyle (1944), accretion by a moving star through a gas became known as Bondi–Hoyle–Lyttleton accretion. Bondi accretion on the other hand, refers to accretion onto a star at rest in regards to the surrounding gas (Bondi, 1952). Spherical accretion is typically encountered in high-mass X-ray binaries (HMXBs) in the form of wind accretion, and in active galactic nuclei (AGN), from gas in the galactic bulge. A compact object in orbit with a massive star will result in the accretion of matter from the winds blown off by the primary star.

Binary (two gravitationally-bound) stars can also exchange matter if their orbital separation is close enough for the outer layers of one of the stars to be disrupted by the other. If a star fills up its Roche lobe, the equipotential surface within which particles are gravitationally bound to the star, material from its surface will spill towards its companion through the first Lagrangian point, where the gravitational potential from each star cancels out. Accretion powered by mass transfer through the first Lagrangian point is termed *Roche-lobe overflow*.

In Roche-lobe overflows and some cases of wind accretion, accretion discs form as a consequence of conservation of angular momentum and its viscous dissipation. When radiation pressure is insignificant, an accretion disc will likely have a scale height much smaller than its radius, and can therefore be considered a 2D flow in the orbital plane. The theory for this *thin disc* approximation was developed by Shakura and Sunyaev (1973), being adopted as the *standard model* of accretion discs. At low Eddington ratios ($\lesssim 0.1$), discs are radiatively inefficient, so that very little of the dissipated energy is released as radiation. In this case, Narayan et al. (1996) proposed that the inner disc is truncated, its central part is a more vertically extended advection-dominated accretion flow (ADAF; Narayan and Yi, 1994), and the outer disc can be described by the standard thin disc. ADAFs are required to explain the much lower luminosities than predicted by the standard disc solution for a given mass accretion rate. ADAFs have successfully been used to infer the presence of an event horizon and explain the low luminosity states of Sgr A* (Narayan et al., 1998), and of black hole X-ray binaries, which have lower quiescent luminosities than neutron stars at the same orbital period (Narayan et al., 1996). Instead of being advected through the event horizon, however, material might also be ejected from the system (Fender et al., 2003).

1.2.3 Outflow

Depending on the properties of the accreting object and inflow, matter can flow out of the system in the form of jets or winds, removing energy and angular momentum from the disc.

Jets

Collimated bipolar jets can be launched during the accretion of matter, and have been observed in many classes of astrophysical sources powered by accretion (Figure 1.2). In many cases these jets are radio–bright and relativistic (e.g. Fender et al., 1999). Even though they are usually associated with black holes (stellar-mass and supermassive), jets can also be observed in neutron stars (Fomalont et al., 2001), white dwarfs (Körding et al., 2008), proto-stars (Anglada et al., 1995), tidal disruption events (Mattila et al., 2018) and γ-ray bursts (Sari et al., 1999). Such jets can appear unresolved or extended, depending on their nature and observational constraints.

First discovered in 1918 (Curtis, 1918), the exact physical mechanism behind jets is uncertain. Black hole jets could be powered by the Penrose process (Penrose and Floyd, 1971), whereby particles gain momentum by directly extracting energy from a spinning black hole. Alternatively, in the Blandford–Znajek model (Blandford and Znajek, 1977), the spin of a black hole could be tapped by a magnetic field penetrating the event horizon. Otherwise, the Blandford–Payne model (Blandford and Payne, 1982) invokes magnetic fields from an accretion disc which can accelerate and collimate disc winds into a jet, and is possible in both neutron stars and black holes. The X-wind model (Migliari and Fender, 2006), developed for proto-stars, has also been suggested to explain how the spin of a neutron star can launch jets (Migliari et al., 2012).

Winds

Radiation from the inner accretion disc can interact with the rest of the disc and blow matter off its surface. Much better understood than jet formation, winds can generally be driven by thermal irradiation (Begelman et al., 1983), radiation pressure (Shlosman et al., 1985), or magnetically (Blandford and Payne, 1982). X-ray heating can produce winds when the local thermal velocity in the disc exceeds the escape velocity. Particles can be pushed off the disc by line absorption of a UV/X-ray continuum, similar to how winds are produced by massive stars (Castor et al., 1975). In comparison to jets, winds typically flow in the equatorial direction, are slower, and carry away more mass.

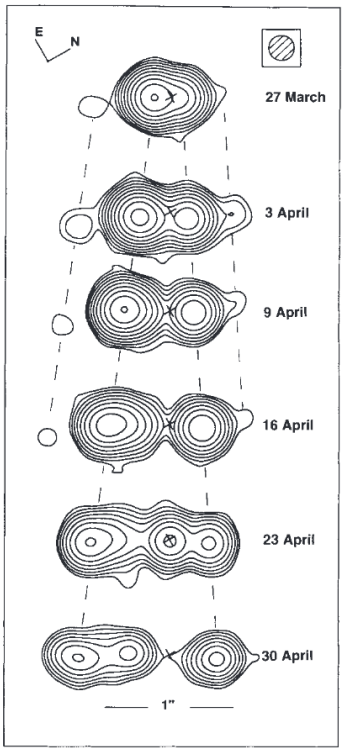

Figure 1.2: Discrete ejecta in the stellar-mass black hole GRS 1915+105, as observed in the radio band with the VLA. Figure from Mirabel and Rodríguez (1994).

Feedback

Depending on the channel of energy output, feedback comes in two flavours: radiative and kinetic. The radiative, or wind mode, typical of quasars, occurs in luminous AGN. In contrast, the kinetic mode associated with weaker AGN is characterised by the mechanical power of radio-loud jets. Radiative and kinetic feedback displace and heat up the interstellar gas in their host galaxies, quenching star formation (Fabian, 2012). In special circumstances, AGN activity can also trigger brief episodes of star formation (Silk, 2013). In a cosmological context, quasars (Barkana and Loeb, 2001; Madau and Haardt, 2015) and HMXBs (Mirabel et al., 2011; Fragos et al., 2013), powered by accretion, could have contributed significantly to the radiation that reionised the early universe. In comparison to AGN, which emit mostly ultraviolet (UV) photons, X-ray binaries are stronger sources of X-rays. As X-rays have a longer mean free path through intergalactic gas, they can reionise it more efficiently.

The understanding of accretion in different astrophysical sources can be facilitated by the study of X-ray binaries, which change accretion states on humanly observable timescales. Our understanding of the balance between radiative and kinetic feedback from AGN can therefore be enhanced by the study of black hole X-ray binaries, which have been shown to be scaled-down analogues of AGN (e.g. McHardy et al., 2003).

The universal physics behind these processes is demonstrated by the existence of scaling relations between accreting stellar-mass and supermassive black holes

(SMBHs), such as the Fundamental Plane of Black Hole Activity (Merloni et al., 2003; Falcke et al., 2004), which demonstrates a correlation among radio luminosity, X-ray luminosity and black hole mass. The timescales of variability between stellar-mass and SMBHs also scale with black hole mass (McHardy et al., 2006).

1.3 Accreting compact objects

X-ray binaries are binary systems in which a compact stellar remnant (neutron star or black hole) accretes matter from a companion star, either from Roche-lobe overflow, or stellar wind accretion (Frank et al., 2002, Chapter 4). About a third of known Galactic X-ray binaries contain black holes (Liu et al., 2007). A schematic for the two main types of X-ray binaries is shown in Figure 1.4.

Depending on the mass of the donor star, X-ray binaries are classified into *low-mass X-ray binaries* (LMXBs; $M_{\rm d} \lesssim 1 M_{\odot}$) or *high-mass X-ray binaries* (HMXBs ; $M_{\rm d} \gtrsim 10 M_{\odot}$), although there is no consensus over the exact mass intervals (Tauris and van den Heuvel, 2006; van den Heuvel, 1975). While a few intermediate-mass X-ray binaries[1] (IMXBs, e.g. V 4641 Sgr; MacDonald et al., 2014) of mass $M_{\rm d} = 1 - 10 M_{\odot}$ and descendants of IMXBs (Podsiadlowski and Rappaport, 2000) are known, their low numbers are thought to be caused by short lifetimes and evolution towards LMXBs (Podsiadlowski et al., 2002). In general, low-mass stars have weak winds, making LMXBs powered by Roche-lobe overflow. In contrast, the more massive OB stars that are associated with HMXBs either have a circumstellar disc or emit strong winds. In these systems, the donor does not need to be overflowing its Roche lobe, and the compact object accretes gas from the circumstellar disc or stellar wind (Tauris and van den Heuvel, 2006). IMXBs can either be powered by Roche-lobe overflow or wind accretion. When intermediate-mass stars do not fill their Roche lobes, their slow winds can still be funnelled through the first Lagrangian point, in which case wind accretion resembles Roche-lobe overflow (Gies and Bolton, 1986; de Val-Borro et al., 2009).

In Roche-lobe overflow systems, the accretion flow can be fed through three main mechanisms. In long period systems, the nuclear evolution and expansion of the secondary pushes its outer envelope outside its Roche lobe. In short period systems, magnetic braking or gravitational wave radiation cause the loss of orbital angular momentum, decreasing the orbital separation and shrinking the Roche lobe around the secondary (Menou et al., 1999). In addition, pulsar winds or the high X-ray fluxes from the inner accretion disc can ablate the surface of companion stars, blowing matter off, and feeding an accretion flow (e.g. Chakrabarty and Morgan, 1998).

[1]Not to be confused with intermediate-mass black holes, which will be discussed later

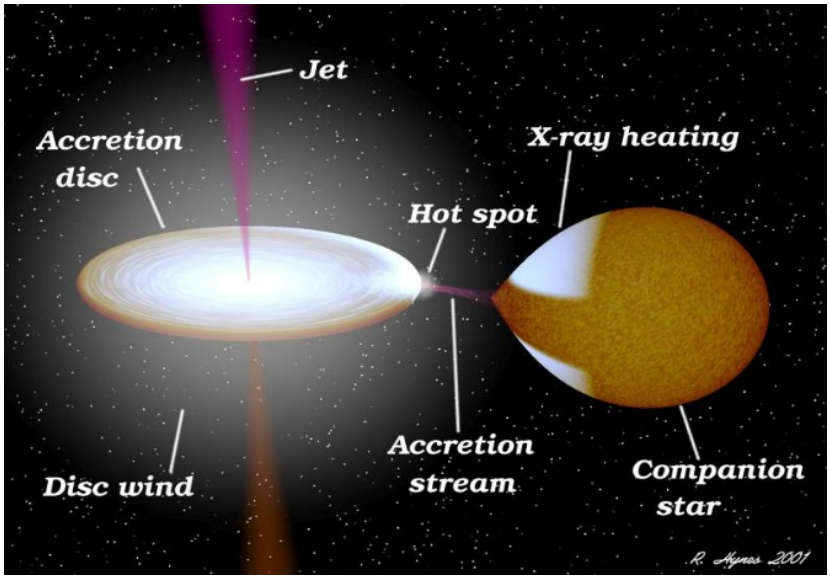

Figure 1.3: Prototypical low-mass X-ray binary, where a compact object (neutron star or black hole) is accreting matter from a Roche-lobe-filling low mass ($M < 1M_{\odot}$) star. The matter forms an accretion disc as it spirals in towards the compact object, and a fraction of it is launched out via relativistic jets and disc winds. Credit: R. Hynes (Software: BINSIM).

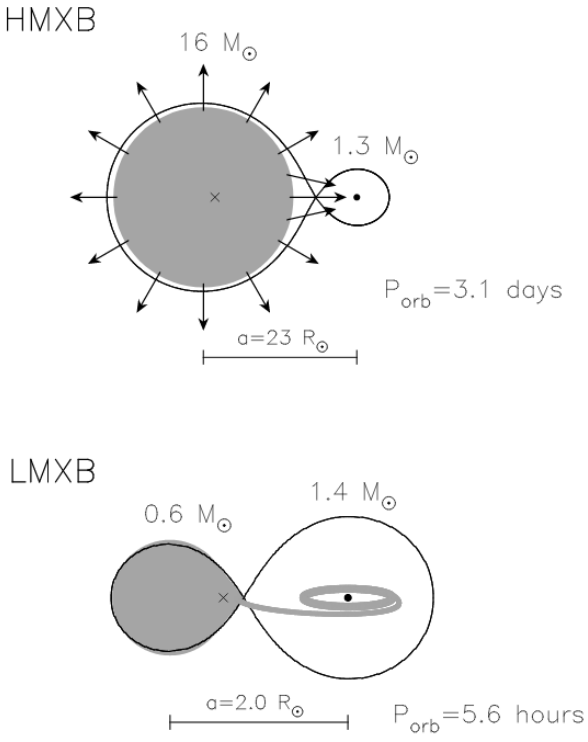

Figure 1.4: Schematic of typical HMXB and LMXB systems. In an HMXB, the companion star does not necessarily fill its Roche lobe, but has strong winds which are accreted by the compact object. In an LMXB, the donor star fills its Roche lobe and feeds an accretion disc around the compact object. Figure from Tauris and van den Heuvel (2006).

1.3.1 LMXB formation

Primordial binaries

In the field, X-ray binaries form from primordial binaries with at least one massive star. As the massive star evolves, it explodes as a supernova or collapses, forming a neutron star or black hole. If the less massive companion survives the supernova, and the supernova kick is not sufficient to unbind the system, Roche-lobe overflow can be triggered when the secondary star evolves off the main sequence and expands (Kalogera and Webbink, 1996, 1998).

Dynamical interactions

In denser environments (mainly globular clusters and the Galactic centre), X-ray binaries mainly form as a result of stellar interactions. The three such forms of interactions are tidal captures (Fabian et al., 1975), direct collisions (Sutantyo, 1975), and exchange interactions (Hills, 1976).

Depending on the distance of closest approach, a tidal capture of a star by a black hole or neutron star can have different outcomes. A long-distance capture can form a wide binary. Close approaches, on the other hand, can mimic the effects of a direct collision, leading to the destruction of the star, or, if a neutron star – giant system does not have enough kinetic energy to dissipate the outer envelope of the star, to a red supergiant with a neutron star core, known as a Thorne – Zytkow object (Ray et al., 1987).

During a direct collision, the stellar remnant passes through the interior of the star, ejecting its outer envelope. Due to their large cross-sectional areas, supergiants are thought to be the main precursors of direct collision events. Depending on the initial conditions of the system, a direct collision can lead to a neutron star/black hole – degenerate core X-ray binary (Sutantyo, 1975).

During an approach between a star and a binary or between two binaries, exchange interactions might disrupt the original binaries, forming new binaries with the most massive components, ejecting the least massive stars (Heggie et al., 1996). Binary disruption is especially likely in soft binaries, in which the binding energy of the system is lower than the mean kinetic energy of the surrounding, unassociated stars. Hard binaries, which have high internal energies relative to cluster stars, become harder (more energetic) from interactions with other stars, which decreases the orbital separation of the two binary components (Heggie, 1975). Hierarchical triples formed in exchange interactions can also lead to mass transfer. The tidal forces exerted by a distant third body on the inner binary cause cyclical variations in eccentricity and inclination (Kozai, 1962). In conjunction with orbital decay due to tidal friction, one of the components of the inner binary can overflow its Roche lobe (Eggleton and

Kisseleva-Eggleton, 2006). In globular clusters, exchange interactions are thought to be the main pathway through which LMXBs (both neutron star and black hole) form (Kalogera et al., 2004; Ivanova et al., 2008, 2010).

Interestingly, Klencki et al. (2017) have suggested that black hole LMXBs in the field can also form through dynamical interactions, without the need for a common envelope. The formation channel they propose is based on very wide binaries (> 500 AU) with a black hole component that are perturbed into highly eccentric orbits, leading to mass transfer at periastron, orbital circularization and the formation of a typical X-ray binary. This would mean that black holes in short period systems may also be found in the field, not just globular clusters.

Millisecond pulsars

Related to X-ray binaries are millisecond pulsars. The formation of radio millisecond pulsars (MSPs) is thought to occur by recycling neutron stars, as described in the review by Patruno and Watts (2012). In this scenario, an initially slow-spinning neutron star is spun up by accretion from a low-mass companion star, becoming an MSP once accretion stops. Recently, this idea has been reinforced by the discovery of accreting millisecond X-ray pulsars (AMXPs) and transitional millisecond X-ray pulsars (tMSPs). These are thought to be the missing links between MSPs and low-mass X-ray binaries (LMXBs); AMXPs are LMXBs which display fast X-ray pulsations at the spin period of the neutron star, but do not yet show radio pulsations because accretion is still active, burying the neutron star's magnetic field (Patruno and Watts, 2012). TMSPs switch between an accreting state, when the system is observed as an LMXB, and a non-accreting state, when the neutron star is observed as an MSP. As of today, there are only three confirmed (Wang et al., 2009; Papitto et al., 2013; Bassa et al., 2014) and one candidate (Bogdanov and Halpern, 2015) tMSPs.

Ultracompact X-ray binaries

An ultracompact X-ray binary is an LMXB in which both the donor (a white dwarf) and accretor (a neutron star or black hole) are compact. Other combinations of compact objects are not included in the ultracompact X-ray binary category. Mass-transferring white dwarf – white dwarf binaries fall under the category of cataclysmic variables as a subset of AM CVn stars (Solheim, 2010), and double neutron star (Abbott et al., 2017) and neutron star – black hole binaries only briefly transfer mass before merging (Kawaguchi et al., 2015). In regions of the Galaxy with high encounter rates, ultracompact X-ray binaries can form efficiently.

Once the white dwarf in orbit with a black hole or neutron star fills its Roche lobe, rapid mass transfer is initiated, becoming an ultracompact X-ray binary (van Haaften

et al., 2012; Sengar et al., 2017). A mass-transferring system consisting of a neutron star and a He white dwarf spends 10^7–10^8 years as a persistent source. Following this, the X-ray binary then becomes transient, undergoing outbursts occasionally (van Haaften et al., 2012). During accretion, the donor loses mass, leading to orbital expansion and thus a continuous decrease in the rate of mass transfer.

About 20 ultracompact X-ray binaries have been found to date (in't Zand et al., 2007, Nelemans and Jonker, 2010). Most of these systems are persistently accreting neutron stars, as indicated by the detection of thermonuclear X-ray bursts. The first black hole ultracompact X-ray binary candidate was found in a globular cluster in the elliptical galaxy NGC 4472. This source exceeds the Eddington luminosity for a black hole. In addition, the difference in luminosity between the faintest and brightest points of its light curve exceed the Eddington luminosity for a neutron star, ruling out the superposition of multiple neutron stars (Maccarone et al., 2007). This source is unlikely to be an ultraluminous X-ray pulsar (e.g., Bachetti et al., 2014) because such objects are thought to require highly magnetised neutron stars and massive donors (Kaaret et al., 2017), both associated with young stellar populations. Such populations do not survive in globular clusters today.

1.3.2 Spectral states

Some LMXBs are observed to undergo outbursts, when their luminosity increases by several orders of magnitude across the electromagnetic spectrum, accompanied by spectral changes and strong outflows. Outbursts recur on time scales of years to decades and typically last for several weeks. The physical explanation behind outbursts is provided by the disc instability model (DIM). The DIM was first proposed by Smak (1971) to explain the outburst behaviour of dwarf nova systems. This model predicts that as matter accumulates in the accretion disc, a critical surface density is reached, at which point the viscosity of the disc suddenly changes, and matter from the disc is dumped on the white dwarf, causing an outburst. The disc instability model was successfully extended to explain the outburst behaviour of black hole and neutron star LMXBs, with the addition of effects such as irradiation and tidal forces (Coriat et al., 2012).

During outbursts, black hole LMXBs are seen to exhibit particular correlations between the X-ray hardness (ratio between flux of high-energy photons and total flux) and X-ray flux, depending on the stage of the outburst. Neutron stars and cataclysmic variables have been observed to behave similarly (Körding et al., 2008). This hardness/intensity diagram is displayed in Figure 1.5.

At the start of an outburst, X-ray binaries are observed in a state of low luminosity characterised by a relatively large fraction of emission of high-energy X-ray photons,

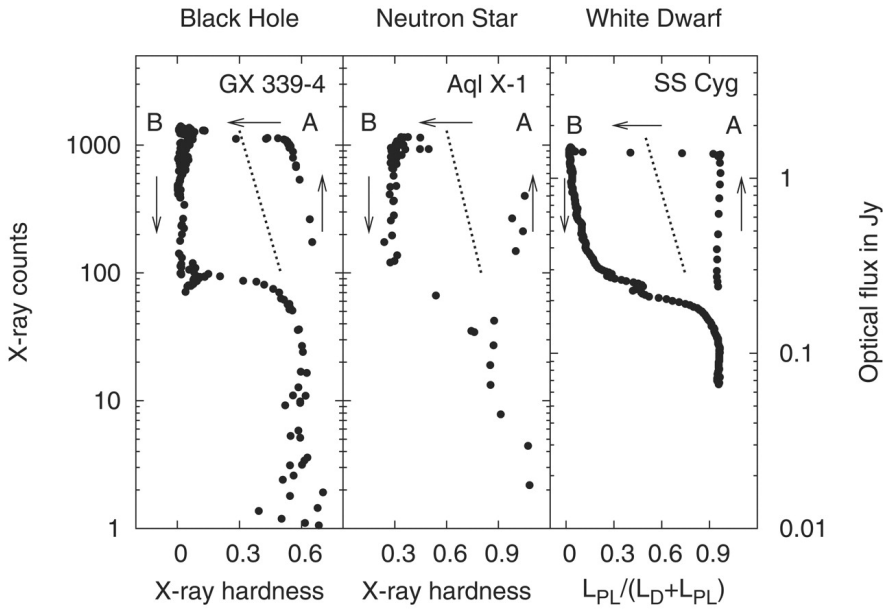

Figure 1.5: The hardness/intensity diagram for black holes and neutron stars, and power-law fraction/intensity diagram for white dwarfs. The hard state is the right-side branch of each path (with quiescence at low intensity), the soft state is on the left side of the diagram (Körding et al., 2008).

termed the *hard state*. The hardest black hole X-ray binary spectra occur at X-ray Eddington ratios of $\approx 10^{-2}$, with a photon index $\Gamma \approx 1.5$ ($N(E) \propto E^{-\Gamma}$, Wu and Gu, 2008). Associated with the hard state is a compact, steady radio jet. Towards the peak of an outburst, the spectrum softens, so that at 10% of the Eddington luminosity, $\Gamma \approx 2.5$. The X-ray spectra of neutron stars in the hard state are typically softer than those of black holes at the same X-ray luminosity (Wijnands et al., 2015; Parikh et al., 2017). At the transition towards the *soft state*, discrete, transient ejections are launched, after which the jet is either completely quenched (Fender et al., 2004c; Russell et al., 2011), or becomes "dark", with a very low radiative output, but still large kinetic power (Drappeau et al., 2017). Jet suppression in the soft state has also been observed in some neutron stars (Migliari et al., 2003; Tudose et al., 2009; Miller-Jones et al., 2010; Migliari, 2011; Gusinskaia et al., 2017). A schematic view of the relationship between spectral states and jet phenomenology is displayed in Figure 1.6.

The *quiescent state* is thought to be an extension of the hard state towards lower luminosities, but it does have different characteristics to the hard state. The photon indices of black holes vary; from the minimum photon index $\Gamma \approx 1.5$ in the hard state at an Eddington ratio of $\sim 10^{-2}$, Γ softens towards Eddington ratios of 10^{-5}, where it then plateaus at $\Gamma \approx 2.1$ (Plotkin et al., 2013, 2017). A black hole X-ray binary is therefore considered to be in quiescence below Eddington ratios of $\approx 10^{-5}$.

The quiescent luminosity of LMXBs is theoretically expected to depend on the orbital period of the system (Menou et al., 1999). For orbital periods longer than $\approx$10

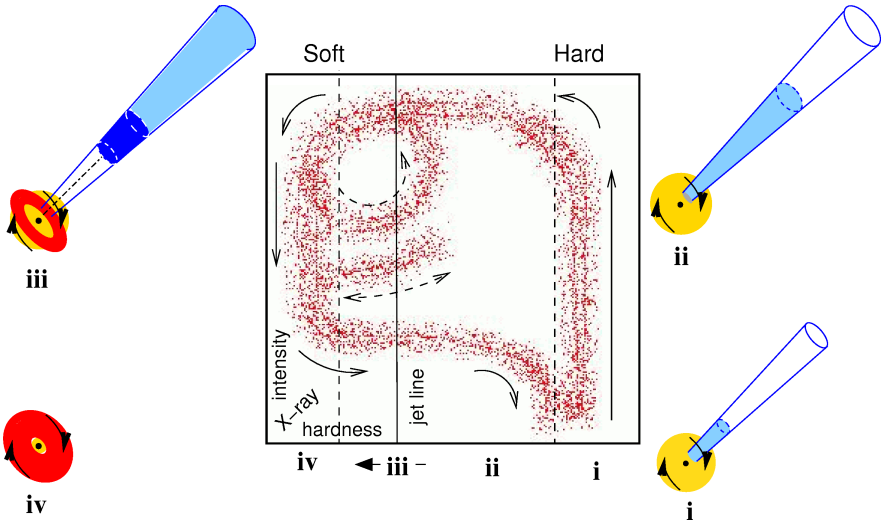

Figure 1.6: A schematic view of the hardness/intensity diagram, including jet phenomenology, and the contribution of different spectral components (red – disc, yellow – corona, blue – jet). The outer diagrams show the X-ray binary at different stages of an outburst: (i) quiescence, (ii) hard state, (iii) soft state with transient jets, (iv) soft state with quenched jet. Figure adapted from Fender et al. (2004c)

hours, the accretion rate in Roche-lobe overflow systems is driven by the evolution of the companion star, which translates to an increase in quiescent X-ray luminosity with binary separation. For shorter periods, mass loss from the orbital decay caused by gravitational wave radiation and magnetic braking becomes significant. Therefore, below periods of ≈3 hours, the quiescent X-ray luminosity increases with decreasing period. Due to the lack of very short period LMXBs, especially black holes, the observational evidence for a bifurcation period is scarce (Gallo et al., 2008a; Armas Padilla et al., 2014).

1.3.3 Disk–jet coupling

The X-ray luminosity of an X-ray binary is expected to scale with the mass accretion rate, $L_{\rm X} \propto \dot{m}^q$. For radiatively-efficient accretion, where all the gravitational potential energy of the accreted gas is converted to radiation, $q = 1$. For radiatively-inefficient accretion, $q \approx 2$ (Falcke and Biermann, 1995; Markoff et al., 2003). As mass outflow depends on mass inflow, the radio luminosity of a jet, which is an indicator of jet power, should indirectly trace mass accretion rate ($L_{\rm R} \propto \dot{m}^{\frac{17}{12}}$, Falcke and Biermann, 1995; Markoff et al., 2003). The theoretical expectation is therefore that $L_{\rm R} \propto L_{\rm X}^{\beta}$, with $\beta = 1.4$ for radiatively-efficient accretion, and $\beta = 0.7$ for the radiatively-inefficient case.

Inefficient accretion is expected in black holes as some of the matter is launched out of the system as strong, relativistic jets or slower, mass-loaded winds, and some can pass through the event horizon. On the other hand, neutron stars are expected to convert

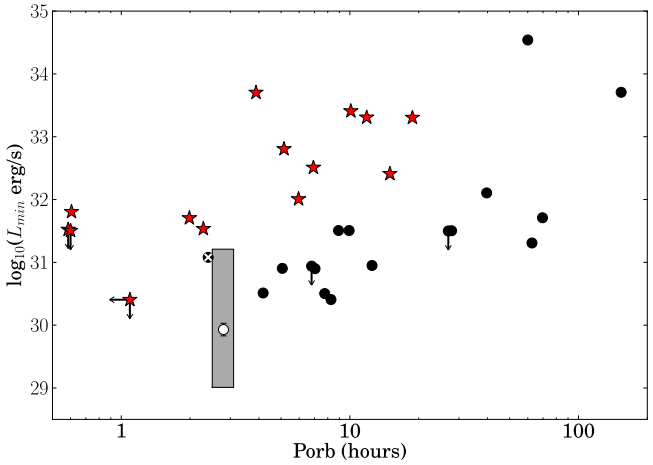

Figure 1.7: Observed quiescent X-ray (0.5–10 keV) luminosities of known neutron star (red stars) and black hole (black circles) LMXBs and their orbital periods. The gray area shows the uncertainty range (due to unknown distance) for Swift J1357.2–0933, the possibly faintest known black hole system. Empirically, luminosity is seen to increase with orbital period, as expected from mass transfer driven by the evolution of the donor star. Due to the low number of systems with short orbital periods ($P_{\rm orb} \lesssim 3$ hours), the existence of the bifurcation period ($P_{\rm orb} \approx 8$ hours) is yet to be confirmed empirically. Figure from Armas Padilla et al. (2014)

most of the available potential energy into radiation, as accreted matter hits the surface although they could still launch jets and winds. Below, we describe the observational evidence for a relationship of this type in black hole and neutron star X-ray binaries.

Black Holes

As radio jets from black hole X-ray binaries are more luminous relative to other accreting compact objects, it has been possible to study their inflow–outflow coupling over 8 orders of magnitude of X-ray luminosity (Figure 1.8; Corbel et al., 2008, 2013; Coriat et al., 2011; Plotkin et al., 2017). Instead of the expected universality of the radio–X-ray correlation, it was observed that individual black hole systems trace different tracks in the radio–X-ray plane, including radiatively efficient ($L_{\rm R} \propto L_{\rm X}^{1.4}$; Coriat et al., 2011; Gallo et al., 2012) and inefficient regimes ($L_{\rm R} \propto L_{\rm X}^{0.7}$; Gallo et al., 2003, 2014). Some of the radiatively-efficient systems are seen to switch to a radiatively-inefficient track as they decay towards quiescence (Jonker et al., 2010; Ratti et al., 2012; Jonker et al., 2012).

Gallo et al. (2014), however, found weak statistical evidence for the existence of two tracks in the black hole population, suggesting that each black hole could follow its own track. The difference in radio-loudness does not yet have a full physical explanation, but may be linked to the inclination angle (Motta et al., 2018; Espinasse and Fender, 2018).

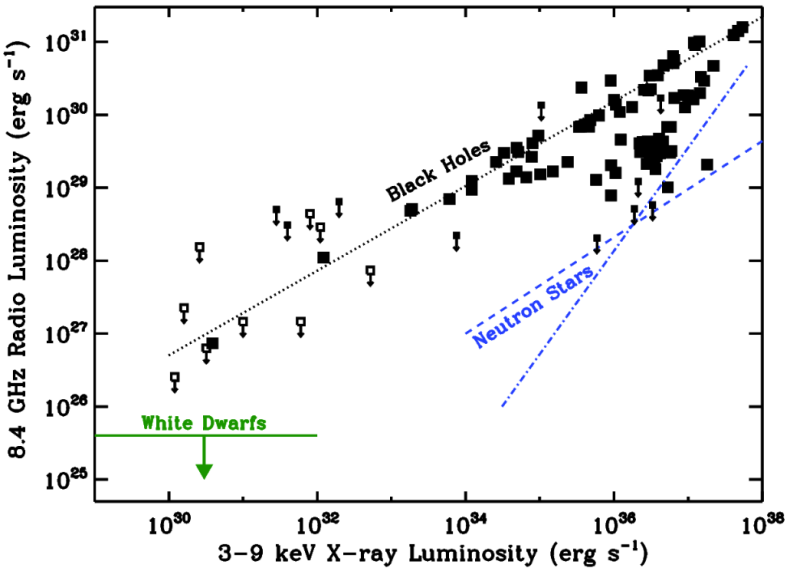

Figure 1.8: The radio X–ray correlation for accreting black holes adapted from Strader et al. (2012b). Neutron stars and white dwarfs are less radio-loud than black holes at the equivalent X-ray luminosity.

Radio and X-ray detections of three black hole LMXBs in quiescence confirm that the radio/X-ray correlation extends into quiescence (Gallo et al., 2006; Corbel et al., 2008; Gallo et al., 2014). In addition, radio and X-ray observations of the HMXBs MWC 656 and Cyg X–1 (Ribó et al., 2017) show that the inflow and outflow mechanisms of black holes are similar across systems, regardless of accretion type (Roche-lobe overflow, or wind-fed). It is possible to extend the radio – X-ray correlation to SMBHs by applying a mass normalization. Sub-Eddington AGN can therefore be unified with X-ray binaries in the hard state through the Fundamental Plane of black hole activity (Figure 1.9; Merloni et al., 2003; Falcke et al., 2004.

Neutron stars

Radio jets from accreting neutron stars are typically a factor of ~20 fainter than black holes at a similar X-ray luminosity (Migliari and Fender, 2006; Gallo et al., 2018). However, with recent radio detections of low-luminosity objects, the distinction in radio luminosity between black hole and neutron star jets is starting to blur (Deller et al., 2015; Tudor et al., 2017).

Disk–jet coupling in neutron stars initially focused on persistently luminous sources. A variety of studies found that radio emission in such systems correlates with their X-ray states (Penninx et al., 1988; Hjellming et al., 1990). Later, Migliari et al. (2003) found the atoll (transient, accreting well below the Eddington luminosity) source 4U 1728–34 follows a relationship of the form $L_{\rm R} \propto L_{\rm X}^{1.5\pm0.2}$, suggesting radiatively-efficient flows, as expected for accretion onto neutron stars. Following this, Migliari and

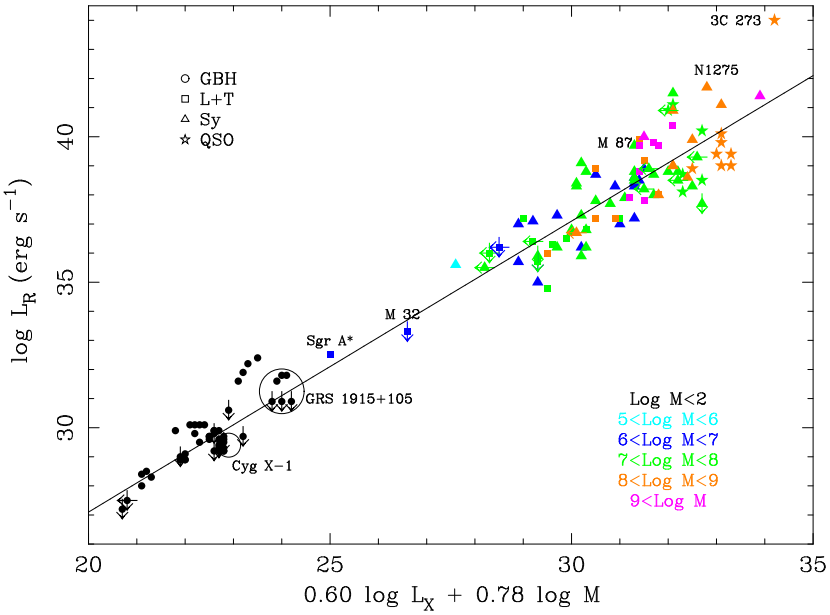

Figure 1.9: The Fundamental Plane of accreting black holes from Merloni et al. (2003). The radio luminosity from the jet scales with the X-ray luminosity from the inner accretion flow, and the mass of the black hole.

Fender (2006) extended their sample with three additional atolls showing $\beta \approx 1.4$, and four AMXPs which are more scattered across the radio–X-ray plane. The atoll source Aql X–1 was found to follow a flatter correlation, with a coupling index of $\beta = 0.8 \pm 0.2$ in the hard state (Tudose et al., 2009; Tetarenko et al., 2016a). During its discovery outburst in the globular cluster Terzan 5, the neutron star EXO 1745–248 traced a very steep ($\beta = 1.7 \pm 0.1$) correlation. For a given X-ray luminosity, it was also a factor of five less luminous in the radio band compared to 4U 1728–34 and Aql X–1 (Tetarenko et al., 2016a), suggesting different sources have different normalisations. However, incorrect distance estimates may contribute to the erroneous normalisation measurements (Jonker et al., 2004). Deller et al. (2015) found that tMSPs are more radio-loud than other neutron star systems without reaching the typical radio luminosities of black holes.They suggested the strong outflows of tMSPs may be ejected in the propeller regime.

Such varied behaviour across these three classes of neutron star LMXBs could be due to having different magnetic fields, spins, jet launching mechanisms and possibly other unknown factors. Compared to black holes, neutron stars do not have an event horizon or an ergosphere, and the strong magnetic fields can modify the structure of the accretion disc (Illarionov and Sunyaev, 1975). Due to the faintness of neutron stars in the radio band, studying these effects is complicated by the narrower range of radio luminosities observable by radio telescopes. For this reason, the studies detailed above generally sampled only one decade of luminosity in individual sources. This makes the true neutron star radio – X-ray correlation unclear.

1.4 Detecting compact objects

1.4.1 Non-accreting systems

The first white dwarf whose nature was identified was 40 Eridani B in 1910, which was recognized as an intrinsically faint, blue star, unlike typical stars known at the time. The first pulsar was discovered in 1967 (Hewish et al., 1968).

As white dwarfs are physically much larger than neutron stars and stellar-mass black holes, they are much easier to observe. While many white dwarfs are visible in the optical spectrum, the intrinsic optical emission from neutron stars and black holes is too faint to be detected. However, neutron stars that are active as pulsars may be observed in the radio band. In fact, most neutron stars have been detected as pulsars in radio timing searches.

The presence of some black holes has also been inferred spectroscopically in a couple of non-interacting binaries based on the motion they impart on a nearby companion star (Thompson et al., 2018; Giesers et al., 2018). Similar binaries are expected to be detected astrometrically by the *Gaia* mission (Perryman et al., 2001; Mashian and Loeb, 2017; Breivik et al., 2017).

Another method of detecting faint objects (including compact objects) is via gravitational lensing. Microlensing surveys have found a number of lenses with masses indicative of black holes. The MAssive Compact Halo Objects (MACHO) survey of the Galactic bulge found three black hole candidates (Poindexter et al., 2005). Similarly, during eight years of observations for the third phase of the Optical Gravitational Lensing Experiment, OGLE–III, three strong black hole candidates have been detected (Wyrzykowski et al., 2016).

Binary systems have long been predicted by general relativistic theory to be gravitational wave sources (Einstein, 1916). Due to technological challenges, the first gravitational wave event was recorded 100 years later by the *Laser Interferometer Gravitational-Wave Observatory* (*LIGO*) in the shape of a binary black hole merger (Abbott et al., 2016). Such events offer a glimpse into compact binaries which cannot be seen through the electromagnetic spectrum. While *LIGO* is designed to detect compact object mergers, which mostly occur outside the Galaxy, the future *Laser Interferometer Space Antenna* (*LISA*) mission will be able to detect close compact object binaries within the Galaxy (Amaro-Seoane et al., 2017).

1.4.2 Accreting systems

In 1962, the first X-ray source outside the solar system was discovered (Giacconi et al., 1962). This source, Scorpius X–1, is an LMXB, and was the first neutron star to be discovered. The first black hole to be discovered was the HMXB Cygnus X–1

(Bolton, 1972). These sources, as well as other neutron stars and the majority of black holes have been discovered not through their intrinsic emission, but as persistently bright, or transient X-ray binaries. Hence, the current sample is biased towards those sources which have bright (detectable by all-sky X-ray monitors, with peak luminosities exceeding $10^{36}\,\mathrm{erg\,s^{-1}}$) and frequent (every ∼50 years or less) outbursts. This bias is most evident when the number of known accreting neutron stars and black holes (∼ 300; Liu et al., 2007, 2006) is compared to the expected number of X-ray binaries (a few thousand), and the total number of neutron stars and black holes ($\sim 10^9$) in the Galaxy.

Other observing strategies aimed at discovering different populations of black holes have been developed. These include the *HAlpha-Width Kilo-degree Survey* (HAWKS), an optical photometric survey of the Galactic field (Casares, 2018); and the *Galactic Bulge Survey* (GBS), an X-ray survey of the Galactic centre (Jonker et al., 2011). A radio survey is another approach to finding black holes, as originally proposed by Maccarone (2005). As these surveys use different search strategies, they suffer from different biases, and are thus complementary to each other.

Isolated black holes can in principle be detected when they are accreting from the interstellar medium (Bondi–Hoyle accretion), although no such object has been detected to date. The faintness of such objects, and the requirement of a very dense environment, make their detection difficult. X-ray follow-up of gravitational lenses indicating strong black hole candidates found no evidence of accretion from the interstellar medium (Nucita et al., 2006; Revnivtsev and Sunyaev, 2002).

Determining the nature of an accreting object is often difficult. The universal way of determining the nature of a compact object is through the measurement of its dynamical mass. Because of faint donors, large distances and high reddening typical of X-ray binaries, dynamical masses can be very difficult to measure. However, other methods can be employed.

In outburst, accreting white dwarfs can be classified based on their optical spectra, but neutron stars and black holes can be harder to differentiate. The detection of a type I X-ray burst (themonuclear explosions of accreted material on the surface of a neutron star) or coherent X-ray pulsations (from a hot spot from the accretion stream impacting the surface of a spinning surface) categorically classifies an object as a neutron star. In the absence of detection of such features, classification relies on modelling the X-ray spectrum. High signal-to-noise spectra may indicate a neutron star if a neutron star surface or atmosphere model can explain the spectrum better than alternative models. In case of lower signal-to-noise spectra, we have already mentioned the X-ray photon index as a potential diagnostic tool (Wijnands et al., 2015). Another approach is through combined radio and X-ray observations, which can be used to track disc–jet coupling in outburst and towards quiescence. The radio faintness of neutron stars at a given X-ray luminosity compared to black holes implies that joint radio and X-ray observations can

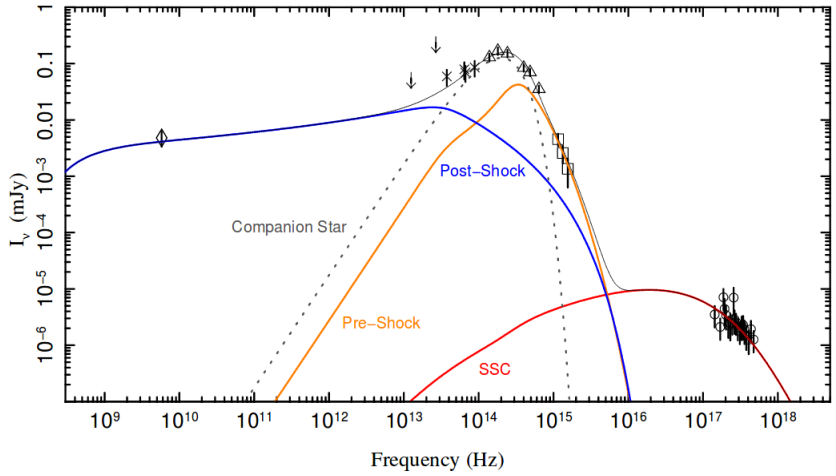

Figure 1.10: The broadband spectrum (radio to X-ray) of the black hole LMXB XTE J1118+480. The companion star is modelled as a black body, the jet (pre-shock and post-shock) emits synchrotron radiation, and the accretion flow is seen as self-synchrotron emission (SSC). Figure from (Plotkin et al., 2015).

be used to identify black hole candidates.

1.5 Radiative processes

The identification of X-ray binary candidates relies on recognising the radiative signatures of their components: the accretor, donor star, inflow and outflow. Each of these can emit through a variety of processes at different wavelengths, the most important of which are radiative transitions, blackbody radiation, inverse Compton scattering and synchrotron radiation (Figure 1.10). In this section, I outline these processes, based on the work of Rybicki and Lightman (1979).

Transitions of electrons between discrete energy levels can occur when they absorb or emit photons. This type of radiation is frequently observed in astrophysical optically-thin media, visible in spectra across the electromagnetic spectrum. Radiative transitions often occur as electrons switch between different electron shells of an atom. As the wavelengths at which they are emitted depend on the composition of the emitting medium, such transitions can be used to constrain element abundances in X-ray binaries. This is especially relevant when confirming ultracompact X-ray binaries, which do not contain hydrogen. Examples of optical spectra from different classes of objects are shown in Figure 1.11.

Blackbody radiation is thermal emission from optically-thick media in local thermodynamic equilibrium, and is homogeneous and isotropic. The brightness (B), which represents the energy emitted per unit time per unit surface per unit solid angle per unit frequency (or wavelength) of a blackbody is given by the Planck function. As a

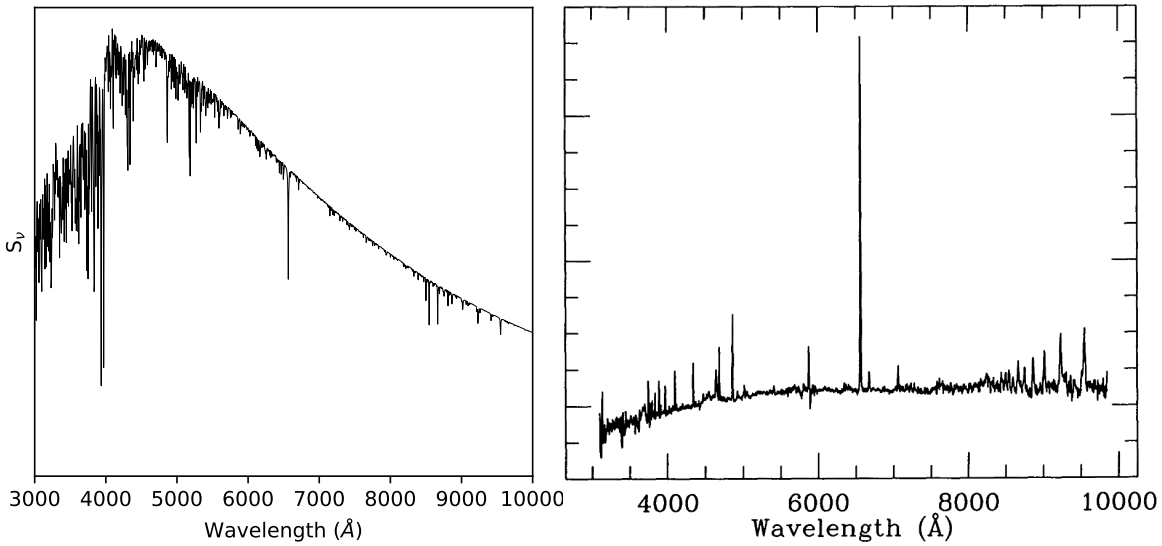

(a) Star (b) Sco X–1

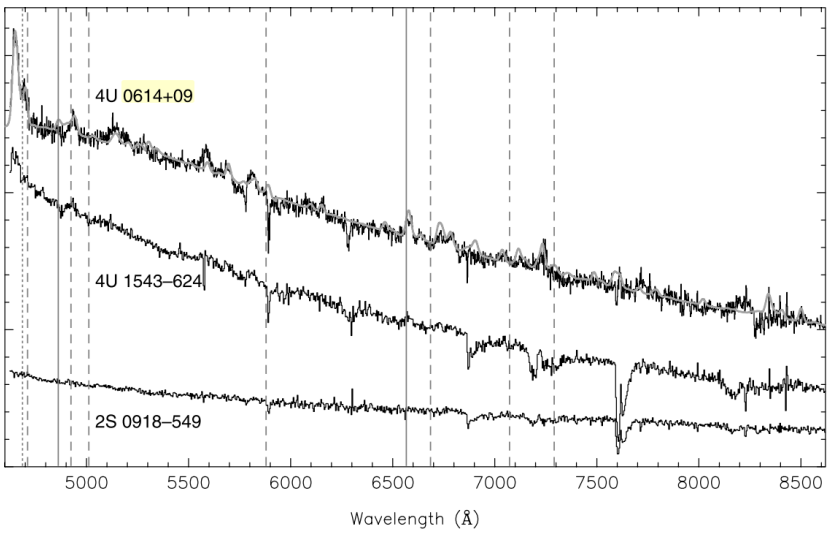

(c) Ultracompact X-ray binaries

Figure 1.11: Examples of optical spectra: (a) star, as absorption lines on a blackbody continuum (synthetic spectrum calculated using BT-Settl models; Allard et al., 2012), (b) the neutron star LMXB Sco X–1, dominated by emission lines from H and He atoms (Figure from Schachter et al., 1989), and (c) three ultracompact X-ray binaries (4U 0614+09, 4U 1543–624 and 2S 0918–549), lacking emission lines from H and He (expected at positions indicated by the vertical full and dashed lines; Figure from Nelemans et al., 2004a).

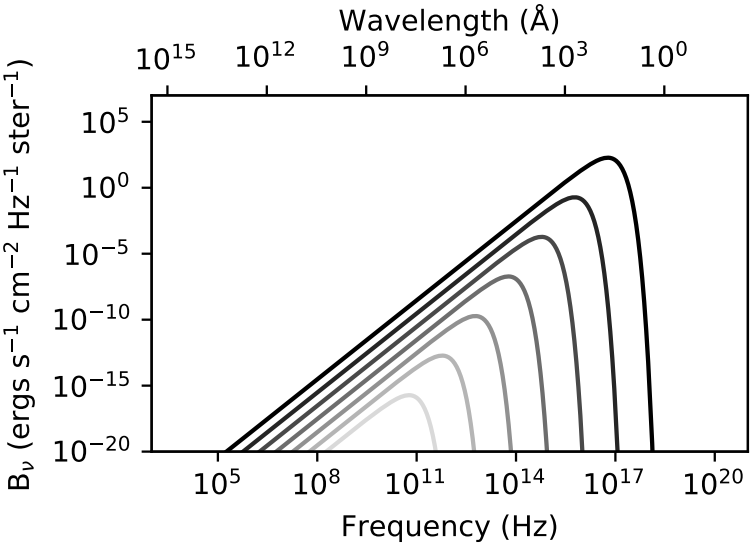

Figure 1.12: Blackbody spectrum for different temperatures, displayed with different shades of grey, for $T = 10^6 K$ (black), to $T = 1K$ (light gray), in steps of $\Delta \log_{10} T = 1$. Figure generated using the ASTROPY package.

function of frequency and temperature, B_ν is given by Equation 1.3:

$$B_\nu = \frac{2h\nu^3/c^2}{\exp(h\nu/kT) - 1}, \tag{1.3}$$

where h, c and k are the Plank constant, speed of light and Boltzmann constant respectively. Examples of black body spectra are shown in Figure 1.12. In the case of X-ray binaries, approximate black body radiation is emitted by the donor star (in the optical band) and the accretion disc (with a temperature gradient, from infrared to X-rays).

Charged particles in magnetic fields are accelerated on helical tracks, emitting electromagnetic radiation. Depending on the velocity of these particles, the direction and spectrum of the emission can change. In the case of relativistic particles, the radiation is known as synchrotron, and is emitted by these particles in a narrow cone with a half-opening angle the size of the pitch angle (α, the angle between the magnetic field and particle velocity), and angular width (θ) defined by the Lorentz factor of the particle ($\theta \approx \gamma^{-1}$, a function of the particle velocity).

All emission processes have a corresponding absorption process. In the case of synchrotron radiation, this corresponds to synchrotron self-absorption, and becomes apparent for populations of charged particles in a field. In this case, a synchrotron photon interacts with one of the charged particles in the magnetic field, transferring some of its energy to the particle. The emission spectrum for a population of electrons is set by the electron energy distribution.

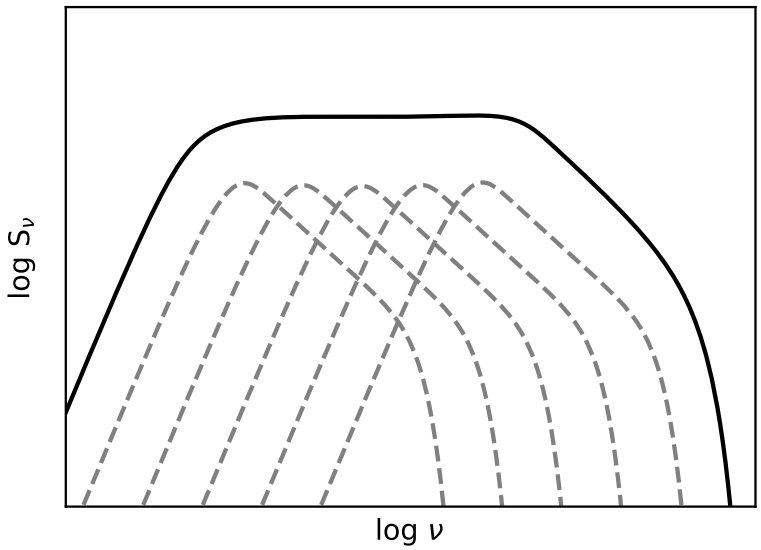

Figure 1.13: In astrophysical compact jets, the emission spectra of multiple populations of relativistic electrons with different energies add up to a flat spectrum across a range of frequencies. Figure generated using the NAIMA package (Zabalza, 2015).

Similar to low-luminosity AGN, the jets of X-ray binaries in the hard state show flat or inverted radio spectra (spectral index $\alpha \approx 0$, where $S_\nu \propto \nu^\alpha$, S_ν is the flux density measured at frequency ν) that extend up to infrared frequencies (Fender, 2001). The physical interpretation of this spectral component is that of synchrotron emission from a partially self-absorbed conical jet with individual self-absorbed spectra from different regions along the jet combining to give an overall flat spectrum.(Figure 1.13; Rybicki and Lightman, 1979).

Inverse-Compton scattering occurs when low-energy photons are up-scattered to higher energies by a population of relativistic electrons. In X-ray binaries, the hard X-rays originate from the comptonization of low-energy seed photons by the base of the jet or electron corona (Markoff et al., 2005), manifesting as a power-law component in the X-ray spectrum above 1 keV. The seed photons can be optical photons emitted by an accretion disc. Otherwise, a population of ultrarelativistic electrons in a magnetic field can up-scatter their own synchrotron radiation, in a process termed synchrotron self-Compton.

1.6 Globular clusters

Globular clusters are old, gravitationally-bound spherical systems of thousands to millions of stars, orbiting galactic centres. 47 Tucanae (NGC 104), is shown in Figure 1.15 as an example of such a cluster in the Milky Way. Globular cluster cores can reach densities of $\approx 10^6$ stars pc^{-3} (Harris, 1996). In comparison, the stellar density in the

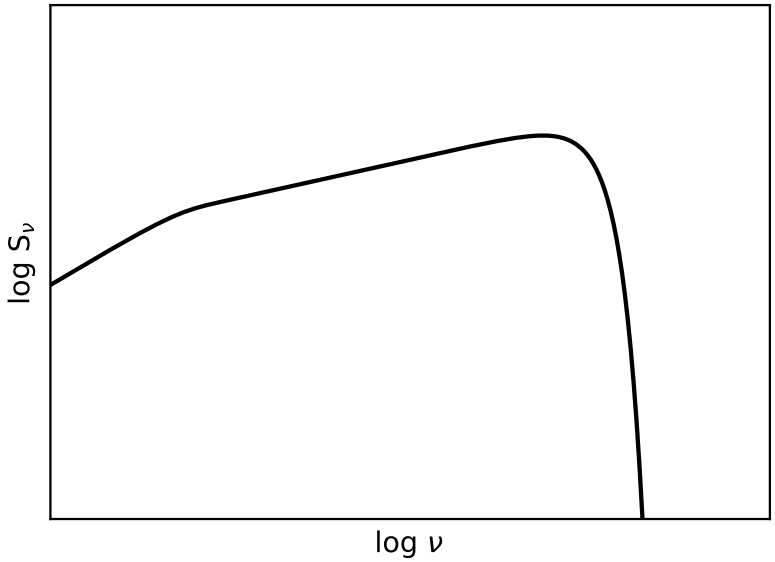

Figure 1.14: Inverse Compton spectrum, emitted by a power-law distribution of electrons within a finite energy range, seeded by a low-temperature blackbody. Figure generated using the NAIMA package (Zabalza, 2015).

Figure 1.15: 47 Tucanae (NGC 104). Image produced using HST data. Credit: J. Mack and G. Piotto

solar neighbourhood is just 0.15 stars pc^{-3} (Latyshev, 1978).

Within globular clusters, compact objects sink towards cluster centres owing to mass segregation, and exotic binaries preferentially form in the densest part of their cores (Hong et al., 2017; Rivera Sandoval et al., 2018). Pulsars are known to be more centrally concentrated than the surrounding stars (most are found within 5 core radii; McConnell and Ables, 2000; Moody and Sigurdsson, 2009; Camilo and Rasio, 2005), but some may also be found at large distances from the cluster centre (e.g., D'Amico et al., 2001).

1.6.1 X-ray binaries in globular clusters

Since the discovery of X-ray binaries, it was recognized that globular clusters are two orders of magnitude more efficient at producing X-ray binaries than the field (Katz, 1975; Clark, 1975). Over time, this effect was confirmed by the multitude of X-ray missions, for Galactic (Grindlay et al., 2001a) and extragalactic globular clusters (Sarazin et al., 2003). The high X-ray binary formation rate in globular clusters was explained theoretically as being caused by the high rate of dynamical interactions, rather than primordial binaries (Clark, 1975). Indeed, observational evidence of this effect confirms that the number of X-ray binaries in a globular cluster is proportional to its stellar encounter rate (Pooley et al., 2003; Maxwell et al., 2012; Bahramian et al., 2013).

Virtually all persistent or transient X-ray sources in globular clusters have so far been found to be neutron stars based on the detection of X-ray thermonuclear bursts or pulsations. Only two such sources may not be neutron stars: IGR J17361–4441 in NGC 6388 may have been a planetary tidal disruption event by a white dwarf (Del Santo et al., 2014), and 1E 1339.8+2837 in M 3 is a cataclysmic variable (Stacey et al., 2011).

In the field, about a third of all X-ray binaries have black holes (Liu et al., 2007). From the ≈18 confirmed neutron star transients or persistent sources detected in Galactic globular clusters (Bahramian et al., 2014) [2], one should also expect ≈6 black hole transients in globular clusters. To date, no such outbursts have been detected, raising the question whether the black hole populations residing in globular clusters are different than those in the Galactic field, or whether they exist at all.

Soon after its formation, thousands of stellar-mass black holes are expected to form in a typical globular cluster. Initially, theoretical studies suggested black holes sink to the cluster centres as they exchange energy with the lighter surrounding stars. The Spitzer mass instability (Spitzer, 1969), which causes the black hole subsystem to collapse at the centre of the cluster, was thought to lead to their efficient ejection via dynamical interactions, on $\lesssim 10^9$ year time scales. Up to four black holes within binaries were expected to remain in the cluster (Kulkarni et al., 1993; Sigurdsson and Hernquist, 1993). This scenario is illustrated in Figure 1.16.

This hypothesis was questioned with the discovery of variable ultraluminous X-ray sources (ULXs) associated with extragalactic globular clusters, which are likely associated with stellar-mass black holes (Maccarone et al., 2007; Shih et al., 2010; Brassington et al., 2010; Irwin et al., 2010; Maccarone et al., 2011). Their classification as black holes is based on their X-ray luminosities exceeding the Eddington luminosity for neutron stars, and their variability, which dismisses the possibility of a superposition

[2] https://bersavosh.github.io/research/gc_lmxbs.html

of multiple neutron star X-ray binaries. These sources are unlikely to be neutron star ULXs (e.g., Bachetti et al., 2014) as such objects are thought to require a young stellar population and pulsars with high magnetic fields, which cannot be found in globular clusters (Dage et al., 2018).

Five black hole candidates have also been discovered in quiescence in Galactic clusters through deep radio observations (Strader et al., 2012a; Chomiuk et al., 2013; Miller-Jones et al., 2015; Shishkovsky et al., 2018). Based on the number of quiescent LMXBs, Miller-Jones et al. (2015) suggest that ≈ 60 black hole X-ray binaries could be found in globular clusters. A rich collection of recent theoretical work now suggests a significant fraction of black holes may be retained to the present day (Sippel and Hurley, 2013; Morscher et al., 2015; Peuten et al., 2016; Rodriguez et al., 2016). In addition, the first dynamical stellar-mass black hole in a globular cluster was found in NGC 3201, although it is not transferring mass (Giesers et al., 2018), demonstrating that black holes can be retained in globular clusters.

These new developments indicate that a large number of black holes can be retained in globular clusters up to present times, which implies they are ejected much slower than previously thought. The discrepancy with previous studies comes from the assumption that all black holes rapidly undergo the Spitzer instability. Morscher et al. (2015) found the most massive black holes sink first, while the lighter ones mix with surrounding stars. Breen and Heggie (2013) found that large cluster cores can be sustained by the black hole subsystem, with core-collapsed clusters having ejected most of their black holes. Therefore, the largest numbers of black holes may be retained in massive clusters with large cores.

The lack of transient or persistent black holes in globular clusters then indicates their nature is different from black hole systems in the field, as a result of their dynamical formation. Kalogera et al. (2004) found that the duty cycle (fraction of time it spends in outburst) of a black hole X-ray binary depends on how it was formed. The duty cycles of X-ray binaries born from exchange interactions are expected to be very low ($\lesssim 10^{-3}$), in contrast to X-ray binaries formed from tidal captures, which are bright, persistent sources. The lack of such sources implies black hole LMXBs in globular clusters are more commonly created from exchange interactions. In the presence of neutron stars and black holes, exchange encounters and physical collisions lead to an efficient formation of ultracompact X-ray binaries (Ivanova et al., 2008, 2010). Even when these systems go into outburst, they still may be too faint to be detected by all-sky X-ray detectors (Knevitt et al., 2014).

Metallicity effects

By studying the population of X-ray binaries in the Galaxy and in the neighbouring M 31, Bellazzini et al. (1995) found that high-metallicity globular clusters are more

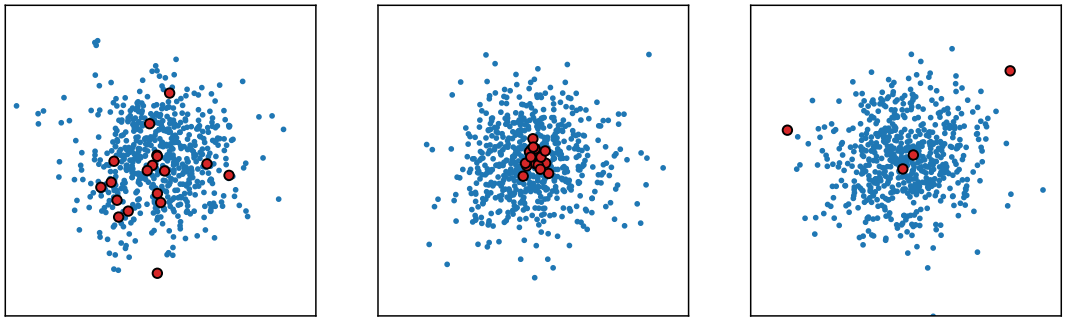

Figure 1.16: Illustration showing the evolution of the globular cluster (blue) population of black holes (red). Black holes form uniformly across a globular cluster (*left*), but sink towards its centre due to dynamical friction (*middle*). Frequent dynamical interactions in the core lead to black hole ejections, with few black holes remaining after a few billion years (*right*).

likely to contain X-ray binaries. However, the low number of globular clusters in the Galaxy (157, Harris, 1996) and M 31 (667, Galleti et al., 2004), and the correlation between metallicity and other parameters, such as galactocentric radius (Zinn, 1980) and size (Jordán et al., 2005), made causation between metallicity and X-ray binary presence uncertain.

Subsequently, from a population of X-ray binaries in a sample of galaxies including ellipticals, which contain higher numbers of globular clusters in comparison with spirals (e.g. M 87 contains an exceptionally high number of ≈13,000 globular clusters McLaughlin et al., 1994), found that increased metallicity does enhance the production of X-ray binaries, independent of other effects. High-metallicity globular clusters are three times more likely to contain an X-ray binary than low-metallicity globular clusters (e.g. Kundu et al., 2002; Smits et al., 2006; Kim et al., 2013).

The effect of metallicity on the formation of LMXBs does not yet have a satisfactory physical explanation, although a number of hypotheses have been proposed. Bellazzini et al. (1995) suggest two possibilities: a metallicity-dependant IMF, or a *natural* effect. The former refers to the flattening of the IMF in high-metallicity clusters. A large number of high-mass stars might self-enrich the cluster with metals (McClure et al., 1986), but will also produce more neutron stars and black holes (Grindlay, 1987). The *natural* effect requires that metal-rich stars be larger and more massive than metal-poor stars, for an increased likelihood of filling up their Roche-lobes in binary systems, and producing an X-ray binary. The observational evidence for these scenarios is poor, given that all globular clusters seem to have similar steep IMFs (Richer et al., 1991), and stellar evolution models indicate that metal-rich stars are generally less massive. Instead of a global natural effect, Ivanova et al. (2012) propose that red giant stars are the pathway through which metallicity leads to high LMXB numbers. As red giants produce LMXBs through exchange interactions and direct collisions, the higher

number and more massive red giants in metal-rich globular clusters will create more LMXBs. Alternatively, Ivanova (2006) proposed that the metallicity effect comes from the different structures of low and high metallicity stars. The absence of an outer convective layer in metal-poor stars leads to an absence of magnetic braking in binaries.

1.6.2 Radio sources

The radio sources which have historically been associated with globular clusters are pulsars (Lyne et al., 1987). Owing to their steep spectra, with $\alpha = -1.4 \pm 1.0$ (Bates et al., 2013), they have mainly been discovered at low frequencies ($\sim$1.4 GHz) in timing searches, but they are also visible in continuum images (Wijers and van Paradijs, 1991; McConnell and Ables, 2000; McConnell et al., 2001). Apart from pulsars, persistent neutron star X-ray binaries (Grindlay and Seaquist, 1986; Machin et al., 1990; Johnston et al., 1991; Johnston and Kulkarni, 1992) and planetary nebulae (Johnson, 1976) have been detected in the radio band since the early days of radio astronomy. With the development of more sensitive instruments, increasing numbers of X-ray binaries, in quiescence and outburst, are being detected in globular clusters in the radio band. In deep observations, other classes of radio sources may also become detectable: accreting white dwarfs (Körding et al., 2008) and black holes (stellar-mass, Fender et al., 2004c; and intermediate-mass, Maccarone, 2004), and magnetically-active stars (Morris and Mutel, 1988). Even though no radio source in a globular cluster has so far been confirmed as such an object, they could exist in large numbers. While the detectable pulsar population of globular clusters is relatively well established, much less is known about these other classes of radio sources.

While CVs are known to be radio emitters in outburst or persistent states (Mason and Gray, 2007; Körding et al., 2008, 2011; Coppejans et al., 2015, 2016; Barrett et al., 2017), they reach typical peak radio luminosities of $L_{\rm R} \approx 10^{26}\,{\rm erg\,s^{-1}}$, with a highest recorded luminosity of $L_{\rm R} \approx 10^{27}\,{\rm erg\,s^{-1}}$ in the case of AE Aqr (Abada-Simon et al., 1993). The white dwarf pulsar AR Sco reaches a similar luminosity (Marsh et al., 2016). Magnetically-active stars can also reach radio luminosities of up to $L_{\rm R} \approx 10^{28}\,{\rm erg\,s^{-1}}$ in quiescence, in the case of RS CVn stars (Benz and Guedel, 1994). These objects are a class of close binaries consisting of at least one cool giant or sub-giant star (Berdyugina, 2005) which may be common in globular clusters (Gendre et al., 2003). However, above $L_{\rm R} \approx 10^{28}\,{\rm erg\,s^{-1}}$, we expect the detectable radio sources within clusters to be dominated by pulsars and X-ray binaries.

1.6.3 Millisecond pulsars

149 pulsars have so far been discovered in Milky Way globular clusters using radio timing searches[3]. The two globular clusters richest in MSPs are Terzan 5 (with 38 known MSPs) and 47 Tuc (with 25 known MSPs). It is estimated that a few thousand (Heinke et al., 2005; Abdo et al., 2010; Turk and Lorimer, 2013) potentially detectable MSPs are present in the Galactic globular cluster system.

Millisecond pulsars with ultracompact X-ray binary progenitors are expected to reside in globular clusters as part of short-period pulsar – pulsar or white dwarf – pulsar binaries. Due to the high accelerations these pulsars might be subjected to, their pulses can be smeared over time, rendering them undetectable to radio pulsation searches. Such short-period systems can provide tests of general relativity. The existence of undiscovered MSPs in globular clusters is indicated by globular clusters with γ-ray emission typical of magnetospheric emission from MSPs (e.g. Abdo et al., 2010). Even if short-period systems are invisible to radio timing searches, continuum emission from these pulsars may still be detectable by imaging observations.

Black hole–pulsar binaries are important general relativity laboratories. Soon after the discovery of the first binary pulsar (Hulse and Taylor, 1975), it was recognized that pulsar–black hole binaries will be able to provide stringent tests of general relativity (Paczynski and Trimble, 1979). The validity of the Kerr metric for a spinning, uncharged black hole, can be tested by such systems (Wex and Kopeikin, 1999). Early predictions estimated $\approx 10^5$ black hole–pulsar binaries should exist in the Galaxy (Narayan et al., 1991). More recently, it was predicted that there likely exists only one or no pulsar–black hole binary across all Galactic globular clusters, and 10 at most (Clausen et al., 2014). No such binary has been found to date.

Similar to short-period binary MSPs, pulsar – black hole binaries could be too accelerated to be detectable by current timing searches, but identifiable in images. Future radio telescopes might be able to confirm such a binary from timing search and the measurement of their mass functions (Liu et al., 2014).

1.6.4 Intermediate-mass black holes

The existence of high-redshift ($z \gtrsim 6$) quasars of masses of a few $10^9 M_\odot$ (Fan et al., 2001) require the formation of "seed" black holes at early times, which grow to SMBH masses via accretion (Volonteri and Rees, 2005) or mergers (Volonteri et al., 2003). Currently, there is no universally-accepted model for the formation of black hole seeds. Proposed models include the direct collapse of low angular momentum gas in protogalaxies (Koushiappas et al., 2004), the direct collapse of massive Population III stars (Madau and Rees, 2001), or supermassive 10^6 $M_\odot$ stars (Begelman, 2010; Fiacconi and

[3] http://www.naic.edu/~pfreire/GCpsr.html

Rossi, 2017), runaway mergers of massive stars (Ebisuzaki et al., 2001) or stellar-mass black holes (Taniguchi et al., 2000) in dense star clusters.

As high-z globular clusters have been proposed as birthing places for the intermediate-mass black hole (IMBH) seeds that later became SMBHs, some present-day globular clusters might still contain massive seeds that never grew to supermassive sizes. Indeed, extrapolating the $M - \sigma$ relation (Ferrarese and Merritt, 2000) to globular clusters, one should expect to find IMBHs at the centres of globular clusters. As Ferrarese and Merritt (2000) caution, however, extrapolation might not be physically reasonable given different formation paths between IMBHs and SMBHs. Still, some dynamical measurements have suggested the existence of IMBHs in several Galactic (Noyola et al., 2008; Lützgendorf et al., 2011, e.g.) and extragalactic (Gebhardt et al., 2005)) globular clusters, although more recent work refutes these findings (with the exception of ω Centauri; Baumgardt, 2017). In addition, the existence of these dynamical IMBHs has never been confirmed by direct detections in radio or X-rays (e.g. Cseh et al., 2010; Lu and Kong, 2011; Strader et al., 2012b; Miller-Jones et al., 2012). The upper mass limits derived from the fundamental plane of accreting black holes are always lower than dynamical mass measurements. Deep radio observations may be the best method of detection the radiative signatures of Bondi accretion of intracluster gas onto IMBHs (Maccarone, 2004).

The inconsistency between the dynamical and fundamental plane mass estimates is currently unexplained. Possible interpretations include a change of the fundamental plane of accretion towards very low luminosity, a large number of dark remnants (neutron stars and stellar-mass black holes) in cluster cores, which mimic the effects of an IMBH, or currently unknown dynamical effects in globular clusters. Other sources of error could originate from limited observational capabilities. The sphere of influence of an IMBH in a globular cluster is an order of magnitude smaller than the cluster core (Baumgardt et al., 2005). This translates to regions of angular sizes of the order of a few arcseconds, where too few stars reside for an accurate dynamical mass measurement, and shot noise drowns out the signal from a potential IMBH.

A steepening of the fundamental plane at low luminosities is not supported by current observational evidence. The stellar-mass black holes A0620–00 and XTE J1118+480, and the SMBH Sgr A*, which have been detected in the radio and X-ray bands at very low Eddington ratios ($L_{\rm X}/L_{\rm Edd} \lesssim 10^{-8.5}$), all follow the fundamental plane of accretion (Merloni et al., 2003; Gallo et al., 2006, 2014).

Apart from dynamically-indicated IMBHs, other candidates have been proposed, based on a number of different arguments. The best IMBH candidate, HLX–1, is estimated to have a mass of $10^4 M_\odot$ (Farrell et al., 2009; Soria et al., 2017), and resides in an old, compact stellar population, possibly a globular cluster orbiting the galaxy ESO 243–49 (Soria et al., 2017). There was also a claim of an intermediate-mass black

hole interacting with a molecular cloud in the Central Molecular Zone of the Galaxy, originating from a globular cluster or accreted dwarf galaxy (Oka et al., 2016, 2017). This source was later shown to be consistent with the collision between two gas clouds, rather than an IMBH (Tanaka, 2018). With a different approach, the presence of IMBHs in globular clusters has also been suggested based on pulsar timing solutions (Perera et al., 2017; Kızıltan et al., 2017), and the discovery of a radio pulsar in the halo of a globular cluster (Colpi et al., 2003). The pulsar dynamics of these clusters, however, can be explained even in the absence of IMBHs (Perera et al., 2017; Freire et al., 2017; Mann et al., 2018).

Another argument for the presence of IMBHs is that some globular clusters, in particular ω Centauri (Bekki and Freeman, 2003) and M 54 (Da Costa and Armandroff, 1995), could be the remnants of tidally-stripped dwarf galaxies. As some dwarf galaxies have been found to host low-mass SMBHs (e.g., Reines et al., 2011), globular clusters with dwarf galaxy progenitors might also have massive black holes at their centres.

1.7 Motivation for this thesis

Most confirmed neutron star and black hole X-ray binaries have been discovered in the Galactic field when they went into outburst. Being biased towards those sources which have luminous and frequent outbursts, this sample does not offer a complete view of X-ray binaries. For a better understanding of accretion, jet launching mechanisms, the inflow–outflow connection, the co-evolution of binaries and their environment, as well as the origin of double-degenerate binaries as sources of gravitational waves, a wider sample of X-ray binaries needs to be selected. This can be achieved by drawing from populations with different formation and evolutionary histories, and using other selection criteria. As nurseries of dynamically-formed X-ray binaries, globular clusters can provide the required laboratories. These star systems have the additional benefit that they are easy to observe (small angular sizes), and their distances are reasonably well known. New X-ray binaries that are not necessarily X-ray-bright, such as black holes and tMSPs, are favourably detected in radio observations. Therefore, such observations can be used to place constraints on the number of stellar-mass and intermediate-mass black holes in globular clusters.

This thesis presents a deep radio survey of globular clusters we conducted to find new populations of compact objects. In Chapter 2, I describe the multi-wavelength (radio, optical and X-ray) observational and analysis techniques used in this work. In Chapter 3 I present the observational strategy of the cluster survey, and quantify the population of radio sources in globular clusters. Chapter 4 contains a study of neutron stars in the radio and X-ray band, used to help quantify the contribution of neutron star X-ray binaries to the globular cluster radio source population. Chapter 5 focuses on

the optical spectrum of 47 Tuc X9, one of the black hole candidates discovered in the survey. In Chapter 6, I discuss a few other interesting sources we have detected as part of the MAVERIC survey. I conclude with Chapter 7, where I provide an interpretation of the observed population of radio sources in globular clusters, and conclude with a view towards the future.

Chapter 2

Instrumentation and calibration

X-ray binaries emit radiation across the electromagnetic spectrum. As evidenced by their name, most of their radiative output is released in the X-ray band, but most of the angular momentum and kinetic energy may flow out of such systems through jets, observed in the radio band. In addition, the donor stars and accretion discs may be optical sources. Hence, the characterization of an X-ray binary through the knowledge of all of its components is best performed through multi-wavelength observations.

This thesis has made use of observations in the previously mentioned electromagnetic bands. In this chapter, I outline the principles behind such observations, based on the works of Pearson and Readhead (1984); Taylor et al. (1999); Thompson et al. (2017) (radio), Howell (2006) (optical) and Arnaud et al. (2011) (X-rays).

Given the large span of frequencies between radio waves ($< 10^{11}$ Hz, but typically 10^{10} Hz in this thesis) and X-ray photons (0.1–100 keV, or $\sim 10^{16} - 10^{19}$ Hz), a range of detectors and techniques need to be employed to perform multi-wavelength observations of an astrophysical source. For ground-based telescopes, the time of day, weather, atmospheric composition, presence of the ionosphere and interstellar gas, as well as the technological performance of a telescope and detector, all contribute towards the observability of an astrophysical object. The atmosphere is only transparent in certain bands across the electromagnetic spectrum: the radio, optical, and some narrow infrared regions (Figure 2.1). These atmospheric windows permit observations from the ground, but X-ray sources need to be observed from high altitudes, generally from satellites in orbit. While optical observations are restricted to clear night skies, radio observations can be carried out during the day, and during rain and overcast skies below $\sim$10 GHz.

Diffraction poses an absolute limit to the resolution of a telescope, independent of its design. Finer details can be resolved using shorter observing wavelengths and larger telescope apertures, such that:

$$\theta \approx \frac{\lambda}{D}, \tag{2.1}$$

where θ is the maximum angular separation between two observed sources at which

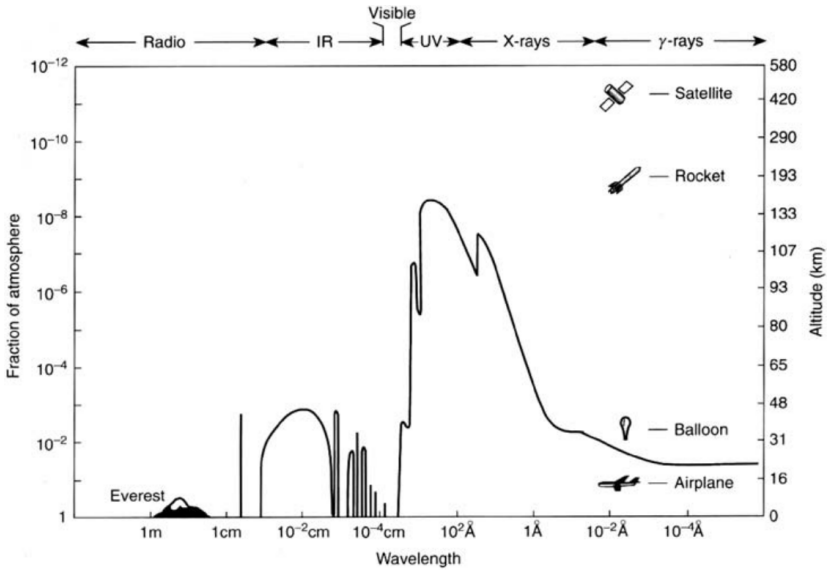

Figure 2.1: Atmospheric transmission of electromagnetic radiation. The full line shows the altitude and fraction of atmosphere by which half the incoming radiation from space has been attenuated. At ground level, the atmosphere offers observing windows in the radio, optical, and some narrow infrared bands. Most of the infrared band, UV radiation, X-rays and γ-rays cannot penetrate the full extent of the atmosphere. Their observation requires high-altitude or orbital detectors. Figure from Seward and Charles (2010).

they can be individually distinguished, λ is the observing wavelength, and D is the diameter of the aperture (similar in size to the reflecting component of the telescope). If the angular size of an astrophysical source is larger than the resolution θ of a telescope, its angular size can be measured directly from an image acquired by the telescope. Otherwise, only an upper limit can be placed on the angular size. From Equation 2.1, it can be seen that shorter wavelengths are more desirable if resolution is important. As we have seen, however, an astrophysical source needs to be studied at a variety of wavelengths for better insight into its nature. Therefore, instead of varying the observing wavelength, telescopes are designed to have larger apertures in order to achieve better resolution. The other important reason for building large telescopes is light gathering power. Larger apertures are able to gather more light in a given time interval than smaller apertures ($\propto D^2$), allowing fainter objects, or more objects to be observed within a set time window. The quest for building ever-larger telescopes across the electromagnetic spectrum is driven by the ambition to see more minute details in any astrophysical source in the shortest time possible.

2.1 Radio observations

From Equation 2.1, the resolution of a radio dish such as the Parkes radio telescope ($D = 64$ m) at a frequency of 1.4 GHz is on the order of $\theta \approx 10'$. Compared to optical

observations, where $\theta \approx 1''$, single-dish radio telescopes have almost three orders of magnitude poorer resolution. In those fields concerned with the multi-wavelength study of small ($< 1''$) sources in crowded fields such as X-ray binaries in globular clusters, this discrepancy in resolution is problematic. While the construction of larger radio dishes is desirable, it is impractical. A solution to this is aperture synthesis. This is an interferometric technique that combines the signal from multiple antennas, producing images that have the same angular resolution as an antenna the size of the whole ensemble, and a field of view set by the size of each antenna. In the simplest case, an interferometer is made up of two receivers separated by a baseline distance b (Figure 2.2). An ensemble of multiple receivers, which combines the signals from N receivers in a pair-wise fashion across $N(N-1)/2$ baselines forms a synthesis array. Different timing delays are electronically introduced at each receiver to compensate for the geometric delay caused by observing sources away from zenith. Through interferometry, arcsecond and sub-arcsecond scales open up to radio observations. The longest baseline of a synthesis array defines the smallest discernible features of a source on the sky, while the shortest baseline sets the largest observable features on the sky. Both scales are described by Equation 2.1, where D is set to the baseline length. With the ATCA, which was the main instrument used in this thesis, resolutions of $\sim 1''$ are achievable in the most sensitive band (5.5–9 GHz) and most extended configuration (6 km). With Very Long Baseline Interferometry (VLBI) observations, which uses few-thousand-kilometre baselines, milliarcsecond resolution can be reached.

The measured interferometer signal is recorded as phase and amplitude information for each baseline at discrete time and frequency intervals, known as the visibility. The visibility is a 2D Fourier transform of the sky brightness, as projected on a plane perpendicular to the source direction, known as the uv plane. The u and v coordinates point East–West and North–South respectively, with uv distances measured in number of wavelengths. During an instantaneous observation, the uv plane is sampled at a number of discrete points equal to twice the number of baselines. Image fidelity increases with sampling of the uv plane, such that more antennas separated by a wide range of baselines are able to better recover the sky brightness. In addition to the number of baselines, the rotation of the Earth can also be employed to fill up the uv plane. As the Earth rotates during an observation of a single source, the baseline projections on the uv plane change length and angle, sampling elliptical tracks on this plane. This technique is known as Earth-rotation synthesis, and it makes the addition of many antennas less critical as far as image fidelity is concerned. Large fractional bandwidths also fill in the uv plane since (u, v) are measured in number of wavelengths. Linear East-West arrays like ATCA (6 antennas) can then recover the sky brightness well as long as the integration times are close to 12 h. Non-linear arrays do not need such long integration times for this purpose, but they require more antennas. The

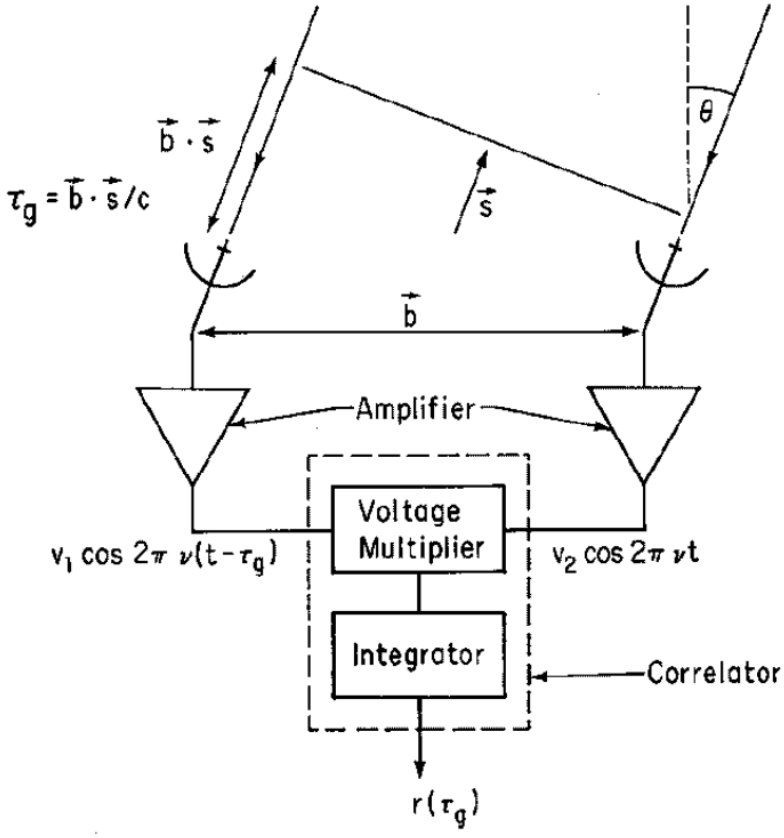

Figure 2.2: Schematic of a two-element interferometer. The two elements are separated by the baseline length b and observe a source at the zenith angle θ. An astrophysical signal arrives at the two receivers with a geometric time delay $\tau_g = b \sin\theta/c$. After the weak astrophysical signals are amplified, they are correlated. Figure from Taylor et al. (1999).

Y-shaped VLA (27 antennas) can then provide high fidelity in snapshot images after deconvolution.

2.1.1 Calibration

Radio-frequency interference (RFI) produced by man-made signals or lightning can corrupt observations. Data corrupted by RFI must be removed before calibration. Having removed the deleterious effects of RFI, we can aim to recover the true sky brightness from observations. This requires correcting for the response of the interferometer and atmospheric effects. For continuum observations, bandpass, flux, phase and amplitude (complex gains) calibration are required. Bandpass calibration consists of correcting the response of the receiver across the observing frequency band. It is performed by observing a bright calibrator source with a well known spectrum and no emission or absorption lines. The flux density of such a source varies little across frequency channels, so any variations in the observed spectrum are likely to be caused by the response of the receiver. Flux calibration is performed by observing a bright source for which the flux density at the observing frequencies are known. The same primary calibrator is often used for bandpass and flux calibration, and observing it once per observing run is sufficient as the bandpass response only varies slowly over time. Phase and amplitude distortions are introduced in the system by the ionosphere and troposphere, and by the electronics of the instrument. These distortions can usually be treated as antenna-based, and can be calibrated. This can be achieved by observing a secondary calibrator. Such a calibrator needs to be sufficiently bright $\gtrsim 1$ Jy, have a well-known position (position uncertainty much smaller than the resolution element), be located within a few degrees of the main target field, and be observed every $\sim$10 min (more often at higher observational frequencies), interspersed with observations of the target field. The phase and amplitude solutions for the target field are derived by interpolation. These conditions listed above are required as phase and amplitude distortions can vary on short time scales, and change across the sky.

For these reasons, the measurement of complex gains based on the secondary calibrator are approximate only. However, a model of the field can be made to solve for the complex gains in the exact direction and at the exact times of the target observations. This is achieved during self-calibration, by exploiting the redundancy of information within a large number of visibility measurements. For arrays with many elements ($N > 4$), there are more baseline-based visibility measurements than antenna-based gains to solve for, and hence the problem is over-constrained, and can be successfully solved. Self-calibration can be used to reduce the calibration errors introduced in previous steps, as it sidesteps the errors associated with transferring solutions from the position and observation times of the secondary calibrator. Special care needs to

be taken during self-calibration, so as not to introduce further errors. Otherwise, the derived gains can be wrong, leading to poor image fidelity, astrometry and flux density scales. If the target field has a high signal-to-noise ratio, self-calibration can, in general, be carried out. As such, the time scales for complex gain changes need to be much longer than the time taken for the noise level to reach the flux density of the field for each antenna. In addition, the emission structure of the field must not be too complex. An incorrect field model can lead to incorrect inferences about source flux densities and positions. Not including all the emission in the sky model can lead to a mismatched flux density scale. Likewise, including spurious structures (caused by calibration errors or noise spikes) to the sky model can lead to similar issues. Self-calibration imposes the assumed astrometry of the model on the data. In the realistic case where the sky model is not perfect, this makes the positions indeterminate. As such, absolute position shifts of up to a fraction of the beam can be induced throughout the field. Relative positions, however, are still valid. In addition, performing self-calibration on sources located away from the phase tracking centre can lead to further astrometric errors stemming from observations through different parts of the atmosphere.

Self-calibration is performed after the standard calibration procedure and initial sky model are obtained. Phase and amplitude corrections are made to minimize the difference between the observed and model visibilities. An updated model is recreated from the newly calibrated visibilities. These steps are run iteratively to improve the visibility models.

2.1.2 Imaging

An image of the observed field is made by inverse Fourier transforming the calibrated data. This initial image is referred to as the *dirty image*. The term comes from the incomplete coverage of the *uv* plane characteristic of interferometric observations (even in Earth-rotation synthesis), which degrades the image. The dirty image is the true sky brightness convolved with the point spread function (PSF) of the observation, known as the *dirty* or *synthesised* beam. The dirty beam is the Fourier transform of the sampling function. For each position in the *uv* plane, the sampling function has a value of 1 where data has been measured, and 0 otherwise. The incomplete coverage of the *uv* plane gives the dirty beam strong sidelobes that degrade the dirty image.

To correct for the incomplete sampling of the *uv* plane, the dirty image can be deconvolved with the dirty beam pattern. The most commonly used deconvolution algorithm is CLEAN. CLEAN works by finding the brightest pixel in a dirty image. At its position, the dirty beam, scaled to the peak flux density, and multiplied by a small factor (the loop gain, $\lesssim$10%), is subtracted from the image. A delta function with the amplitude and position of the removed (clean) component is added to a model image.

This procedure is repeated until no more islands of emission remain in this residual image. The final model image is convolved with the restoring beam, which is set to a Gaussian the size and shape of the main lobe of the dirty beam, and added to the residual image, resulting in a cleaned image. This cleaned image can then be used for self-calibration if the field contains bright sources. Otherwise, it is ready to be used for science.

2.2 Optical–ultraviolet observations

Modern optical observatories use mirrors to focus the light of an astrophysical source onto a charge-coupled device (CCD) detector. These devices convert incoming photons to electrons via the photoelectric effect. The number of electrons produced (analog signal) in each pixel of the CCD is converted to a digital number (referred to as counts or analog-to-digital units) on a 16-bit scale, and recorded on file. The gain of the CCD is the number of electrons required to produce one count, and is an integer typically with value < 10.

As they are silicon-based, CCDs most easily absorb light between 3000 and 11000 Å. Different phosphorus-based coatings, which re-emit UV photons to longer wavelength photons, can be applied to CCDs to increase response below 3000 Å. The ability of a detector to convert incoming photons to electrons is termed quantum efficiency. An ideal CCD with quantum efficiency of 100% would detect all incoming photons, but CCDs typically reach quantum efficiencies of 80%. Combined with the reflectivity of telescope mirrors, transparency of filters and contaminants on the detector, the quantum efficiency contributes to the throughput of the telescope. System throughputs for different detectors and filters for the *Hubble Space Telescope* (*HST*) are shown in Figure 2.3.

CCD imaging is prone to a variety of imperfections, such as pixels with different sensitivities, dead and hot pixels, and cosmic rays. These effects are compounded with other imperfections along the optical path of the telescope, such as dust on the detector, and its non-uniform illumination. These problems can be mitigated by using bias, dark and flat frames. A bias frame is a zero-exposure image, and a dark frame is a long exposure taken with a closed shutter. These two types of frames are used to characterise the read-out and thermal currents for each pixel of the CCD. Hot pixels can then be identified in dark frames. Flat frames are images of uniformly-illuminated fields (such as the sky at dawn). They are used to find cold and dead pixels, correct for pixel-to-pixel variations in sensitivity, dust on the CCD, and for the non-uniform illumination of the CCD. Cosmic rays can be removed by stacking multiple images and rejecting outlier pixels. The defects of cold and hot pixels can also be removed using a similar procedure, with the addition of dithering between consecutive exposures.

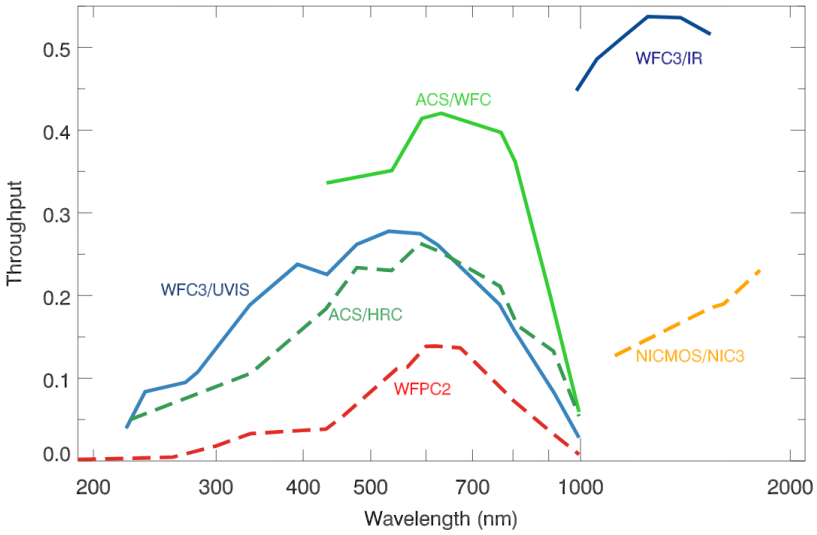

Figure 2.3: System throughputs as a function of wavelength for different detectors mounted on HST. Typical peak throughputs are <60%. Figure from Ryon (2018).

Dithering is the slight change in the pointing of a telescope when observing the same field, so that the same area of the sky is observed by different pixels.

2.2.1 Photometry

Photometry is the measurement of the flux emitted by an astrophysical source at specific wavelengths. Photometric studies can be based on images acquired on a CCD detector. A simple method to measure source fluxes is aperture photometry. This technique consists of an aperture centred on a star, which contains the combined signal from the source and underlying background, and an annulus surrounding it, used to estimate the level of the background. An illustration of this technique is shown in Figure 2.4. The collected intensity within the aperture (I) is measured by summing up all the counts from all the N pixels within the aperture. The background level per pixel (B) is estimated by taking the median pixel value within the annulus. The median is used because it is less sensitive to outliers such as cosmic rays, bad pixels and close-by astronomical objects. The background flux within the source aperture is then estimated by multiplying the number of pixels within the aperture with the median background pixel value. The source intensity contained within the aperture is the difference between the total intensity and the background intensity. The total source flux (intensity normalized to the exposure time, t) is not all contained within the boundary of the aperture, as the stellar PSF can extend beyond it. The aperture correction factor (k, which depends on the sizes of the aperture and the PSF), is used to convert the measured flux to the total flux. These steps are summarized in Equation 2.2.

$$F_\star = \frac{I - N \times B}{t \times k} \tag{2.2}$$

A physical interpretation of $F_\star$ can only be achieved via absolute flux calibration. This step is achieved by knowing the sensitivity of the observing setup, or how the observed count rate on a CCD translates to the true flux density of the observed source at a given wavelength. Placing $F_\star$ on an absolute magnitude scale is done using a zero-point (ZP), which is a function of the sensitivity, as described by Equation 2.3. The zero-point is unique for each combination of telescope, filter and photometric system. It is measured using a suite of bright stars with known flux densities, known as photometric standards, and used as calibrators.

$$m = ZP - 2.5 \log_{10} F_\star, \tag{2.3}$$

The magnitude m in Equation 2.3 is referred to as apparent magnitude, as it represents the magnitude of a source as observed from Earth. The atmosphere and interstellar medium attenuate emission originating from Galactic distances, making objects appear dimmer than they would otherwise. This effect is stronger at shorter wavelengths, which makes astrophysical objects seem "redder" than they actually are. Removing the effects of interstellar extinction on the apparent magnitude is done using Equation 2.4:

$$m' = m - A_\lambda, \tag{2.4}$$

where A_λ is the absorption in magnitudes at the observing wavelength (λ), and m' is the dereddened apparent magnitude. In the V-band, the absorption (A_V) is given by Equation 2.5:

$$A_\mathrm{V} = R_\mathrm{V} \times E(B-V). \tag{2.5}$$

In the Milky Way, $R_\mathrm{V} = 3.1$ on average, but changes with the line of sight, such that the standard deviation of R_V measurements is $\sigma R_\mathrm{V} = 0.18$; (Schlafly et al., 2016). $E(B-V)$ is the colour excess, which depends on the column density of gas towards the observed source, and not on its properties.

2.2.2 Spectroscopy

Spectroscopy is the measurement of flux densities as a function of wavelength. Whereas photometry uses broadband (∼500 nm-wide) and narrow-band filters (∼30 nm-wide), spectroscopy can achieve much finer spectral resolution ($\lesssim$ 1 nm) across hundreds of nm simultaneously. To achieve this high resolution, the incoming light through a telescope is focused on a narrow aperture (commonly a slit), and then dispersed through a diffraction grating before being refocused on the CCD. Examples of raw and calibrated optical spectra are displayed in Figure 2.5.

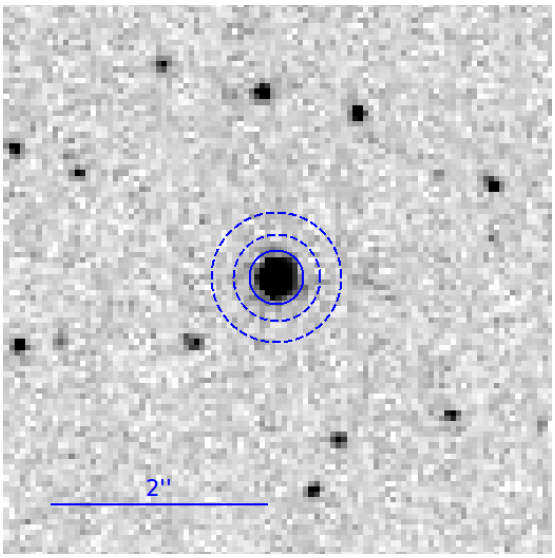

Figure 2.4: An example of a star field. The inner aperture ($r = 0.25''$) encloses 91% of the star's flux. The outer dashed annulus is used to estimate the value of the sky within the star aperture. The colours are inverted, so that darker colour represent higher fluxes. The image was acquired with the ACS/WFC detector on the *HST*, using the F435W filter, and is a section of an observation of the globular cluster NGC 6388 (P.I. Pritzl).

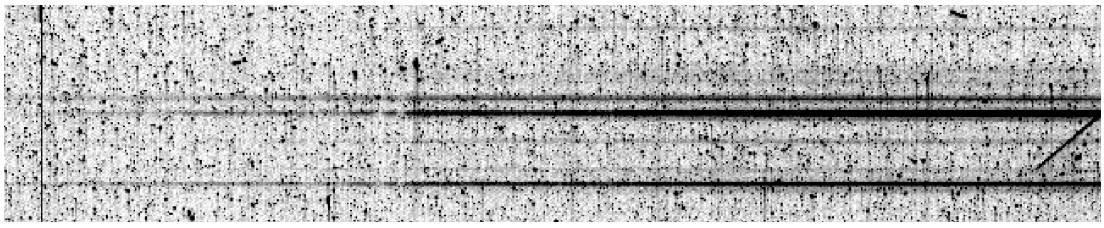

(a) Raw spectrum

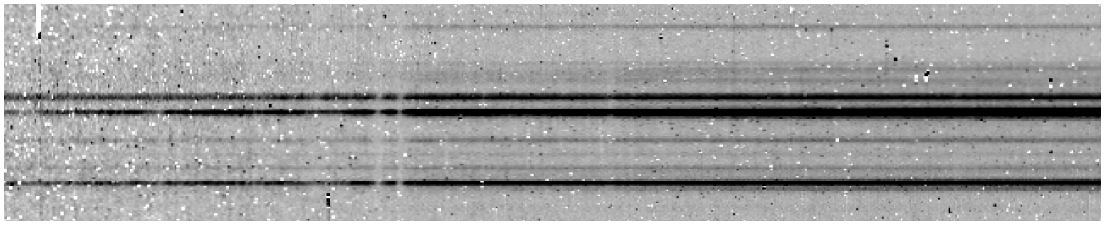

(b) Calibrated spectrum

Figure 2.5: Example of a 2D optical long-slit spectrum, (a) pre-calibration and (b) post-calibration) in inverted colours. These spectra cover 3300 Å (left side) to 5100 Å (right side), and $6''$ along the slit (in the y direction). The spectra of multiple stars can be identified as dark horizontal lines. The two vertical features seen left of the centre are the Ca II H&K absorption lines. The raw spectrum is covered by imperfections such as hot pixels (saturated pixels unassociated with the stars), bleeding pixels (vertical streaks originating from saturated pixels) and cosmic rays (streak on the right side). The loss of stellar flux at shorter wavelengths is mainly caused by the varying throughput across the spectrum. These issues have been mitigated by combining multiple exposures, and correcting for the loss of sensitivity at bluer wavelengths in the calibrated spectrum. This spectrum is a section of a spectrum acquired with the STIS spectrograph on the *HST* (P.I. Miller-Jones), which I will discuss in Chapter 5.

2.3 X-ray observations

Due to the short wavelength of X-ray radiation, it typically penetrates, or is attenuated by any material it is incident on. Under small grazing angles ($< 1°$), however, 0.1–10 keV X-rays can be reflected by metals with high atomic numbers such as gold. The optical design of an X-ray telescope therefore has to be different to that of an optical telescope. To maximize their effective areas, X-ray telescopes therefore use many sets of (almost) cylindrical mirrors of different radii, nested within each other. Similar to optical telescopes, the detectors of choice are CCDs. As X-rays are much more energetic than optical waves, they release many more electrons from the silicon detector as a result of the photoelectric effect. Where an optical photon generates $\sim$1 electron, one X-ray photon can release hundreds to thousands of electrons, depending on its energy. This property, coupled with the low count rates of X-ray sources, allow the position, energy, and time of arrival to be recorded for individual photons. This information is stored in event files.

The calibration of X-ray data includes the removal of non-X-ray backgrounds (caused by cosmic rays) and background flares (caused by solar flares). Pile-up is caused by the arrival on the detector of at least two X-ray photons within the same time frame. Such an event is caused by observing bright sources, and is recorded as a single photon of higher energy. As X-ray detectors are usually CCDs, they have similar issues as optical astronomy: hot and dead pixels. The calibration of event files is typically run through pipelines, and the observer does not need to do this work themselves.

In contrast to radio and optical observations, the calibration of X-ray data does not include the removal of the instrumental response. Instead, instrumental effects, and the conversion of events to physical units are accounted for during analysis using calibration files. These files include the response matrix file (RMF) and the ancillary response file (ARF). The RMF describes the probability of an incident photon with a given energy to be recorded as an event in a particular energy bin in the spectrum. It includes the quantum efficiency of the detector, and the attenuation caused by any filters. The ARF represents the energy-dependent effective area of the telescope.

2.4 Astrometry

The recorded positions of astrophysical objects on the sky may be subject to systematic errors causing them to deviate from the absolute frame of reference of the International Celestial Reference Frame (ICRF; Ma et al., 2009). Such systematic offsets are a concern especially for studies using multiple images separated by time, acquired by different instruments, or observed in different bands. As such, the measured position of an X-ray source may be significantly offset from the measured position of its radio

counterpart. This may arise even if the physical emission regions are the same, purely due to imperfect calibration at either band.

The identification of multi-wavelength counterparts to astrophysical sources requires such systematic offsets to be corrected. In other words, the different images need to be aligned to the same frame of reference. Astrometric alignment between different frames is performed using sources with known counterparts in all the images. All-sky catalogues that are locked to the ICRF (e.g., 2MASS, Skrutskie et al., 2006; Gaia, Gaia Collaboration et al., 2016) can be very useful in this regard. If only a few such sources can be identified, a simple translation of the coordinate system of one image is best. Otherwise, field rotations and distortions can also be corrected for.

The frame of reference of a radio image is most commonly used as the basis for astrometric alignment, as it is the wavelength of choice for the ICRF. For a radio image, the astrometry is set during phase referencing, relative to the position of the secondary calibrator. The direction and magnitude of the shift in position between calibrator and target are determined by comparing their phase delays. Secondary calibrators are chosen to have negligible position uncertainties, which are continuously refined through regular VLBI observations carried out under astrometric and geodetic programs. Rather than uncertainties on the position of secondary calibrators, target position errors are caused by atmospheric phase instabilities. The magnitude of such errors are therefore proportional to calibrator throw, i.e. the relative separation between target and calibrator sources (Pradel et al., 2006). In the case of ATCA, the errors on the absolute astrometry are expected to be at the level of $< 0.4''$ (Caswell, 2009; Smolčić et al., 2016). This value is smaller than a synthesised beam at 5.5 GHz at 6 km configuration.

2.5 Timing

Astrophysical sources, and especially accreting sources, are often variable across the electromagnetic spectrum. Orbital motions, spins and other periodicities are often measured in timing studies. Variability can be used to cross-identify optical–X-ray counterparts in crowded fields like globular clusters. In addition, the way variability at different bands correlates is indicative of the radiative processes that are active in a system.

To perform timing studies, it is critical to use a reference system that is independent of the location and motion of the observer relative to the observed source. The Barycentric celestial reference system was created for this purpose. It takes the centre of mass (barycentre) of the solar system as its origin. Converting instrumental time to barycentric time requires correcting for Earth's orbital and spin motion, and accounting for general relativistic effects caused by proximity to Earth. Space observatories would

also need to have their own orbital motion corrected for.

2.6 Summary

For a full-picture view of an X-ray binary, all of its components (accretor, donor, accretion disc and jet) need to be studied. As rapidly evolving systems in which a variety of radiative processes are at play, emitting across the electromagnetic spectrum, X-ray binaries are best studied through time-resolved multi-wavelength observations. The jet is best observed through radio interferometric observations, while the donor star and accretion disc are seen in the optical–UV bands, with the highly energetic inner flows visible to X-ray telescopes. As these multi-wavelength data come from different observatories (ground or space-based), they need to be aligned to the same spatial and temporal frames of reference for an accurate description of their physics.

Chapter 3

Radio survey of globular clusters

Adapted from:

Vlad Tudor et al.; *to be submitted*

The content of this chapter is my own work, excepting the following. Some observations with ATCA were carried out by J. C. A. Miller-Jones, T. D. Russell and A. K. Tzioumis. Discussions were contributed to by members of the MAVERIC team – L. Chomiuk, C. O. Heinke, T. J. Maccarone, J. C. A. Miller-Jones, L. Shishkovsky, G. R. Sivakoff, and J. Strader, as well as by my supervisory panel – J. C. A. Miller-Jones, R. M. Plotkin, G. E. Anderson, and R. Soria.

In this chapter, I describe a radio continuum survey of globular clusters to assess the occurrence rate of radio sources within these systems. This survey was conducted as part of the MAVERIC project, and included 26 nearby, massive globular clusters in the Southern hemisphere ($\delta \lesssim -25°$), observed with ATCA at 5.5 and 9.0 GHz, reaching a median central rms $\approx 4\,\mu$Jy. We describe the observations in Section 3.1. Based on the source counts, we estimate the number of radio sources within the globular clusters of our sample, which is expected to be dominated by compact objects (accreting and non-accreting), and some planetary nebulae. We present our results in Section 3.3 and discuss them in Section 3.4.

3.1 Observations

3.1.1 Sample selection

We retrieved most cluster properties (distances and radii) from the 2010 version of the Harris catalogue of Milky Way globular clusters (Harris, 1996). For Liller 1, we adopted the values of Saracino et al. (2016). For Terzan 1, we re-calculated the position, core and half-light radii, and for NGC 6522 just the position, based on 2MASS data. We use the cluster masses reported by Baumgardt and Hilker (2018). One cluster (NGC 6652) in our sample was not covered by this study, in which case we used a mass-to-light ratio $\Upsilon = 2\,M_\odot L_\odot^{-1}$ to estimate the cluster mass based on its absolute visual magnitude (M_V) (McLaughlin and van der Marel, 2005). From the Southern globular clusters ($\delta < -25°$), we selected nearby ($D \lesssim 9$ kpc, for sensitivity), massive clusters ($M \gtrsim 10^5\,M_\odot$, which may host larger numbers of black holes), to maximise the chances of detection of radio sources within clusters. We also included a few other more distant, massive globular clusters which may contain intermediate-mass black holes, and others with high interaction rates or bright quiescent X-ray sources. Among the surveyed sample is NGC 6624, which contains the most luminous steady X-ray source in any Galactic globular cluster (Bahramian et al., 2014). In Figure 3.1 we show the masses and distances to our globular cluster sample, relative to the Galactic clusters in the Harris (1996) catalog. In Figure 3.2, we show the target distribution in Galactic coordinates – most of our sample is contained within 10° from the Galactic centre.

In Table 3.1, we list some basic properties for our sample which may correlate with the number of radio sources they contain. The stellar encounter rates (Γ) have been estimated by Bahramian et al. (2013) using the integrated surface brightness profile and velocity dispersion for most clusters, normalized to the encounter rate of 47 Tuc, requiring $\Gamma_{47\mathrm{Tuc}} = 1000$. They also provided simpler estimates for Γ, needed for those clusters for which the main method could not be employed. For our sample, we used these simple estimates for NGC 4833 (Γ based on the core radius, central surface

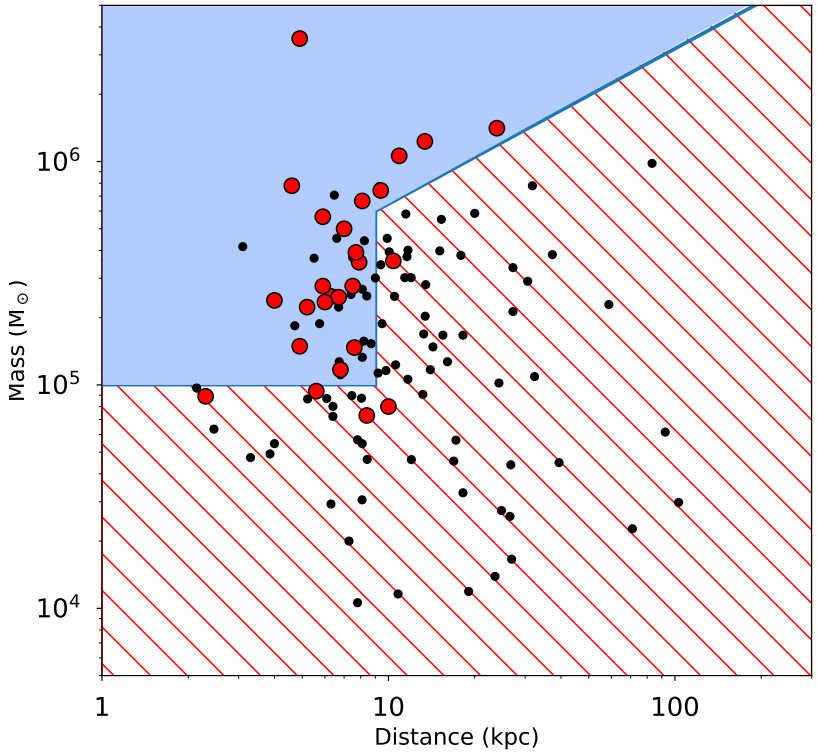

Figure 3.1: Globular cluster sample, selected based on mass ($M \gtrsim 10^5\,M_\odot$) and distance ($D \lesssim 9$ kpc). We also include a few more distant clusters with masses $M \gtrsim 10^6\,M_\odot$, which may contain intermediate-mass black holes. These selection criteria are displayed as a blue region (included sample) and red-hashed region (excluded sample). We also observed a few lower-mass clusters ($M \lesssim 10^5\,M_\odot$) with bright X-ray sources. All globular clusters from the Harris (1996) catalogue are shown in small black circles, and the 26 surveyed clusters are shown in large red circles.

brightness and velocity dispersion), and Liller 1 and Djorg 2 (Γ based on the core radius and central surface brightness). The γ-ray fluxes (including detections and non-detections) are those reported by Hooper and Linden (2016) using Fermi Gamma-Ray Space Telescope (Atwood et al., 2009) data. The number of pulsars within each cluster is taken from the ATNF pulsar catalogue[1].

3.1.2 Setup

The radio observations with the ATCA were carried out when the array was in any extended configuration (6 km maximum baseline) under project code C2877 from 2013 until 2015. We observed simultaneously in two bands, centred at 5.5 and 9.0 GHz, each with a 2 GHz bandwidth subdivided in 2048 × 1-MHz channels. We observed the source PKS 1934–638 as a primary and bandpass calibrator for an integration time of ≈10 minutes each observing run. Secondary calibrators were observed for 1.5 or 2 minute intervals each cycle depending on their flux density, and alternated with target

[1] `http://www.atnf.csiro.au/people/pulsar/psrcat/`

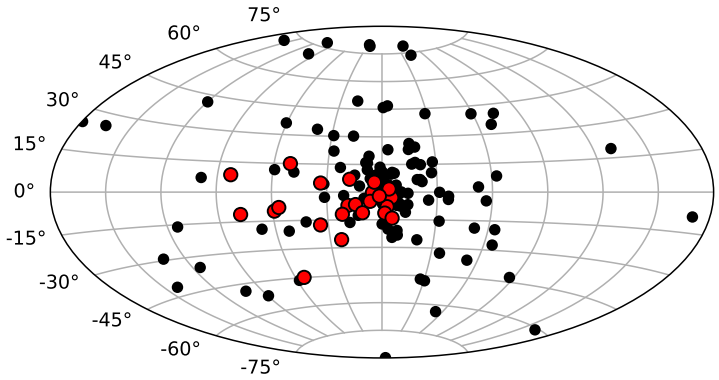

Figure 3.2: Galactic coordinate map in the Mollweide projection showing the distribution of clusters across the celestial sphere. The symbols are the same as in Figure 3.1. The southern clusters are mostly visible in the Western Galactic hemisphere, and are concentrated towards the Galactic centre.

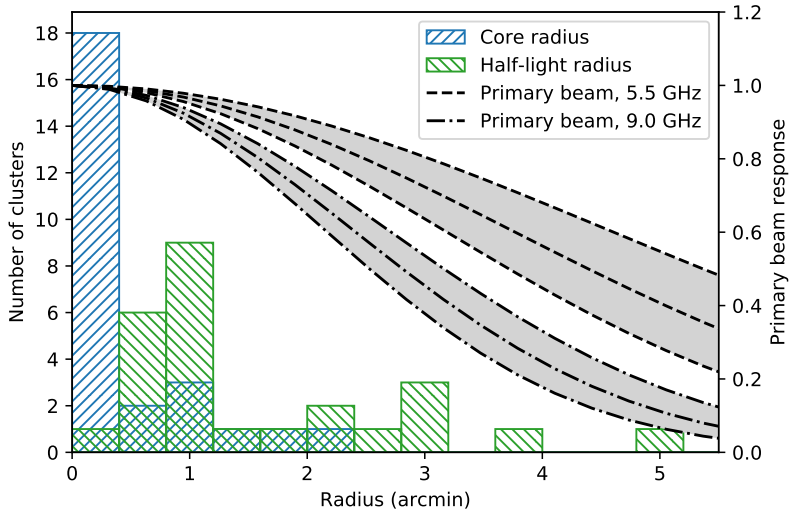

Figure 3.3: The distribution of core and half-light radii for the sample of 26 globular clusters, in relation to the primary beam responses at the observed frequencies 5.5 GHz and 9.0 GHz. The primary beam response at a given radius and central frequency covers a band of values due to the large observing bandwidth (2 GHz). Most clusters fit well within the primary beam.

Table 3.1: Properties of the globular clusters in the sample: the heliocentric distance (D), mass (M), half-light radius ($R_{\rm h}$), core radius ($R_{\rm c}$), flag indicating whether the cluster is core-collapsed (cc), number of known pulsars (PSRs), stellar encounter rate (Γ), and γ-ray flux in the 0.1–100 GeV band.

Cluster	D (kpc)	M ($10^5\,M_\odot$)	$R_{\rm h}$ (arcsec)	$R_{\rm c}$ (arcsec)	cc	Known PSRs	Γ	γ-ray flux ($\times 10^{-12}$ erg s^{-1})
NGC 104	4.6	7.79	190.2	21.6		25	1000.0	24.40
NGC 2808	9.4	7.42	48.0	15.0		0	923.0	3.55
NGC 3201	4.9	1.49	186.0	78.0		0	717.0	1.99
NGC 4372	6.3	2.49	234.6	105.0		0	0.2	3.00
NGC 4833	6.7	2.47	144.6	60.0		0	23.0	2.42
NGC 5139	4.9	35.50	300.0	142.2		0	90.0	5.90
NGC 5927	7.9	3.54	66.0	25.2		0	68.0	3.55
NGC 6139	10.4	3.59	51.0	9.0		0	307.0	5.33
NGC 6304	5.9	2.77	85.2	12.6		0	123.0	5.98
NGC 6352	5.6	0.94	123.0	49.8		0	6.7	6.17
NGC 6362	7.6	1.47	123.0	67.8		0	4.6	1.71
Liller 1	8.1	6.66	30.5	5.4		0	391.0	4.95
Terzan 1	5.2	2.23	23.8	2.0	✓	0	0.3	4.95
NGC 6388	10.9	10.60	31.2	7.2		0	899.0	17.30
NGC 6397	2.3	0.89	174.0	3.0	✓	1	84.0	6.39
Terzan 5	5.9	5.66	43.2	9.6		38	6800.0	59.70
NGC 6441	13.4	12.30	34.2	7.8		4	2300.0	12.50
Terzan 6	6.8	1.17	26.4	3.0	✓	0	2500.0	5.46
Djorg 2	7.0	5.00	63.0	19.8		0	46.0	5.56
NGC 6522	7.7	3.92	60.0	3.0	✓	4	360.0	2.19
NGC 6541	7.5	2.77	63.6	10.8	✓	0	390.0	3.25
NGC 6553	6.0	2.35	61.8	31.8		0	69.0	1.63
NGC 6624	8.4	0.73	49.2	3.6	✓	6	1100.0	2.77
NGC 6652	10.0	0.80	28.8	6.0		1	700.0	4.50
NGC 6715	23.9	14.10	49.2	5.4		0	2500.0	1.76
NGC 6752	4.0	2.39	114.6	10.2	✓	5	400.0	2.87

observations of 5 – 20 minutes integration times, depending on the atmospheric stability and calibrator brightness. The on-source integration time per cluster varied between 8.7 and 35.7 h, with a total of 499 h on-source time, which also includes the archival data of Lu and Kong (2011) for 47 Tuc and ω Cen (project code C2158). A summary of the radio observations is provided in Table 3.2.

The primary beam of ATCA (down to a 20% response) is well described by a Gaussian profile with $FWHM \approx A/\nu$, where $A = 50.6$ and $A = 48.3$ arcmin GHz at 5.5 GHz and 9.0 GHz, respectively (M. Wieringa & M. Kesteven's memo; AT Memo 39.3/024[2]), and ν is the observing frequency in GHz. Most globular clusters fit within the primary beam for ATCA, with the exception of ω Cen, which we cannot observe out to the half-light radius at 9 GHz (Figure 3.3).

3.1.3 Data reduction

Data reduction and calibration were performed using the MIRIAD v1.5 (Sault et al., 1995) software package using standard procedures. We calibrated the 5.5 and 9.0 GHz data separately. We imaged and deconvolved the Stokes I data in CASA v5.1.0 (McMullin et al., 2007) using the multi-frequency, multi-scale CLEAN (Clark, 1980; Sault and Wieringa, 1994) algorithm with 2 Taylor coefficients, which takes into account spectral indices, and Briggs weighting of robustness 1 (Briggs, 1995), which gives a good compromise between sensitivity and spatial resolution. We imaged the 5.5 and 9.0 GHz data and their stack (7.25 GHz) separately. The stack of visibilities between the two wave bands was performed to increase sensitivity to flat-spectrum point sources. As such, the stacked data has more visibilities, and the rms level in their image is lower than either of the individual bands. We used pixel sizes of 0.33″, 0.24″ and 0.24″ for the 5.5, 9.0 and 7.25 GHz images respectively. To improve dynamic range, self-calibration can be employed to better characterise phase information. Due to signal–to–noise considerations, self-calibration is only possible for fields containing sources brighter than ≈3 mJy total flux. We performed this step for five fields: Djorg 2, NGC 6441, NGC 6624 and NGC 6715 (M 54) and NGC 6752. We cropped the resulting images within the 20% primary beam response, which we corrected for using the task `widebandpbcor`. For cropping the stacked image, we used the 20% response of the 9 GHz primary beam. This resulted in image radii of 6.6′, 4.2′ and 4.2′ at 5.5, 9.0 and 7.25 GHz respectively. The achieved resolutions and sensitivities are listed in Table 3.3.

[2] `http://www.atnf.csiro.au/observers/memos/d97f7b~1.pdf`

Table 3.2: Table of radio observations with the ATCA.

Cluster	Date	On-source time (h)	Phase calibrator
NGC 104	2010 Jan 24 [a,b]	7.8	2353-686
(47 Tucanae)	2010 Jan 25 [a,b]	10.5	
	2013 Nov 12 [b]	8.7	
	2015 Feb 02 [b]	8.7	
NGC 2808	2014 Dec 26	7.9	J0845-6527
	2014 Dec 27	7.6	
	2014 Dec 28	7.8	
NGC 3201	2014 Feb 05	9.3	1012-44
	2014 Feb 06	8.8	
NGC 4372	2015 Jan 04	8.4	1251-713
	2015 Jan 05	8.9	
NGC 4833	2015 Jan 07	8.5	1251-713
	2015 Jan 08	8.4	
NGC 5139	2010 Jan 22 [a]	10.1	1320-446
(ω Centauri)	2010 Jan 23 [a]	7.6	
	2014 Dec 04	2.8	
	2014 Dec 06	1.9	
	2015 Jan 09	7.0	
NGC 5927	2015 Jan 10	8.8	1511-47
	2015 Jan 11	9.3	
NGC 6139	2014 Dec 30	8.7	1606-39
	2014 Dec 31	4.9	
	2015 Jan 01	3.0	
NGC 6304	2015 Jan 02	8.1	1710-269
	2015 Jan 03	8.3	
NGC 6352	2013 Nov 07	10.4	1740-517
	2013 Nov 08	10.0	
NGC 6362	2014 Dec 02	9.9	1718-649
	2014 Dec 05	5.1	
	2015 Apr 23	10.1	
Liller 1	2015 Jan 06	8.7	1714-336
Terzan 1	2015 Apr 20	8.2	1741-312
	2015 Apr 29	8.1	
NGC 6388	2014 Dec 12	8.8	1714-397
	2014 Dec 13	9.2	
	2014 Dec 14	9.1	
NGC 6397	2013 Nov 09	8.8	1740-517
	2013 Nov 10	6.9	
Terzan 5	2015 Apr 16 [c]	8.0	1748-253
	2015 June 23 [c]	8.0	
NGC 6441	2015 Apr 14	6.2	1729-37
	2015 Apr 15	8.2	
	2015 May 02	8.1	
Terzan 6	2015 Apr 17	8.0	1741-312
	2015 Apr 18	7.9	
Djorg 2	2015 Apr 26	8.1	1748-253
	2015 Apr 27	8.0	
NGC 6522	2015 Jan 16	8.5	1817-254
	2015 Jan 17	8.2	
NGC 6541	2015 Jan 14	8.1	1759-39
	2015 Jan 15	8.3	
NGC 6553	2015 Apr 30	7.9	1817-254
	2015 May 01	8.4	
NGC 6624	2015 Apr 24	7.8	1817-254
	2015 Apr 25	8.5	
NGC 6652	2015 Apr 19	8.5	1849-36
	2015 June 21	9.7	
	2015 June 22	7.9	
NGC 6715	2014 Dec 05	6.3	1921-293
(M 54)	2014 Dec 06	5.0	
NGC 6752	2014 Feb 06	2.6	1925-610
	2014 Feb 07	8.7	
	2014 Feb 07	9.1	

Notes.
[a] Archival data used by Lu and Kong (2011).
[b] Data used by Miller-Jones et al. (2015) and Bahramian et al. (2017).
[c] Data used by Tetarenko et al. (2016b).

Table 3.3: The FWHM of the synthesised beam – major axis ($B_{\rm maj}$), minor axis ($B_{\rm min}$) and position angle ($B_{\rm pa}$, measured from north toward east), and the central rms, for each of the three frequencies – 5.5 GHz, 9 GHz and their stack (7.25 GHz).

	Frequency											
	5.5 GHz				9 GHz				7.25 GHz			
Source	$B_{\rm maj}$ ($''$)	$B_{\rm min}$ ($''$)	$B_{\rm pa}$ (deg)	rms (μJy)	$B_{\rm maj}$ ($''$)	$B_{\rm min}$ ($''$)	$B_{\rm pa}$ (deg)	rms (μJy)	$B_{\rm maj}$ ($''$)	$B_{\rm min}$ ($''$)	$B_{\rm pa}$ (deg)	rms (μJy)
NGC 104	2.2	1.7	32	3.8	1.5	1.1	39	4.7	1.9	1.4	32	3.2
NGC 2808	2.6	1.5	9	3.7	1.7	1.0	9	4.3	2.0	1.3	13	2.9
NGC 3201	2.9	1.5	4	3.9	2.2	1.1	4	4.1	2.2	1.1	4	3.5
NGC 4372	2.2	1.6	0	4.1	1.5	1.1	0	4.6	1.8	1.3	0	3.0
NGC 4833	2.3	1.6	-3	4.1	1.6	1.1	-3	4.5	1.9	1.3	-4	3.0
NGC 5139	3.0	1.6	-16	3.7	2.0	1.1	-18	4.5	2.4	1.3	-18	2.9
NGC 5927	2.6	1.7	0	4.2	1.7	1.2	-1	5.3	2.1	1.4	-1	3.3
NGC 6139	2.9	1.8	9	4.2	2.0	1.3	6	4.9	2.3	1.5	6	3.3
NGC 6304	4.1	1.6	0	3.9	2.8	1.1	0	4.2	3.3	1.3	0	2.9
NGC 6352	2.6	1.7	0	3.6	1.8	1.2	7	4.3	2.1	1.4	3	2.8
NGC 6362	2.1	1.7	11	3.3	1.4	1.2	5	3.9	1.7	1.4	6	2.5
Liller 1	3.6	1.6	1	6.2	2.5	1.1	0	6.1	3.0	1.3	0	4.4
Terzan 1	4.2	1.5	0	5.6	2.9	1.1	-1	4.1	3.4	1.3	0	2.9
NGC 6388	3.2	1.8	-2	3.5	2.0	1.2	-7	3.4	2.5	1.4	-4	2.6
NGC 6397	2.9	1.5	0	4.6	1.9	1.0	-3	4.8	2.2	1.2	-2	3.3
Terzan 5	5.1	1.5	1	5.1	3.5	1.0	-1	6.5	4.2	1.3	0	4.9
NGC 6441	3.8	1.5	2	3.5	2.4	1.0	4	3.4	2.8	1.2	4	2.6
Terzan 6	4.2	1.6	3	4.7	2.8	1.1	4	5.1	3.4	1.3	4	3.6
Djorg 2	4.8	1.5	0	4.2	3.1	1.0	-1	4.2	3.8	1.2	0	3.2
NGC 6522	4.0	1.6	-1	4.1	2.7	1.1	-1	4.3	3.2	1.3	-1	3.0
NGC 6541	3.0	1.6	-2	5.4	2.1	1.1	-2	4.6	2.7	1.5	-2	3.7
NGC 6553	5.0	1.6	1	4.1	3.4	1.1	1	4.3	4.0	1.3	1	3.0
NGC 6624	4.2	1.6	0	4.0	2.8	1.1	0	4.2	3.3	1.3	0	3.0
NGC 6652	3.7	1.5	-1	3.3	2.7	1.1	0	3.5	3.1	1.3	-1	2.5
NGC 6715	4.4	1.6	-12	5.3	3.1	1.4	-20	9.7	3.9	1.5	-14	5.7
NGC 6752	2.8	1.5	-15	3.8	1.8	1.0	-17	4.3	2.3	1.3	-17	2.9

3.2 Methods

3.2.1 Source finding

We use the source extraction software PYBDSF v1.8.13 (Mohan and Rafferty, 2015) to find radio sources in the 5.5, 9.0, and 7.25 (the stack between the latter bands) GHz images. This tool works by estimating the local background mean and rms using a sliding box algorithm. We set the size of the sliding box to 150×150 pixels, measured in steps of 30 pixels. For bright sources of SNR $\geq$ 50, around which imaging artefacts are more likely, we use a smaller box of 50×50 pixels in steps of 10 pixels. Because the response of the primary beam decreases quickly towards its edge, we estimated the rms and background maps from the non-primary-beam-corrected images, and then corrected them for the primary beam response. Source finding was run on the primary-beam-corrected images. Since we cropped all images at the 20% primary beam response, the uncertainty in the primary beam model only minimally affects the flux measurements. Primary beam effects are even less important for sources towards globular clusters, as these are typically found close to the phase centre. At these frequencies, systematic errors in the absolute flux density scale are expected to be at the level of $\sim$ 2 percent.

Hence, for most sources, we expect flux density errors to be dominated by signal-to-noise constraints. We therefore report the flux density errors as statistical errors from the fit.

Those pixels with values larger than three times the rms above the mean are identified as islands of emission. Island boundaries are expanded to include adjacent pixels with values larger than 3σ, and are then fit with one or more Gaussians fixed to the shape of the synthesised beam. We assume each contiguous island of emission is a single source, with a flux density equal to the modelled total flux density, integrated over all of the Gaussian components (equal to the peak flux density for point sources).

We then cross-match the catalogs at the three different frequencies. We consider a match as any two sources (at different frequencies) that lie closer than 3σ in position from each other. A source may not have a counterpart at both frequencies because: (a) it lies outside of the 20% primary beam response at the higher frequency, (b) any signal is buried by the noise (primarily due to the faster primary beam drop-off at the higher frequency), or (c) the morphology of an extended source is significantly different between each image. In case (a), we do not report the flux density of any source missing from the 9 GHz or 7.25 GHz catalogue (the primary beams at these frequencies are smaller than at 5.5 GHz). In case (b), we take the non-detection as an upper limit at 3× rms. In case (c), we take the value of the upper limit as the value of the pixel at the position of the source, plus 3× rms.

After cross-matching between the three catalogs, we only keep those sources with SNR ≥ 5 in at least one band, to ensure the catalog is reliable. We measure the spectral index ($S_\nu \propto \nu^\alpha$) as $\alpha = \log(S_{5.5}/S_9)/\log(5.5/9)$. If a radio source is only visible in one band, we can place a limit on the spectral index by fixing the value of the flux density in the other band to its upper limit. Errors on the spectral index are estimated by resampling the flux density measurements assuming Gaussian errors, and recalculating the spectral index 1000 times for each source. As the differences between the negative and positive errors of spectral indices do not typically exceed values of ~0.1, we report symmetric spectral index errors as the geometric mean of the two errors.

3.2.2 Source injection

We performed a test to assess whether the completeness, reliability, and flux recovery performance of PyBDSF using the method described in Section 3.2.1 are optimal. This consisted of simulating a simple radio observation by injecting 2000 sources into one of our measurement sets (of NGC 2808), into a 500″×500″ field 1 deg away from the phase centre, to suppress any real sources. We injected these sources at positions at least 7″ away from each other, with flux densities corresponding to SNR in the range 3 to 8. The rms is 4.2 μJy, and the beam size is 1″×1.75″. After imaging the simulated field,

we extracted the sources as described in the previous section, and cross-matched them with the true source catalogue. In Figure 3.4, we show the statistics associated with source extraction. We find that across the recovered sources, the standardised residuals, $(S_{\rm true} - S_{\rm obs})/\Delta S_{\rm obs}$, have a mean $\mu = -0.31$ and standard deviation $\sigma = 1.01$. The measured flux densities are over-estimated (expected $\mu = 0$), as a form of Eddington bias (Eddington, 1913), which makes faint sources more likely to be detected if they coincide with noise peaks. For sources with true SNR $> 5\sigma$, this bias is minimal ($\mu = -0.08$). Above this significance level, we find the completeness and reliability to be above the 90% level. For these reasons, we choose to set the threshold for defining a detection at 5σ.

3.2.3 Source counts

Radio source counts ($\log N/\log S$ as a function of $\log S$) have been used since the early days of radio astronomy as a tool for exploring the evolution of the Universe (Longair, 1966). High flux density sources are mostly Active Galactic Nuclei (AGN), but star-forming galaxies dominate at the faint end (Seymour et al., 2008; Condon et al., 2012). The different populations of astrophysical sources can be seen as a flattening of the source counts below 1 mJy (Windhorst et al., 1984). Sample variance (due to the anisotropic distribution of sources across the sky) can induce deviations in the radio source counts measured in a given survey, depending on flux density and survey area (Heywood et al., 2013). In general, however, field-to-field variations in source counts are caused by instrumental and analysis effects (Condon, 2007).

We use radio source counts as a tool to identify the putative excess of radio sources towards globular clusters. In radio astronomy, population statistics are usually based on differential, rather than cumulative, source counts. The reason behind this is that cumulative source counts are likely to be prone to biases caused by observational, instrumental, and analysis effects (Crawford et al., 1970). However, excesses of radio sources towards targets of interest are typically quantified based on cumulative source counts (e.g., Best et al., 2002). As long as the aforementioned biases are the same between comparison fields (one field to measure the excess over, and one to estimate the background level), using cumulative source counts for this purpose is justified.

The number of sources per unit flux density and unit sky area, known as differential source counts, $n(S_j)$, is given by (Ehlert et al., 2013):

$$n(S_j) = \frac{dN}{dS d\Omega} = \frac{\sum_{i=1}^{i=m} \frac{1}{\Omega_i}}{\Delta S_j}, \tag{3.1}$$

where j is the flux bin between S_0 and S_1 of mean S_j and width $\Delta S_j = S_1 - S_0$, which contains m sources. Ω_i is the surveyed area of the sky that is sensitive enough to detect

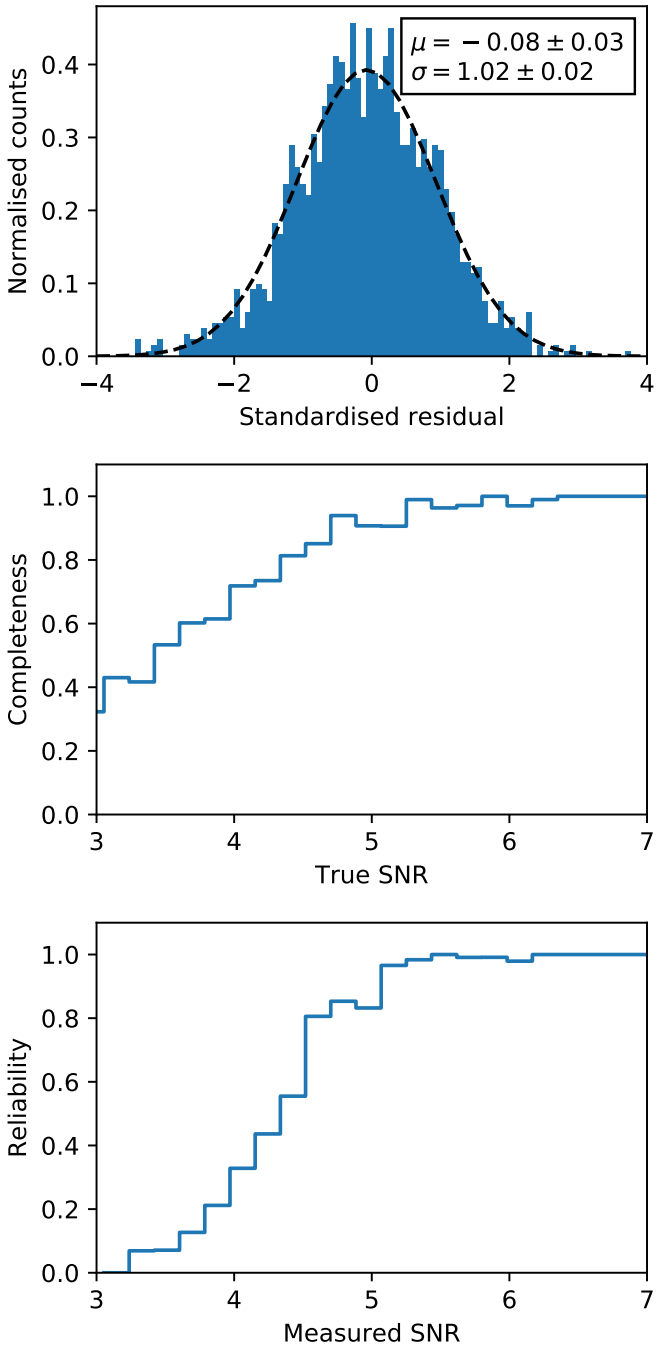

Figure 3.4: Source recovery statistics. *Top:* normalised histogram of standardised residuals for the matched sources, $(S_{\text{true}} - S_{\text{obs}})/\Delta S_{\text{obs}}$. The dashed black line shows the normal distribution of best fit. *Middle:* completeness as a function of input SNR. Sources are virtually complete above 5σ. *Bottom:* reliability as a function of measured SNR. Above 5σ, sources are reliably identified.

sources of flux density S_i with at least 5σ confidence. We take S_j to be the geometric mean $\sqrt{S_0 S_1}$.

To estimate the errors on the source counts, we first investigate how dominant the sources of error are: Poisson errors, errors in the sensitivity map, or flux density errors. The fractional error of the rms is $\sigma_{\rm rms}/{\rm rms} = (1/2N_{\rm beams})^{1/2}$ (Condon et al., 2012), where $N_{\rm beams}$ is the number of resolution elements (synthesised beams) within an area. For a 100×100 pixel box, $N_{\rm beams} \approx 60$, so the error on the rms is at the 10% level. For flux density bin widths (we use 0.1 dex, i.e. a width of 5μJy for a bin centred at $20\,\mu$Jy) that are much larger than typical flux density errors for individual sources ($\approx 4\mu$Jy), the errors in the source counts associated with measurement errors are negligible. Therefore, for low number counts (< 100 counts bin^{-1}), the errors in the measured source counts are dominated by Poisson errors.

3.2.4 Testing for an excess in clusters

To estimate the magnitude of any excess in the number of radio sources towards globular clusters, we first need to estimate how many non-cluster sources lie on the same line of sight with the clusters. There are four methods that can be employed: using (*i*) theoretical source counts, (*ii*) empirical source counts from other surveys, (*iii*) empirical source counts from our survey, or (*iv*) the same as (*iii*), but on a per-cluster basis. Option (*i*) is likely to miss real physical features in the source counts, to miss Galactic sources, and it does not take into account instrumental effects. Option (*ii*) may result in biased conclusions owing to the different observational and analysis techniques employed previously. Option (*iii*) offers the benefit of a uniform observational and analysis strategy for determining the number of sources in and out of clusters. However, a disadvantage is that estimating the overall background from all 26 pointings, and applying it on a per-cluster basis may bias the source counts if the field-to-field variations are larger than the Poisson uncertainties. Option (*iv*) gives the least biased estimate of the local background, at the expense of poorer SNR, by at least a factor $\sim \sqrt{26} \approx 5$. Larger clusters provide a smaller background area to estimate the local background level in, in which case the decrease in SNR is larger than a factor of 5.

To assess which of options (*iii*) and (*iv*) is best, we require an estimate of the cosmic variance across the MAVERIC fields. Heywood et al. (2013) found that for survey areas of 0.01 and 0.03 deg^2[3], cosmic variance exceeds Poisson errors for flux densities below $20\,\mu$Jy and $50\,\mu$Jy respectively. The source counts over smaller areas are dominated by Poisson noise. In conclusion, cosmic variance is likely to have little effect on the source counts between different globular cluster pointings with sensitivities $\gtrsim 20\,\mu$Jy.

[3]The ATCA primary beam out to 20% response covers 0.037 deg^2 and 0.015 deg^2 at 5.5 and 9 GHz respectively

We therefore opt to use the source counts measured across the whole survey to quantify the excess in each cluster (option (*iii*)). In case the globular cluster system contains a global signal that is too faint to be detected in individual clusters, we also search for an excess by considering the cluster sample in its entirety.

We check for a cluster excess by comparing the source counts inside and outside of a given radius (R/R_c), relative to the core radius (R_c), for each cluster. The SNR of any putative cluster excess depends on the radius of the aperture within which the excess is to be measured. A relatively small aperture might miss a large fraction of the excess, whereas a relatively large aperture might include too many background sources and thus dilute any signal above the background. To find the radius that gives the best SNR for the excess, we vary the radius of the cluster aperture between the values of 0.5, 1, 2, 4, 8 and 16 R_c. We keep the separation between the inner radius of the background annulus and the radius of the cluster aperture to $1R_c$ to minimise the potential contamination of the background annulus with cluster sources.

To estimate the number of radio sources which reside within individual clusters, we compare the total number of sources in the same sensitivity range inside and outside each given radius. The expected number of background sources within each cluster aperture is estimated by rescaling the number of sources in the background annulus (detected over some sensitivity area) to the sensitivity area within the cluster aperture. We remind the reader these sensitivity areas represent the areas over which the sources in question could be detected (mostly owing to primary beam sensitivity limits), rather than the total area of the aperture or annulus. On a cluster-by-cluster basis, we can therefore only estimate the number of cluster sources bright enough to also be detected in the background annulus. The uncertainty on the observed number of background sources within each cluster aperture is estimated via simulation. Assuming Poisson statistics, for each cluster and for each flux density bin, we draw a random sample of 100 mean background rates from a continuous probability distribution, which would give the observed number of sources in the background annulus. For each of the drawn mean background rates, we draw a random sample of 100 observations of background sources within the cluster aperture, from a discrete probability distribution. The simulated distribution of the total number of background sources in the cluster aperture is given by the sum of the individual distributions for each flux density bin. The most likely value for the number of background sources is the mode of this distribution. We take the 1σ (3σ) confidence interval as the inner 68.27th (99.73rd) percentile of the distribution. The most likely value and 1σ (3σ) uncertainties are integers as they represent a number of sources, rather than a rate of occurrence.

We take the excess of sources as the number of detected radio sources above the background, $N_{\rm excess} = N_{\rm total} - N_{\rm background}$, where $N_{\rm total}$ is the total number of detected sources, and $N_{\rm background}$ is the most likely number of background sources within the

same aperture. $N_{\rm total}$ and $N_{\rm background}$ are measured over the same flux density range. $N_{\rm excess} = 0$ indicates no excess, while $N_{\rm excess} > 0$ shows an excess of sources in globular clusters, and $N_{\rm excess} < 0$ would mean there are fewer sources towards globular clusters than expected. The latter case is unphysical, and no clusters should contain a significant negative excess. Given the uncertainties in the number of background sources, the measurement of $N_{\rm excess}$ can be negative. We consider the detection of an excess to be real at the $>3\sigma$ level. Given 26 fields, two frequencies (and their stack) and six search radii, we do not expect any spurious detections of an excess.

3.2.5 Spectral index analysis

An additional tool that can be employed when analysing the population of radio sources within globular clusters is the comparison of the distribution of spectral indices inside and outside the cluster. A combination of factors – the generally steep spectra of radio sources ($\alpha \approx -0.6$), and the smaller primary beam at 9 GHz – makes it so a large fraction of the sources detected at 5.5 GHz are not detectable at 9 GHz. A significant portion of sources will therefore only have upper limits for the spectral index measurement, which need to be incorporated in the analysis.

To incorporate upper limits in the analysis of spectral indices, we use survival analysis using the package ASURV v1.2 (Lavalley et al., 1992), which implements the statistical methods developed by Feigelson and Nelson (1985) and Isobe et al. (1986), as part of the software suite PYRAF v2.1.14 (Tody, 1993). The Peto-Prentice test (Prentice and Marek, 1979) is a nonparametric, univariate test comparing two samples to assess the probability that they are drawn from the same parent distribution. Given this test is little affected by the censoring pattern of the measurements (whether the likelihood of an upper or lower limit is correlated with its value; Latta, 1981; Feigelson and Nelson, 1985), we use this statistical test to characterise the similarity between the spectral index distribution inside versus outside globular clusters.

To estimate errors on the probability that the two distributions differ, we resample 10000 times the distribution of spectral indices via bootstrapping (drawing random samples with replacement and with the same size as the observed distribution) and perturbation (randomly changing the value of each measurement by an amount described by its uncertainty).

3.3 Results

3.3.1 Catalogue of radio sources

We have detected a total of 1290 sources, 330 of which have counterparts at both 5.5 and 9.0 GHz, and for which a spectral index could be calculated. 36 sources are located within one core radius, and 110 sources within one half-light radius. We make the following information available in the source catalogue (which will be made available online at a later date):

1. Source ID
2. Field: the globular cluster in the direction of which the radio source resides
3. Right ascension (RA)
4. Declination (DEC)
5. 1σ error in RA (Δ RA)
6. 1σ error in DEC (Δ DEC)
7. Flux density at 5.5 GHz ($S_{5.5}$)
8. 1σ error in $S_{5.5}$ ($\Delta\, S_{5.5}$)
9. Flux density at 7.25 GHz ($S_{7.25}$)
10. 1σ error in $S_{7.25}$ ($\Delta\, S_{7.25}$)
11. Flux density at 9 GHz (S_9)
12. 1σ error in $S_{9.0}$ ($\Delta\, S_9$)
13. Spectral index α
14. 1σ error in α
15. Distance from the centre in units of core radii (R/R_c)
16. Distance from the centre in units of half-light radii (R/R_h)

We show the survey images and catalogues in Appendix 3.A.

3.3.2 Source counts

We show the source counts measured from all of our sampled fields outside of clusters, at three different frequencies, and compare them with the previous estimates of the radio source counts of de Zotti et al. (2010) and Wilman et al. (2008). De Zotti et al. (2010) provide a collation of source counts measured from different surveys at various frequencies, and with different sensitivities. Wilman et al. (2008) performed a semi-empirical simulation of the radio sky covering $20 \times 20\,\mathrm{deg}^2$ down to 10 nJy at four different frequencies. To convert the observed source counts of de Zotti et al. (2010) to our observing frequencies, we rescaled their 4.86 GHz source counts to 5.5 GHz, and their 8.4 GHz source counts to 7.25 and 9.0 GHz, assuming a constant spectral index $\alpha = -0.7$ (Condon, 1984). We calculated the theoretical source counts from Wilman et al. (2008) first by measuring the spectral index for each source in their catalogue using the total flux densities at 4.86 GHz and 18 GHz, and then interpolating to 5.5, 7.25 and 9.0 GHz. To mitigate the contamination with globular cluster sources for our sample, we have excluded the regions within $5R_c$ of cluster centres. We show the source counts in Figure 3.5.

3.3.3 Excess of sources

Only five radio sources in our catalogue are associated with some of the 73 previously known pulsars with a known position in our sample: in NGC 104 (pulsar D), in Terzan 5 (3 radio sources; pulsars P, A and C, and possibly others, blended; Prager et al., 2017), and in NGC 6397 (the only known pulsar; D'Amico et al., 2001). As expected, these sources have steep spectral indices, $\alpha \sim -2$. No radio source is detected at the position of the black hole in NGC 3201 (Giesers et al., 2018), with a 3σ upper limit of $S_\nu < 14\,\mu$Jy at 7.25 GHz. This is expected, as radio jets are unlikely to be present in a detached binary system that is not transferring mass.

In Figure 3.6, and Tables 3.4 and 3.5, we show the measured excess for each cluster (and their stack) at the radius (between 0.5, 1, 2, 4, 8 or 16 R_c) with the highest 3σ lower limit for the excess (and highest excess for those radii with the same lower limit). We choose this strategy (instead of using the same aperture size for all clusters) for two reasons: (*i*) not all clusters can be measured out to the same large radius, owing to large core radii, and finite image size; (*ii*) the radial distribution of radio sources is not necessarily constant across clusters. We find that half the globular clusters in our sample (13 out of 26) contain at least one radio source above the background (with 1σ significance). Five clusters contain a significant ($> 3\sigma$) number of sources: Terzan 5, NGC 6397, NGC 6624, Terzan 1 and Terzan 6. We do not find a significant excess in the overall sample at any of the search radii or frequency. The uncertainties associated with each excess are dominated by the sizes of cluster apertures. We show the cumulative

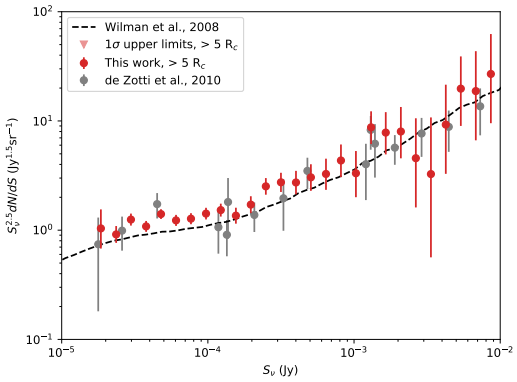

(a) Source counts at 5.5 GHz

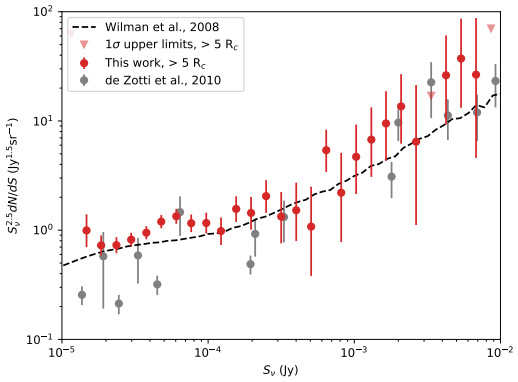

(b) Source counts at 7.25 GHz

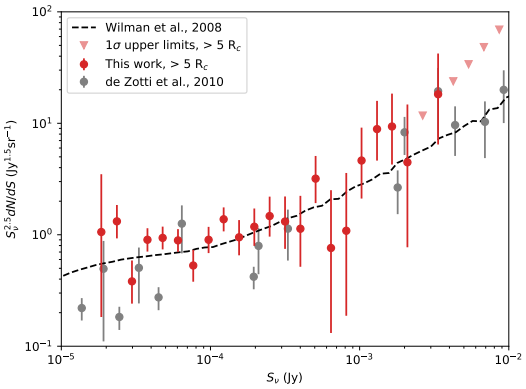

(c) Source counts at 9.0 GHz

Figure 3.5: Differential source counts outside clusters ($> 5R_c$) at three different frequencies, compared to the collated measurements of de Zotti et al. (2010), and the theoretical estimates of Wilman et al. (2008). The error bars represent 1σ uncertainties, and the triangles represent 1σ upper limits. The source counts derived from our work are consistent with previous estimates within a factor of 2. Disparities are due to observational and processing biases rather than cosmic variance.

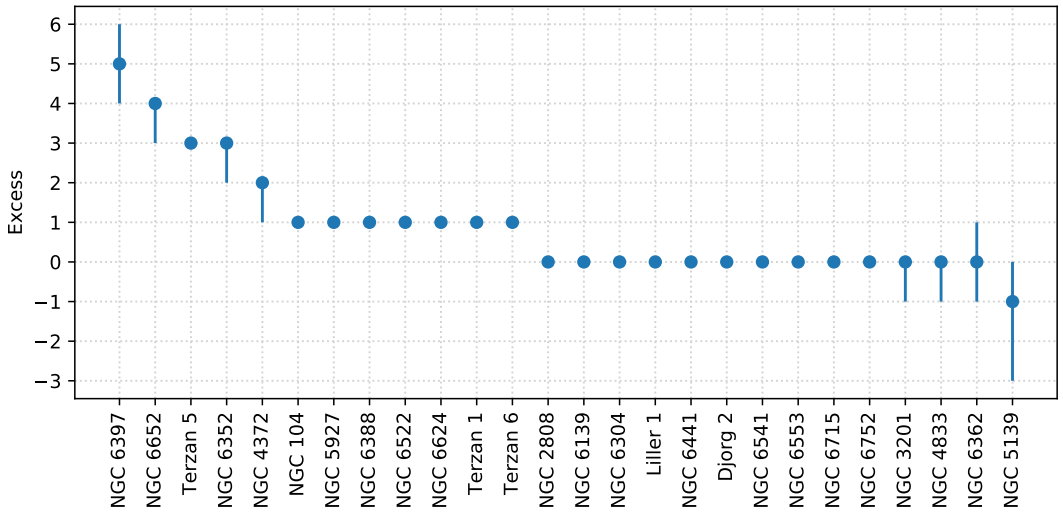

Figure 3.6: The number of detected radio sources which reside within each globular cluster after subtracting the expected number of background/foreground radio sources. The uncertainties represent 1σ confidence intervals on the background counts in the cluster field. Seven out of 26 clusters show an excess at more than 3σ significance.

number counts for NGC 6397 (which has a significant excess of more than one source) in Figure 3.7.

Next, we investigate whether the excess of sources is correlated with any cluster property. For this, we remove from the sample those clusters with core radii larger than 15″ (to ensure all clusters can be well sampled), or located at extreme distances (NGC 6397 at 2.3 kpc and NGC 6715 at 23.9 kpc, for sensitivity concerns). We plot the excess of sources within $4R_c$ (chosen to maximize the measured excess, and minimize the sensitivity variation across the aperture) against the number of known radio pulsars within the cluster, the estimated stellar encounter rate, total cluster mass, γ-ray luminosity, galactocentric distance, core and half-light radii in parsecs, metallicity and distance (Figure 3.8). To assess the significance of any correlations, we calculate the Spearman rank (ρ) for 1000 bootstrapped samples of each property pair. The p-value is the fraction of ρ measurements which are greater (less) than 0 if the median $\rho > 0$ ($\rho < 0$). We consider significant any pair with $p < 0.003$ (corresponding to 3σ). No trends can be identified.

3.3.4 Spectral indices

Having found evidence for an excess of radio sources towards globular clusters, we explore their radio spectral properties. In Figure 3.9, we show the distribution of 5.5–9.0 GHz spectral indices inside and outside $4R_c$. The survival analysis shows that sources within this threshold radius have the same spectral properties as those outside of this radius. Repeating the test for different radii (0.5, 1, 2, 8 and 16 R_c) returns

Table 3.4: The number of detected radio sources above the background, for individual clusters and across the whole sample. We report the source excess (E), its associated uncertainties ($-\delta E$ and $+\delta E$), and 3σ lower ($E_{\rm LL}$) and upper ($E_{\rm UL}$) limits within the radius (R/R_c) which gives the highest 3σ lower limit for the excess.

GC	N	N_{bkg}	E	$-\delta$E	$+\delta$E	E_{LL}	E_{UL}	R/R_c
NGC 6397	6	1	5	1	1	1	6	16
NGC 6652	4	0	4	1	0	0	4	4
Terzan 5	3	0	3	0	0	1	3	2
NGC 6352	3	0	3	1	0	0	3	0.5
NGC 4372	2	0	2	1	0	-2	2	0.5
NGC 104	1	0	1	0	0	0	1	0.5
NGC 5927	1	0	1	0	0	0	1	0.5
NGC 6388	1	0	1	0	0	0	1	0.5
NGC 6522	1	0	1	0	0	0	1	2
NGC 6624	1	0	1	0	0	1	1	0.5
Terzan 1	1	0	1	0	0	1	1	0.5
Terzan 6	1	0	1	0	0	1	1	0.5
NGC 2808	0	0	0	0	0	-1	0	0.5
NGC 6139	0	0	0	0	0	-1	0	0.5
NGC 6304	0	0	0	0	0	-1	0	0.5
Liller 1	0	0	0	0	0	0	0	0.5
NGC 6441	0	0	0	0	0	-1	0	0.5
Djorg 2	0	0	0	0	0	-1	0	0.5
NGC 6541	0	0	0	0	0	-1	0	0.5
NGC 6553	0	0	0	0	0	-2	0	0.5
NGC 6715	0	0	0	0	0	0	0	0.5
NGC 6752	0	0	0	0	0	-1	0	0.5
NGC 3201	0	0	0	1	0	-4	0	0.5
NGC 4833	0	0	0	1	0	-3	0	0.5
NGC 6362	1	1	0	1	1	-4	1	0.5
NGC 5139	0	1	-1	2	1	-7	0	0.5

Table 3.5: Same as Table 3.4, but over the whole survey. In each stack only those globular clusters which have been imaged out to the search radius (R/R_c) have been included.

GC	N	N_{bkg}	E	$-\delta$E	$+\delta$E	E_{LL}	E_{UL}	R/R_c
Stack	12	9	3	3	3	-7	10	0.5
Stack	28	34	-6	7	5	-28	10	1
Stack	90	124	-34	11	13	-72	2	2
Stack	242	270	-28	18	19	-85	30	4
Stack	339	325	14	24	21	-58	73	8
Stack	305	324	-19	25	20	-91	20	16

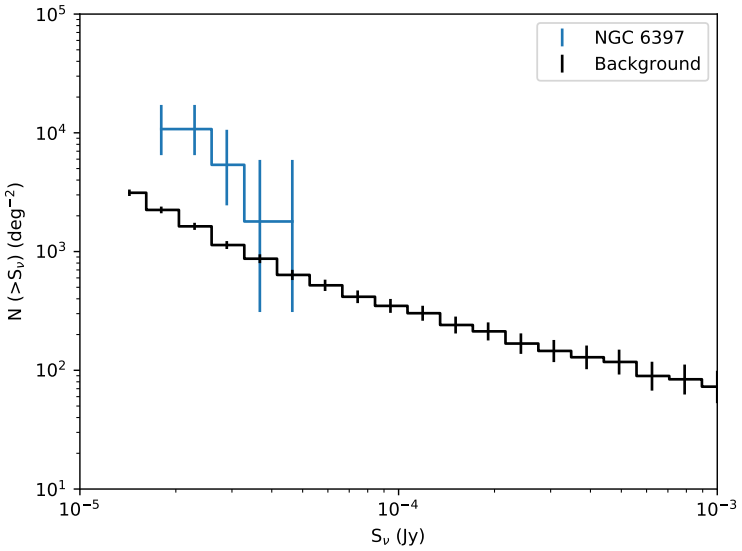

Figure 3.7: Cumulative number counts for the background and the cluster NGC 6397 at 7.25 GHz, within $16R_c$. This cluster contain a significant excess of radio sources.

similar results.

3.4 Discussion and conclusions

Out of the ∼1300 source detections, we estimated at most 70 (at 3σ confidence) are located within clusters. We find some clusters contain an excess of sources when taken on their own, but we do not find a global signal. This means that globular clusters with radio sources persistent at $S_\nu \gtrsim 20\,\mu$Jy are the exception rather than the rule. As only few radio sources in globular clusters reach such flux density levels, deeper follow-up studies are required to sample this population to higher completeness.

Out of the five clusters in which we detected a significant excess, four are core-collapsed (Terzan 1, NGC 6397, Terzan 6 and NGC 6624) and one is not (Terzan 5). On the other hand, six clusters in our sample are core-collapsed, and 20 are not. This, however, does not necessarily imply that core-collapsed clusters are more likely to host radio sources. Instead, the larger cores of non-collapsed clusters make the Poisson noise on background counts drown out any signal from cluster sources. An example of this would be 47 Tuc. In this cluster we detected two radio sources which are known to be part of it: pulsar D and the X-ray binary X9 (covered in Chapter 5), located at 1.6 R_c and 0.4 R_c from its centre respectively. Our measurement for the source excess at 5.5 GHz within 2 R_c for this cluster is $E = 1 \pm 1$. While this result encompasses the two sources known to be part of the cluster, it is also consistent with no excess. This highlights the need for the X-ray, optical and timing characterisation of radio sources to better constrain their numbers and nature in globular clusters. In this light, in Chapter 7

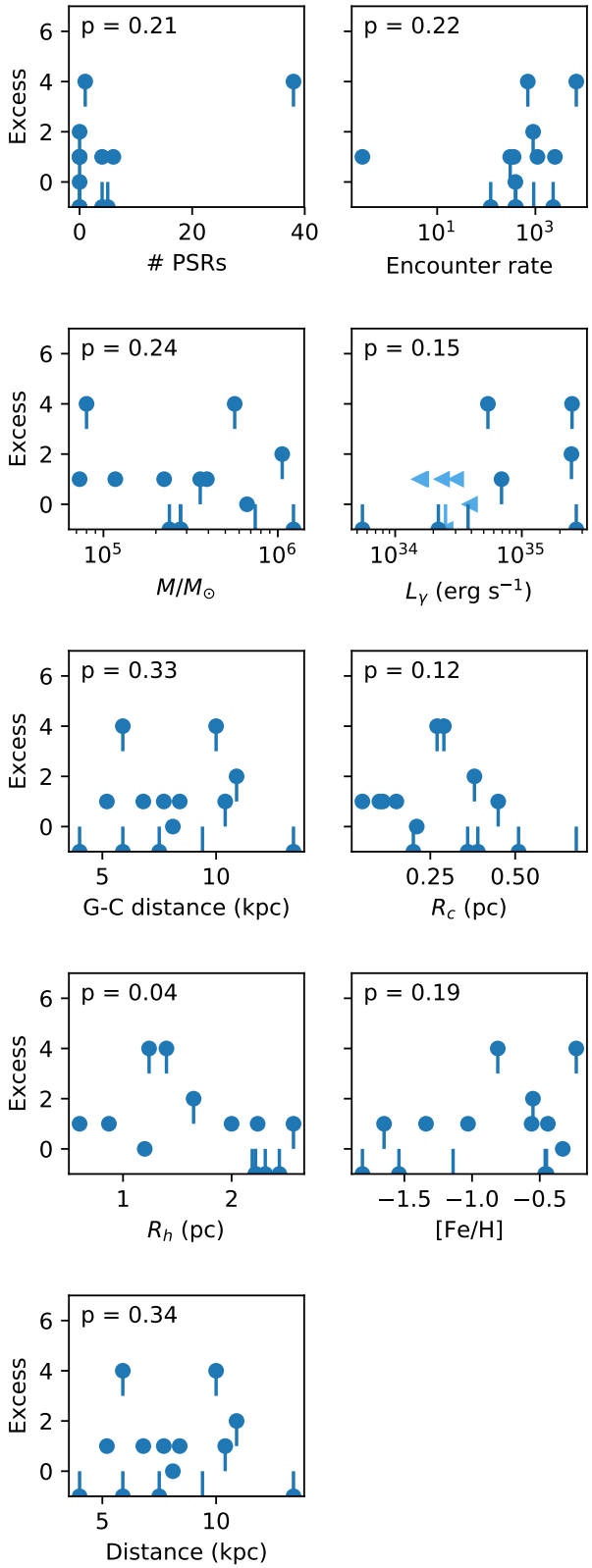

Figure 3.8: The measured excess at 7.25 GHz and a radius of $4R_c$ (in units of parsecs), for those globular clusters with core radii smaller than 15″, disregarding NGC 6397 and NGC 6715 (the two clusters at extreme distances). We do not observe strong trends between the cluster excesses and their properties, as shown by the non-significant p-values.

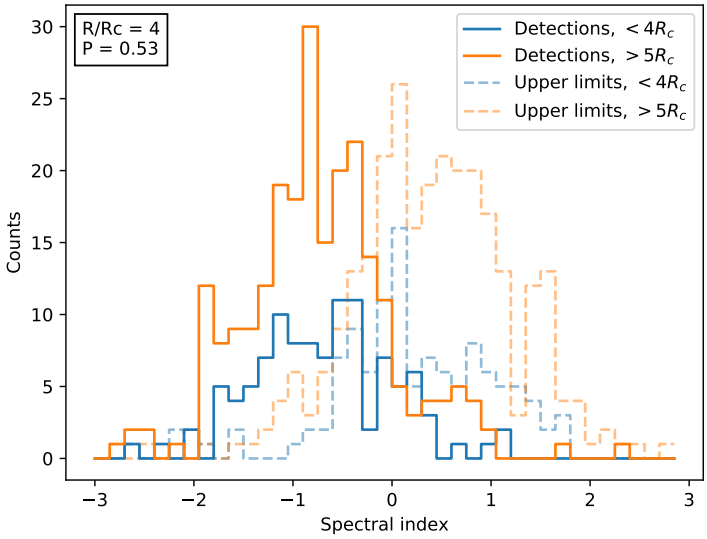

Figure 3.9: Histogram of 5.5–9 GHz spectral indices inside $4R_c$ and outside $5R_c$, showing both detections and upper limits. The probability that both spectral index samples (inside vs outside) are drawn from the same parent population is 49 per cent.

we investigate some of the clusters with an excess (significant or not).

We found the spectral index distribution of sources at small angular distances from globular cluster centres is statistically similar to those of sources further away from clusters. This reinforces the idea that most radio sources in the direction of globular clusters are extragalactic sources. In those clusters where radio sources do exist, they are most likely associated with pulsars and X-ray binaries, but may include other types of compact accreting objects or planetary nebulae.

NGC 6388, for which we found a significant number of radio sources, is one of the clusters that has been singled out by Moody and Sigurdsson (2009) (together with NGC 6441), based on its high mass and metallicity, as potentially retaining large population of black holes. Our results, however, do not show a strong correlation between either the cluster mass and metallicity with the number of radio sources. This may well be because of the low number of radio sources in each individual cluster, and the small lever arm in these properties.

In summary, in this chapter we presented the 26 Southern globular clusters observed with ATCA. We found that some globular clusters host radio sources above the background level, with at least 1–2 sources per cluster. However, most globular clusters do not host radio sources. We will further discuss the nature of the radio sources in those clusters with an excess in Chapter 6.

3.A Survey images and source catalogues

This Appendix contains the for each cluster in the survey. I show the full extent of the 5.5 and 9 GHz images, as well as the inner 10″ in case of their stack. The two red concentric circles show the core and half-light radii, and the smaller green circles show each source detected at SNR > 5 in each band. The source catalogues (described in Section 3.3.1) only contain the innermost 20 sources of each cluster, sorted by distance from the centre. These catalogues will be provided in their entirety following publication.

Table 3.6: NGC 104

ID	Field	RA	DEC	ΔRA ($''$)	ΔDEC ($''$)	$S_{5.5}$ (μJy)	$\Delta S_{5.5}$ (μJy)	$S_{7.25}$ (μJy)	$\Delta S_{7.25}$ (μJy)	S_9 (μJy)	ΔS_9 (μJy)	α	$\Delta\alpha$	R/R_c	R/R_h
1	NGC 104	00:24:04.33	-72:04:57.80	0.24	0.04	34.7	3.8	32.6	3.2	29.1	4.7	-0.37	0.41	0.39	0.04
2	NGC 104	00:24:13.90	-72:04:43.72	0.48	0.15	24.1	3.9	16.0	3.3	<17.6	-	<-0.64	0.33	1.79	0.20
3	NGC 104	00:23:52.35	-72:03:56.48	0.03	0.02	31.0	3.9	26.5	3.6	<29.9	-	<-0.07	0.26	3.85	0.44
4	NGC 104	00:24:13.35	-72:03:32.59	0.28	0.07	87.7	3.9	61.8	3.7	36.3	5.9	-1.79	0.34	4.03	0.46
5	NGC 104	00:24:22.24	-72:04:08.51	0.27	0.13	24.7	4.0	21.5	3.7	<33.4	-	<0.61	0.33	4.07	0.46
6	NGC 104	00:24:18.13	-72:06:19.14	0.47	0.09	24.6	4.2	24.7	4.0	<29.6	-	<0.38	0.35	4.82	0.55
7	NGC 104	00:23:40.87	-72:05:11.64	0.06	0.02	170.0	4.1	120.0	4.2	70.7	6.8	-1.78	0.2	5.38	0.61
8	NGC 104	00:24:27.99	-72:06:03.94	0.49	0.06	29.4	4.2	26.3	4.3	<36.0	-	<0.41	0.3	5.80	0.66
9	NGC 104	00:23:58.13	-72:07:00.41	0.48	0.12	<16.6	-	18.2	4.4	40.6	7.2	>1.82	0.36	6.15	0.70
10	NGC 104	00:24:08.00	-72:07:05.13	0.01	0.06	<18.1	-	22.2	4.4	38.8	7.1	>1.55	0.38	6.17	0.70
11	NGC 104	00:24:35.06	-72:05:01.50	0.06	0.10	30.4	4.3	21.0	4.5	<32.5	-	<0.14	0.29	6.29	0.71
12	NGC 104	00:24:07.92	-72:02:35.98	0.10	0.05	<18.6	-	18.1	4.5	41.6	7.4	>1.64	0.36	6.32	0.72
13	NGC 104	00:24:08.60	-72:07:08.48	0.00	0.09	28.5	4.5	22.4	4.5	<25.2	-	<-0.25	0.32	6.34	0.72
14	NGC 104	00:24:03.33	-72:02:34.80	0.30	0.05	24.5	4.3	19.0	4.5	<34.7	-	<0.71	0.37	6.38	0.72
15	NGC 104	00:24:13.29	-72:02:25.08	0.16	0.09	25.0	4.5	24.8	4.7	<41.3	-	<1.02	0.37	7.00	0.80
16	NGC 104	00:23:46.13	-72:07:15.14	0.32	0.02	25.2	4.7	25.0	5.2	<45.1	-	<1.18	0.38	7.83	0.89
17	NGC 104	00:24:10.32	-72:07:41.33	0.11	0.10	71.9	4.7	58.9	5.2	50.0	9.2	-0.73	0.39	7.89	0.90
18	NGC 104	00:23:28.55	-72:03:53.73	0.43	0.10	28.2	5.0	30.6	5.5	<43.6	-	<0.89	0.36	8.39	0.95
19	NGC 104	00:24:35.73	-72:07:10.13	0.18	0.11	29.3	5.3	26.1	6.2	<51.5	-	<1.15	0.37	9.05	1.03
20	NGC 104	00:24:48.92	-72:04:19.87	0.44	0.36	31.1	5.1	21.5	6.1	<47.8	-	<0.87	0.34	9.35	1.06

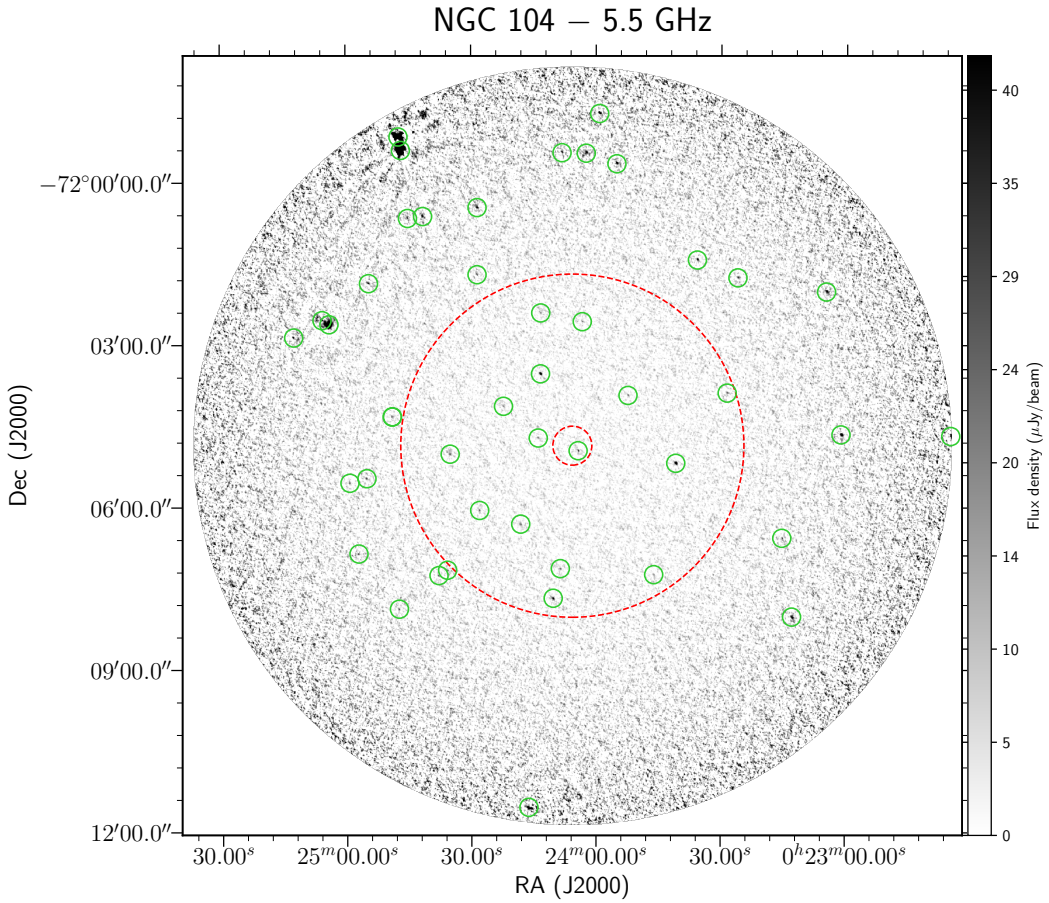
NGC 104 – 5.5 GHz
−72°00′00.0″
03′00.0″
06′00.0″
09′00.0″
12′00.0″
Dec (J2000)
30.00s
25m00.00s
30.00s
24m00.00s
30.00s
0h23m00.00s
RA (J2000)
Flux density (μJy/beam)
40
35
29
24
20
14
10
5
0

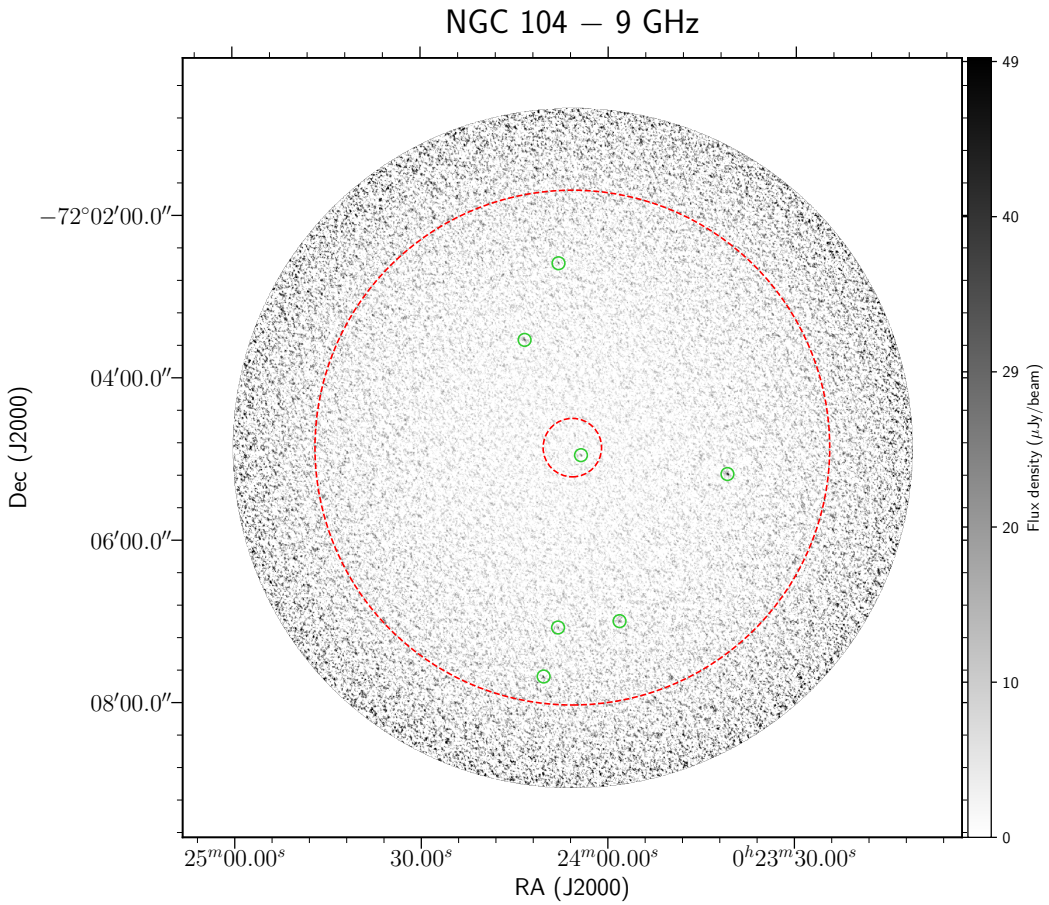
NGC 104 – 9 GHz
−72°02′00.0″
04′00.0″
06′00.0″
08′00.0″
Dec (J2000)
25m00.00s
30.00s
24m00.00s
0h23m30.00s
RA (J2000)
Flux density (μJy/beam)
49
40
29
20
10
0

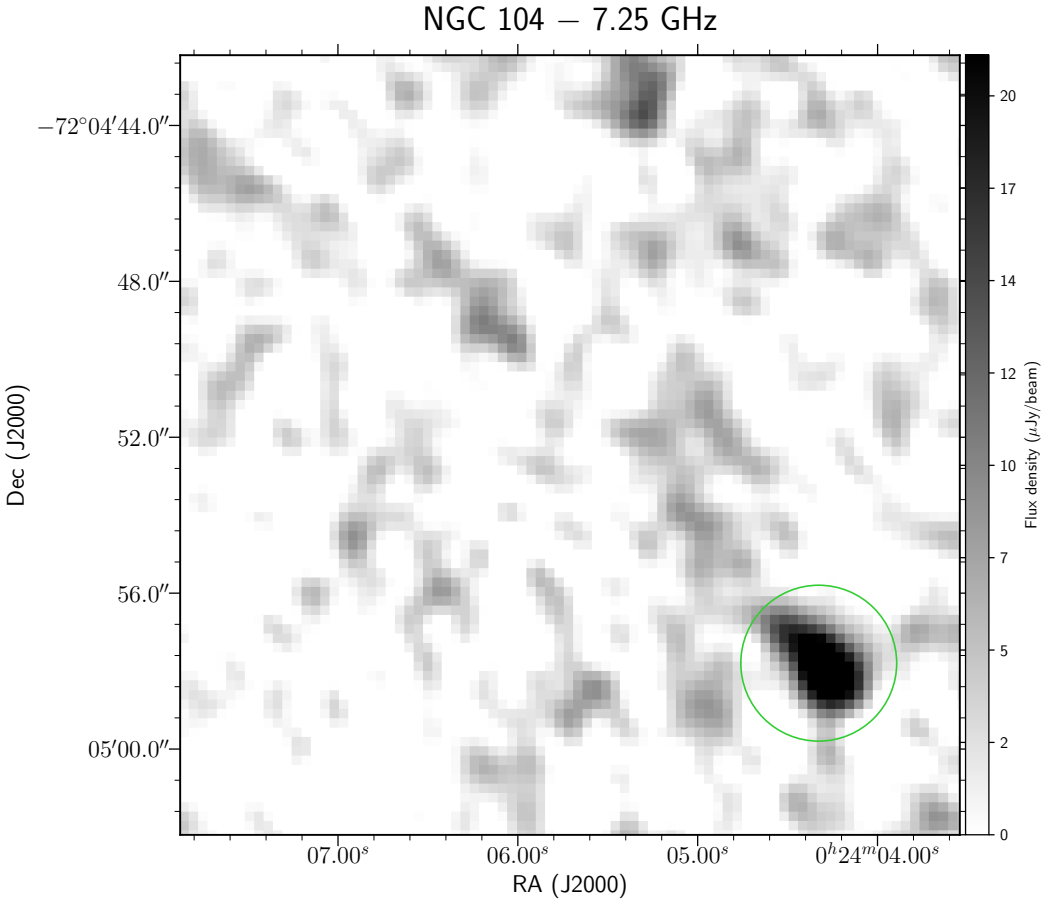
NGC 104 – 7.25 GHz
−72°04′44.0″
48.0″
52.0″
56.0″
05′00.0″
Dec (J2000)
07.00s
06.00s
05.00s
0h24m04.00s
RA (J2000)
Flux density (μJy/beam)
20
17
14
12
10
7
5
2
0

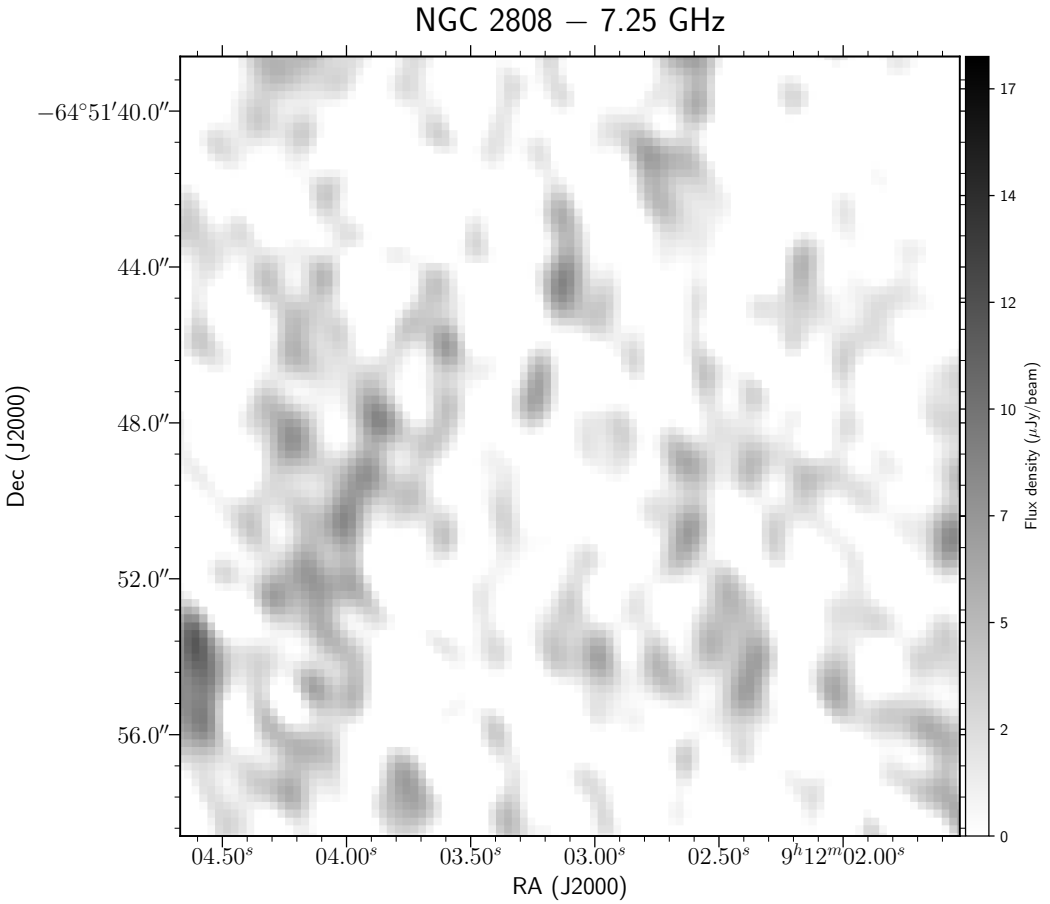
NGC 2808 – 7.25 GHz
−64°51′40.0″
44.0″
48.0″
52.0″
56.0″
Dec (J2000)
04.50s
04.00s
03.50s
03.00s
02.50s
9h12m02.00s
RA (J2000)
Flux density (μJy/beam)
17
14
12
10
7
5
2
0

Table 3.7: NGC 2808

ID	Field	RA	DEC	Δ RA ($''$)	Δ DEC ($''$)	$S_{5.5}$ (μJy)	$\Delta S_{5.5}$ (μJy)	$S_{7.25}$ (μJy)	$\Delta S_{7.25}$ (μJy)	S_9 (μJy)	ΔS_9 (μJy)	α	$\Delta\alpha$	R/R_c	R/R_h
1	NGC 2808	09:12:05.10	-64:51:09.52	0.42	0.15	18.1	3.7	49.8	10.2	19.1	4.5	0.11	0.68	2.74	0.86
2	NGC 2808	09:12:07.18	-64:52:35.15	0.14	0.09	15.7	3.7	15.5	2.8	<26.9	-	<1.09	0.48	3.55	1.11
3	NGC 2808	09:12:10.66	-64:52:35.31	0.32	0.32	23.4	3.8	22.8	3.0	20.6	4.5	-0.27	0.57	4.47	1.40
4	NGC 2808	09:12:12.94	-64:50:51.79	0.05	0.06	49.5	3.7	37.6	3.3	23.9	5.0	-1.49	0.45	5.64	1.76
5	NGC 2808	09:11:55.05	-64:52:58.04	0.10	0.26	20.1	3.8	<19.3	-	<15.5	-	<-0.53	0.38	5.75	1.80
6	NGC 2808	09:12:09.88	-64:53:04.82	0.09	0.12	19.2	3.6	20.3	3.2	19.2	4.9	0.01	0.65	5.84	1.82
7	NGC 2808	09:11:51.48	-64:52:41.88	0.51	0.10	28.5	3.8	22.7	3.7	23.7	5.1	-0.37	0.5	6.08	1.90
8	NGC 2808	09:11:48.72	-64:52:13.00	0.50	0.29	27.2	4.0	21.2	3.7	21.5	5.4	-0.49	0.58	6.32	1.98
9	NGC 2808	09:11:51.65	-64:53:01.97	0.13	0.05	22.3	3.8	17.3	3.5	<24.1	-	<0.16	0.35	6.90	2.15
10	NGC 2808	09:11:44.44	-64:51:28.02	0.04	0.20	38.2	4.0	36.3	4.0	27.8	5.9	-0.64	0.49	8.04	2.51
11	NGC 2808	09:11:43.30	-64:51:41.15	0.58	0.31	27.4	4.1	18.1	4.0	<37.5	-	<0.64	0.3	8.43	2.63
12	NGC 2808	09:12:03.51	-64:49:37.94	0.19	0.08	30.0	4.1	23.8	4.1	<31.9	-	<0.13	0.28	8.71	2.72
13	NGC 2808	09:12:09.33	-64:53:57.25	0.07	0.05	93.8	4.0	87.0	4.1	53.2	6.3	-1.15	0.26	8.98	2.80
14	NGC 2808	09:12:25.44	-64:52:16.41	0.04	0.13	25.3	4.2	22.4	4.6	<33.9	-	<0.60	0.34	9.67	3.02
15	NGC 2808	09:12:24.66	-64:51:02.18	0.12	0.15	33.0	4.2	27.4	4.7	<32.7	-	<-0.02	0.26	9.67	3.02
16	NGC 2808	09:11:51.22	-64:49:43.92	0.21	0.14	26.0	4.1	22.8	4.3	<30.7	-	<0.34	0.33	9.73	3.04
17	NGC 2808	09:11:41.80	-64:50:28.46	1.70	0.42	33.3	4.6	16.4	4.8	<38.3	-	<0.28	0.28	10.51	3.28
18	NGC 2808	09:11:41.70	-64:50:28.14	0.14	0.28	33.3	4.6	28.9	5.1	<39.8	-	<0.36	0.28	10.56	3.30
19	NGC 2808	09:12:07.23	-64:49:11.70	0.23	0.17	125.0	16.1	137.0	16.6	55.9	7.1	-1.63	0.37	10.61	3.31
20	NGC 2808	09:11:35.58	-64:51:59.52	0.35	0.03	41.0	4.9	34.1	5.7	<43.4	-	<0.12	0.25	11.71	3.66

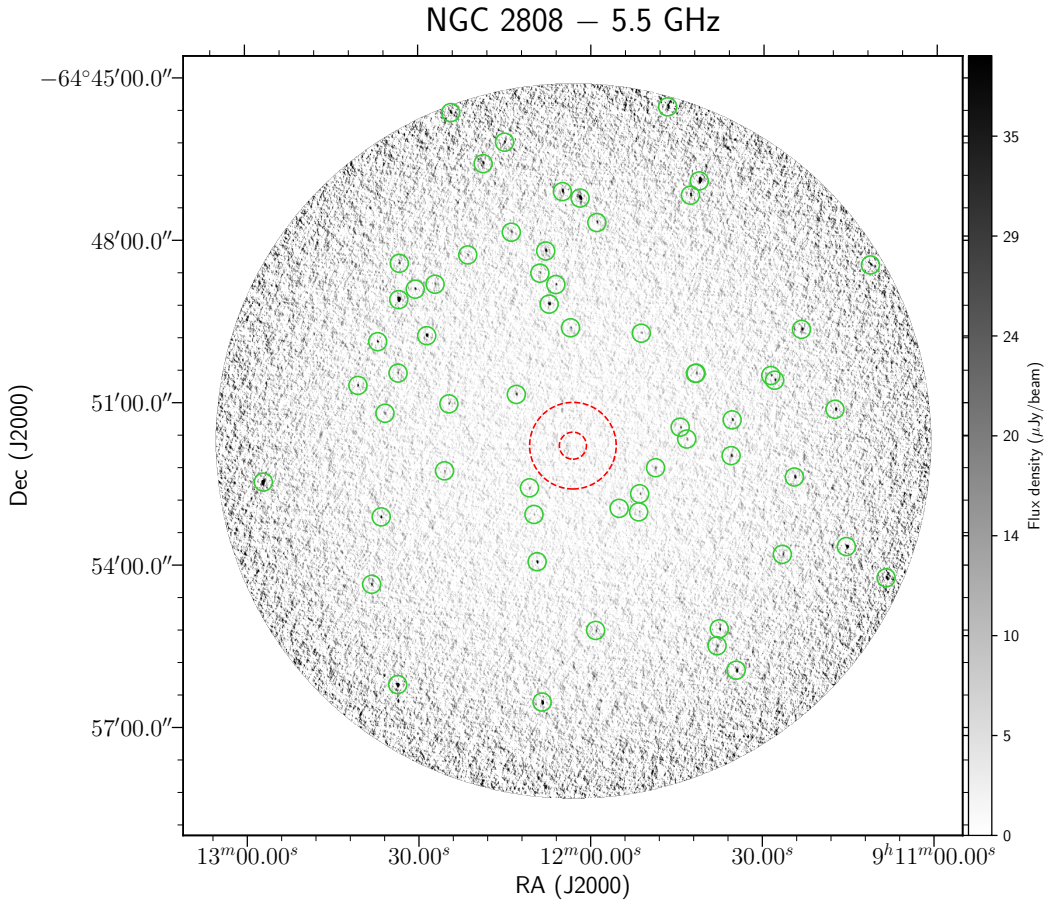
NGC 2808 – 5.5 GHz
−64°45′00.0″
48′00.0″
51′00.0″
54′00.0″
57′00.0″
Dec (J2000)
13^m00.00^s
30.00^s
12^m00.00^s
30.00^s
9^h11^m00.00^s
RA (J2000)
Flux density (μJy/beam)
0
5
10
14
20
24
29
35

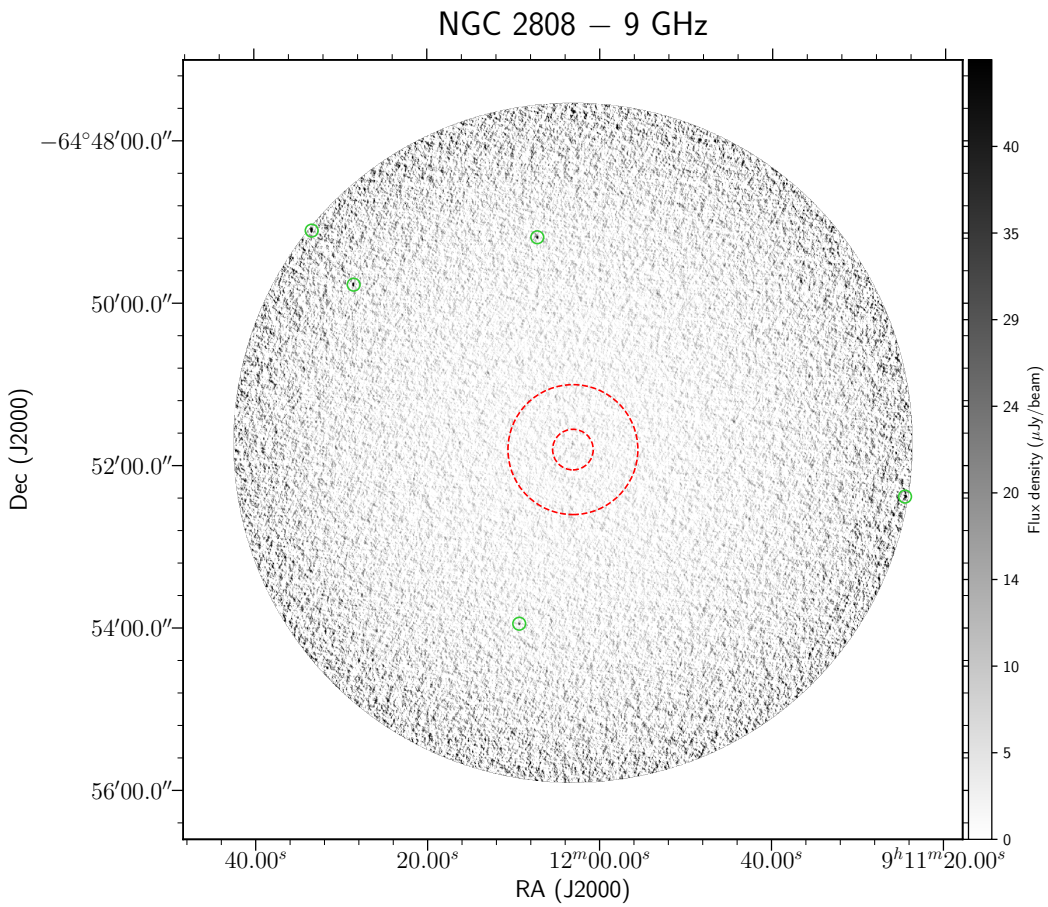
NGC 2808 – 9 GHz
−64°48′00.0″
50′00.0″
52′00.0″
54′00.0″
56′00.0″
Dec (J2000)
40.00^s
20.00^s
12^m00.00^s
40.00^s
9^h11^m20.00^s
RA (J2000)
Flux density (μJy/beam)
0
5
10
14
20
24
29
35
40

Table 3.8: NGC 3201

ID	Field	RA	DEC	Δ RA ($''$)	Δ DEC ($''$)	$S_{5.5}$ (μJy)	$\Delta S_{5.5}$ (μJy)	$S_{7.25}$ (μJy)	$\Delta S_{7.25}$ (μJy)	S_9 (μJy)	ΔS_9 (μJy)	α	$\Delta\alpha$	R/R$_c$	R/R$_h$
1	NGC 3201	10:17:42.67	-46:24:54.26	0.15	0.12	25.4	3.7	19.9	3.8	16.6	4.3	-0.87	0.61	0.78	0.33
2	NGC 3201	10:17:26.71	-46:25:04.56	0.65	0.24	26.6	4.0	15.3	4.1	<24.9	-	<-0.13	0.31	1.36	0.57
3	NGC 3201	10:17:32.31	-46:26:26.16	0.11	0.31	16.6	3.9	24.1	4.0	21.3	5.2	0.47	0.7	1.43	0.60
4	NGC 3201	10:17:31.16	-46:26:42.88	0.05	0.06	26.5	4.2	25.4	4.7	<29.5	-	<0.22	0.32	1.69	0.71
5	NGC 3201	10:17:44.74	-46:26:31.96	0.34	0.20	24.6	4.5	22.2	4.8	22.8	5.8	-0.15	0.64	1.73	0.72
6	NGC 3201	10:17:46.69	-46:23:06.03	0.02	0.22	52.0	4.5	44.0	5.1	41.4	7.3	-0.48	0.41	1.82	0.76
7	NGC 3201	10:17:29.26	-46:26:43.95	0.04	0.02	133.0	4.4	108.0	4.5	69.4	6.2	-1.32	0.19	1.83	0.77
8	NGC 3201	10:17:43.83	-46:22:36.64	0.10	0.02	28.7	4.5	27.9	4.7	<38.6	-	<0.60	0.32	1.89	0.79
9	NGC 3201	10:17:23.72	-46:23:22.62	0.12	0.38	24.9	5.0	25.2	4.8	<44.0	-	<1.16	0.41	2.03	0.85
10	NGC 3201	10:17:21.43	-46:25:36.17	0.25	0.07	30.1	4.8	23.2	5.0	<27.9	-	<-0.15	0.33	2.14	0.90
11	NGC 3201	10:17:48.94	-46:22:45.16	0.03	0.05	182.0	16.3	202.0	23.8	156.0	26.9	-0.30	0.41	2.22	0.93
12	NGC 3201	10:17:27.93	-46:27:12.67	0.11	0.08	29.2	4.9	30.5	5.1	<40.2	-	<0.65	0.35	2.23	0.94
13	NGC 3201	10:17:49.98	-46:22:54.06	0.23	0.93	25.0	5.5	32.7	5.7	<35.9	-	<0.74	0.45	2.25	0.94
14	NGC 3201	10:17:40.92	-46:21:44.95	0.17	0.17	43.6	5.5	36.6	6.3	<50.3	-	<0.29	0.26	2.37	0.99
15	NGC 3201	10:17:39.95	-46:27:54.44	0.13	0.87	29.2	5.2	27.3	5.6	32.9	8.5	0.23	0.67	2.47	1.03
16	NGC 3201	10:17:39.95	-46:27:54.92	0.04	0.13	29.2	5.2	27.3	5.6	38.1	8.6	0.54	0.6	2.47	1.04
17	NGC 3201	10:17:25.68	-46:27:23.35	0.07	0.24	<31.2	-	31.0	5.7	<45.6	-	-	-	2.51	1.05
18	NGC 3201	10:17:54.24	-46:26:11.65	0.13	0.08	35.8	5.5	27.3	6.5	<54.5	-	<0.85	0.31	2.56	1.07
19	NGC 3201	10:17:26.30	-46:27:35.09	0.10	0.64	32.9	5.8	35.2	6.0	43.8	9.9	0.60	0.59	2.59	1.09
20	NGC 3201	10:17:26.03	-46:21:54.16	0.03	0.08	101.0	5.8	98.0	6.5	47.7	10.8	-1.51	0.48	2.62	1.10

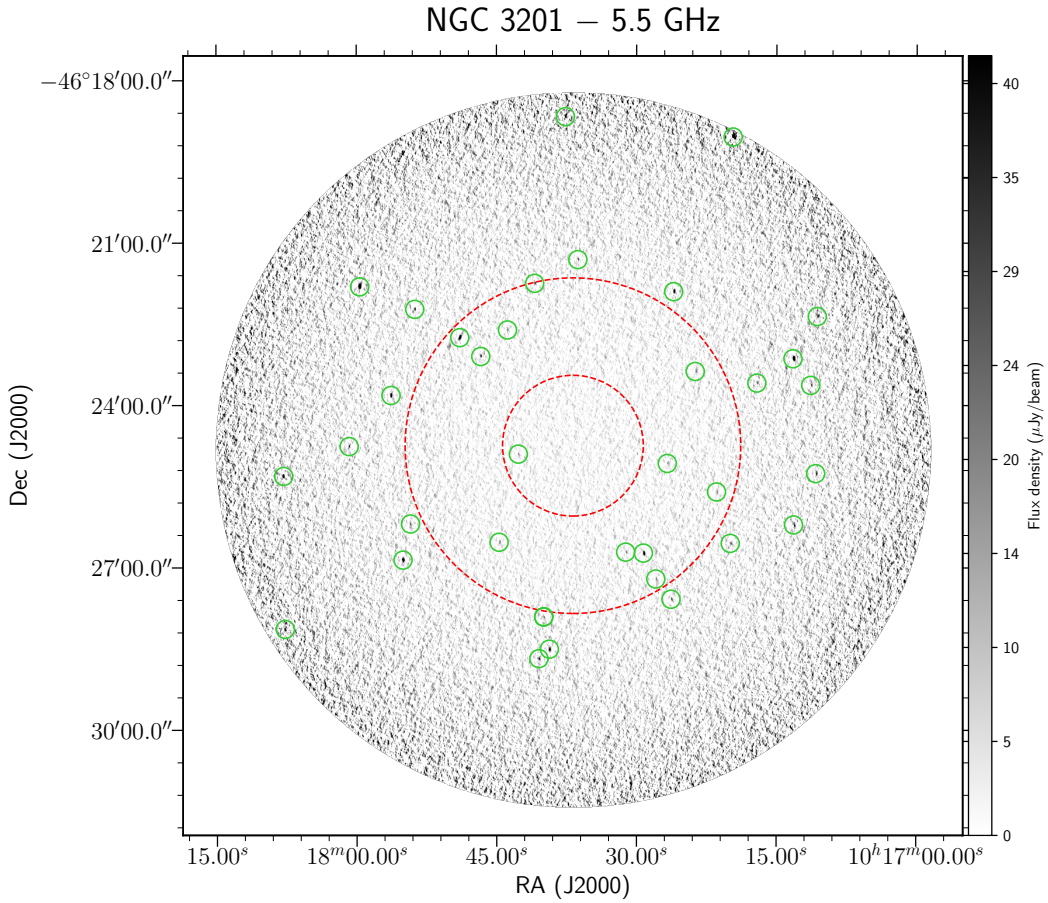
NGC 3201 — 5.5 GHz
−46°18′00.0″
21′00.0″
24′00.0″
27′00.0″
30′00.0″
Dec (J2000)
15.00s
18m00.00s
45.00s
30.00s
15.00s
10h17m00.00s
RA (J2000)
Flux density (μJy/beam)
0
5
10
14
20
24
29
35
40

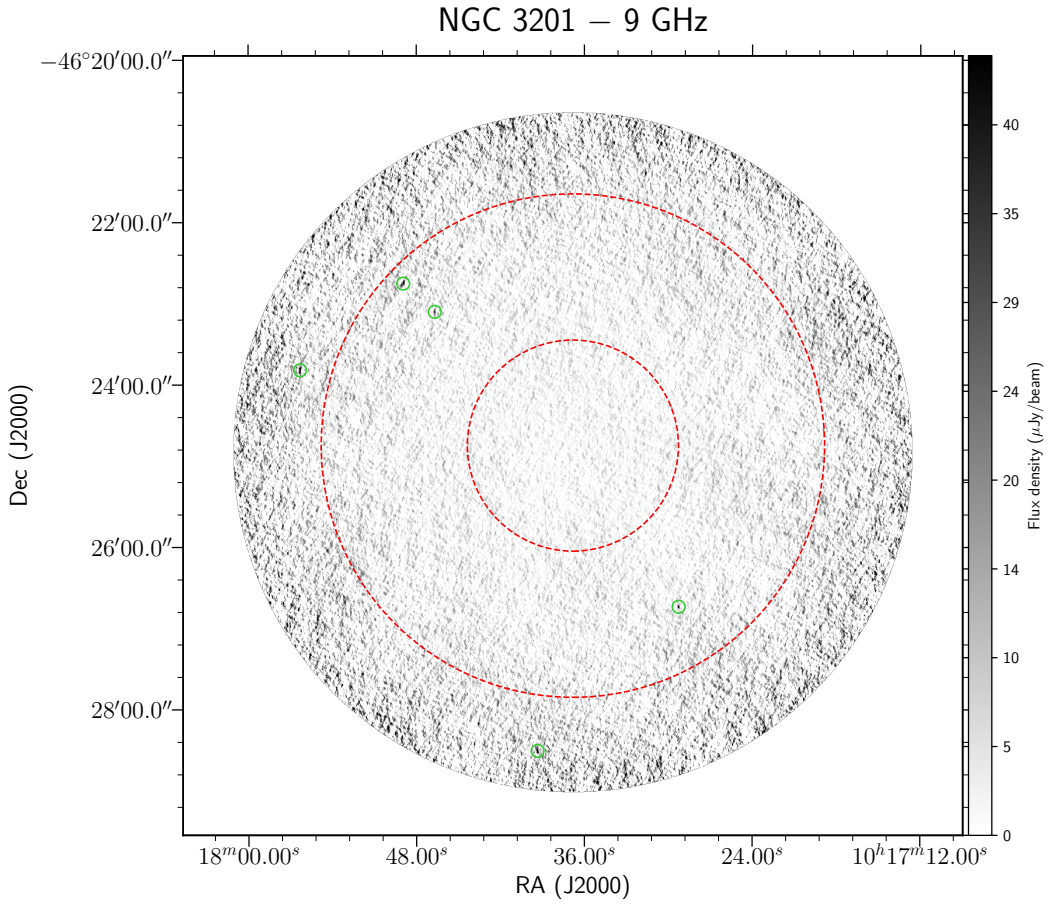
NGC 3201 — 9 GHz
−46°20′00.0″
22′00.0″
24′00.0″
26′00.0″
28′00.0″
Dec (J2000)
18m00.00s
48.00s
36.00s
24.00s
10h17m12.00s
RA (J2000)
Flux density (μJy/beam)
0
5
10
14
20
24
29
35
40

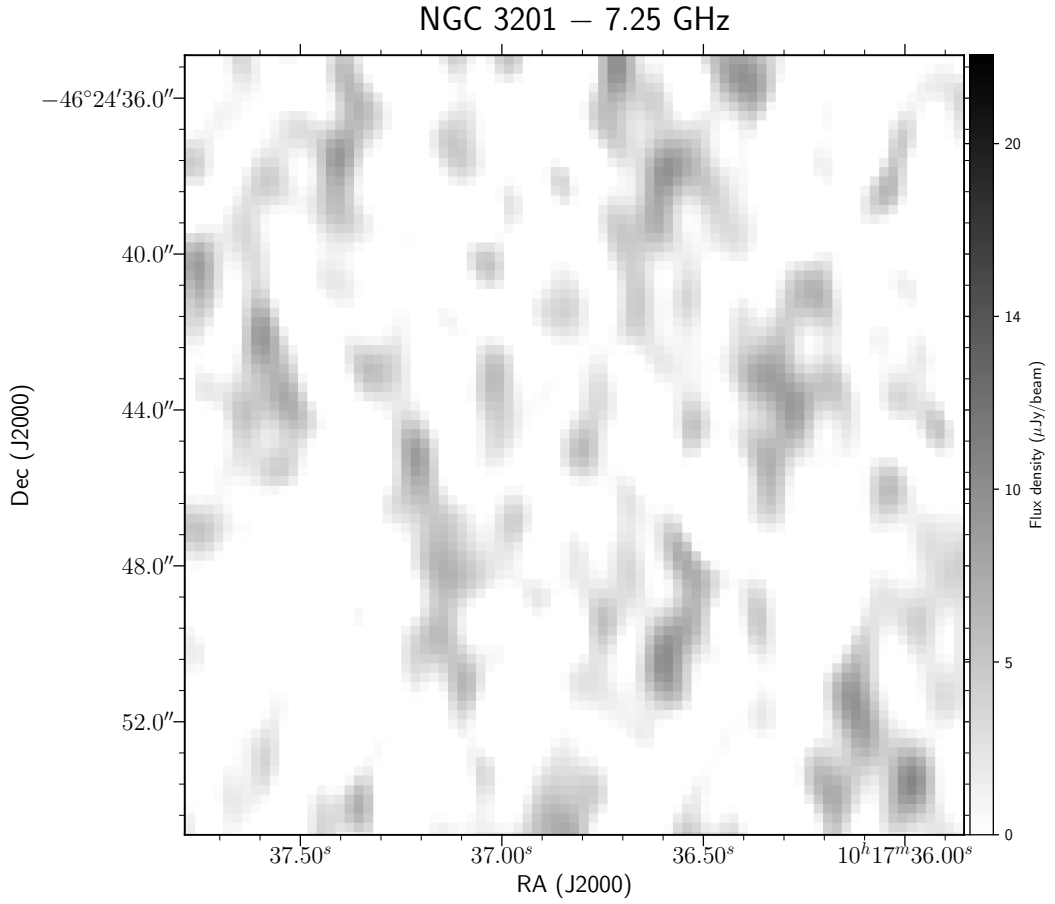
NGC 3201 – 7.25 GHz
−46°24′36.0″
40.0″
44.0″
48.0″
52.0″
Dec (J2000)
37.50s
37.00s
36.50s
10h17m36.00s
RA (J2000)
Flux density (μJy/beam)
0
5
10
14
20

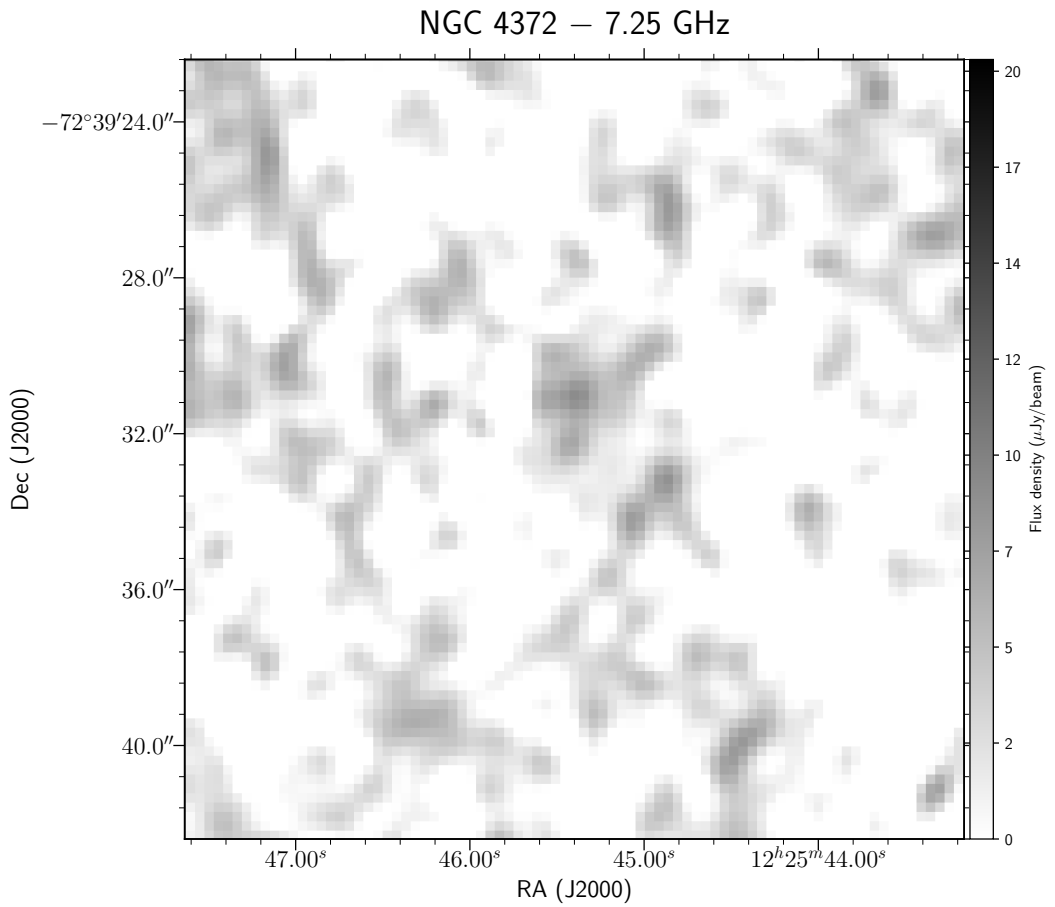
NGC 4372 – 7.25 GHz
−72°39′24.0″
28.0″
32.0″
36.0″
40.0″
Dec (J2000)
47.00s
46.00s
45.00s
12h25m44.00s
RA (J2000)
Flux density (μJy/beam)
0
2
5
7
10
12
14
17
20

Table 3.9: NGC 4372

ID	Field	RA	DEC	Δ RA ($''$)	Δ DEC ($''$)	$S_{5.5}$ (μJy)	$\Delta S_{5.5}$ (μJy)	$S_{7.25}$ (μJy)	$\Delta S_{7.25}$ (μJy)	S_{9} (μJy)	ΔS_{9} (μJy)	α	$\Delta\alpha$	R/R$_c$	R/R$_h$
1	NGC 4372	12:25:54.63	-72:39:41.72	0.09	0.06	44.0	4.1	36.1	3.2	29.2	4.9	-0.85	0.4	0.40	0.18
2	NGC 4372	12:25:46.00	-72:40:15.96	0.17	0.14	37.8	4.0	33.6	3.1	29.7	4.8	-0.48	0.4	0.42	0.19
3	NGC 4372	12:25:44.14	-72:40:32.28	0.32	0.15	25.3	4.1	18.3	3.2	<25.2	-	<-0.01	0.33	0.57	0.26
4	NGC 4372	12:26:06.11	-72:39:58.06	0.03	0.01	484.0	4.8	445.0	4.6	400.0	7.1	-0.39	0.04	0.91	0.41
5	NGC 4372	12:25:24.51	-72:40:04.69	0.39	0.10	35.0	4.3	30.5	3.5	21.0	5.8	-1.03	0.61	0.94	0.42
6	NGC 4372	12:26:04.23	-72:40:58.07	0.11	0.11	29.2	4.7	20.3	4.1	<29.8	-	<0.04	0.33	1.14	0.51
7	NGC 4372	12:25:33.07	-72:37:41.31	0.42	0.10	24.8	4.5	18.5	3.8	<32.2	-	<0.53	0.37	1.18	0.53
8	NGC 4372	12:25:49.01	-72:41:39.85	0.01	0.04	234.0	4.9	186.0	4.0	126.0	6.9	-1.25	0.12	1.22	0.55
9	NGC 4372	12:25:32.79	-72:41:28.62	0.21	0.08	34.3	4.8	32.3	4.0	42.2	6.8	0.42	0.43	1.23	0.55
10	NGC 4372	12:25:27.82	-72:37:29.56	0.27	0.12	22.0	4.8	23.7	4.2	<48.8	-	<1.62	0.45	1.39	0.62
11	NGC 4372	12:26:15.54	-72:40:47.27	0.15	0.08	63.6	5.4	52.5	4.8	40.5	8.1	-0.92	0.45	1.47	0.66
12	NGC 4372	12:25:45.27	-72:36:45.22	0.37	0.03	36.3	5.1	37.4	4.5	43.0	8.5	0.33	0.5	1.59	0.71
13	NGC 4372	12:25:54.67	-72:36:46.55	0.12	0.08	47.3	5.2	42.5	4.8	37.1	8.7	-0.49	0.52	1.63	0.73
14	NGC 4372	12:25:35.65	-72:36:37.24	0.15	0.13	28.6	5.4	24.5	5.0	<47.8	-	<1.04	0.39	1.72	0.77
15	NGC 4372	12:25:19.53	-72:37:07.27	0.26	0.14	28.5	5.4	28.5	5.0	<56.5	-	<1.39	0.39	1.77	0.79
16	NGC 4372	12:25:04.09	-72:40:03.47	0.18	0.11	43.7	5.5	36.0	5.2	<52.9	-	<0.39	0.26	1.78	0.80
17	NGC 4372	12:25:51.42	-72:42:40.02	0.53	0.02	43.9	6.0	44.4	5.6	40.4	11.1	-0.18	0.66	1.81	0.81
18	NGC 4372	12:25:31.72	-72:36:26.56	0.08	0.05	33.1	5.6	25.6	5.5	<37.6	-	<0.26	0.35	1.86	0.83
19	NGC 4372	12:25:52.89	-72:36:16.25	0.01	0.05	41.7	5.8	35.6	5.5	<56.0	-	<0.60	0.29	1.90	0.85
20	NGC 4372	12:26:14.65	-72:42:05.27	0.02	0.02	2080.0	39.3	1720.0	38.8	926.0	16.7	-1.64	0.05	1.91	0.86

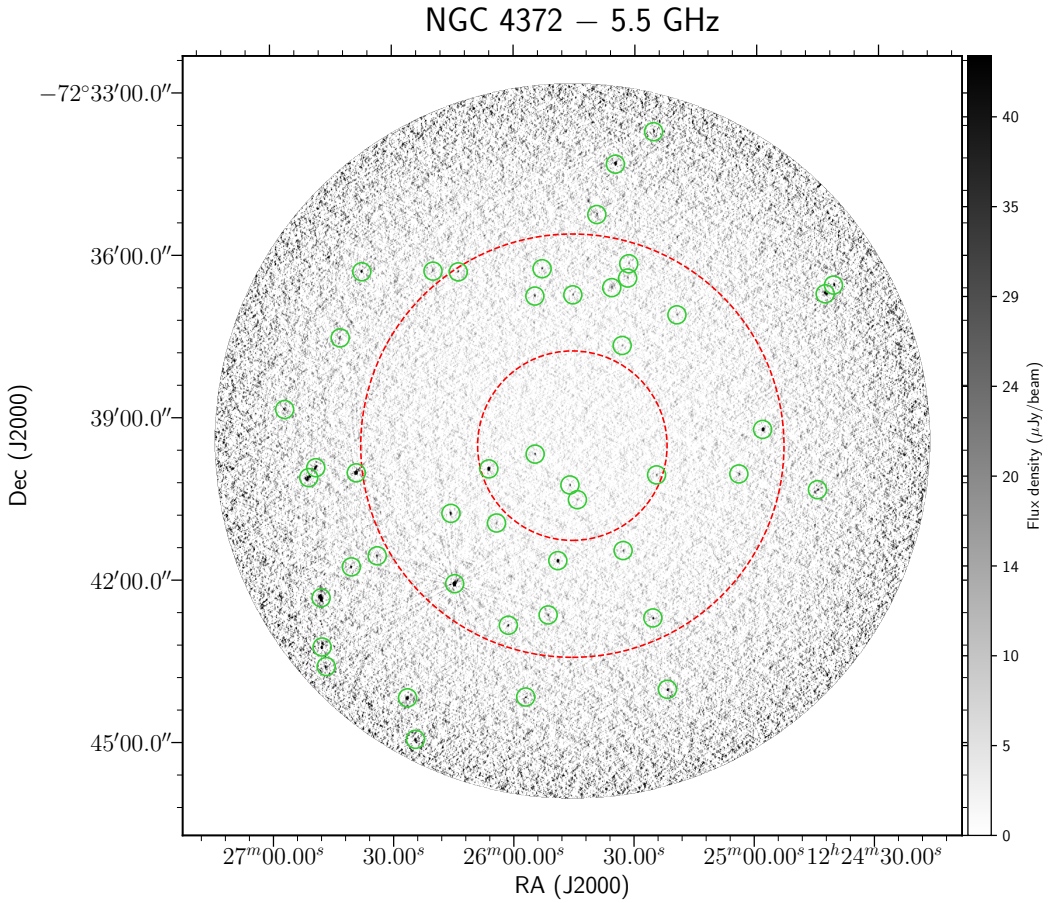
NGC 4372 – 5.5 GHz
−72°33′00.0″
36′00.0″
39′00.0″
42′00.0″
45′00.0″
Dec (J2000)
27m00.00s
30.00s
26m00.00s
30.00s
25m00.00s
12h24m30.00s
RA (J2000)
Flux density (μJy/beam)
0
5
10
14
20
24
29
35
40

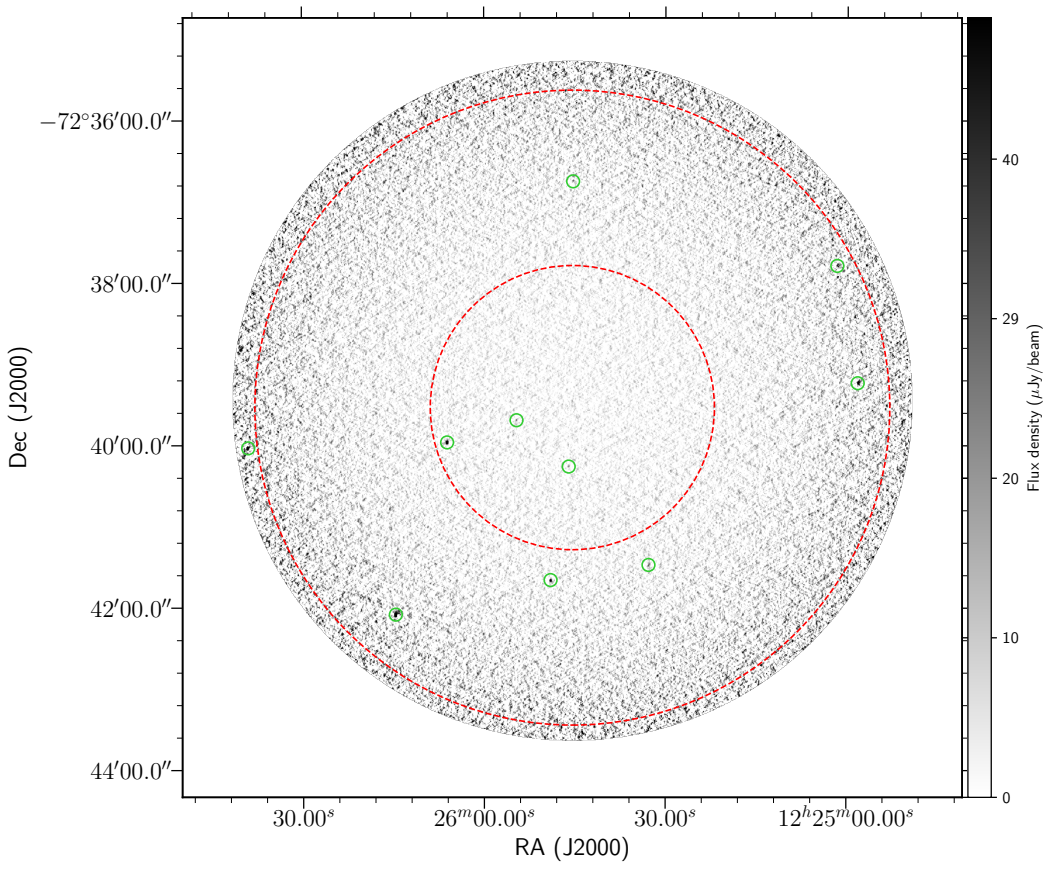
NGC 4372 – 9 GHz
−72°36′00.0″
38′00.0″
40′00.0″
42′00.0″
44′00.0″
Dec (J2000)
30.00s
26m00.00s
30.00s
12h25m00.00s
RA (J2000)
Flux density (μJy/beam)
0
10
20
29
40

Table 3.10: NGC 4833

ID	Field	RA	DEC	Δ RA ($''$)	Δ DEC ($''$)	$S_{5.5}$ (μJy)	$\Delta S_{5.5}$ (μJy)	$S_{7.25}$ (μJy)	$\Delta S_{7.25}$ (μJy)	S_{9} (μJy)	ΔS_{9} (μJy)	α	$\Delta\alpha$	R/R_c	R/R_h
1	NGC 4833	12:59:39.82	-70:53:25.54	0.07	0.06	135.0	4.0	105.0	3.1	77.3	4.6	-1.13	0.14	0.97	0.40
2	NGC 4833	12:59:34.92	-70:53:40.09	0.59	0.13	93.5	12.4	85.6	9.5	50.6	4.7	-1.24	0.32	1.08	0.45
3	NGC 4833	12:59:34.54	-70:53:39.97	0.06	0.14	<37.0	-	<33.3	-	28.7	4.7	>-0.51	0.34	1.08	0.45
4	NGC 4833	12:59:31.81	-70:51:23.45	0.22	0.33	24.1	4.1	21.9	3.2	21.9	4.8	-0.19	0.6	1.21	0.50
5	NGC 4833	12:59:49.02	-70:51:43.44	0.08	0.05	122.0	4.3	108.0	3.4	94.3	5.4	-0.53	0.13	1.51	0.63
6	NGC 4833	12:59:37.80	-70:50:56.50	0.01	0.02	510.0	4.6	485.0	5.2	464.0	8.4	-0.19	0.04	1.68	0.70
7	NGC 4833	12:59:26.93	-70:50:50.43	0.04	0.14	18.8	4.4	18.9	3.6	<35.6	-	<1.30	0.49	1.84	0.76
8	NGC 4833	12:59:15.86	-70:54:02.35	1.52	0.10	36.6	4.6	27.2	3.8	<36.1	-	<-0.03	0.26	2.07	0.86
9	NGC 4833	12:59:11.84	-70:51:22.75	0.22	0.01	33.1	4.5	30.8	3.8	28.8	6.2	-0.28	0.54	2.18	0.90
10	NGC 4833	12:59:41.88	-70:54:51.55	0.70	0.20	31.6	4.6	32.4	4.2	36.8	7.3	0.30	0.5	2.36	0.98
11	NGC 4833	13:00:04.46	-70:52:16.86	0.07	0.14	53.7	5.1	41.0	4.4	30.3	7.3	-1.15	0.53	2.52	1.05
12	NGC 4833	12:59:38.23	-70:55:08.06	0.05	0.09	238.0	15.0	210.0	15.7	114.0	8.1	-1.49	0.19	2.57	1.07
13	NGC 4833	12:59:03.25	-70:51:43.90	0.20	0.05	<24.1	-	21.2	4.2	39.4	7.5	>1.00	0.39	2.66	1.10
14	NGC 4833	12:59:23.48	-70:49:53.02	0.16	0.12	<31.3	-	24.3	4.5	40.7	8.2	>0.53	0.42	2.84	1.18
15	NGC 4833	13:00:06.41	-70:51:32.92	0.07	0.04	47.5	5.5	42.9	4.7	<54.3	-	<0.27	0.23	2.86	1.19
16	NGC 4833	12:59:04.85	-70:50:53.29	0.16	0.02	172.0	5.3	160.0	4.8	150.0	8.5	-0.28	0.13	2.93	1.21
17	NGC 4833	13:00:08.66	-70:51:46.36	0.09	0.19	<39.0	-	25.9	4.9	<46.0	-	-	-	2.96	1.23
18	NGC 4833	13:00:08.78	-70:51:42.12	0.74	0.90	88.3	16.7	32.0	5.1	<44.8	-	<-1.38	0.39	2.99	1.24
19	NGC 4833	12:59:21.89	-70:49:42.00	0.22	0.20	160.0	16.5	71.7	5.0	47.6	9.5	-2.46	0.46	3.05	1.27
20	NGC 4833	12:58:57.41	-70:51:30.37	0.07	0.06	128.0	5.3	113.0	5.1	81.7	10.1	-0.91	0.27	3.18	1.32

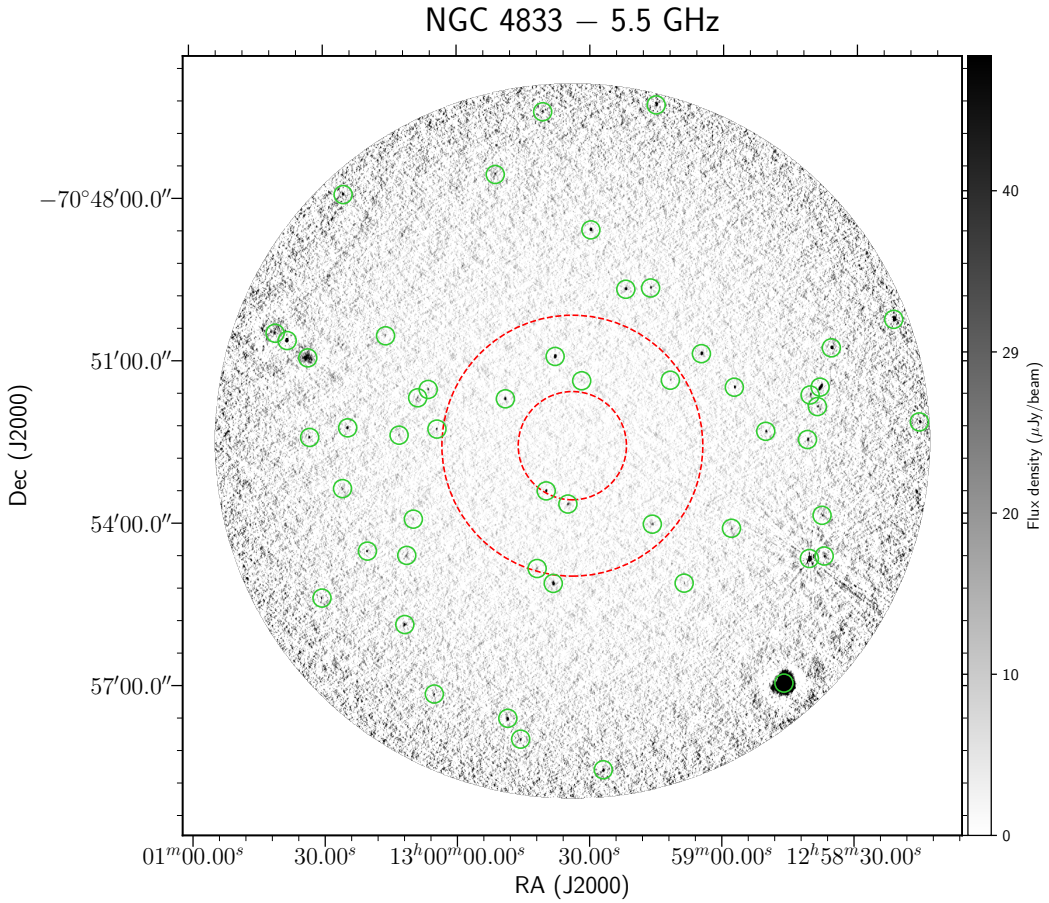
NGC 4833 – 5.5 GHz
−70°48′00.0″
51′00.0″
54′00.0″
57′00.0″
Dec (J2000)
01m00.00s
30.00s
13h00m00.00s
30.00s
59m00.00s
12h58m30.00s
RA (J2000)
Flux density (μJy/beam)
0
10
20
29
40

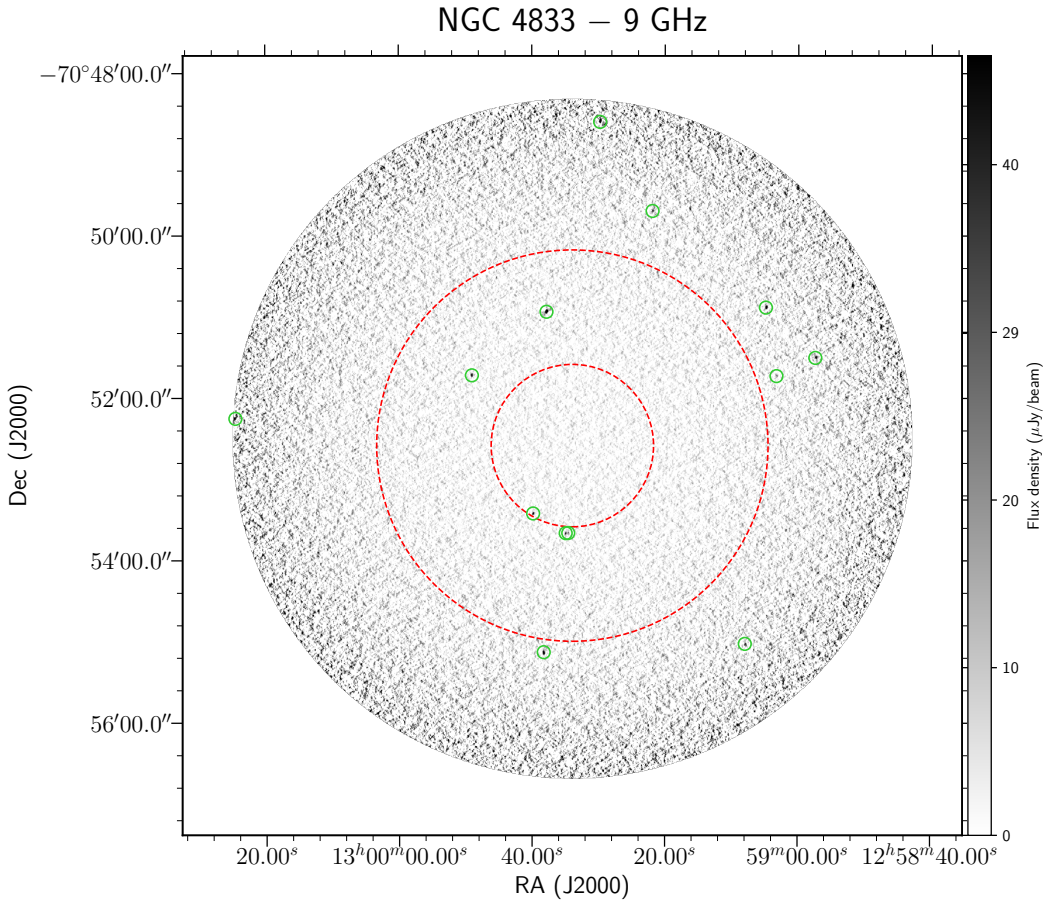
NGC 4833 – 9 GHz
−70°48′00.0″
50′00.0″
52′00.0″
54′00.0″
56′00.0″
Dec (J2000)
20.00s
13h00m00.00s
40.00s
20.00s
59m00.00s
12h58m40.00s
RA (J2000)
Flux density (μJy/beam)
0
10
20
29
40

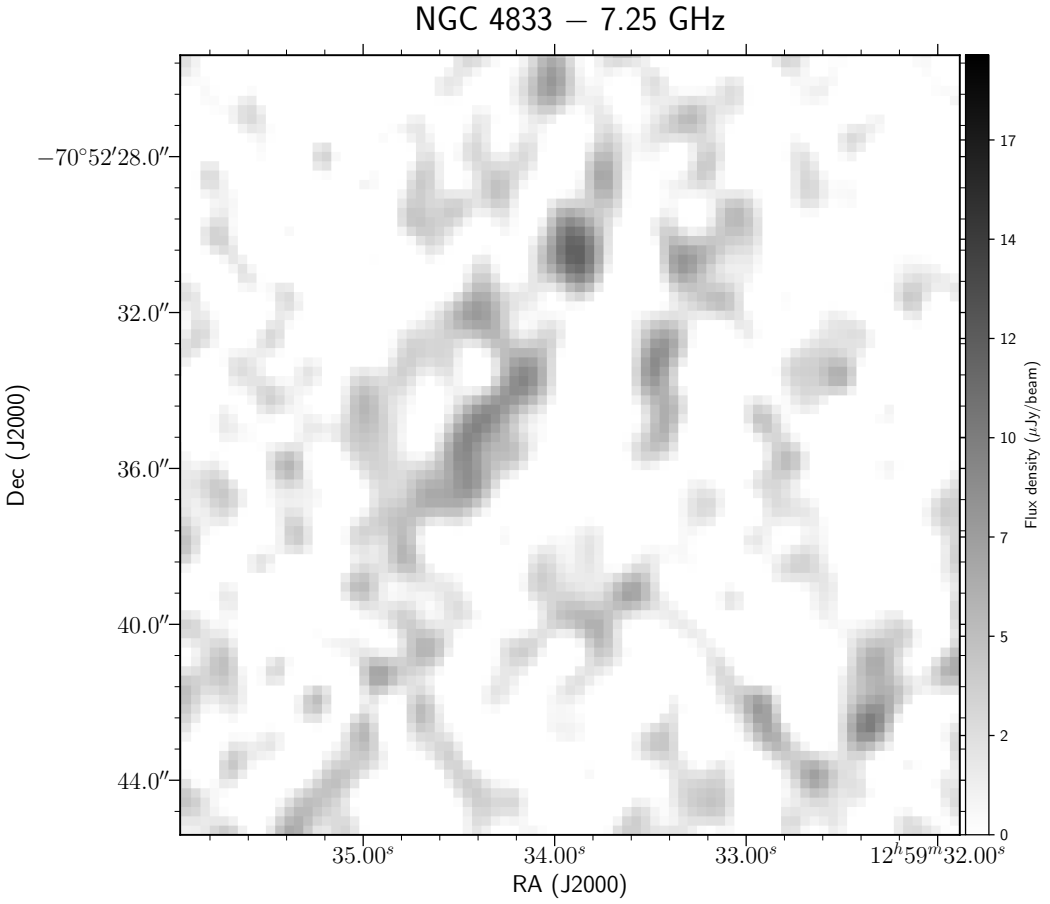
NGC 4833 – 7.25 GHz
−70°52′28.0″
32.0″
36.0″
40.0″
44.0″
Dec (J2000)
35.00s
34.00s
33.00s
12h59m32.00s
RA (J2000)
Flux density (μJy/beam)
17
14
12
10
7
5
2
0

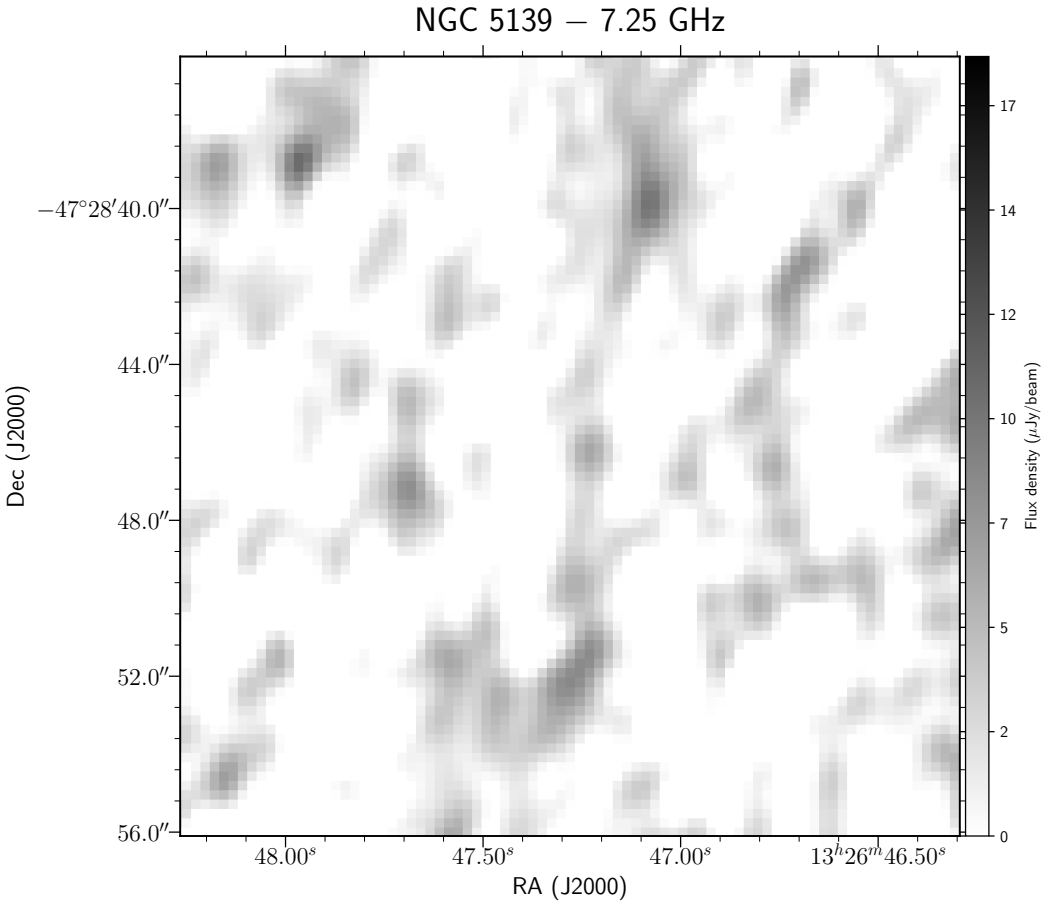
NGC 5139 – 7.25 GHz
−47°28′40.0″
44.0″
48.0″
52.0″
56.0″
Dec (J2000)
48.00s
47.50s
47.00s
13h26m46.50s
RA (J2000)
Flux density (μJy/beam)
17
14
12
10
7
5
2
0

Table 3.11: NGC 5139

ID	Field	RA	DEC	Δ RA ($''$)	Δ DEC ($''$)	$S_{5.5}$ (μJy)	$\Delta S_{5.5}$ (μJy)	$S_{7.25}$ (μJy)	$\Delta S_{7.25}$ (μJy)	S_9 (μJy)	ΔS_9 (μJy)	α	$\Delta\alpha$	R/R_c	R/R_h
1	NGC 5139	13:26:41.76	-47:29:19.42	0.19	0.12	39.7	3.9	27.4	3.1	17.9	4.8	-1.61	0.58	0.46	0.22
2	NGC 5139	13:26:39.03	-47:28:49.47	0.03	0.15	26.8	3.9	18.4	3.3	<22.9	-	<-0.32	0.29	0.59	0.28
3	NGC 5139	13:26:38.29	-47:29:03.85	0.47	1.20	234.0	25.7	136.0	19.8	22.4	5.8	-4.76	0.58	0.65	0.31
4	NGC 5139	13:26:56.28	-47:28:29.46	0.26	0.01	26.7	3.8	26.6	3.2	26.8	6.0	0.01	0.52	0.65	0.31
5	NGC 5139	13:26:38.20	-47:28:56.49	0.08	0.05	<24.1	-	15.4	3.4	39.6	5.7	>1.01	0.29	0.65	0.31
6	NGC 5139	13:26:38.38	-47:29:05.15	0.56	0.80	234.0	25.7	136.0	19.8	35.6	5.8	-3.82	0.41	0.65	0.31
7	NGC 5139	13:26:38.13	-47:29:04.73	0.98	0.84	234.0	25.7	136.0	19.8	172.0	30.7	-0.63	0.43	0.67	0.32
8	NGC 5139	13:26:38.12	-47:29:11.01	0.30	1.14	<42.6	-	86.0	15.2	34.7	6.4	>-0.42	0.38	0.68	0.32
9	NGC 5139	13:26:47.65	-47:30:31.87	0.16	0.10	27.9	4.0	20.9	3.3	<22.9	-	<-0.40	0.3	0.74	0.35
10	NGC 5139	13:26:54.76	-47:30:04.17	0.02	0.11	<22.0	-	19.1	3.4	31.5	6.1	>0.73	0.4	0.77	0.36
11	NGC 5139	13:26:39.30	-47:30:44.10	0.07	0.04	35.4	4.7	30.9	4.2	28.4	6.7	-0.45	0.54	1.01	0.48
12	NGC 5139	13:26:45.37	-47:31:13.36	0.75	0.63	<21.9	-	22.2	4.0	28.0	7.5	>0.50	0.56	1.04	0.50
13	NGC 5139	13:26:41.16	-47:31:16.51	0.16	0.35	20.4	4.6	24.0	4.3	37.0	7.9	1.20	0.65	1.14	0.54
14	NGC 5139	13:26:45.00	-47:25:57.28	0.01	0.01	41.4	4.6	32.5	4.2	<42.9	-	<0.07	0.23	1.20	0.57
15	NGC 5139	13:26:34.37	-47:30:42.59	0.12	0.14	29.4	4.7	30.3	4.5	32.3	8.4	0.21	0.64	1.23	0.58
16	NGC 5139	13:26:28.57	-47:28:19.42	0.22	0.25	29.2	5.0	25.0	5.0	<42.2	-	<0.75	0.35	1.35	0.64
17	NGC 5139	13:27:06.49	-47:28:53.47	0.37	0.30	29.0	5.2	20.1	5.2	<61.0	-	<1.51	0.37	1.37	0.65
18	NGC 5139	13:26:30.41	-47:27:11.99	0.05	0.09	61.6	5.4	52.3	5.3	39.3	8.7	-0.91	0.5	1.37	0.65
19	NGC 5139	13:26:57.22	-47:31:34.87	0.03	0.08	81.6	5.1	71.6	5.4	55.5	12.8	-0.77	0.49	1.38	0.66
20	NGC 5139	13:26:58.69	-47:31:40.69	1.57	0.54	19.0	5.3	31.7	6.0	<47.8	-	<1.87	0.59	1.47	0.70

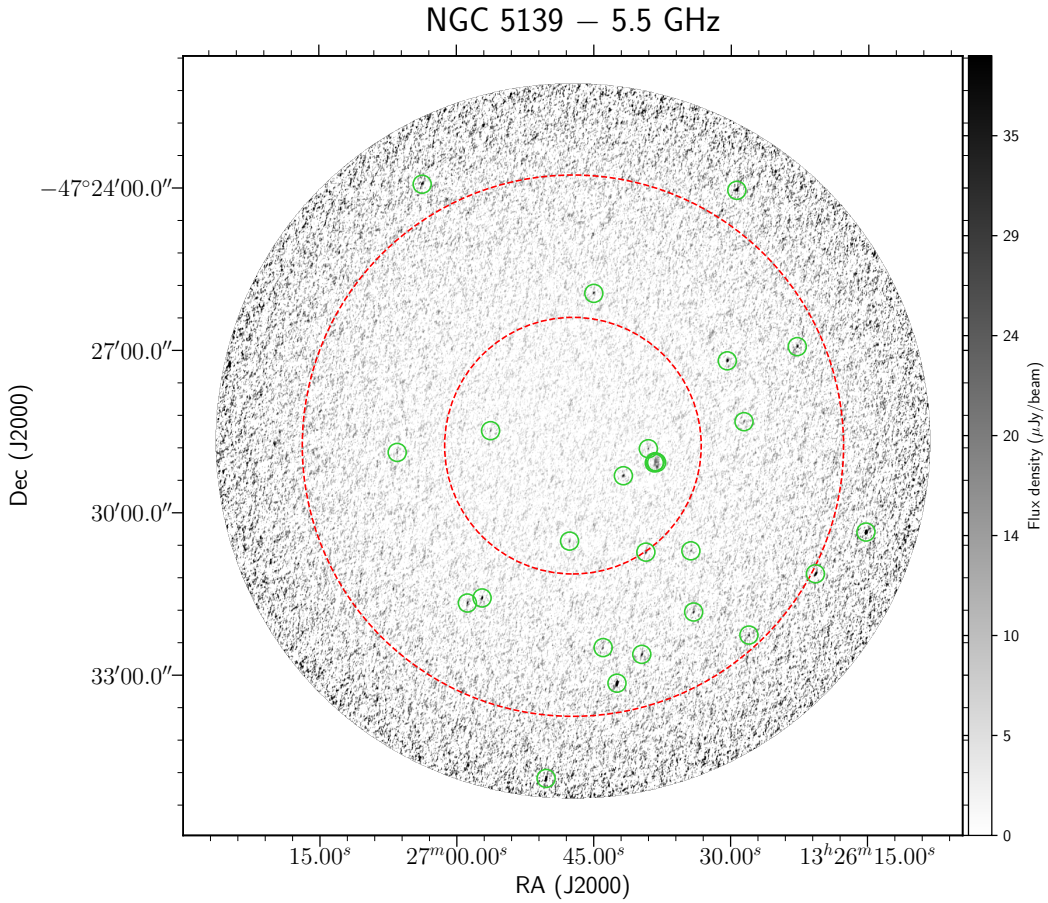
NGC 5139 — 5.5 GHz
−47°24′00.0″
27′00.0″
30′00.0″
33′00.0″
Dec (J2000)
15.00s
27m00.00s
45.00s
30.00s
13h26m15.00s
RA (J2000)
Flux density (μJy/beam)
35
29
24
20
14
10
5
0

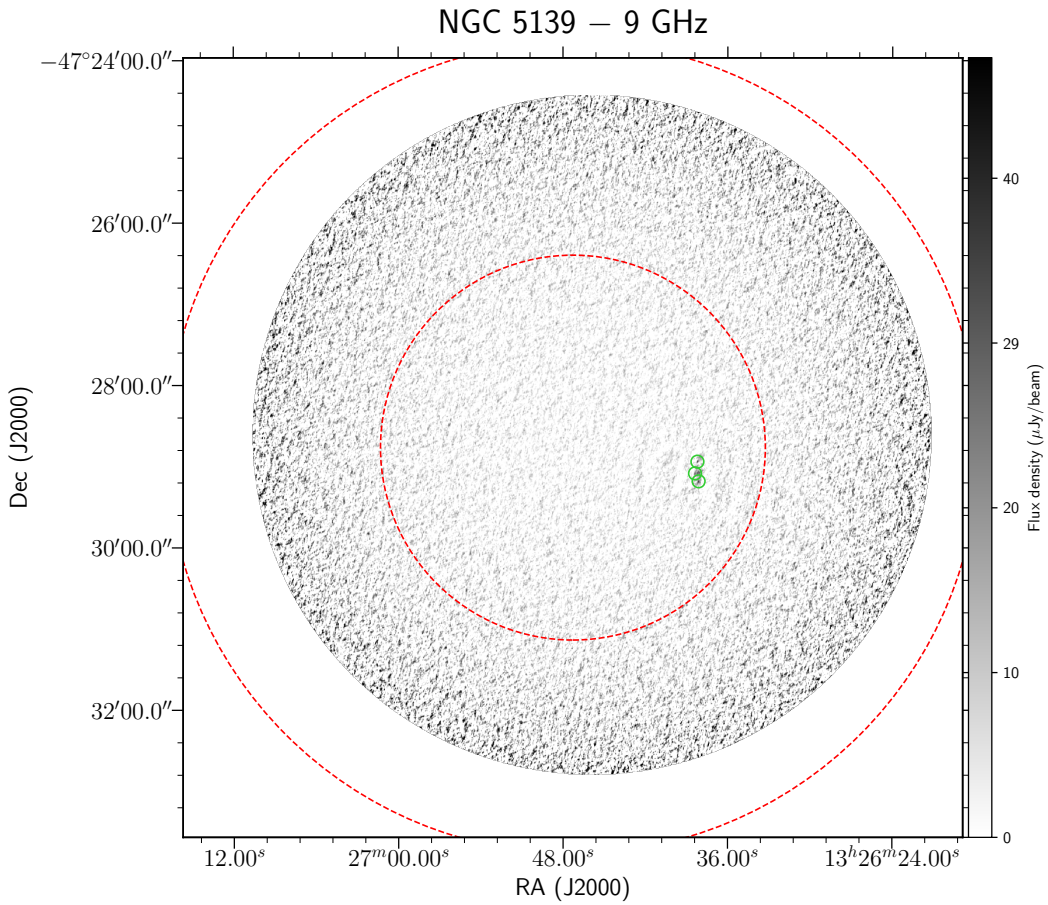
NGC 5139 — 9 GHz
−47°24′00.0″
26′00.0″
28′00.0″
30′00.0″
32′00.0″
Dec (J2000)
12.00s
27m00.00s
48.00s
36.00s
13h26m24.00s
RA (J2000)
Flux density (μJy/beam)
40
29
20
10
0

Table 3.12: NGC 5927

ID	Field	RA	DEC	Δ RA ($''$)	Δ DEC ($''$)	$S_{5.5}$ (μJy)	$\Delta S_{5.5}$ (μJy)	$S_{7.25}$ (μJy)	$\Delta S_{7.25}$ (μJy)	S_{9} (μJy)	ΔS_{9} (μJy)	α	$\Delta\alpha$	R/R_c	R/R_h
1	NGC 5927	15:28:00.67	-50:40:18.23	0.07	0.15	<12.6	-	<18.1	-	30.5	5.1	>1.80	0.34	0.19	0.07
2	NGC 5927	15:28:00.23	-50:41:02.50	0.09	0.03	81.7	4.3	64.9	3.4	46.9	5.4	-1.14	0.25	1.58	0.60
3	NGC 5927	15:27:58.63	-50:39:35.60	0.10	0.24	21.4	4.2	19.1	3.4	19.2	5.4	-0.22	0.73	2.03	0.78
4	NGC 5927	15:27:53.86	-50:39:25.81	0.19	0.03	<35.6	-	28.7	3.8	31.3	6.1	>-0.26	0.4	3.43	1.31
5	NGC 5927	15:27:53.65	-50:39:25.85	0.71	0.12	35.4	4.6	20.7	3.8	<32.3	-	<-0.19	0.27	3.49	1.33
6	NGC 5927	15:28:07.46	-50:41:25.99	0.01	0.02	87.8	4.4	93.5	3.7	90.2	6.5	0.05	0.18	3.58	1.37
7	NGC 5927	15:28:09.88	-50:39:51.66	0.09	0.11	105.0	17.5	83.6	16.4	<29.9	-	<-2.55	0.34	3.68	1.41
8	NGC 5927	15:28:10.29	-50:41:32.71	0.05	0.06	54.0	4.7	53.5	4.2	47.4	7.3	-0.26	0.37	4.56	1.74
9	NGC 5927	15:27:49.54	-50:39:38.04	0.18	0.04	42.1	4.6	40.6	4.0	44.8	6.9	0.13	0.39	4.57	1.74
10	NGC 5927	15:28:07.45	-50:42:00.16	0.18	0.03	24.5	4.8	22.0	4.2	<37.0	-	<0.84	0.4	4.63	1.77
11	NGC 5927	15:28:00.79	-50:38:19.52	0.16	0.34	25.9	4.8	28.6	4.1	27.3	7.0	0.13	0.69	4.90	1.87
12	NGC 5927	15:28:10.56	-50:38:57.68	0.23	0.08	21.2	4.9	21.4	4.1	<33.9	-	<0.95	0.47	5.03	1.92
13	NGC 5927	15:28:03.89	-50:42:38.70	0.16	0.18	28.5	5.0	23.8	4.6	<42.4	-	<0.81	0.36	5.52	2.11
14	NGC 5927	15:27:51.67	-50:42:17.08	0.07	0.05	71.5	5.0	46.4	4.7	<51.5	-	<-0.67	0.14	5.67	2.16
15	NGC 5927	15:28:02.61	-50:42:44.96	0.29	0.07	30.3	5.2	21.5	4.7	<25.7	-	<-0.33	0.35	5.68	2.17
16	NGC 5927	15:27:57.21	-50:38:00.48	0.24	0.13	55.7	5.1	45.3	4.5	41.4	8.1	-0.60	0.46	5.80	2.22
17	NGC 5927	15:28:06.35	-50:42:41.18	0.18	0.17	84.4	5.3	60.7	4.9	40.3	8.9	-1.50	0.47	5.89	2.25
18	NGC 5927	15:27:56.46	-50:43:21.78	0.02	0.04	198.0	5.7	170.0	5.8	145.0	11.9	-0.63	0.18	7.28	2.78
19	NGC 5927	15:27:43.16	-50:41:46.03	0.06	0.10	56.5	5.7	51.7	5.8	49.1	12.1	-0.29	0.54	7.39	2.82
20	NGC 5927	15:27:40.73	-50:40:01.92	0.05	0.01	255.0	5.9	222.0	6.1	167.0	12.6	-0.86	0.16	7.57	2.89

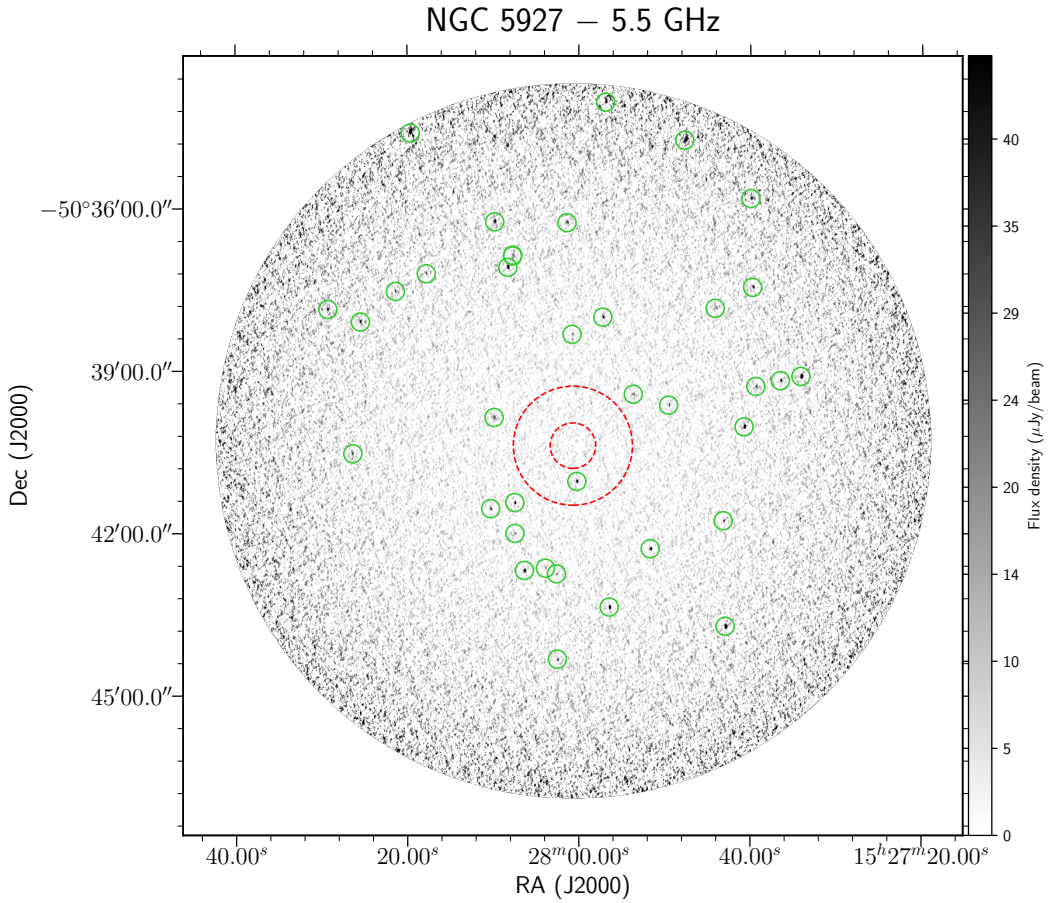
NGC 5927 – 5.5 GHz
−50°36′00.0″
39′00.0″
42′00.0″
45′00.0″
Dec (J2000)
40.00s
20.00s
28m00.00s
40.00s
15h27m20.00s
RA (J2000)
Flux density (μJy/beam)
0
5
10
14
20
24
29
35
40

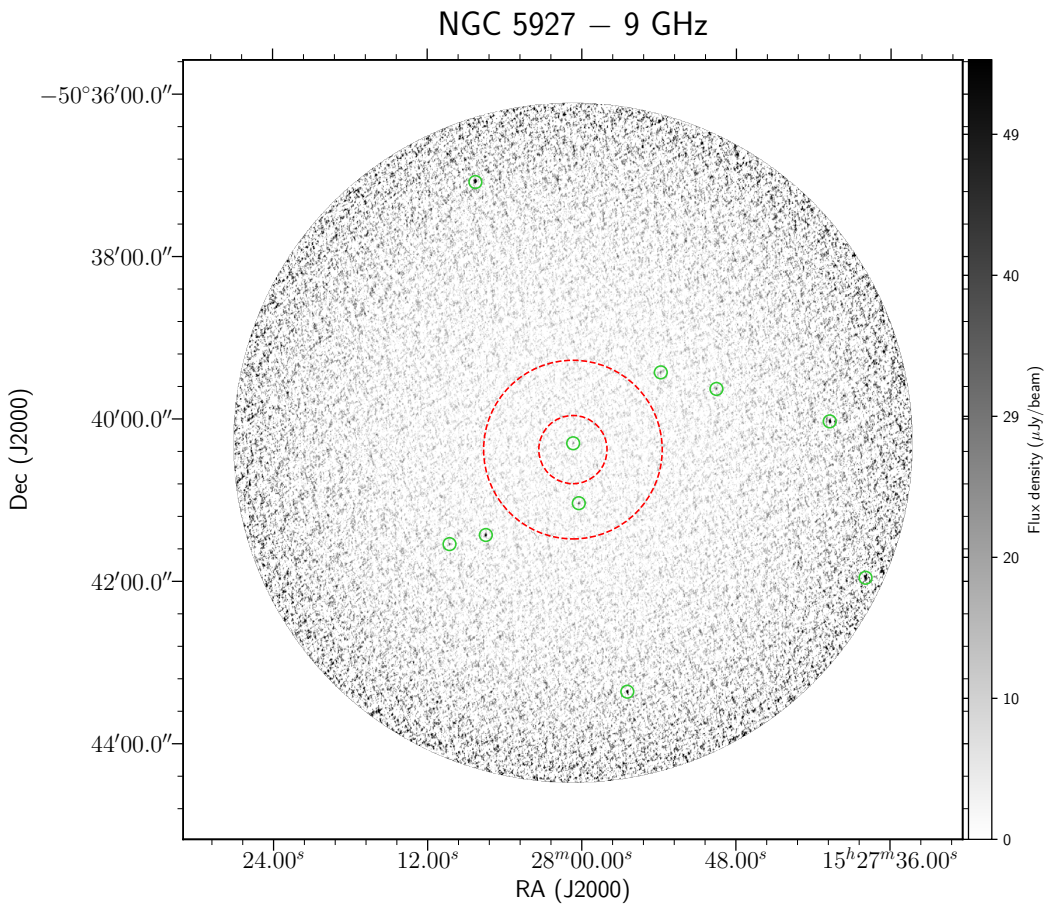
NGC 5927 – 9 GHz
−50°36′00.0″
38′00.0″
40′00.0″
42′00.0″
44′00.0″
Dec (J2000)
24.00s
12.00s
28m00.00s
48.00s
15h27m36.00s
RA (J2000)
Flux density (μJy/beam)
0
10
20
29
40
49

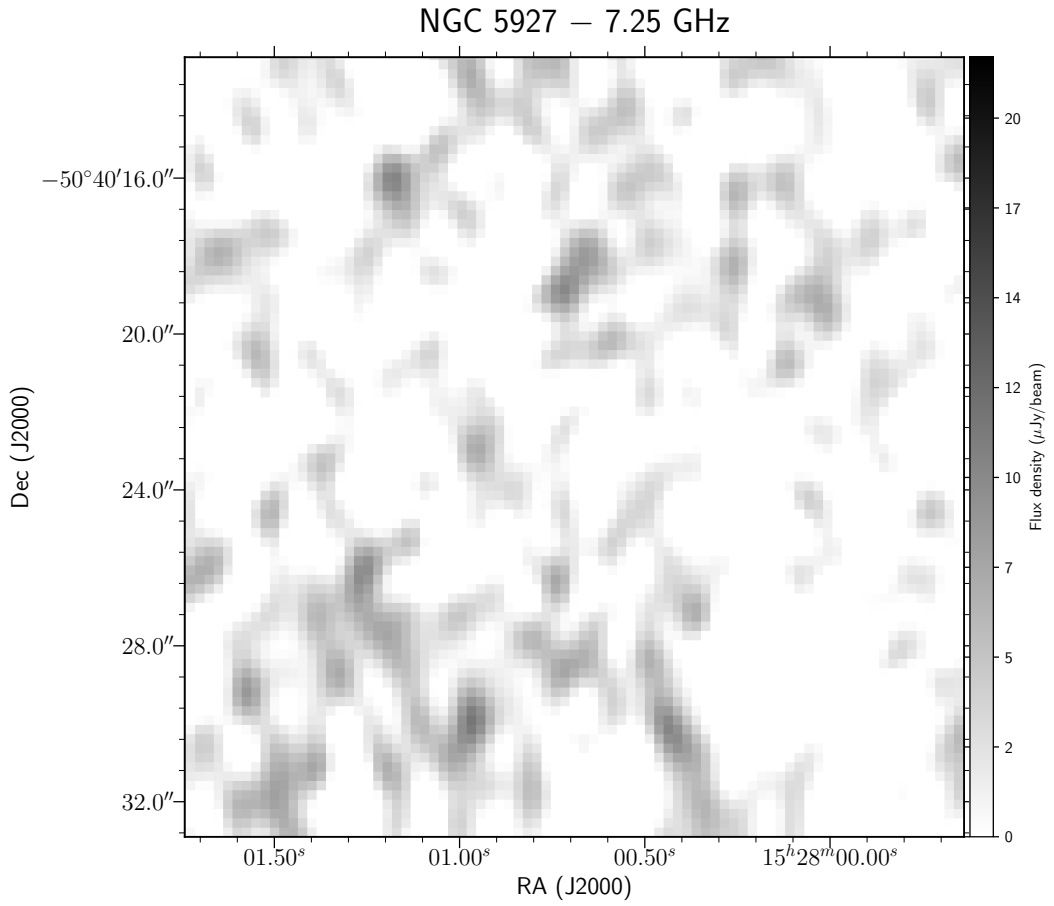
NGC 5927 — 7.25 GHz
−50°40′16.0″
20.0″
24.0″
28.0″
32.0″
Dec (J2000)
01.50s
01.00s
00.50s
15h28m00.00s
RA (J2000)
Flux density (μJy/beam)
0
2
5
7
10
12
14
17
20

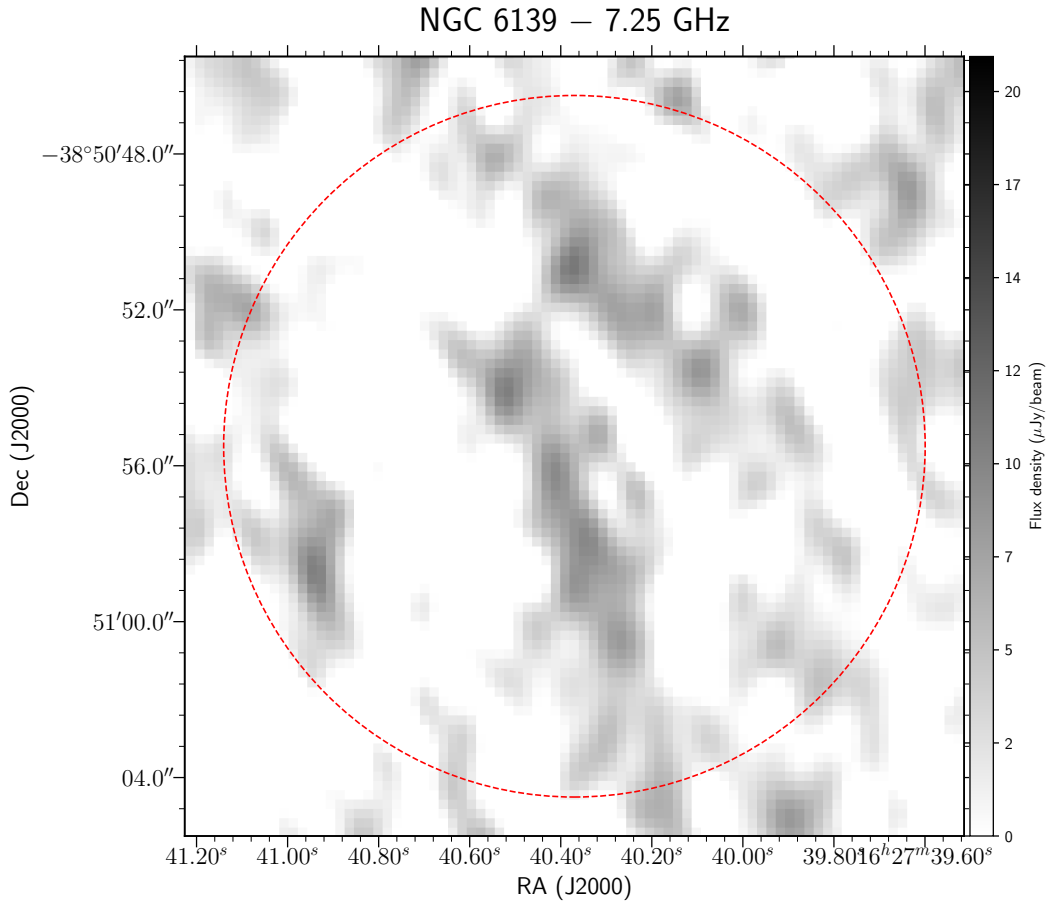
NGC 6139 — 7.25 GHz
−38°50′48.0″
52.0″
56.0″
51′00.0″
04.0″
Dec (J2000)
41.20s
41.00s
40.80s
40.60s
40.40s
40.20s
40.00s
39.80
16h27m39.60s
RA (J2000)
Flux density (μJy/beam)
0
2
5
7
10
12
14
17
20

Table 3.13: NGC 6139

ID	Field	RA	DEC	Δ RA ($''$)	Δ DEC ($''$)	$S_{5.5}$ (μJy)	$\Delta S_{5.5}$ (μJy)	$S_{7.25}$ (μJy)	$\Delta S_{7.25}$ (μJy)	S_{9} (μJy)	ΔS_{9} (μJy)	α	$\Delta\alpha$	R/R$_c$	R/R$_h$
1	NGC 6139	16:27:42.09	-38:50:33.74	0.20	0.35	26.6	4.2	19.7	3.4	21.8	4.7	-0.40	0.56	3.29	0.58
2	NGC 6139	16:27:44.12	-38:50:54.32	0.02	0.01	175.0	4.5	169.0	11.9	76.3	5.1	-1.69	0.14	4.87	0.86
3	NGC 6139	16:27:39.44	-38:49:50.30	1.01	0.23	23.6	4.3	11.4	3.3	<26.6	-	<0.24	0.38	7.34	1.30
4	NGC 6139	16:27:34.87	-38:50:39.99	0.23	0.04	28.9	4.3	24.9	3.3	18.3	4.9	-0.91	0.63	7.35	1.30
5	NGC 6139	16:27:47.95	-38:50:53.33	0.08	0.19	134.0	14.1	111.0	12.3	57.5	5.5	-1.71	0.29	9.85	1.74
6	NGC 6139	16:27:46.02	-38:51:54.99	0.04	0.12	80.5	4.3	60.2	3.7	39.3	5.6	-1.45	0.31	9.88	1.74
7	NGC 6139	16:27:49.67	-38:51:11.55	0.05	0.03	77.5	4.6	61.9	3.7	57.3	5.9	-0.62	0.24	12.20	2.15
8	NGC 6139	16:27:41.21	-38:53:01.36	0.09	0.40	29.0	4.9	29.5	4.2	29.9	6.8	0.08	0.55	14.03	2.48
9	NGC 6139	16:27:41.18	-38:53:01.52	0.28	0.37	29.0	4.9	29.5	4.2	26.4	6.9	-0.19	0.62	14.04	2.48
10	NGC 6139	16:27:50.88	-38:52:05.36	0.01	0.04	254.0	6.1	188.0	4.5	109.0	7.3	-1.72	0.15	15.69	2.77
11	NGC 6139	16:27:41.90	-38:53:25.40	0.02	0.00	56.9	5.1	53.0	4.3	49.4	7.8	-0.29	0.39	16.77	2.96
12	NGC 6139	16:27:53.36	-38:50:13.48	0.09	0.09	31.2	5.0	23.2	4.4	<33.0	-	<0.12	0.33	17.50	3.09
13	NGC 6139	16:27:42.13	-38:48:01.51	0.22	0.13	41.3	6.8	24.9	6.3	<37.1	-	<-0.22	0.34	19.47	3.44
14	NGC 6139	16:27:30.90	-38:48:27.93	0.18	0.25	45.4	5.4	41.7	5.2	49.7	9.4	0.18	0.48	20.49	3.62
15	NGC 6139	16:27:31.16	-38:53:31.28	0.13	0.07	32.1	6.0	26.8	5.6	<44.6	-	<0.67	0.38	21.03	3.71
16	NGC 6139	16:27:24.22	-38:51:22.46	0.05	0.48	44.6	5.9	31.8	5.7	<49.0	-	<0.19	0.27	21.18	3.74
17	NGC 6139	16:27:36.17	-38:47:50.98	0.12	0.03	33.3	5.9	29.4	5.6	<61.1	-	<1.23	0.36	21.21	3.74
18	NGC 6139	16:27:43.44	-38:47:36.16	0.03	0.01	1260.0	38.2	1270.0	53.3	1280.0	75.3	0.03	0.13	22.51	3.97
19	NGC 6139	16:27:48.64	-38:53:54.35	0.12	0.04	54.2	6.2	37.5	6.1	<55.2	-	<0.04	0.23	22.59	3.99
20	NGC 6139	16:27:27.85	-38:54:04.94	0.00	0.04	44.6	7.2	34.8	8.0	<79.9	-	<1.18	0.33	26.59	4.69

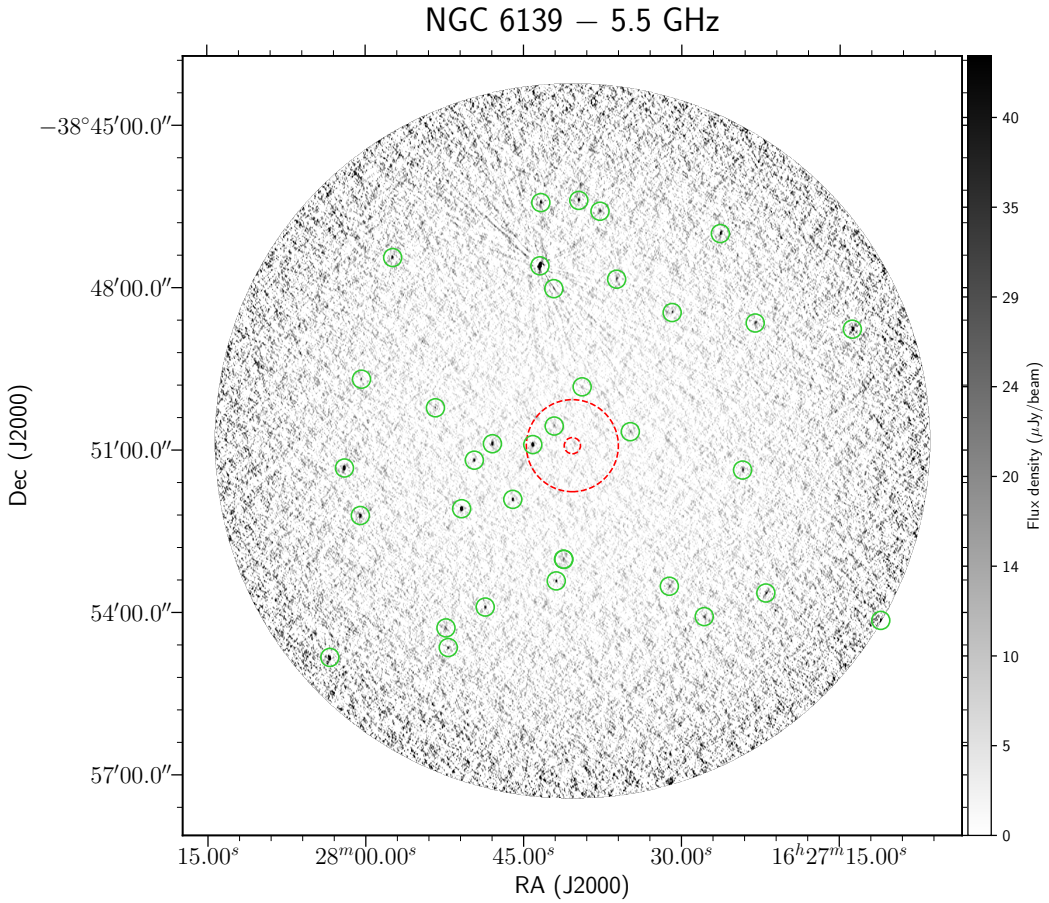
NGC 6139 – 5.5 GHz
−38°45′00.0″
48′00.0″
51′00.0″
54′00.0″
57′00.0″
Dec (J2000)
15.00s
28m00.00s
45.00s
30.00s
16h27m15.00s
RA (J2000)
Flux density (μJy/beam)
0
5
10
14
20
24
29
35
40

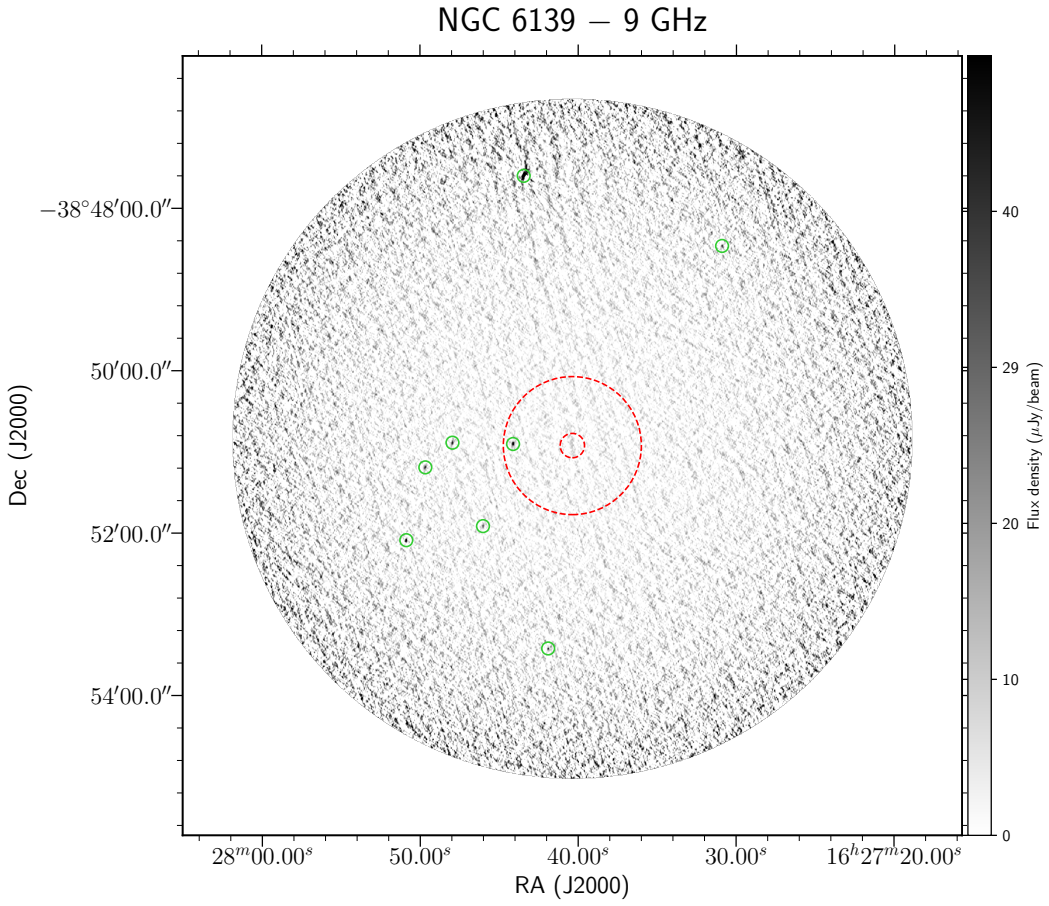
NGC 6139 – 9 GHz
−38°48′00.0″
50′00.0″
52′00.0″
54′00.0″
Dec (J2000)
28m00.00s
50.00s
40.00s
30.00s
16h27m20.00s
RA (J2000)
Flux density (μJy/beam)
0
10
20
29
40

Table 3.14: NGC 6304

ID	Field	RA	DEC	Δ RA ($''$)	Δ DEC ($''$)	$S_{5.5}$ (μJy)	$\Delta S_{5.5}$ (μJy)	$S_{7.25}$ (μJy)	$\Delta S_{7.25}$ (μJy)	S_{9} (μJy)	ΔS_{9} (μJy)	α	$\Delta\alpha$	R/R$_c$	R/R$_h$
1	NGC 6304	17:14:30.47	-29:27:29.84	0.01	0.14	20.2	3.4	11.0	2.8	<17.2	-	<-0.33	0.34	2.13	0.32
2	NGC 6304	17:14:33.10	-29:26:34.42	0.05	0.08	75.0	4.7	57.5	3.4	43.9	4.7	-1.09	0.26	5.54	0.82
3	NGC 6304	17:14:34.28	-29:28:56.08	0.22	0.31	25.7	4.4	17.9	3.3	21.1	4.0	-0.40	0.51	6.15	0.91
4	NGC 6304	17:14:28.95	-29:28:47.95	0.07	0.27	<23.0	-	15.3	2.6	18.4	4.0	>-0.45	0.45	6.17	0.91
5	NGC 6304	17:14:33.27	-29:26:23.22	0.03	0.02	33.3	4.8	24.9	3.5	22.3	4.2	-0.82	0.49	6.44	0.95
6	NGC 6304	17:14:38.60	-29:29:00.08	0.12	0.20	25.6	3.9	20.4	3.1	<26.4	-	<0.06	0.31	8.97	1.33
7	NGC 6304	17:14:23.84	-29:27:11.58	0.08	0.23	19.8	4.0	20.1	3.2	<33.4	-	<1.06	0.42	9.08	1.34
8	NGC 6304	17:14:23.21	-29:27:08.48	0.14	0.22	24.6	4.1	17.2	3.3	<23.7	-	<-0.08	0.34	9.77	1.44
9	NGC 6304	17:14:23.80	-29:28:41.75	0.00	0.08	31.3	4.1	21.3	3.9	<31.1	-	<-0.01	0.27	9.91	1.46
10	NGC 6304	17:14:42.08	-29:26:51.83	0.06	0.37	<31.3	-	21.4	3.5	<33.7	-	-	-	10.98	1.62
11	NGC 6304	17:14:42.32	-29:28:26.39	0.02	0.09	27.4	4.8	21.3	3.4	<30.1	-	<0.19	0.36	10.98	1.62
12	NGC 6304	17:14:22.86	-29:28:47.40	0.09	0.04	28.9	4.3	19.1	3.6	<28.8	-	<-0.01	0.3	10.99	1.62
13	NGC 6304	17:14:21.41	-29:27:31.45	0.02	0.29	19.2	4.4	21.2	3.5	<35.3	-	<1.24	0.47	11.28	1.67
14	NGC 6304	17:14:20.28	-29:28:17.36	0.03	0.03	38.8	4.5	29.5	4.4	<39.6	-	<0.04	0.24	12.70	1.88
15	NGC 6304	17:14:25.32	-29:25:28.37	0.02	0.06	109.0	5.2	84.9	4.6	61.3	6.9	-1.17	0.25	12.90	1.91
16	NGC 6304	17:14:23.45	-29:25:18.04	0.02	0.27	31.1	4.9	28.5	5.3	<52.8	-	<1.08	0.32	14.70	2.17
17	NGC 6304	17:14:20.97	-29:25:47.27	0.15	0.14	28.8	4.9	24.2	4.5	<45.6	-	<0.93	0.35	14.88	2.20
18	NGC 6304	17:14:27.40	-29:24:39.87	0.01	0.22	64.6	4.9	46.6	5.4	<58.4	-	<-0.20	0.16	15.40	2.28
19	NGC 6304	17:14:43.48	-29:25:11.14	0.05	0.17	76.2	6.5	63.2	5.4	<62.4	-	<-0.41	0.17	16.77	2.48
20	NGC 6304	17:14:40.32	-29:24:15.03	0.06	0.11	753.0	14.3	770.0	43.0	528.0	50.4	-0.72	0.19	18.53	2.74

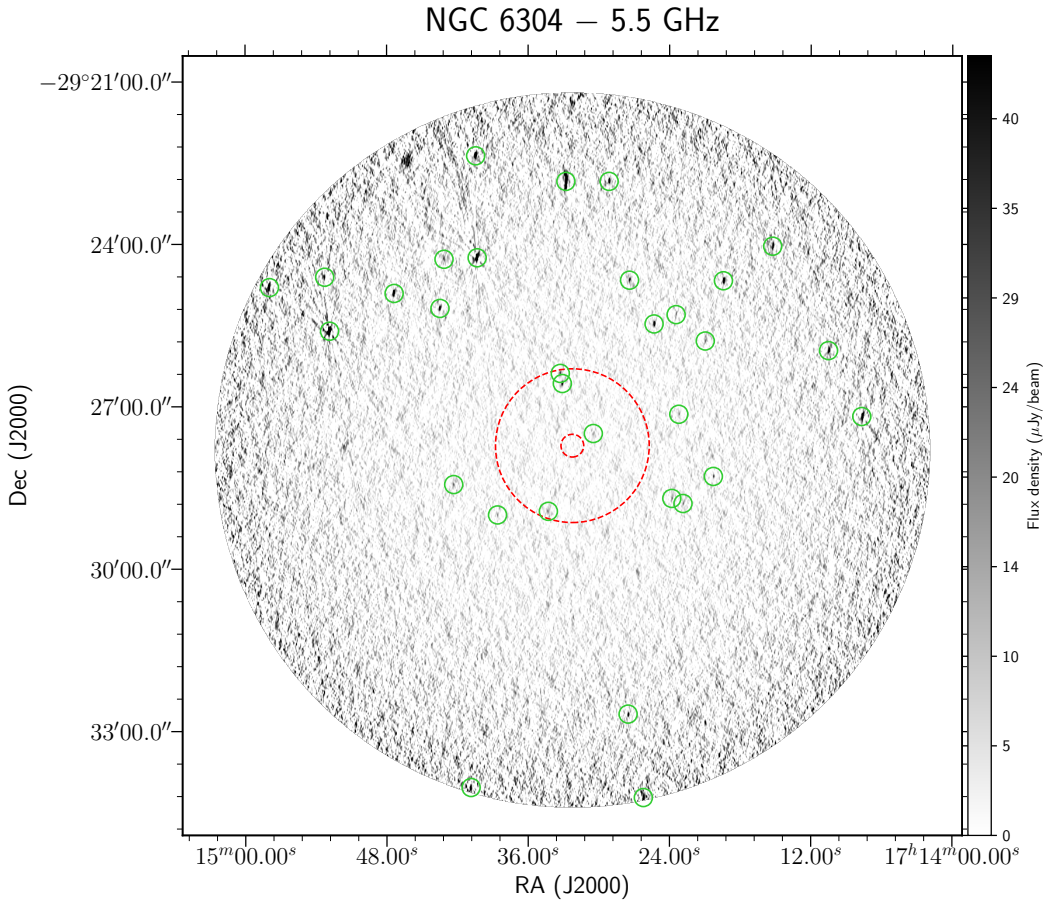
NGC 6304 – 5.5 GHz
−29°21′00.0″
24′00.0″
27′00.0″
30′00.0″
33′00.0″
Dec (J2000)
15^m00.00^s
48.00^s
36.00^s
24.00^s
12.00^s
17^h14^m00.00^s
RA (J2000)
Flux density (μJy/beam)
0
5
10
14
20
24
29
35
40

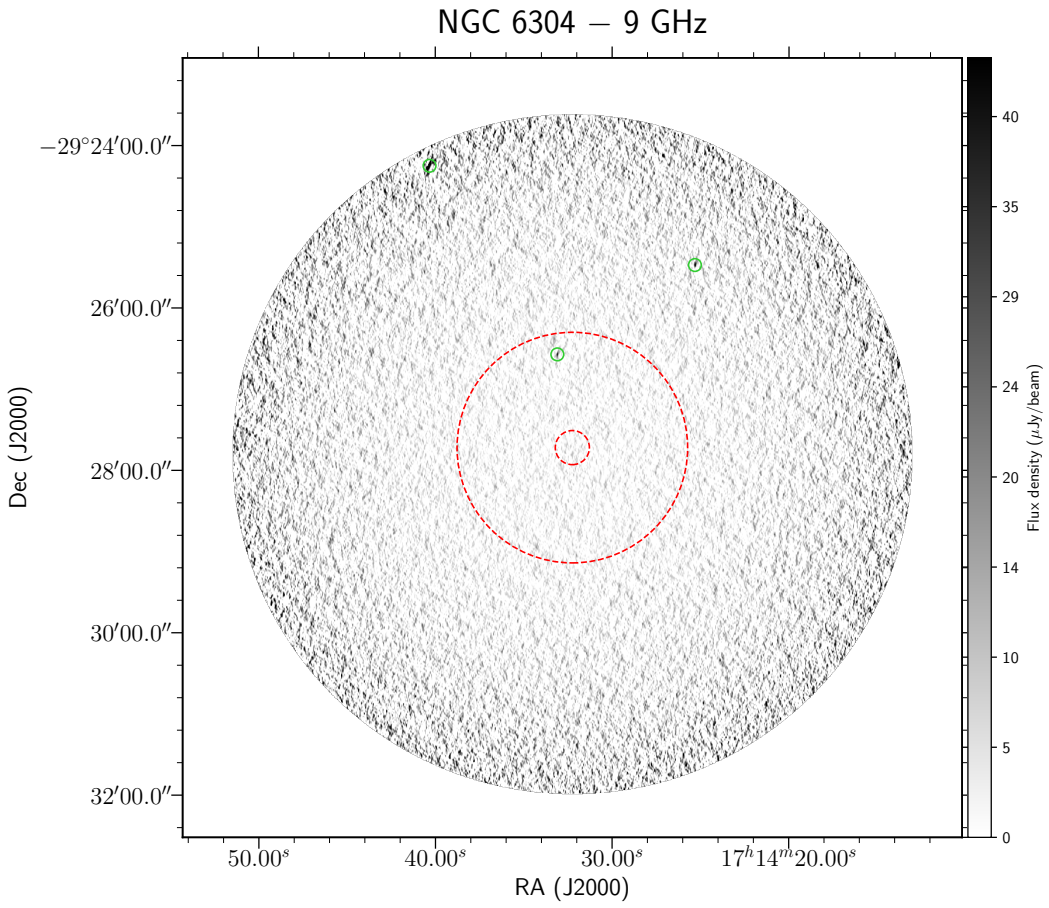
NGC 6304 – 9 GHz
−29°24′00.0″
26′00.0″
28′00.0″
30′00.0″
32′00.0″
Dec (J2000)
50.00^s
40.00^s
30.00^s
17^h14^m20.00^s
RA (J2000)
Flux density (μJy/beam)
0
5
10
14
20
24
29
35
40

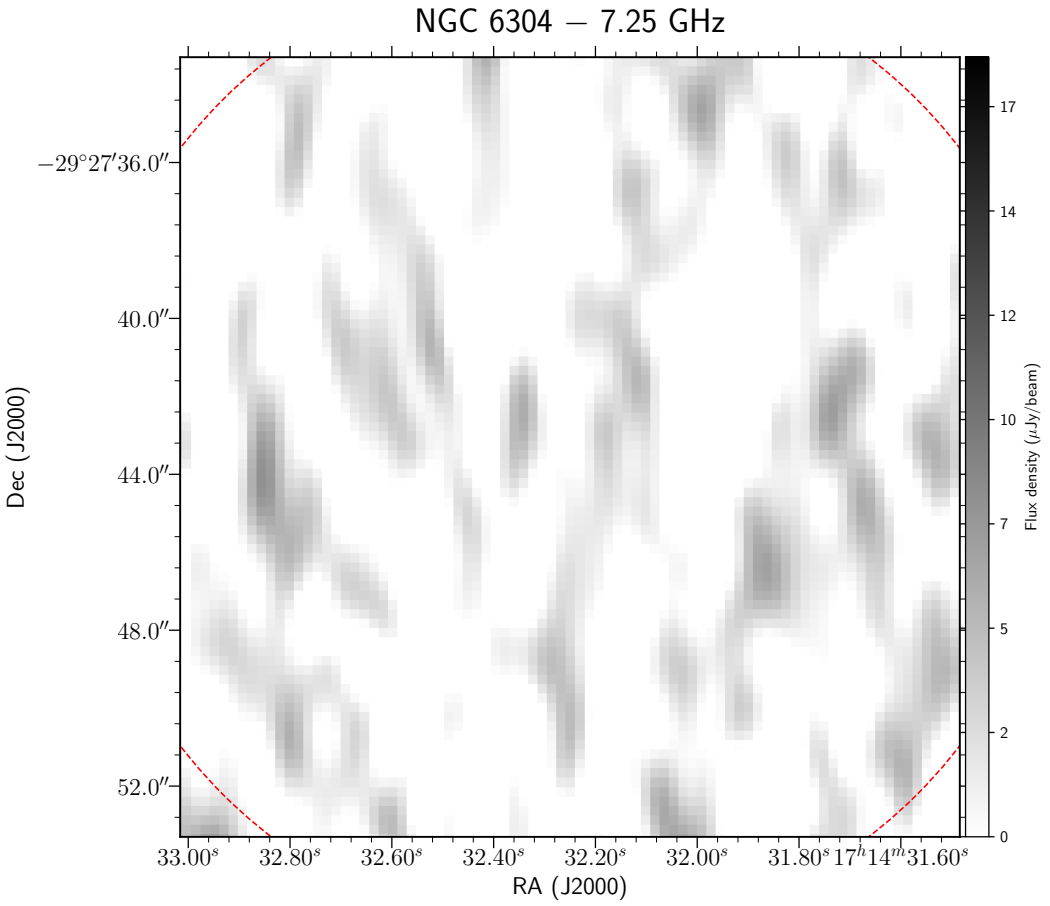
NGC 6304 — 7.25 GHz
−29°27′36.0″
40.0″
44.0″
48.0″
52.0″
Dec (J2000)
33.00s
32.80s
32.60s
32.40s
32.20s
32.00s
31.80s
17h14m31.60s
RA (J2000)
Flux density (μJy/beam)
0
2
5
7
10
12
14
17

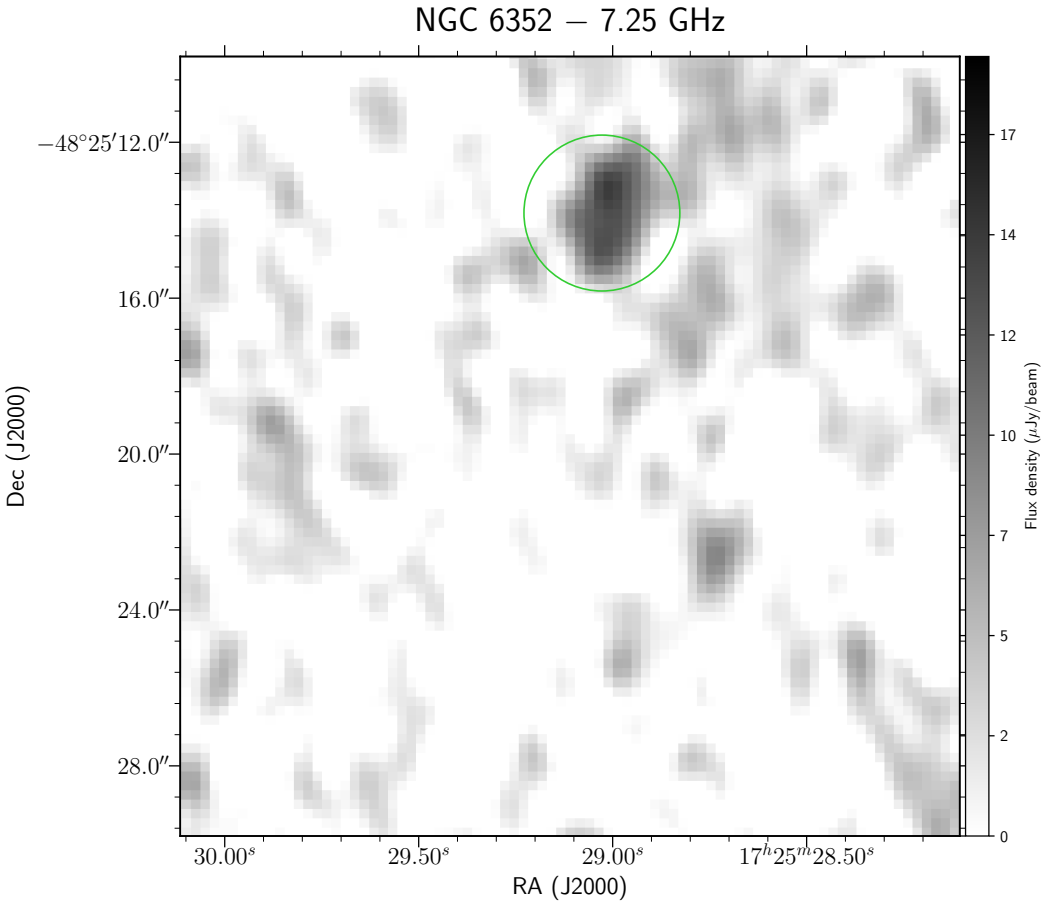
NGC 6352 — 7.25 GHz
−48°25′12.0″
16.0″
20.0″
24.0″
28.0″
Dec (J2000)
30.00s
29.50s
29.00s
17h25m28.50s
RA (J2000)
Flux density (μJy/beam)
0
2
5
7
10
12
14
17

Table 3.15: NGC 6352

ID	Field	RA	DEC	Δ RA ($''$)	Δ DEC ($''$)	$S_{5.5}$ (μJy)	$\Delta S_{5.5}$ (μJy)	$S_{7.25}$ (μJy)	$\Delta S_{7.25}$ (μJy)	S_9 (μJy)	ΔS_9 (μJy)	α	$\Delta\alpha$	R/R_c	R/R_h
1	NGC 6352	17:25:29.03	-48:25:13.82	0.38	0.06	24.0	3.6	15.9	2.9	<24.2	-	<0.02	0.31	0.12	0.05
2	NGC 6352	17:25:27.32	-48:25:09.06	0.03	0.02	163.0	3.5	163.0	3.1	164.0	4.1	0.01	0.07	0.42	0.17
3	NGC 6352	17:25:29.08	-48:24:56.83	0.20	0.07	29.3	3.5	21.7	2.7	15.5	4.1	-1.27	0.61	0.46	0.19
4	NGC 6352	17:25:25.86	-48:25:31.06	0.05	0.01	20.5	3.5	15.1	2.9	<23.0	-	<0.23	0.35	0.69	0.28
5	NGC 6352	17:25:25.04	-48:24:59.73	0.02	0.03	65.7	3.6	50.4	2.8	37.1	4.4	-1.17	0.26	0.91	0.37
6	NGC 6352	17:25:32.57	-48:24:45.06	0.08	0.28	25.1	3.8	18.2	2.9	<25.8	-	<0.06	0.31	0.98	0.40
7	NGC 6352	17:25:30.61	-48:26:08.54	0.12	0.08	50.2	3.7	38.4	2.9	27.0	4.6	-1.26	0.38	1.02	0.41
8	NGC 6352	17:25:23.97	-48:24:59.35	0.18	0.59	15.0	3.6	15.1	2.8	15.1	4.4	0.02	0.76	1.11	0.45
9	NGC 6352	17:25:29.88	-48:24:14.01	0.06	0.07	42.3	3.9	31.6	2.8	20.4	4.5	-1.49	0.5	1.33	0.54
10	NGC 6352	17:25:23.53	-48:26:06.62	0.00	0.19	19.6	3.7	13.7	3.1	<21.3	-	<0.17	0.38	1.46	0.59
11	NGC 6352	17:25:37.89	-48:25:06.03	0.32	0.15	22.0	3.8	20.9	3.3	23.6	5.2	0.16	0.58	1.78	0.72
12	NGC 6352	17:25:27.88	-48:26:52.41	0.49	0.28	24.0	3.9	15.1	3.2	<24.7	-	<0.06	0.33	1.88	0.76
13	NGC 6352	17:25:37.98	-48:25:58.87	0.02	0.01	185.0	3.9	139.0	3.3	88.5	5.5	-1.50	0.13	1.94	0.79
14	NGC 6352	17:25:27.29	-48:23:40.13	0.16	0.05	21.0	4.0	14.0	3.2	<28.5	-	<0.62	0.39	2.03	0.82
15	NGC 6352	17:25:36.50	-48:26:37.28	0.10	0.10	33.0	3.9	22.3	3.5	<34.0	-	<0.06	0.24	2.14	0.87
16	NGC 6352	17:25:19.50	-48:23:58.65	0.07	0.08	140.0	4.0	133.0	3.4	121.0	6.0	-0.30	0.12	2.52	1.02
17	NGC 6352	17:25:20.21	-48:27:08.63	0.14	0.04	24.5	4.2	17.1	3.8	<29.5	-	<0.38	0.35	2.82	1.14
18	NGC 6352	17:25:22.95	-48:27:27.56	0.08	0.18	<12.7	-	<20.9	-	36.2	6.9	>2.13	0.39	2.85	1.15
19	NGC 6352	17:25:19.12	-48:23:34.37	0.12	0.16	19.4	4.1	19.4	3.7	<35.1	-	<1.21	0.44	2.91	1.18
20	NGC 6352	17:25:33.58	-48:22:56.11	0.07	0.05	96.2	4.6	83.9	4.0	72.4	7.0	-0.58	0.22	3.02	1.22

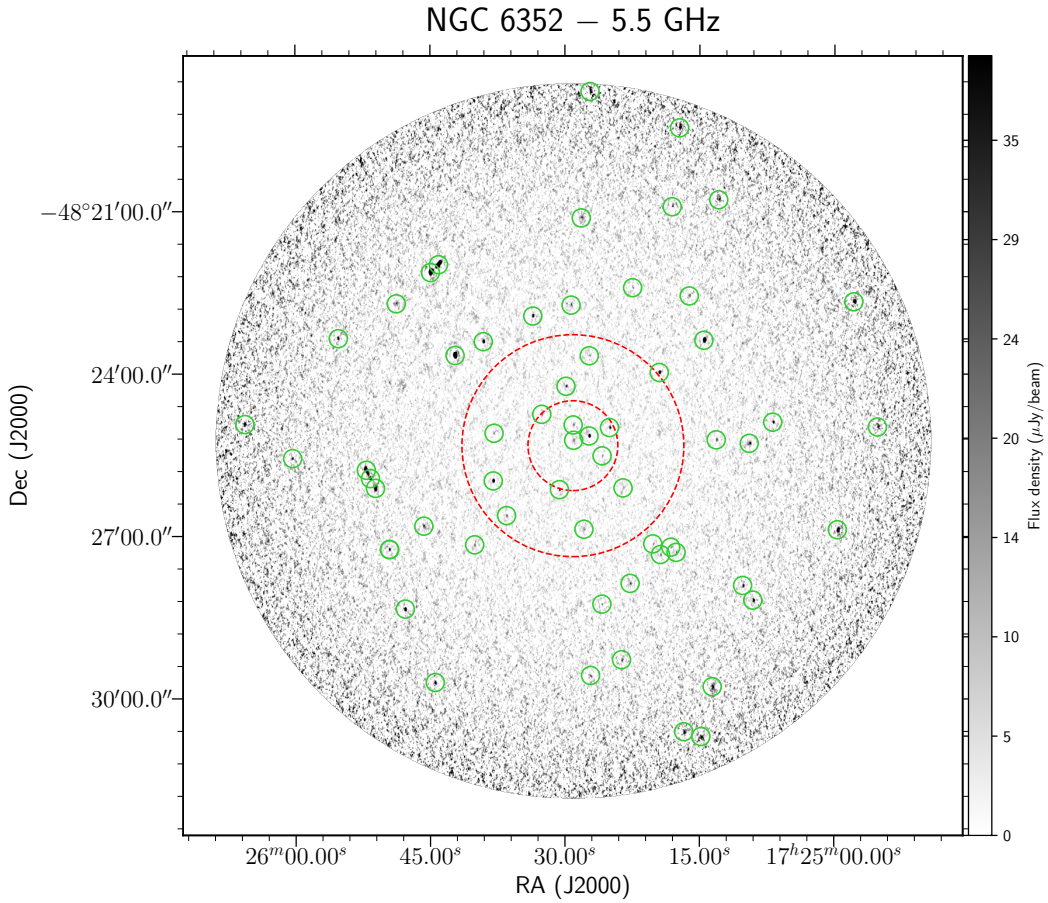
NGC 6352 — 5.5 GHz
−48°21′00.0″
24′00.0″
27′00.0″
30′00.0″
Dec (J2000)
26^m00.00^s
45.00^s
30.00^s
15.00^s
17^h25^m00.00^s
RA (J2000)
Flux density (μJy/beam)
35
29
24
20
14
10
5
0

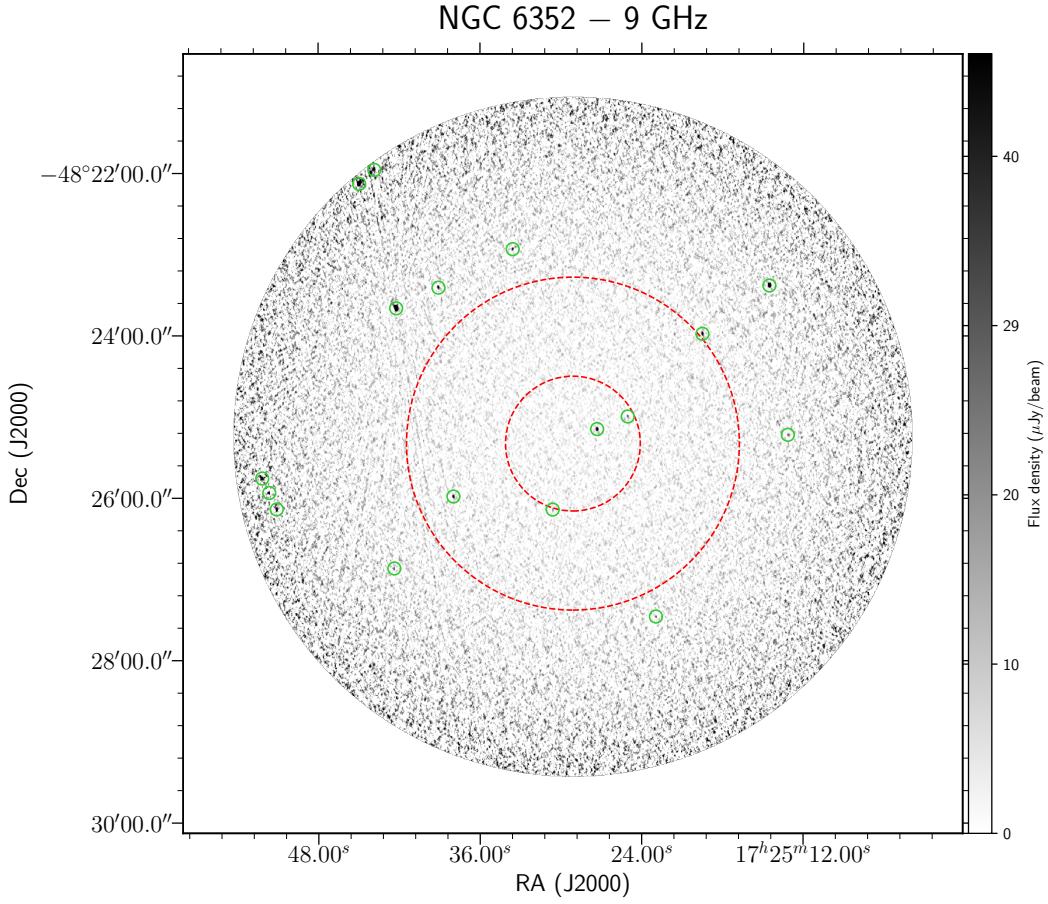
NGC 6352 — 9 GHz
−48°22′00.0″
24′00.0″
26′00.0″
28′00.0″
30′00.0″
Dec (J2000)
48.00^s
36.00^s
24.00^s
17^h25^m12.00^s
RA (J2000)
Flux density (μJy/beam)
40
29
20
10
0

Table 3.16: NGC 6362

ID	Field	RA	DEC	Δ RA ($''$)	Δ DEC ($''$)	$S_{5.5}$ (μJy)	$\Delta S_{5.5}$ (μJy)	$S_{7.25}$ (μJy)	$\Delta S_{7.25}$ (μJy)	S_9 (μJy)	ΔS_9 (μJy)	α	$\Delta\alpha$	R/R$_c$	R/R$_h$
1	NGC 6362	17:31:55.00	-67:02:49.30	0.54	0.19	18.1	3.3	15.3	2.5	16.3	3.8	-0.20	0.62	0.07	0.04
2	NGC 6362	17:31:47.12	-67:02:58.64	0.13	0.04	24.8	3.5	18.2	2.6	<22.3	-	<-0.22	0.29	0.68	0.38
3	NGC 6362	17:31:46.38	-67:03:07.15	0.17	0.14	20.2	3.5	14.3	2.6	<18.5	-	<-0.18	0.35	0.77	0.42
4	NGC 6362	17:31:53.75	-67:01:42.23	0.01	0.07	14.8	3.4	14.2	2.6	<25.2	-	<1.08	0.48	1.06	0.59
5	NGC 6362	17:31:58.77	-67:01:44.76	0.49	0.05	28.0	3.5	21.4	2.6	20.8	4.2	-0.61	0.49	1.07	0.59
6	NGC 6362	17:31:53.12	-67:01:26.88	0.28	0.02	23.9	3.5	15.3	2.7	<21.8	-	<-0.19	0.3	1.30	0.71
7	NGC 6362	17:31:38.60	-67:03:07.97	0.26	0.06	20.3	3.8	13.6	2.7	<21.0	-	<0.07	0.38	1.43	0.79
8	NGC 6362	17:32:13.35	-67:03:08.53	0.17	0.07	169.0	4.0	128.0	2.9	105.0	5.2	-0.97	0.11	1.60	0.88
9	NGC 6362	17:31:35.79	-67:03:30.96	0.21	0.28	35.1	3.9	26.6	2.9	25.0	5.3	-0.71	0.49	1.74	0.96
10	NGC 6362	17:31:34.51	-67:03:29.78	0.16	0.08	50.7	3.9	30.8	2.9	24.0	5.5	-1.52	0.5	1.84	1.02
11	NGC 6362	17:31:35.19	-67:03:56.27	0.07	0.04	47.5	3.9	40.2	3.0	44.3	5.9	-0.12	0.33	1.94	1.07
12	NGC 6362	17:32:11.88	-67:01:24.61	0.24	0.04	69.9	4.0	48.8	3.0	39.5	5.8	-1.16	0.32	1.97	1.08
13	NGC 6362	17:32:14.12	-67:04:09.71	0.03	0.05	53.9	4.2	43.7	3.0	41.5	6.0	-0.55	0.34	1.99	1.10
14	NGC 6362	17:31:49.64	-67:05:05.79	0.13	0.08	37.0	4.1	27.2	3.0	22.0	5.9	-1.07	0.6	2.00	1.10
15	NGC 6362	17:32:06.10	-67:00:54.42	0.39	0.04	63.4	4.0	48.9	2.9	31.4	5.8	-1.41	0.42	2.01	1.11
16	NGC 6362	17:31:45.07	-67:00:44.85	0.46	0.10	34.6	3.9	25.7	2.9	23.8	5.9	-0.75	0.56	2.09	1.15
17	NGC 6362	17:32:17.70	-67:04:00.47	1.27	0.07	46.3	4.7	27.9	3.4	29.0	6.7	-0.95	0.54	2.19	1.21
18	NGC 6362	17:32:17.65	-67:04:00.49	1.23	0.07	<51.4	-	27.9	3.4	29.0	6.7	>-1.16	0.48	2.19	1.21
19	NGC 6362	17:32:17.74	-67:04:00.43	0.53	0.03	46.3	4.7	27.9	3.4	<20.3	-	<-1.67	0.21	2.19	1.21
20	NGC 6362	17:32:17.77	-67:04:15.41	0.14	0.03	32.6	4.9	21.0	3.5	<37.3	-	<0.27	0.31	2.30	1.27

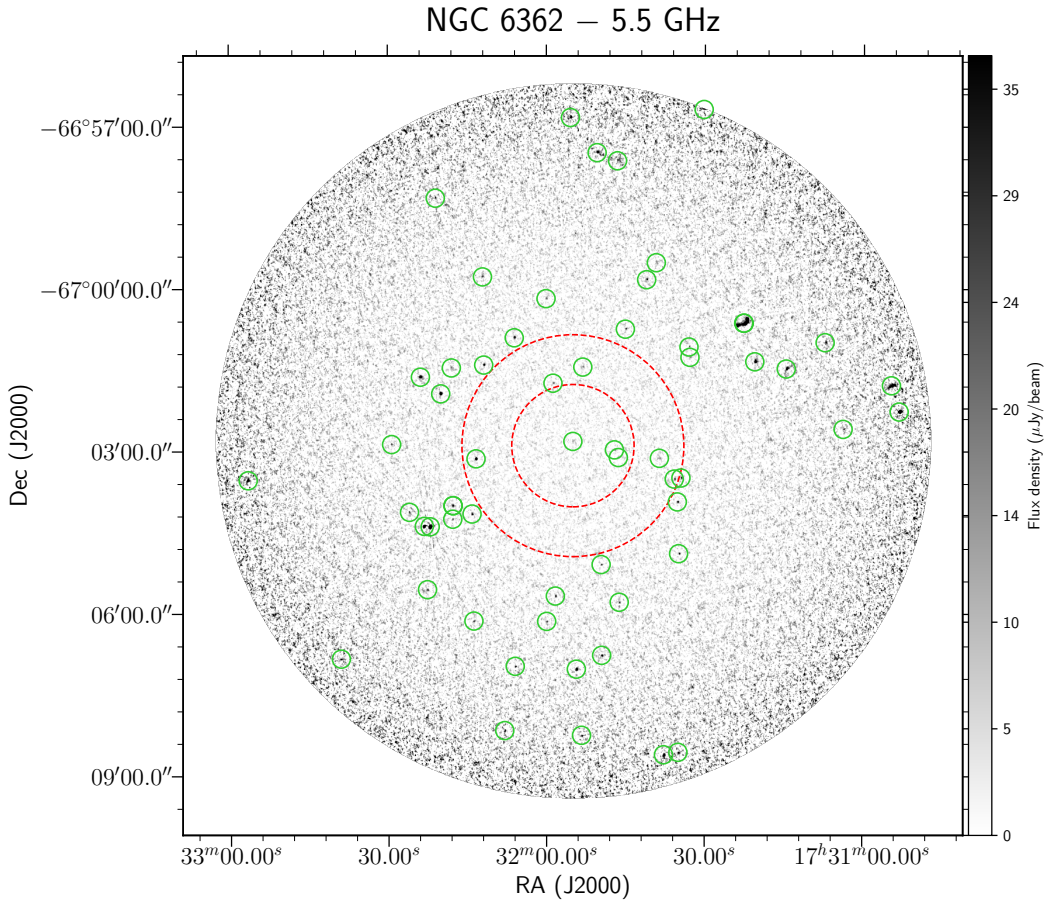
NGC 6362 — 5.5 GHz
−66°57′00.0″
−67°00′00.0″
03′00.0″
06′00.0″
09′00.0″
Dec (J2000)
33m00.00s
30.00s
32m00.00s
30.00s
17h31m00.00s
RA (J2000)
Flux density (μJy/beam)
0
5
10
14
20
24
29
35

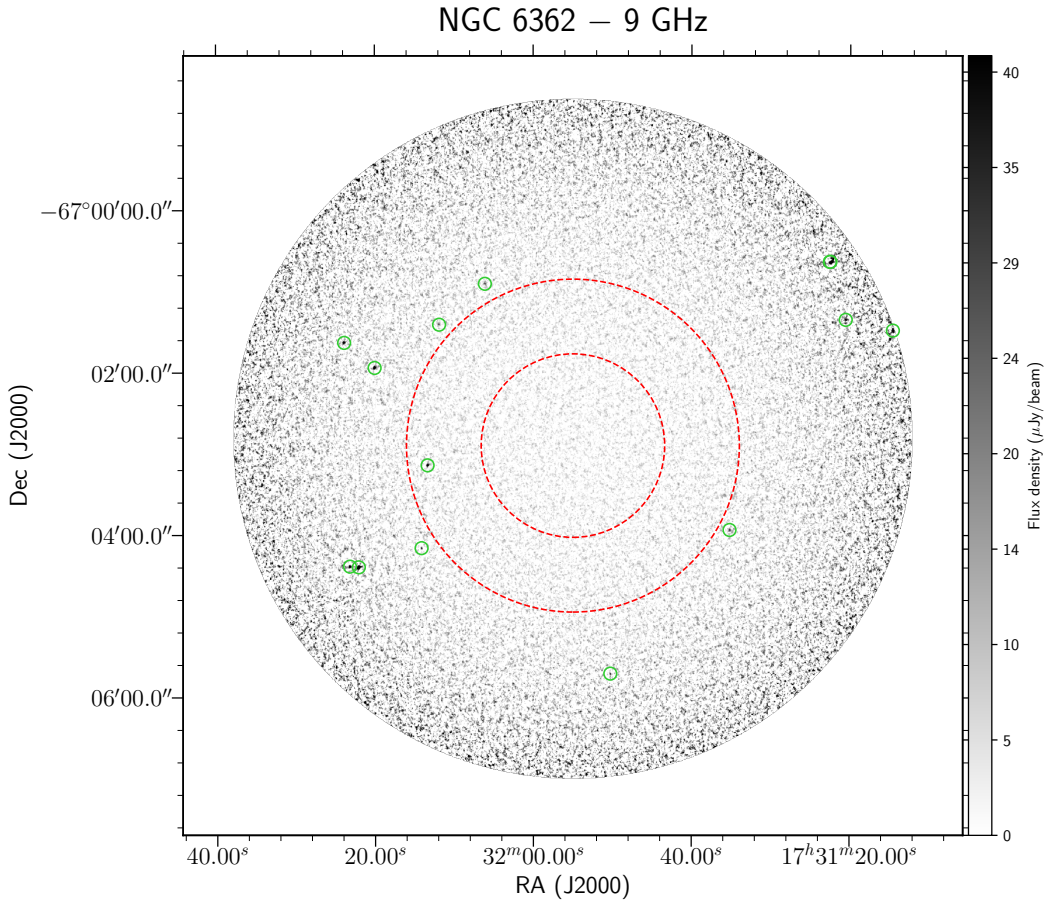
NGC 6362 — 9 GHz
−67°00′00.0″
02′00.0″
04′00.0″
06′00.0″
Dec (J2000)
40.00s
20.00s
32m00.00s
40.00s
17h31m20.00s
RA (J2000)
Flux density (μJy/beam)
0
5
10
14
20
24
29
35
40

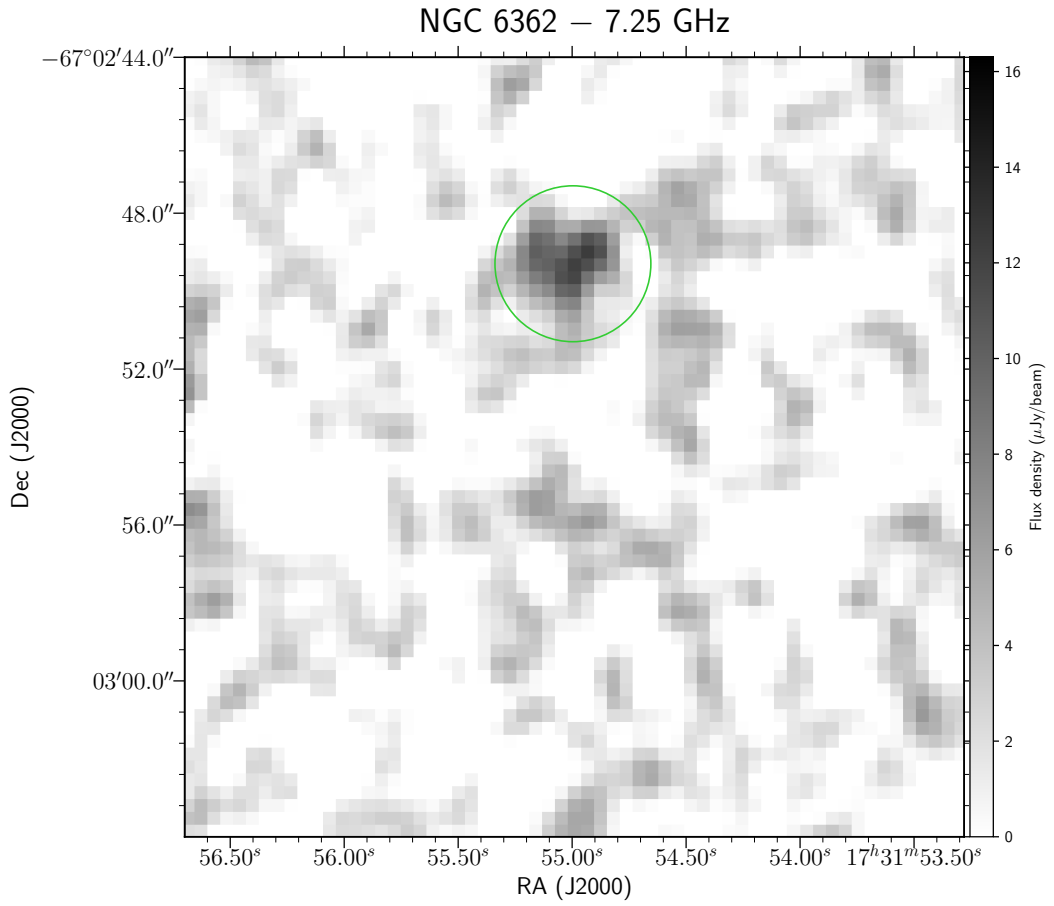
NGC 6362 — 7.25 GHz
−67°02′44.0″
48.0″
52.0″
56.0″
03′00.0″
Dec (J2000)
56.50s
56.00s
55.50s
55.00s
54.50s
54.00s
17h31m53.50s
RA (J2000)
Flux density (μJy/beam)
0
2
4
6
8
10
12
14
16

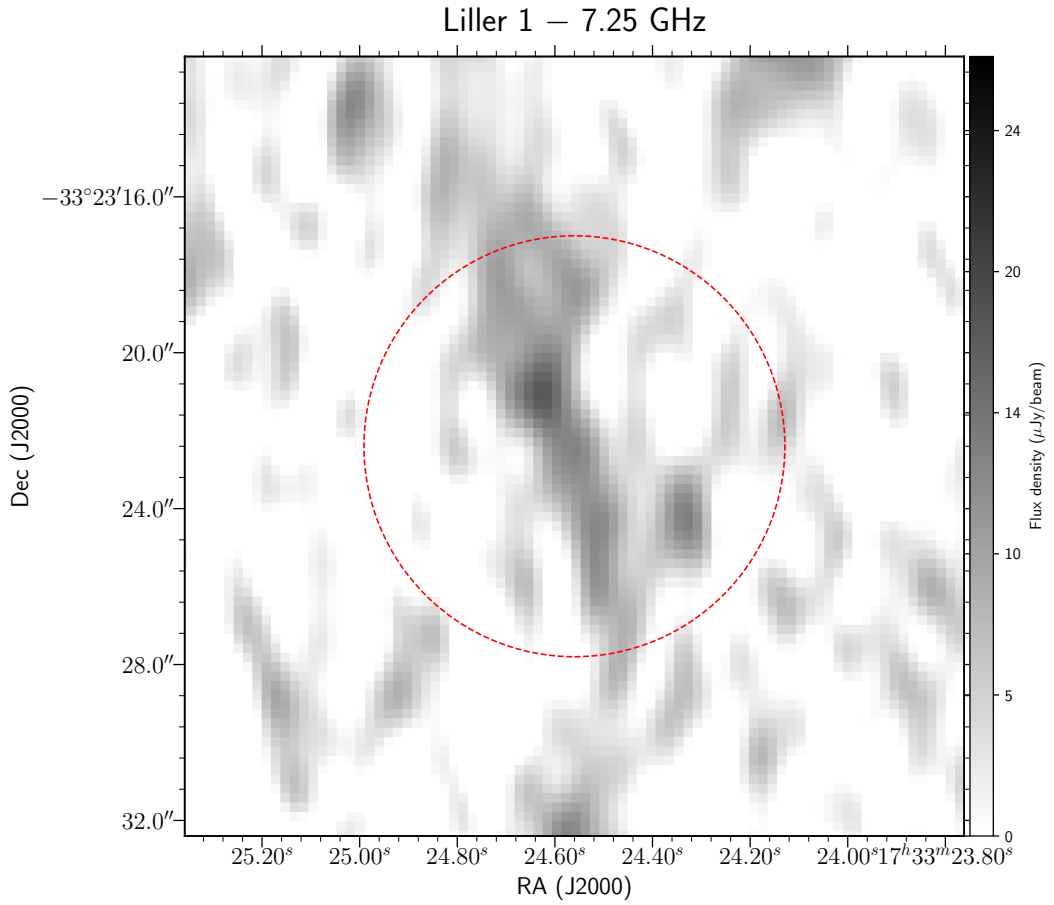
Liller 1 — 7.25 GHz
−33°23′16.0″
20.0″
24.0″
28.0″
32.0″
Dec (J2000)
25.20s
25.00s
24.80s
24.60s
24.40s
24.20s
24.00s17h33m23.80s
RA (J2000)
Flux density (μJy/beam)
0
5
10
14
20
24

Table 3.17: Liller 1

ID	Field	RA	DEC	Δ RA ($''$)	Δ DEC ($''$)	$S_{5.5}$ (μJy)	$\Delta S_{5.5}$ (μJy)	$S_{7.25}$ (μJy)	$\Delta S_{7.25}$ (μJy)	S_9 (μJy)	ΔS_9 (μJy)	α	$\Delta\alpha$	R/R$_c$	R/R$_h$
1	Liller 1	17:33:19.86	-33:22:58.88	0.07	0.28	34.5	5.5	20.0	4.7	<31.2	-	<-0.20	0.33	11.75	2.08
2	Liller 1	17:33:21.48	-33:24:17.54	0.09	0.12	33.7	5.4	21.8	4.1	<25.5	-	<-0.57	0.33	12.46	2.21
3	Liller 1	17:33:30.41	-33:22:41.38	0.02	0.32	46.3	6.0	34.1	5.3	30.7	6.5	-0.83	0.51	15.56	2.76
4	Liller 1	17:33:21.92	-33:22:00.68	0.02	0.03	52.8	6.4	41.2	4.9	27.9	6.5	-1.30	0.55	16.33	2.89
5	Liller 1	17:33:27.65	-33:25:09.31	0.14	0.14	39.3	6.9	31.6	5.5	<47.3	-	<0.38	0.36	21.06	3.73
6	Liller 1	17:33:31.53	-33:21:10.47	0.02	0.09	81.3	6.7	60.7	6.0	<51.1	-	<-0.94	0.17	29.29	5.19
7	Liller 1	17:33:24.59	-33:26:13.41	0.09	0.06	47.7	6.7	46.2	5.9	<75.2	-	<0.92	0.29	31.67	5.61
8	Liller 1	17:33:31.31	-33:26:00.73	0.05	0.12	45.4	7.2	35.1	6.1	<63.6	-	<0.69	0.33	33.23	5.88
9	Liller 1	17:33:10.68	-33:24:25.99	0.07	0.23	194.0	8.2	181.0	6.9	142.0	13.8	-0.63	0.21	34.28	6.07
10	Liller 1	17:33:25.91	-33:20:09.22	0.06	0.01	65.4	7.8	52.0	8.3	<92.8	-	<0.71	0.24	35.91	6.36
11	Liller 1	17:33:29.76	-33:26:41.66	0.03	0.46	39.9	7.9	44.0	7.4	<87.2	-	<1.59	0.41	38.82	6.87
12	Liller 1	17:33:36.81	-33:20:59.09	0.10	0.03	63.2	9.3	43.9	9.0	<70.2	-	<0.21	0.3	38.89	6.89
13	Liller 1	17:33:11.64	-33:25:38.39	0.03	0.11	114.0	9.1	118.0	7.6	103.0	15.6	-0.21	0.35	39.14	6.93
14	Liller 1	17:33:43.48	-33:23:49.02	0.06	0.05	396.0	10.9	352.0	10.9	248.0	22.9	-0.95	0.2	44.15	7.82
15	Liller 1	17:33:41.07	-33:21:12.17	0.11	0.12	<42.3	-	44.6	9.4	143.0	23.8	>2.47	0.34	45.27	8.01
16	Liller 1	17:33:04.68	-33:23:44.36	0.06	0.32	<59.9	-	57.5	9.7	<180.0	-	-	-	46.28	8.19
17	Liller 1	17:33:43.88	-33:24:39.86	0.23	0.13	96.0	11.0	-	-	-	-	-	-	47.05	8.33
18	Liller 1	17:33:04.68	-33:24:53.87	0.05	0.29	81.5	10.1	-	-	-	-	-	-	49.12	8.70
19	Liller 1	17:33:08.58	-33:20:14.29	0.07	0.08	685.0	17.8	-	-	-	-	-	-	50.87	9.01
20	Liller 1	17:33:46.51	-33:23:51.58	0.06	0.33	77.3	10.9	-	-	-	-	-	-	51.20	9.07

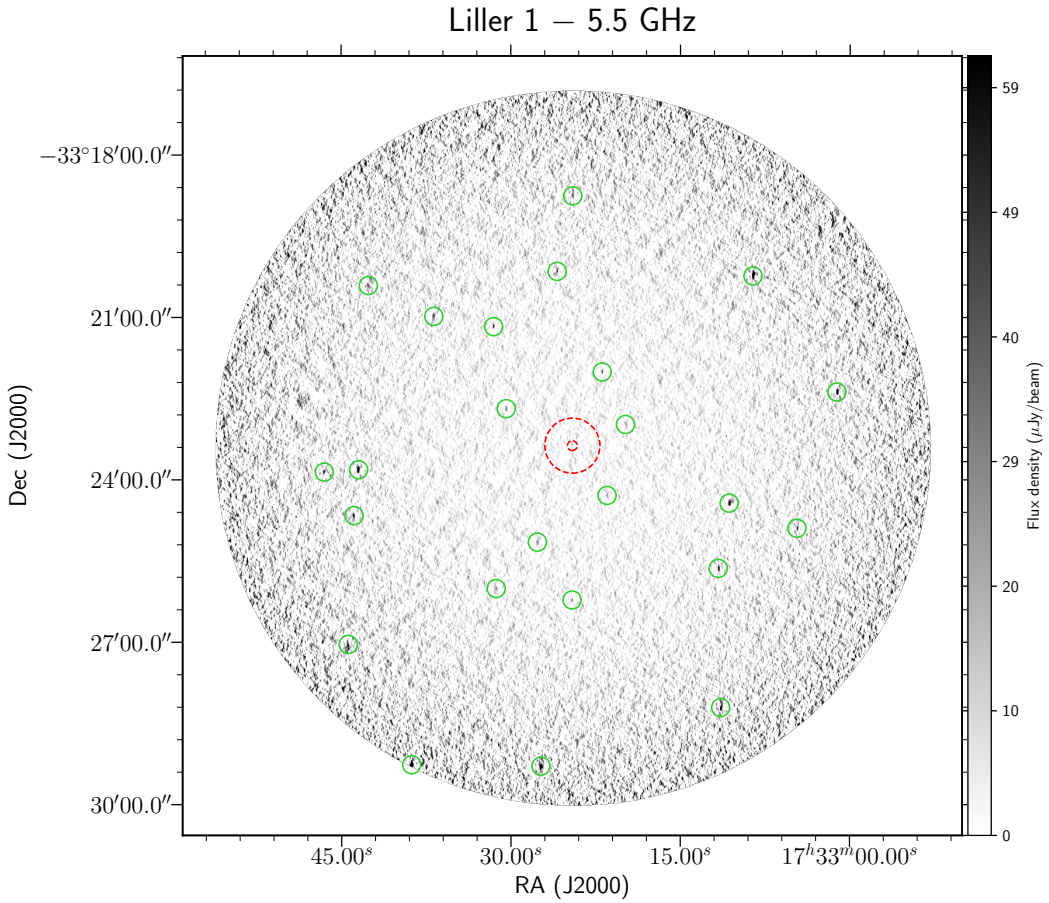
Liller 1 – 5.5 GHz
−33°18′00.0″
21′00.0″
24′00.0″
27′00.0″
30′00.0″
Dec (J2000)
45.00ˢ
30.00ˢ
15.00ˢ
17ʰ33ᵐ00.00ˢ
RA (J2000)
Flux density (μJy/beam)
59
49
40
29
20
10
0

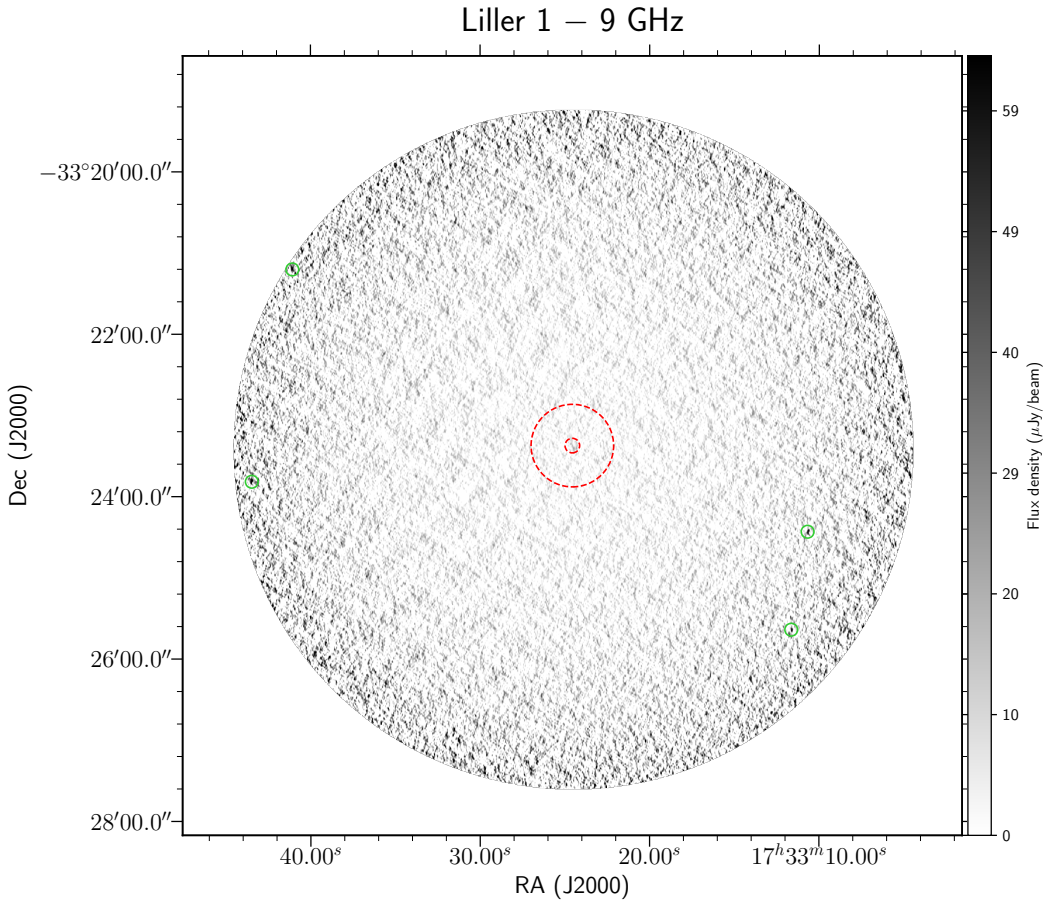
Liller 1 – 9 GHz
−33°20′00.0″
22′00.0″
24′00.0″
26′00.0″
28′00.0″
Dec (J2000)
40.00ˢ
30.00ˢ
20.00ˢ
17ʰ33ᵐ10.00ˢ
RA (J2000)
Flux density (μJy/beam)
59
49
40
29
20
10
0

Table 3.18: Terzan 1

ID	Field	RA	DEC	Δ RA ($''$)	Δ DEC ($''$)	$S_{5.5}$ (μJy)	$\Delta S_{5.5}$ (μJy)	$S_{7.25}$ (μJy)	$\Delta S_{7.25}$ (μJy)	S_{9} (μJy)	ΔS_{9} (μJy)	α	$\Delta\alpha$	R/R$_c$	R/R$_h$
1	Terzan 1	17:35:47.19	-30:28:54.62	0.17	0.16	79.8	5.7	55.0	3.0	27.0	4.2	-2.21	0.35	0.12	0.01
2	Terzan 1	17:35:49.57	-30:28:40.67	0.07	0.04	28.9	4.8	26.3	3.1	25.0	4.3	-0.30	0.49	16.77	1.41
3	Terzan 1	17:35:50.74	-30:29:04.03	0.11	0.82	24.4	4.8	16.7	3.2	<25.1	-	<0.06	0.4	23.39	1.97
4	Terzan 1	17:35:50.82	-30:29:03.79	0.20	0.28	20.7	4.8	16.7	3.2	<28.3	-	<0.64	0.48	23.84	2.00
5	Terzan 1	17:35:42.86	-30:28:16.39	0.04	0.08	41.7	4.8	31.0	2.6	25.1	3.7	-1.04	0.36	33.86	2.85
6	Terzan 1	17:35:40.00	-30:28:57.90	0.05	0.39	<33.0	-	17.3	2.8	<28.6	-	-	-	46.56	3.91
7	Terzan 1	17:35:54.85	-30:27:39.25	0.30	0.15	<38.9	-	19.7	3.5	<28.8	-	-	-	62.10	5.22
8	Terzan 1	17:35:54.33	-30:27:16.44	0.09	0.57	43.6	5.3	33.8	3.0	23.0	5.3	-1.31	0.52	67.25	5.65
9	Terzan 1	17:35:41.33	-30:30:47.63	0.10	0.07	55.2	5.9	42.4	3.8	<51.2	-	<-0.15	0.22	68.14	5.73
10	Terzan 1	17:35:36.76	-30:29:19.65	0.00	0.08	35.7	5.7	25.2	4.4	<33.1	-	<-0.15	0.33	68.65	5.77
11	Terzan 1	17:35:36.16	-30:28:44.95	0.11	0.45	32.3	5.6	31.7	3.7	35.1	6.1	0.16	0.5	71.54	6.01
12	Terzan 1	17:35:55.85	-30:30:27.73	0.01	0.03	1190.0	8.7	958.0	4.5	619.0	9.4	-1.33	0.03	72.81	6.12
13	Terzan 1	17:35:36.10	-30:28:18.80	0.03	0.14	27.0	5.8	25.1	3.5	<41.2	-	<0.86	0.44	73.90	6.21
14	Terzan 1	17:35:41.06	-30:31:00.43	0.04	0.19	50.2	6.3	42.9	4.2	38.0	7.9	-0.55	0.52	74.46	6.26
15	Terzan 1	17:35:38.10	-30:30:32.59	0.15	0.92	<46.2	-	26.2	4.8	44.5	9.2	>-0.07	0.42	76.59	6.44
16	Terzan 1	17:35:47.23	-30:31:36.58	0.05	0.36	<44.9	-	30.1	4.5	<49.8	-	-	-	81.09	6.81
17	Terzan 1	17:36:00.06	-30:28:23.40	0.06	0.07	1450.0	51.5	1220.0	44.6	1150.0	58.5	-0.47	0.12	84.53	7.10
18	Terzan 1	17:35:55.46	-30:26:12.04	0.03	0.09	116.0	5.9	112.0	3.4	109.0	6.1	-0.12	0.15	97.16	8.16
19	Terzan 1	17:35:31.86	-30:29:10.63	0.21	0.21	54.2	7.1	40.4	5.0	<53.5	-	<-0.03	0.27	99.48	8.36
20	Terzan 1	17:35:48.36	-30:25:32.65	0.00	0.29	36.7	5.9	28.6	3.6	<41.8	-	<0.27	0.33	101.15	8.50

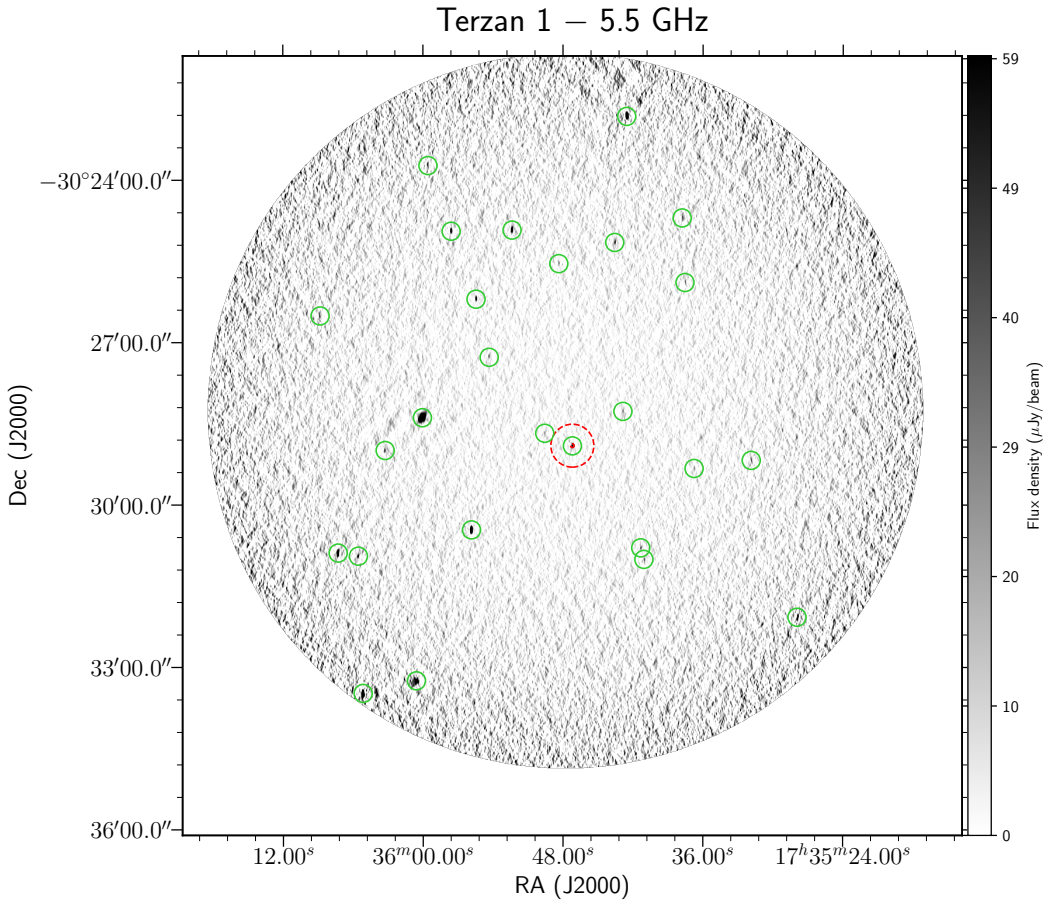
Terzan 1 – 5.5 GHz
−30°24′00.0″
27′00.0″
30′00.0″
33′00.0″
36′00.0″
Dec (J2000)
12.00s
36m00.00s
48.00s
36.00s
17h35m24.00s
RA (J2000)
59
49
40
29
20
10
0
Flux density (μJy/beam)

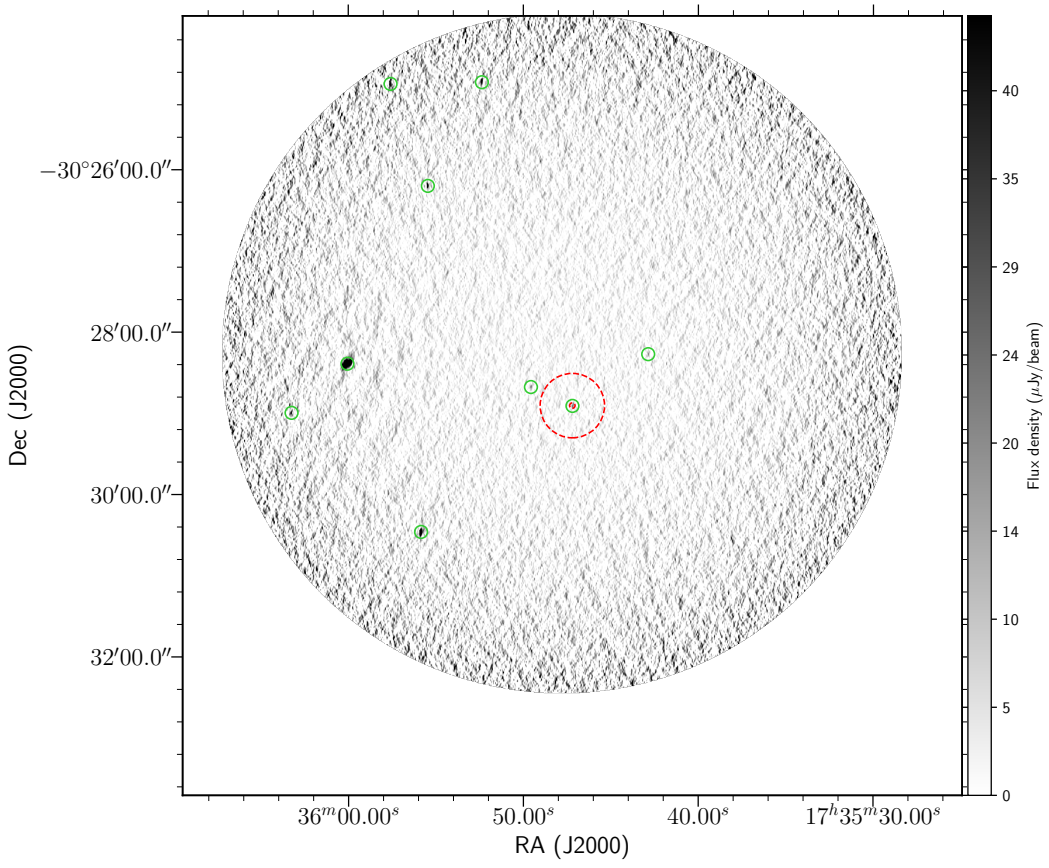
Terzan 1 – 9 GHz
−30°26′00.0″
28′00.0″
30′00.0″
32′00.0″
Dec (J2000)
36m00.00s
50.00s
40.00s
17h35m30.00s
RA (J2000)
40
35
29
24
20
14
10
5
0
Flux density (μJy/beam)

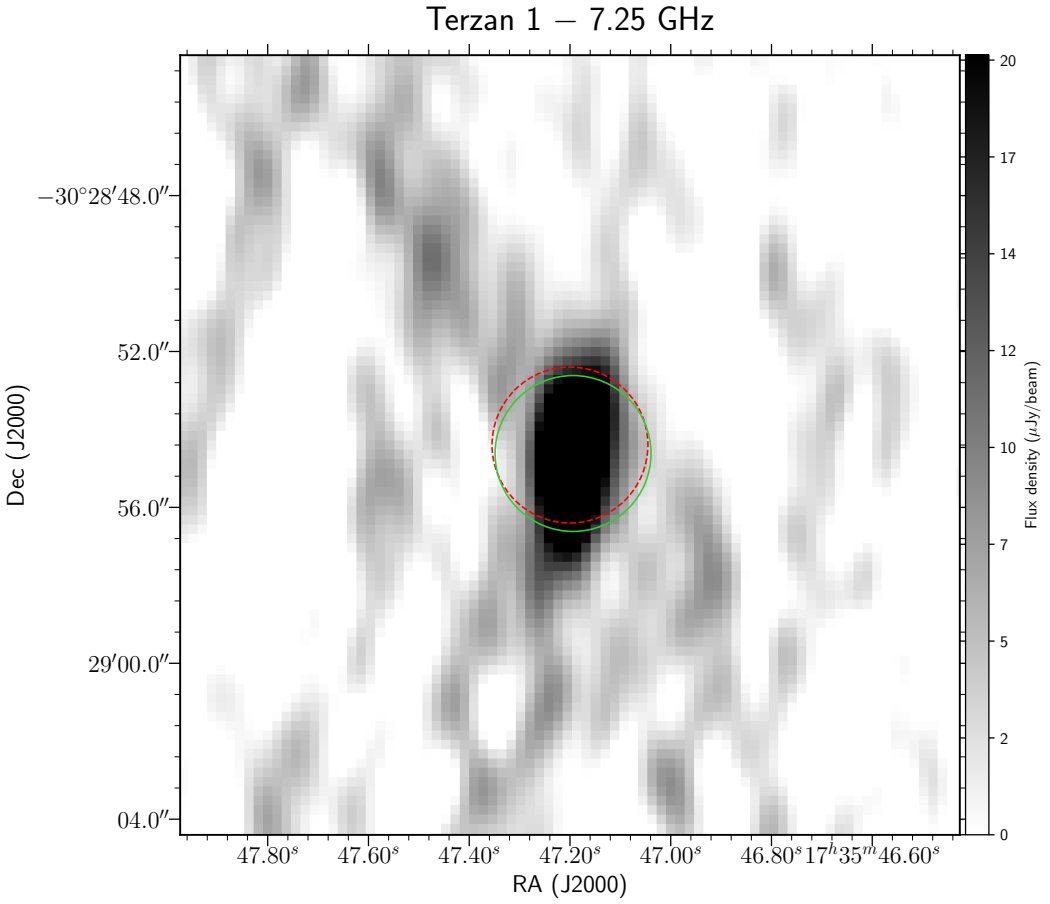
Terzan 1 – 7.25 GHz
−30°28′48.0″
52.0″
56.0″
29′00.0″
04.0″
Dec (J2000)
47.80s
47.60s
47.40s
47.20s
47.00s
46.80s
17h35m46.60s
RA (J2000)
Flux density (μJy/beam)
20
17
14
12
10
7
5
2
0

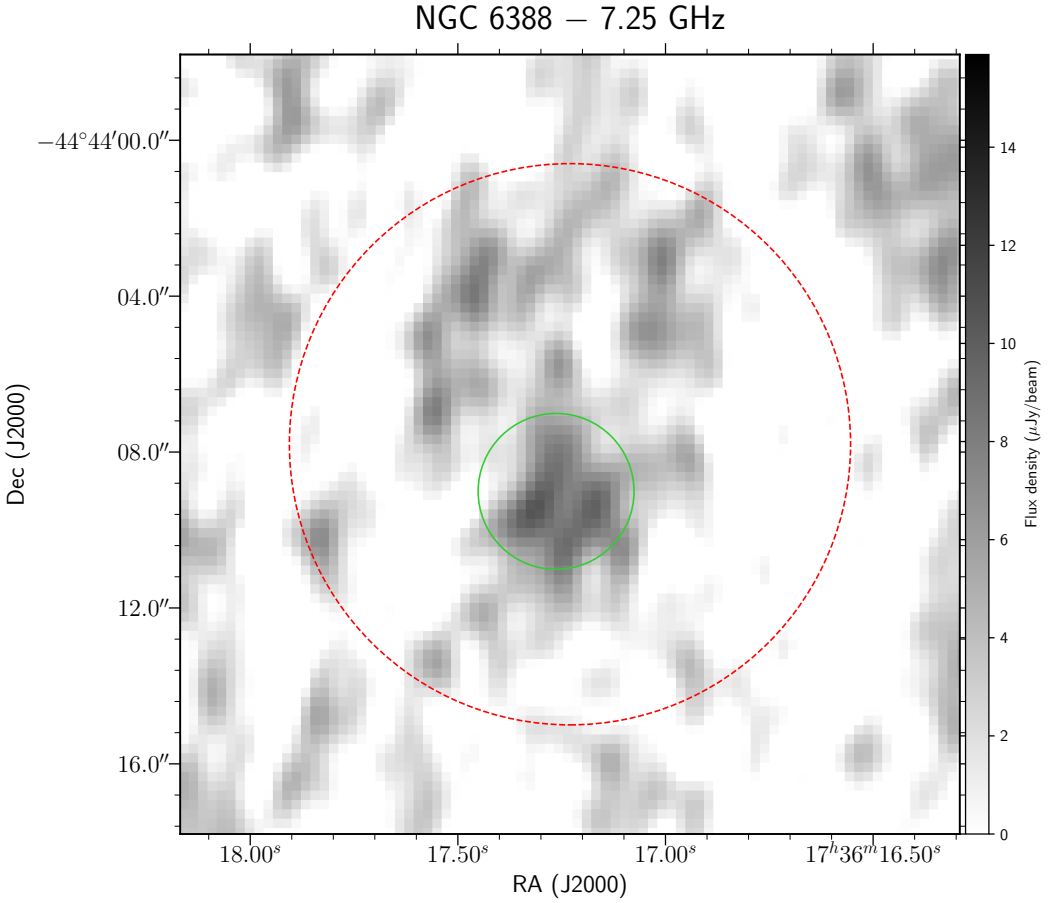
NGC 6388 – 7.25 GHz
−44°44′00.0″
04.0″
08.0″
12.0″
16.0″
Dec (J2000)
18.00s
17.50s
17.00s
17h36m16.50s
RA (J2000)
Flux density (μJy/beam)
14
12
10
8
6
4
2
0

Table 3.19: NGC 6388

ID	Field	RA	DEC	Δ RA ($''$)	Δ DEC ($''$)	$S_{5.5}$ (μJy)	$\Delta S_{5.5}$ (μJy)	$S_{7.25}$ (μJy)	$\Delta S_{7.25}$ (μJy)	S_9 (μJy)	ΔS_9 (μJy)	α	$\Delta\alpha$	R/R$_c$	R/R$_h$
1	NGC 6388	17:36:17.26	-44:44:09.01	0.21	0.35	15.2	3.5	13.4	2.4	<13.8	-	<-0.20	0.48	0.18	0.04
2	NGC 6388	17:36:17.87	-44:43:44.75	0.02	0.01	44.4	3.3	48.6	2.4	51.6	3.2	0.30	0.21	3.34	0.77
3	NGC 6388	17:36:14.81	-44:44:32.83	0.24	0.03	24.3	3.5	19.4	2.5	14.6	3.4	-1.02	0.57	4.99	1.15
4	NGC 6388	17:36:14.62	-44:44:43.09	0.13	0.22	24.4	3.7	16.8	2.4	<16.5	-	<-0.79	0.31	6.24	1.44
5	NGC 6388	17:36:17.68	-44:44:53.29	0.42	0.53	66.8	10.9	54.5	9.0	19.1	3.6	-2.52	0.5	6.35	1.47
6	NGC 6388	17:36:17.96	-44:45:17.78	0.03	0.20	36.1	3.5	27.2	2.5	17.2	3.9	-1.50	0.52	9.78	2.26
7	NGC 6388	17:36:15.73	-44:45:17.38	0.13	0.05	16.8	3.5	16.0	2.6	15.4	3.7	-0.16	0.7	9.92	2.29
8	NGC 6388	17:36:24.80	-44:42:54.57	0.00	0.11	<16.2	-	12.4	2.8	23.2	4.2	>0.73	0.37	15.13	3.49
9	NGC 6388	17:36:09.56	-44:45:34.13	0.02	0.16	19.8	3.9	15.2	3.1	<21.2	-	<0.14	0.41	16.51	3.81
10	NGC 6388	17:36:27.37	-44:43:02.19	0.13	0.35	<148.0	-	145.0	11.0	71.2	4.9	>-1.49	0.14	17.56	4.05
11	NGC 6388	17:36:27.49	-44:43:01.29	0.15	0.16	284.0	16.8	<13.0	-	<14.8	-	<-6.00	0.12	17.78	4.10
12	NGC 6388	17:36:27.67	-44:43:00.34	0.12	0.07	<101.0	-	69.8	3.2	48.9	5.0	>-1.47	0.21	18.07	4.17
13	NGC 6388	17:36:26.02	-44:42:35.36	0.09	0.14	<24.1	-	16.4	3.0	21.1	4.8	>-0.27	0.47	18.28	4.22
14	NGC 6388	17:36:30.26	-44:43:46.72	0.00	0.10	174.0	4.1	143.0	3.3	107.0	5.1	-0.99	0.11	19.51	4.50
15	NGC 6388	17:36:17.51	-44:46:29.92	0.03	0.06	23.8	3.8	20.2	3.2	<28.5	-	<0.37	0.33	19.74	4.56
16	NGC 6388	17:36:24.37	-44:46:24.45	0.14	0.15	87.6	4.4	72.5	3.7	55.6	6.2	-0.93	0.25	21.72	5.01
17	NGC 6388	17:36:31.12	-44:45:07.48	0.20	0.18	23.6	4.0	20.6	3.4	<29.1	-	<0.43	0.35	22.16	5.11
18	NGC 6388	17:36:34.04	-44:44:12.04	0.06	0.09	74.6	4.5	66.2	3.9	50.8	6.8	-0.78	0.3	24.88	5.74
19	NGC 6388	17:36:26.03	-44:41:30.37	0.10	0.09	43.5	4.3	32.5	3.9	<32.7	-	<-0.58	0.2	25.45	5.87
20	NGC 6388	17:36:21.33	-44:47:11.57	0.01	0.04	<15.2	-	16.7	4.0	44.9	7.9	>2.20	0.36	26.23	6.05

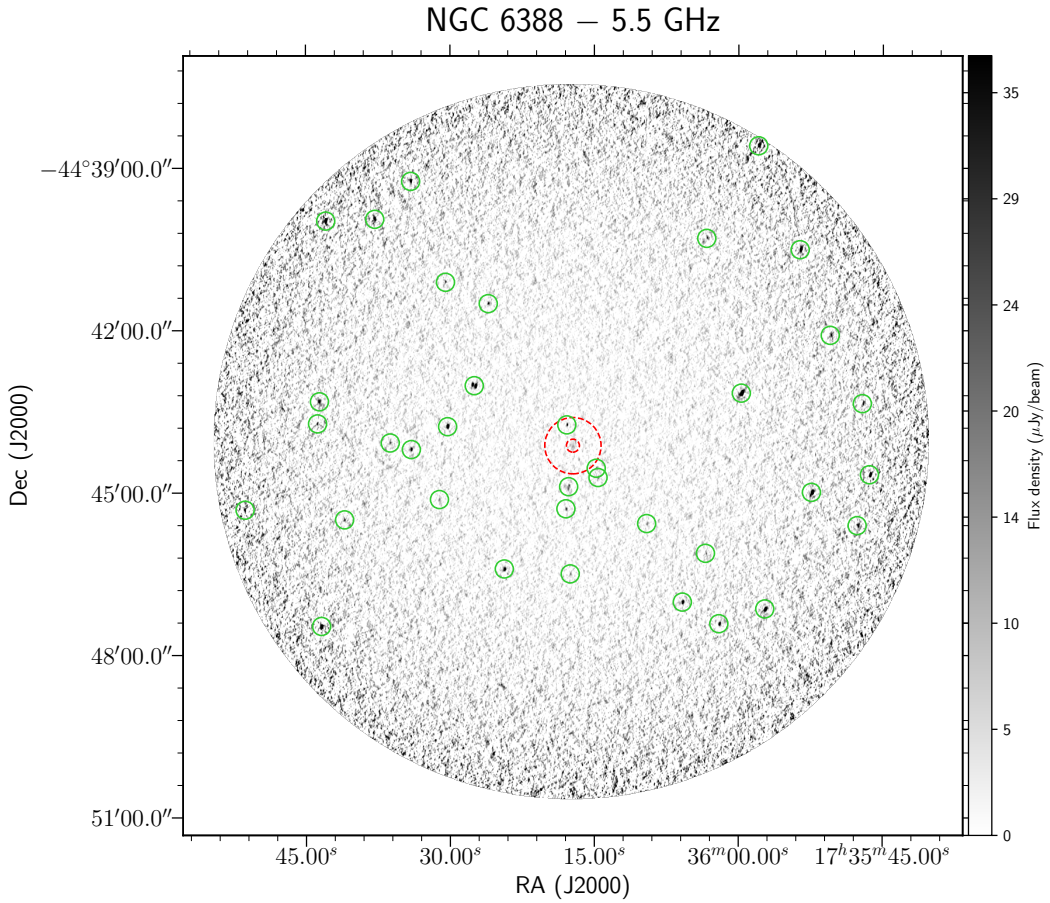
NGC 6388 – 5.5 GHz
−44°39′00.0″
42′00.0″
45′00.0″
48′00.0″
51′00.0″
Dec (J2000)
45.00s
30.00s
15.00s
36m00.00s
17h35m45.00s
RA (J2000)
Flux density (μJy/beam)
35
29
24
20
14
10
5
0

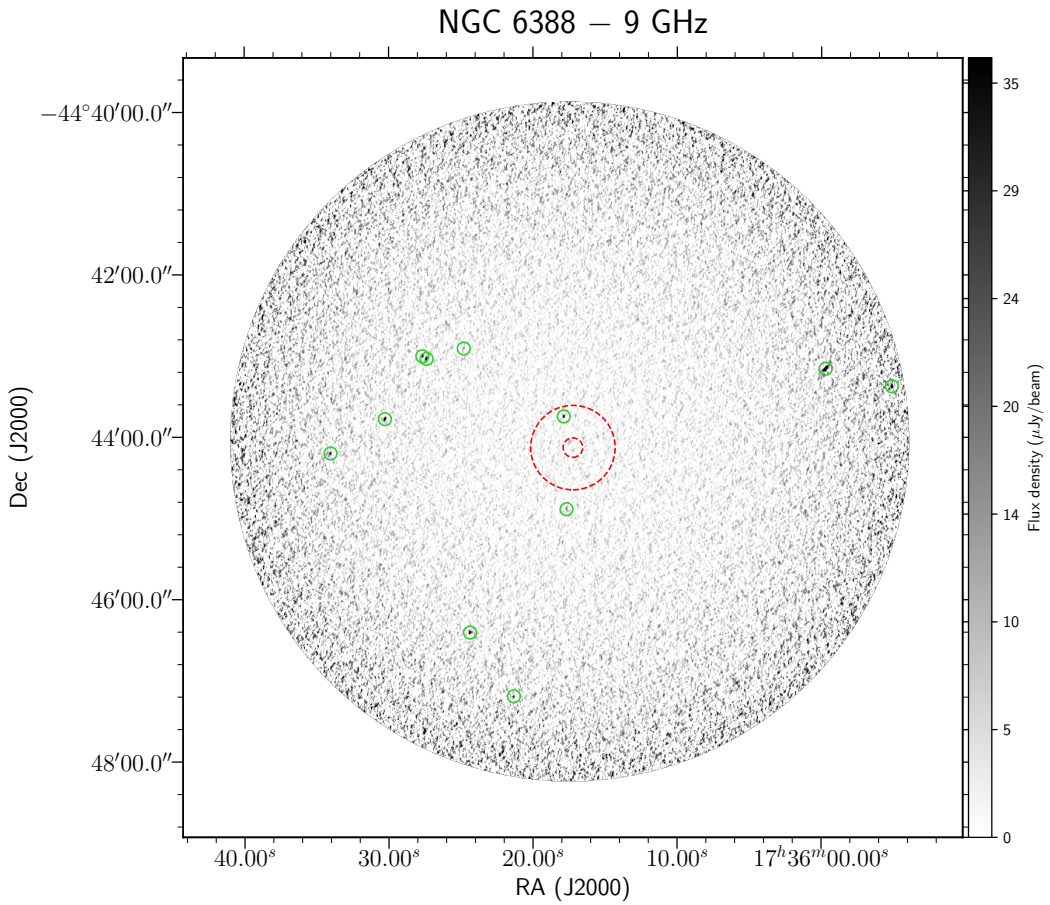
NGC 6388 – 9 GHz
−44°40′00.0″
42′00.0″
44′00.0″
46′00.0″
48′00.0″
Dec (J2000)
40.00s
30.00s
20.00s
10.00s
17h36m00.00s
RA (J2000)
Flux density (μJy/beam)
35
29
24
20
14
10
5
0

Table 3.20: NGC 6397

ID	Field	RA	DEC	Δ RA ($''$)	Δ DEC ($''$)	$S_{5.5}$ (μJy)	$\Delta S_{5.5}$ (μJy)	$S_{7.25}$ (μJy)	$\Delta S_{7.25}$ (μJy)	S_{9} (μJy)	ΔS_{9} (μJy)	α	$\Delta\alpha$	R/R$_c$	R/R$_h$
1	NGC 6397	17:40:42.63	-53:40:28.06	0.02	0.08	54.7	4.3	36.0	3.3	21.6	4.4	-1.89	0.45	1.60	0.03
2	NGC 6397	17:40:39.51	-53:40:33.57	0.22	0.08	38.9	4.1	28.4	3.2	20.8	4.8	-1.26	0.52	7.89	0.14
3	NGC 6397	17:40:41.58	-53:40:03.95	0.04	0.43	28.0	4.6	60.7	11.3	20.7	4.5	-0.61	0.58	8.03	0.14
4	NGC 6397	17:40:44.64	-53:40:41.87	0.13	0.01	36.7	4.3	28.3	3.1	<25.0	-	<-0.78	0.24	8.93	0.15
5	NGC 6397	17:40:43.94	-53:40:05.65	0.20	0.17	34.1	4.7	24.1	3.3	18.6	4.5	-1.21	0.58	9.14	0.16
6	NGC 6397	17:40:43.94	-53:41:04.04	0.04	0.04	43.5	4.3	27.3	3.3	<24.7	-	<-1.15	0.2	13.33	0.23
7	NGC 6397	17:40:48.08	-53:41:27.74	0.29	0.03	29.2	4.7	25.5	3.6	27.7	5.4	-0.10	0.52	26.77	0.46
8	NGC 6397	17:40:32.54	-53:41:13.16	0.25	0.13	48.8	4.6	34.1	3.9	21.5	5.3	-1.66	0.55	32.11	0.55
9	NGC 6397	17:40:52.16	-53:39:48.68	0.10	0.15	34.9	4.5	24.0	3.5	<26.8	-	<-0.54	0.26	32.53	0.56
10	NGC 6397	17:40:52.37	-53:39:16.61	0.02	0.01	35.5	4.7	27.5	3.8	<38.9	-	<0.19	0.27	38.57	0.66
11	NGC 6397	17:40:37.48	-53:42:38.04	0.18	0.32	30.1	5.3	26.6	4.9	<49.0	-	<0.99	0.36	45.57	0.79
12	NGC 6397	17:40:57.13	-53:39:32.25	0.23	0.91	<29.5	-	23.3	4.3	34.1	7.8	>0.30	0.47	48.23	0.83
13	NGC 6397	17:40:58.50	-53:40:15.46	0.30	0.17	26.9	5.0	24.3	4.5	<35.8	-	<0.58	0.38	48.79	0.84
14	NGC 6397	17:40:56.21	-53:39:11.06	0.05	0.08	163.0	5.0	120.0	4.8	65.0	8.9	-1.87	0.28	48.99	0.84
15	NGC 6397	17:40:37.93	-53:42:57.35	0.12	0.29	2040.0	47.9	1840.0	71.1	969.0	55.0	-1.51	0.12	51.41	0.89
16	NGC 6397	17:40:42.29	-53:37:44.63	0.01	0.00	56.6	5.7	41.1	4.9	<43.7	-	<-0.52	0.21	54.33	0.94
17	NGC 6397	17:41:00.43	-53:40:41.80	0.04	0.04	99.2	5.7	81.9	4.6	53.0	9.2	-1.27	0.39	54.53	0.94
18	NGC 6397	17:40:48.74	-53:43:05.36	0.05	0.16	31.5	5.8	25.0	5.0	<39.4	-	<0.46	0.38	56.15	0.97
19	NGC 6397	17:40:33.10	-53:37:49.74	0.05	0.02	85.1	5.4	65.6	4.8	<54.8	-	<-0.89	0.13	58.98	1.02
20	NGC 6397	17:40:24.43	-53:41:52.15	0.12	0.36	67.7	6.4	53.9	6.1	<49.4	-	<-0.64	0.19	59.41	1.02

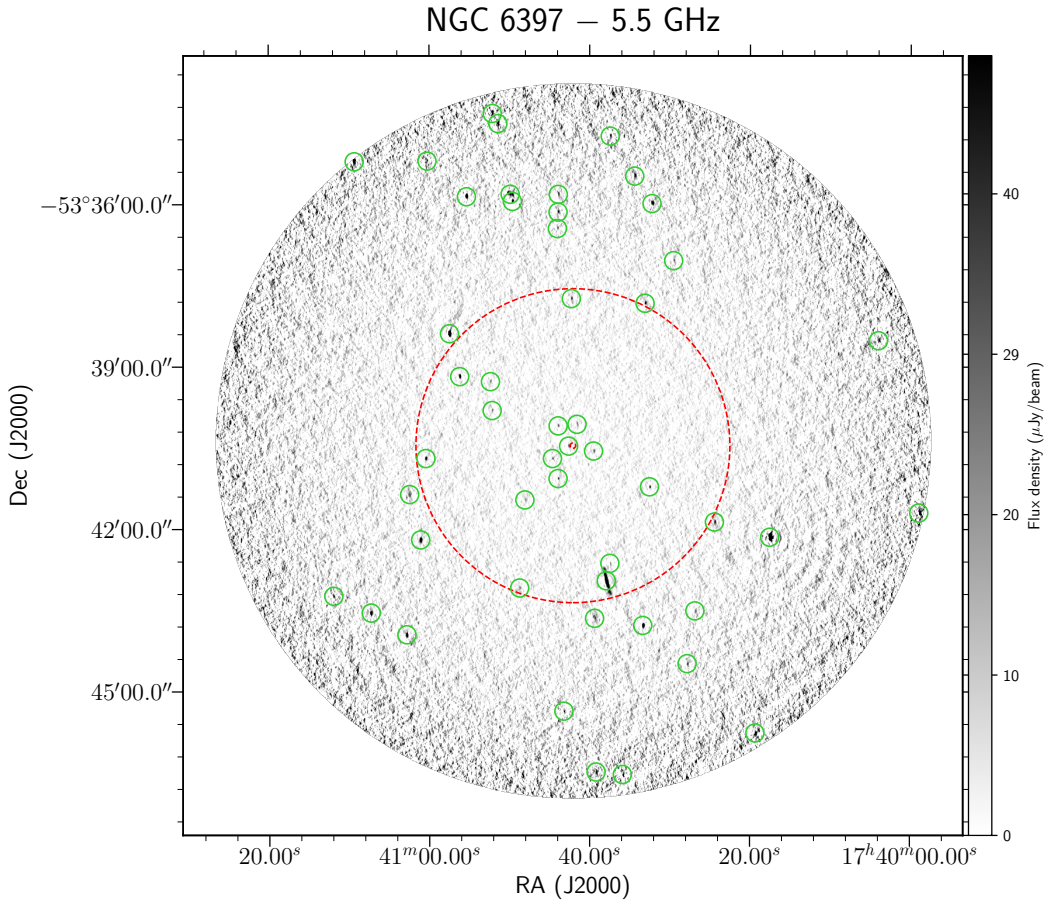
NGC 6397 — 5.5 GHz
−53°36′00.0″
39′00.0″
42′00.0″
45′00.0″
Dec (J2000)
20.00s
41m00.00s
40.00s
20.00s
17h40m00.00s
RA (J2000)
Flux density (μJy/beam)
0
10
20
29
40

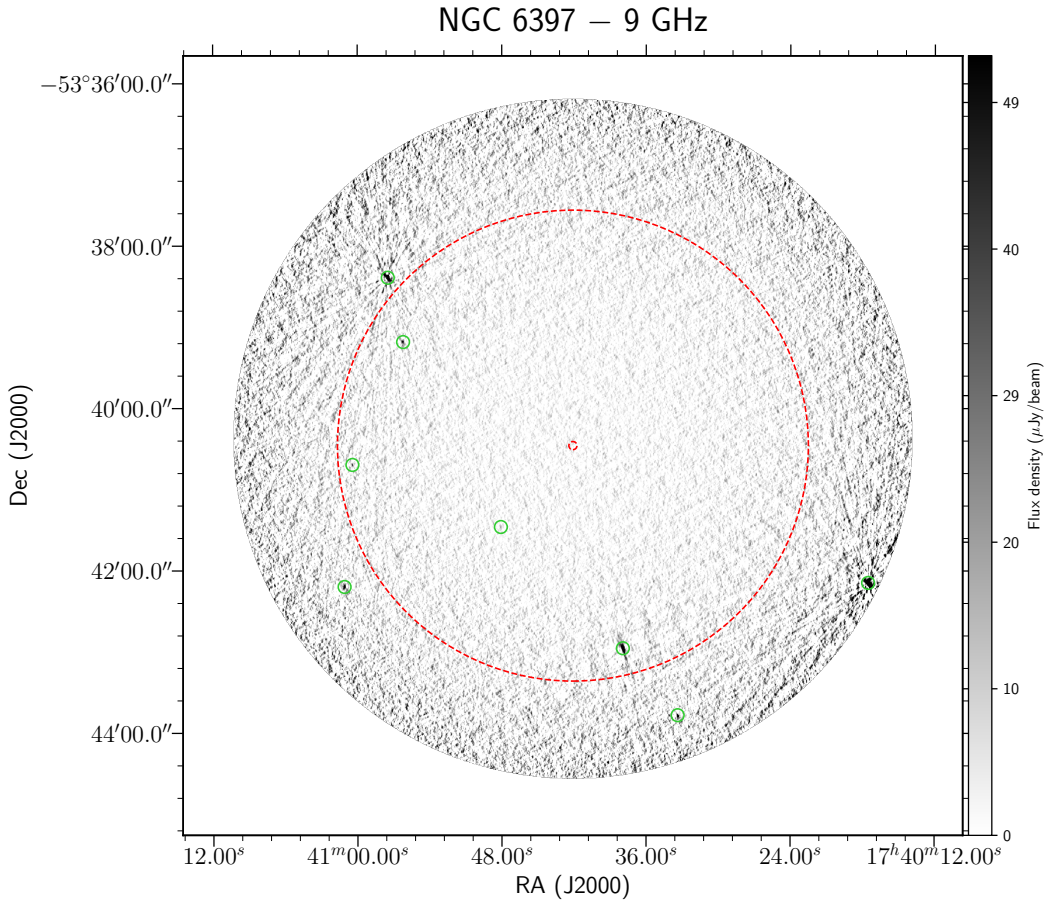
NGC 6397 — 9 GHz
−53°36′00.0″
38′00.0″
40′00.0″
42′00.0″
44′00.0″
Dec (J2000)
12.00s
41m00.00s
48.00s
36.00s
24.00s
17h40m12.00s
RA (J2000)
Flux density (μJy/beam)
0
10
20
29
40
49

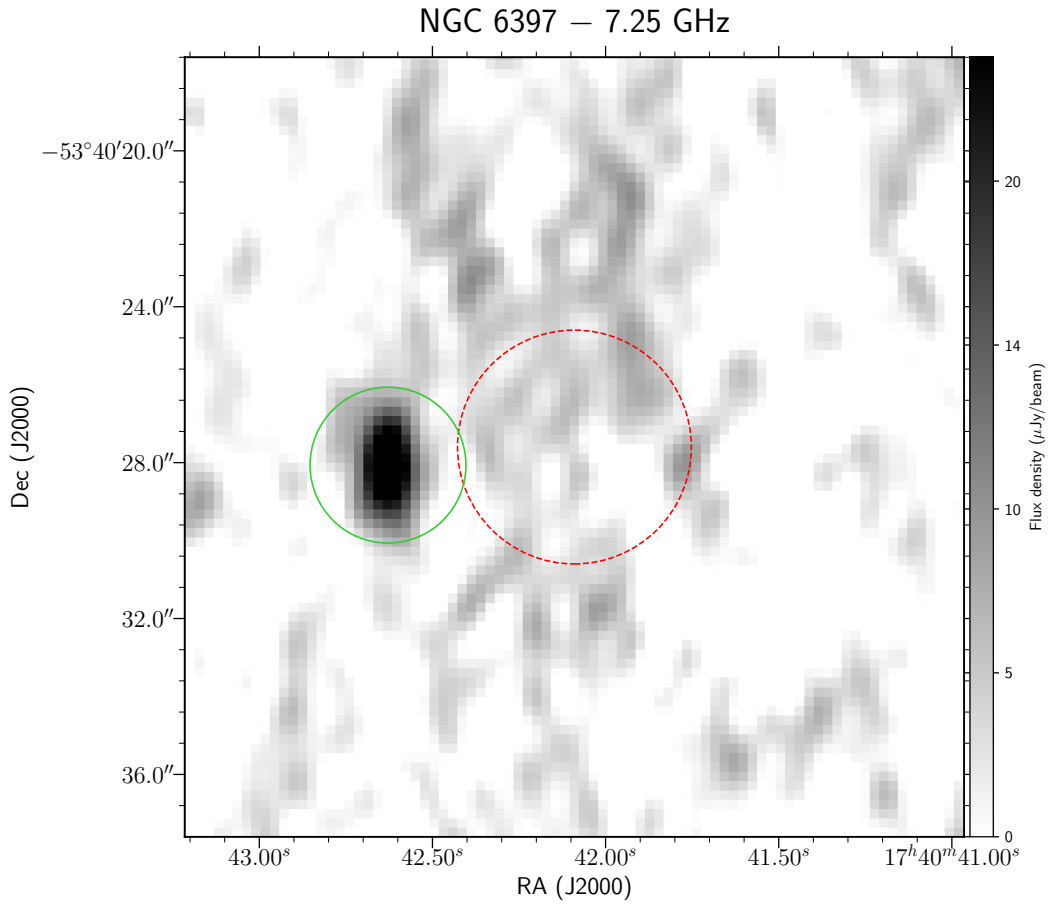
NGC 6397 — 7.25 GHz
−53°40′20.0″
24.0″
28.0″
32.0″
36.0″
Dec (J2000)
43.00s
42.50s
42.00s
41.50s
17h40m41.00s
RA (J2000)
Flux density (μJy/beam)
0
5
10
14
20

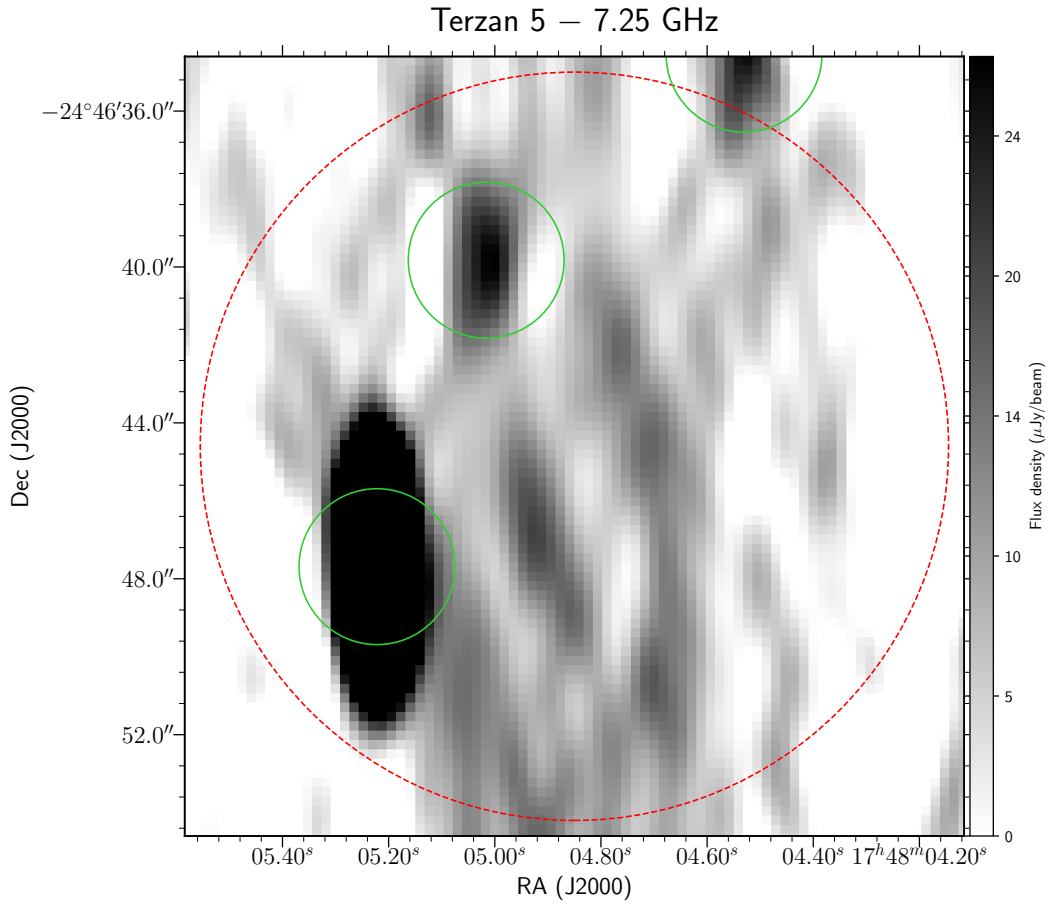
Terzan 5 — 7.25 GHz
−24°46′36.0″
40.0″
44.0″
48.0″
52.0″
Dec (J2000)
05.40s
05.20s
05.00s
04.80s
04.60s
04.40s
17h48m04.20s
RA (J2000)
Flux density (μJy/beam)
0
5
10
14
20
24

Table 3.21: Terzan 5

ID	Field	RA	DEC	Δ RA ($''$)	Δ DEC ($''$)	$S_{5.5}$ (μJy)	$\Delta S_{5.5}$ (μJy)	$S_{7.25}$ (μJy)	$\Delta S_{7.25}$ (μJy)	S_9 (μJy)	ΔS_9 (μJy)	α	$\Delta\alpha$	R/R$_c$	R/R$_h$
1	Terzan 5	17:48:05.17	-24:46:46.54	0.21	0.13	282.0	14.7	<160.0	-	<107.0	-	<-1.97	0.11	0.50	0.11
2	Terzan 5	17:48:05.02	-24:46:39.83	0.04	0.48	<46.3	-	29.8	4.3	<43.8	-	-	-	0.55	0.12
3	Terzan 5	17:48:05.22	-24:46:47.69	0.00	0.03	<204.0	-	349.0	7.8	331.0	8.3	>0.98	0.05	0.62	0.14
4	Terzan 5	17:48:04.53	-24:46:34.54	0.01	0.10	30.1	3.9	28.3	3.9	<33.2	-	<0.20	0.26	1.14	0.25
5	Terzan 5	17:48:02.25	-24:46:37.62	0.27	0.02	102.0	3.5	23.7	3.4	<36.3	-	<-2.10	0.07	3.76	0.84
6	Terzan 5	17:48:01.73	-24:46:27.88	0.15	0.23	45.0	3.5	47.2	3.4	39.2	6.7	-0.27	0.37	4.76	1.06
7	Terzan 5	17:48:08.06	-24:46:00.82	0.03	0.23	26.8	3.4	34.0	3.5	33.7	5.1	0.45	0.4	6.45	1.43
8	Terzan 5	17:48:08.87	-24:47:34.54	0.18	0.94	33.7	4.6	33.6	3.6	27.5	5.4	-0.42	0.52	7.72	1.72
9	Terzan 5	17:48:06.40	-24:45:05.08	0.04	0.08	181.0	3.4	157.0	4.8	133.0	6.0	-0.63	0.1	10.60	2.36
10	Terzan 5	17:48:00.14	-24:48:05.50	0.04	0.22	130.0	14.2	98.8	17.5	68.8	13.1	-1.30	0.45	10.76	2.39
11	Terzan 5	17:47:59.82	-24:48:02.50	0.00	0.06	949.0	17.2	862.0	13.7	737.0	11.8	-0.51	0.05	10.81	2.40
12	Terzan 5	17:48:10.92	-24:45:40.52	0.01	0.06	166.0	3.4	142.0	4.9	131.0	5.9	-0.48	0.1	10.90	2.42
13	Terzan 5	17:48:10.35	-24:47:59.42	0.12	0.57	24.6	3.6	18.8	3.8	<39.4	-	<0.96	0.3	11.03	2.45
14	Terzan 5	17:47:59.43	-24:48:01.61	0.37	0.27	74.5	10.9	<95.5	-	<62.9	-	<-0.34	0.3	11.11	2.47
15	Terzan 5	17:47:57.13	-24:45:21.42	0.13	0.49	46.1	3.9	33.9	5.7	38.0	7.1	-0.39	0.41	13.97	3.10
16	Terzan 5	17:48:09.89	-24:48:57.90	0.01	0.16	80.0	3.9	49.0	6.0	<51.0	-	<-0.91	0.1	15.62	3.47
17	Terzan 5	17:47:54.48	-24:45:44.82	0.01	0.11	33.1	4.1	29.7	4.6	<47.2	-	<0.72	0.25	15.98	3.55
18	Terzan 5	17:48:15.76	-24:45:58.86	0.00	0.25	27.6	3.8	30.1	4.5	<57.9	-	<1.51	0.28	16.20	3.60
19	Terzan 5	17:47:53.15	-24:46:51.70	0.07	0.14	46.2	4.2	28.8	4.9	<58.0	-	<0.46	0.19	16.62	3.69
20	Terzan 5	17:48:16.81	-24:46:42.23	0.04	0.05	156.0	4.0	132.0	4.9	116.0	8.8	-0.60	0.16	16.97	3.77

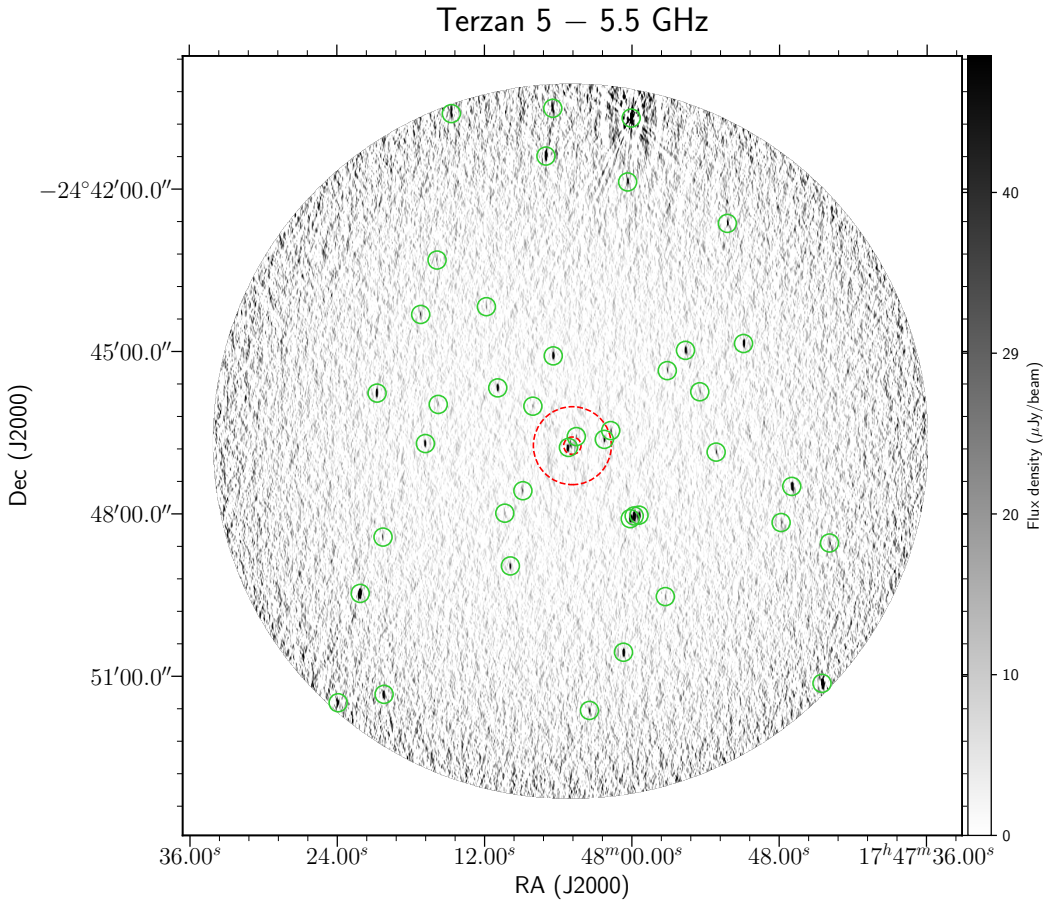
Terzan 5 – 5.5 GHz
−24°42′00.0″
45′00.0″
48′00.0″
51′00.0″
Dec (J2000)
36.00s
24.00s
12.00s
48m00.00s
48.00s
17h47m36.00s
RA (J2000)
Flux density (μJy/beam)
0
10
20
29
40

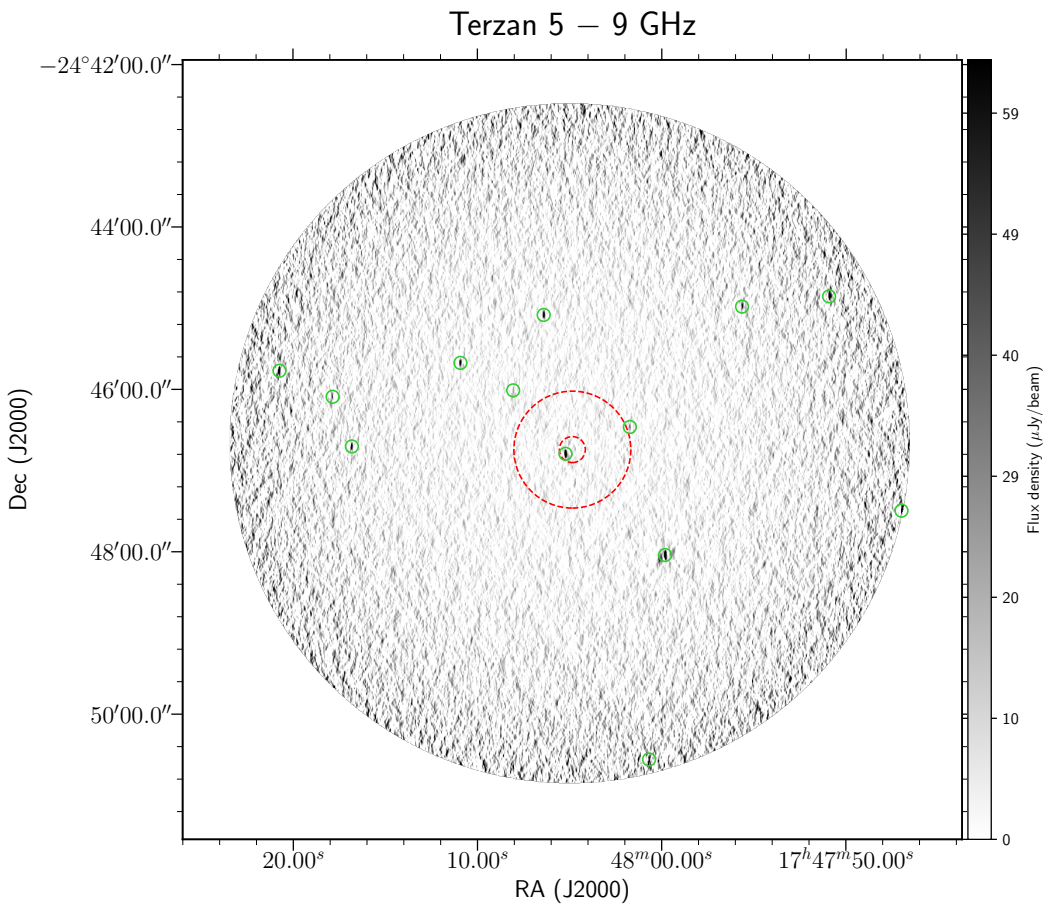
Terzan 5 – 9 GHz
−24°42′00.0″
44′00.0″
46′00.0″
48′00.0″
50′00.0″
Dec (J2000)
20.00s
10.00s
48m00.00s
17h47m50.00s
RA (J2000)
Flux density (μJy/beam)
0
10
20
29
40
49
59

Table 3.22: NGC 6441

ID	Field	RA	DEC	Δ RA ($''$)	Δ DEC ($''$)	$S_{5.5}$ (μJy)	$\Delta S_{5.5}$ (μJy)	$S_{7.25}$ (μJy)	$\Delta S_{7.25}$ (μJy)	S_{9} (μJy)	ΔS_{9} (μJy)	α	$\Delta\alpha$	R/R$_c$	R/R$_h$
1	NGC 6441	17:50:10.95	-37:03:27.24	0.13	0.09	323.0	15.7	317.0	15.9	239.0	19.2	-0.62	0.2	4.30	0.98
2	NGC 6441	17:50:13.04	-37:02:30.44	0.07	0.07	21.6	3.4	20.6	2.6	19.4	3.0	-0.20	0.47	4.46	1.02
3	NGC 6441	17:50:16.45	-37:03:05.38	0.01	0.03	138.0	3.0	99.9	2.6	66.0	3.4	-1.50	0.12	5.20	1.18
4	NGC 6441	17:50:13.77	-37:02:03.92	0.06	0.32	<19.5	-	12.9	2.2	<21.9	-	-	-	7.93	1.81
5	NGC 6441	17:50:13.66	-37:04:10.98	0.06	0.38	22.4	3.3	<21.3	-	<12.2	-	<-1.23	0.3	8.48	1.93
6	NGC 6441	17:50:16.87	-37:02:14.60	0.12	0.13	83.3	11.7	66.7	8.7	16.7	3.5	-3.26	0.55	8.74	1.99
7	NGC 6441	17:50:16.58	-37:04:00.82	0.01	0.14	36.6	3.2	26.9	3.2	17.2	3.3	-1.52	0.41	8.94	2.04
8	NGC 6441	17:50:12.94	-37:04:27.22	0.05	0.26	<11.8	-	<24.7	-	23.9	4.0	>1.43	0.34	10.52	2.40
9	NGC 6441	17:50:16.83	-37:01:42.18	0.07	0.24	24.9	3.6	22.0	2.3	16.6	3.3	-0.82	0.51	12.11	2.76
10	NGC 6441	17:50:21.18	-37:02:46.43	0.16	0.09	18.5	3.1	16.3	2.6	<24.1	-	<0.54	0.35	12.69	2.89
11	NGC 6441	17:50:04.79	-37:03:01.61	0.66	0.71	24.6	3.3	12.3	3.0	<24.8	-	<0.02	0.27	12.70	2.90
12	NGC 6441	17:50:11.57	-37:01:27.34	0.04	0.22	14.7	3.1	14.3	2.5	14.7	3.5	-0.00	0.64	12.75	2.91
13	NGC 6441	17:50:05.25	-37:03:53.61	0.16	0.08	16.0	3.2	17.9	2.9	<14.4	-	<-0.21	0.41	13.50	3.08
14	NGC 6441	17:50:21.54	-37:02:34.04	0.02	0.01	18.8	3.6	18.5	2.6	<12.3	-	<-0.86	0.4	13.62	3.11
15	NGC 6441	17:50:20.05	-37:01:56.77	0.46	0.27	17.9	3.0	12.9	2.4	<17.6	-	<-0.03	0.35	13.86	3.16
16	NGC 6441	17:50:09.03	-37:01:27.86	0.01	0.27	15.9	3.2	17.3	2.6	<25.6	-	<0.97	0.42	13.93	3.18
17	NGC 6441	17:50:20.09	-37:01:56.17	0.50	1.16	17.9	3.0	10.4	2.4	<20.0	-	<0.23	0.35	13.96	3.18
18	NGC 6441	17:50:22.81	-37:02:41.07	0.01	0.18	136.0	3.8	109.0	3.2	80.1	4.4	-1.08	0.13	15.28	3.49
19	NGC 6441	17:50:07.38	-37:01:20.51	0.03	0.13	48.9	3.4	39.2	2.9	33.3	3.9	-0.79	0.29	16.00	3.65
20	NGC 6441	17:50:02.97	-37:03:37.40	0.11	0.26	21.1	3.4	19.8	3.1	<30.5	-	<0.75	0.33	16.03	3.66

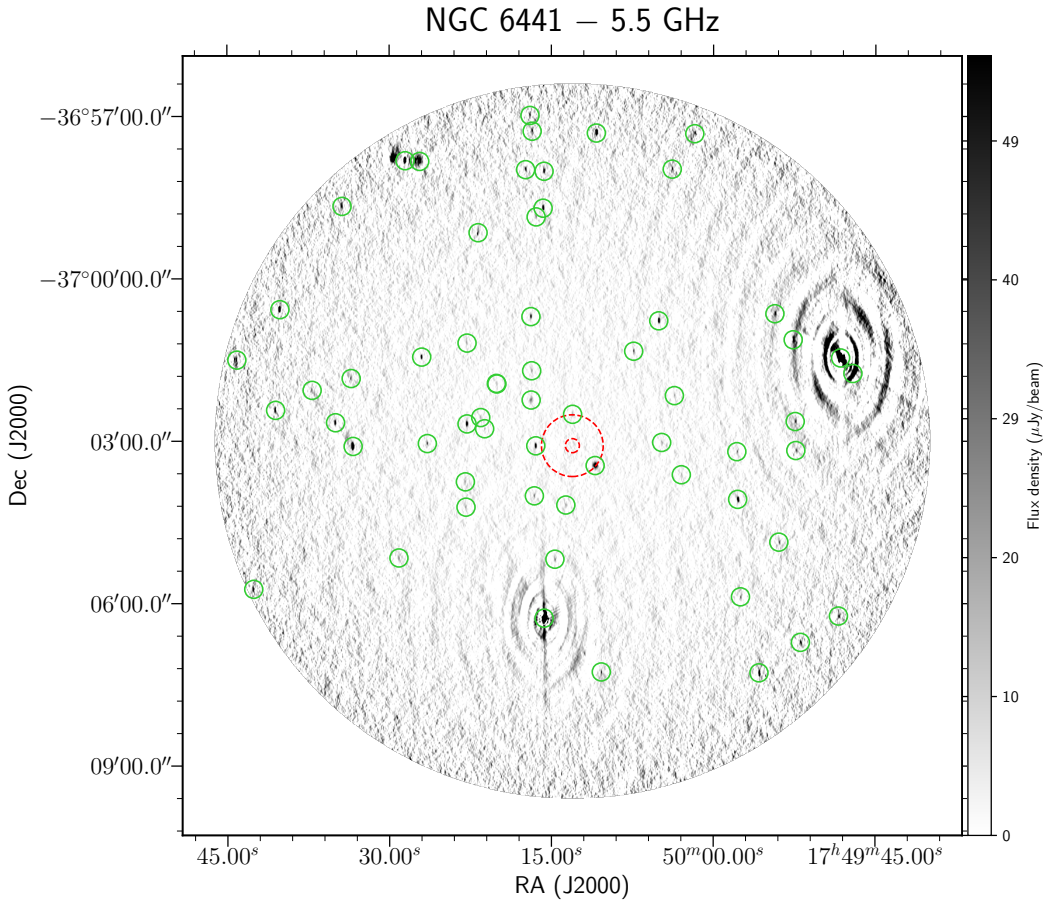
NGC 6441 – 5.5 GHz
−36°57′00.0″
−37°00′00.0″
03′00.0″
06′00.0″
09′00.0″
Dec (J2000)
45.00s
30.00s
15.00s
50m00.00s
17h49m45.00s
RA (J2000)
Flux density (μJy/beam)
0
10
20
29
40
49

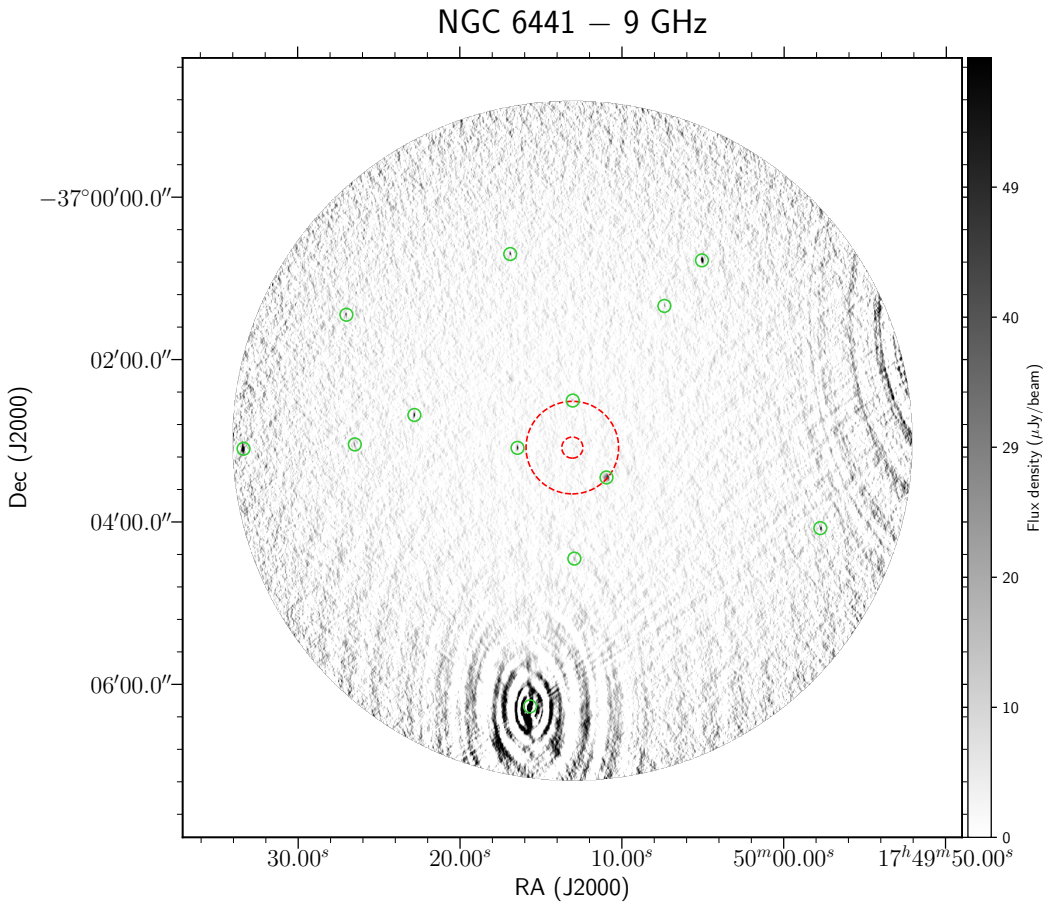
NGC 6441 – 9 GHz
−37°00′00.0″
02′00.0″
04′00.0″
06′00.0″
Dec (J2000)
30.00s
20.00s
10.00s
50m00.00s
17h49m50.00s
RA (J2000)
Flux density (μJy/beam)
0
10
20
29
40
49

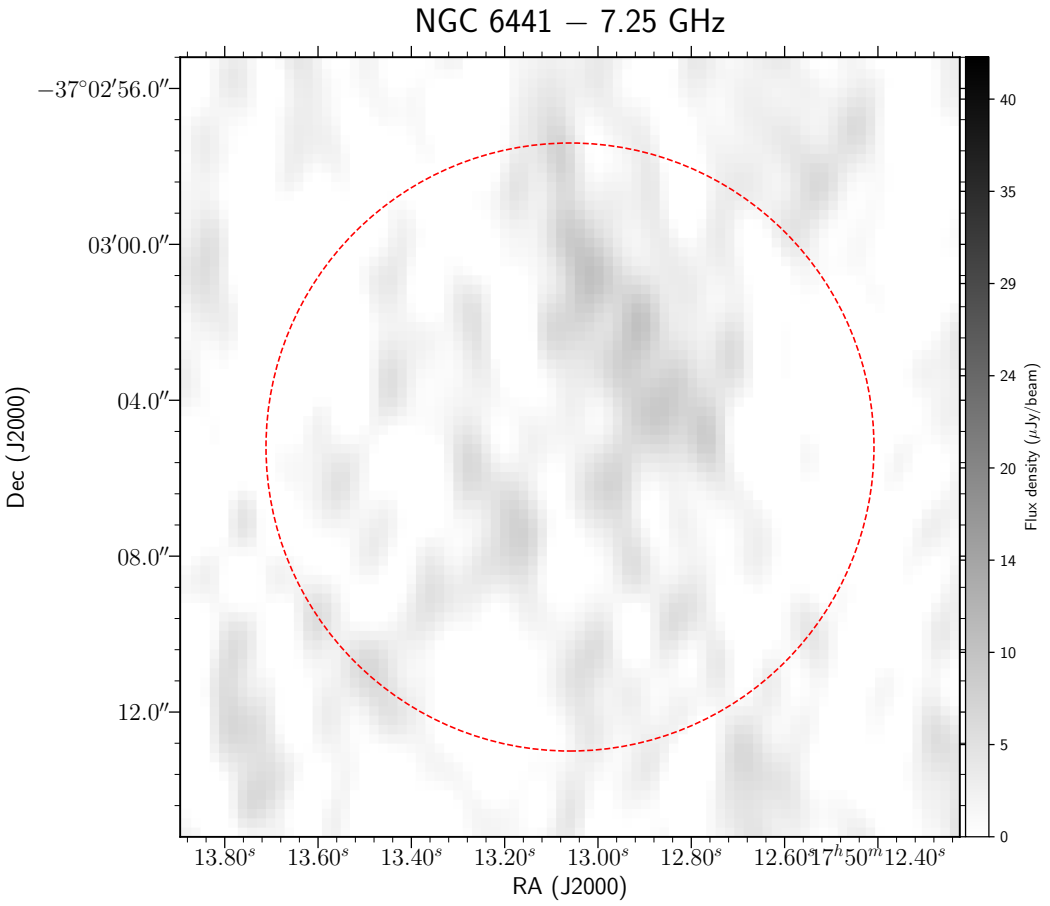
NGC 6441 — 7.25 GHz
−37°02′56.0″
03′00.0″
04.0″
08.0″
12.0″
Dec (J2000)
13.80s
13.60s
13.40s
13.20s
13.00s
12.80s
12.60s
17h50m12.40s
RA (J2000)
Flux density (μJy/beam)
40
35
29
24
20
14
10
5
0

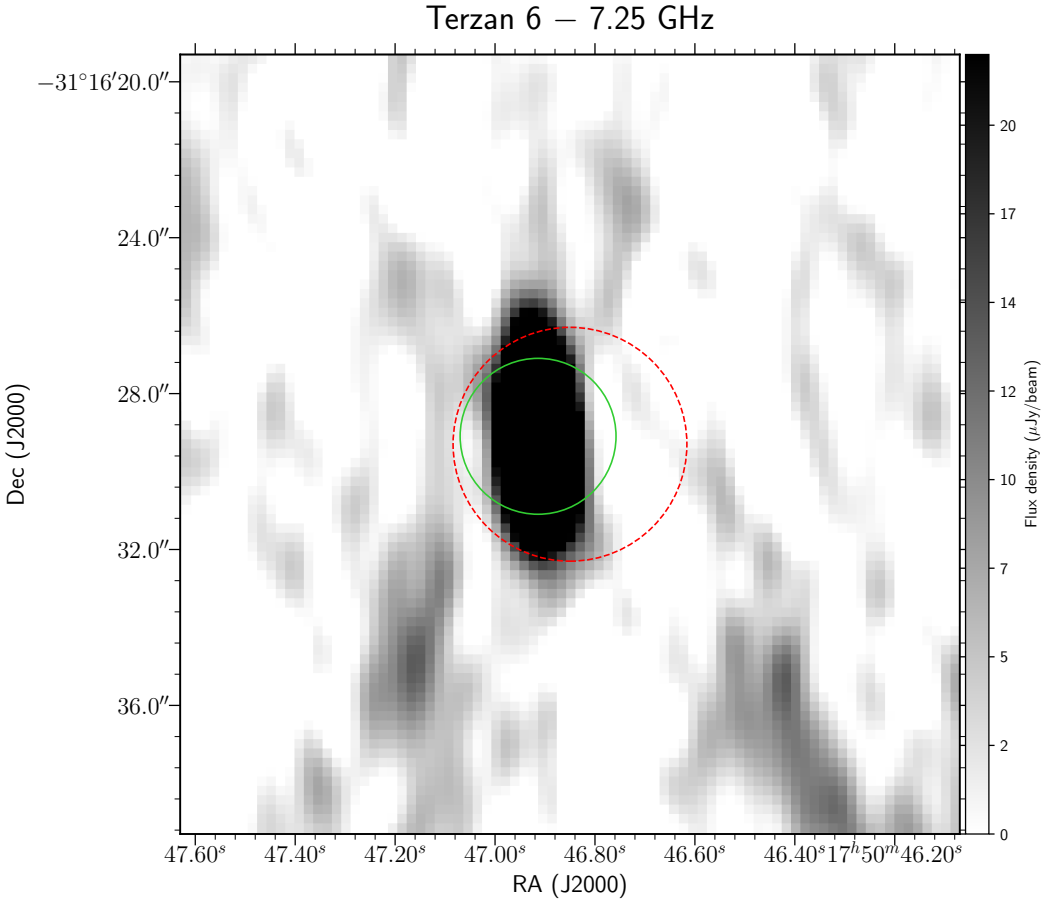
Terzan 6 — 7.25 GHz
−31°16′20.0″
24.0″
28.0″
32.0″
36.0″
Dec (J2000)
47.60s
47.40s
47.20s
47.00s
46.80s
46.60s
46.40s
17h50m46.20s
RA (J2000)
Flux density (μJy/beam)
20
17
14
12
10
7
5
2
0

Table 3.23: Terzan 6

ID	Field	RA	DEC	Δ RA ($''$)	Δ DEC ($''$)	$S_{5.5}$ (μJy)	$\Delta S_{5.5}$ (μJy)	$S_{7.25}$ (μJy)	$\Delta S_{7.25}$ (μJy)	S_9 (μJy)	ΔS_9 (μJy)	α	$\Delta\alpha$	R/R_c	R/R_h
1	Terzan 6	17:50:46.91	-31:16:29.10	0.00	0.09	203.0	4.8	190.0	3.5	166.0	5.2	-0.41	0.08	0.28	0.03
2	Terzan 6	17:50:48.51	-31:16:46.35	0.03	0.46	37.9	4.0	35.9	3.0	32.4	5.1	-0.35	0.38	9.10	1.03
3	Terzan 6	17:50:51.83	-31:16:44.95	0.06	0.21	23.6	3.9	19.1	3.0	<22.2	-	<-0.12	0.34	21.91	2.49
4	Terzan 6	17:50:46.60	-31:15:19.99	0.01	0.15	91.6	3.9	68.4	3.7	48.3	5.7	-1.30	0.25	23.13	2.63
5	Terzan 6	17:50:45.63	-31:15:16.97	0.12	0.05	40.6	4.0	26.7	3.7	23.7	4.8	-1.09	0.45	24.66	2.80
6	Terzan 6	17:50:49.70	-31:15:10.11	0.00	0.39	36.7	4.2	21.8	4.0	<22.7	-	<-0.97	0.23	29.07	3.30
7	Terzan 6	17:50:44.61	-31:17:57.02	0.12	0.18	25.3	4.0	20.6	3.2	<33.9	-	<0.59	0.33	30.77	3.50
8	Terzan 6	17:50:54.01	-31:16:16.48	0.01	0.33	37.7	3.9	32.1	3.1	24.3	5.2	-0.90	0.48	30.90	3.51
9	Terzan 6	17:50:49.56	-31:18:03.12	0.07	0.25	227.0	14.4	182.0	13.5	115.0	6.2	-1.38	0.16	33.34	3.79
10	Terzan 6	17:50:44.25	-31:14:45.62	0.18	0.87	27.3	4.4	20.4	3.6	<38.0	-	<0.67	0.33	36.30	4.13
11	Terzan 6	17:50:44.23	-31:14:44.16	0.44	1.26	27.3	4.4	14.8	3.7	<28.7	-	<0.10	0.33	36.80	4.18
12	Terzan 6	17:50:38.46	-31:17:00.34	0.05	0.36	37.2	4.1	42.5	3.4	51.0	6.4	0.64	0.32	37.31	4.24
13	Terzan 6	17:50:48.09	-31:18:25.99	0.05	0.32	<15.8	-	<15.8	-	34.2	5.7	>1.57	0.34	39.25	4.46
14	Terzan 6	17:50:43.21	-31:14:34.62	0.71	0.40	26.1	4.5	23.0	4.5	25.8	6.1	-0.01	0.6	41.27	4.69
15	Terzan 6	17:50:54.38	-31:17:49.29	0.08	0.32	30.0	4.3	23.6	3.7	<38.5	-	<0.51	0.3	41.79	4.75
16	Terzan 6	17:50:43.47	-31:18:41.99	0.14	0.33	33.8	4.5	34.9	4.0	33.7	6.4	-0.00	0.47	46.53	5.29
17	Terzan 6	17:50:35.51	-31:16:10.71	0.23	0.19	37.5	4.3	33.4	4.6	28.9	6.9	-0.52	0.55	48.87	5.55
18	Terzan 6	17:50:35.38	-31:15:17.99	0.00	0.03	270.0	4.7	220.0	5.0	169.0	9.6	-0.95	0.12	54.48	6.19
19	Terzan 6	17:50:57.74	-31:15:00.38	0.01	0.00	39.1	5.9	38.4	4.5	<54.4	-	<0.67	0.31	55.18	6.27
20	Terzan 6	17:50:52.22	-31:19:05.31	0.03	0.38	34.2	4.7	25.1	5.1	<37.3	-	<0.18	0.28	56.84	6.46

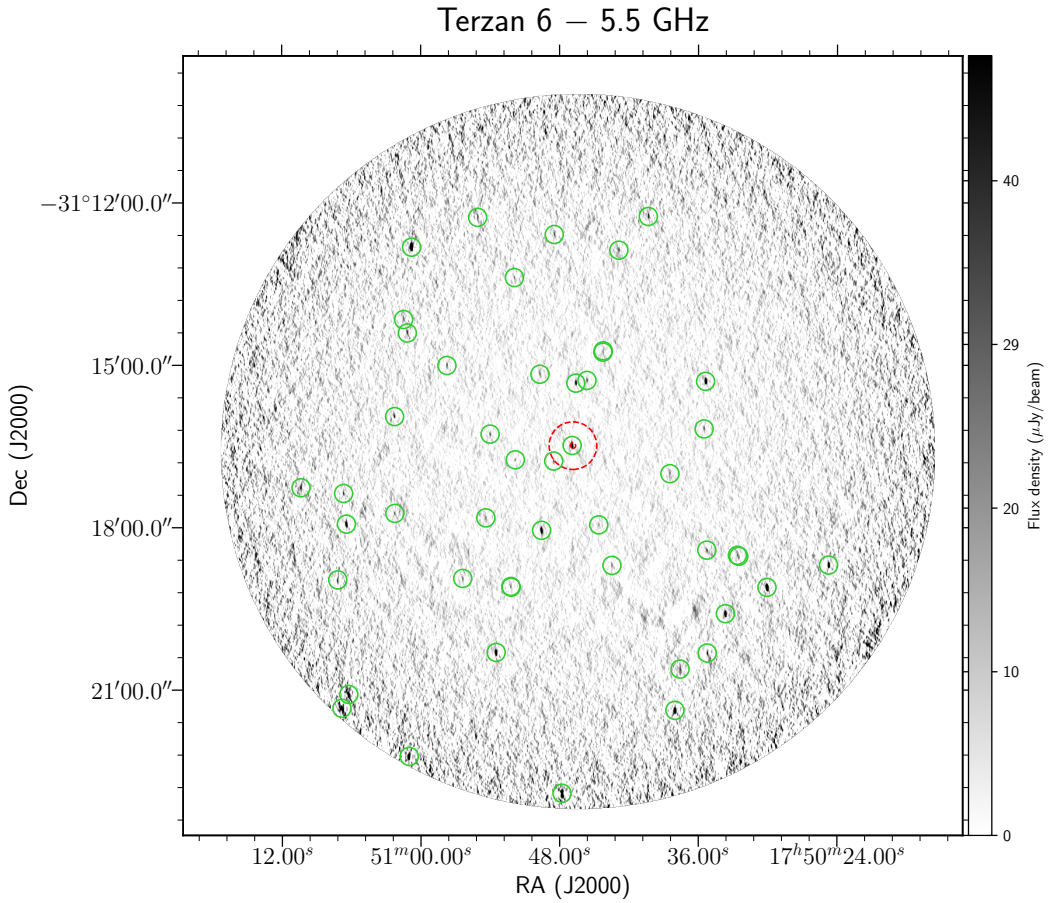
Terzan 6 – 5.5 GHz
−31°12′00.0″
15′00.0″
18′00.0″
21′00.0″
Dec (J2000)
12.00s
51m00.00s
48.00s
36.00s
17h50m24.00s
RA (J2000)
Flux density (μJy/beam)
0
10
20
29
40

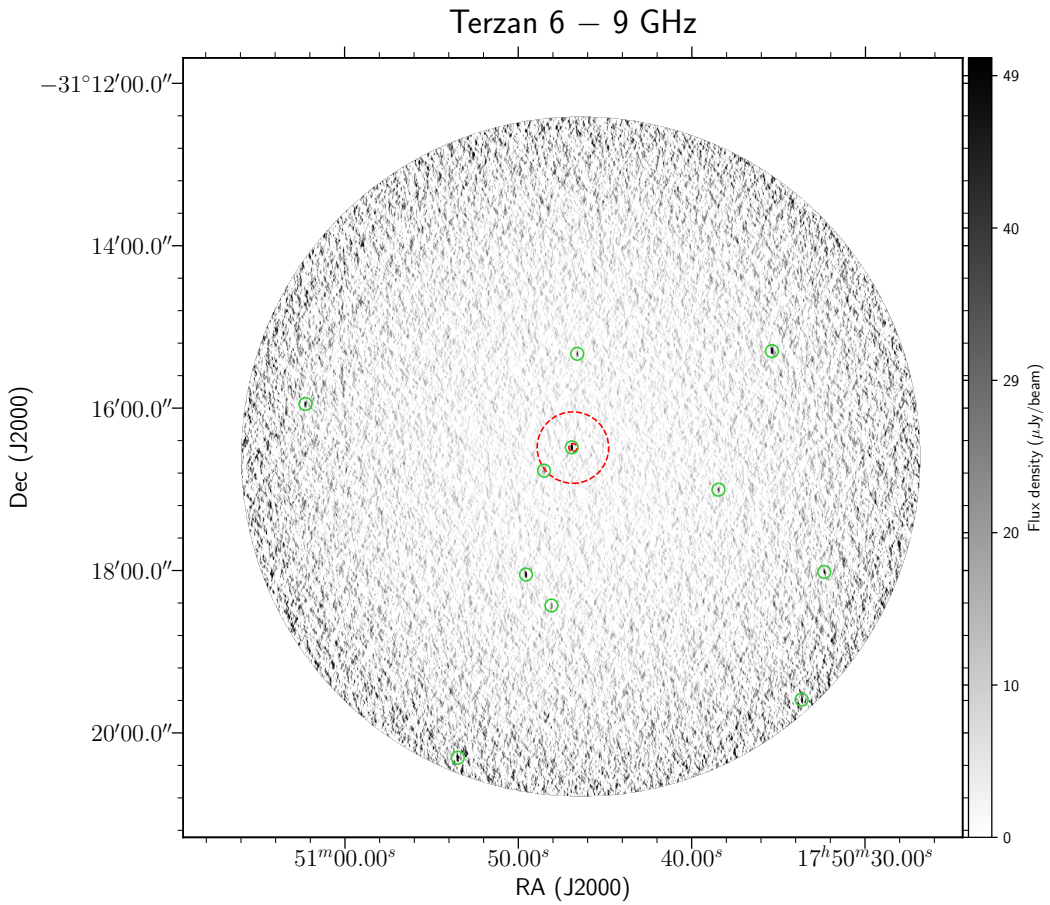
Terzan 6 – 9 GHz
−31°12′00.0″
14′00.0″
16′00.0″
18′00.0″
20′00.0″
Dec (J2000)
51m00.00s
50.00s
40.00s
17h50m30.00s
RA (J2000)
Flux density (μJy/beam)
0
10
20
29
40
49

Table 3.24: Djorg 2

ID	Field	RA	DEC	Δ RA ($''$)	Δ DEC ($''$)	$S_{5.5}$ (μJy)	$\Delta S_{5.5}$ (μJy)	$S_{7.25}$ (μJy)	$\Delta S_{7.25}$ (μJy)	S_9 (μJy)	ΔS_9 (μJy)	α	$\Delta\alpha$	R/R$_c$	R/R$_h$
1	Djorg 2	18:01:48.88	-27:48:57.98	0.27	0.67	21.0	3.3	18.5	2.6	19.1	3.5	-0.20	0.51	1.78	0.56
2	Djorg 2	18:01:48.01	-27:49:00.24	0.00	0.86	21.6	3.3	15.9	2.7	<19.8	-	<-0.18	0.31	1.81	0.57
3	Djorg 2	18:01:45.56	-27:49:33.95	0.07	0.05	25.5	3.3	16.4	2.5	<18.4	-	<-0.66	0.26	2.37	0.75
4	Djorg 2	18:01:52.88	-27:49:19.60	0.02	0.46	31.9	3.6	27.7	4.0	21.4	3.6	-0.82	0.45	2.62	0.82
5	Djorg 2	18:01:47.97	-27:50:22.92	0.14	0.11	26.6	3.4	21.0	2.5	<20.0	-	<-0.58	0.26	2.63	0.83
6	Djorg 2	18:01:46.10	-27:50:19.02	0.04	0.25	37.8	3.3	33.0	2.6	26.0	3.7	-0.75	0.34	3.07	0.97
7	Djorg 2	18:01:46.08	-27:50:19.49	1.10	1.17	14.3	3.3	<20.6	-	26.0	3.7	1.21	0.56	3.10	0.97
8	Djorg 2	18:01:44.71	-27:49:07.51	0.12	0.03	15.4	3.4	19.4	2.7	<25.5	-	<1.02	0.45	3.21	1.01
9	Djorg 2	18:01:51.16	-27:48:33.58	0.22	0.59	21.5	3.5	18.9	3.2	19.7	3.7	-0.17	0.53	3.30	1.04
10	Djorg 2	18:01:54.24	-27:48:44.23	0.12	0.22	38.6	3.8	28.6	3.5	23.8	4.0	-0.97	0.38	4.23	1.33
11	Djorg 2	18:01:57.37	-27:48:56.01	0.01	0.04	28.2	4.1	19.6	4.4	<25.6	-	<-0.20	0.3	5.85	1.84
12	Djorg 2	18:01:45.79	-27:51:22.07	0.07	0.05	24.5	3.7	18.6	3.1	<22.4	-	<-0.18	0.31	5.94	1.87
13	Djorg 2	18:01:58.08	-27:49:57.77	0.01	0.04	72.6	4.4	71.3	4.8	48.0	4.9	-0.84	0.24	6.15	1.93
14	Djorg 2	18:01:54.94	-27:51:07.45	0.32	1.40	3950.0	139.0	2470.0	147.0	<53.8	-	<-8.72	0.07	6.17	1.94
15	Djorg 2	18:01:54.63	-27:51:11.65	0.31	0.16	<247.0	-	<164.0	-	56.3	9.7	>-3.00	0.35	6.21	1.95
16	Djorg 2	18:01:40.88	-27:48:15.56	0.20	0.04	1580.0	35.0	1420.0	35.5	1180.0	39.5	-0.59	0.08	6.75	2.12
17	Djorg 2	18:01:58.70	-27:48:48.89	0.06	0.32	39.8	4.2	37.4	3.8	27.5	5.3	-0.76	0.46	6.81	2.14
18	Djorg 2	18:01:51.59	-27:47:21.18	0.05	0.28	24.1	4.0	22.5	3.6	<41.0	-	<1.08	0.34	6.86	2.16
19	Djorg 2	18:01:55.03	-27:51:28.72	0.04	0.37	<555.0	-	<360.0	-	133.0	21.3	>-2.90	0.33	7.07	2.22
20	Djorg 2	18:01:43.07	-27:47:37.05	0.03	0.06	38.2	4.1	28.5	4.4	23.2	5.4	-1.04	0.53	7.12	2.24

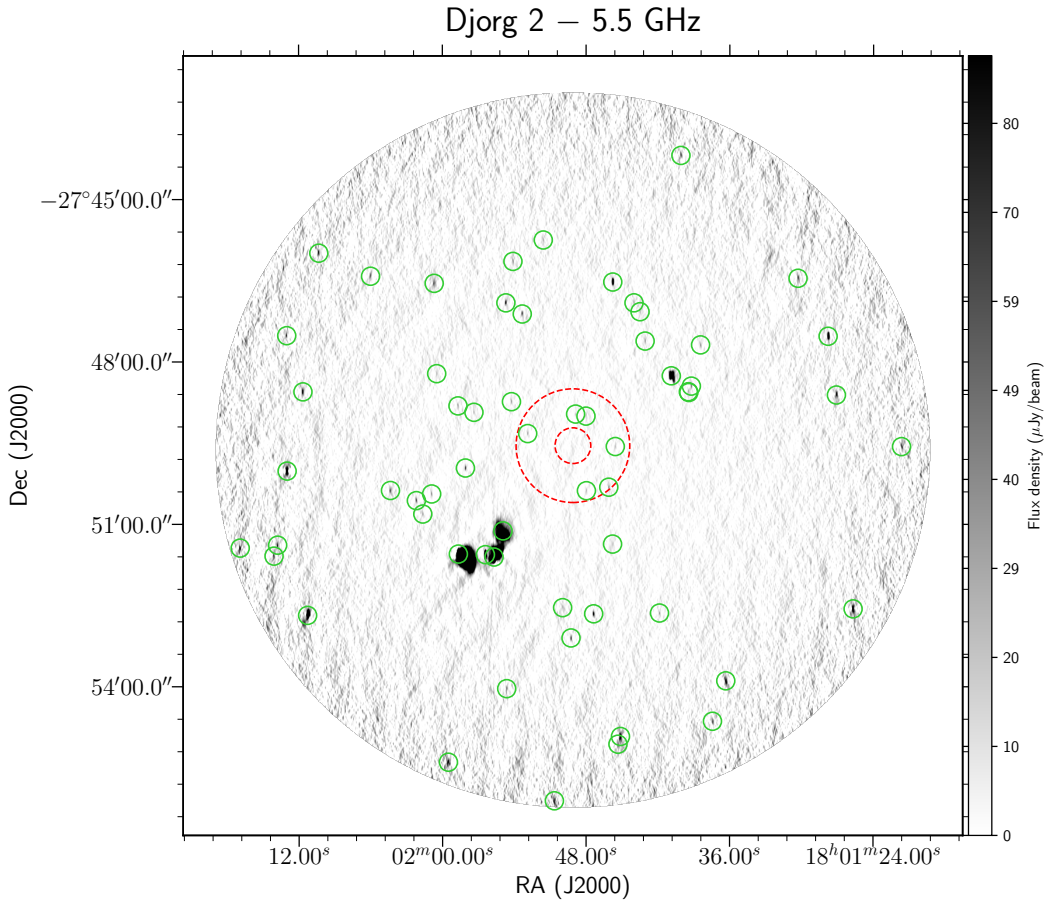
Djorg 2 — 5.5 GHz
−27°45′00.0″
48′00.0″
51′00.0″
54′00.0″
Dec (J2000)
12.00s
02m00.00s
48.00s
36.00s
18h01m24.00s
RA (J2000)
Flux density (μJy/beam)
80
70
59
49
40
29
20
10
0

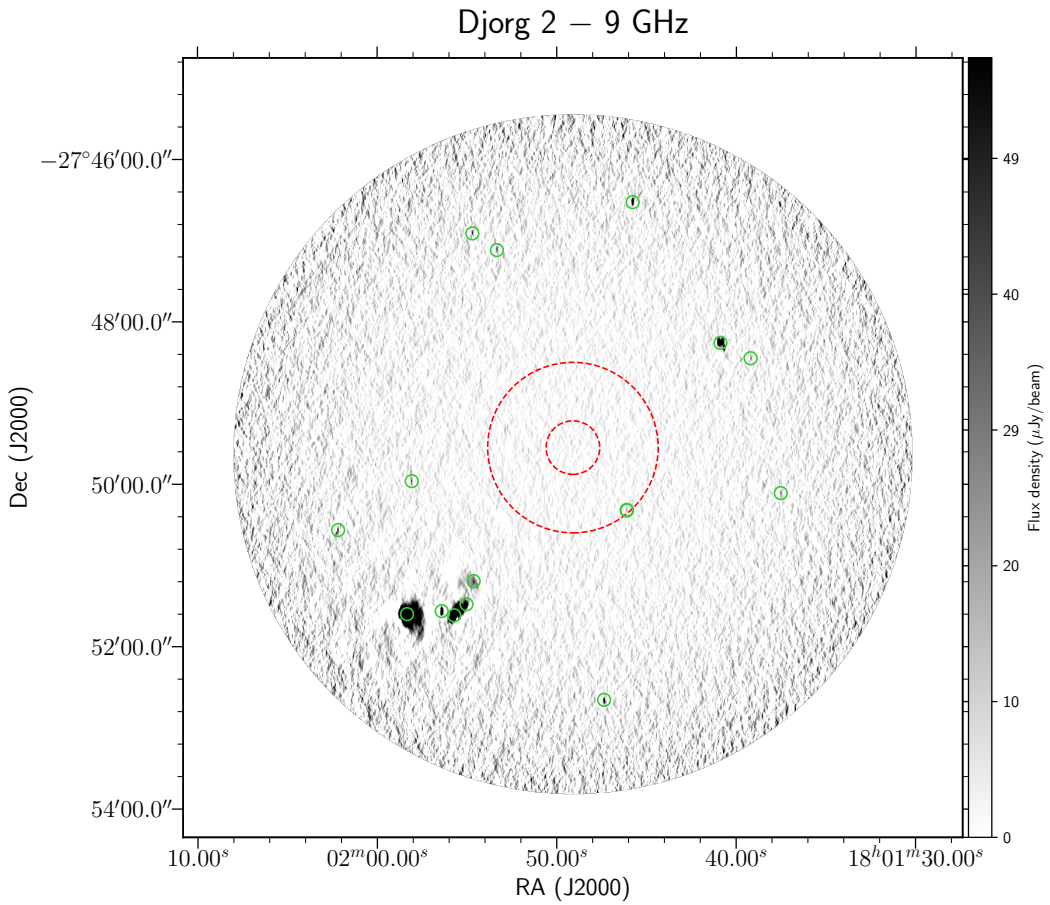
Djorg 2 — 9 GHz
−27°46′00.0″
48′00.0″
50′00.0″
52′00.0″
54′00.0″
Dec (J2000)
10.00s
02m00.00s
50.00s
40.00s
18h01m30.00s
RA (J2000)
Flux density (μJy/beam)
49
40
29
20
10
0

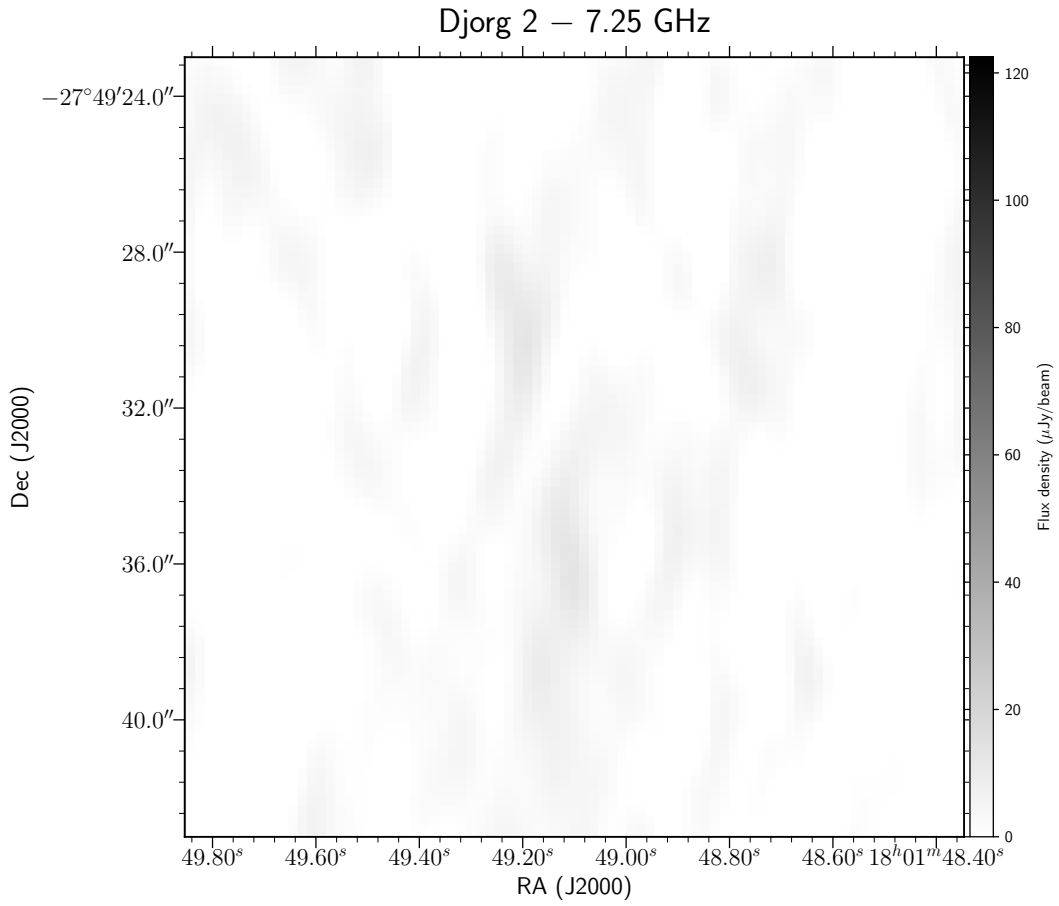
Djorg 2 – 7.25 GHz
−27°49′24.0″
28.0″
32.0″
36.0″
40.0″
Dec (J2000)
49.80s
49.60s
49.40s
49.20s
49.00s
48.80s
48.60s
18h01m48.40s
RA (J2000)
Flux density (μJy/beam)
120
100
80
60
40
20
0

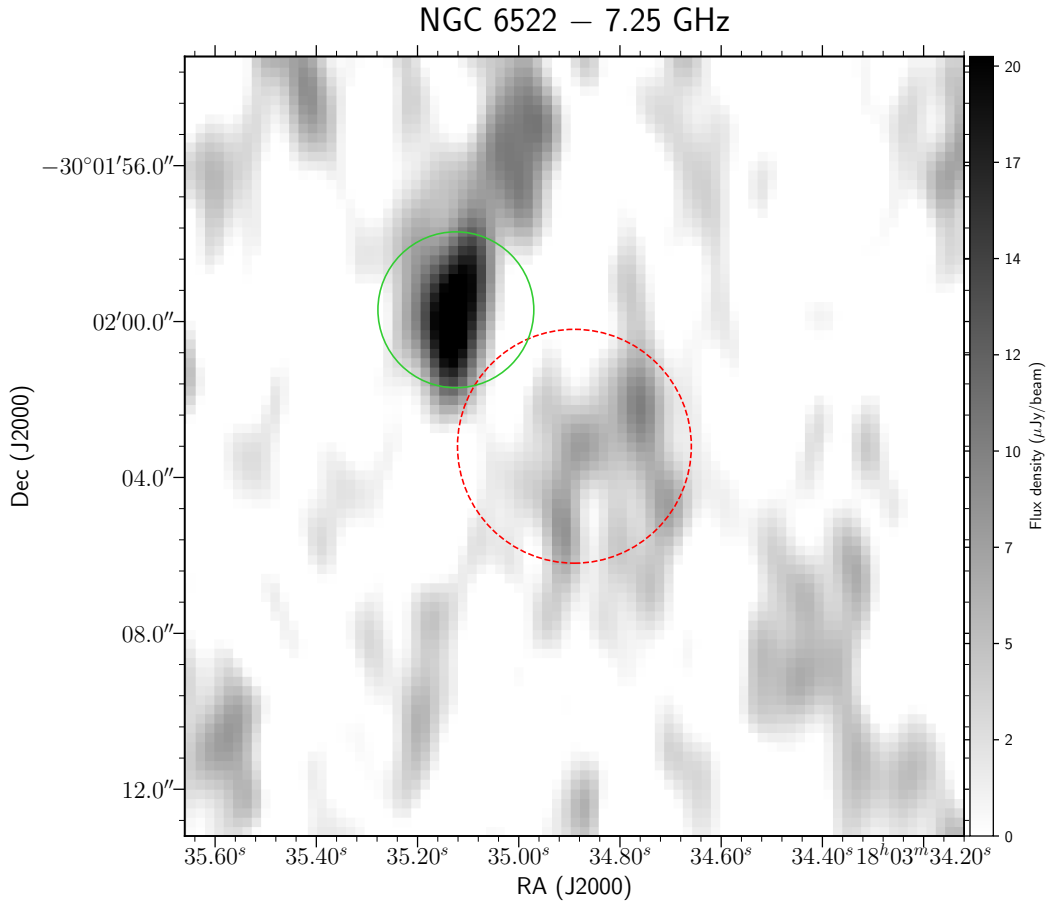
NGC 6522 – 7.25 GHz
−30°01′56.0″
02′00.0″
04.0″
08.0″
12.0″
Dec (J2000)
35.60s
35.40s
35.20s
35.00s
34.80s
34.60s
34.40s
18h03m34.20s
RA (J2000)
Flux density (μJy/beam)
20
17
14
12
10
7
5
2
0

Table 3.25: NGC 6522

ID	Field	RA	DEC	Δ RA ($''$)	Δ DEC ($''$)	$S_{5.5}$ (μJy)	$\Delta S_{5.5}$ (μJy)	$S_{7.25}$ (μJy)	$\Delta S_{7.25}$ (μJy)	S_9 (μJy)	ΔS_9 (μJy)	α	$\Delta\alpha$	R/R_c	R/R_h
1	NGC 6522	18:03:35.12	-30:01:59.70	0.06	0.08	31.4	4.1	25.1	3.0	19.4	3.7	-0.97	0.48	1.55	0.08
2	NGC 6522	18:03:37.45	-30:02:16.72	0.33	0.12	24.1	3.5	19.5	3.0	22.5	3.9	-0.13	0.46	11.97	0.60
3	NGC 6522	18:03:31.42	-30:01:42.93	0.02	0.19	41.0	3.4	40.7	2.9	38.8	4.4	-0.11	0.28	16.47	0.82
4	NGC 6522	18:03:32.99	-30:00:59.97	0.04	0.35	23.4	3.5	20.4	2.6	17.1	4.1	-0.63	0.59	22.62	1.13
5	NGC 6522	18:03:28.49	-30:02:17.41	0.05	0.06	57.3	3.6	45.1	3.1	36.3	4.2	-0.93	0.26	28.12	1.41
6	NGC 6522	18:03:28.13	-30:01:43.66	0.01	0.07	26.1	3.5	26.8	2.8	25.0	4.9	-0.08	0.48	29.96	1.50
7	NGC 6522	18:03:41.23	-30:01:21.24	0.01	0.04	62.3	4.3	59.8	3.4	60.1	4.8	-0.07	0.22	30.81	1.54
8	NGC 6522	18:03:41.84	-30:02:27.96	0.07	0.15	17.3	4.4	17.7	3.0	<26.9	-	<0.90	0.53	31.18	1.56
9	NGC 6522	18:03:27.68	-30:01:14.41	0.16	0.12	28.7	4.3	23.6	3.4	<31.4	-	<0.18	0.31	35.18	1.76
10	NGC 6522	18:03:39.49	-30:03:42.06	0.17	0.25	34.2	4.5	30.3	3.8	28.0	5.1	-0.42	0.47	38.50	1.93
11	NGC 6522	18:03:27.91	-30:03:20.05	0.02	0.05	108.0	4.7	86.6	3.8	63.3	4.8	-1.08	0.19	39.61	1.98
12	NGC 6522	18:03:36.29	-30:00:00.21	0.15	0.27	29.8	4.7	23.2	4.0	<29.0	-	<-0.05	0.32	41.44	2.07
13	NGC 6522	18:03:27.52	-30:00:19.08	0.02	0.03	64.0	4.1	52.4	3.4	43.4	6.7	-0.79	0.34	47.14	2.36
14	NGC 6522	18:03:27.69	-30:03:55.37	0.21	0.58	38.2	4.2	27.0	3.5	<32.2	-	<-0.35	0.22	48.67	2.43
15	NGC 6522	18:03:23.57	-30:01:57.58	0.01	0.07	94.7	4.0	76.8	4.0	59.9	6.6	-0.92	0.24	49.04	2.45
16	NGC 6522	18:03:41.30	-30:04:07.76	0.02	0.07	158.0	5.1	150.0	4.5	146.0	6.4	-0.16	0.11	49.93	2.50
17	NGC 6522	18:03:31.53	-30:04:28.17	0.02	0.02	188.0	4.3	165.0	3.6	130.0	6.0	-0.75	0.1	50.47	2.52
18	NGC 6522	18:03:33.06	-29:59:29.26	0.02	0.10	24.1	5.1	25.5	3.9	<47.6	-	<1.38	0.44	51.92	2.60
19	NGC 6522	18:03:35.95	-29:59:25.56	0.02	0.01	27.9	5.2	24.0	4.5	<39.4	-	<0.70	0.38	52.75	2.64
20	NGC 6522	18:03:24.58	-30:00:28.67	0.04	0.04	121.0	4.9	103.0	4.2	79.2	7.7	-0.86	0.22	54.65	2.73

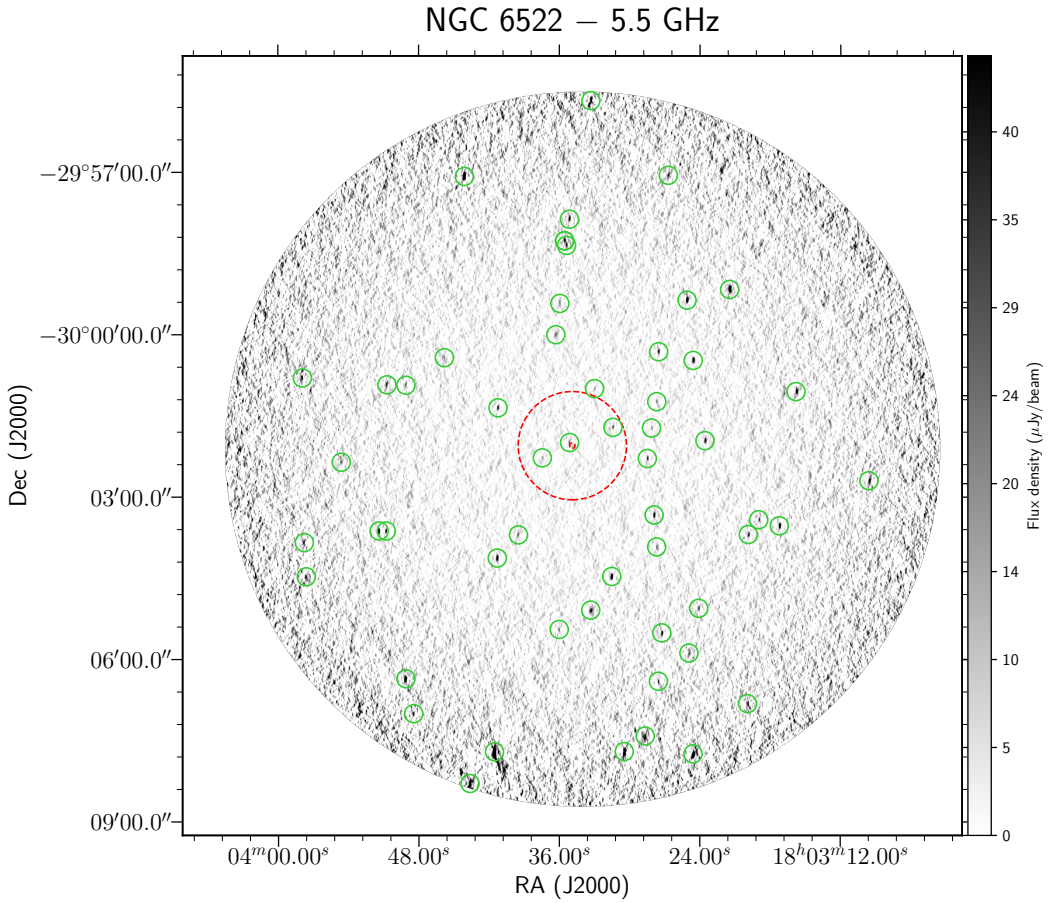
NGC 6522 – 5.5 GHz
−29°57′00.0″
−30°00′00.0″
03′00.0″
06′00.0″
09′00.0″
Dec (J2000)
04^m00.00^s
48.00^s
36.00^s
24.00^s
18^h03^m12.00^s
RA (J2000)
Flux density (μJy/beam)
40
35
29
24
20
14
10
5
0

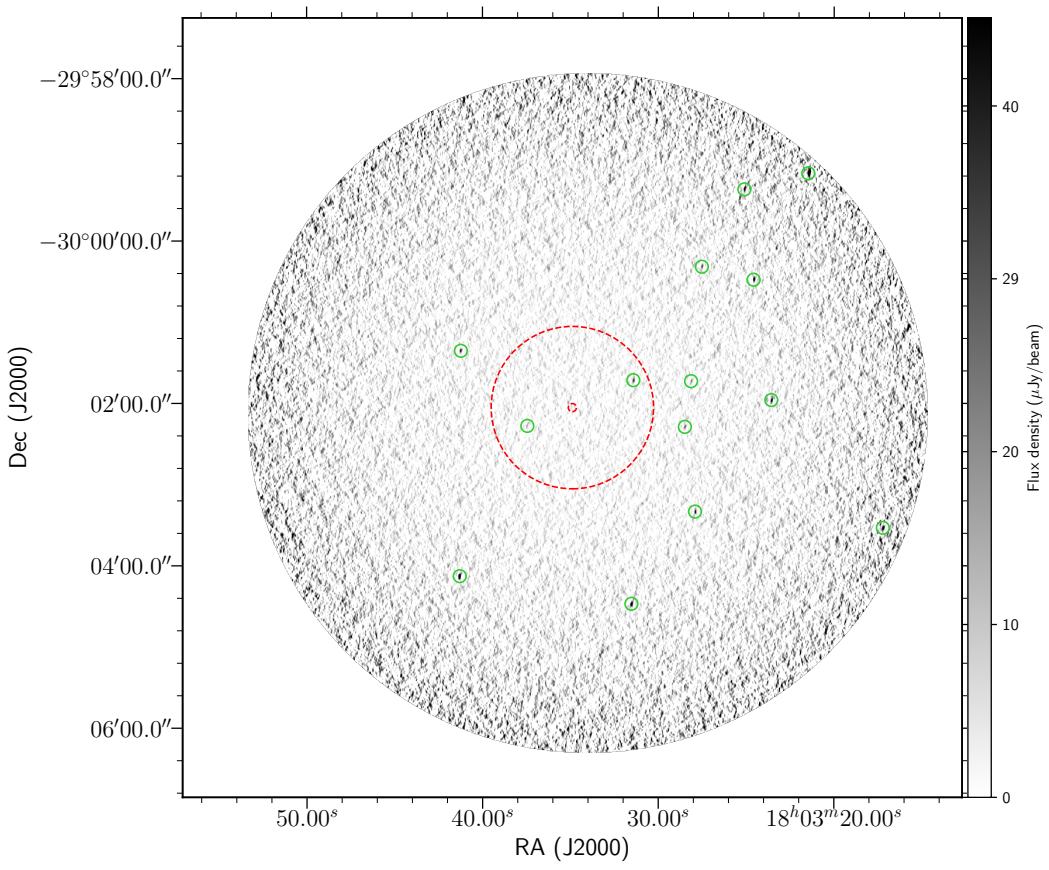
NGC 6522 – 9 GHz
−29°58′00.0″
−30°00′00.0″
02′00.0″
04′00.0″
06′00.0″
Dec (J2000)
50.00^s
40.00^s
30.00^s
18^h03^m20.00^s
RA (J2000)
Flux density (μJy/beam)
40
29
20
10
0

Table 3.26: NGC 6541

ID	Field	RA	DEC	Δ RA ($''$)	Δ DEC ($''$)	$S_{5.5}$ (μJy)	$\Delta S_{5.5}$ (μJy)	$S_{7.25}$ (μJy)	$\Delta S_{7.25}$ (μJy)	S_9 (μJy)	ΔS_9 (μJy)	α	$\Delta\alpha$	R/R$_c$	R/R$_h$
1	NGC 6541	18:08:00.60	-43:43:37.90	0.02	0.01	653.0	28.8	596.0	27.5	533.0	32.4	-0.41	0.15	4.47	0.76
2	NGC 6541	18:07:56.24	-43:42:20.01	0.08	0.06	27.8	4.9	19.3	3.4	<25.5	-	<-0.17	0.36	6.89	1.17
3	NGC 6541	18:08:05.69	-43:43:58.62	0.25	0.03	43.8	5.3	29.2	3.6	20.5	4.5	-1.53	0.5	6.89	1.17
4	NGC 6541	18:08:05.21	-43:44:02.99	0.21	0.14	<15.9	-	<20.1	-	25.0	4.9	>0.92	0.4	7.03	1.19
5	NGC 6541	18:08:10.55	-43:41:24.00	0.55	0.20	40.5	5.7	27.1	4.4	22.2	5.6	-1.22	0.59	11.68	1.98
6	NGC 6541	18:08:05.90	-43:40:44.97	0.05	0.12	30.8	5.8	20.1	4.3	<22.9	-	<-0.60	0.39	12.43	2.11
7	NGC 6541	18:08:16.03	-43:44:34.31	0.07	0.07	208.0	6.9	152.0	5.7	67.2	9.0	-2.30	0.29	16.59	2.82
8	NGC 6541	18:07:45.93	-43:41:03.28	0.08	0.11	70.7	7.5	56.0	6.4	<60.9	-	<-0.30	0.22	19.40	3.30
9	NGC 6541	18:08:05.71	-43:46:21.39	0.03	0.04	270.0	7.9	231.0	7.0	151.0	12.9	-1.17	0.19	19.53	3.32
10	NGC 6541	18:07:42.67	-43:43:52.68	0.13	0.02	205.0	8.4	156.0	7.7	89.3	13.0	-1.69	0.31	20.51	3.48
11	NGC 6541	18:07:41.78	-43:43:00.99	0.03	0.07	253.0	8.3	201.0	7.4	108.0	13.9	-1.72	0.28	20.67	3.51
12	NGC 6541	18:08:05.09	-43:39:06.78	0.11	0.08	<216.0	-	<175.0	-	92.0	14.5	>-1.73	0.32	21.18	3.60
13	NGC 6541	18:08:05.26	-43:39:05.98	0.00	0.02	659.0	37.9	569.0	38.9	<85.4	-	<-4.15	0.12	21.28	3.61
14	NGC 6541	18:07:41.30	-43:43:29.81	0.13	0.13	54.3	8.2	50.2	8.2	<70.1	-	<0.52	0.31	21.40	3.63
15	NGC 6541	18:08:21.63	-43:44:34.82	0.19	0.41	46.3	7.8	31.2	7.9	<55.8	-	<0.38	0.35	21.49	3.65
16	NGC 6541	18:08:21.69	-43:41:13.65	0.10	0.31	41.6	7.5	37.4	7.5	67.5	14.0	1.00	0.57	21.50	3.65
17	NGC 6541	18:07:41.65	-43:44:47.72	0.09	0.08	173.0	9.0	-	-	-	-	-	-	23.32	3.96
18	NGC 6541	18:08:16.88	-43:46:19.94	0.07	0.22	68.6	8.9	-	-	-	-	-	-	24.03	4.08
19	NGC 6541	18:07:47.98	-43:38:52.62	0.06	0.07	2170.0	88.3	-	-	-	-	-	-	26.58	4.51
20	NGC 6541	18:08:28.30	-43:41:42.22	0.03	0.04	848.0	17.3	-	-	-	-	-	-	26.87	4.56

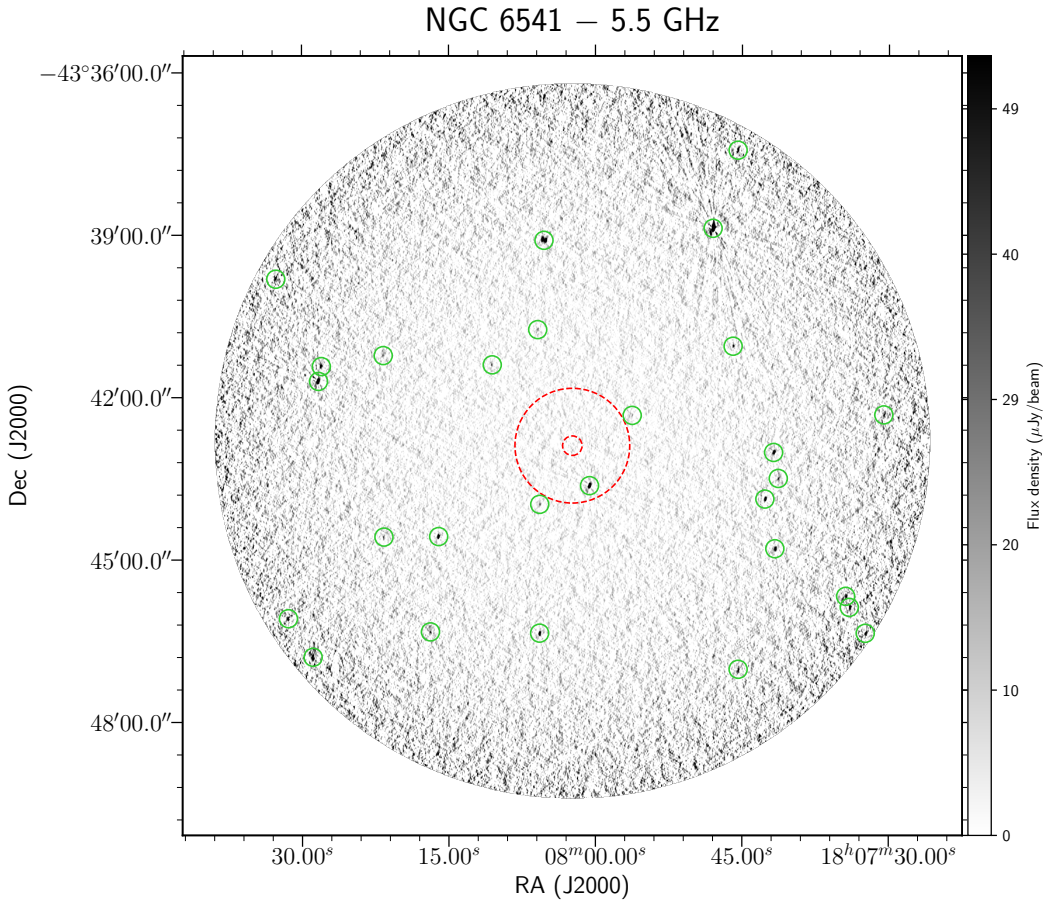
NGC 6541 – 5.5 GHz
−43°36′00.0″
39′00.0″
42′00.0″
45′00.0″
48′00.0″
Dec (J2000)
30.00s
15.00s
08m00.00s
45.00s
18h07m30.00s
RA (J2000)
Flux density (μJy/beam)
0
10
20
29
40
49

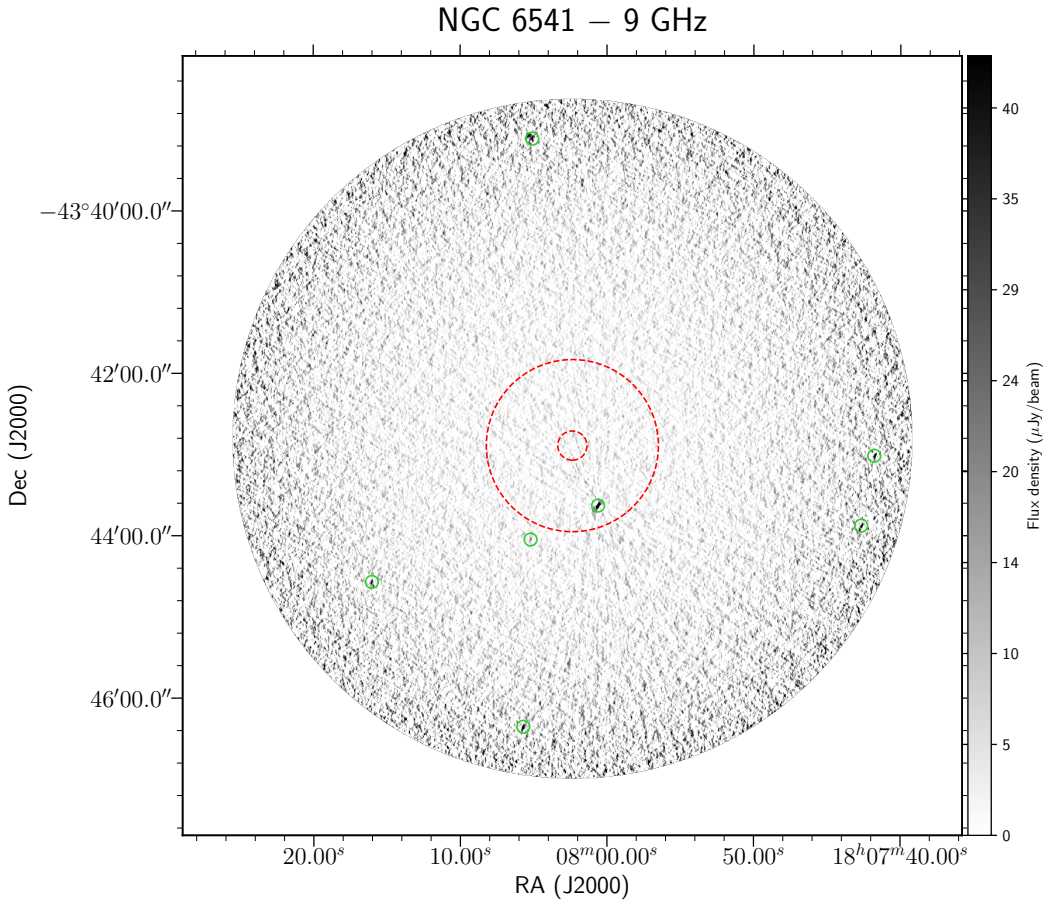
NGC 6541 – 9 GHz
−43°40′00.0″
42′00.0″
44′00.0″
46′00.0″
Dec (J2000)
20.00s
10.00s
08m00.00s
50.00s
18h07m40.00s
RA (J2000)
Flux density (μJy/beam)
0
5
10
14
20
24
29
35
40

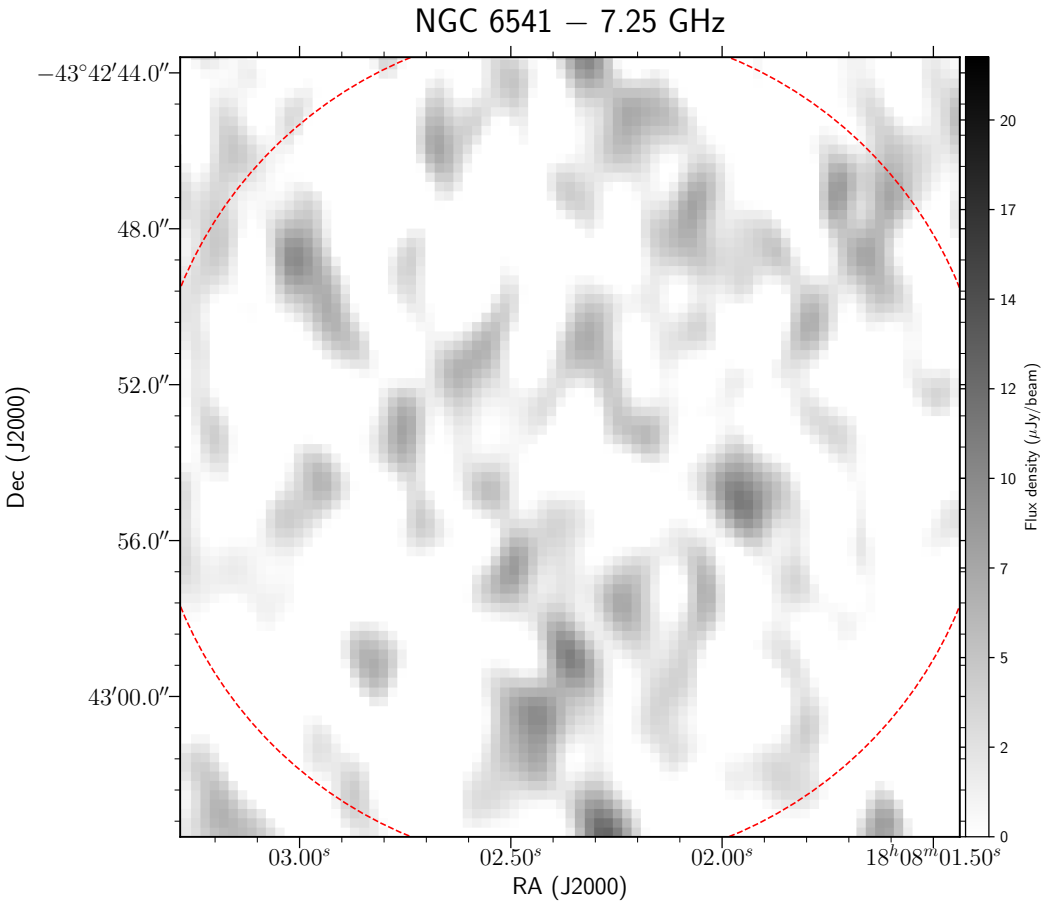
NGC 6541 — 7.25 GHz
−43°42′44.0″
48.0″
52.0″
56.0″
43′00.0″
Dec (J2000)
03.00s
02.50s
02.00s
18h08m01.50s
RA (J2000)
Flux density (μJy/beam)
0
2
5
7
10
12
14
17
20

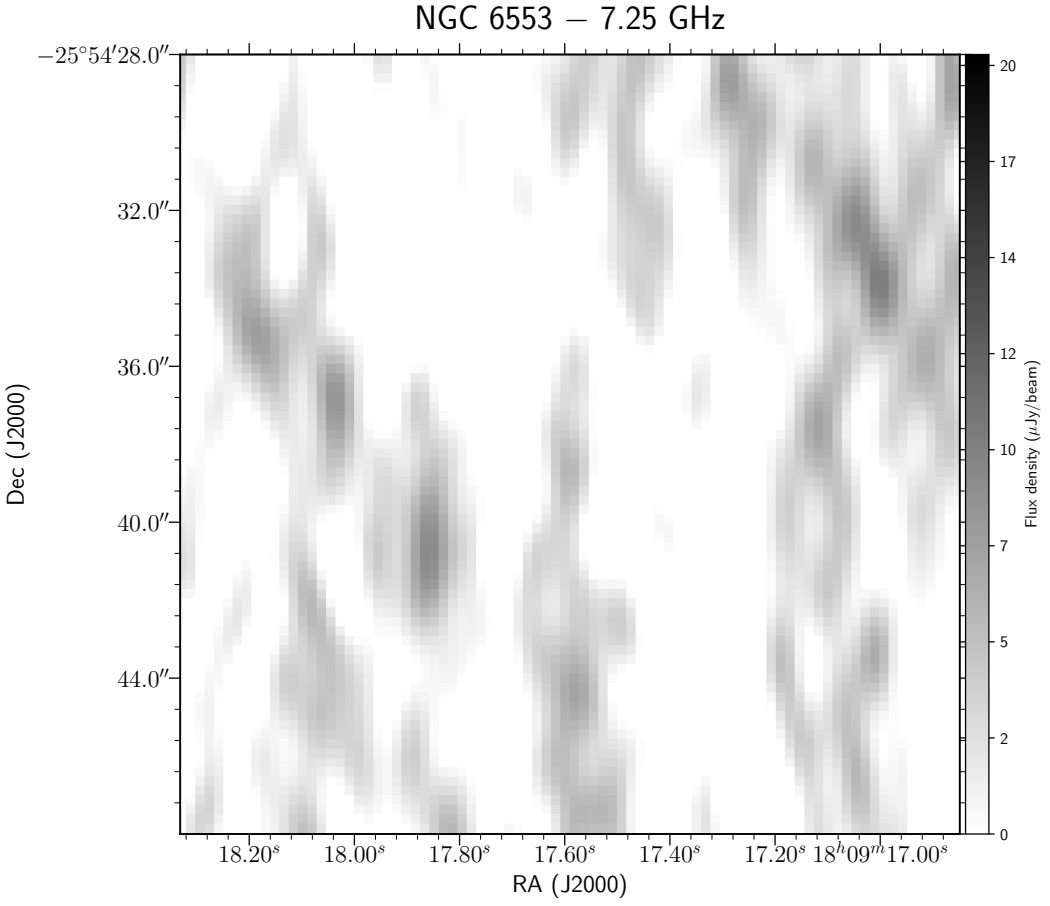
NGC 6553 — 7.25 GHz
−25°54′28.0″
32.0″
36.0″
40.0″
44.0″
Dec (J2000)
18.20s
18.00s
17.80s
17.60s
17.40s
17.20s
18h09m17.00s
RA (J2000)
Flux density (μJy/beam)
0
2
5
7
10
12
14
17
20

Table 3.27: NGC 6553

ID	Field	RA	DEC	Δ RA ($''$)	Δ DEC ($''$)	$S_{5.5}$ (μJy)	$\Delta S_{5.5}$ (μJy)	$S_{7.25}$ (μJy)	$\Delta S_{7.25}$ (μJy)	S_9 (μJy)	ΔS_9 (μJy)	α	$\Delta\alpha$	R/R_c	R/R_h
1	NGC 6553	18:09:16.28	-25:53:54.51	0.05	0.18	32.2	3.2	30.1	2.5	26.0	3.6	-0.43	0.33	1.48	0.76
2	NGC 6553	18:09:19.69	-25:53:58.39	0.03	0.14	18.3	3.3	16.8	2.5	<21.1	-	<0.29	0.37	1.53	0.79
3	NGC 6553	18:09:17.80	-25:55:28.20	0.29	0.77	26.2	3.3	19.1	3.4	23.5	3.8	-0.22	0.41	1.58	0.81
4	NGC 6553	18:09:16.99	-25:55:57.97	0.01	0.10	35.4	3.5	25.8	2.8	<28.6	-	<-0.43	0.2	2.53	1.30
5	NGC 6553	18:09:13.85	-25:55:45.41	0.22	0.31	21.9	3.4	17.8	2.7	<28.0	-	<0.50	0.31	2.65	1.36
6	NGC 6553	18:09:11.50	-25:55:04.43	0.09	0.38	25.0	3.4	19.1	2.8	<26.4	-	<0.11	0.28	2.71	1.40
7	NGC 6553	18:09:16.91	-25:53:08.88	0.07	0.18	40.4	3.4	34.9	2.8	31.4	4.4	-0.50	0.34	2.82	1.45
8	NGC 6553	18:09:13.43	-25:53:20.95	0.17	0.23	22.1	3.5	12.8	2.8	<22.6	-	<0.05	0.32	3.00	1.54
9	NGC 6553	18:09:19.89	-25:56:10.95	0.00	0.05	37.7	3.4	21.9	3.4	<25.8	-	<-0.77	0.18	3.08	1.59
10	NGC 6553	18:09:10.96	-25:55:17.86	0.53	2.17	24.4	3.5	12.6	2.9	<31.0	-	<0.49	0.29	3.08	1.58
11	NGC 6553	18:09:10.98	-25:55:19.00	0.05	0.11	24.4	3.5	15.9	2.8	<21.2	-	<-0.28	0.29	3.09	1.59
12	NGC 6553	18:09:21.13	-25:53:08.66	0.02	0.29	29.9	3.7	23.6	3.8	23.6	4.4	-0.47	0.45	3.19	1.64
13	NGC 6553	18:09:15.07	-25:56:29.73	0.93	2.22	26.5	3.7	12.4	2.9	<29.3	-	<0.20	0.29	3.67	1.89
14	NGC 6553	18:09:15.04	-25:56:30.80	0.05	0.09	26.5	3.7	24.8	3.0	<42.9	-	<0.98	0.29	3.71	1.91
15	NGC 6553	18:09:16.78	-25:52:26.55	0.05	0.27	44.8	4.9	35.7	4.0	24.9	5.2	-1.18	0.49	4.15	2.13
16	NGC 6553	18:09:24.35	-25:56:16.08	0.13	0.47	66.3	5.3	43.3	4.5	29.6	6.8	-1.64	0.49	4.21	2.17
17	NGC 6553	18:09:25.05	-25:56:19.09	0.06	0.11	53.7	4.2	36.2	3.8	<41.8	-	<-0.51	0.16	4.49	2.31
18	NGC 6553	18:09:16.24	-25:52:11.59	0.01	0.13	31.2	3.9	23.4	4.3	<33.7	-	<0.16	0.26	4.64	2.39
19	NGC 6553	18:09:25.67	-25:56:23.44	0.16	0.18	30.4	5.5	24.5	5.0	26.8	6.1	-0.27	0.62	4.77	2.45
20	NGC 6553	18:09:10.63	-25:52:33.48	0.12	0.40	34.5	4.1	23.3	4.7	31.7	6.0	-0.17	0.46	4.91	2.52

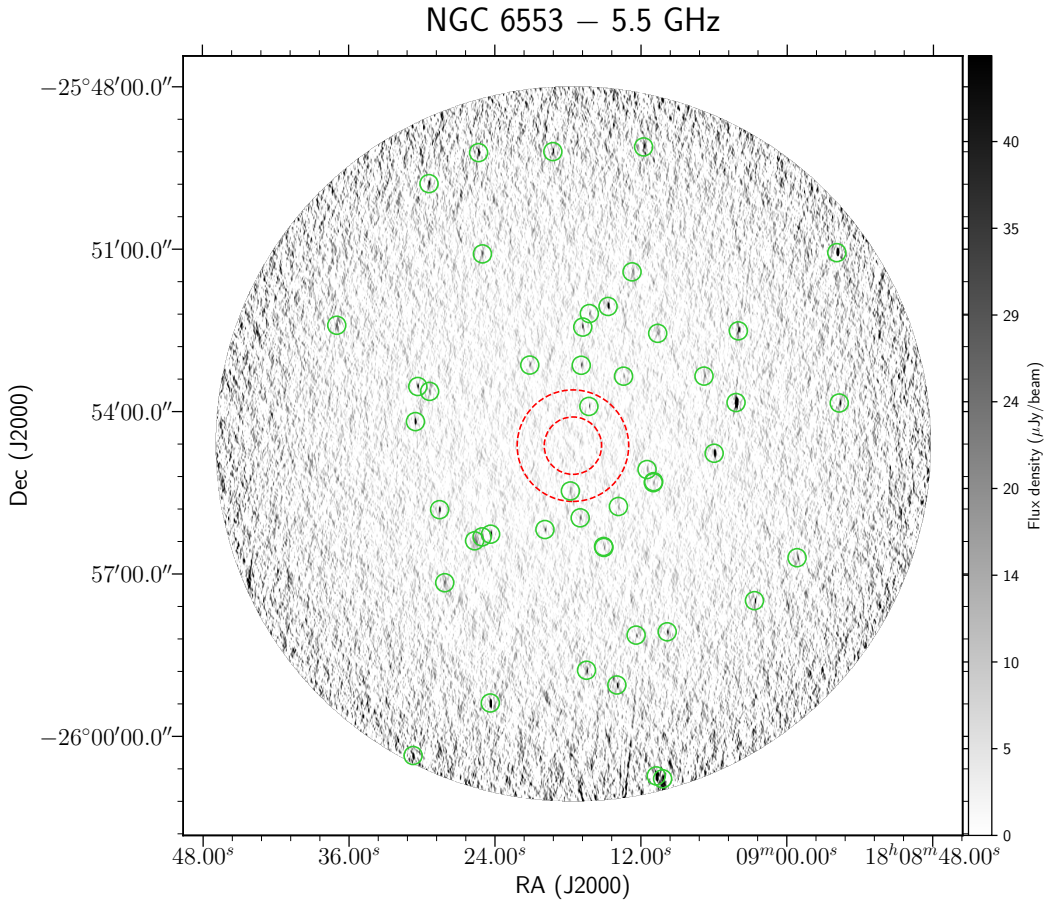
NGC 6553 — 5.5 GHz
−25°48′00.0″
51′00.0″
54′00.0″
57′00.0″
−26°00′00.0″
Dec (J2000)
48.00s
36.00s
24.00s
12.00s
09m00.00s
18h08m48.00s
RA (J2000)
Flux density (μJy/beam)
0
5
10
14
20
24
29
35
40

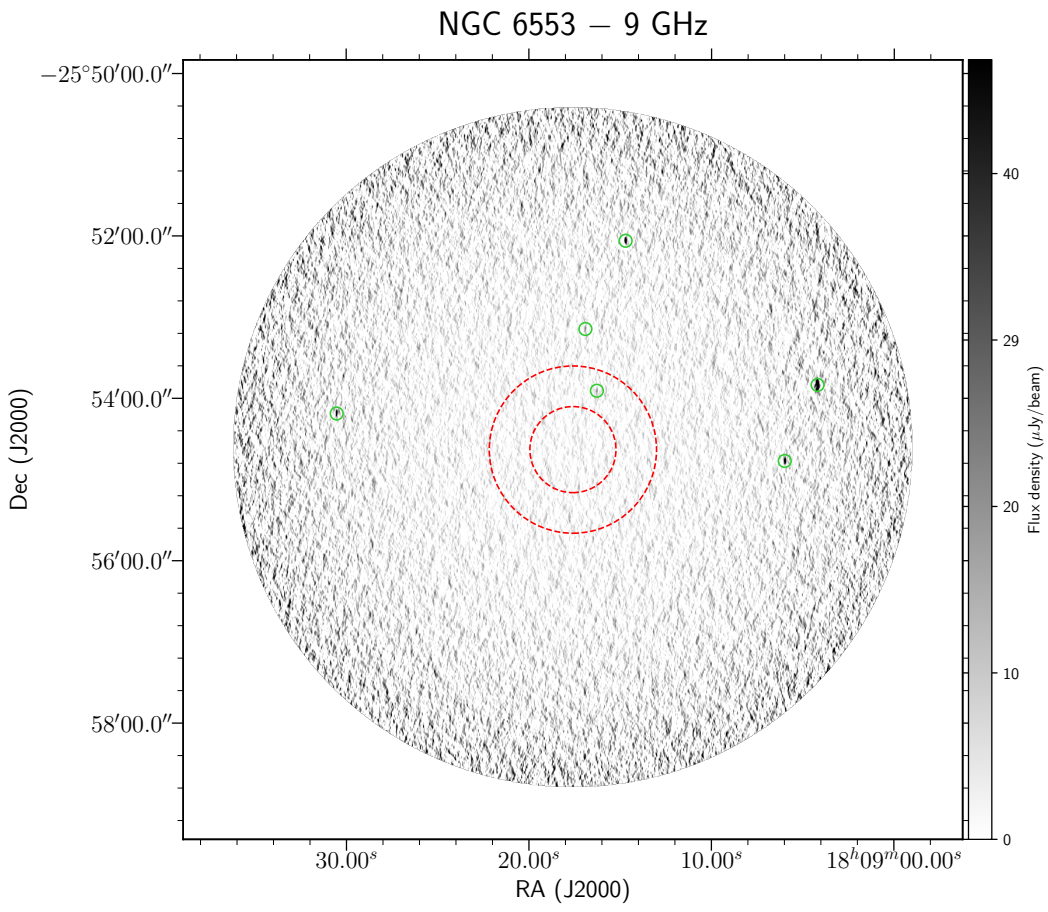
NGC 6553 — 9 GHz
−25°50′00.0″
52′00.0″
54′00.0″
56′00.0″
58′00.0″
Dec (J2000)
30.00s
20.00s
10.00s
18h09m00.00s
RA (J2000)
Flux density (μJy/beam)
0
10
20
29
40

Table 3.28: NGC 6624

ID	Field	RA	DEC	Δ RA ($''$)	Δ DEC ($''$)	$S_{5.5}$ (μJy)	$\Delta S_{5.5}$ (μJy)	$S_{7.25}$ (μJy)	$\Delta S_{7.25}$ (μJy)	S_{9} (μJy)	ΔS_{9} (μJy)	α	$\Delta\alpha$	R/R$_c$	R/R$_h$
1	NGC 6624	18:23:40.50	-30:21:40.07	0.01	0.01	235.0	4.9	222.0	3.2	196.0	4.2	-0.37	0.06	0.11	0.01
2	NGC 6624	18:23:38.00	-30:21:31.55	0.01	0.03	131.0	4.0	120.0	2.9	115.0	3.6	-0.26	0.08	9.30	0.68
3	NGC 6624	18:23:36.90	-30:21:02.32	0.03	0.06	55.5	3.3	46.4	2.5	36.4	3.8	-0.86	0.24	16.63	1.22
4	NGC 6624	18:23:35.21	-30:22:11.97	0.23	0.09	42.6	3.5	35.4	3.3	37.3	4.2	-0.27	0.29	21.05	1.54
5	NGC 6624	18:23:45.91	-30:22:23.47	0.42	0.15	20.1	4.2	44.1	7.9	16.5	4.3	-0.40	0.7	22.89	1.67
6	NGC 6624	18:23:46.03	-30:22:23.67	0.23	0.46	20.1	4.2	44.1	7.9	27.5	4.3	0.64	0.56	23.29	1.70
7	NGC 6624	18:23:34.36	-30:22:30.39	0.06	0.21	86.8	3.7	68.2	3.6	57.8	4.5	-0.82	0.18	26.20	1.92
8	NGC 6624	18:23:31.73	-30:21:28.85	0.02	0.22	34.7	4.4	33.2	3.1	29.4	5.8	-0.33	0.47	31.73	2.32
9	NGC 6624	18:23:50.32	-30:21:16.56	0.15	0.58	25.4	3.9	18.7	3.4	<33.6	-	<0.57	0.31	35.86	2.62
10	NGC 6624	18:23:38.58	-30:24:03.93	0.10	0.11	25.0	4.1	20.0	4.3	<32.7	-	<0.55	0.33	40.66	2.98
11	NGC 6624	18:23:29.37	-30:21:02.08	0.03	0.48	37.7	4.9	47.1	3.4	57.4	5.9	0.85	0.33	41.39	3.03
12	NGC 6624	18:23:46.69	-30:19:25.73	0.00	0.41	28.3	4.1	23.3	4.2	<31.0	-	<0.19	0.3	43.34	3.17
13	NGC 6624	18:23:36.44	-30:19:11.34	0.02	0.21	25.5	4.0	23.3	3.5	<35.9	-	<0.70	0.32	43.73	3.20
14	NGC 6624	18:23:33.14	-30:24:08.97	0.03	0.11	101.0	5.4	80.6	5.0	48.5	7.8	-1.49	0.35	49.21	3.60
15	NGC 6624	18:23:26.49	-30:21:38.50	0.09	0.20	24.2	4.5	29.6	4.1	36.5	7.9	0.85	0.55	50.39	3.69
16	NGC 6624	18:23:30.09	-30:23:49.93	0.05	0.35	<29.9	-	27.8	4.3	<47.4	-	-	-	52.07	3.81
17	NGC 6624	18:23:26.07	-30:22:24.05	0.02	0.02	319.0	4.8	304.0	5.8	286.0	9.0	-0.22	0.07	53.37	3.91
18	NGC 6624	18:23:39.33	-30:18:14.05	0.09	0.11	33.8	4.9	28.4	5.6	<47.0	-	<0.67	0.29	57.28	4.19
19	NGC 6624	18:23:24.36	-30:21:11.21	0.02	0.04	128.0	6.0	108.0	5.6	76.3	10.3	-1.04	0.29	58.60	4.29
20	NGC 6624	18:23:55.02	-30:20:03.61	0.02	0.04	1690.0	8.3	1560.0	30.7	1030.0	17.9	-1.00	0.04	58.61	4.29

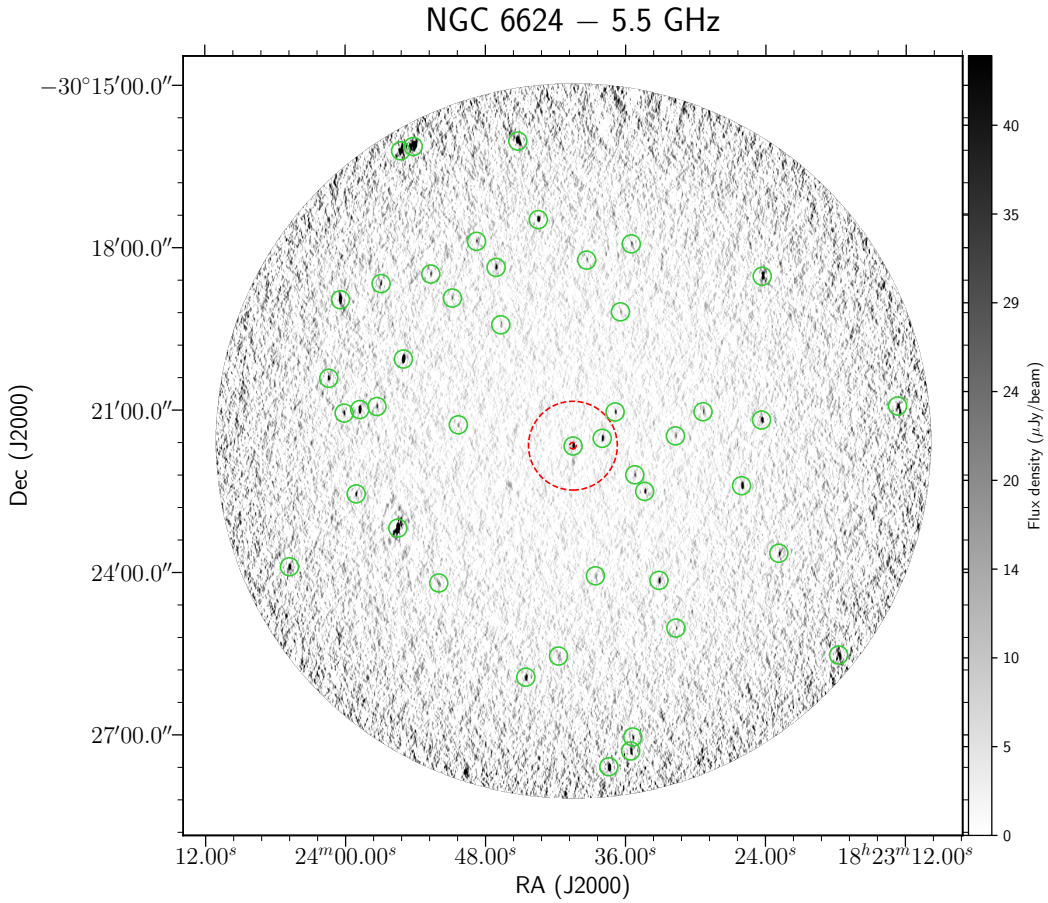
NGC 6624 — 5.5 GHz
−30°15′00.0″
18′00.0″
21′00.0″
24′00.0″
27′00.0″
Dec (J2000)
12.00s
24m00.00s
48.00s
36.00s
24.00s
18h23m12.00s
RA (J2000)
Flux density (μJy/beam)
0
5
10
14
20
24
29
35
40

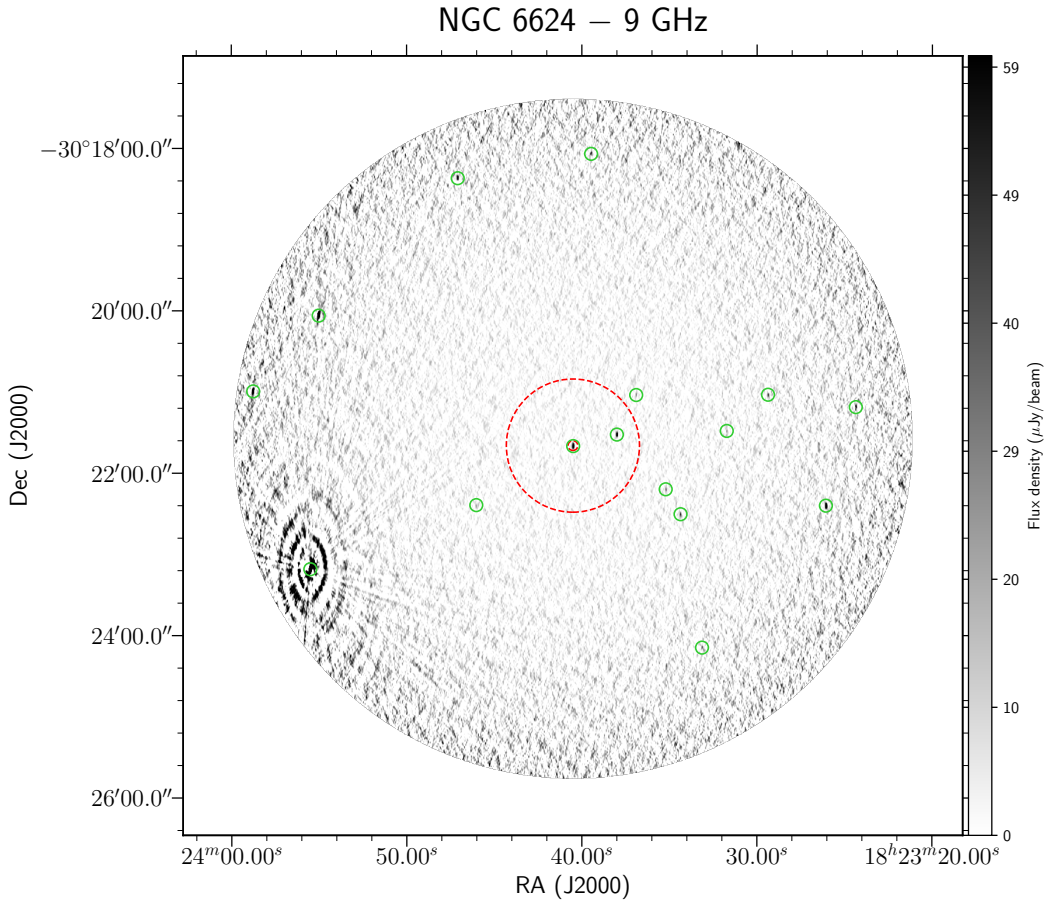
NGC 6624 — 9 GHz
−30°18′00.0″
20′00.0″
22′00.0″
24′00.0″
26′00.0″
Dec (J2000)
24m00.00s
50.00s
40.00s
30.00s
18h23m20.00s
RA (J2000)
Flux density (μJy/beam)
0
10
20
29
40
49
59

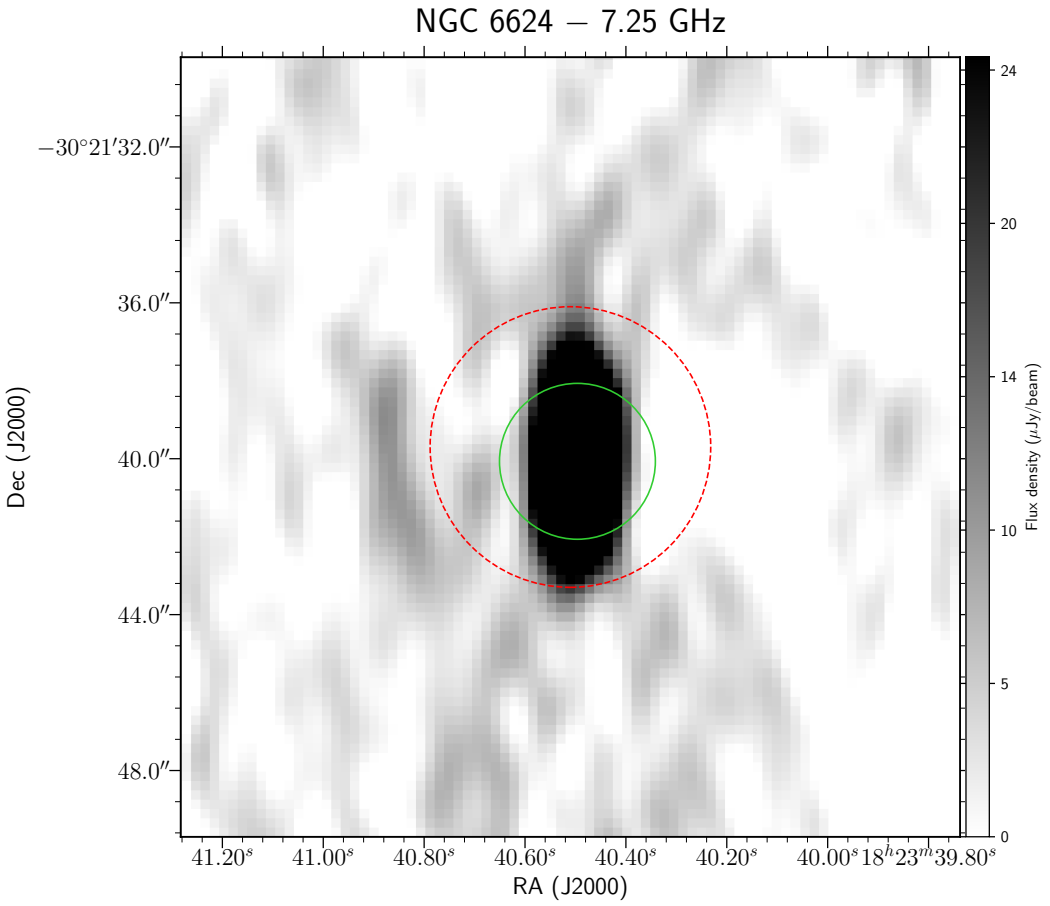
NGC 6624 — 7.25 GHz
−30°21′32.0″
36.0″
40.0″
44.0″
48.0″
Dec (J2000)
41.20ˢ
41.00ˢ
40.80ˢ
40.60ˢ
40.40ˢ
40.20ˢ
40.00ˢ
18ʰ23ᵐ39.80ˢ
RA (J2000)
Flux density (μJy/beam)
0
5
10
14
20
24

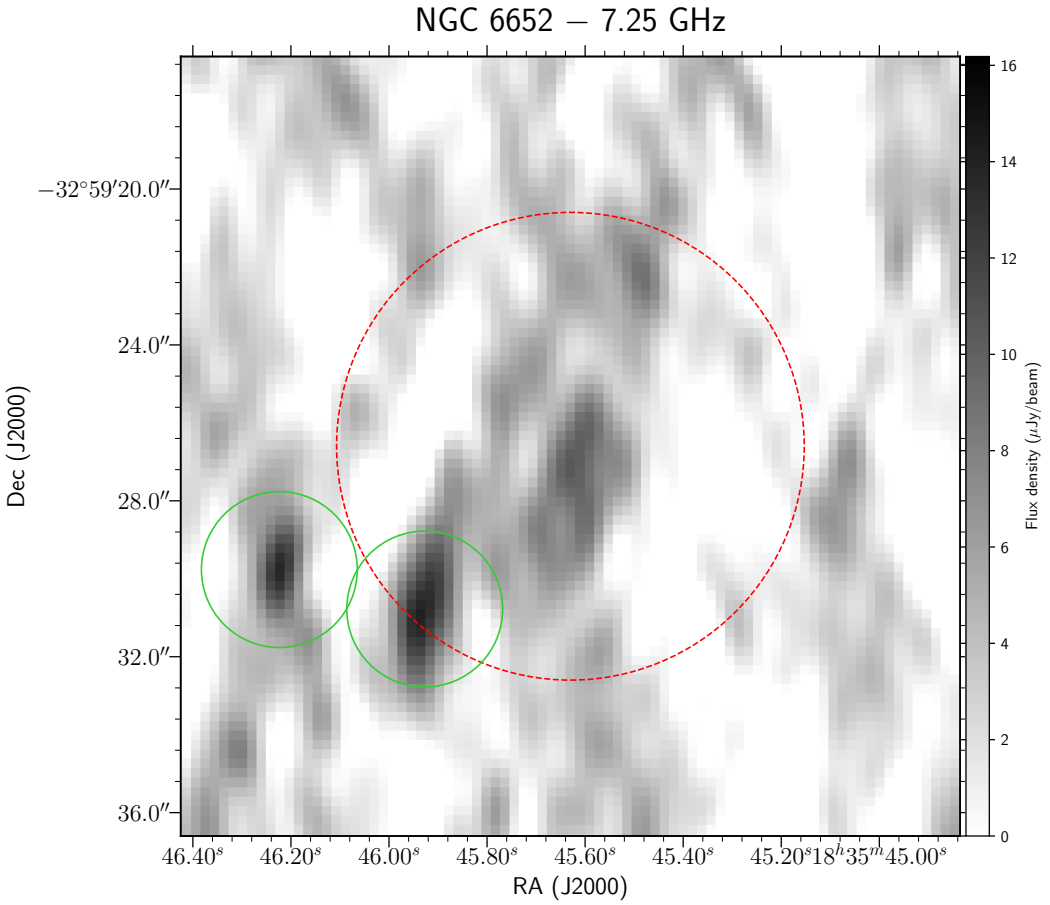
NGC 6652 — 7.25 GHz
−32°59′20.0″
24.0″
28.0″
32.0″
36.0″
Dec (J2000)
46.40ˢ
46.20ˢ
46.00ˢ
45.80ˢ
45.60ˢ
45.40ˢ
45.20ˢ
18ʰ35ᵐ45.00ˢ
RA (J2000)
Flux density (μJy/beam)
0
2
4
6
8
10
12
14
16

Table 3.29: NGC 6652

ID	Field	RA	DEC	Δ RA ($''$)	Δ DEC ($''$)	$S_{5.5}$ (μJy)	$\Delta S_{5.5}$ (μJy)	$S_{7.25}$ (μJy)	$\Delta S_{7.25}$ (μJy)	S_9 (μJy)	ΔS_9 (μJy)	α	$\Delta\alpha$	R/R_c	R/R_h
1	NGC 6652	18:35:45.93	-32:59:30.78	0.08	0.28	<20.7	-	13.9	2.5	17.8	3.4	>-0.31	0.4	0.93	0.19
2	NGC 6652	18:35:46.22	-32:59:29.76	0.05	0.05	<13.0	-	13.0	2.2	18.9	3.0	>0.76	0.32	1.35	0.28
3	NGC 6652	18:35:44.54	-32:59:38.69	0.03	0.05	65.5	2.8	69.5	2.5	75.7	3.5	0.30	0.13	3.04	0.63
4	NGC 6652	18:35:46.28	-32:59:48.66	0.06	0.01	16.5	2.8	13.5	2.2	<20.0	-	<0.39	0.36	3.92	0.82
5	NGC 6652	18:35:47.74	-32:59:20.10	0.11	0.15	19.5	3.0	15.0	2.2	13.7	3.0	-0.71	0.55	4.56	0.95
6	NGC 6652	18:35:48.78	-32:59:21.24	0.02	0.07	40.7	3.5	32.4	2.5	29.7	3.0	-0.65	0.28	6.68	1.39
7	NGC 6652	18:35:43.05	-32:59:56.64	0.16	0.23	14.0	2.8	14.1	2.0	<20.5	-	<0.78	0.41	7.37	1.54
8	NGC 6652	18:35:49.48	-32:59:38.53	0.02	0.15	19.1	3.3	15.7	2.4	<20.2	-	<0.11	0.36	8.30	1.73
9	NGC 6652	18:35:47.03	-32:58:24.90	0.01	0.02	42.7	2.9	38.7	2.2	29.0	3.9	-0.79	0.3	10.69	2.23
10	NGC 6652	18:35:48.70	-32:58:21.38	0.08	0.22	45.5	2.9	32.4	2.2	22.3	3.5	-1.46	0.34	12.63	2.63
11	NGC 6652	18:35:45.34	-32:58:03.80	0.06	0.32	14.3	2.9	15.1	2.2	<23.8	-	<1.04	0.41	13.81	2.88
12	NGC 6652	18:35:52.68	-32:59:46.32	0.03	0.12	22.2	3.4	20.9	2.7	20.4	3.5	-0.17	0.46	15.14	3.15
13	NGC 6652	18:35:44.15	-33:00:56.40	0.02	0.71	59.6	10.1	26.1	2.3	18.4	4.0	-2.38	0.55	15.29	3.18
14	NGC 6652	18:35:51.42	-32:58:24.93	0.17	0.02	18.3	3.6	15.3	2.4	<20.8	-	<0.26	0.4	15.91	3.32
15	NGC 6652	18:35:44.18	-33:01:02.00	0.05	0.30	<23.5	-	15.5	2.3	<25.6	-	-	-	16.19	3.37
16	NGC 6652	18:35:53.22	-33:00:22.03	0.02	0.12	14.1	3.0	15.7	2.4	21.5	3.8	0.85	0.55	18.40	3.83
17	NGC 6652	18:35:40.21	-32:57:53.95	0.04	0.28	21.8	3.0	20.9	2.7	25.1	4.0	0.30	0.43	19.18	4.00
18	NGC 6652	18:35:50.87	-32:57:51.93	0.01	0.03	47.6	3.3	40.9	2.6	36.1	4.8	-0.56	0.3	19.22	4.00
19	NGC 6652	18:35:36.51	-32:59:03.86	0.04	0.16	19.5	3.0	15.0	2.4	<21.9	-	<0.24	0.32	19.50	4.06
20	NGC 6652	18:35:54.49	-32:58:50.28	0.15	0.04	21.5	3.2	21.1	3.0	19.5	4.2	-0.22	0.52	19.55	4.07

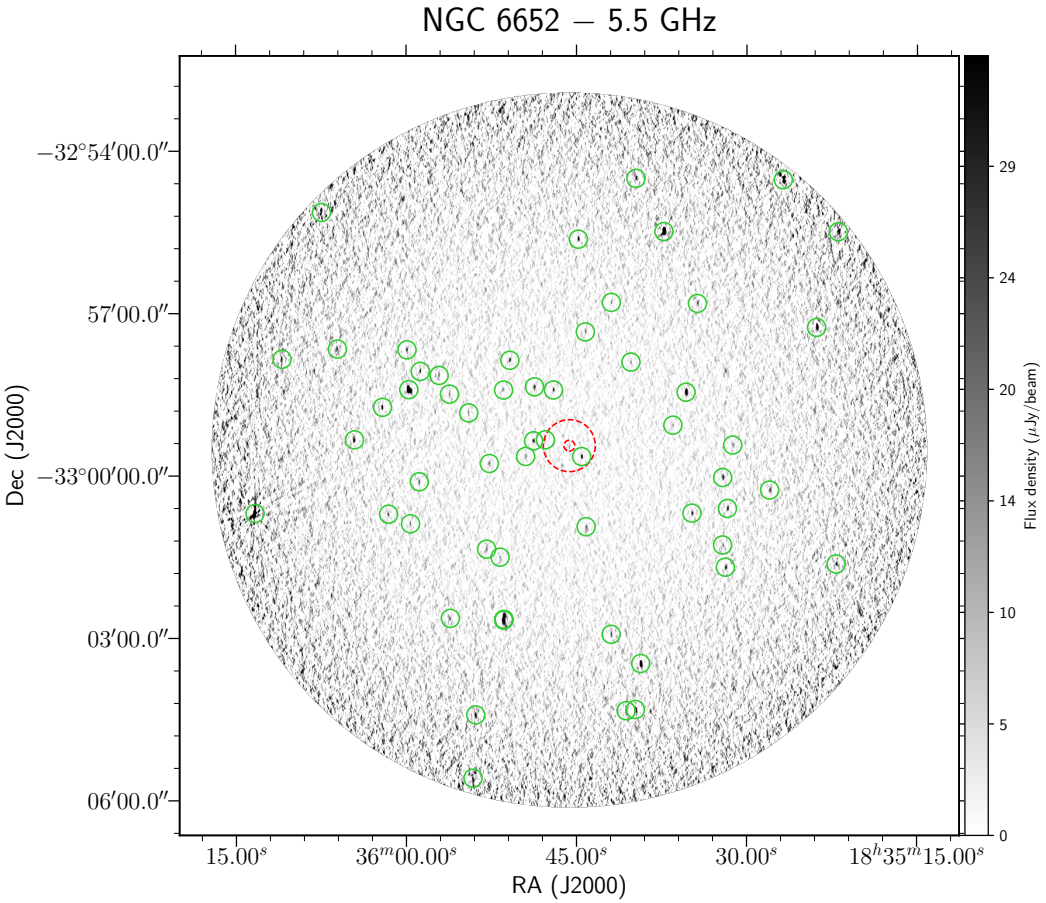
NGC 6652 – 5.5 GHz
−32°54′00.0″
57′00.0″
−33°00′00.0″
03′00.0″
06′00.0″
Dec (J2000)
15.00s
36m00.00s
45.00s
30.00s
18h35m15.00s
RA (J2000)
Flux density (μJy/beam)
0
5
10
14
20
24
29

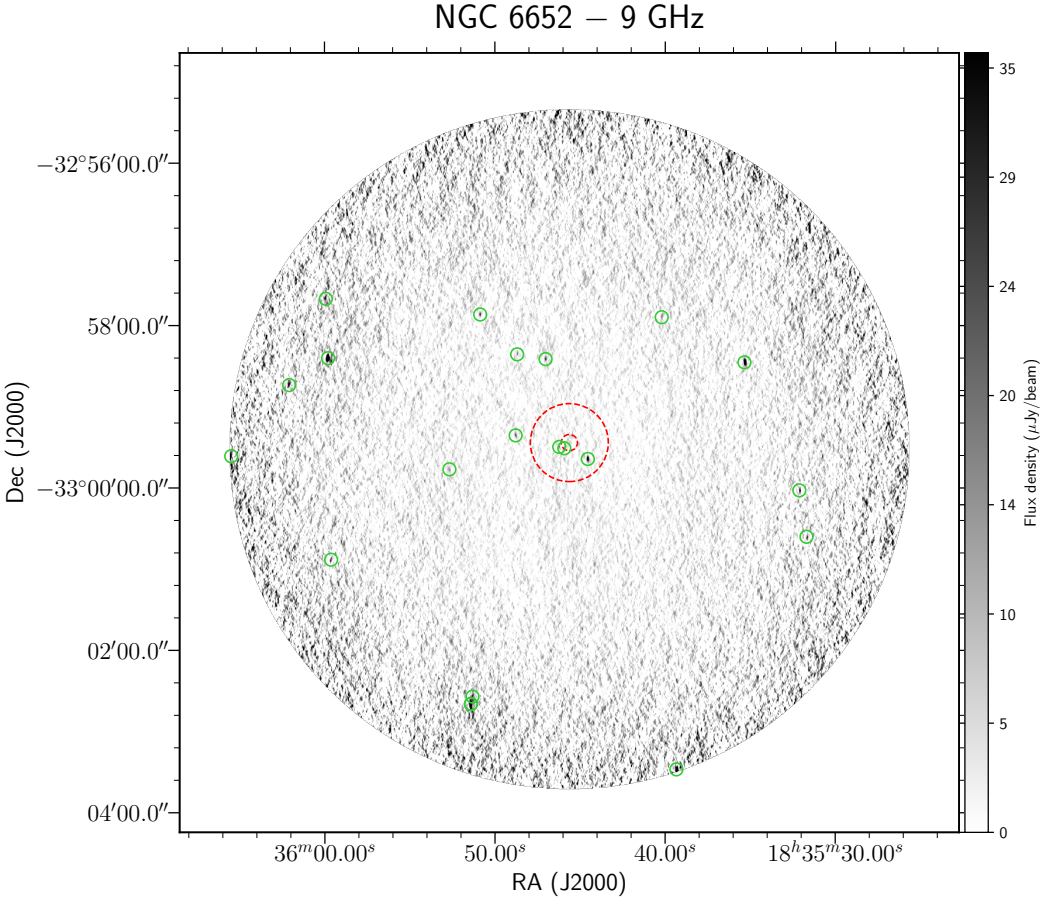
NGC 6652 – 9 GHz
−32°56′00.0″
58′00.0″
−33°00′00.0″
02′00.0″
04′00.0″
Dec (J2000)
36m00.00s
50.00s
40.00s
18h35m30.00s
RA (J2000)
Flux density (μJy/beam)
0
5
10
14
20
24
29
35

Table 3.30: NGC 6715

ID	Field	RA	DEC	Δ RA ($''$)	Δ DEC ($''$)	$S_{5.5}$ (μJy)	$\Delta S_{5.5}$ (μJy)	$S_{7.25}$ (μJy)	$\Delta S_{7.25}$ (μJy)	S_{9} (μJy)	ΔS_{9} (μJy)	α	$\Delta\alpha$	R/R$_c$	R/R$_h$
1	NGC 6715	18:54:58.45	-30:29:32.37	0.10	0.18	67.6	5.2	61.3	6.0	54.9	10.9	-0.41	0.43	14.34	1.57
2	NGC 6715	18:54:59.42	-30:27:25.06	0.23	0.56	32.8	5.7	27.3	5.4	<55.6	-	<1.07	0.36	17.91	1.97
3	NGC 6715	18:54:59.29	-30:27:24.54	0.56	0.68	32.8	5.7	23.3	5.4	<56.6	-	<1.11	0.36	18.15	1.99
4	NGC 6715	18:55:00.12	-30:30:49.69	0.13	0.01	1260.0	24.3	1440.0	45.4	1680.0	79.9	0.58	0.1	23.90	2.62
5	NGC 6715	18:54:52.92	-30:29:09.83	0.08	0.06	76.0	6.5	55.9	7.4	<82.4	-	<0.16	0.17	25.27	2.77
6	NGC 6715	18:55:10.67	-30:26:51.31	0.09	0.04	1500.0	22.5	1840.0	58.5	2130.0	104.0	0.71	0.11	27.77	3.05
7	NGC 6715	18:54:52.65	-30:26:56.76	0.14	0.07	36.0	5.5	56.1	7.3	93.6	17.4	1.93	0.5	32.79	3.60
8	NGC 6715	18:54:53.89	-30:26:14.25	0.08	0.88	<31.5	-	50.6	10.1	122.0	21.6	>2.75	0.36	36.28	3.98
9	NGC 6715	18:55:11.77	-30:25:57.62	0.00	0.12	69.2	7.1	52.8	13.3	<146.0	-	<1.52	0.21	37.39	4.10
10	NGC 6715	18:54:54.23	-30:25:34.36	0.13	0.32	<25.2	-	<73.3	-	173.0	30.5	>3.91	0.36	41.88	4.60
11	NGC 6715	18:54:51.57	-30:25:47.70	0.77	0.60	<26.5	-	<59.1	-	192.0	36.3	>4.02	0.39	43.60	4.79
12	NGC 6715	18:55:21.42	-30:29:19.49	0.23	0.21	<23.9	-	58.4	10.1	198.0	31.5	>4.29	0.33	43.71	4.80
13	NGC 6715	18:54:59.27	-30:24:47.32	0.43	0.25	70.5	9.1	-	-	-	-	-	-	45.53	5.00
14	NGC 6715	18:54:50.78	-30:25:06.82	0.07	0.29	93.0	8.9	-	-	-	-	-	-	50.73	5.57
15	NGC 6715	18:54:41.81	-30:29:43.68	0.13	0.50	55.6	9.2	-	-	-	-	-	-	52.56	5.77
16	NGC 6715	18:55:24.01	-30:30:23.91	0.12	0.11	177.0	10.4	-	-	-	-	-	-	52.61	5.77
17	NGC 6715	18:54:47.80	-30:25:17.16	0.13	0.50	58.1	9.7	-	-	-	-	-	-	53.85	5.91
18	NGC 6715	18:55:13.33	-30:24:13.84	0.39	0.37	771.0	70.1	-	-	-	-	-	-	56.06	6.15
19	NGC 6715	18:54:40.17	-30:27:50.09	0.26	0.22	72.3	13.0	-	-	-	-	-	-	56.45	6.20
20	NGC 6715	18:55:26.80	-30:29:44.28	0.41	0.33	255.0	41.0	-	-	-	-	-	-	57.16	6.27

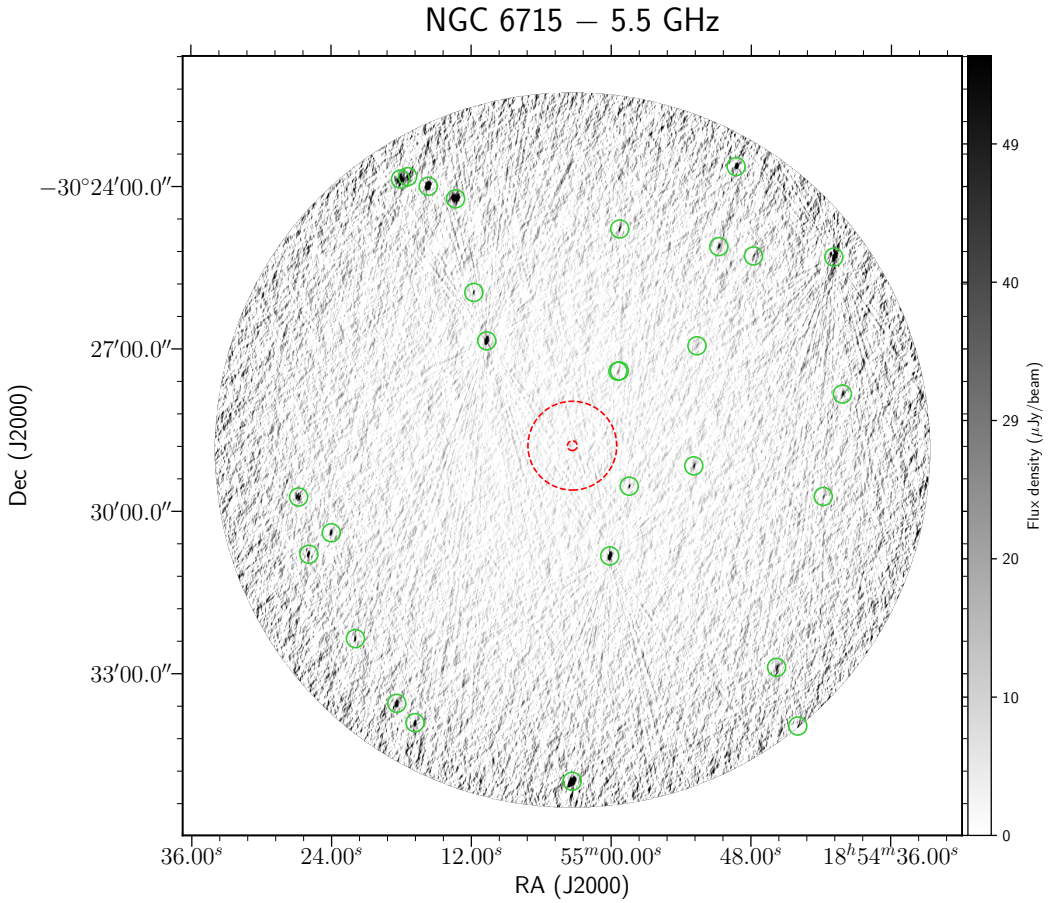
NGC 6715 – 5.5 GHz
−30°24′00.0″
27′00.0″
30′00.0″
33′00.0″
Dec (J2000)
36.00s
24.00s
12.00s
55m00.00s
48.00s
18h54m36.00s
RA (J2000)
Flux density (μJy/beam)
0
10
20
29
40
49

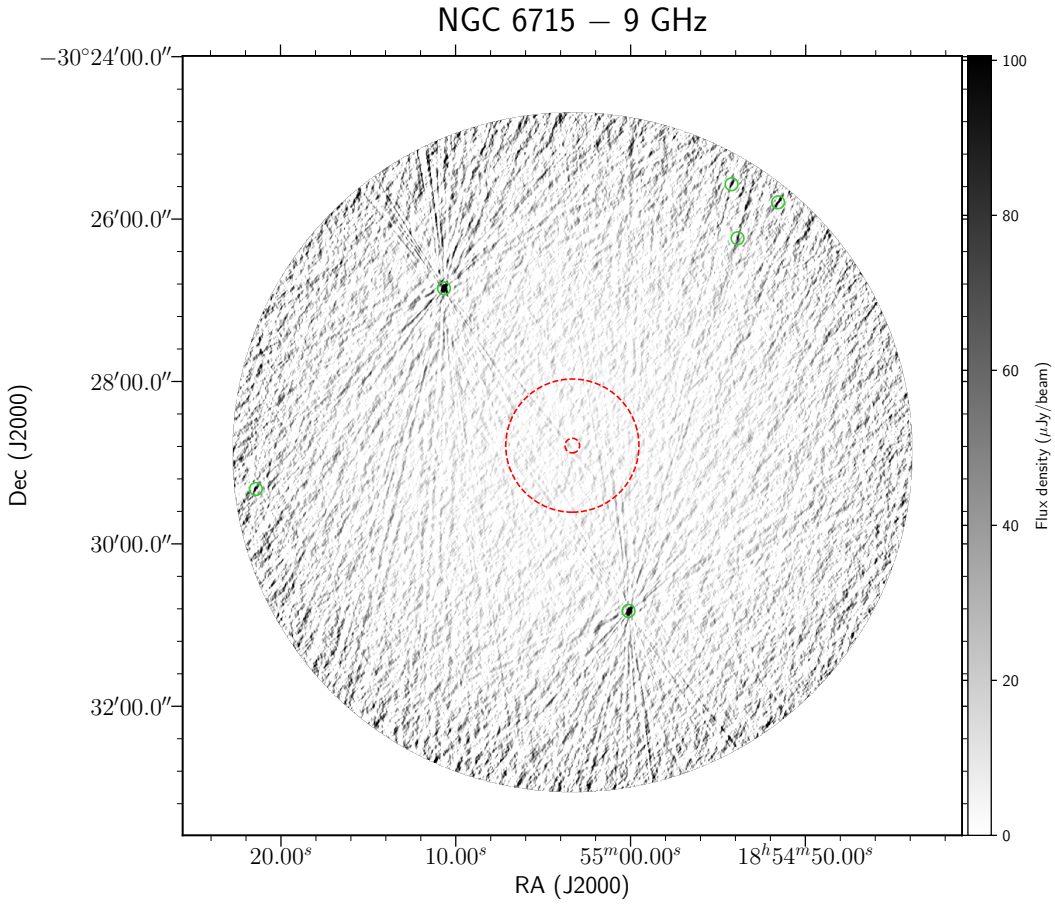
NGC 6715 – 9 GHz
−30°24′00.0″
26′00.0″
28′00.0″
30′00.0″
32′00.0″
Dec (J2000)
20.00s
10.00s
55m00.00s
18h54m50.00s
RA (J2000)
Flux density (μJy/beam)
0
20
40
60
80
100

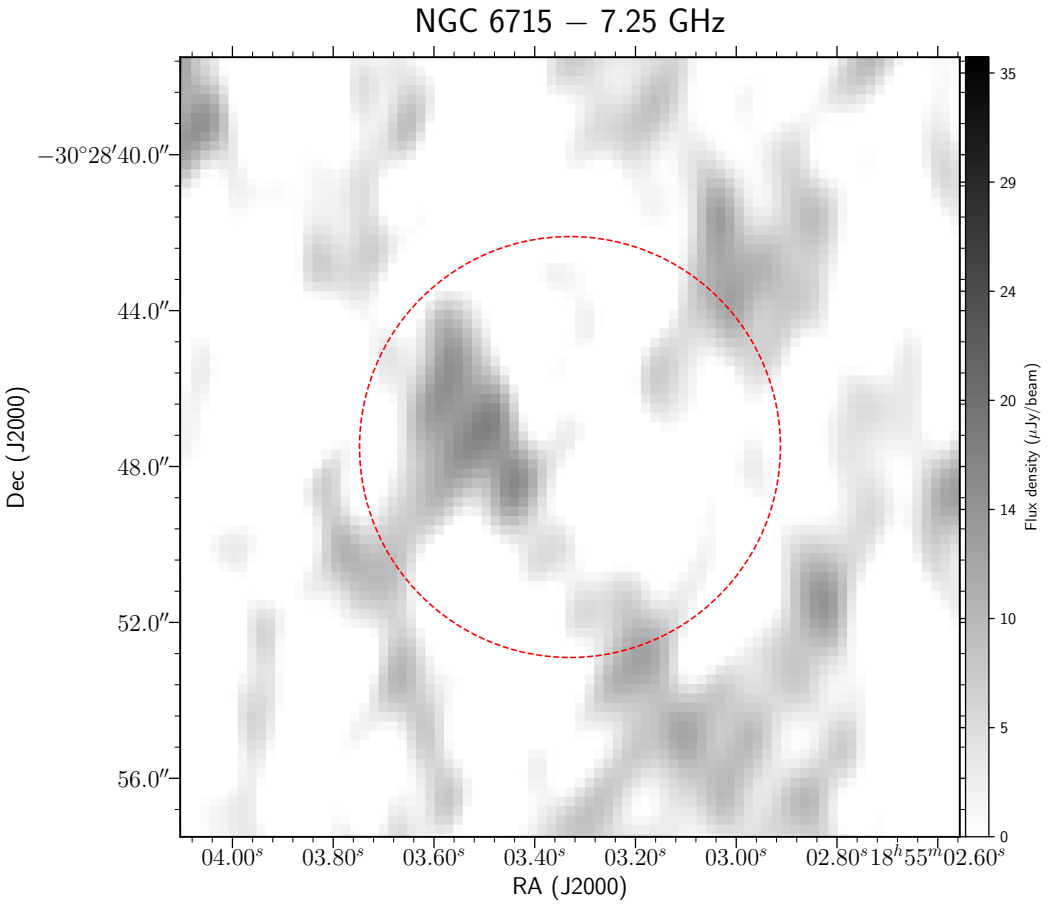
NGC 6715 – 7.25 GHz
−30°28′40.0″
44.0″
48.0″
52.0″
56.0″
Dec (J2000)
04.00s
03.80s
03.60s
03.40s
03.20s
03.00s
02.80s
18h55m02.60s
RA (J2000)
Flux density (μJy/beam)
35
29
24
20
14
10
5
0

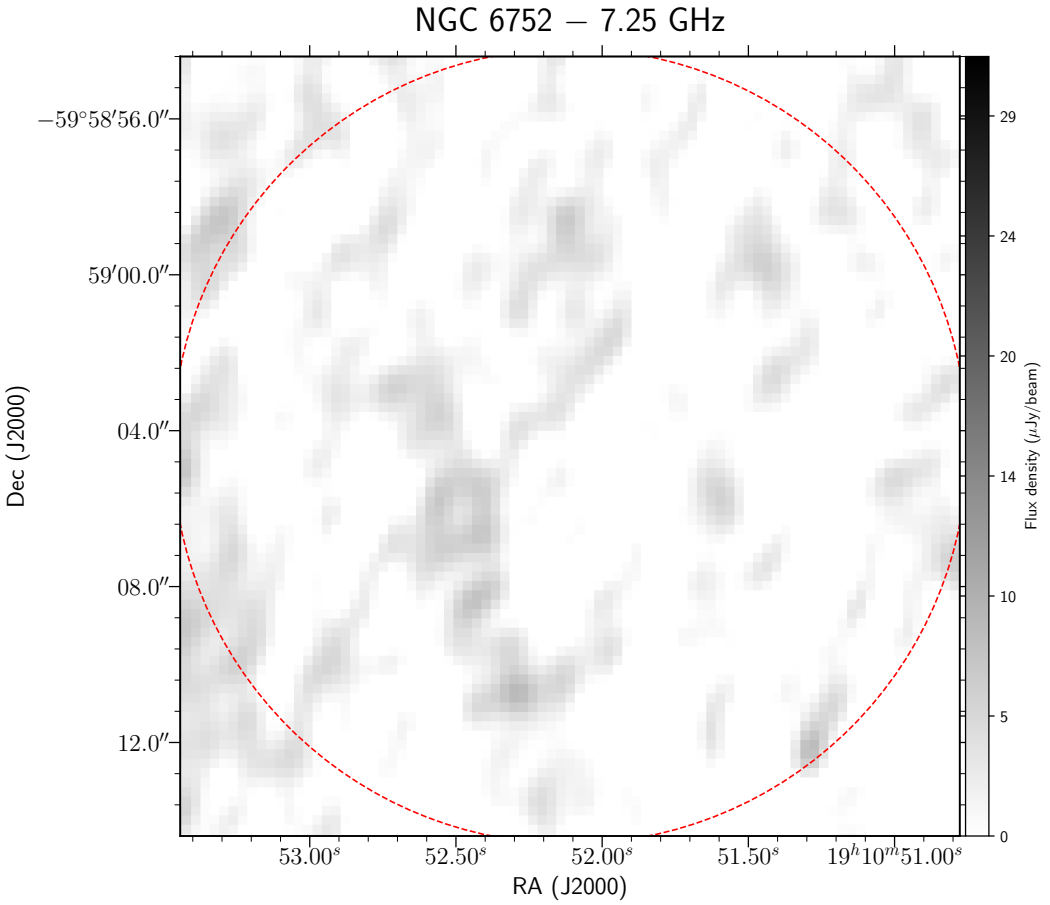
NGC 6752 – 7.25 GHz
−59°58′56.0″
59′00.0″
04.0″
08.0″
12.0″
Dec (J2000)
53.00s
52.50s
52.00s
51.50s
19h10m51.00s
RA (J2000)
Flux density (μJy/beam)
29
24
20
14
10
5
0

Table 3.31: NGC 6752

ID	Field	RA	DEC	Δ RA ($''$)	Δ DEC ($''$)	$S_{5.5}$ (μJy)	$\Delta S_{5.5}$ (μJy)	$S_{7.25}$ (μJy)	$\Delta S_{7.25}$ (μJy)	S_{9} (μJy)	ΔS_{9} (μJy)	α	$\Delta\alpha$	R/R$_c$	R/R$_h$
1	NGC 6752	19:10:57.65	-59:59:25.44	0.10	0.23	<20.9	-	16.0	2.8	<24.2	-	-	-	4.57	0.41
2	NGC 6752	19:11:01.14	-59:58:58.02	0.44	0.09	18.3	3.9	19.4	3.1	19.4	4.9	0.09	0.68	6.68	0.59
3	NGC 6752	19:10:48.11	-60:00:07.25	0.10	0.06	41.7	4.2	37.0	3.2	33.4	4.5	-0.45	0.34	6.83	0.61
4	NGC 6752	19:10:48.84	-59:57:57.67	0.05	0.09	18.1	3.9	17.7	3.5	<25.0	-	<0.66	0.44	6.97	0.62
5	NGC 6752	19:11:05.29	-59:59:04.34	0.08	0.03	187.0	10.5	185.0	13.6	131.0	19.1	-0.74	0.33	9.69	0.86
6	NGC 6752	19:11:00.52	-59:57:48.34	0.13	0.03	21.8	4.1	22.3	3.2	<29.7	-	<0.63	0.39	9.69	0.86
7	NGC 6752	19:10:38.92	-59:59:22.97	0.25	0.26	23.5	4.3	21.3	3.4	23.4	5.0	0.00	0.59	9.87	0.88
8	NGC 6752	19:10:43.11	-59:57:45.34	0.45	0.41	22.0	4.0	16.0	3.3	<22.8	-	<0.07	0.38	10.20	0.91
9	NGC 6752	19:10:46.40	-59:57:10.97	0.05	0.02	36.6	4.6	35.2	3.6	25.7	5.8	-0.72	0.55	11.89	1.06
10	NGC 6752	19:10:59.84	-60:00:55.02	0.10	0.62	20.8	4.1	18.8	3.4	<27.3	-	<0.55	0.41	12.25	1.09
11	NGC 6752	19:10:52.04	-60:01:10.30	0.24	0.02	26.5	4.0	17.5	3.4	<18.6	-	<-0.72	0.31	12.34	1.10
12	NGC 6752	19:10:35.58	-59:58:26.63	0.16	0.14	23.5	4.2	16.5	3.7	<24.0	-	<0.04	0.37	12.71	1.13
13	NGC 6752	19:11:04.76	-60:00:33.43	0.21	0.12	27.2	4.2	22.7	3.5	<36.7	-	<0.61	0.32	12.76	1.14
14	NGC 6752	19:10:35.21	-59:57:59.45	0.10	0.15	<14.0	-	15.7	3.8	36.8	6.5	>1.96	0.36	13.97	1.24
15	NGC 6752	19:10:40.09	-60:01:05.67	0.01	0.04	25.6	4.5	16.8	4.3	<23.9	-	<-0.14	0.36	14.81	1.32
16	NGC 6752	19:10:45.31	-60:01:40.55	0.25	0.17	42.4	4.7	77.9	13.3	30.5	7.2	-0.66	0.52	16.10	1.43
17	NGC 6752	19:10:48.86	-59:56:19.61	0.09	0.06	43.7	4.8	42.2	4.4	46.0	7.8	0.12	0.41	16.33	1.45
18	NGC 6752	19:10:45.90	-59:56:19.50	0.32	0.07	35.3	4.9	30.9	4.4	<56.4	-	<0.95	0.28	16.80	1.50
19	NGC 6752	19:11:00.46	-59:56:21.47	0.04	0.04	5240.0	53.5	4550.0	72.3	3370.0	97.8	-0.90	0.06	17.12	1.52
20	NGC 6752	19:10:46.26	-60:01:53.46	0.04	0.15	51.7	4.8	50.6	4.4	37.9	7.8	-0.63	0.46	17.12	1.52

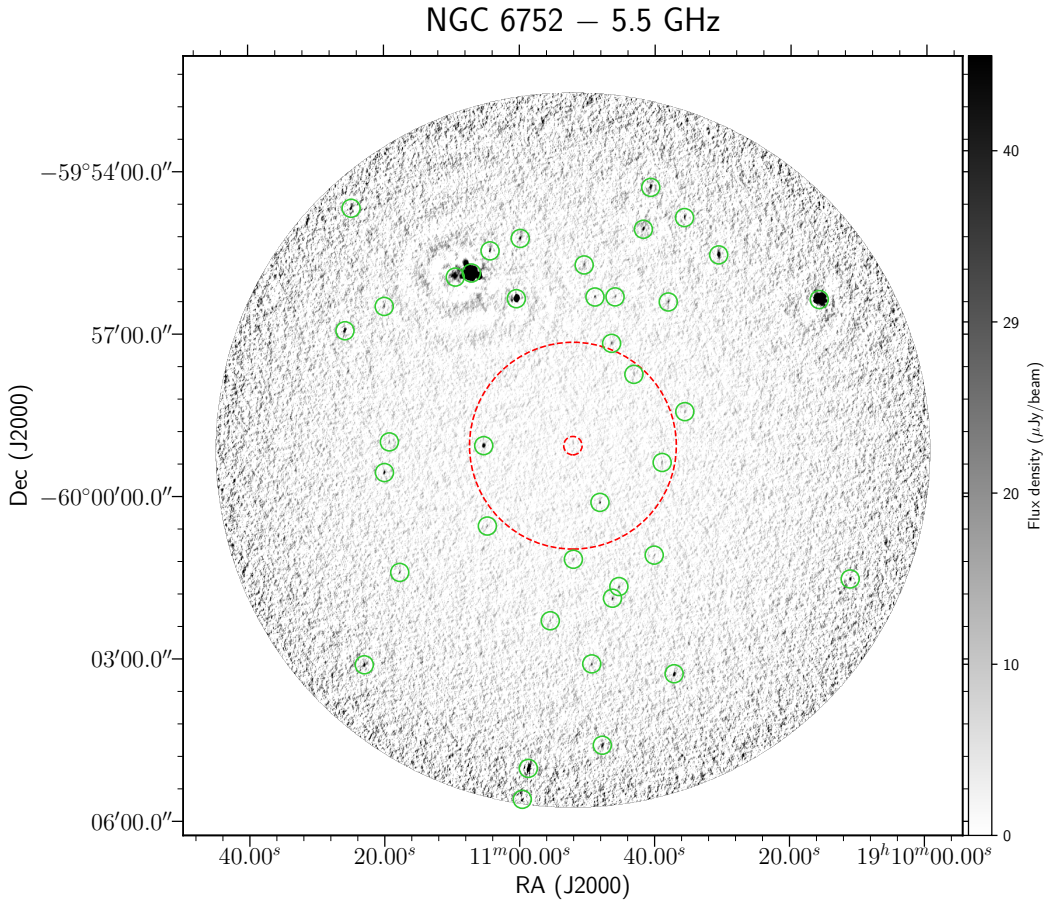
NGC 6752 — 5.5 GHz
−59°54′00.0″
57′00.0″
−60°00′00.0″
03′00.0″
06′00.0″
Dec (J2000)
40.00ˢ
20.00ˢ
11ᵐ00.00ˢ
40.00ˢ
20.00ˢ
19ʰ10ᵐ00.00ˢ
RA (J2000)
Flux density (μJy/beam)
0
10
20
29
40

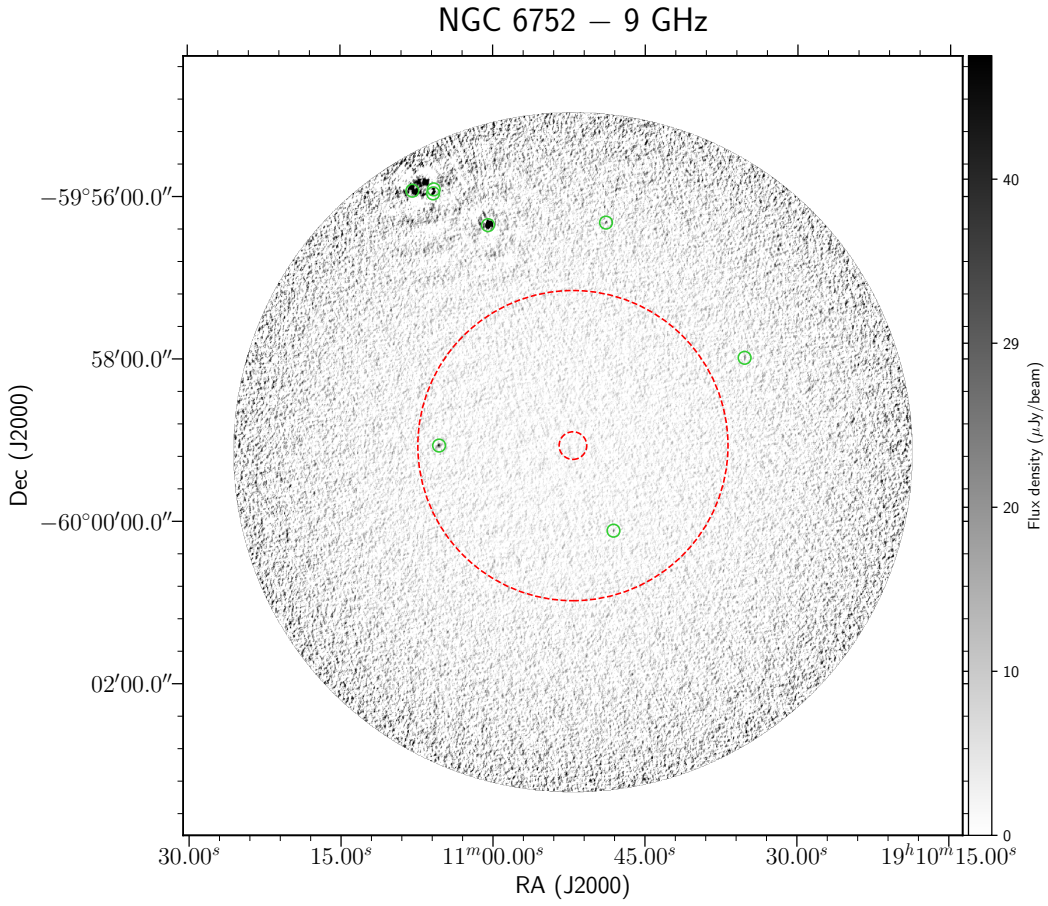
NGC 6752 — 9 GHz
−59°56′00.0″
58′00.0″
−60°00′00.0″
02′00.0″
Dec (J2000)
30.00ˢ
15.00ˢ
11ᵐ00.00ˢ
45.00ˢ
30.00ˢ
19ʰ10ᵐ15.00ˢ
RA (J2000)
Flux density (μJy/beam)
0
10
20
29
40

Chapter 4

Disk–jet coupling in low–luminosity accreting neutron stars

Adapted from:

> **V. Tudor**, J. C. A. Miller-Jones, A. Patruno, C. R. D'Angelo, P. G. Jonker, D. M. Russell, T. D. Russell, F. Bernardini, F. Lewis, A. T. Deller, J. W. T. Hessels, S. Migliari, R. M. Plotkin, R. Soria and R. Wijnands; *Monthly Notices of the Royal Astronomical Society, 470, 324 (2017)*

The content of this chapter is my own work, excepting the following. The *Swift*/XRT analysis for SAX J1808.4–3658 was performed by A. Patruno, for IGR J00291+5934 by T. D. Russell, and for Cen X–4 partly by P. G. Jonker. D. M. Russell, F. Bernardini and F. Lewis provided and performed the analysis for the optical observations of SAX J1808.4–3658.

To establish the relative contribution of accreting neutron stars to the radio source population of radio clusters, we first need to establish whether neutron stars power jets at low accretion rates ($L_X \lesssim 10^{36}$ erg s^{-1}), and if they do, what their radio luminosities are. For this purpose, in this chapter we report new and archival radio and X-ray observations of four neutron star X-ray binaries. Our target sample consists of three accreting millisecond X-ray pulsars (IGR J17511–3057, SAX J1808.4–3658 and IGR J00291+5934) during their outbursts in 2015, and of the non-pulsing neutron star Cen X–4 in quiescence (2015) and in outburst (1979), it being the closest known neutron star low mass X-ray binary (1.2 kpc).

We did not detect the radio counterpart of IGR J17511–3057 in outburst or of Cen X–4 in quiescence, but did detect IGR J00291+5934 and SAX J1808.4–3658, showing that at least some neutron stars launch jets at low accretion rates. While the radio and X-ray emission in IGR J00291+5934 seem to be tightly correlated, the relationship in SAX J1808.4–3658 is more complicated. We find that SAX J1808.4–3658 produces jets during the reflaring tail, and we explore a toy model to ascertain whether the radio emission could be attributed to the onset of a strong propeller, whereby the spinning magnetic field ejects infalling matter. The lack of a universal radio/X-ray correlation, with different behaviours in different neutron star systems (with various radio/X-ray correlations; some being radio faint and others not), points at distinct disc–jet interactions in individual sources, while always being fainter in the radio band than black holes at the same X-ray luminosity.

4.1 Targets

4.1.1 Quiescent neutron star transient

Cen X–4

Cen X–4, a likely atoll source, was discovered during an outburst in 1969 (Conner et al., 1969; Evans et al., 1970). During a subsequent outburst in 1979 (Kaluzienski et al., 1980), it was also detected in the radio band by the VLA, which was being built at the time (Hjellming, 1979; Hjellming et al., 1988). Cen X–4 has been in quiescence ever since, although the currently variable X-ray emission indicates that it is still actively accreting, albeit at a very low level ($L_X = 10^{32}$ erg s^{-1}; Campana et al., 2000, 2004b; Cackett et al., 2010; Bernardini et al., 2013). Given the radio detection of the tMSP PSR J1023+0038 in its accretion state (Deller et al., 2015), during which it has a similar X-ray luminosity as Cen X–4 in quiescence, and indications of a jet in the quiescent AMXP XTE J1814–338 (Baglio et al., 2013), we hypothesise that a jet could still be launched in Cen X–4 even at extremely low X-ray luminosities ($L_X \approx 10^{-6}\ L_{Edd}$).

Based on the theoretical Eddington luminosity for a neutron star, the Type I X-ray

bursts of Cen X–4 place it at a distance of 1.2 ± 0.3 kpc (Chevalier et al., 1989). Using the empirical Eddington luminosity calibrated for neutron stars in globular clusters, González Hernández et al. (2005) report a similar distance of 1.4 ± 0.3 kpc. For consistency with other studies of Cen X–4, we adopt a distance of 1.2 kpc. We note that since these results have been published, the parallax of Cen X–4 was measured at 0.46 ± 0.15 mas as part of *Gaia* DR2 (Lindegren et al., 2018). To convert this measurement into distance, the Lutz-Kelker bias (Lutz and Kelker, 1973) needs to be accounted for. Using the implementation of Luri et al. (2018) with an exponentially decreasing space density prior (Bailer-Jones, 2015; Astraatmadja and Bailer-Jones, 2016), we find the most likely distance for Cen X–4 is 2.3 kpc, with a 90% confidence interval of 1.7–5.8 kpc. This value is larger than the previously accepted value of 1.2 kpc. As a 3σ measurement, however, the inferred distance is heavily influenced by the choice of prior. In this case, we still favour the previous, independent distance estimates. The higher distance (2.3 vs 1.2 kpc) would change the luminosities by a factor of ~ 3.7, but no other conclusions from this chapter.

As the most nearby known neutron star X-ray binary, Cen X–4 is a good laboratory for testing whether ordinary neutron stars launch jets in quiescence. Previous radio observations of the quiescent Cen X–4, however, have failed to detect a jet, with a 4σ upper limit of ≈ 0.4 mJy (Kulkarni et al., 1992). This upper limit ($L_{\rm R} < 3 \times 10^{27}$ erg s^{-1}) is unconstraining compared to black holes at the same X-ray luminosity ($L_{\rm R} \approx 10^{27}$ erg s^{-1}).

4.1.2 AMXPs in outburst

IGR J17511–3057

Discovered in 2009 by the *INTErnational Gamma-Ray Astrophysics Laboratory* (*INTEGRAL*) (Baldovin et al., 2009), IGR J17511–3057 was later classified as an AMXP after the detection of 245 Hz X-ray pulsations (Markwardt et al., 2009). Since its 2009 outburst, it has undergone two additional outbursts, in 2012 and 2015. Previous radio observations were conducted by Miller-Jones et al. (2009) during the September 2009 outburst, but no emission was detected, with 3σ upper limits of 0.17 mJy.

Based on the peak X-ray flux of its thermonuclear bursts, Altamirano et al. (2010) placed an upper limit of 6.9 kpc on its distance. Papitto et al. (2010) found a similar lower limit of 6.5 kpc by assuming that the emission during the outburst decay comes from the neutron star surface. The pulsation timing analysis of Riggio et al. (2011) pointed towards two possible distances (6.3 or 3.6 kpc), the first of which is comparable with previous estimates. We adopt a distance of 6.9 kpc for IGR J17511–3057 for consistency with previous studies.

SAX J1808.4–3658

The first detected and most extensively studied AMXP, SAX J1808.4–3658 was discovered in 1996 with the *BeppoSAX* satellite (in 't Zand et al., 1998), and classified as an AMXP after the discovery of a 401 Hz spin (Wijnands and van der Klis, 1998). It was previously detected in the radio band during three of its outbursts, in 1998, 2002 and 2005 (Gaensler et al., 1999; Rupen et al., 2002, 2005).

Based on the fluence and recurrence times of its outbursts, Galloway and Cumming (2006) estimated a distance to SAX J1808.4–3658 of 3.4–3.6 kpc, which is consistent with the distance derived from Type I X-ray bursts (3.1–3.8 kpc). We adopt a distance of 3.5 kpc for SAX J1808.4–3658.

The X-ray light curves of SAX J1808.4–3658 are similar between different outbursts. After a quick rise to the outburst peak, the source slowly decays for 15–20 days, followed by a faster decay over ≈ 3 days, after which the source reflares for a few tens of days, each reflare lasting a few days (Patruno et al., 2016b). Episodic accretion of matter in the propeller regime could be the mechanism behind the reflares (Patruno et al., 2016b). At $L_{\rm X} \approx 10^{33}\,{\rm erg\,s^{-1}}$, the magnetosphere reaches the light cylinder of the neutron star, so that in quiescence SAX J1808.4–3658 should turn on as a radio pulsar (Campana et al., 2002). However, no radio pulsations have been detected so far (Burgay et al., 2003; Iacolina et al., 2010; Patruno et al., 2016a) in quiescence (quiescent $L_{\rm X} \approx 10^{31}\,{\rm erg\,s^{-1}}$; Campana et al., 2002), when a typical radio pulsar should have been detected, although the presence of a radio pulsar has been indirectly inferred (Burderi et al., 2003; Campana et al., 2004a).

IGR J00291+5934

Following the discovery of IGR J00291+5934 in 2004 by *INTEGRAL* (Eckert et al., 2004), the detection of a 599 Hz spin frequency by the *Rossi X-ray Timing Explorer Mission* (*RXTE*) classified it as an AMXP (Galloway et al., 2005). Similar to SAX J1808.4–3658, IGR J00291+5934 goes into outburst every 3–4 years. During its discovery outburst, the source was also detected in the radio band (Pooley, 2004; Fender et al., 2004a; Rupen et al., 2004), but no radio emission was detected during its two fainter outbursts in 2008 (Linares et al., 2008; Lewis et al., 2010). Similar to SAX J1808.4–3658, there is some evidence that IGR J00291+5934 might become active as a radio pulsar during quiescence (Jonker et al., 2008).

A Type I X-ray burst from IGR J00291+5934 was detected for the first time during the 2015 outburst, placing it at a distance of 4.2 ± 0.3 kpc (Bozzo et al., 2015b; De Falco et al., 2017). This measurement is in line with the lower limit of ≈ 4 kpc based on the fluence of the 2004 outburst (Galloway et al., 2005). However, Jonker et al. (2005) and Torres et al. (2008) found that IGR J00291+5934 should lie 2–3.6 kpc away, assuming

a similar quiescent X-ray flux as other AMXPs. Torres et al. (2008) also estimated a lower limit of 1.8–3.8 kpc based on the timing of the fast decay in its X-ray light curve, and assumptions on disc ionization states. In this chapter, we assume a distance of 4.2 kpc to IGR J00291+5934, since it is based on Type I X-ray bursts.

4.2 Observations

4.2.1 Cen X–4

On 2015 January 17, we observed Cen X–4 in quiescence simultaneously with the Karl G. Jansky Very Large Array (VLA, program 14B–117, PI: J.C.A. Miller-Jones) and the *Swift* X-ray Telescope (XRT; Gehrels et al., 2004; Burrows et al., 2005), under a Target of Opportunity observation (ObsID 00035324066, PI: P. G. Jonker). The VLA observations were carried out when the array was in the CnB configuration, at 8–12 GHz, between 13:06 – 13:48 UT, with an on-source integration time of 34 minutes. The XRT observations started at 13:25 UT, for a deadtime-corrected exposure time of 936 s in photon counting mode.

4.2.2 IGR J17511–3057

An outburst from IGR J17511–3057 was detected by *INTEGRAL* on 2015 March 23 (Bozzo et al., 2015a; Papitto et al., 2016). We observed this source with the VLA (program 14B–153, PI: D. M. Russell) on three occasions over two weeks, during a period of X-ray monitoring with *Swift*/XRT (detailed in Papitto et al., 2016). Our radio observations were carried out when the VLA was in B configuration, at 8–12 GHz. Because IGR J17511–3057 remained undetected in all these observations, we then switched to observing SAX J1808.4–3658, which went into outburst during our monitoring campaign on IGR J17511–3057.

4.2.3 SAX J1808.4–3658

The *Swift* Burst Alert Telescope (BAT) monitor detected a new outburst from SAX J1808.4–3658 on 2015 April 9 (Sanna et al., 2015), which we subsequently monitored with the VLA (program 14B–153) in B configuration, during the decay phase in April and May. On April 19, we observed this source simultaneously in the C (4–8 GHz) and K (18–26.5 GHz) bands, for improved spectral information at peak luminosity. The high-frequency K band observations required pointing calibration, for which we observed the bright calibrator J1820–2528. All the other observations were taken in the X (8–12 GHz) band. The outburst was monitored in X-rays with *Swift*/XRT with almost daily cadence (the observation log is given in Table 4.1, PIs Patruno, Chakrabarty, Sanna).

For comparison with the X-ray and radio data, we also report optical observations; Bernardini et al., in preparation).

We monitored the 2015 outburst of SAX J1808.4–3658 at optical wavelengths with the 2-m robotic Faulkes Telescopes North and South, located at Haleakala on Maui and Siding Spring, Australia, respectively, as part of an ongoing monitoring campaign of $\sim$ 40 low-mass X-ray binaries (Lewis et al., 2008). During the outburst we increased the cadence and made additional observations with five of the robotic 1-m telescopes in the Las Cumbres Observatory (LCO) network; namely one located at the Cerro Tololo Inter-American Observatory, Chile, two at the South African Astronomical Observatory, Sutherland, South Africa, and two at Siding Spring Observatory, Australia. Photometric observations were made using four filters; Bessell B-band, V-band, R-band and Sloan Digital Sky Survey (SDSS) i'-band. Here, we present the data in i'-band only, which have the most number of observations during the outburst, and are sufficient to characterise the optical light curve, identify flares, and compare to the X-ray and radio light curves.

4.2.4 IGR J00291+5934

Following the X-ray discovery of a new outburst from IGR J00291+5934 on 2015 July 24 by *Swift*/BAT (Cummings et al., 2015), in August we carried out three radio observations over three days, each with an on-source integration time of 36 minutes. These observations were carried out with the VLA in A configuration, at 8–12 GHz, under Director's Discretionary Time (program 15B–339, PI: T. D. Russell), during monitoring with the *Swift*/XRT (PI. Sanna).

4.2.5 Data analysis

VLA

The radio observations of all four systems are summarised in Table 4.2. We calibrated the radio data from the VLA with the Common Astronomy Software Applications package (CASA v4.2.1; McMullin et al., 2007) using standard procedures. The source 3C48 was used as a flux calibrator for IGR J00291+5934, and 3C286 for the other sources. For all four sources, we switched between phase calibrator and science target on 5 minute cycles (3 minutes for the 22 GHz observations). We imaged the Stokes I data using Briggs weighting with a robustness parameter of 1 as a compromise between sidelobe contamination and point source sensitivity. We performed deconvolution using the multi-frequency, multi-scale `clean` algorithm with two Taylor coefficients to account for sky frequency dependence. No self-calibration was performed. The flux density of each detected source was measured by fitting the source in the image plane

Table 4.1: Swift/XRT observations of SAX J1808.4–3658 in window timing (WT) and photon counting (PC) modes.

Program IDs	Obs. Number	Obs. Mode	Date	Exposure (s)
30034	74	WT	2015-04-13	5184
	76	WT	2015-04-14	1618
	77	WT	2015-04-15	839
81453	01	WT	2015-04-16	1794
33737	01	WT	2015-04-17	5179
30034	78	WT	2015-04-18	1848
	79	WT	2015-04-19	389
	80	WT	2015-04-20	621
	81	WT	2015-04-21	1969
	82	WT	2015-04-22	2188
33737	02	PC	2015-04-24	3719
	03	PC	2015-04-29	2544
	04	PC	2015-04-30	5444
33034	83	PC	2015-05-02	418
	84	PC	2015-05-03	1118
	85	PC	2015-05-04	1003
	86	PC	2015-05-05	684
	87	PC	2015-05-06	1118
33737	05	PC	2015-05-09	5855
30034	88	PC	2015-05-09	975
	90	PC	2015-05-10	1041
	89	PC	2015-05-10	1076
	91	PC	2015-05-12	1166
	92	PC	2015-05-13	968
33737	06	PC	2015-05-15	3707
30034	94	PC	2015-05-19	995

Table 4.2: Summary of VLA radio observations.

Source	Project ID	Date (2015)	Integration time (min)	Array configuration	Observing band (GHz)	Phase calibrator
Cen X–4	14B-117	17 Jan	34	CnB	X (8.0–12.0)	J1522-2730
IGR J17511–3057	14B-153	26 Mar	13	B	X	J1744–3116
		2 Apr	13		X	
		8 Apr	12		X	
SAX J1808.4–3658	14B-153	18 Apr	11	B	X	J1744–3116
		19 Apr	11		K (18.0–26.5)	
		19 Apr	15		C (4.0–8.0)	
		22 Apr	11		X	
		27 Apr	12		X	
		5 May	11		X	
		7 May	22		X	
		10 May	23		X	
IGR J00291+5934	15B-339	11 Aug	36	A	X	J0102+5824
		15 Aug	36		X	
		18 Aug	36		X	

using the `imfit` task. We forced a point-source fit, with an elliptical Gaussian of the shape of the synthesised beam. The flux uncertainty is taken as the rms of the residual image, with an additional systematic uncertainty of 2%, typical of flux calibration with the VLA at these frequencies. Given that no self-calibration was performed, the flux errors could be underestimated. The observing frequencies (primarily centred at 10 GHz), and the short phase-referencing cycle times (5 min), should help minimize the effects of phase decorrelation. While the lack of other point sources in the fields of view of our targets means we cannot quantify the level of phase decorrelation, we assume it to be negligible for the reasons stated above. Our final flux density measurements are given in Table 4.3. The flux density upper limits on non-detections are reported at 3 times the local rms.

To measure the radio spectral index of SAX J1808.4–3658, we split each 10 GHz observation into two sub-bands (8–10 GHz and 10–12 GHz) and imaged them separately. On April 19, we carried out 6 GHz and 22 GHz observations for a more precise measurement of the spectral index. We use the flux densities measured at each of these two frequencies to obtain the spectral index α following the $S_\nu \propto \nu^\alpha$ convention (where S_ν is the flux density measured at the central frequency ν).

We also calibrated previously unpublished VLA observations of IGR J00291+5934 taken during the 2004 (program AR545 on December 11 and 14, taken in A configuration at 4.86 GHz) and 2008 (program MPRTST on September 30 in D configura-

tion at 8.46 GHz) outbursts. As in our 2015 observations, the phase calibrator was J0102+5824 for all these observations, and the flux calibrator was 3C286 in 2004 and 3C147 in 2008. For these archival observations, we used only one Taylor coefficient during deconvolution (suitable for these single-frequency observations) and natural weighting (to maximize point source sensitivity).

Swift

Swift/XRT data were analysed with HEAsoft, as part of the HEASARC software suite (Arnaud, 1996). To generate the *Swift*/BAT light curves, we used the *Swift*/BAT light curve database (Krimm et al., 2013).

During our single X-ray observation of Cen X–4 on January 17, 2015 (MJD 56650.4), *Swift*/XRT operated in photon-counting mode (PC, 2.5 s resolution). Within a 20″ radius of its position, only 7 total counts are detected (corresponding to a count rate of 7.5×10^{-3} counts/s). The background level was measured in an area offset from visible X-ray sources. Given the low number of counts, we do not fit its spectrum, but assume the same spectral shape as that reported by Bernardini et al. (2013) for the faintest state of Cen X–4 (count rate < 0.07 counts/s), and use Poisson statistics (Kraft et al., 1991) to estimate the 90% confidence interval for its count rate. We assume a low-luminosity spectrum for Cen X–4 consisting of a thermal component (which dominates at energies below ≈ 2 keV) and a power-law component ($\Gamma = 2.0$), absorbed by a column density $N_{\rm H} = 8 \times 10^{20}$ cm^{-2} (Bernardini et al., 2013). When calculating the uncertainty in the count rate, we only take into consideration the errors associated with the low number of counts, since they will dominate over the errors associated with the spectral model. We use XSPEC (12.9.0) and WebPIMMS[1] (Mukai, 1993) to convert from count rate to unabsorbed flux.

For IGR J17511-3057, we use the light curve and spectral information provided by Papitto et al. (2016), observed with *Swift*/XRT in window-timing (WT, 1.76 ms resolution) and PC modes. They fit the spectra with an absorbed power-law, and reported the fluxes in the 0.5–10 keV range (for the same 6.9 kpc distance assumed in this chapter), which we converted to 1–10 keV fluxes in WebPIMMS, using their measured absorption column and photon indices.

For SAX J1808.4–3658, we analyzed all pointed Swift/XRT observations taken between April 13, 2015 (MJD 57125.4) and May 19, 2015 (MJD 57161.8). A total of 26 observations were taken, with Program IDs 33034, 33737 and 81453. The X-Ray Telescope operated either in WT or PC mode. The source counts were extracted in an energy range of 1–10 keV, as is commonly used in recent literature, from a circular region of radius 20″, and the background was extracted from an area far from

[1]https://heasarc.gsfc.nasa.gov/docs/software/tools/pimms.html

known sources in the field. The events and X-ray spectra were extracted with the tool XSELECT (v2.4d) and the spectral analysis was done with XSPEC. Each spectrum was fitted with a simple absorbed power-law model plus a multiplicative component (CFLUX) used to calculate the unabsorbed flux in the 1–10 keV band (and its 90% confidence interval).

For IGR J00291+5937, we use a procedure similar to that described for SAX J1808.4–3658. The observation campaign carried out with *Swift*/XRT on this source will be described in full in Russell et al., in preparation.

Ariel V

For the 1979 outburst of Cen X–4, we use the X-ray data reported by Kaluzienski et al. (1980), observed with the *Ariel V* All-Sky X-ray Monitor (ASM) (Holt, 1976), and retrieved from the public archive. We converted the reported 3–6 keV flux to 1–10 keV unabsorbed flux using WebPIMMS, by assuming a power-law spectrum with photon index $\Gamma = 1.6$ (as adopted by Bernardini et al., 2016) and absorption ($N_{\rm H} = 8 \times 10^{20}$ cm^{-2}; Bernardini et al., 2013).

RXTE

To estimate the X-ray fluxes of IGR J00291+5934 at those times when the source was not detected in the radio band during its outbursts in 2004 and 2008, we used the X-ray data reported by Galloway et al. (2005) and Lewis et al. (2010), observed with the *RXTE* Proportional Counter Array (PCA). These data were retrieved from the *RXTE* Mission-Long Source Catalog. We converted the 2–9 keV count rate from IGR J00291+5934 to the 1–10 keV unabsorbed flux using WebPIMMS, by assuming a power-law spectrum with photon index $\Gamma = 2.06$ and absorption $N_{\rm H} = 4.3 \times 10^{21}$ cm^{-2}, which describes the 0.4–10 keV spectrum (Paizis et al., 2005).

LCO

The i'-band magnitudes were extracted using PHOT in IRAF and calibrated using the three comparison stars listed in Greenhill et al. (2006). i'-band magnitudes of the three comparison stars were calculated from R-band and I-band magnitudes using the conversion of Jordi et al. (2006), in the same way as mentioned in Elebert et al. (2009).

4.3 Results

4.3.1 Cen X–4

We did not detect Cen X–4 in the radio band, although we place constraints on the emission (<14 μJy; Table 4.2) that are a factor of $\approx$ 20 deeper than previous radio observations in quiescence (Kulkarni et al., 1992). In the X-ray band, we detected only 7 total photons (including background) from Cen X–4, as our observations were conducted during a particularly faint X-ray state (Fig. 4.1). The 90% confidence interval for its background-subtracted 1–10 keV luminosity is $L_X = 8.0 \times 10^{30} - 5.6 \times 10^{31}$ erg s^{-1}.

4.3.2 IGR J17511–3057

We conducted radio observations of IGR J17511–3057 during its slow X-ray decay (Fig. 4.2). Similar to previous outbursts, it remained undetected in the radio band, although our constraints (<21 μJy; Table 4.2) are a factor of $\approx$ 8 deeper than previous radio observations at similar X-ray luminosity (Miller-Jones et al., 2009).

4.3.3 IGR J00291+5934

Our radio observations were conducted during the fast X-ray decay of IGR J00291+5934 (Fig. 4.4), and we detected it in the first two of three epochs (Table 4.2). We did not detect the source in the archival observations taken on December 11 (<132 μJy) and 14 (<111 μJy), 2004 or on September 30, 2008 (<156 μJy). Coupled with previous detections, IGR J00291+5934 now has a well-sampled X-ray luminosity range, meaning that we can track its disc–jet coupling from the peak of the outburst towards quiescence, assuming that it follows the same path over multiple outbursts, as seen in the black holes GX 339–4 (Corbel et al., 2013) and V404 Cyg (Plotkin et al., 2017).

4.3.4 SAX J1808.4–3658

Light curves

The seven radio detections of SAX J1808.4–3658 (labelled sequentially A–G) at different times across a single outburst make it an excellent source for tracing the inflow–outflow coupling in an AMXP. Observations during previous outbursts have identified SAX J1808.4–3658 as a radio-loud neutron star (Migliari and Fender, 2006), and in addition to the main outburst, we are now also able to track its multiwavelength behaviour in the fainter states (Fig. 4.3).

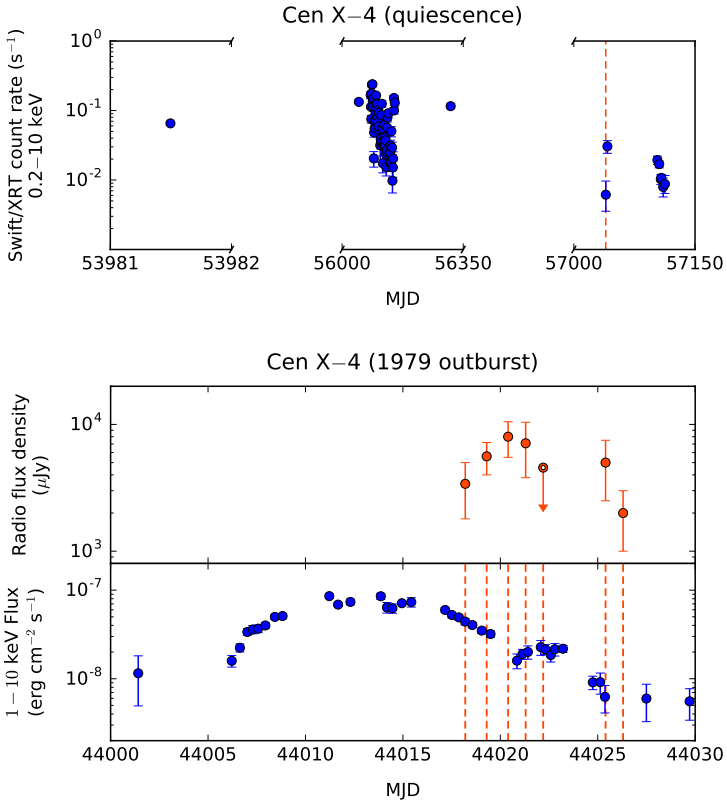

Figure 4.1: *Top*: quiescent X-ray light curve of Cen X–4, as observed by *Swift*/XRT in PC mode. We show all observations with the *Swift*/XRT (over the years 2006/2012/2015) as a visual representation of the quiescent flux of Cen X–4. The blue points show individual snapshots and the vertical dashed line indicates the timing of our VLA observations in 2015, carried out simultaneously with an XRT observation when the system was in a particularly faint state. *Bottom*: The radio and X-ray light curves of Cen X–4 during its 1979 outburst, as observed with the VLA (Hjellming et al., 1988) and *Ariel V ASM (Kaluzienski et al., 1980). Cen X–4 was detected in the radio band multiple times during the X-ray decay.*

In X-rays, SAX J1808.4–3658 behaved during its 2015 outburst similarly to previous outbursts: a slow decay (until MJD $\approx$ 57141), a fast decay (MJD $\approx$ 57141 – 57143), and a reflaring tail (after MJD $\approx$ 57143). A radio reflare was also observed, but the X-ray and radio reflares do not seem to be coincident (observations F, G in Fig. 4.3). Radio detections during X-ray reflares show that the jet survives during the reflaring tail. The last two radio observations show unexpected behaviour, as the source undergoes a radio reflare during an X-ray minimum (observation F, although an X-ray reflare at that time could have been missed, see Section 4.4.3), and no increase in radio flux is observed during a rapid increase in X-ray flux at the start of an X-ray reflare (observation G). We find little evidence of intra-observation variability during these two radio observations (consistent with a constant flux over 2 min and 10 min timescales within $\approx 2\sigma$ uncertainty).

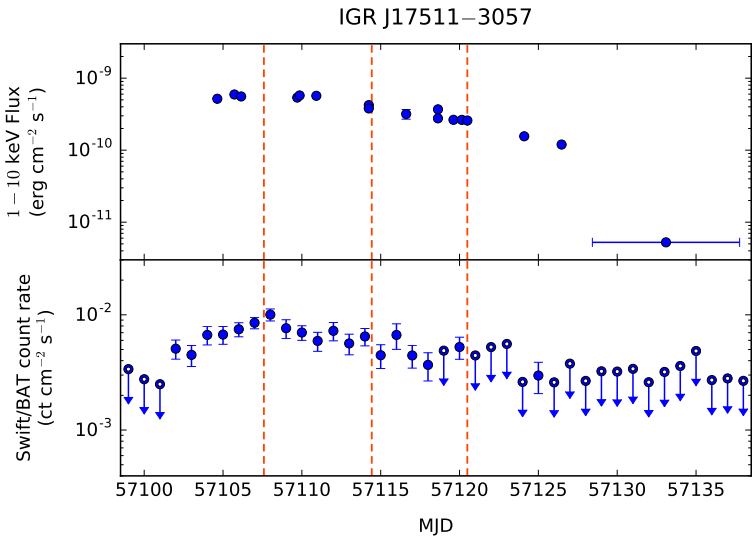

Figure 4.2: X-ray light curves of IGR J17511–3057 during its outburst in 2015, as observed by *Swift*/XRT (1–10 keV flux) and *Swift*/BAT (15–150 keV count rate). The blue points show individual observations and the vertical dashed lines indicate the timing of our VLA observations. All radio observations were carried out during the slow X-ray decay. We did not detect the source in any of our VLA observations.

Radio spectral indices

The 6 and 22 GHz observations from April 19 were taken within 20 minutes of each other, during which time we do not expect the source to have varied (see 4.3.4). Indeed, we do not find evidence for variability during either observation on that day (both C and K band data are consistent with a constant flux within each observation within 1σ uncertainty). We find the spectral index to be close to flat ($\alpha = -0.24 \pm 0.10$, assuming no change in flux between the two observations), similar to the compact jets of other X-ray binaries, although we cannot rule out a steep spectrum within uncertainties. We find that the spectral index measurements within the 10 GHz band on the other observing epochs are typically unconstraining (with a typical error of ±0.5, due to the faintness of the radio emission and the small lever arm in frequency), so we cannot distinguish between optically thin and thick emission. The spectral index measurements for all epochs are listed in Table 4.3.

4.3.5 The radio–X-ray correlation

The radio ($L_{\rm R} = 4\pi D^2 \nu S_\nu$, where D is the distance to the source) and X-ray luminosities of our sample are displayed in Fig. 4.5 individually, and together in Fig. 4.6, with the addition of other black hole and neutron star systems from the literature, as of 2016.

Positions of X-ray binaries on the radio – X-ray plane are best measured from strictly simultaneous observations. Among our multi-wavelength campaign, Cen X–4 has strictly simultaneous data. For the other sources, we interpolate the X-ray light

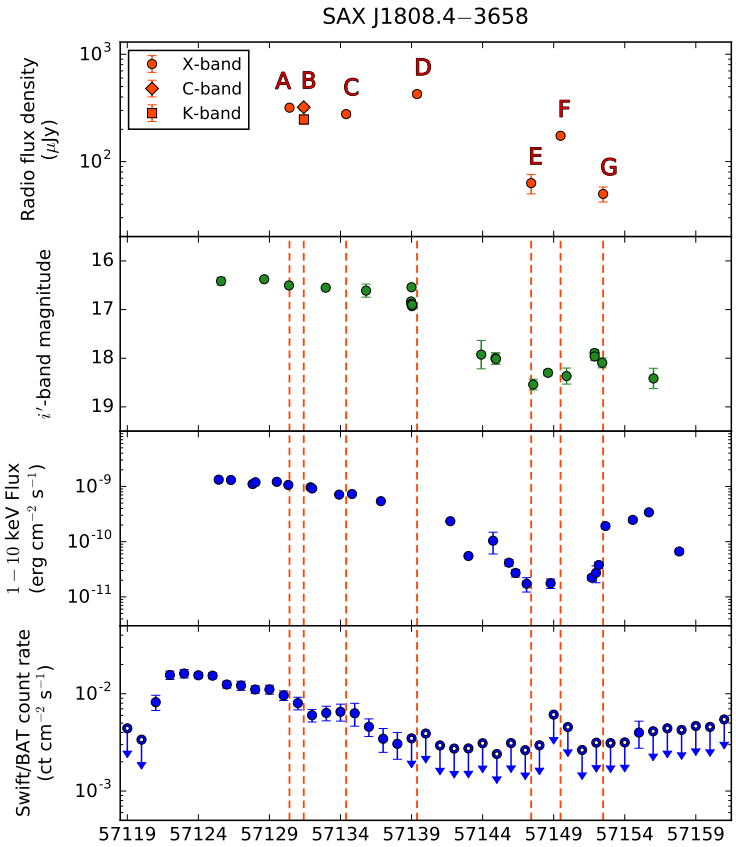

Figure 4.3: Radio (VLA), optical (LCO) and X-ray (*Swift*/XRT, 1–10 keV flux; *Swift*/BAT, 15–150 keV count rate) light curves of SAX J1808.4–3658 during its 2015 outburst. The orange dashed lines indicate the times of the radio observations, individually labelled from A to G. During the slow X-ray decay, the source undergoes a radio reflare (observation F).

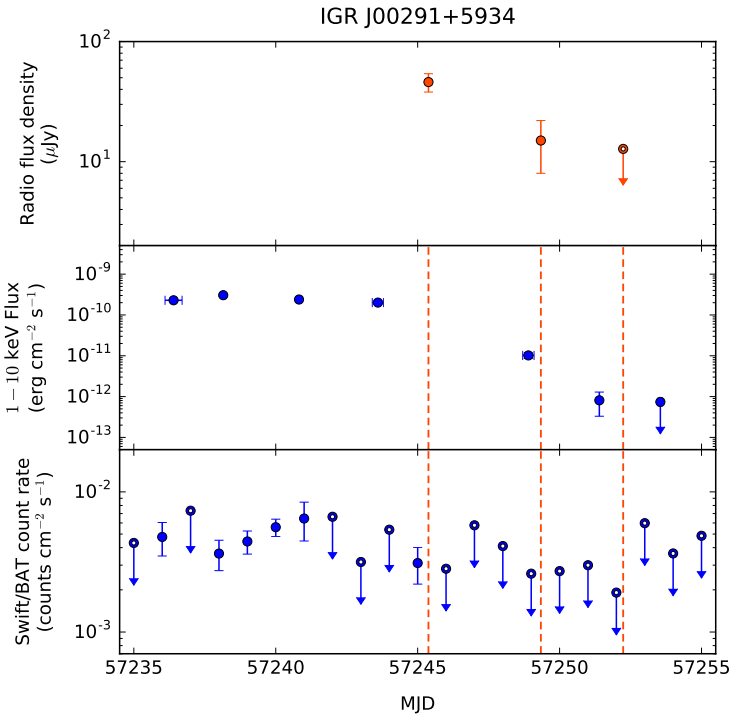

Figure 4.4: The radio (VLA) and X-ray (*Swift*/XRT, 1–10 keV flux; *Swift*/BAT, 15–150 keV count rate) light curves of IGR J00291+5934 during the late stages of its 2015 outburst. We detect the source in the first two out of our three observations.

Table 4.3: Radio monitoring results. Source distances are assumed as discussed in Section 4.1.

Source	D (kpc)	MJD	$F^{a}_{1-10\,\mathrm{keV}}$ ($\times 10^{-11}$ erg cm^{-2} s^{-1})	ν (GHz)	S_ν (μJy bm^{-1})	α
Cen X–4	1.2	56650.409	$(8.5 \pm 5.4) \times 10^{-3}$	10.0	< 14	–
IGR J17511–3057	6.9	57107.592	58.5 ± 10.1	10.0	< 22	–
		57114.432	38.9 ± 6.7	10.0	< 21	–
		57120.494	27.0 ± 4.6	10.0	< 28	–
SAX J1808.4–3658	3.5	57130.411	98.7 ± 5.5	10.0	317 ± 24	0.05 ± 0.45
		57131.413	91.4 ± 5.1	22.0	238 ± 23	–[b]
		57131.427	91.4 ± 5.1	6.0	321 ± 25	-0.24 ± 0.10[b]
		57134.397	73.0 ± 4.1	10.0	277 ± 22	-0.51 ± 0.56
		57139.386	50.0 ± 2.8	10.0	426 ± 24	-0.21 ± 0.60
		57147.415	1.6 ± 0.1	10.0	63 ± 13	–[c]
		57149.484	1.9 ± 0.1	10.0	174 ± 9	-0.26 ± 0.57
		57152.478	11.1 ± 0.6	10.0	50 ± 8	–[c]
IGR J00291+5934	4.2	57245.376	19.6 ± 7.2	10.0	46 ± 8	–[c]
		57249.335	0.65 ± 0.16	10.0	15 ± 7	–[c]
		57252.241	$(3.6 \pm 2.8) \times 10^{-2}$	10.0	< 12	–

Notes.
[a] Estimated at the time of the radio observation
[b] The 6 and 22 GHz observations were used to derive a single spectral index measurement.
[c] The signal-to-noise ratio is too low for a meaningful spectral index measurement.

curve to estimate the X-ray flux at the time of the radio observations, by fitting a piecewise linear function in the log L_X/time space.

The 3 σ upper limit of 14 μJy on the radio emission of Cen X–4 in quiescence only constrains its radio luminosity to being less than that of the radio-fainter black hole jets (e.g. XTE J1118+480; Gallo et al., 2014). The limit lies just above the proposed tMSP track, slightly below the quiescent black hole systems.

In addition, we also place the 1979 outburst of Cen X–4 on the radio/X-ray plane for the first time. For the radio luminosity, we use the data reported by Hjellming et al. (1988) in two bands (at 1.49 and 4.9 GHz). For days when observations were carried out in both radio bands, we use the measurement with smaller uncertainties, with the assumption of a flat spectrum. We find that during the 1979 outburst, Cen X–4 reached radio and X-ray luminosities similar to the atoll sources. Assuming it follows a single, continuous radio–X-ray correlation from the peak of the outburst down to quiescence (like the black hole systems V404 Cyg, Corbel et al., 2008; and GX 339–4, Corbel et al., 2013), we obtain a lower limit for its correlation slope $\beta \gtrsim 0.5$.

The upper limits for IGR J17511–3057 make it less luminous in the radio band than typical atoll sources (Fig. 4.6), but we cannot rule out radio emission at a level similar to that of EXO 1745–248, the radio-detected neutron star with the lowest disc–jet coupling normalization (Tetarenko et al., 2016a).

Previous radio detections of SAX J1808.4–3658 sample just one decade of X-ray luminosity ($L_X \approx 10^{35}$ to 10^{36} erg s^{-1}; Migliari et al., 2011). Here, we extend the range of detections down to $L_X \approx 10^{34}$ erg s^{-1}. The radio behaviour of SAX J1808.4–3658 during the slow X-ray decay seems to be reproducible between different outbursts, with a clustering of detections at $L_X \approx 10^{36}$ erg s^{-1} and $L_R \approx 10^{28}$ erg s^{-1}. As it fades, SAX J1808.4–3658 is seen to alternate between the atoll sources and tMSPs in the radio–X-ray plane. This points to temporal changes in the radiative efficiency, which does not reach the same levels as for black hole systems.

Similar to SAX J1808.4–3658, our radio observations of IGR J00291+5934 make it possible to study the jet over two decades of X-ray luminosity, in the range $L_X \approx 10^{34}$ to 10^{36} erg s^{-1}. In contrast to SAX J1808.4–3658, IGR J00291+5934 is consistent with following a $L_R \propto L_X^{\beta}$ correlation. We find a correlation slope $\beta = 0.77 \pm 0.18$ (90% uncertainty range, assuming reproducible outbursts), which is similar to the primary black hole track, to the proposed tMSP track, and to Aql X–1 (above 10^{36} erg s^{-1}; Tetarenko et al., 2016a), at a luminosity similar to that of atoll sources.

4.4 Discussion

Our results reinforce the idea of different behaviours in different neutron star systems – with reflares and no consistent radio–X-ray relationship (SAX J1808.4–3658), with a

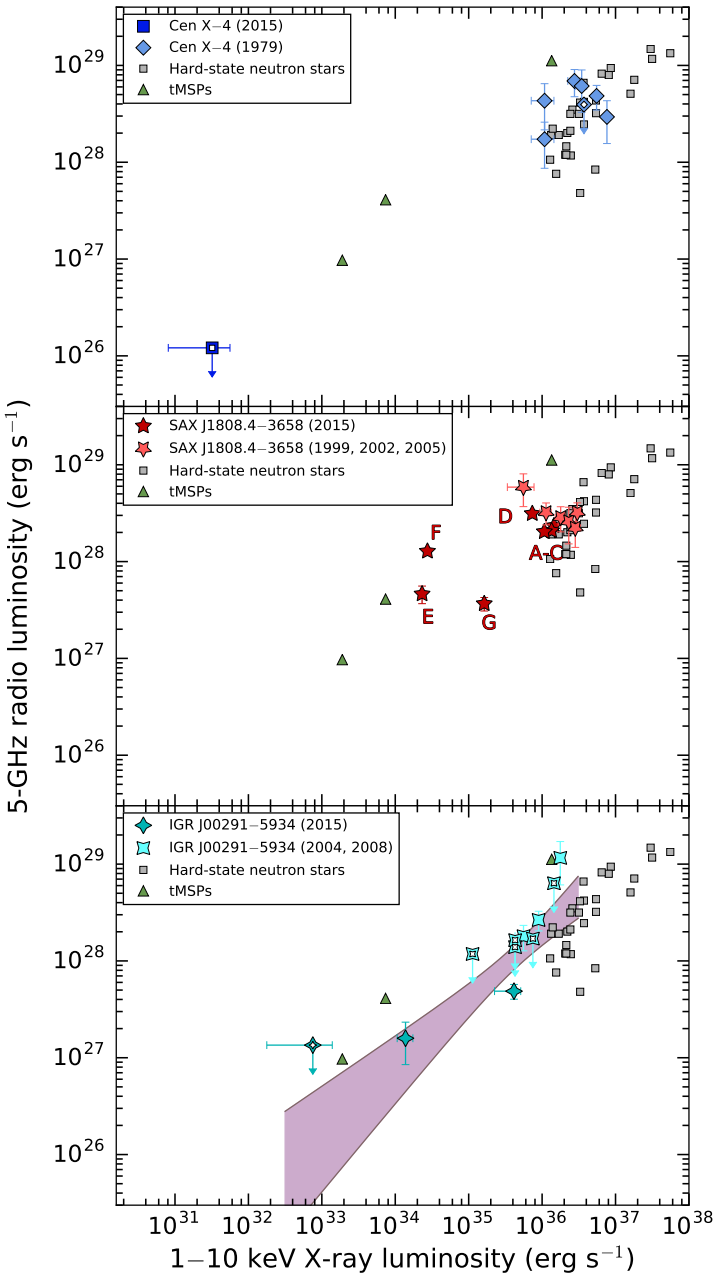

Figure 4.5: The radio and X-ray luminosities of Cen X–4, SAX J1808.4–3658 and IGR J00291+5934. Hollow symbols mark upper limits on radio luminosities. The labelled data points of SAX J1808.4–3658 refer to the same observations in Fig. 4.3. IGR J00291+5934 (and possibly SAX J1808.4–3658, but with larger scatter) seems to follow the familiar $L_{\rm R} \propto L_{\rm X}^{\beta}$ correlation seen in black holes and some atoll sources, with $\beta = 0.77 \pm 0.18$ (90% confidence interval, shaded area).

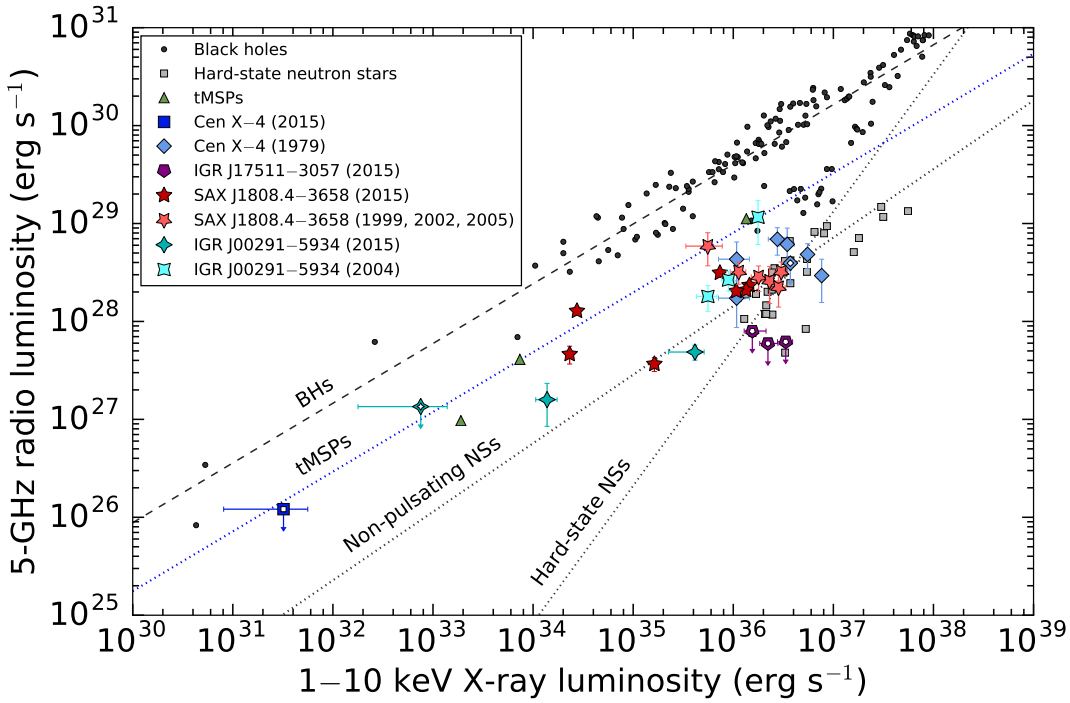

Figure 4.6: Radio and X-ray luminosities of low-mass X-ray binaries. The black dashed line represents the radio–X-ray correlation of accreting black holes (β = 0.6; Gallo et al., 2014), and the three dotted lines are the proposed relations for tMSPs (β = 0.6; Deller et al., 2015), non-pulsating neutron stars (NS) regardless of spectral state (β = 0.7), and hard-state neutron stars only (β = 1.4; Migliari and Fender, 2006; Migliari et al., 2011). Hollow symbols indicate upper limits in radio luminosity. The upper limits from the previous outbursts of IGR J00291+5934 are not plotted for better visibility.

well-fitting radiatively inefficient flow (IGR J00291+5934), long-term steady, but with flipping between X-ray modes (tMSPs), etc. Our observations strengthen the evidence for atoll sources and AMXPs being fainter in the radio band than black holes at the same X-ray luminosity. Some AMXPs can be faint (IGR J00291+5934) or fainter than non-pulsating neutron stars (IGR J17511–3057). During outbursts, however, some AMXPs (SAX J1808.4–3658) can become as radio-bright as tMSPs (a conclusion also supported by the tMSP M28I, which was observed in outburst as an AMXP; Papitto et al., 2013).

The above hints at a maximum radio luminosity achievable by neutron stars, a factor of ≈ 5 fainter than radiatively inefficient black holes at the same X-ray luminosity, as proposed by Deller et al. (2015). One expects radio jets from more massive accretors to be more luminous at comparable X-ray luminosities, as indicated by the fundamental plane of accreting black holes ($\log L_{\rm R} = 0.8 \log M + 0.6 \log L_{\rm X} + 7$; Merloni et al., 2003; Falcke et al., 2004). Therefore, as already noted by Deller et al. (2015), the difference in mass between black holes ($\approx 8 M_{\odot}$; Özel et al., 2010; Kreidberg et al., 2012) and neutron stars ($\approx 1.4 M_{\odot}$; Özel et al., 2012) could account for a factor of ≈ 4 between the radio luminosity of the two classes of X-ray binaries, if their accretion mechanisms are otherwise similar. This could possibly explain some of the difference between the radiatively inefficient black holes, and the most radio-luminous neutron stars (the tMSPs, and the radio-loud epochs of SAX J1808.4–3658). However, the mass term of the fundamental plane cannot explain the difference in radio luminosity between neutron stars and black holes. Even considering bolometric luminosities, and the radiative output of the boundary layer in neutron stars, black holes still remain a factor of 2.5 radio-louder than neutron stars (Gallo et al., 2018).

Because of different disc–jet coupling behaviours in different neutron stars, highlighted by the contrast between IGR J00291–3658, with a coupling index $\beta \approx 0.7$, and EXO 1745–248, with $\beta \approx 1.7$ (Tetarenko et al., 2016a), we do not attempt to fit a single radio/X-ray correlation for the whole population of neutron stars (as previously done by Migliari and Fender, 2006). Such a fit would be biased towards radio-loud neutron stars, and would thus not offer further insights into the accretion process, nor better predictive power. As a tool to identify new black holes and neutron star candidates below $L_{\rm X} \lesssim 10^{36}\,{\rm erg\,s^{-1}}$, we therefore advise only using the maximal radio luminosity (neutron stars at least a factor of ≈ 5 fainter than black holes) suggested above.

Below we discuss each source in our sample, considering in most detail the case of SAX J1808.4–3658, the source for which we obtained the best-sampled multi-wavelength coverage.

4.4.1 Cen X–4

The X-ray flux of Cen X–4 during our observations was an order of magnitude lower than its median quiescent flux (see Fig. 4.1). Its quiescent X-ray luminosity (Cackett et al., 2010; Bernardini et al., 2013), is typically in the range $L_X = 0.7-4.3\times10^{32}$ erg s^{-1} in the 1–10 keV band (assuming a photon index $\Gamma = 1.5$). In contrast, we measure a luminosity $L_X \approx 0.05 - 0.24 \times 10^{32}$ erg s^{-1} (90% uncertainty range), which means that we cannot place constraints on jet production in Cen X–4 in quiescence, deeper than that of some black holes.

During its outburst in 1979, Cen X–4 had similar radio ($L_R = 10^{28} - 10^{29}$ erg s^{-1}) and X-ray luminosities ($L_X = 10^{36} - 10^{37}$ erg s^{-1}) as most of the non-pulsating systems. The signal-to-noise ratio of these early radio detections, however, is too low to check if the two wavebands are correlated. Including our radio upper limit during quiescence, the radio–X-ray correlation index is only restricted to $\beta \gtrsim 0.5$, so we cannot differentiate between radiatively efficient or inefficient accretion in this system.

Had we observed Cen X–4 at a more typical quiescent X-ray luminosity, a radio observation would have likely either detected or disproved the formation of a jet as powerful as that of tMSPs. We therefore encourage future simultaneous radio and X-ray observations of Cen X–4.

4.4.2 IGR J17511–3057

The radio non-detection of IGR J17511–3057 could potentially be attributed to several factors: an incorrect distance estimate, a quenching of the jet in the soft state, or suppression of jet formation by a high magnetic field. IGR J17511–3057 would need to be located approximately 30 kpc away for its upper limits to be consistent with the $\beta = 0.7$ correlation for neutron stars. Given that multiple distance estimates point towards a source distance of less than 7 kpc (see Section 4.1.2), we consider that its non-detection has a physical origin. Jet quenching at high Eddington ratios has previously been observed in the atoll sources Aql X-1 (Tudose et al., 2009, Miller-Jones et al., 2010), GX 9+9 (Migliari, 2011), and 4U 1728–34 (Migliari et al., 2003), but it has not been seen in all neutron stars (Rutledge et al., 1998; Migliari et al., 2004). The hard spectral state and power spectrum of the low luminosity outburst of IGR J17511–3057 (Papitto et al., 2016) point towards a canonical hard state (Shaposhnikov and Titarchuk, 2006) and hence, against the non-detections being caused by jet quenching in the soft state.

The high magnetic fields of pulsars may also inhibit the formation of jets (for fields $\gtrsim 10^{11}$ G; Fender and Hendry, 2000; Migliari et al., 2012), although the magnetic field of IGR J17511–3057 has been estimated to be similar to that of other AMXPs ($\sim 10^8$ G; Mukherjee et al., 2015, Papitto et al., 2016). The detection of type I bursts (Altamirano

et al., 2010) also rules out a high magnetic field (Joss and Li, 1980).

Given that radio emission at the same level as EXO 1745–248 is not ruled out, it is possible that IGR J17511–3057 has an X-ray to radio normalization that is lower than that of other AMXPs and atolls. Contrary to the common assumption that AMXPs are more radio-loud than non-pulsating sources, IGR J17511–3057 would then be a clear example that this rule does not hold for all AMXPs. Since IGR J17511–3057 has a similar spin ($\nu = 245$ Hz) and magnetic field strength ($B \approx 10^8$ G) to other AMXPs (Mukherjee et al., 2015), it appears that the magnitude of the spin and magnetic field are not the only properties that produce strong jets in the other AMXPs and tMSPs, and that other factors, as yet unidentified, could be at least as important.

4.4.3 SAX J1808.4–3658

The atypical radio behaviour of SAX J1808.4–3658 might be interpreted in a variety of ways, which we explore below. Throughout this section, we refer to our radio epochs as A–G, as labelled in Fig. 4.3. Of these, we refer to those epochs that are close to the proposed radio/X-ray correlation for tMSPs as "radio-loud" (our observations D, E, F, and the detection by Gaensler et al., 1999).

Insufficient light curve sampling

Sparse X-ray coverage could be invoked to explain the apparent high radio luminosity of the radio-loud epochs, and their deviation from the proposed radio/X-ray tracks for neutron stars. For example, *Swift*/XRT observations might have missed an X-ray reflare coincident with the radio reflare of observation F. The X-ray reflares can last as little as ≈ 0.3 days (Wijnands et al., 2001). In comparison, the two *Swift*/XRT observations adjacent to the radio reflare (observation F) are separated by ≈ 3 days. We therefore examine hard X-ray (*Swift*/BAT, 15–50 keV) and optical (LCO) light curves for evidence of flares or dips of other wavebands at the times of the radio observations. We find the optical and soft X-ray fluxes in SAX J1808.4–3558 track each other well during the outburst (Fig. 4.3; a full description of the optical–X-ray correlation will be presented in Bernardini et al.), similar to previous outbursts (Patruno et al., 2016b). In previous outbursts, however, the X-ray lagged the optical emission by 1.5–4 days (Giles et al., 1999; Patruno et al., 2016b), and the optical and X-ray fluxes during some reflares were anti-correlated or uncorrelated (Wijnands, 2006; Patruno et al., 2016b). Given the lack of *Swift*/XRT data, we therefore look for evidence of reflares primarily in the *Swift*/BAT light curve.

For radio observations D, E, F, the optical and hard X-ray light curves do not show evidence of reflares (with the previously described caveat of possible uncorrelated X-ray/optical behaviour). In addition, observation E was probably carried out at the

end of a stable X-ray decay (as shown by the preceding *Swift*/XRT observations, MJD ~57144 to ~57148). In observation F, the radio flux density increased by a factor of ≈ 3 over the two days since observation E, with no apparent corresponding increase in the 1–10 keV flux. Unfortunately, the coincidentally large uncertainties in the daily *Swift*/BAT data adjacent to this radio observation were not particularly constraining ($F_{1-10\,\mathrm{keV}} < 10^{-10}\,\mathrm{erg\,cm^{-2}\,s^{-1}}$, 3σ limit, assuming a photon index $\Gamma = 1.8$), so a relatively faint ($L_\mathrm{X} < 1.5 \times 10^{35}\,\mathrm{erg\,s^{-1}}$), fast X-ray flare without a corresponding optical flare could have been missed. There was also no significant detection in the orbital *Swift*/BAT light curve around observation F. We find it unlikely that the other radio-loud epochs were caused by insufficient sampling of its multi-wavelength light curve.

Observations D, E, F, together with previous radio observations, show that SAX J1808.4–3658 can reach quasi-simultaneous radio/X-ray luminosities similar to those of tMSPs. The sparse 1–10 keV sampling around observations D and F could potentially be the reason behind their apparently high radio luminosities, but observation E and that of Gaensler et al. (1999), might require a physical explanation. Below, we investigate possible physical causes.

A collision of the jet with a nearby medium

The enhanced flux during the radio-loud epochs could be caused by additional radio emission from a shock. Thus, a significant fraction of the radio emission could originate from radio lobes or hot spots from the interaction of the jet with the interstellar medium. We do not resolve any extended emission in SAX J1808.4–3658 that might indicate lobes. Based on the size of the synthesised beam at 22 GHz ($3.4'' \times 0.9''$), we place an upper limit of $\lesssim 2 \times 10^{17}$ cm on the size of the radio source (at a distance of 3.5 kpc). Separations between the two radio lobes produced by outbursting X-ray binaries have been seen to reach similar dimensions (e.g. Bower et al., 2005). Travelling the above distance at velocity c takes 0.2 years, however. Since this is longer than the outburst timescale, the reflares cannot be associated with lobes of such size. We cannot dismiss the possibility of smaller radio lobes based on physical size alone. However, the low density environment of SAX J1808.4–3658 ($N_\mathrm{H} = 1.4 \times 10^{21}\,\mathrm{cm^{-2}}$, inferred from the X-ray spectrum; Pinto et al., 2013) argues against the presence of a dense interstellar medium in its vicinity for a jet to interact with. However, we still cannot rule out the (somewhat unlikely) possibility of a cloud adjacent to the neutron star that does not intervene along our line of sight towards it, which requires a finely-tuned geometry.

Instead of the high-density interstellar medium that SAX J1808.4–3658 would need to be embedded in, the jet could interact with a smaller, localized circumbinary structure, produced by accretion/ejection processes in the system, from the current or previous outbursts. Such material would likely lead to accelerated orbital decay (Taam

and Spruit, 2001). SAX J1808.4–3658, however, undergoes orbital expansion (Patruno et al., 2012), which we take as evidence against the existence of a massive circumbinary structure around the system.

Alternatively, the radio emission could be caused by collisions of a high-velocity collimated jet with slow, wide-angle winds. This scenario is thought to occur in SS433, a black hole system in a very different evolutionary state to SAX J1808.4–3658, which is accreting close to the Eddington luminosity from a supergiant companion, producing heavy outflows driven by strong radiation pressure (Blundell and Hirst, 2011). The coexistence of jets and winds is thought to occur in a few other black hole and neutron star systems at high X-ray luminosities ($L_{\rm X} \gtrsim 0.3\ L_{\rm Edd}$; Homan et al., 2016a). In contrast, SAX J1808.4–3658 only reaches luminosities $L_{\rm X} \lesssim 0.1\ L_{\rm Edd}$, although it does launch winds (Pinto et al., 2014). If winds are still launched down to $L_{\rm X} = 10^{33}$ erg s^{-1} (possibly by the propeller mode of accretion; Romanova et al., 2009; Lii et al., 2014), the jet could blow into them, producing the observed radio–X-ray behaviour. In comparison, compact radio and γ-ray emission from cataclysmic variables in outburst originates at the interface between slow and fast outflows (Chomiuk et al., 2014). The possibility of coexisting jets and winds in SAX J1808.4–3658 can be tested in future outbursts with simultaneous radio and high spectral resolution X-ray observations.

Another possibility is that the radio flares are produced by a jet colliding with the accretion disc or the donor star. This could occur if the spin of the neutron star is severely misaligned with respect to the orbit of the donor star, and the accretion disc is warped (Bardeen and Petterson, 1975; Maccarone, 2002; Butt et al., 2003). If this were the case, we should expect the same mechanism to operate in some black hole systems. The fact that no black hole low-mass X-ray binary in the hard state is known to display as much scatter in the radio/X-ray plane as SAX J1808.4–3658, suggests that such a geometry and emission mechanism are unlikely. In addition, the small donor ($M = 0.03 - 0.06 M_{\odot}$; Wang et al., 2013), which covers $\approx 1\%$ of the sky as seen from the neutron star, makes a collision between it and the jet unlikely.

Information about the nature of the radio emission can in principle be gleaned from the spectral index. Radio lobes typically have steep spectral indices ($\alpha \approx -0.7$), similar to discrete, transient jets, whereas steady, compact jets have flat spectra ($\alpha \approx 0$; Blandford and Konigl, 1978; Fender, 2001). As discussed in section 4.3.4, the best constrained spectral index measurement of SAX J1808.4–3658 is $\alpha = -0.24 \pm 0.10$, but we cannot confidently ($<3\sigma$ confidence) favour any emission mechanism, although a flat-spectrum jet during the slow decay is slightly more favourable. The slightly shallower spectral index than expected for neutron stars (with an average $\alpha \approx 0.2$; Russell et al., 2007) could imply contamination from optically thin regions.

Another observational test that would confirm collisions of the jet with a surrounding medium would be a rebrightening in the radio band simultaneous with an increase in

optical line flux (e.g. Hα), during constant, or decaying, optical continuum level (e.g. Gallo et al., 2005).

Collisions within the jet

Shocks within a jet have previously been invoked to explain the radio properties of jets in general (Kaiser et al., 2000; Fender et al., 2004c; Jamil et al., 2010; Malzac, 2013) and the behaviour of individual X-ray binaries in particular (Fomalont et al., 2001; Ratti et al., 2012). A luminosity-dependent Lorentz factor of the ejecta (invoked by Soleri and Fender, 2011 and Russell et al., 2015 to explain the X-ray/radio luminosity tracks of radio-faint black holes) could in principle lead to delayed radio reflares. Fast ejecta launched at the peak of an X-ray reflare could collide with previous slower ejecta, and cause a radio brightening of the source. The typical durations and peak fluxes of the reflares of SAX J1808.4–3658, which are so far unique to this source, might be responsible for the scatter in the radio–X-ray plane that has not been observed in other X-ray binaries.

A large delay between the radio and X-ray emission

The scatter in the radio/X-ray plane could be caused by the rapid variability of SAX J1808.4–3658 and a large delay between the radio and X-ray light curves. In the black hole X-ray binary GX 339–4, infrared emission from the jet lags X-ray emission by 100 ms (Casella et al., 2010); in another black hole system, GRS 1915+105, X-rays lead the radio by ≈ 0.1 h (Mirabel et al., 1998). Such a short time-lag ($\ll 1$ h) cannot explain the radio-loud observations (D, E, F) in SAX J1808.4–3658. A neutron star with a different ejection mechanism (e.g. the propeller mode of accretion/ejection) could potentially show a longer delay between the radio and X-ray bands (on the order of hours). Such a time delay produced by the propeller effect could be common among AMXPs, but it has so far not been detected due to the poor radio sampling of AMXP outbursts.

Still, delays of less than a day would only give a significantly different result for the last radio observation (G), such that its corresponding X-ray flux would be an order of magnitude fainter, making it radio-loud.

It could also be that the radio emission is delayed with respect to the X-ray emission by a few days. Given the sparse sampling of the radio light curve, a cross-correlation test for finding the delay between the radio and X-ray emission will not be robust for our data set. Below, we highlight two possible time delays, but a detailed quantitative analysis will require better sampled multi-wavelength light curves.

It is plausible that the radio flare of observation F could actually be produced by the X-ray reflare at MJD ~57144, with a delay of ~5 days. Such long delays have previously

been observed between the core and knots in the jet of the neutron star HMXB Cir X–1 (Fender et al., 2004b). The knots in the jets of Cir X–1, however, are resolved on 1″ scales, and are likely to be produced during an interaction with the surroundings, which we do not find evidence for in SAX J1808.4–3658 (see Section 4.4.3).

Less likely (as outflows typically follow inflows) is for the radio emission to precede the X-ray emission such that observation F and the reflare at MJD $\gtrsim$ 57152 are directly linked. However, a possible explanation for the radio preceding the X-ray emission could be a timescale for the diffusion through the magnetosphere that is longer than the ejection timescale, such that a fraction of an infalling supply of gas is ejected before its remainder penetrates the magnetosphere, as seen in the simulations of Lii et al. (2014).

The ejection of matter in the "propeller" mode

The radio emission could come from material ejected by the propeller effect, as suggested by Gaensler et al. (1999), who detected the strongest radio emission from SAX J1808.4–3658 a day after the start of the fast X-ray decay during its outburst in 1998. In the propeller mode of accretion, the magnetic pressure of the magnetosphere balances the ram pressure of the infalling matter, accelerating the inner regions of the accretion disc (Illarionov and Sunyaev, 1975). If the gas velocity exceeds the escape velocity of the neutron star, outflows are launched from the system (strong propeller). Such outflows prevent most of the disc material from accreting onto the surface of the neutron star, decreasing the radiative efficiency of the flow (Campana and Stella, 2000). However, matter may accumulate in the disc, and accrete quasi-periodically on the neutron star even in the strong propeller mode (Lii et al., 2014).

In the case of SAX J1808.4–3658, the propeller effect has been invoked as a possible mechanism behind the rapid X-ray decay during its outbursts (Gilfanov et al., 1998), the re-flares following the main outburst (Patruno et al., 2009, 2016b), and the light curve modulations seen during the main outburst (1–5 Hz; Bult and van der Klis, 2014) and reflares (1 Hz; Patruno et al., 2009). This makes it a possible candidate to explain the variable radio emission. At low luminosities, the jet would be dominated by propeller emission, and at higher luminosities it would transition to a jet similar to those of atoll sources. The dipolar and stable magnetic field of SAX J1808.4–3658 (Li et al., 1999) could play a part in the efficient ejection of matter at low accretion rates.

We develop a toy model to explore whether the strong propeller mode of accretion could account for the radio-loud epochs of SAX J1808.4–3658. Given the radio and X-ray properties of tMSPs in the accreting state, in which the propeller is thought to operate (Deller et al., 2015), we expect the kinetic and emission properties of propeller-driven jets to be similar to those of other X-ray binary jets (collimated, flat spectrum). The radio luminosity might therefore be expected to scale with the kinetic power (Heinz

and Sunyaev, 2003) according to:

$$L_{\rm radio} = L_0 \left(\frac{W_{\rm jet}}{W_0} \right)^{1.42} . \tag{4.1}$$

From approximations of the kinetic and radiative powers of the jets of three radio galaxies, Heinz and Grimm (2005) found $W_0 = 6.2 \times 10^{37}\,{\rm erg\,s^{-1}}$, with an estimated order of magnitude uncertainty, by setting $L_0 = 1.6 \times 10^{30}\,{\rm erg\,s^{-1}}$, as determined empirically from the fundamental plane of accreting black holes (Merloni et al., 2003; Falcke et al., 2004). The large uncertainties come from the difficulty of measuring the kinetic power of jets, and from the orders of magnitude difference between the radiative and kinetic energies of jets.

To estimate the kinetic energy of an outflow, we use energy conservation in the system, which is expressed as:

$$\dot{E}_{\rm pot} + \dot{E}_{\rm sd} = L_\star + L_{\rm flow} + W_{\rm jet} \,, \tag{4.2}$$

where $\dot{E}_{\rm pot}$ is the rate of gravitational potential release, $\dot{E_{\rm sd}}$ is the spin-down power supplied by the neutron star, $L_\star$ and $L_{\rm flow}$ are the radiated luminosities from the impact stream onto the surface of the neutron star and in the accretion flow, and $W_{\rm jet}$ is the kinetic energy carried by the jet. The total rate of gravitational potential energy release is given by:

$$\dot{E}_{\rm pot} = \frac{GM\dot{M}_d}{R_\star} \,, \tag{4.3}$$

where M and $R_\star$ are the mass and radius of the neutron star respectively.

To estimate the kinetic power flowing into the jet, we use the analysis of D'Angelo et al. (2015, Fig. 2) for a 2 ms accreting pulsar with a 10^8 G field, which was based on the numerical work of Ustyugova et al. (2006) and Lii et al. (2014). Their formulation for the radiative efficiency ($\mathcal{F} = (L_{\rm flow} + L_\star)/\dot{E}_{\rm pot}$) shows what fraction of the gravitational potential energy is radiated. When the accretion disc truncates below the corotation radius, all matter accretes onto the neutron star, resulting in a radiative efficiency $\mathcal{F} = 1$. At larger truncation radii (set by the magnetospheric radius), matter is redirected into jets, decreasing $\mathcal{F}$ below unity. We can estimate the radiative power of the system as:

$$\mathcal{F}\dot{E}_{\rm pot} = GM\dot{M}_d \left(\frac{1 - f_{\rm out}}{R_\star} + \frac{1}{2}\frac{f_{\rm out}}{R_{\rm in}} \right) \tag{4.4}$$

(where the factor of 1/2 is from the virial theorem), which we use to estimate the fraction of mass lost to the jet ($f_{\rm out}$). This assumes that the fraction of radiative power originating from spin-down is negligible. Indeed, we expect less than 1% of the spin-down power to be converted to X-rays (Possenti et al., 2002). To obtain a lower limit

for the kinetic power of the jet ($W_{\rm jet} = 0.5 f_{\rm out} \dot{M}_d v_{\rm jet}^2$), we assume matter is ejected at the escape velocity ($v_{\rm jet} = \sqrt{2GM/R_{\rm in}}$).

In the propeller regime, the jet draws power from the spin of the neutron star, which in turn loses rotational energy at a rate $\dot{E}_{\rm sd} = 4\pi^2 I \nu \dot{\nu}$, where I is the moment of inertia of the neutron star ($I = 10^{45}\,{\rm g\,cm^2}$). We provide an upper limit on the power of the jet by assuming a constant spin-down rate of $\dot{\nu} = 2.5 \times 10^{-14}\,{\rm Hz\,s^{-1}}$ (the upper limit found by Hartman et al., 2008 during outbursts), and that the value of W_0 is one order of magnitude lower than reported by Heinz and Grimm (2005) (who estimate an order of magnitude uncertainty on W_0). When $R_{\rm in}$ is close to the corotation radius, it is expressed as (Spruit and Taam, 1993):

$$R_{\rm in} \approx \left(\frac{\mu^2}{4\Omega \dot{M}_d} \right)^{1/5} , \tag{4.5}$$

where μ is the magnetic moment of the star ($\mu = B R_\star^2$, where B is the magnetic field strength).

The X-ray luminosity in the 1–10 keV band represents a fraction of the radiative power of the system, such that $L_{\rm X} = \eta \mathcal{F} \dot{E}_{\rm pot}$ ($\eta = 0.5$ is the bolometric correction), and the radio luminosity is given by Equation 4.1. Under these assumptions, the inner disc radius is 2.5 times the corotation radius at $L_{\rm X} = 10^{33}\,{\rm erg\,s^{-1}}$, making Equation 4.5 valid at the X-ray luminosities sampled here ($L_{\rm X} = 10^{34} - 10^{37}\,{\rm erg\,s^{-1}}$). Fig. 4.7 (bottom) shows the results of our model. We find that the radio luminosity estimate from the spin-down of the neutron star is compatible with the values derived using the analysis of D'Angelo et al. (2015). The empirical upper limit on the spin-down rate during the outbursts of SAX J1808.4–3658 ($\dot{\nu} < 2.5 \times 10^{-14}\,{\rm Hz\,s^{-1}}$; Hartman et al., 2008) is also compatible with the maximum spin-down rate in the above model ($\dot{\nu} = 1.7 \times 10^{-14}\,{\rm Hz\,s^{-1}}$). We find, however, that the radio luminosity predicted by our model is at least one order of magnitude too low for it to account for the behaviour of SAX J1808.4–3658, making it unlikely that the propeller effect is solely responsible for its radio-bright jet. This discrepancy might be explained by a large fraction of the gravitational potential energy being directed to the jet, or by the poorly known scaling between the power of the jet and radio luminosity, especially in the case of the propeller regime. In addition, simulations show that two kinds of outflows are driven as a consequence of the strong propeller: a slow, matter-dominated disc wind, and a collimated magnetically-dominated Poynting jet (Ustyugova et al., 2006; Romanova et al., 2009; Lii et al., 2014). In contrast, our model assumes a jet typical of X-ray binaries, which are often considered to be energetically equipartitioned (not magnetically dominated). Moreover, some X-ray emission is likely to originate at the magnetosphere–disc interface, and the flow is thought to be less radiatively efficient (Papitto and Torres, 2015).

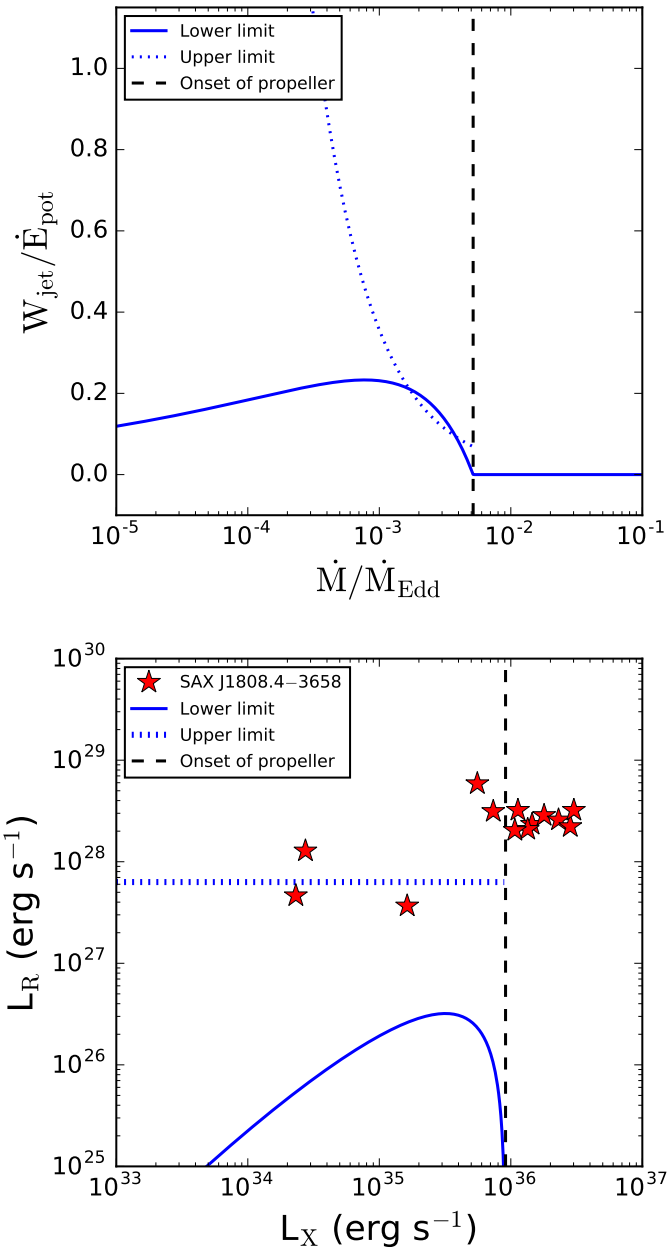

Figure 4.7: *Top*: Ratio between jet power and gravitational potential energy release, given as a lower limit (continuous line) and upper limit (dotted line). *Bottom*: Radio emission from the strong propeller for our toy model, using the analysis of D'Angelo et al., 2015 (as a lower limit), and using the upper limit on spin-down energy (as an upper limit). The jet of SAX J1808.4–3658 is unlikely to be caused by a propeller effect described by our model.

To provide more rigorous tests of the connection between propeller outflows and radio luminosity, additional simultaneous radio and X-ray observations of propeller-mode sources are necessary. Focusing on luminosities at which the strong propeller is thought to switch on will assist in quantifying the differences between standard X-ray binary jets and propeller jets. To robustly determine whether propeller outflows are responsible for strong radio emission, an empirical characterisation of the connection between the kinetic and radiative signatures of propeller-mode systems is required. Hydrodynamical simulations would be needed to fully explain the observed emission in tMSPs, the radio-loud and radio-faint AMXPs.

4.4.4 IGR J00291+5934

For the first time, we report a radio–X-ray correlation index β for a neutron star low-mass X-ray binary in the range $L_X \approx 10^{34}$ to 10^{36} erg s^{-1}, using the detections of IGR J00291+5934. In contrast to SAX J1808.4–3658, IGR J00291+5934 shows correlated decay in the two bands. A correlation slope $\beta = 0.77 \pm 0.18$ in IGR J00291+5934, indicates radiatively inefficient accretion, albeit with weaker radio emission than tMSPs. Different radio–X-ray normalizations have previously been observed between non-pulsating neutron stars (Tetarenko et al., 2016a), and a similar behaviour could occur in pulsating neutron stars.

The correlation index is different than measured over the limited $L_X \approx 10^{36}$ to 10^{37} erg s^{-1} range for the atoll sources in the hard state (Migliari and Fender, 2006; Tetarenko et al., 2016a). This does not, however, preclude IGR J00291+5934 and some atoll sources from sharing similar radiatively inefficient emission mechanisms, especially since IGR J00291+5934 has a similar radio–X-ray normalization to the atolls 4U 1728–34 and Aql X–1.

The presence of reflares in SAX J1808.4–3658 and lack thereof in IGR J00291+5934 (e.g. Hartman et al., 2011) highlights additional differences between the two sources. However, as SAX J1808.4–3658 and IGR J00291+5934 are the only two neutron stars with radio coverage in the range $L_X \approx 10^{34}$ to 10^{36} erg s^{-1}, no firm conclusion can be drawn as to the causes of their different behaviour. As such differences may only become apparent at low luminosities, deep, high-cadence, multi-wavelength observations such as these, will be necessary in the future.

4.5 Conclusions

For the first time, multi-wavelength observations of SAX J1808.4–3658 and IGR J00291+5934 have allowed us to study the inflow/outflow coupling within individual neutron stars in the $L_X \approx 10^{34}$–10^{36} erg s^{-1} range. We find that SAX J1808.4–3658 is strongly radio-

variable and that it does not follow an obvious L_R–L_X relationship, although at the peak of the outburst it has similar radio and X-ray luminosities as other neutron stars. A combination of factors, such as sparse sampling during the reflares, a long time delay, and strong ejections driven by a propeller, are probably responsible for its behaviour. IGR J00291+5934, on the other hand, has a more well-defined radio–X-ray correlation, with $\beta = 0.77 \pm 0.18$. We do not detect IGR J17511–3057, but we place stringent limits on its radio emission. The outburst detections and quiescent non-detection of Cen X–4 are compatible with the radio and X-ray luminosities of other atoll sources. Overall, neutron stars are always at least a factor of five fainter than the radiatively inefficient black hole track (Gallo et al., 2014).

Such varied behaviour across neutron star classes (and even within AMXPs) could be due to the jet launching mechanism, as impacted by the magnetic field and spin of the neutron star. At high X-ray luminosities, where the disc truncates below the corotation radius, there is evidence of different normalizations for each system (Tetarenko et al., 2016a). As the mass accretion rate decreases, some systems might enter a strong propeller mode, where matter is ejected more efficiently, increasing the radio flux, possibly contributing to the different correlations seen below $L_X \lesssim 10^{36}$ erg s^{-1}. It is possible, however, that even without the effects of the propeller mode, neutron stars do not follow a unique radio–X-ray relationship and each system might have a unique behaviour, as suggested by Gallo et al. (2014) for black holes.

The varied behaviour of neutron stars at low X-ray luminosities ($L_X \lesssim 0.01\ L_{Edd}$) is in contrast to black holes, which seem to all settle on a similar radiatively-inefficient track. This emphasises the need to accumulate more data on neutron stars, rather than black holes, since there seem to be several classes of neutron stars. The difficulty of carrying out these observations due to radio faintness, however, could be addressed by the upcoming next-generation radio interferometers, such as MeerKAT (Jonas, 2009) and SKA (Dewdney et al., 2009).

We propose that during its next outburst, SAX J1808.4–3658 should be monitored approximately twice daily for about three weeks in the X-ray and radio bands. Such dense sampling during the fast X-ray decay and reflares is essential for tracking the disc–jet coupling in the propeller regime, measuring a radio/X-ray time lag, quantifying the differences in the radio spectra at low and high radio luminosities, and ultimately identifying the mechanism behind the radio emission. Even without a radio detection, Cen X–4 remains a good candidate for future campaigns for testing whether any non-pulsating neutron stars produce jets at the faintest X-ray luminosities ($L_X \approx 10^{32}$ erg s^{-1}).

Chapter 5

HST spectrum and timing of the ultra-compact X-ray binary candidate 47 Tuc X9

Adapted from:

> **V. Tudor**, J. C. A. Miller-Jones, C. Knigge, T. J. Maccarone, T. M. Tauris, A. Bahramian, L. Chomiuk, C. O. Heinke, G. R. Sivakoff, J. Strader, R. M. Plotkin, R. Soria, M. D. Albrow, G. E. Anderson, M. van den Berg, F. Bernardini, S. Bogdanov, C. T. Britt, D. M. Russell, D. R. Zurek; *Monthly Notices of the Royal Astronomical Society, 476, 1889 (2018)*

The content of this chapter is my own work, excepting the following. The FUV spectrum was provided by C. Knigge, along with the optical/FUV timing analysis, writing its corresponding sections (Sections 5.1.3 and 5.2.3), and making Figures 5.3 and 5.4. The sections detailing the interpretation of the X-ray spectrum (Section 5.3.6), and the estimated rate of bright black hole ultracompact X-ray binaries (second half of Section 5.3.9) were written by T. Maccarone. The binary simulation (first half of Section 5.3.9) was run by T. Tauris, along with making Figures 5.12 and 5.13. The X-ray data plotted in Figure 5.9 were provided by A. Bahramian, and the optical/X-ray data for V404 Cyg and Cen X–4 were provided by F. Bernardini and D. M. Russell.

In this chapter, we investigate the optical spectral properties of the first black hole candidate identified in the ATCA MAVERIC survey. The source, X9, is located in the massive globular cluster 47 Tucanae ($M = (6.5 \pm 0.5) \times 10^5\,M_\odot$; Kimmig et al., 2015) located at a distance of 4.53 ± 0.08 kpc (Bogdanov et al., 2016), with foreground reddening $E(B-V) = 0.04 \pm 0.02$ (Salaris et al., 2007), and is also the first Galactic candidate for an ultracompact system with a black hole accretor (Miller-Jones et al., 2015). Originally proposed to be a cataclysmic variable (Paresce et al., 1992; Grindlay et al., 2001a), X9 has recently been found to be a source of strong radio emission (relative to the X-ray luminosity), making it a black hole candidate (Miller-Jones et al., 2015). Its relatively high X-ray luminosity ($L_{0.5-10\,\mathrm{keV}} \approx 10^{33} - 10^{34}\,\mathrm{erg\,s^{-1}}$), broadband FUV–optical–infrared spectrum, and C IV emission lines (Knigge et al., 2008) suggested a degenerate donor (Miller-Jones et al., 2015). There is some evidence from narrowband *Hubble Space Telescope* (*HST*) colours for weak H α emission with $-\mathrm{EW} \approx 10$ Å, but both the presence of H α emission and its exact EW depend strongly on the model assumed for the underlying continuum (Miller-Jones et al., 2015). Based on X-ray timing and spectroscopy, Bahramian et al. (2017) suggested a short orbital period ($P_\mathrm{orb} = 28.2$ min), and identified oxygen lines (<1 keV, similar to the neutron star ultracompact 4U 1626–67; Krauss et al., 2007) that support the presence of a C/O white dwarf donor. The previous suggestions of periodicities (of low significance) in photometric studies with *HST* ($P_\mathrm{orb} \approx 6$ hours; Paresce et al., 1992, or ≈ 3.5 hours; Edmonds et al., 2003) are likely to be spurious (Bahramian et al., 2017). Bahramian et al. (2017) concluded that 47 Tuc X9 might be more likely to host a black hole accretor, on account of its radio and X-ray behaviour, although we stress that the nature of the accreting object is still unknown.

5.1 Observations & Data analysis

5.1.1 Spectroscopy

We observed X9 with STIS on 16 June 2016, using the CCD detector and the $52'' \times 0.1''$ E1 slit position. The program (GO–14203, PI: J.C.A. Miller-Jones) was allocated a total of four orbits, acquiring a total of five and six (for cosmic-ray rejection) low-resolution spectra ($R \sim 500$) with the G430L (spectral range 2900–5700 Å, dispersion $\Delta\lambda = 2.73$ Å pixel^{-1}) and G750L (5240–10270 Å, $\Delta\lambda = 4.92$ Å pixel^{-1}) gratings, respectively. The observations were not dithered. After each of the G750L observations, we observed fringe flats to improve the removal of fringes (caused by interference between incident and reflected beams in the CCD) on the redward side of the spectra (Malumuth et al., 2003). A summary of the science observations is provided in Table 5.1.

We retrieved the calibrated 2-D spectra from the Mikulski Archive for Space Tele-

Table 5.1: Summary of *HST* / *STIS* observations on 16 June 2016, using the 52″×0.1″E1 slit.

Gratings	Dataset	Start (UT)	Exp (s)
G430L	OCXP02010	06:56	2×661
G430L	OCXP02020	07:42	3×1052
G750L	OCXP02030	09:17	3×1078
G750L	OCXP02050	10:52	3×1051

scopes (MAST). These data frames were reduced with the *STIS* pipeline (CALSTIS v3.4), using the calibration files closest in time to the science observations. We processed these spectra using the recommended PyRAF (v2.1.14; Tody, 1993) and Space Telescope Science Data Analysis System (STSDAS v3.17) tools. We recalibrated the wavelength solution using the GO-wavecal exposures, removed the fringes on each of the G750L spectra above 6000 Å using their associated flat files, and merged the individual spectra of each grating into a G430L stack and a G750L stack. We extracted the two stacked spectra using the task `x1d`, adopting a three pixel aperture (corresponding to 0.15″). We subtracted the background using two emission-free regions adjacent to X9. We smoothed the background in these two regions using a median boxcar filter with a 9 pixel window. We inferred the sky values at the position of X9 by taking the mean of the two background regions, and we fitted the resulting sky spectrum with a fourth order polynomial (as a function of wavelength).

The extracted spectrum still contains a relatively high number of outliers, which can be distinguished from line emission or absorption because their point spread function is undersampled. The presence of such data points can be explained as hot and cold pixels that could not be removed when stacking individual spectra because the observations have not been dithered. Since these deviant points have not been flagged by the `x1d` task as being of poor data quality, we need to remove them using a different strategy. First, we created a smooth, low-resolution spectrum from the extracted 1D spectrum by convolving it with a Gaussian with FWHM = 7 pixels. We removed from the original spectrum those data points that deviated by more than 4 standard deviations from the smoothed spectrum. Less than 1% of the data were removed in this process, and we manually checked that no emission or absorption lines found in typical X-ray binaries were removed. This edited version of the original spectrum (with full resolution) was used in subsequent analysis.

5.1.2 Calibration checks

To verify the quality of the calibration, we used the spectrum of a star within 0.5 pixels of the centre of the slit near X9 (J002404.30–720457.7, 0.4″ NE of X9), which we

extracted with a similar procedure as for X9 using the same sky regions.

To find the spectral class of the check star, we used BT-Settl model grids of theoretical spectra (Allard et al., 2012) with surface gravity $\log g = 4.5$, overall metal abundance [M/H] = –0.5 and [M/H] = –1.0, and reddening $E(B-V) = 0.04$. We convolved these with the spectral resolution of *STIS*. We searched for the spectral template that best fit the observed spectrum by using a χ^2 minimization approach that left the flux normalisation and radial velocity as free parameters. For each model spectrum, we formed a grid of possible radial velocities (from –300 to 300 km s^{-1} in steps of 50 km s^{-1}; 47 Tuc has a heliocentric radial velocity of –18 km s^{-1} and a central velocity dispersion of 11 km s^{-1}, Harris, 1996).

We found the best-matching template for the check star was a $T = 6{,}600$ K, $M \approx 0.6\,M_\odot$ dwarf. The 3,000–8,500 Å flux of such a star is consistent with the measured flux in our spectrum, thus confirming that flux calibration has been correctly performed. The spectrum at wavelengths longer than ≈ 8,500 Å was systematically brighter than indicated by the spectral template (where the background dominates), so we ignored this part of our spectra in the remaining analysis of the check star and X9. A comparison of the observed check star spectrum to the template in the 3,000–8,500 Å range (which covers the G430L and G750L gratings) results in $\chi^2_\nu = 4.8$, indicating that the error bars produced by CALSTIS are underestimated by a factor $k \approx \sqrt{\chi^2_\nu} \approx 2.2$. The required rescaling is similar for G430L and G750L. The spectral template might be a poor match for the star, so we take the value of $k = 2.2$ as an upper limit to the rescaling factor. As another method of estimating the rescaling factor, we also fit power-law functions to line-free spectral regions (from visually inspecting the observed and template spectra): 4,600–4,800 Å on G430L, and 6,700–8,500 Å on G750L. For G430L, we find $k = 1.5$, and for G750L, $k = 1.9$. We chose to rescale the error bars by these factors. After rescaling, we measure the equivalent width of the H α line in absorption, and its radial velocity, for this check star. We find $\mathrm{EW}_{\mathrm{H}\,\alpha} = 3 \pm 1$ Å, and a radial velocity $V_\mathrm{r} = 210 \pm 150$ km s^{-1}. We estimate a radial velocity shift of up to 100 km s^{-1} in this check star owing to its misaligned position in the slit, which might explain the large radial velocity estimate. The spectrum of this star, with rescaled error bars, and the contribution of each point to χ^2, are shown in Figure 5.1. Apart from the spectral region around the Ca II H and K lines, between 3,900 and 4,000 Å, the observed and template spectra match well. The high χ^2 value can therefore be attributed to a general underestimate of the error bars, and hence the method described above remains valid.

5.1.3 Timing analysis

To investigate the orbital ($P \approx 28$ min) and superorbital ($P \approx 7$ days) modulations found in the X-ray band (Bahramian et al., 2017), we performed timing analyses on

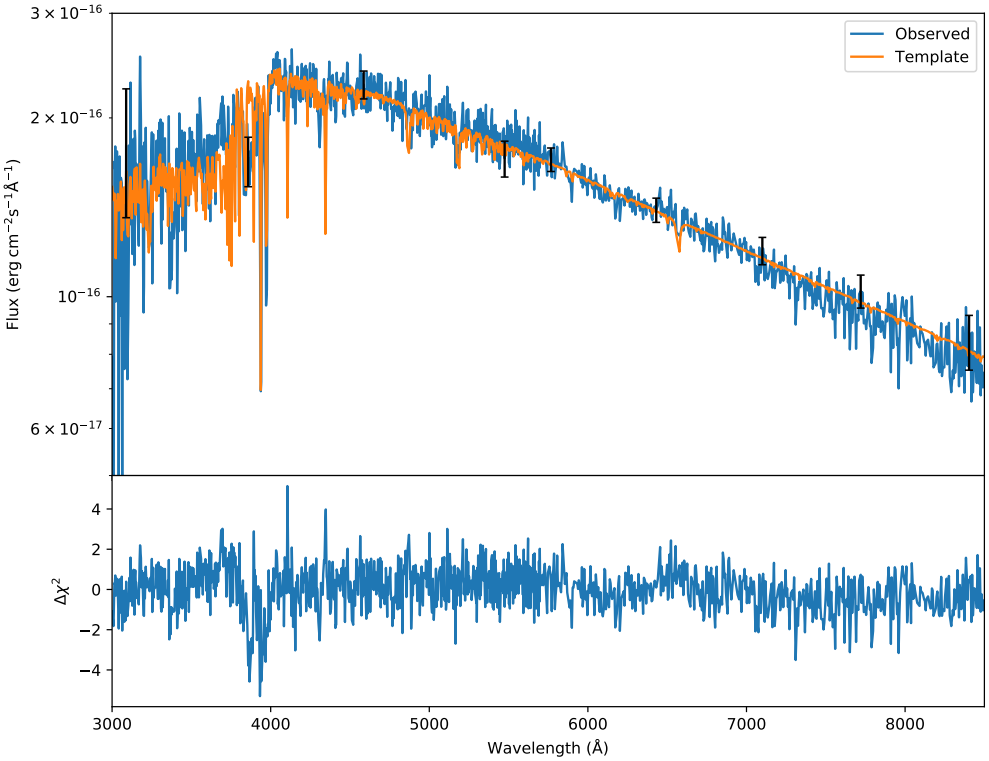

Figure 5.1: *Top*: The observed and template spectra for the check star. We show only some of the error bars for clarity. *Bottom*: The contribution to χ^2 for each point in the spectrum.

archival FUV and optical *HST* observations of 47 Tuc, previously reported by Knigge et al. (2008), Gilliland et al. (2000) and Albrow et al. (2001).

The FUV data, taken as part of a campaign to study exotic objects in 47 Tuc, were taken with the FUV-MAMA detector on the *STIS* spectrograph (program GO–8279). The observations were composed of six distinct epochs, with the first occurring almost a year before the other five. We only included the spectroscopic data (there are only two photometric data points per epoch), which was performed in slitless mode, and we summed the entire flux in the spectrum of X9 in each exposure. We analysed the entire data set jointly, which favours the detection of highly coherent signals. Importantly, the exposure times were typically 600s, approximately one-third of the $\approx$ 28 min orbital period seen in the X-rays. This will smooth out the amplitude and significance of any signal at such a short period.

The optical data, taken with the F555W and F814W filters of the Wide Field Planetary Camera 2, were obtained over a period of 8.3 days, using 160 s exposures (program GO–8267). We reanalysed the differential time series photometry reported by Albrow et al. (2001), who refer to X9 as PC1-V47, which they classify as a variable with a 6.39 day period.

Time conversion to Barycentric Julian Dates in the Barycentric Dynamical Time standard was done using the online calculator from Eastman et al. (2010). To search for

significant periodicities in the FUV and optical datasets, we used the Generalised Lomb-Scargle algorithm (Zechmeister and Kürster, 2009), as implemented in AstroML (which accounts for heteroscedastic errors; Vanderplas et al., 2012). We evaluated the statistical significance via randomization (i.e. keeping the magnitudes of each measurement, and shuffling their observation times); errors on the period were estimated via bootstrapping (i.e. selecting random samples from the original dataset). In both cases, 10,000 fake data sets were used. In analysing the optical data, we allowed for a $\sigma_m = 0.085$ magnitude intrinsic dispersion (accounting for source variability), which brings $\chi^2_\nu \approx 1$ for a sine wave fit to the folded light curve (with the period fixed to the most significant peak in the power spectrum).

5.2 Results

5.2.1 Continuum

The optical spectrum of X9 is featureless and blue (Figure 5.2), with the colour $(B - R) = 0.3$ (Vega magnitudes; obtained by convolving the spectrum through *HST* filter throughput curves[1]) and $F_\nu \propto \nu^{-0.2}$ ($F_\lambda \propto \lambda^{-1.8}$; obtained by fitting a reddened power-law over the 3,000 to 8,500 Å range). The blue colour of the source, determined from broadband data, has previously been reported in the literature (Paresce et al., 1992; Knigge et al., 2008), and we measure the same $(B - R)$ value as Miller-Jones et al. (2015) from quasi-simultaneous photometric measurements taken in 2002.

5.2.2 Line significance

No strong lines can be readily identified in the 3,000–8,500 Å spectrum of the optical counterpart of X9. We measure the colour $(H\,\alpha - B) = -0.3$ (Vega magnitudes; obtained by convolving the spectrum through *HST* filter throughput curves), which is similar to that reported by Miller-Jones et al. (2015). We have estimated the upper limits on the strongest H and He lines seen in typical X-ray binaries (Shahbaz et al., 1996), and also on the C/N/O lines/complexes of other ultracompacts that have been reported by Nelemans et al. (2004a) to have emission $-\mathrm{EW} > 3$ Å. To estimate these upper limits, we first use a power-law model, `redden` × `pow` in XSPEC (v12.9.1; Arnaud, 1996) to fit the continuum in a $4 \times \mathrm{FWHM_{C\,IV}}$ ($\mathrm{FWHM_{C\,IV}} = 3600\,\mathrm{km\,s^{-1}}$; see Section 5.3.5) window centred on a given wavelength (the central wavelengths are listed in Table 5.2), ignoring the central $1.09 \times \mathrm{FWHM_{C\,IV}}$ (corresponding to 80% of a Gaussian line emission) to avoid line emission. Secondly, we re-add to the data set the previously ignored central window, and add to the model a Gaussian component (`agauss`) centred on the given

[1] http://www.stsci.edu/hst/acs/analysis/throughputs

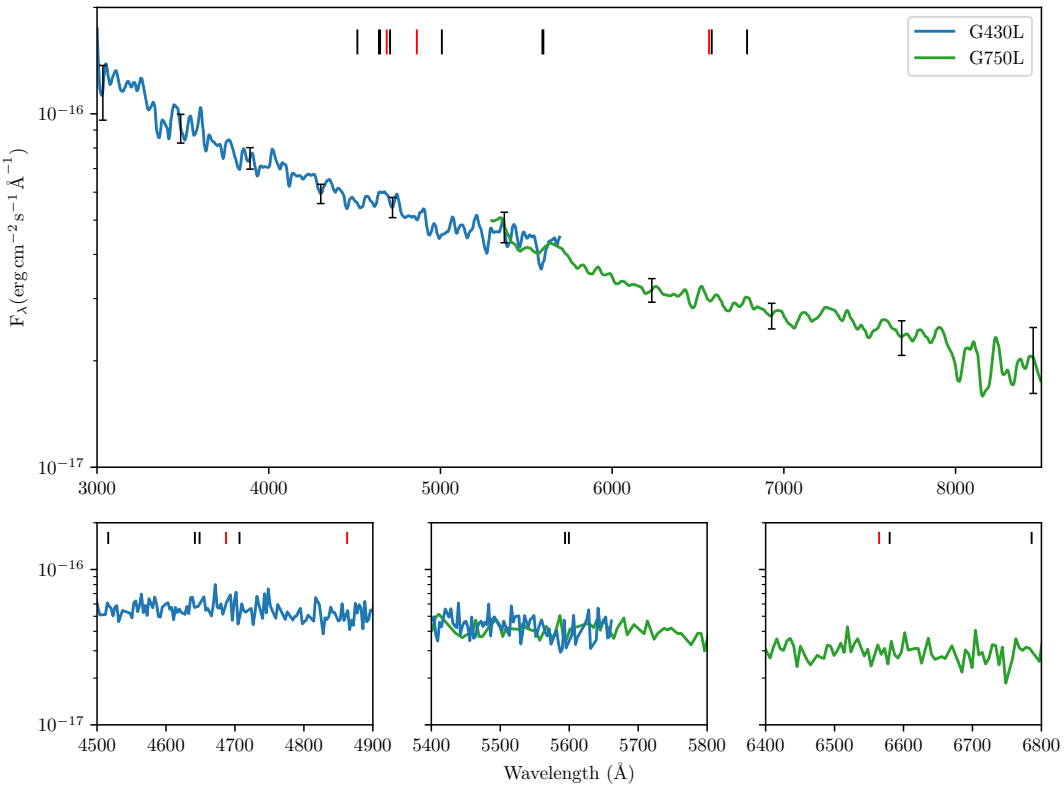

Figure 5.2: *Top*: Smoothed optical spectrum of X9 (convolved with a Gaussian with FWHM = 7 pixels). We show only some of the error bars for clarity. *Bottom:* Zoomed-in regions of the non-smoothed spectrum. The vertical ticks above the spectrum indicate the wavelengths of the H α λ6564, H β λ4862 and He II λ4687 lines (red ticks) typical of ordinary X-ray binaries, and the brightest C/N/O emission features (black ticks) in ultracompact systems (with emission $-$EW $>$ 3 Å in at least one of the three systems studied by Nelemans et al., 2004a), which may be expected in X9. No obvious emission lines are visible. The upper limits on the EW (in emission and absorption) for these lines are listed in Table 5.2.

Table 5.2: Limits for the EWs of selected lines, assuming a FWHM = 3600 km s^{-1}

Species	Line[a] (Å)	EW[b] (absorption, Å)	−EW[b] (emission, Å)
He II	4687	2.5	8.8
H β	4862	5.9	6.4
H α	6564	8.5	13.7
N III	4516	7.8	3.7
N III[c]	4641	4.6	6.9
C III[c]	4648	3.7	8.7
O II	4706	4.0	7.8
[O III]	5008	12.0	1.2
O III	5593	12.3	8.0
O V	5599	11.3	9.2
C II	6579	8.7	13.4
C II	6785	8.3	17.9

Notes.
[a] Vacuum wavelengths
[b] 3σ limits
[c] Strongest lines in Bowen blend

wavelength, with FWHM = 3600 km s^{-1}. We fit the line model by fixing the continuum level, line FWHM, and central wavelength, and letting only the normalisation of the Gaussian (the total line flux) be free to vary. Using the `error` task, we take the upper limit for the line flux to correspond to $\Delta\chi^2 = 9.0$ (3σ). The equivalent width of the Gaussian component is measured with the `eqwidth` task. No significant line emission was found. Line upper limits are reported in Table 5.2. The central wavelength of a line could be offset from the assumed position by less than 1 px. The absolute wavelength calibration for STIS is accurate to within 0.2 px (Woodgate et al., 1998), and the central velocity dispersion of 47 Tuc is 11 km s^{-1}, or < 0.1 px (Harris, 1996). Any line offset from the assumed centres should therefore have minimal impact on the reported EW upper limits. The FWHM of an optical line, however, could be lower than that of the C IV line. Repeating the fitting procedure by letting the FWHM free to vary between the spectral resolution of the instrument and the C IV FWHM (3600 km s^{-1}), we derive similar upper limits (within 10%). This demonstrates the robustness of the EW upper limits presented in Table 5.2.

5.2.3 Timing

Optical

We detect the seven-day period (0.14 cycles day^{-1}) from Bahramian et al. (2017) with very high significance in both V and I bands (Figure 5.3). The bootstrap simulations show the period estimate is fully consistent with the X-ray-based one. The optical

data spans just over one cycle of this period, so, taken alone, its persistence would be questionable. However, coupled with its detection in the X-ray band at different epochs, we consider this superorbital period to be real and stable. The semi-amplitude of the signal is ≈ 0.05 mag (i.e. about 5% of flux). Thus, in the optical band, this seven-day modulation has an amplitude two orders of magnitude smaller than the corresponding X-ray signal (which has a semi-amplitude of a factor of about three).

Unfortunately, due to the long stretch of time between the optical observations (July 1999) and the X-ray observations when the superorbital phase was well known (Jan 2006; Bahramian et al., 2017), we cannot determine if the optical and X-ray modulations vary in phase with each other.

We also detect significant peaks at ≈ 15 and ≈ 30 cycles day^{-1}. The former are most likely associated with *HST*'s orbit (≈ 96 min), and the latter are probably associated with its first harmonic. The signal that Edmonds et al. (2003) tentatively mentioned in their paper corresponds to the peak near 6 cycles day^{-1} (i.e. ≈ 4 hours). However, this has low significance (false alarm probability $p > 0.1$) in the V-band power spectrum and is almost absent in the I-band data. In addition, we do not find evidence for power around 28.2 min in either band. The 3σ upper limits (in the V and I bands) for this signal have semi-amplitudes of < 0.025 mag (2% of the flux). No signal at half that period (as expected for ellipsoidal variations) is detected either.

FUV

The strongest peak in the FUV power spectrum occurs at a frequency of 53 cycles day^{-1}, i.e. 27.2 min (false alarm probability $p < 0.05$; Figure 5.4). The second strongest peak in the power spectrum (28 cycles day^{-1}) may not be caused by any aliases of the orbital period of X9 or of *HST*. It is possible that this weaker signal is partly responsible for the flickering observed in individual FUV epochs, and may be drowning out the orbital signal of X9. The light curve phased on the 27.2 min period shows a smooth varying signal (similar to the orbital modulation in X-rays), with a semi-amplitude of about 5%. We consider this a lower limit, since the long exposure times imply that a significant part of the true signal in each exposure has been averaged. All individual epochs show the same signal in the folded light curve, showing the detected periodicity cannot be associated with variability between the epochs. If the FUV signal is real, the discrepancy between the FUV and X-ray periods is significant. Of the 10,000 bootstrap simulations, only $\approx 0.1\%$ return a peak frequency in the range 28.18 ± 0.02 min, determined from X-ray observations. Even though this 27.2 min signal is only significant at the 2σ level, we further investigate it in subsequent discussions (Sections 5.3.7, 5.3.8) due to its proximity to the X-ray signal.

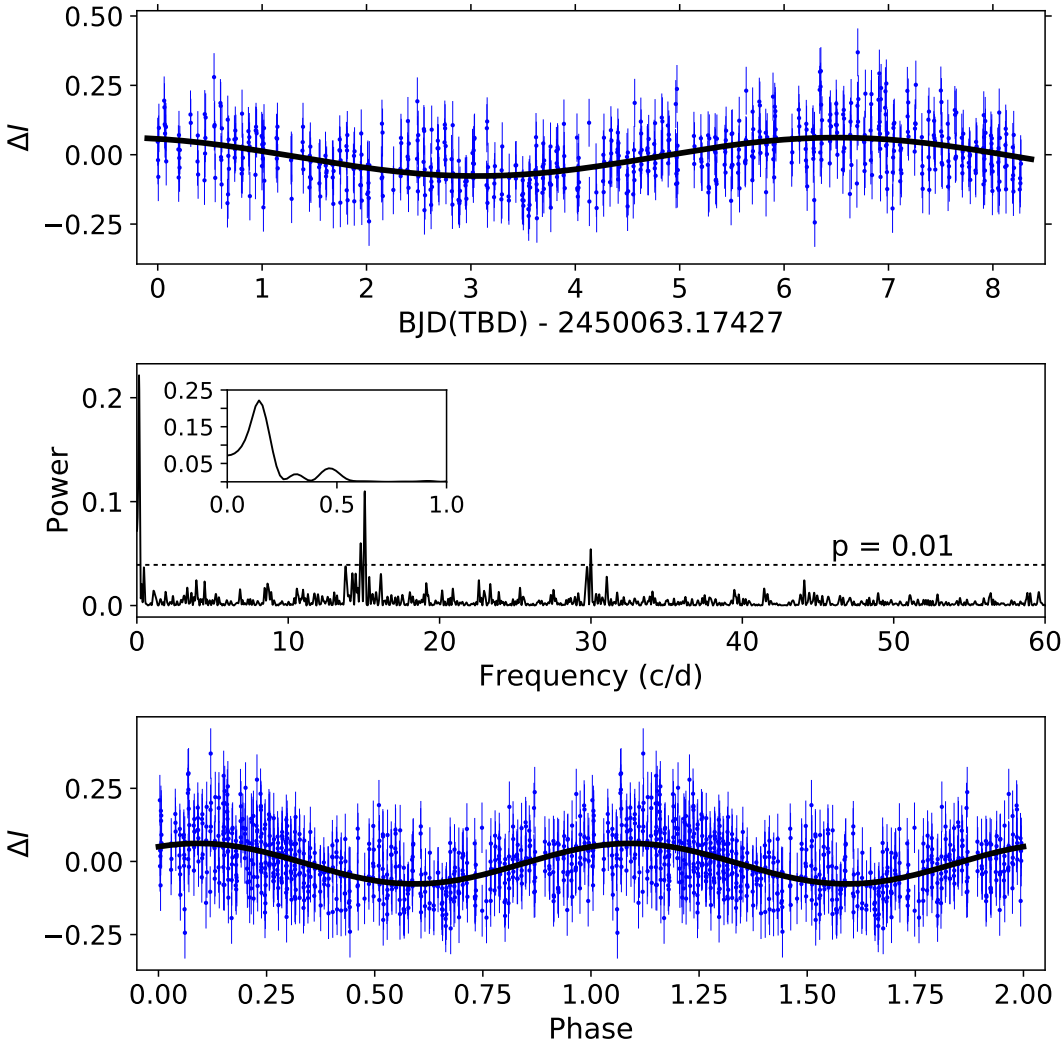

Figure 5.3: Timing analysis on the I-band data of Gilliland et al. (2000). *Top:* normalised light curve showing the sine-wave signal (black curve) retrieved from the power spectrum and folded light curve. *Middle:* power spectrum (horizontal dotted line indicating the false alarm probability $p = 0.01$). The most significant peak ($P = 0.14$ cycles day^{-1} = 7.1 days) coincides with the superorbital period reported by Bahramian et al. (2017), while the peaks at ≈ 15 and ≈ 30 cycles day^{-1} are likely to be associated with the orbital period of the HST and its first harmonic. No orbital modulation ($P = 51$ cycles day^{-1}) is detected in this dataset. *Bottom:* the light curve folded on the most significant period, revealing a superorbital modulation with a semi-amplitude of 5%. The timing analysis on the V-band data gives similar results.

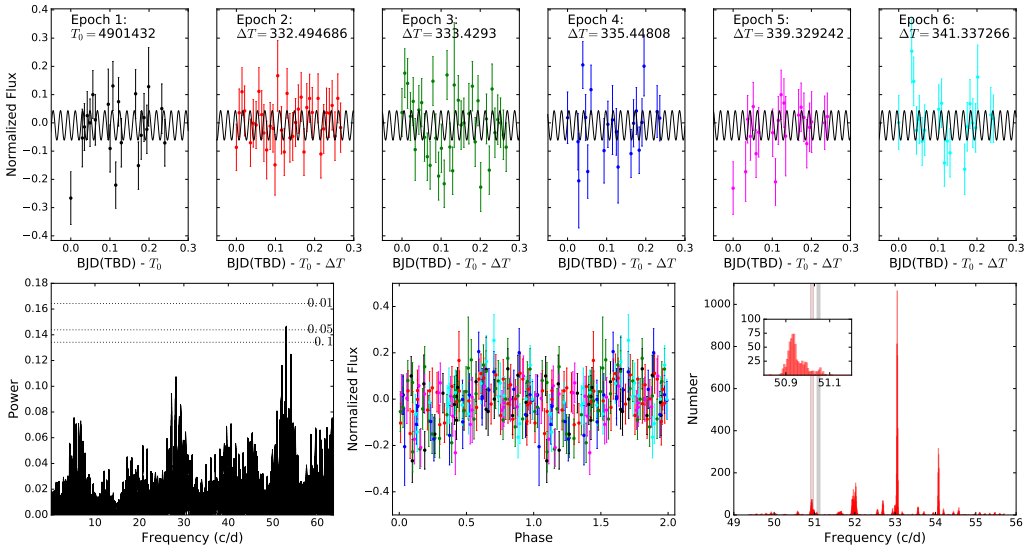

Figure 5.4: Timing analysis on the FUV data of Knigge et al. (2008). *Top:* normalized light curves for the individual epochs; the associated error bars have been increased by $\sigma_{\rm m} = 0.085$ to account for source flickering. The parameters of the shown sine-wave curve (black) are those found through the power spectrum and folded light curve. *Bottom left:* power spectrum (horizontal dotted lines indicating false-alarm probabilities, the strongest signal just exceeds the 2σ level); *bottom middle:* folded light curve (on the most significant period – 27.2 min, with a semi-amplitude of $\approx 5\%$), with different epochs shown in the same colors as in the top panel; *bottom right:* the result of the bootstrapping simulations, showing what periods are plausible, highlighting (gray region) the suggested orbital period based on X-ray data (28.18 ± 0.02 min; Bahramian et al., 2017). The period measured from the FUV data (53 cycles day^{-1}; 27.2 min) is close to, but not statistically consistent with the X-ray period.

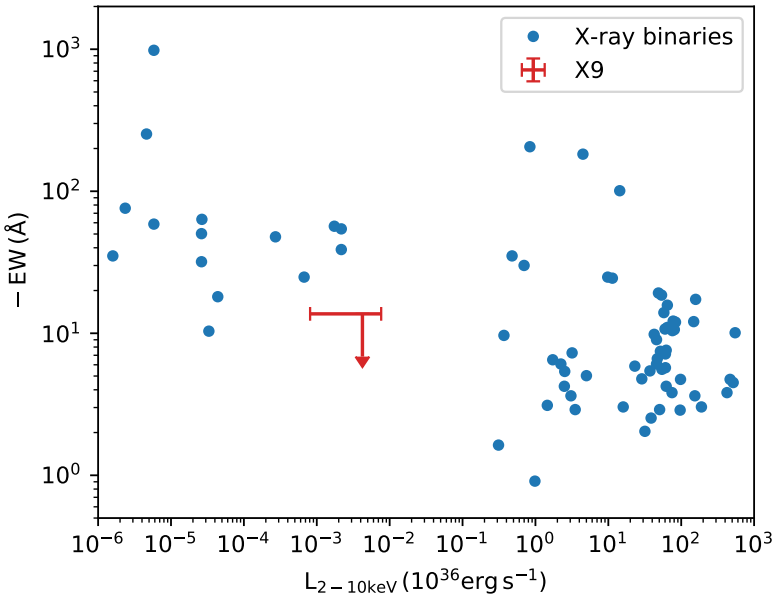

Figure 5.5: The empirical relationship between the H α EW and X-ray luminosity for X-ray binaries (including black holes and neutron stars) from Fender et al. (2009). The upper limit on the H α emission in X9 is lower than the emission seen from typical X-ray binaries at a similar X-ray luminosity, as expected for a H-poor donor.

5.3 Discussion

5.3.1 Comparison with other systems

H α EW vs X-ray luminosity

The trend between the EW of the H α line in emission and the X-ray luminosity of X-ray binaries reported by Fender et al. (2009) can be used to estimate the expected EW of the H α line for X9. Taking into account the X-ray variability of X9 ($L_X = 10^{33} - 10^{34}$ erg s^{-1}; Bahramian et al., 2017), we would expect $-\mathrm{EW}_{\mathrm{H}\,\alpha} \sim 50$ Å (Figure 5.5). However, we found $-\mathrm{EW}_{\mathrm{H}\,\alpha} < 14$ Å (3σ upper limit). The large scatter ($\gtrsim 1$ dex) of $\mathrm{EW}_{\mathrm{H}\,\alpha}$ measurements for a given L_X in the well-sampled $L_X = 10^{30} - 10^{32}$ erg s^{-1} and $L_X = 10^{35} - 10^{39}$ erg s^{-1} ranges suggests a similar scatter may be expected in the range $L_X = 10^{32} - 10^{34}$ erg s^{-1} (which only contains five $\mathrm{EW}_{\mathrm{H}\,\alpha}$ measurements). In addition, the Fender et al. (2009) sample contains sources that are quiescent or decaying from the peak of the outburst, in which the H α emission is produced by residual discs. With its persistently high X-ray luminosity, X9 is dissimilar to this sample. Still, our upper limit on the H α line strengthens the case for a H-deficient system, and thus for a C/O white dwarf donor.

Optical spectral index

We compare the optical spectrum of X9 with the spectra of other ultracompact candidates: 4U 0614+091, XTE J0929–314, 4U 1626–67, XB 1916–05 (Nelemans et al., 2006), 2S 0918–549 and 4U 1543–624 (Nelemans et al., 2004a). The spectral indices ($F_\nu \propto \nu^\alpha$) in these sources are $\alpha = -1$ to 0. For X9, we measure a similarly blue continuum, with $\alpha = -0.2$. Most emission lines in these systems are faint ($-\mathrm{EW} < 10$ Å). In particular, the strongest emission line in the optical spectrum of 2S 0918–549 is C II λ6785 with $-\mathrm{EW} \approx 4$ Å), indicating that a lack of bright optical emission lines ($-\mathrm{EW} \gtrsim 10$ Å) in ultracompact X-ray binaries may be a common occurrence. In 4U 0614+091, however, the C III feature at $\lambda \approx 4648$ Å has $-\mathrm{EW} \approx 10$ Å, which, if present, would have been marginally detected in X9.

5.3.2 Nature of donor

The lack of H and He in the optical spectrum reported in this chapter, coupled with the C IV $\lambda\lambda$1548, 1550 emission and lack of He II λ1640 in the FUV spectrum (Knigge et al., 2008), and the detection of oxygen features in the soft X-ray spectra (Bahramian et al., 2017), indicate the donor is likely a C/O white dwarf.

In Figure 5.6 we show the mass-radius relationship for degenerate stars of C and O composition based on the equation of state derived by Deloye and Bildsten (2003), together with the mass-radius relationship for a Roche-lobe-filling companion to both a neutron star and black hole, using the Eggleton (1983) relation. A $M_2 \approx 0.01\,M_\odot$ C/O white dwarf donor in an X-ray binary is likely to have a core temperature in the range $T_{\rm core} = 10^5 - 10^6$ K (Bildsten, 2002; Nelson and Rappaport, 2003). For an orbital period of 28.2 minutes, the mass and radius of a C/O white dwarf are likely to lie between $M_2 = 0.010\,M_\odot$, $R_2 = 0.032\,R_\odot$ (for a cool, $T_{\rm core} = 10^4\,K$ O white dwarf), and $M_2 = 0.016\,M_\odot$, $R_2 = 0.037\,R_\odot$ (for a hot, $T_{\rm core} = 3 \times 10^6\,K$ white dwarf), with a weak dependence on the mass of the primary (for $M_2 \ll M_1$ and a given orbital period, the density of the secondary is approximately constant; Eggleton, 1983). The Roche lobe of the secondary can accommodate a smaller and lighter donor if it contains a significant presence of Ne or Mg.

Since we do not see evidence of emission from the surface of the donor (no absorption lines, and X9 flickers across all wavelengths), we can also estimate the upper limit on the effective temperature of the white dwarf donor when we know its size. For this purpose, we overlay the template spectrum of a carbon white dwarf ($\log g = 8$, $T = 22,000$ K; Dufour et al., 2008), scaled to a radius $R_2 = 0.035\,R_\odot$ and distance $D = 4.53$ kpc, over the UV-optical spectrum of X9 (Figure 5.7). We found that the donor in X9 likely has an extremely low mass. Using $M_2 \approx 0.013\,M_\odot$ (the middle value of the allowed range), results in a surface gravity $\log g = 5.5$. This surface gravity is

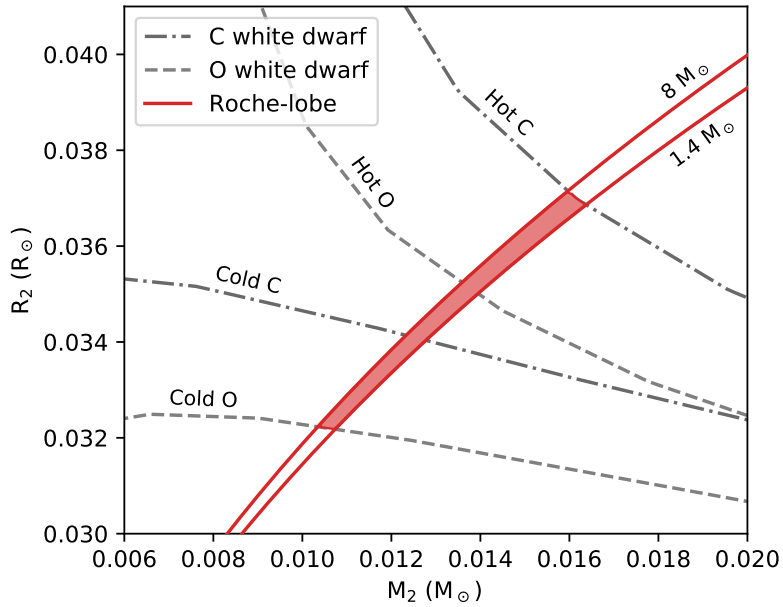

Figure 5.6: The mass–radius relationships (gray curves) for cold ($T = 10^4\,K$, lower curves) and hot ($T = 3 \times 10^6\,K$, upper curves) O (dashed curve) and C (dot-dashed) low-mass white dwarfs (Deloye and Bildsten, 2003), and the mass-radius relationship (red curves) for a Roche-lobe filling donor in a 28.2 minute orbital period with a $1.4\,M_\odot$ (lower curve) or $8\,M_\odot$ (upper curve) primary. The donor is likely to have a mass and radius between $M_2 = 0.010\,M_\odot$, $R_2 = 0.032\,R_\odot$ (for a cool O white dwarf), and $M_2 = 0.016\,M_\odot$, $R_2 = 0.037\,R_\odot$ (for a hot C white dwarf).

almost three orders of magnitude lower than that of the template white dwarf spectrum, and X9 contains additional atomic species (in particular oxygen). Thus, the template spectrum we have used should not be taken as a quantitative match to the donor in X9. We also overlay a black body spectrum with the same parameters for comparison. We find that the donor cannot be much hotter than $T = 22,000$ K, since otherwise it would start diluting the flickering activity seen in the FUV and optical bands.

5.3.3 Mass accretion rate

Next, we investigate whether the mass accretion rate inferred from the X-ray luminosity is compatible with the theoretical prediction of mass transfer driven by gravitational wave radiation in the cases of a neutron star or black hole.

The conversion of mass to radiation is determined by the radiative efficiency (η), such that $L_{\rm bol} = \eta \dot{M} c^2$. For black holes, we assume $\eta = 0.1$ in the soft state (independent of mass accretion rate), and $\eta \propto \dot{M}$ in the hard state and quiescence, with a continuous transition between the two regimes (Narayan and McClintock, 2008). For neutron stars, we assume $\eta = 0.1$ regardless of mass transfer rate or spectral state (the innermost stable circular orbit for a neutron star is similar in size to its radius). The hard-to-soft

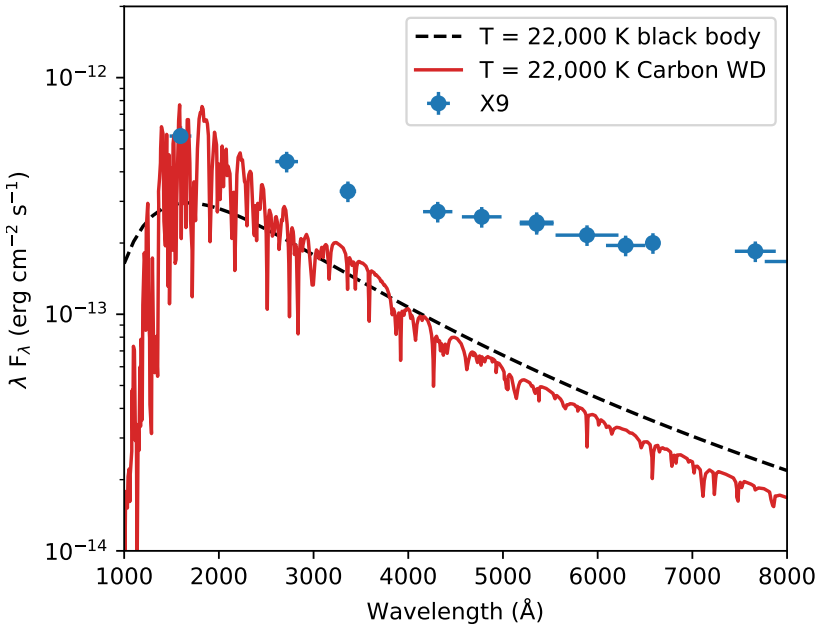

Figure 5.7: Model spectrum for a carbon-atmosphere white dwarf of $T = 22,000\,\mathrm{K}$ (Dufour et al., 2008), scaled to $R_2 = 0.035 R_\odot$ and $D = 4.53\,\mathrm{kpc}$, compared with the spectrum of X9. The donor in X9 is likely to be cooler than $T \approx 22,000\,\mathrm{K}$, otherwise it would start dominating the broadband spectrum of X9 in the UV.

transitions of X-ray binaries (neutron stars and black holes) occur at Eddington ratios $L_{\mathrm{bol,tr}}/L_{\mathrm{Edd}} = 0.004 - 0.25$, with an average of $L_{\mathrm{bol,tr}}/L_{\mathrm{Edd}} = 0.02$ (Maccarone, 2003; Kalemci et al., 2013). We therefore adopt $L_{\mathrm{bol,tr}}/L_{\mathrm{Edd}} = 0.02$ for X9, which could be uncertain by an an order of magnitude. The bolometric luminosity is then given by:

$$L_{\mathrm{bol}} = \eta_0 \frac{\dot{M}^2}{\dot{M}_{\mathrm{tr}}} c^2, \tag{5.1}$$

where η_0 and $\dot{M}_{\mathrm{tr}}$ are the transition efficiency and mass transfer rate respectively. Bahramian et al. (2017) found the 0.5–10 keV luminosity of X9 to vary in the range $L_{\mathrm{X}} = (2 - 7) \times 10^{33}\,\mathrm{erg\,s^{-1}}$ on the seven-day period. Assuming a cut-off power-law for the X-ray spectrum, with $\Gamma = 1.1$ and $E_{\mathrm{fold}} = 50\,\mathrm{keV}$ (Bahramian et al., 2017), the bolometric correction for X9 is $L_{0.5-10\,\mathrm{keV}}/L_{0.5-200\,\mathrm{keV}} = 0.13$. Therefore, its bolometric (0.5–200 keV) luminosity varies between $L_{\mathrm{bol}} = (15 - 54) \times 10^{33}\,\mathrm{erg\,s^{-1}}$, owing to the seven-day superorbital modulation (Bahramian et al., 2017). Using Equation 5.1, for a black hole (assuming a typical mass $M_1 = 8\,M_\odot$; Özel et al., 2010) this range corresponds to a radiative efficiency $\eta_{\mathrm{BH}} = (3 - 5) \times 10^{-3}$ and a mass accretion rate through the disc $\dot{M}_{\mathrm{BH}} = (9 - 18) \times 10^{-11}\,M_\odot\,\mathrm{yr^{-1}}$. If X9 instead hosts a neutron star ($M_1 = 1.4\,M_\odot$, $R_1 = 10\,\mathrm{km}$), the accretion rate ranges between $\dot{M}_{\mathrm{NS}} = (0.3 - 1.0) \times 10^{-11}\,M_\odot\,\mathrm{yr^{-1}}$. Note that these values assume the luminosity variations are due to variations in mass accretion rate. If instead the variability is

caused by geometric effects, the mass accretion rates derived above are lower limits only.

The mass transfer rate for conservative mass transfer driven by gravitational wave radiation is given by Landau and Lifshitz (1975), Verbunt (1993):

$$\frac{\dot{M}_2}{M_2} = 2\frac{\dot{J}}{J}\frac{1}{n_{\rm R} + 5/3 - 2M_2/M_1}, \tag{5.2}$$

where $n_{\rm R}$ describes the change of the donor's radius as its mass changes, and J and $\dot{J}$ are the angular momentum of the system and the angular momentum loss rate respectively, given by Peters (1964):

$$\frac{\dot{J}}{J} = -\frac{32}{5}\frac{G^3}{c^5}\frac{M_1 M_2 (M_1 + M_2)}{a^4}, \tag{5.3}$$

where a is the orbital separation; $a_{\rm BH} = 4.3 \times 10^{10}$ cm or $a_{\rm NS} = 2.4 \times 10^{10}$ cm using Kepler's third law for a 28.2 min orbital period. For a C/O white dwarf donor of mass $M_2 = 0.010-0.016\,M_\odot$, $|n_{\rm R}| < 0.1$ (Deloye and Bildsten, 2003), making it negligible in Equation 5.2. For a black hole primary ($M_1 = 8\,M_\odot$), $\dot{M}_{2,\rm BH} = (5-11)\times10^{-11}\,M_\odot\,{\rm yr}^{-1}$ (with higher rate for a more massive donor). For a neutron star, we obtain a mass transfer rate in the range $\dot{M}_{2,\rm NS} = (1-4)\times10^{-11}\,M_\odot\,{\rm yr}^{-1}$. We stress these estimates are based on the assumption of conservative mass transfer.

If X9 is a transient system in quiescence, the mass lost by the donor should be larger than the rate of mass transfer reaching the primary ($|\dot{M}_2| > \dot{M}$), such that matter accumulates in the disc. The mean mass accretion rates estimated above from the X-ray luminosity and conservative mass transfer are compatible both with a neutron star or black hole.

5.3.4 Source of optical emission

The sources of optical/UV continuum and line (C IV) emission could originate from the accretion disc (viscous dissipation or X-ray reprocessing), the impact point of the accretion stream on the disc, the donor star (intrinsic or reprocessed spectrum), and/or the optically-thin part of the jet. The corona, base of the jet, or an inner advection-dominated accretion flow (ADAF) might also contribute UV-blue photons. It is thought, however, that the optical emission (disregarding the companion star) in X-ray binaries is most often dominated by X-ray reprocessing in the disc (Vrtilek et al., 1990; Russell et al., 2006; Bernardini et al., 2016).

Before we investigate the likely scenario of disc irradiation, we discuss the other potential sources of optical emission. In the absence of outflows, an ADAF is expected to have a sharp peak at $\nu_{\rm peak} \sim 10^{15}(M/M_\odot)$ Hz (Narayan and Yi, 1994; Quataert and

Narayan, 1999). Since we do not observe such a peak in the optical/UV spectrum (Figure 5.9), an ADAF is unlikely to be dominating in these bands. The radio flux density of X9 is at the level of $S_\nu \approx 30\,\mu$Jy (Miller-Jones et al., 2015; Bahramian et al., 2017). Assuming a flat radio spectrum, this corresponds to $\sim 50\%$ of the measured optical flux, so it is possible that the jet could contribute to the optical emission. The jet in the hard state, however, is thought to turn over at frequencies lower than $\nu_{\rm break} \lesssim 10^{14}\,$Hz $\approx 10^4\,$Å (Russell et al., 2013), making it unlikely to dominate the optical emission, especially towards bluer wavelengths. The jet could, however, contribute on the red side of the spectrum.

The maximum luminosity that may be reached by the stream-impact point is estimated as the release of gravitational energy as matter falls from the first Lagrangian point (R_{L1}) to the minimum impact radius on the disc (half the circularization radius, $R_{\rm circ}$) (Menou and McClintock, 2001):

$$L_{\rm impact} < GM_1\dot{M}_2\left(\frac{1}{0.5R_{\rm circ}} - \frac{1}{R_{L1}}\right). \tag{5.4}$$

Using the formulations for $R_{\rm circ}$ from Verbunt and Rappaport (1988, their Equation 13) and for $R_{\rm L1}$ from van Haaften et al. (2012, their Equation C.3), and taking $M_1 = 8\,M_\odot$, $\dot{M} = 10^{-10}\,M_\odot$ (the maximum allowed from gravitational wave radiation for $M_2 = 0.016\,M_\odot$), the maximum stream-impact luminosity is $L_{\rm impact} < 3\times10^{32}\,$erg s^{-1}. This value is a factor of $\sim$3 lower than the mean monochromatic optical/FUV luminosity ($L = \lambda F_\lambda \approx 1\times10^{33}\,$erg s^{-1}), meaning that it is unlikely to be produced at the impact point. The bulk of the disc and possibly the jet are most likely the sources of optical emission in X9. Next, we explore how bright the reprocessed emission in X9 should be, by comparing X9 to sources where reprocessing is known to occur.

Disc irradiation

In their optical/X-ray correlation study, Bernardini et al. (2016) focused on the black hole and neutron star X-ray binaries V404 Cyg and Cen X–4. They found that the correlations between the total optical (R or V band) and X-ray (3–9 keV) luminosities in the two systems have different correlation indices and normalisations, V404 Cyg being more optically bright than Cen X–4 at the same X-ray luminosity. However, when only the reprocessed optical and bolometric X-ray flux (0.5–200 keV) are considered, the two sources have virtually indistinguishable optical/X-ray correlations in outburst and quiescence. This suggests the optical/X-ray correlation for reprocessed X-rays could be universal across neutron stars and black holes with different mass ratios.

To compare X9 with V404 Cyg and Cen X–4, we follow the steps laid out by Bernardini et al. (2016), and calculate the 0.5–200 keV luminosity and normalise the optical flux to that of Cen X–4. Since there is no soft X-ray component reminiscent of

emission from the surface of a neutron star, we do not subtract any surface contribution from the X-ray luminosity. Because the inclination of X9 is poorly constrained ($i \gtrsim 30°$; see Section 5.3.7), but comparable to V404 Cyg ($i = 67^{\circ+3}_{-1}$; Khargharia et al., 2010) and Cen X–4 ($32^{\circ+8}_{-2}$; Shahbaz et al., 2014; Hammerstein et al., 2018), we do not correct for inclination effects.

The reprocessed emission from the accretion disc depends on its size (and hence on the orbital period and the mass of the primary, via Kepler's third law). Therefore, to make an effective comparison, the optical luminosity of X9 ($L_{\rm opt} \approx 6 \times 10^{32}\,{\rm erg\,s^{-1}}$, calculated from the V-band flux) needs to be normalised to that of Cen X–4 accounting for its mass and orbital period using $L_{\rm opt} \propto M_1^{1/3} P_{\rm orb}^{2/3}$ (for $M_2 \ll M_1$; van Paradijs and McClintock, 1994; Bernardini et al., 2016). Moreover, one must also take into account the bolometric luminosity (which irradiates the disc). Taking the mass to be either $1.4 M_\odot$ or $8 M_\odot$, we find the normalised optical monochromatic luminosities to be $L_{\rm opt} \approx 3.2 \times 10^{33}\,{\rm erg\,s^{-1}}$ and $L_{\rm opt} \approx 1.8 \times 10^{33}\,{\rm erg\,s^{-1}}$ for a neutron star and black hole respectively. The normalised optical luminosity is a factor of three (for a black hole) to six (for a neutron star) larger than those of V404 Cyg and Cen X–4 at similar bolometric luminosities ($L_{\rm opt} \approx 5 \times 10^{32}\,{\rm erg\,s^{-1}}$; Figure 5.8). X9 is relatively optically bright for its X-ray luminosity, suggesting the disc reprocesses more of the irradiating X-ray flux (if the disc has a lower albedo, or a larger aspect ratio H/R than typical X-ray binaries), or the jet contributes significantly in the optical band.

In typical X-ray binaries, it is usually assumed the albedo of the disc to grazing X-rays is $A \gtrsim 0.9$ (de Jong et al., 1996), where the albedo determines what fraction of the incident X-rays is reprocessed to optical emission ($L_{\rm repro} \propto (1 - A)$). As O-rich gas effectively absorbs X-rays, the effective albedo of the disc could be lower than that of Cen X–4. Still, the reflection signatures in the X-ray spectrum of X9 (Bahramian et al., 2017) show the disc albedo is significant, and we expect a value in the range of $A_{X9} = (0.1 - 1.0) \times A_{\rm CenX-4}$, implying the reprocessed optical emission in X9 would have been a factor of $\lesssim 10$ fainter if it had solar metallicity. As long as the inclination of the system $i \lesssim 70°$ (when emission from the heated face of the disc dominates over emission from the edge of the disc), the minimum fractional disc contribution to the optical light is $\gtrsim 1/6$ for a neutron star, and $\gtrsim 1/3$ for a black hole (Figure 5.8), but a low albedo can account for 100% of optical emission as originating from the irradiated disc. The optical emission from the disc in a high inclination ($i \gtrsim 70°$) system could appear fainter ($< 1/6$ contribution) because only its edge would be visible (as a black body). In such a case, the jet would need to contribute significantly to the optical emission. Next, we fit the spectral energy distribution for X9 to further constrain the relative contributions of the jet and disc.

Table 5.3: Parameters for the best fits to the broadband spectrum, using three different models. $R_{1,2}$ and $T_{1,2}$ are the projected sizes of the black body components and their respective temperatures. For `discir`, T_1 is the temperature at the inner truncation radius R_1. In all cases, R_2 is the radius of the outer edge of the disc. α is the spectral index of the optically thick jet emission. For each fit, we show the χ^2 statistic of the fit and the degrees of freedom (ndf) for the optical range only. We compare the size of the disc from these models, $R_{\mathrm{d,model}} = R_2/(\cos i)^{1/2}$ (assuming $i = 60°$) with the theoretical disc size for a neutron star and a black hole (for a disc that extends out to 90% of the primary's Roche lobe; van Haaften et al., 2012).

Parameter	`pow + bbody`	`2× bbody`	`discir`
T_1 (10^4 K)	–	2.6	17.4
R_1 (10^8 cm)	–	34 ± 14	1.0 ± 0.02
T_2 (10^4 K)	2.6	0.6	–
R_2 (10^8 cm)	33 ± 5	250 ± 46	770 ± 190
α	0.02 ± 0.01	–	–
χ^2/ndf	1576/1305	1570/1306	1573/1304
$R_{\mathrm{d,model}}/R_{\mathrm{d,NS}}$	0.30 ± 0.04	2.3 ± 0.4	4.9 ± 1.2
$R_{\mathrm{d,model}}/R_{\mathrm{d,BH}}$	0.16 ± 0.04	1.2 ± 0.4	2.6 ± 0.6

Broadband spectra

Following Gallo et al. (2007), we start by fitting two different physically motivated XSPEC models to the broadband spectrum: a broken power-law and a black body (to represent the jet and disc, respectively), and a double black body (to represent the outer disc and the inner accretion flow). In addition, we also fit an irradiated disc model. The model parameters are listed in Table 5.3.

For the *broken power-law + black body* model, we fix the spectral index of the optically-thin part of the jet to $\alpha = -0.8$ (Gallo et al., 2007). We find the projected size of the disc is only $R_{\mathrm{d,model}} = 3 \times 10^9$ cm (compared to the expected $R_{\mathrm{d,NS}} = 24 \times 10^9$ cm for a neutron star and a disc filling up 90% of its Roche lobe). While the emission in the optical band is mostly dominated by the jet, the projected size of the black body component requires an edge-on system.

In the *double black body* model, the size of the large, cool component ($R_2 \approx 2.5 \times 10^{10}$ cm) identified with the outer disc indicates either a face-on disc around a neutron star, or a black hole seen at intermediate inclination angles. The small, hot component could be the viscously-heated inner disc, an ADAF, the base of the jet, or the disc/stream impact point. Both of these simple fits show that both a neutron star and black hole are compatible with the observed broadband spectrum.

Assuming the optical emission in X9 originates from X-ray reprocessing alone, we can fit an irradiated disc model (`discir`; Gierliński et al., 2008) to the 3,000–8,500 Å spectrum reported in this chapter, assuming a 1–10 keV power-law ($\Gamma = 1.1$) X-ray spectrum with a luminosity $L_{1-10\,\mathrm{keV}} = 10^{34}\,\mathrm{erg\,s^{-1}}$ representing the unobscured

corona. We do not include the broadband optical and FUV measurements reported by Knigge et al. (2008) because they have not been taken simultaneously with our data, and variability (especially in the FUV band) might compromise the fit.

We fix the radius of the Compton-illuminated disc $r_{\rm irr} = 1.2$ (relative to the inner disc radius), the electron temperature $kT_{\rm e} = 100\,{\rm keV}$, and the fraction of luminosity in the Compton tail that is thermalised in the inner disc $f_{\rm in} = 0.1$. These values have been chosen as typical for X-ray binaries in the hard state (Poutanen et al., 1997). In addition, we fix the temperature of the inner disc $T_{\rm in} = 0.015\,{\rm keV}$, chosen so that the soft X-ray emission from the inner disc does not become visible in the X-rays.

We find the irradiated disc model to be a good representation of the observed broadband spectrum. Repeating the fit with different values of $kT_{\rm e}$ and $T_{\rm in}$ does not change these results significantly. We find that for an inclination angle $i = 60°$, the data are best described by a disc extending out to $R_{\rm d} = (8 \pm 2) \times 10^{10}\,{\rm cm}$, or factors of $R_{\rm d,model}/R_{\rm d,NS} = 4.9 \pm 1.2$ and $R_{\rm d,model}/R_{\rm d,BH} = 2.6 \pm 0.6$ times larger than expected for a neutron star or black hole respectively. An explanation for this discrepancy is the inclination angle. For a face-on system, the parameters of best fit would correspond to disc radii $R_{\rm d,model}/R_{\rm d,NS} = 2.2 \pm 0.5$ and $R_{\rm d,model}/R_{\rm d,BH} = 1.2 \pm 0.3$. In this case, a neutron star is disfavoured, but a black hole is compatible, as long as $i \lesssim 30°$.

In summary, we find that the optical emission can originate from the following sources: a jet and a disc ($i \approx 90°$, regardless of the nature of the primary), a disc and an inner accretion flow ($i \lesssim 30°$ for a neutron star, or $i \approx 60°$ for a black hole), or X-ray reprocessing by the disc (only for a $i \lesssim 30°$ black hole).

5.3.5 C IV emission

We have found the optical spectrum of X9 to be featureless. In the FUV, however, Knigge et al. (2008) have unambiguously detected C IV emission. Because of its double-peaked profile, they attributed it to a rotating medium, possibly the accretion disc or disc wind. Absorption towards the system (intrinsic or extrinsic), however, could result in a similar shape of the profile. For example, Homer et al. (2002) have attributed the double-peaked profile of the C IV doublet in the carbon-rich ultracompact X-ray binary 4U 1626–67 to absorption near the line centres, superposed on the emission line. The lack of absorption lines in the FUV spectrum of X9, in contrast to their presence in 4U 1626–67 (Homer et al., 2002), shows that the double-peaked nature of the lines is more readily explained by a rotating medium in X9.

The FWHM of the C IV doublet and the orbital period can be used to estimate the mass of the primary object by using the FWHM – K_2 (where K_2 is the projected velocity amplitude of the donor; Casares, 2015) and the DP/FWHM–q (where DP is the double-peak separation; Casares, 2016) relations. Following the same procedure

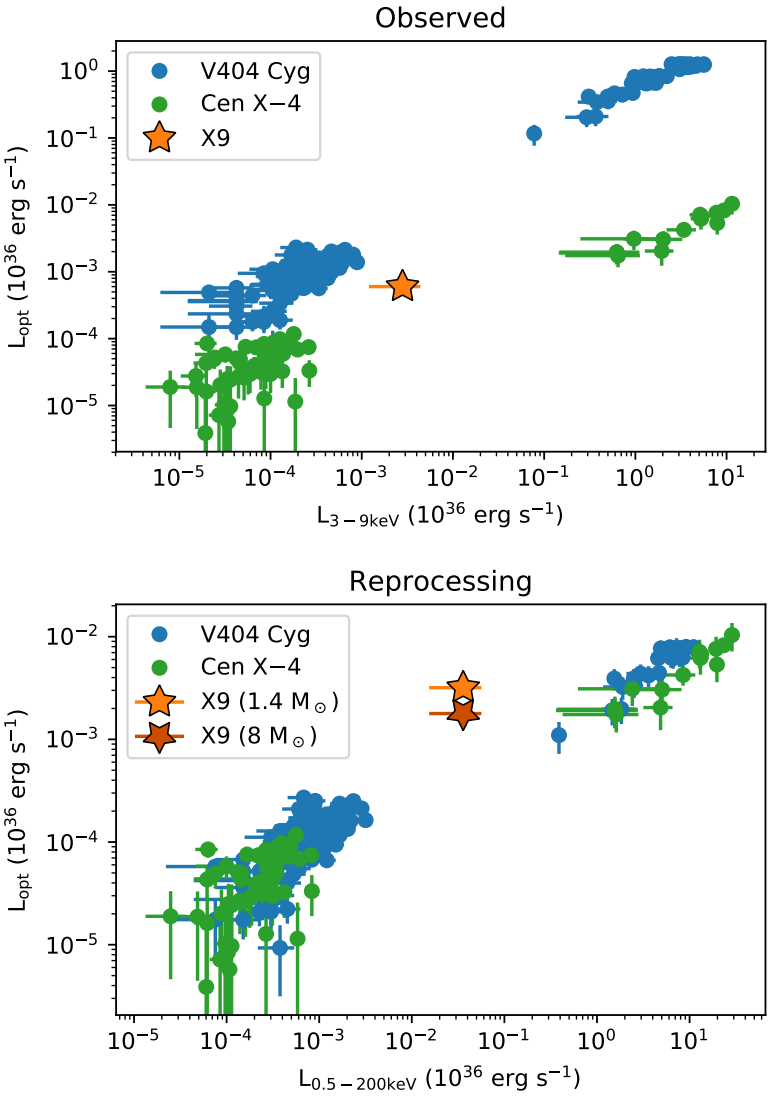

Figure 5.8: *Top*: the relationship between the observed optical and X-ray luminosities of the accreting neutron star Cen X–4 and black hole V404 Cyg, in comparison to X9. *Bottom*: for the same sources, the optical and X-ray luminosities associated with reprocessing only (removed contributions from the donor and jet for Cen X–4 and V404 Cyg), normalised to the primary mass ($M = 1.4\,M_\odot$) and orbital period ($P = 0.629$ days) of Cen X–4. This Figure was adapted from Bernardini et al. (2016). The optical emission of X9 is brighter than expected when compared to V404 Cyg and Cen X–4, indicating more efficient reprocessing of X-rays, or the significant contribution of a jet at optical wavelengths.

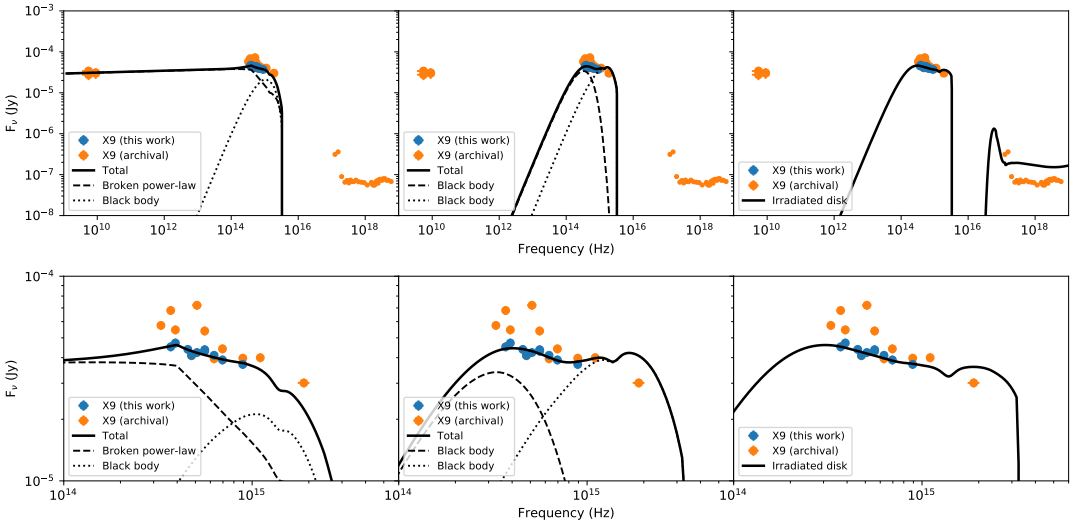

Figure 5.9: Observed broadband spectrum for X9 (radio data from Miller-Jones et al., 2015 and Bahramian et al., 2017, archival FUV–infrared data from Knigge et al., 2008, optical data from this chapter (displayed as broadband fluxes calculated from our spectrum), and X-ray data from Bahramian et al., 2017), with superimposed models. For fitting the models, we excluded the FUV–infrared data from (Knigge et al., 2008). In the `power-law + black body` model, we also included the radio data in the fit, and for the `diskir` model we assumed a 1–10 keV power-law spectrum ($\Gamma = 1.1$), with $L_{1-10\,\mathrm{keV}} = 10^{34}\,\mathrm{erg\,s^{-1}}$, representing the likely intrinsic X-ray luminosity of X9 (see Section 5.3.8), which is brighter than the apparent luminosity. *Left:* a broken power-law + black body, where the jet dominates up to the optical band; *middle:* two black bodies, with emission from a large, cool disc, and a small, hot inner disc or stream/disc impact point; *right*: an irradiated disc. *Bottom*: The same spectrum and models, zoomed-in on the optical data.

as Casares (2015) and Casares (2016), we fit the C IV doublet with two symmetrical Gaussians (one for each line in the doublet) to measure its FWHM, and with 2×2 symmetrical Gaussians to measure the double-peak separation. We find FWHM = $3600 \pm 140\,\mathrm{km\,s^{-1}}$, and DP = $2070 \pm 70\,\mathrm{km\,s^{-1}}$ (Figure 5.10). We note the reason behind the poor fit ($\chi_\nu = 1.50$) in Figure 5.10 is forcing the two peaks to have the same normalization, to follow the same procedure as Casares (2016). Leaving the relative intensities of the blue and red peaks free to vary leads to a statistically better fit ($\chi_\nu = 1.13$), but to a similar value DP = $2190 \pm 60\,\mathrm{km\,s^{-1}}$. Changing the relative intensities within the doublet to the theoretical ratio $I_{\lambda1548}/I_{\lambda1550}$ = 2:1 (Flower et al., 1982) does not change the FWHM and DP significantly. With a total exposure time for the FUV spectrum of 82,200 s (Knigge et al., 2008), i.e. almost 50 binary orbits, we assume the measured C IV profile is representative of the average emission in the system. We do not correct the FWHM for the instrumental resolution because of its small value ($\Delta\lambda = 1.2$ Å).

Compared to the H α line in quiescent X-ray binaries, the FWHM of the C IV doublet in X9 is one of the highest observed (Casares, 2015). The FWHM of the C IV doublet lies in the tentatively defined forbidden region for cataclysmic variables ($\mathrm{FWHM_{H\,\alpha}} \gtrsim 2600\,\mathrm{km\,s^{-1}}$; Casares, 2015), further strengthening the evidence against such an object. Because the C IV doublet has higher energy than the H α line, the former might originate from closer in to the primary object in an X-ray binary, where the disc is hotter. In contrast to this idea, the FUV and optical spectra (albeit non-simultaneous) of A0620–00 in quiescence show that the emission features of C IV and H α have similar FWHM ($\approx 2000\,\mathrm{km\,s^{-1}}$; Marsh et al., 1994; Froning et al., 2011). Even in outburst, the optical spectrum of the black hole X-ray binary MAXI J1659–152 includes many emission lines between 3,000–10,000 Å with similar FWHM = $1500 - 2000\,\mathrm{km\,s^{-1}}$ (Kaur et al., 2012), indicating that at a given luminosity, emission lines likely originate from similar characteristic radii, regardless of their species. It is unknown, however, if the relationships of Casares (2015) and Casares (2016) hold for the extreme mass ratios in ultracompact X-ray binaries because the sample of Casares (2015) includes only H-rich X-ray binaries with orbital periods longer than $P_{\mathrm{orb}} = 0.17$ days.

The accreting neutron star 4U 1626–67 is a good candidate for testing if the Casares relations hold for the C IV line in ultracompacts. It has strong C IV emission (Homer et al., 2002), a short orbital period (41 min; Middleditch et al., 1981) and a low-mass donor ($M_2 \approx 0.02\,M_\odot$), seen at an inclination angle $i \lesssim 33°$; Verbunt et al., 1990; Chakrabarty, 1998). In this source, the C IV FWHM $\approx 1500\,\mathrm{km\,s^{-1}}$. Using $K_2 = (0.233 \pm 0.013) \times \mathrm{FWHM}$ (Casares, 2015), we predict $K_2 \approx 350\,\mathrm{km\,s^{-1}}$. Using the primary mass function, $f(M_1) = P_{\mathrm{orb}}K_2^3/2\pi G = M_1 \sin^3 i/(1+q)^2$, we find a primary mass $M_1 \gtrsim 0.8\,M_\odot$, which is compatible with the canonical mass for a neutron star ($M_1 = 1.4\,M_\odot$). While this value supports the same FWHM–K_2 relationship for

the C IV line in ultracompacts as the H α line in typical X-ray binaries, we cannot be confident about this interpretation because of the poorly known inclination angle for 4U 1626–67, and the lack of other test sources.

Applied to X9, we predict $K_2 = 850 \pm 60\,\mathrm{km\,s^{-1}}$ using the FWHM–K_2 relation. Similarly, we can use the empirically-found ratio between the outer disc velocity (K_d) and the orbital velocity of the donor star (K_2) to reach a similar conclusion. This approach has previously been used to constrain the nature of the X-ray transient Swift J1357.2–0933 as a black hole (Corral-Santana et al., 2013). This ratio has been found to lie in the range $K_\mathrm{d}/K_2 = 1.1 - 1.2$ (Orosz et al., 1994). Estimating K_2 based on DP is also more suitable than the FWHM-based method in the case of edge-on systems, where all of the line emission comes from the outer disc. In X9, DP = $2070 \pm 70\,\mathrm{km\,s^{-1}}$ implies $K_2 = K_\mathrm{d}/1.15 = (\mathrm{DP}/2)/1.15 = 900 \pm 30\,\mathrm{km\,s^{-1}}$. Both methods (FWHM–$K_2$ and DP–K_2) give similar K_2 values. The mass function implies a minimum primary mass $M_1 \geq 1\,M_\odot$ (for an edge-on system, $i = 90°$, and a negligible donor mass), compatible with both a neutron star and a black hole. Alternatively, comparing the mass ratio and DP/FWHM in X9 with those of other X-ray binaries, we find that a neutron star is a slightly better fit than a black hole (Figure 5.11). The low DP/FWHM values in X9 could be explained by double peaks that originate further out in the Roche lobe than assumed for other X-ray binaries; in quiescent ultracompact X-ray binaries, the outer disc is likely to truncate at a larger radius relative to the Roche lobe (van Haaften et al., 2012).

The C IV emission could alternatively originate from the bright spot at the outer edge of the disc. The line luminosity emitted by the C IV doublet is $L_\mathrm{C\,IV} \approx 6 \times 10^{30}\,\mathrm{erg\,s^{-1}}$. In addition, the predicted luminosity of the stream/disc impact point was $L_\mathrm{impact} < 3 \times 10^{32}\,\mathrm{erg\,s^{-1}}$ (Section 5.3.4), up to a factor of 50 larger than the line luminosity, so it is also possible for the C IV emission to originate from there as well. In this case, time-resolved spectroscopy of the line would reveal a periodic change in its radial velocity – an S-wave (Honeycutt et al., 1987). As we have not performed this investigation on the existing FUV data, it is an avenue for future studies.

For an inclination angle $i \gtrsim 30°$ (Section 5.3.7), we restrict the primary mass to the range $M_1 \lesssim 10\,M_\odot$. The threshold inclination angle (for $M_1 = 3\,M_\odot$, between a neutron star and a black hole) is $i \approx 50°$. We highlight that these estimates are based on the assumption that there is no C IV absorption, the double-peaked C IV emission is due to motion of the accretion disc, and that it originates from the same characteristic radius as the H α line in typical X-ray binaries. The mass and inclination angle estimates presented above could therefore be subject to large systematic errors, and should therefore only be used as rough guides.

In summary, the C IV emission suggests $i \gtrsim 50°$ for a neutron star, or $i \lesssim 50°$ for a black hole. Using these results to constrain the model predictions from Section 5.3.4,

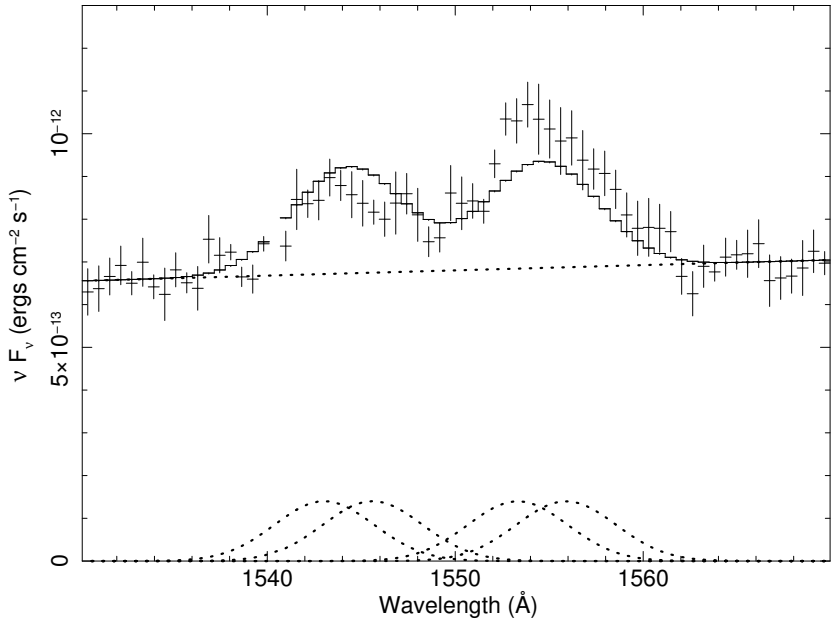

Figure 5.10: The C IV $\lambda\lambda$1549, 1551 doublet in X9, fit with two sets of two symmetrical Gaussian line profiles added to the local continuum. Each model component is displayed with a dotted line, and the total model is shown in the full line.

we find the optical emission in a neutron star to most likely come both from the jet and disc. For a black hole, the emission would come from X-ray reprocessing in the disc.

5.3.6 X-ray spectrum

One of the peculiarities of this source is that its X-ray spectrum is considerably harder than the spectra of other X-ray binaries with either a black hole or neutron star primary, at similar X-ray luminosities. This may, in fact, be a natural consequence of the abundances of the accreted material, and if this is the case, there are important implications for the likelihood that the accretor is a black hole, and for understanding emission mechanisms from accreting black holes at low accretion rates.

In the context of ADAF models (Narayan and Yi, 1995), there are three major processes that can contribute to the X-ray emission: synchrotron emission, inverse compton emission, and bremsstrahlung emission. The seed photons for the Compton scattering may be the synchrotron photons, the bremsstrahlung photons, or, in the case of neutron star accretors, the photons produced in the boundary layer where the excess energy carried by the flow is dissipated near the surface of the neutron star. Ordinarily, the bremsstrahlung emission dominates only in the very outer parts of the emission region. In an ultracompact binary, however, the bremsstrahlung emission should become considerably more important, since bremsstrahlung emissivity scales as $\langle Z^2 \rangle$, where Z is the charge per nucleus. The bremsstrahlung emission in a system with a C/O white dwarf mass donor should be $\sim$ 50 times more important than in a system

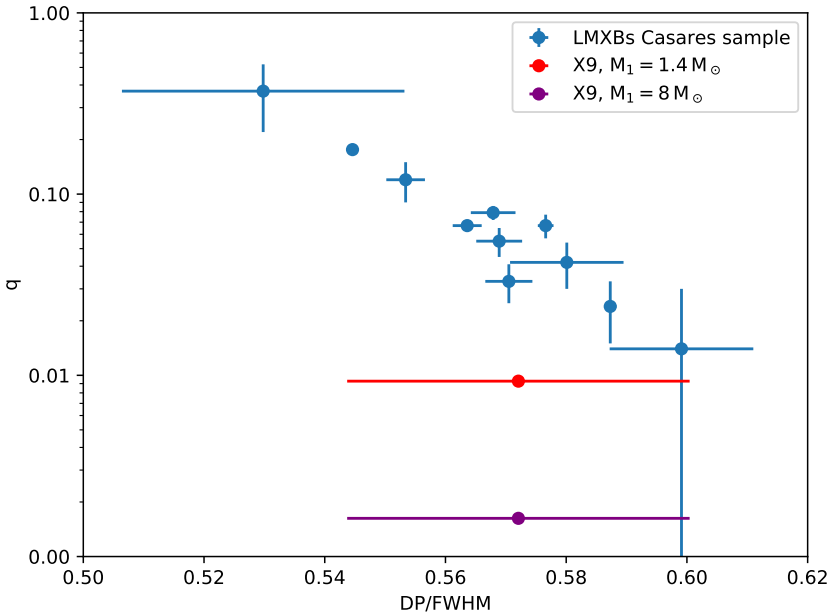

Figure 5.11: Mass ratio (q) versus DP/FWHM of the C IV doublet of X9, compared with the H α line for the low-mass X-ray binary (LMXB) sample of Casares (2016). The X9 data are consistent with the system hosting either a neutron star or a black hole, but the signal to noise ratio of the C IV doublet in X9 is too low to distinguish between the two scenarios.

with a H donor. Systems with He white dwarf donor stars should have intermediate properties.

A full treatment of this effect is well beyond the scope of this chapter, but we can examine Figures 6 & 7 of Narayan and Yi (1995) to obtain some intuition about how important the effect is likely to be. In their Figure 6(b), it is clear that, for neutron stars, the Compton emission dominates heavily over bremsstrahlung across the range of radii where nearly all the emission is produced. Therefore, if we assume that the reason for the hard X-ray spectrum is the relative importance of bremsstrahlung emission, a neutron star accretor is disfavoured. Indeed, neutron star ultracompact systems have X-ray spectra as soft as those seen in other neutron star systems (e.g. for the persistent C/O-rich 2S 0918–549 and 4U 0614+091, $\Gamma \approx 2.1$; in't Zand et al., 2005, and $\Gamma \approx 2.2$; Migliari et al., 2010, respectively). There is no other obvious mechanism, either, for getting an especially hard X-ray spectrum from an accretion disc corona (ADC) source. For black hole accretors, on the other hand, Figure 6(a) of Narayan and Yi (1995) shows that, at the critical accretion rate, the bremsstrahlung emission is a factor of about 100 below the synchrotron level at the inner edge of the accretion disc, and falls off much more slowly with distance from the black hole. Furthermore, from their Figure 7, we see that, as the accretion rate drops, the crossover radius between bremsstrahlung and synchrotron / synchrotron self-Compton emission moves inwards.

We propose that the harder X-ray spectrum of X9 relative to other low-accretion-

rate systems is due to its C/O-dominated chemical composition, which boosts the bremsstrahlung component of the X-ray emission in the case of a black hole accretor. If so, high X-ray spectral hardness will be a key selection criterion to discovering more such objects in large surveys. A more detailed modelling of how the bremsstrahlung / synchrotron ratio changes with metallicity and nature of the primary is a promising avenue to uncover if X9 is a neutron star or black hole.

5.3.7 Origin of orbital modulations

In the X-ray timing analysis of X9, Bahramian et al. (2017) suggested an orbital period of 28.2 minutes. This orbital modulation is characterised by long ($\sim$ 30% of the orbit) and shallow drops in the X-ray light curve ($\approx$ 15% of flux), while the 27.2 min FUV signal is shallower ($\approx$ 5% of flux).

In X-rays, orbital modulations can arise from the obscuration of the X-ray source, the reflection of X-rays by the companion star, or from changes in the mass accretion rate. Obscuration can be provided by cold clouds in the disc, a flared or warped disc, the stream/disc impact point (X-ray dips), or by the donor star (total or partial eclipses). Since the donor is too small to be obscuring the X-ray source (as already noted in Bahramian et al., 2017), the alternative is that X9 is similar to an X-ray dipper, where clumps in the disc are blocking a fraction of the X-rays. Indeed, periodic X-ray dips reflective of the binary period have been observed in a number of high-inclination X-ray binaries such as XB 1916–053 (White and Swank, 1982). Such dips are produced by a bulge in the disc from the collision of the accretion stream with the disc, and can appear at the outer disc edge (White and Holt, 1982), at the circularization radius (Frank et al., 1987), or between the circularization radius and outer disc (Armitage and Livio, 1996). Regardless of where these impact bulges are located in the disc, they are stationary in the binary frame. Such bulges can stretch over a large fraction of the disc, potentially explaining the large fraction of the orbital period X9 spends in partial obscuration. An inner warped disc, which is likely in a dynamically-formed system where the spin of the primary is misaligned with respect to the orbital plane, could potentially supply the required obscuration even in more face-on configurations.

The modulation could also potentially arise from X-rays reflected off the donor. If the primary is a neutron star ($M_1 = 1.4\,M_\odot$), then $a = 0.34\,R_\odot$. For a radius $R_2 = 0.04\,R_\odot$, the donor occupies $f = 1/4\,(R_2/a)^2 \approx 0.3\%$ of the sky as seen from the primary, meaning that up to 0.3% of the X-ray flux is reflected by the donor (less in the case of a heavier primary). The source of the orbital modulation (in X-rays) is therefore unlikely to be associated with reflection from the donor. The last possibility is that the orbital modulations are caused by an oscillating mass accretion rate. Zdziarski et al. (2009) found this to be unlikely in low-mass X-ray binaries because the viscous time-

scale of the disc is much longer than the orbital period, dampening any variations in the mass accretion at the edge of the disc. We therefore conclude the orbital modulation in the X-ray band is most likely caused by obscuring material in the disc. Next, we attempt to constrain the inclination angle of the system.

For a donor of mass $M_2 = 0.013\,M_\odot$, the lack of X-ray eclipses in X9 restricts the inclination angle to $i \lesssim 85°$ (assuming a point source for the X-ray emission, and a disc much thinner than the size of the donor; Frank et al., 1987). Alternatively, the disc could fully shadow the donor star (a viable option for a disc opening angle $\theta \lesssim 5°$; Section 5.3.8), or the signal to noise ratio of the phased X-ray orbital modulation might be too low to show eclipses, in which case edge-on systems ($i = 90°$) are also allowed. Our interpretation of the orbital modulation as obscuration by features in the disc suggests $i \gtrsim 60°$ (Frank et al., 1987). Comparing the orbital modulation profile of X9 with other sources whose inclination is known is not straightforward. For many systems, the inclination angle is only an upper or lower limit based on the presence or lack of dips or eclipses in their light curves. There are a handful of examples of sources showing orbital modulations in X-rays, for which better estimates for their inclination angles exist. For Sco X–1, which has an orbital inclination of $i \approx 40° - 50°$ (Steeghs and Casares, 2002), there is evidence for a 1% orbital modulation in the X-ray band (Vanderlinde et al., 2003), although its physical origin is unclear. 4U 1820–30 has a 685 s orbital modulation with a 1.5% amplitude (Stella et al., 1987). The inclination of this system is $i \approx 20° - 50°$ (Anderson et al., 1997; Ballantyne and Strohmayer, 2004).

Based on the presence of orbital modulations in the X-ray light curve of X9, its inclination is likely to be in the range $i \gtrsim 60°$, but could be as low as $i \approx 30°$. These values are compatible with the acceptable spectral fits of Bahramian et al. (2017) in the 1–79 keV band ($i < 68°$) and in the 0.4–79 keV band ($i < 66°$). Bahramian et al. (2017) warn, however, that their estimates of the inclination angle could be inaccurate, since they rely on spectral models which do not take into account the metallicity of the reflecting disc.

5.3.8 Origin of superorbital period

We have recovered the seven-day superorbital period of Bahramian et al. (2017) in the V and I bands, confirming the suggestion of a periodic X-ray modulation (Bahramian et al., 2017). The three significant periods in X9 (28.2 min, 27.2 min and seven days) are not consistent with being related by a beat relation. Specifically, we have $\Delta f \approx 1.95$ cycles per day (between the two short periods), but the long period of seven-days corresponds to 0.14 cycles per day.

Superorbital modulations can occur due to a change in the mass accretion rate, obscuration of the source, or a change in the inclination. These can be induced by

precession (nodal – of the inclination of disc plane, or apsidal – of an eccentric disc in a fixed plane), which can have a variety of physical origins.

The semi-amplitude of the superorbital modulations is a factor of 1.9 in the X-rays, whereas in the optical it is only 5%. For reprocessed X-rays, the optical emission should vary as $L_{\rm opt} \propto L_{\rm X}^{\beta}$, where $\beta = 1/2$ (van Paradijs and McClintock, 1994). For X9, one would then naively expect a semi-amplitude of a factor of ≈ 1.4 in the optical band. Similarly, if the optical emission is dominated by the viscously heated disc, $\beta = 0.17 - 0.5$, or if the jet is the the source of emission, $\beta = 0.7 - 1.4$, in all cases predicting much larger (by at least a factor of two) superorbital modulations than what is observed. The two ways for a steadily accreting source to have such a large disparity between the modulations of the two bands is if a non-variable optical source dominates the optical emission in X9, or if these modulations are not driven by changes in mass accretion. The former scenario can occur by emission from the donor, or if an additional stellar companion, or another unassociated cluster star that dominates the optical luminosity. If that were the case, however, the star would need to be at least as bright as the accretion flow. The spectral energy distribution would then be closer to a white dwarf atmosphere (with absorption lines), and the superorbital modulations would likely be different between the V and I bands (set by the different temperatures of the star and accretion flow). We do not observe any of these three features, so it is unlikely that a stellar object (donor or otherwise) drowns out the superorbital variability from the accretion flow.

Geometric effects such as occultation or changes of projected surface area are more likely to be causing the observed modulations. In the case of viewing angle effects and assuming $F_{\rm X} \propto (\cos i)^{1/2}$ (if X-rays are emitted from close to the disc surface), a face-on disc ($i = 0$) at maximum flux would require an almost edge-on disc ($i \approx 85^{\circ}$) at minimum flux. It is therefore difficult to invoke simple oscillations in the projected disc area as an explanation. We therefore find periodic obscuration to be the most likely interpretation for the superorbital period. In that case, the intrinsic bolometric luminosity of X9 needs to be at least as large as the maximum observed bolometric luminosity ($L_{\rm bol} \gtrsim 5 \times 10^{34}\,{\rm erg\,s^{-1}}$).

If mass transfer is driven solely by gravitational wave radiation, the maximum luminosity allowed by mass transfer to a neutron star or black hole is $L_{\rm bol,NS} \lesssim 2 \times 10^{35}\,{\rm erg\,s^{-1}}$ or $L_{\rm bol,BH} \lesssim 2 \times 10^{34}\,{\rm erg\,s^{-1}}$, respectively (Section 5.3.3). The former value is compatible with the estimated bolometric luminosity, but the latter value is a factor of ~2.5 smaller than required for a black hole. However, the uncertainties associated with calculating the mass accretion rate may be as large as an order of magnitude, so we cannot rule out a black hole.

One explanation for the high measured radio to X-ray luminosity ratio, relative to neutron stars (Miller-Jones et al., 2015; Bahramian et al., 2017), could be that X9 is

an ADC source, which would reduce the observed X-ray luminosity due to obscuration of the inner disc by a bulge in the disc. This shows that if X9 is an ADC source, its intrinsic X-ray ($L_{1-10\,\mathrm{keV}} \sim 10^{36}\,\mathrm{erg\,s^{-1}}$) and radio luminosities would be in line with other neutron stars. Otherwise, a black hole would be the most radio-faint at that X-ray luminosity.

The large difference between the observed superorbital amplitudes in the X-ray and optical bands is either caused by a more variable obscuration fraction in the X-rays, or by a larger absorption cross-section at short wavelengths. Depending on the geometry of the system, different obscuration factors for the X-ray and optical sources can be achieved. If $i \approx 90°$, the obscuration of the optical source (be it the jet or edge of the disc, but not the surface of the disc) varies little as the disc precesses, but how much of the X-ray emission is absorbed depends on the geometry of the outer disc. If $i < 80°$, and the optical emission is dominated by emission at the disc surface, only the inner regions of the disc may periodically occult the central X-ray source (otherwise the superorbital modulations would be prominent in the optical band too).

Next, we investigate whether the outer disc can reach the required height to obscure a significant part of the X-ray corona. In the simple case of a thin disc, the height of the disc at the outer edge is given by $H \approx c_\mathrm{s} P_\mathrm{orb}/(2\pi)$ (Frank et al., 2002), where c_s is the local sound speed, $c_\mathrm{s} = \sqrt{k_\mathrm{B} T/(\mu m_\mathrm{H})}$ (k_B is Boltzmann's constant, T is the temperature at the outer disc, μ is the mean atomic weight of the accreted gas, and m_H is the atomic weight for atomic H). Taking $T = 22,000\,\mathrm{K}$ (the estimated upper limit for the donor; Section 5.3.2) and $\mu = 7$ (for a singly-ionized C/O mixture), we find $H \approx 10^8\,\mathrm{cm}$, or a disc opening angle $\theta < 1°$. Such a small opening angle cannot produce the observed superorbital modulations. However, energy deposited by the accretion stream on the outer edge of the disc can thicken it (White and Holt, 1982). In typical low-mass X-ray binaries, the opening (semi-)angle of the disc is $\theta \approx 12°$ (de Jong et al., 1996), but metal-rich discs can be a factor of ≈2 thinner (keeping all other disc parameters the same; Dunkel et al., 2006). Coupled with a weak dependence of the aspect ratio on the radius ($H/R \propto R^{1/8}$; Frank et al., 2002), the outer disc in X9 is likely to be on the order of $\theta \approx 5°$. The surface layer of the accretion disc is likely to be optically thin, so we take the above value as an upper limit to the height of the optically-thick region. The disc obscures the X-ray corona and inner disc for inclination angles $i \gtrsim 85°$.

In view of the broadband modelling (Section 5.3.4) and C IV emission (Section 5.3.5) results, the X-ray corona can either be obscured by the inner or outer discs in the case of a neutron star ($i > 60°$, disc and jet emission), but only by the inner disc in the case of a black hole ($i < 30°$, disc emission only).

Next, we investigate the potential mechanisms behind disc precession, which are detailed in Appendix 5.A. We find that the seven-day superorbital period in the X9 system could either be driven by tidal effects, or the Kozai mechanism (in a hierarchical

triple system) in the case of a neutron star. In the case of a black hole, we have not found a mechanism that could give rise to the observed superorbital period. We cannot readily find a physical explanation to the short FUV period (27.2 min, in conflict with the 28.2 min X-ray period), which, at just over 2σ significance, could be spurious. The broadband models and the C IV emission cannot be used to distinguish between a neutron star and a black hole. Given the lack of an explanation for the observed superorbital period in the case of a black hole, but the presence of a hard X-ray spectrum ($\Gamma \approx 1.1$), which is more likely to be produced in a black hole system, the nature of the primary remains unsolved.

5.3.9 Formation and evolution

Simulation

Given that there are already many binary evolution calculations in the literature for neutron star ultracompact X-ray binaries, but essentially none for ultracompacts with black hole primaries, we decided to explore at least one simple channel that might produce such a system (illustrated in Figure 5.12).

We evolved a 2.0 $M_\odot$ He-star and a 5 $M_\odot$ black hole with an initial orbital period of 0.1673 days (4.015 hr). These initial masses were chosen to reflect the likely properties of the components of X9: a C/O white dwarf donor (evolved from a He-star of mass $M < 2.1\,M_\odot$; Dewi et al., 2002, and a light black hole; see Section 5.3.5). Such a He-star may originate from a $5 - 6\,M_\odot$ star formed in the globular cluster 10–12 Gyr ago, which subsequently lost its outer layers of H in a stellar collision or mass-transfer episode. For this simulation, we used the BEC binary evolution code, originally developed by Braun (1997) on the basis of a single-star code (Langer, 1998) which solves the hydrodynamic structure and evolution equations (Kippenhahn and Weigert, 1990) using Lagrangian methods. More details about an updated version of this code applied to X-ray binaries can be found in Tauris et al. (2012), Istrate et al. (2014) and Tauris et al. (2015).

We assume the binary to be losing orbital angular momentum via gravitational radiation only (no significant magnetic braking is expected to occur because the He-star does not have an outer convective zone; Podsiadlowski et al., 2002). The binary shrinks its orbit due to gravitational wave radiation until the He-star fills its Roche lobe and initiates mass transfer. For the first 3.1 Myr of the simulation, before Roche-lobe overflow (RLO) starts, the donor is burning He in a convective core. After 3.1 Myr, the C/O core (which is not massive enough to fuse heavier elements) becomes degenerate, and He-burning continues in the radiative shell (Figure 5.13a). Due to the subsequent radial expansion of the star, mass transfer is initiated after 3.25 Myr (Case BB RLO; Tauris et al., 2015), at a rate of $\dot{M}_2 \approx 10^{-6} - 10^{-5}\,M_\odot \mathrm{yr}^{-1}$ (Figure 5.13c). In this

super-Eddington regime, excess material is blown away from the vicinity of the black hole (isotropic re-emission). This rapid mass loss leads to an almost naked C/O core (with a tiny $0.04\,M_\odot$ surface layer of He) which will detach after 1.5×10^5 yr and produce a C/O white dwarf. The outcome is thus a $1.062\,M_\odot$ C/O white dwarf orbiting a $5.016\,M_\odot$ black hole with $P_{\rm orb} = 0.830$ days (19.9 hr). As a result of gravitational wave radiation, this system will become an ultracompact X-ray binary (i.e. a progenitor to X9) after 9.81 Gyr (less than the age of the cluster, ≈ 11 Gyr; Gratton et al., 2003), thereby quickly losing the leftover white dwarf surface layer of He. Adjusting the initial orbital period can lead to an ultracompact X-ray binary after 1–13 Gyr. Hence, we find that an initial binary made up of a black hole and a He-star can lead to the formation of an ultracompact X-ray binary with a C/O white dwarf donor within the lifetime, or in the recent history of 47 Tuc. This formation path need not necessarily have been followed by X9 (if it is a black hole), and we only suggest it as a possible scenario. It is also possible that any initial binary would exchange energy with surrounding stars/binaries via dynamical interactions in the cluster (Ivanova et al., 2010), especially in the early stages of its evolution.

Previously, similar simulations of He-star and neutron star binaries leading to the formation of ultracompact systems have been performed (e.g. van Haaften et al., 2013; Heinke et al., 2013). In certain cases, these calculations show rapid contraction of the orbit while the He-star is transferring mass and burning He, only switching to orbital expansion at later stages. This is in contrast to our simulation, where the binary undergoes orbital expansion at all stages of the mass transfer (Figure 5.13b). This difference is the result of applying different component masses and initial orbital periods. In particular, van Haaften et al. (2013) followed low mass ($0.35 - 1.0\ M_\odot$) He-stars transferring mass to a $1.4\ M_\odot$ neutron star and assuming initial orbital periods between 17–48 min. In our simulation, the component masses are $2.0\ M_\odot$ and $5.0\ M_\odot$, and the initial orbital period is 96 min. Despite the larger masses, the long orbital period strongly decreases the efficiency of loss of orbital angular momentum from gravitational wave radiation. Also, a more massive He-star evolves much faster, and the initial mass ratio in our case is $q = 0.4$, whereas in the work of van Haaften et al. (2013) the applied mass ratio was often closer to unity. Lastly, our He-star initiates RLO while it is still undergoing He shell burning (hence, a (sub)giant donor star), and thus the evolutionary time-scale during mass transfer is relatively small. All of these effects will cause our system to widen once RLO starts.

Occurrence rates of ultracompact black holes in globular clusters

We can also consider the plausibility of the black hole scenario in light of the already existing evidence for at least one ultracompact X-ray binary with a black hole primary observed as a ultraluminous X-ray source (ULX) in an extragalactic globular cluster.

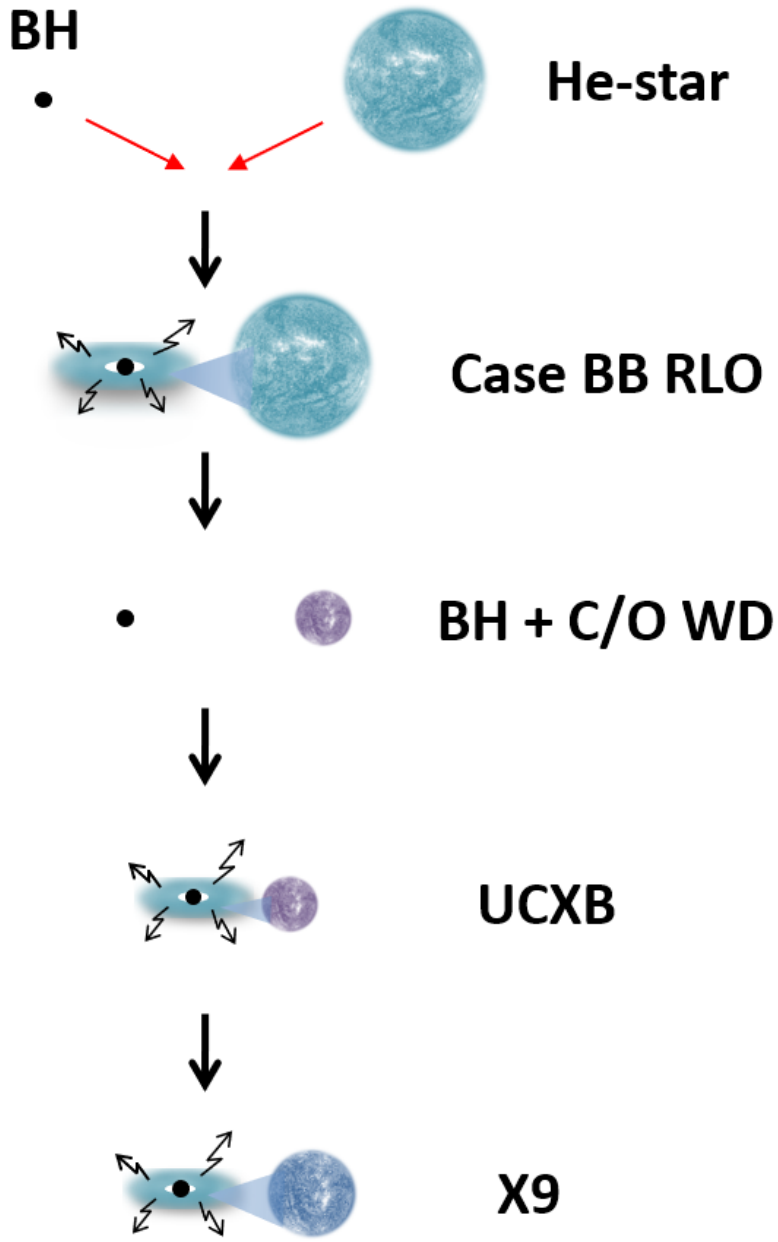

Figure 5.12: Illustration showing the evolutionary sequence of a 2.0 $M_{\odot}$ He-star in orbit with a 5.0 $M_{\odot}$ black hole (BH). The binary loses angular momentum via gravitational wave radiation, leading to case BB mass transfer (after core He is exhausted, before carbon ignition), and eventually to a black hole and C/O white dwarf (WD) binary. The next stage of this system is an ultracompact X-ray binary (UCXB) resembling X9.

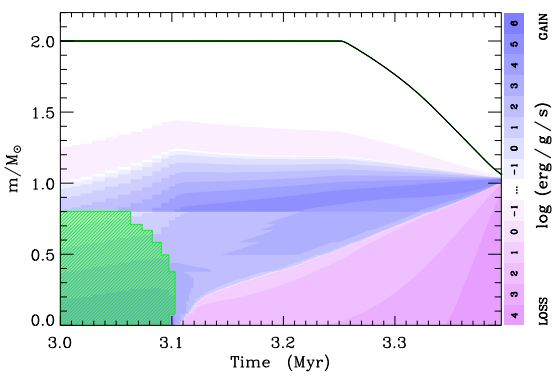

(a) Kippenhahn diagram

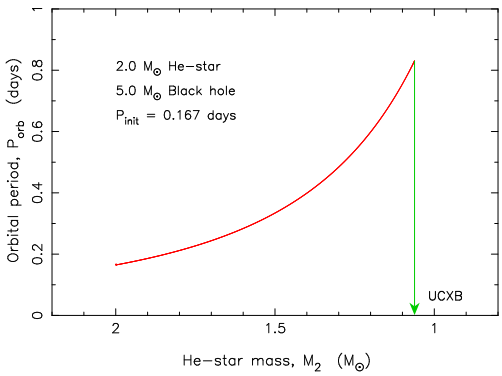

(b) Evolution of the orbital period

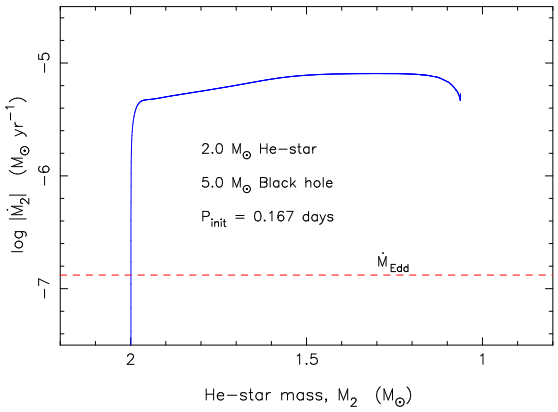

(c) Evolution of the mass-transfer rate

Figure 5.13: The evolution of a 2.0 $M_\odot$ He-star + 5 $M_\odot$ black hole binary, starting at an initial orbital period $P_{\rm orb} = 0.167$ d. (a) Kippenhahn diagram (mass coordinate against time) of the donor. The color bar shows the rate of nuclear energy generation, which can either be positive (purple), or negative (pink). At the beginning of the simulation, He burns in a convective core (green area) surrounded by a radiative shell. Once central He is exhausted, the star continues to burn He in a shell (purple) around the degenerate C/O core (pink), driving the star to expand, leading to RLO (starting at 3.25 Myr). (b) Orbital expansion as a result of mass transfer from the donor star (evolution from left to right). (c) Mass-loss rate from the donor star ($\dot{M}_2 \approx 10^{-6} - 10^{-5}\ M_\odot\ {\rm yr}^{-1}$) exceeding the Eddington accretion rate of the black hole ($\dot{M}_2 \approx 10^{-7}\ M_\odot\ {\rm yr}^{-1}$, red dashed line), leading to isotropic re-emission of matter from the system.

Although at least some ULXs ($L_X > 10^{39}\,\mathrm{erg}^{-1}$) host neutron stars (Bachetti et al., 2014; Israel et al., 2017a,b), the majority of globular cluster ULXs may still host black hole primaries. This is because ULXs powered by accretion on to neutron stars are thought to require high surface magnetic fields ($B > 10^{11}$ G; Ekşi et al., 2015; Tsygankov et al., 2016; King and Lasota, 2016). In globular clusters, however, pulsars typically have much weaker magnetic fields ($B \approx 10^9$ G), with only four out of >140 known globular cluster pulsars reaching $B \approx 10^{11} - 10^{12}$ G (Boyles et al., 2011).

The best candidate for a black hole with a white dwarf donor in a ULX is XMMU J122939.7+075333 (Maccarone et al., 2007), associated with the globular cluster RZ 2109 in the Virgo galaxy NGC 4472 (Rhode and Zepf, 2001). It has an X-ray luminosity of about 5×10^{39} erg s^{-1} and shows clear evidence for strong forbidden oxygen emission lines, with stringent upper limits for H or He emission lines (Zepf et al., 2007, 2008; Steele et al., 2014). The lack of any other globular cluster in NGC 4472 with similar emission lines (Peacock et al., 2012) strongly argues against anisotropic emission being responsible for the brightness of the source, since the emission from the forbidden lines should be isotropic. Another system, CXOU J1229410+075744, in the same galaxy, shows variability of a factor of four with a peak luminosity of about 2×10^{39} erg s^{-1}, but is persistent over a time-scale of more than a decade (Maccarone et al., 2011). This persistently bright emission could be explained through either a long period binary with a highly evolved donor (e.g., Truss and Done, 2006), or an ultracompact binary. Another candidate is CXOKMZ J033831.7–353058 in NGC 1399 in the Fornax cluster (Shih et al., 2010).

It is not straightforward to determine the number of globular clusters observed by Chandra in which one could have established the presence of a source which varies by significantly more than the Eddington luminosity of a neutron star. However, simply by adding the numbers of clusters detected by *HST* in the Virgo and Fornax cluster surveys, we are likely to incur uncertainties no larger than the uncertainties that come from basing our population statistics on the mere presence of XMMU J122939.7+075333. In the Virgo cluster, there are about 13,000 globular clusters in *HST* data (Jordán et al., 2009), and in the Fornax cluster survey, there are about 9,000 (Jordán et al., 2015). To be clear, there are other galaxies which have been well observed by Chandra for which there are catalogues of globular clusters from either *HST* or ground-based data; and there are, as well, wider-field ground-based data for globular clusters in Virgo. On the other hand, many of the smaller Virgo Cluster galaxies have X-ray data only from the AGN Multiwavelength Survey of Early-type galaxies in the Virgo cluster (AMUSE-Virgo) project (Gallo et al., 2008b). It is reasonable to estimate that about 20,000 clusters have been well-enough observed by Chandra to allow for the identification of strong ultracompact black hole candidates, and that ∼1 of them has been discovered. Thus, we can estimate that at least 10^{-5} of clusters contain bright ultracompact black hole

X-ray binaries, and use this number to determine whether it is plausible to find a much fainter one in the Milky Way's globular cluster system.

Next, we look at the evolutionary time-scales of ultracompact black hole X-ray binaries (van Haaften et al., 2012). If we take XMMU J122939.7+075333 to have an orbital period of about 5 minutes, as would be expected given its X-ray luminosity, its lifetime should be just under 10^5 years. For a source with an orbital period of half an hour, the expected characteristic age is just under 10^8 years. There should, thus, be ≈ 1000 black hole X-ray binaries at an orbital period of half an hour for every one at an orbital period of 5 minutes. In turn, assuming the 10^{-5} fraction from above, and the number of globular clusters in the Milky Way (> 100; Harris, 1996) we expect $\sim$1 Milky Way cluster to have a black hole X-ray binary at an orbital period of less than half an hour. It is thus reasonable that we have seen such an object. Furthermore, assuming that these systems formed mostly relatively early in the lifetimes of the clusters ($\sim 10^{10}$ years), we may expect $\sim$ 100 times as many ultracompact black hole X-ray binaries at any orbital period (i.e. of order one per cluster, but with a higher concentration expected in the clusters with higher stellar interaction rates). Similarly, Ivanova et al. (2017) estimate globular clusters should contain about one faint black hole – white dwarf binary per $10^5\,M_\odot$. These additional systems should be at longer periods, be considerably fainter, and exhibit transient outbursts. In quiescence, some of them could be nearly indistinguishable from cataclysmic variables, except in observations using radio emission or optical/UV spectroscopy, and they may easily be among the sources classified as quiescent dwarf novae in existing Chandra work. However, the majority of these old, longer-period ($\sim$2 h) systems might be too faint to be detectable.

5.4 Conclusions

We acquired a broadband optical (3,000–10,000 Å) spectrum of X9, finding a blue continuum with no identifiable emission (or absorption) lines. In particular, we place a 3σ upper limit on the H α line in emission of $-\mathrm{EW} < 14$ Å. This limit is below that of H-rich X-ray binaries observed at similar X-ray luminosities ($L_{2-10\,\mathrm{keV}} = 10^{33} - 10^{34}$ erg s^{-1}), which typically have $-\mathrm{EW}_{\mathrm{H}\,\alpha} \sim 50$ Å. This result strengthens the evidence for a C/O white dwarf donor as identified by Bahramian et al. (2017).

Performing a timing analysis on archival photometric V and I-band data, we find the most significant period is $P \approx 7$ days, consistent with the superorbital period suggested by Bahramian et al. (2017) based on X-ray data. In these bands there is no evidence for any signal at the orbital period. Timing analysis of archival FUV data returns one marginally significant period (at less than 3σ significance): 27.2 min. This value is close to, but not equal to the 28.2 min orbital period identified by Bahramian et al. (2017) (who estimated a significance of $> 5\sigma$ for this period).

The superorbital modulations are weak in the optical bands (5% semi-amplitude), and strong in the X-ray band (factor of 3 semi-amplitude), suggesting the occultation of an extended X-ray corona is probably driving this variability. If this interpretation is correct, the intrinsic luminosity of X9 could be stable at a level of $L_{2-10\,\mathrm{keV}} = 10^{34} - 10^{35}\,\mathrm{erg\,s^{-1}}$. In this case, its radio luminosity makes a neutron star a more likely interpretation. Otherwise, it would be the radio-faintest known black hole at this X-ray luminosity. The C IV doublet and the broadband spectrum indicate that if X9 is a neutron star, it is observed at a high inclination ($i > 60°$) and the optical emission is dominated by the jet and disc. For a black hole, the emission would be dominated by reprocessing of X-rays by the disc, and is seen at a low inclination ($i < 30°$). While the seven-day superorbital modulation can be explained by the precession of the disc due to tidal torques exerted by the companion star to a neutron star, we cannot find a way to produce the same modulation for a black hole. The estimate for the inclination angle based on the presence of orbital modulations in the X-ray band ($i \gtrsim 60°$, favouring a neutron star) is slightly at odds with the estimation based on the X-ray spectrum ($i \lesssim 45°$ to $i \lesssim 68°$ depending on the model, favouring a black hole). The hardness of the X-ray spectrum is easier to explain in the context of a black hole. Presently, not all the observables of X9 can easily be explained by either a neutron star or black hole.

While we know of neutron star ultracompact systems and theoretical pathways to produce such objects, the latter pathways have not been proposed for black hole ultracompacts. We therefore performed binary evolution calculations of a 2.0 $M_\odot$ He-star and a 5.0 $M_\odot$ black hole binary, to show that if X9 does host a black hole, such a system could indeed be produced in a globular cluster. Stronger still, Church et al. (2017) found that based on hydrodynamic simulations, C/O white dwarf donors in globular clusters can form X-ray binaries with stable mass transfer only if their primaries are black holes.

The easiest way to confirm the nature of this system would be if it went into a bright outburst; pulsations or thermonuclear bursts would then verify a neutron star nature. Otherwise, phase-resolved FUV spectroscopy, through the C IV or Mg II lines, might be used to solve the system parameters if they arise from the heated face of the donor. Unfortunately, the Bowen fluorescence lines (driven by He II emission) typically used for this purpose will not be produced in a C/O donor. Another way to confirm the parameters of X9 might be the detection of its gravitational waves. The strain amplitude for a binary with a circular orbit is given by (Nelemans et al., 2004b):

$$h = 5 \times 10^{-22} \left(\frac{\mathcal{M}}{M_\odot}\right)^{5/3} \left(\frac{P_{\mathrm{orb}}}{1\mathrm{hr}}\right)^{-2/3} \left(\frac{d}{1\mathrm{kpc}}\right)^{-1}, \tag{5.5}$$

where $\mathcal{M} = (M_1 M_2)^{3/5}/(M_1 + M_2)^{1/5}$ is the chirp mass of the system. For $M_1 = 8\,M_\odot$, $M_2 = 0.016\,M_\odot$, $h = 1 \times 10^{-23}$. At the gravitational wave frequency $\nu_{\mathrm{GW}} = 1.2 \times$

10^{-3} Hz (twice the orbital frequency), X9 will not be detectable to the gravitational wave detector *LISA* even if it hosts a black hole, as it falls below the Galactic foreground noise from double white dwarfs (Nelemans et al., 2004b).

5.A Potential mechanisms behind the superorbital modulation

5.A.1 Superhumps

In cataclysmic variables, the accretion disc is often tidally unstable, becoming eccentric and precessing. The periodically variable tidal dissipation in the outer parts of the disc gives rise to light curve modulations known as superhumps, which have time-scales slightly longer (by a few percent) than the orbital period (Whitehurst, 1988; Hirose and Osaki, 1990). Similar to cataclysmic variable systems, the 28.2 min period could be related to the superhump mechanism (as already noted by Bahramian et al., 2017), and the 27.2 min period could be the orbital period. Superhumps have also been proposed for a number of X-ray binaries like 4U 1820–30 (Wang and Chakrabarty, 2010) and XB 1916–053 (Retter et al., 2002), both ultracompacts. Calculating the period excess as is typically done for superhumps, $\epsilon = (P_{\rm sh} - P_{\rm o})/P_{\rm o}$, we obtain $\epsilon \approx 0.04$. Taking the calibration of Patterson et al. (2005) for superhumps in cataclysmic variables, $\epsilon = 0.18q + 0.29q^2$, we estimate $q = 0.17$ for X9 (if the same relationship holds for all mass ratios in X-ray binaries), which is much larger than the expected $q < 0.01$. If the donor mass is $M_2 \approx 0.02\,M_\odot$, $q = 0.17$ gives $M_1 \approx 0.1\,M_\odot$, much lower than expected for a neutron star. Instead, the orbital period could be longer than the superhump period (negative superhumps). In this case, observations (Retter et al., 2002; Olech et al., 2009) and simulations (Wood et al., 2009) show that for very small q values ($q \lesssim 0.1$), the negative and positive superhumps should have similar values. We therefore rule out the 27.2 min signal as a classical superhump.

Superhumps typically seen in cataclysmic variables are due to the 3:1 resonance (for each orbit of the secondary, the material in the disc orbits three times), and are encountered in systems with mass ratio $q \lesssim 0.25$. For more extreme mass ratios ($q \lesssim 0.025$), the 2:1 resonance can be reached, because the disc can be larger (as a fraction of the orbital separation; Whitehurst and King, 1991).

In quiescent systems with mass ratios $q \lesssim 0.25$, accretion discs are thought to extend up to the 3:1 resonance radius (Hirose and Osaki, 1990). During outbursts, however, the outer disc can expand to reach the tidal truncation radius (Paczynski, 1977; Papaloizou and Pringle, 1977; Whitehurst, 1988). In addition, the discs of systems with extreme mass ratios ($q \lesssim 0.01$) in quiescence are likely to occupy a large fraction of the Roche

lobe (extending beyond the 2:1 resonance radius), while still being constrained by it (Priedhorsky and Verbunt, 1988; van Haaften et al., 2012).

In X9, for a donor mass $M_2 = 0.010-0.016\,M_\odot$, the value $P_{\rm long}/P_{\rm orb} = 357$ requires $M_1 = 1.8-2.8\,M_\odot$ if the long period is caused by precession of the 2:1 resonance radius (Pearson, 2003). The beat (long) period between the superhump and orbital periods is not usually observed in cataclysmic variables. The large amplitude of the long-period modulation in X-rays is therefore surprising, but could arise in some circumstances. For example, an elliptical disc with a given aspect ratio H/R will reach maximum thickness at its apoapsis, and minimum thickness at periapsis (White and Holt, 1982; Osaki, 1985). If the X-ray emitting corona is of similar size to the maximum disc thickness, the fraction occulted by the edge of the disc will vary sinusoidally on the precession period.

5.A.2 Other tidal effects

To check if the superorbital modulation could be caused by nodal precession from tidal forces, we use the relationship of Larwood (1998, Equation 5), between the ratio of orbital to precession periods, and system parameters:

$$\frac{P_{\rm orb}}{P_{\rm long}} = \frac{3}{7}\beta^{3/2}\frac{q\,r_{\rm L}^{3/2}\cos\delta}{(1+q)^{1/2}}, \tag{5.6}$$

where $P_{\rm long}$ is the precession period, β is the disc size as a fraction of the primary's Roche lobe, δ is the tilt between the planes of the disc and the orbit. The minimum precession period occurs when the inner and outer disc are aligned ($\delta = 0$), for the maximum mass ratio ($q = 0.016/1.4$). We find that for $P = 28.2\,$min and $\beta = 0.9$ (van Haaften et al., 2012), the minimum nodal precession period is $P_{\rm long} \gtrsim 7.8\,$d, only slightly larger than the measured 7 d period. This suggests that tidal precession could be the source of the superorbital modulation if the primary is a neutron star (similar to the 2:1 superhump interpretation above). The requirement of a small misalignment angle, and the large amplitude of this modulation, suggest a nearly edge-on view of the system, as suggested also by the C IV doublet in the case of a neutron star.

Wijers and Pringle (1999) provide descriptions for forced precession (by tidal forces from the donor star) and for radiatively-driven precession. Their conclusion is that the superorbital periods observed in X-ray binaries can be explained by radiatively driven precession (with a factor of 2 scatter between the predicted and observed periods, owing to unknowns in system parameters). In the case of X9, however, the low mass ratio ($q < 0.02$) and low X-ray luminosity (relative to persistent and soft states) suggest tidal disc precession is more likely, unless X9 is an ADC source. (Ogilvie and Dubus, 2001; Kotze and Charles, 2012). As described by Ogilvie and Dubus (2001), radiation-

driven warping can only be important in soft X-ray transients during outbursts. Using the formulations of Wijers and Pringle (1999), the period associated with forced tidal precession respectively is given by:

$$\left(\frac{P_{\rm long}}{1\ {\rm d}}\right) = 7.64 \times 10^{-6} \pi \left(\frac{P_{\rm orb}}{1\ {\rm min}}\right)^2 \left(\frac{1+q}{q}\right) M_{1.4}^{1/2} R_{11}^{-3/2}, \tag{5.7}$$

where $M_{1.4}$ is the primary mass in units of 1.4 $M_\odot$, and R_{11} is the disc radius in units of 10^{11} cm. We find $P_{\rm long} \approx 190$ days for a black hole and $P_{\rm tidal} = 40$ days for a neutron star.

Summarizing, we find the tidal precession model of Larwood (1998) may be able to explain the superorbital period in X9 for an edge-on neutron star.

5.A.3 Lense-Thirring precession

In the vicinity of neutron stars and black holes, accretion discs experience general relativistic frame-dragging effects. In particular, the Lense–Thirring effect (Lense and Thirring, 1918) is the nodal precession of an accretion disc due to the spin of the accreting object. When the orbital plane of an X-ray binary is tilted with respect to the spin axis of an accreting compact object (as would be expected in a dynamically-formed system), the accretion disc can warp, so that the outer disc lies in the orbital plane, but the inner disc is aligned with the spin axis of the compact object (Bardeen and Petterson, 1975). When this occurs, the Lense-Thirring precession of the inner disc may be observed through modulations in the X-ray light curve of the binary.

For a disc that precesses like a solid body, the Lense–Thirring precession is given by Fragile et al. (2007, their Equation 43). For constant surface density, and $R_{\rm out} \gg R_{\rm in}$:

$$P_{\rm long} = \frac{\pi G M_1}{5c^3} \frac{r_{\rm out}^{\frac{5}{2}} r_{\rm in}^{\frac{1}{2}}}{a}, \tag{5.8}$$

where in this case a is the dimensionless spin of the black hole, $r_{\rm out}$ and $r_{\rm in}$ are the outer and inner disc radii in units of gravitational radii. Taking a slow-spinning $a = 0.1$, 8 $M_\odot$ black hole, and $r_{\rm in} = 500\, r_{\rm g}$, Equation 5.8 requires $r_{\rm out} \approx 1600\, r_{\rm g}$ for the precession period to match the observed $P_{\rm long} = 7$ days. The transition between the inner, precessing disc, and outer disc (the Bardeen–Petterson radius) could occur at a radius of up to a few hundred gravitational radii (Bardeen and Petterson, 1975; Nelson and Papaloizou, 2000; Fragile et al., 2001). We find, however, that the precessing disc in our test case needs to extend beyond $10^3\, r_{\rm g}$, where the misalignment between the disc plane and the orbital plane is likely to be very small (a few degrees), regardless of the spin axis of the black hole. Other warping mechanisms or a neutron star are equally unlikely to provide a larger tilt; low-mass X-ray binaries are only prone to radiation

warping during outbursts (Ogilvie and Dubus, 2001). For the X-ray superorbital period to have the large amplitude that is observed, the disc would need to be seen nearly edge-on. As discussed in Section 5.3.5, however, the double-peak separation of the C IV doublet is incompatible with a black hole system seen edge-on.

5.A.4 Hierarchical triple

A hierarchical triple system can drive the eccentricity and inclination of the inner binary to oscillate via the Kozai mechanism (Kozai, 1962). This mechanism is thought to be the main channel for creating black hole – white dwarf binaries in globular clusters (Ivanova et al., 2010) and can explain the superorbital modulations of some ultracompact X-ray binaries (Zdziarski et al., 2007; Maccarone et al., 2010). The Kozai mechanism could explain the difference between the short optical and X-ray periods, and the superorbital modulation.

In the core of 47 Tuc ($\sigma = 11\,\mathrm{km\,s^{-1}}$), double neutron star binaries with semi-major axes smaller than $\approx$ 20 A.U. ($P_{\mathrm{orb}} < 50$ years; angular separation $< 0.01''$) are stable against dynamical disruption by neighbouring cluster stars (Hills, 1984), but are susceptible to chaging their eccentricities from fly-by encounters. Low mass main-sequence stars are less likely as a third body because they require shorter periods, making the triple less stable. The maximum mass for a main-sequence star that can fit in within the broadband spectrum of X9 is $M_3 \approx 0.5\,M_\odot$, but the third companion could instead be a heavy white dwarf or a neutron star. This scenario is not unlikely; Giersz and Heggie (2011) find that half of the mass in the core of 47 Tuc is likely to be made up of white dwarfs. According to the globular cluster simulations of Ivanova (2008, see their Table 1), the fractions of hierarchical triples with main sequence stars and white dwarfs as outer companions are 79% and 20% respectively. Theoretically, ≈5% of all binaries in the core of a globular cluster as dense as 47 Tuc are expected to form stable hierarchical triples in one Gyr (Ivanova, 2008).

For XB 1916–053, such a system was invoked to explain a 1% difference between the optical and X-ray periods (50 min) seen in conjunction with a 199 day superorbital period[2](Grindlay et al., 1988; Chou et al., 2001). In that case, the beat between the optical and X-ray periods is the period of the outer companion. In the case of X9, the outer companion would have a period of $P_3 \approx 13$ hours (the beat between the optical 27.2 min and X-ray 28.2 min). For $M_2 \ll M_1$, and a nearly circular inner orbit, the Kozai period is approximately $P_{\mathrm{long}} \approx P_3^2 (M_1 + M_3) M_3^{-1} P_1^{-1}$ (Mazeh and Shaham, 1979; Ford et al., 2000). For $P_1 = 28.2$ min and $P_3 = 13$ hours, we obtain a lower limit for the Kozai period of $P_{\mathrm{long}} \gtrsim 15$ days (for $M_3 \gg M_1$), in contrast to the found

[2]It was later shown that negative superhumps could explain the optical–X-ray period excess in XB 1916–053, without the need to invoke a third body (Retter et al., 2002).

period of $P_{\rm long} \approx 7$ days. This argues against the Kozai mechanism as the source of period excess between the optical and X-ray periods, and of the superorbital period. Disregarding the short FUV period (which has low significance), the Kozai mechanism can still explain the superorbital period as a variation of the inclination angle of the inner binary (and thus of the disc). Again, this scenario requires an edge-on view of the system, making a neutron star more likely.

Chapter 6

Case studies

In Chapter 3, we found the globular clusters NGC 6397, Terzan 5, NGC 6624, Terzan 1 and Terzan 6 contain a significant excess of radio sources above the background. In addition to these, NGC 6652 and NGC 6352 may contain the largest excesses in our sample (3–5 sources, albeit not significant at 3σ). By preliminarily cross-matching our radio source catalogue with published *Chandra* catalogues, we have identified a number of sources with emission in both bands. All these sources reside in the aforementioned clusters, as well as in NGC 104 and NGC 6388. In this chapter I investigate the multi-wavelength properties for some of the radio sources in these clusters.

In Terzan 5, the most significant excess (3 sources within $2R_c$) can be attributed to known pulsars and the neutron star X-ray binary EXO 1745–248, which was in outburst at the time (Chapter 3). The one-source excess in NGC 6624 is due to the well-known neutron star X-ray binary 4U 1820–30 (e.g, Díaz Trigo et al., 2017). In NGC 104, the radio–X-ray match is X9, which I discussed in Chapter 5. For the rest of this chapter, I focus on the other clusters, which have not been as well studied previously.

6.1 NGC 6652

By cross-matching the MAVERIC source catalogue with the X-ray catalogue of Stacey et al. (2012) for NGC 6652, we have identified three sources with emission in both bands. These are the X-ray sources B, E and F (Figure 6.1). The brightest X-ray source in the cluster, NGC 6652 A, is a neutron star, but remains undetected in our radio images. Stacey et al. (2012) find NGC 6652 B to be a luminous, variable, hard–spectrum ($\Gamma = 1.3 \pm 0.1$) X-ray binary, but the natures of NGC 6652 E and F are less well known. Given their faintness in the X-ray band, their spectra could not be well constrained (for E, $\Gamma = 2.2^{+1.1}_{-0.8}$, and for F, $\Gamma = 1.7^{+1.1}_{-0.5}$). They do not appear to be variable in the X-ray band (Stacey et al., 2012). In the radio band, we find E and F to have spectral indices $\alpha = +0.8 \pm 0.3$ and $\alpha = -0.7 \pm 0.6$ respectively. These properties

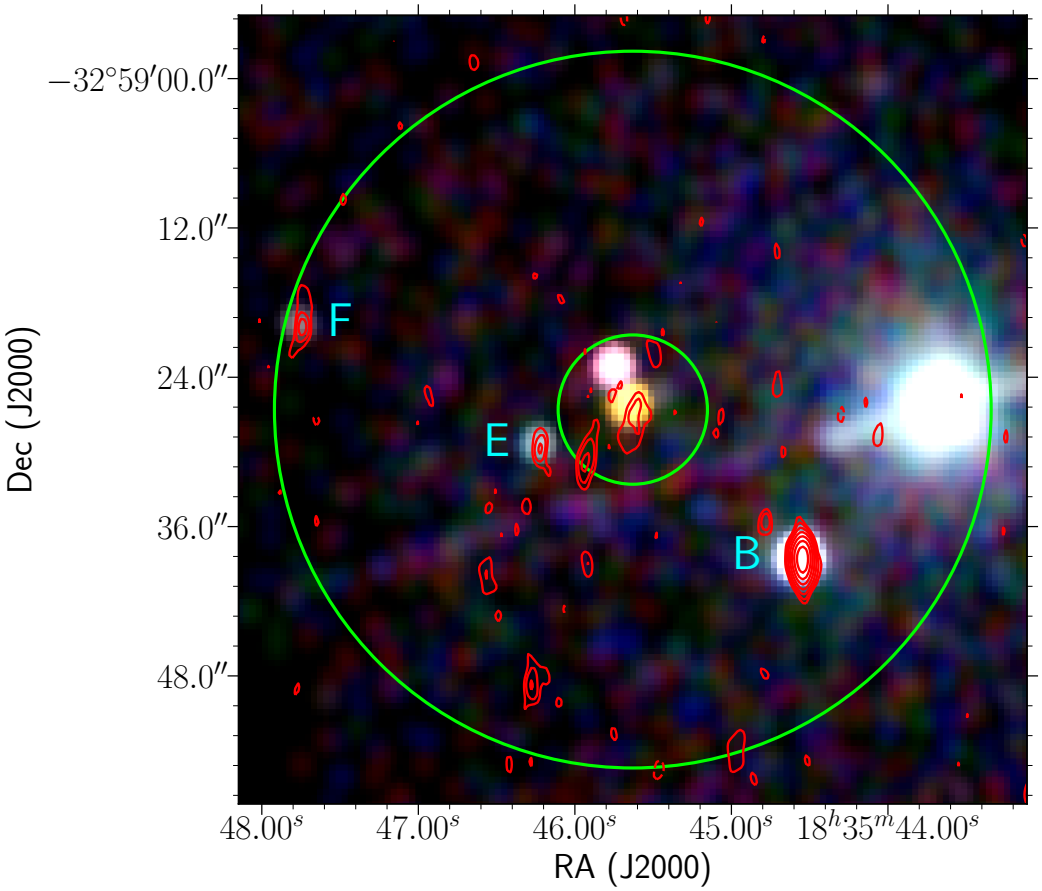

Figure 6.1: A colour X-ray image of the globular cluster NGC 6652 (red: 0.3–1 keV, green: 1–2 keV, blue: 2–7 keV), overlaid with radio contours at 5.5 GHz (red, at levels $\sqrt{2}^{\mathrm{n}} \times$ rms, where $n = -2, 2, 3, \ldots$, and rms $= 3.2\,\mu$Jy). The concentric green circles represent the core and half-light radius of the cluster. The brightest radio source in the cluster is coincident with the second-brightest X-ray source, NGC 6652 B. NGC 6652 E and F also have radio counterparts, and there is a hint of emission from the core of the cluster. The brightest X-ray source is NGC 6652 A, a known neutron star X-ray binary.

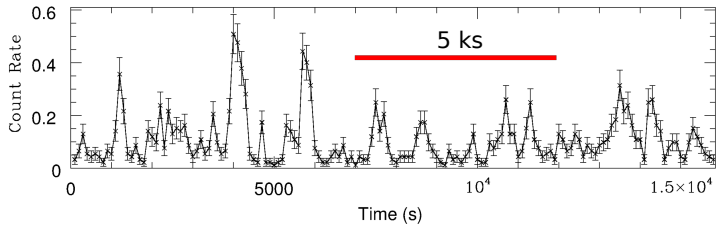

(a) NGC 6652 B

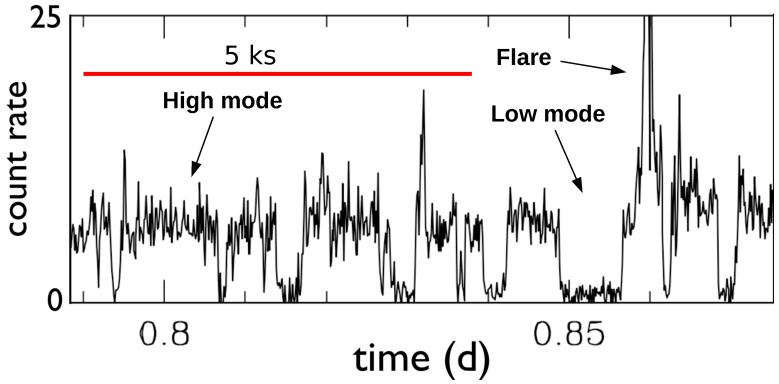

(b) PSR J1023+0038

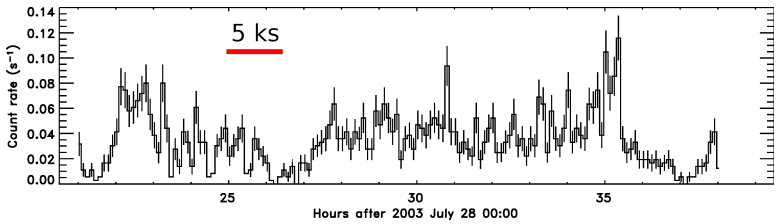

(c) V404 Cyg in quiescence

Figure 6.2: X-ray light curves of (a) NGC 6652 B (Stacey et al., 2012), (b) the tMSP J1023+0038 (Bogdanov et al., 2015), and (c) V404 Cyg, a black hole X-ray binary (Hynes et al., 2004). NGC 6652 B is more variable than V404 Cyg, but it does not have a bimodal behaviour like J1023+0038.

make these sources consistent with X-ray binaries. For the rest of this section, we focus on NGC 6652 B.

NGC 6652 B has an inverted spectral index $\alpha = 0.38 \pm 0.13$ ($S_\nu \propto \nu^\alpha$), with an average flux density of $76 \pm 4\,\mu$Jy at 9 GHz, corresponding to a luminosity of $10^{29}\,\mathrm{erg\,s^{-1}}$. At a distance of 10 kpc, it has an X-ray luminosity of $\approx 2 \times 10^{34}\,\mathrm{erg\,s^{-1}}$ (the second brightest X-ray source in its host cluster; Stacey et al., 2012). The radio properties of NGC 6652 B have immediate implications for the nature of the X-ray binary. The only known sources at this X-ray luminosity that show flat to inverted continuum radio emission at this luminosity are black hole X-ray binaries or tMSPs.

NGC 6652 B is highly variable in the X-ray (Figure 6.2a; Coomber et al., 2011; Stacey et al., 2012) and optical bands (Deutsch et al., 2000; Engel et al., 2012), changing flux by a factor of a few on minute timescales. Over 20 years, the source has been

detected at similar average luminosities by *ROSAT* HRI in 1994 (Coomber et al., 2011), *Chandra*/HRC in 2000 (Heinke et al., 2001), and *Chandra*/ACIS-S in 2008 (Coomber et al., 2011) and 2011 (Stacey et al., 2012). The cause of its high short-timescale variability is currently unknown, but the low intrinsic absorption rules out obscuration effects (Stacey et al., 2012); this suggests a fluctuating inflow. Non-simultaneous observations (separated by 4 years) place NGC 6652 B on the radio–X-ray correlation for accreting black holes. To ensure this position on the correlation is not spurious due to its high variability, we also requested simultaneous radio and X-ray observations with the VLA (10 GHz) and *Chandra*. Because of the proximity to NGC 6652 A (X1832–330), a bright, $\approx 10^{-10}\,\mathrm{erg\,cm^{-2}\,s^{-1}}$ X-ray source only $\approx 17''$ away from NGC 6652 B, *Chandra* is the only X-ray telescope capable of resolving the spectrum and variability of NGC 6652 B. The VLA is required for the short-timescale sensitivity and snapshot imaging capability. In this simultaneous dataset, we found the radio and X-ray light curves to be highly variable. Considering the mean luminosities during this strictly simultaneous observation, this source maintains its position on the radio–X-ray correlation for hard-state black holes (Figure 6.11). By inspecting their light curves, the radio and X-ray emission do not appear to be well correlated (Figure 6.3). To measure any delay between the radio and X-ray light curves, we performed a cross-correlation test between the two bands. For this purpose, we used a modified version of the algorithm of (Peterson et al., 1998), implemented in the software package `PyCCF` (Sun et al., 2018). We assessed the significance of any putative delays via randomisation of the X-ray light curve (keeping the fluxes of each measurement, and randomly permuting their observation times). Errors on measured time delays are measured via random subsample selection and flux randomisation. 10,000 trials were used to estimate significances and errors. We show the cross-correlation function in Figure 6.4. By restricting the search to delays between -0.01 and 0.01 days, we find the most likely delay is 331 ± 100 s. This delay is larger than the time resolution of the observations (100 s), and corresponds to a negative correlation coefficient, indicating that for this source, the X-rays may be lagging and may be anti-correlated to the radio emission.

Following the radio detection, we acquired optical spectra with the Goodman spectrograph (Clemens et al., 2004) mounted on the SOAR 4 m telescope. These show double-peaked Balmer lines, which prove that the object is an accreting binary, and a radial velocity member of the globular cluster, but it also reveals remarkable variations. On a time scale of hours, it switches from an accretion-dominated spectrum with double-peaked emission lines of H and He to an absorption-line spectrum with no apparent emission (Figure 6.5). However, given that no periodic radial velocities were detected and the source shows no periodic photometric variability, the mass of the accretor cannot be established. Unfortunately these spectra cannot be used for flux

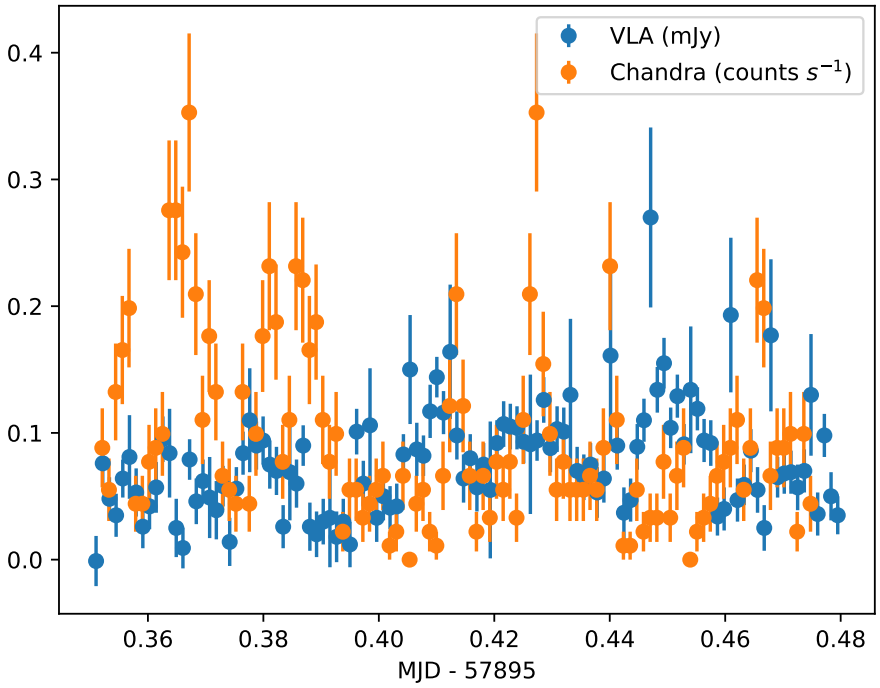

Figure 6.3: The strictly simultaneous radio (VLA) and X-ray (*Chandra*) light curves of NGC 6652 B, binned to 100 s. Both bands show large-amplitude variability on minute time scales.

measurements due to variable sky conditions.

Given the low Eddington ratio of the source ($\sim 10^{-4}$ or $\sim 10^{-5}$ of the Eddington luminosity for a neutron star or black hole), it is exceptionally unlikely there is a strong enough disc wind that could generate optical absorption lines. Instead, we consider the emission/absorption reversal to be most likely caused by the emergence of the stellar continuum and photospheric absorption lines during low-flux states of the disc. A system can switch between emission and absorption spectra in a process similar to dwarf novae. The accretion discs of some dwarf novae with luminous donors and long orbits are seen to change from emission in quiescence, to absorption during the rise to outburst, accompanied by a brightness change of several magnitudes (Clarke et al., 1984). In this case, the variability of the optical spectrum can be explained by the alternating dominance of light from the secondary star ($H\alpha$ in absorption), and accretion disc ($H\alpha$ in emission) during periods of low and high luminosity disc states, respectively. In most dwarf novae, however, the disc dominates at all stages. Such "passive" and "active" optical states have previously been observed in the quiescent light curve variations of the black hole X-ray binary A0620–00 (Cantrell et al., 2008).

Its position on the color-magnitude diagram of the cluster varies between observations and photometric bands (Deutsch et al., 2000; Heinke et al., 2001; Engel et al.,

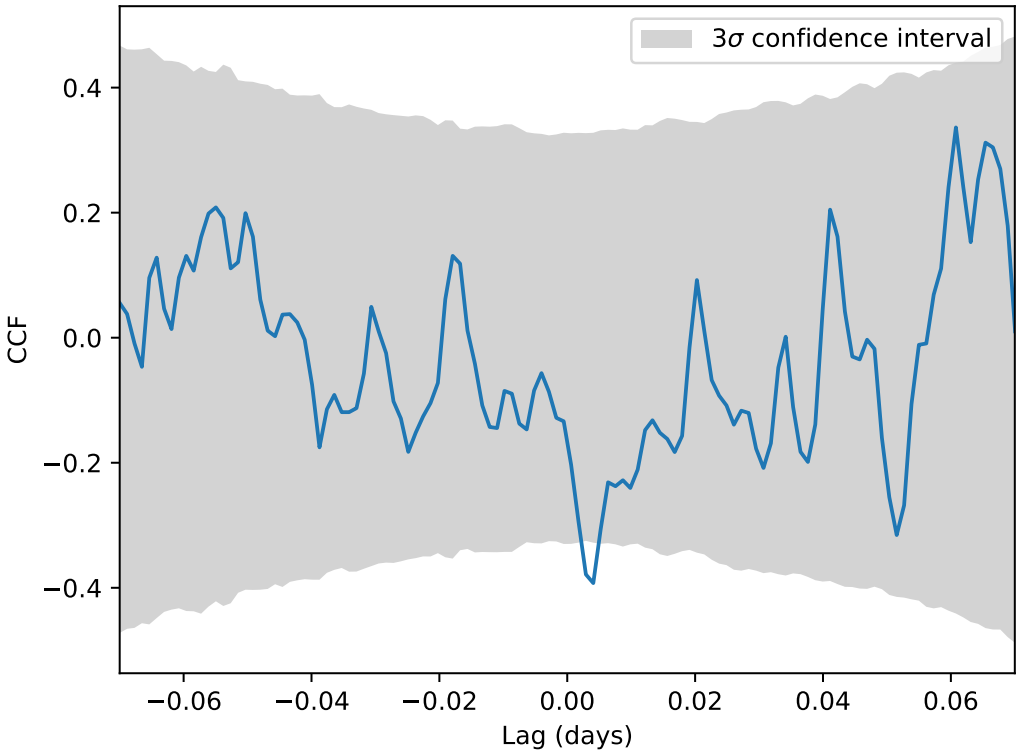

Figure 6.4: Cross-correlation function (CCF) between the radio (VLA) and X-ray (*Chandra*) bands. A positive lag corresponds to the X-rays being delayed relative to the radio. A positive (negative) CCF means the two bands are correlated (anti-correlated). A delay can be identified at 331 ± 100 s. With a marginal significance at the $\sim 3\sigma$ level, this delay could be spurious.

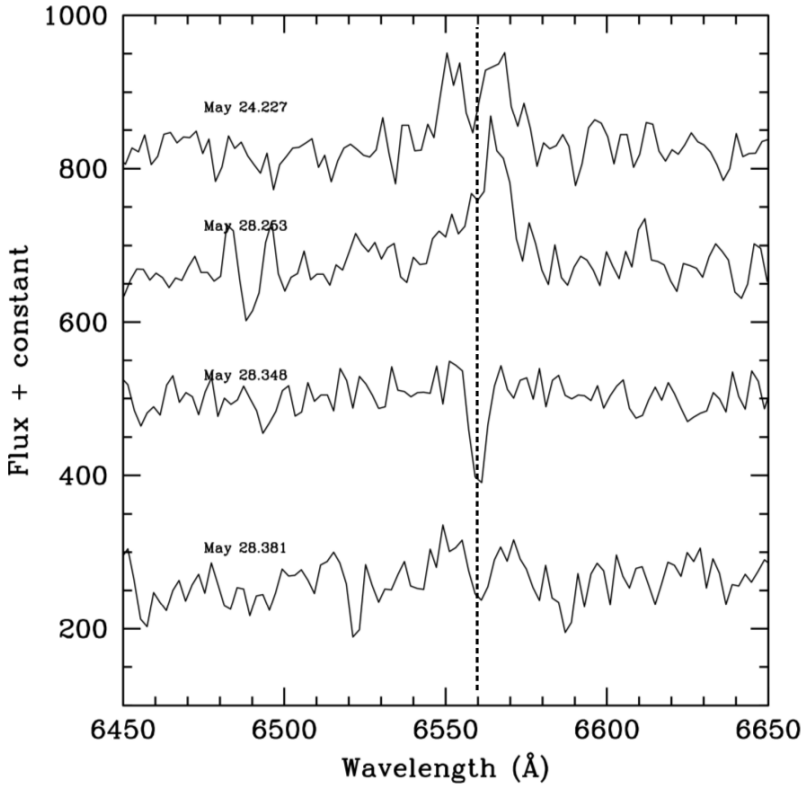

Figure 6.5: Optical spectra of NGC 6652 B in arbitrary flux units, centred on the $H\alpha$ line, showing double–peaked emission, a strong indicator of accretion from a disc. The spectrum is seen to change during the course of a night, with emission lines shifting to absorption.

2012; Skottfelt et al., 2015), with a similar physical explanation as the variable $H\alpha$ line. Assuming the secondary dominates the optical flux at the faintest point in the light curve (Deutsch et al., 2000), at $V \approx 20$, it is slightly fainter than the turnoff point of the cluster. Assuming a main-sequence star, it would be a G2 solar analogue ($M \approx 1 M_{\odot}$) just starting its evolution towards the red giant branch, which evolution might explain the Roche-lobe overflow inferred in the system from the accretion signature. Combining the period–density relation in Roche-overflow systems (Frank et al., 1987)), with the mass–radius relation for main-sequence stars (Kippenhahn and Weigert, 1990), a period–mass relation is obtained: $M \approx 0.11 P_{\rm h}$. This makes the orbital period of NGC 6652 B likely to be ∼10 hr. At this orbital period, the relation between quiescent X-ray luminosity and orbital period in X-ray binaries (Armas Padilla et al., 2014) point towards a neutron star primary, although the large uncertainties do not rule out a black hole. To constrain the nature of the accretor, first we must clearly identify the companion type. Because the SOAR data were taken in poor seeing conditions ($> 1''$), the absorption features could not be used for meaningful surface gravity or orbital period measurements. Given the highly variable nature of the source, high-quality wide-band spectra, acquired at ∼0.7″ seeing, are required to explore the nature of the system. The absorption features are a promising avenue for dynamical mass measurements in the future.

Stellar-mass black holes in the quiescent state show substantial (more than a factor of 2–10) variability in both radio and X-ray bands (e.g. Corbel et al., 2006; Miller-Jones et al., 2008; Hynes et al., 2009). NGC 6652 B shows short flares in its X-ray light curve that recur quasi-periodically every ∼ 5 minutes. Even though black hole X-ray binaries do show sub-hour variability in quiescence (e.g., Hynes et al., 2004), the timescales are usually longer than seen in NGC 6652 B (See Figure 6.2c for a typical black hole X-ray light curve).

Compared to known quiescent black hole X-ray binaries outside globular clusters, the X-ray luminosity of NGC 6652 B is slightly higher ($\approx 10^{34}$ erg s^{-1} vs $10^{30.5}$–$10^{33.5}$; Remillard and McClintock, 2006), and the spectrum is harder than expected (the photon index, $\Gamma = 1.3 \pm 0.1$ vs ≈ 2.1; Plotkin et al., 2013). At this luminosity, the photon index is also atypical of neutron stars, which in general have softer spectra than black holes at these X-ray luminosities. However, this spectrum is similar to 47 Tuc X9 ($\Gamma \approx 1.1$), which has been proposed as a candidate black hole (Miller-Jones et al., 2015; Bahramian et al., 2017), although we found that the nature of the accretor could not be definitively determined (Chapter 5).

The radio and X-ray luminosities of NGC 6652 B argue for a black hole primary. However, some neutron star systems display properties that make them difficult to distinguish from black holes. tMSP systems are variable on short time scales across the electromagnetic spectrum (Bogdanov et al., 2015; Shahbaz et al., 2015). A feature

unique and common to all four known tMSPs is their bimodal X-ray flux distribution (e.g. Bogdanov and Halpern, 2015). When they are not flaring, tMSPs switch between a high-state mode and a low-state mode (Figure 6.2b). The available *Chandra* light curves of NGC 6652 B (Figure 6.2a, and Stacey et al., 2012; Coomber et al., 2011) do not show the characteristic bimodal distribution, although this could perhaps be explained by a continuous flaring state (e.g. Tendulkar et al., 2014). The similarities between the 2008, 2011 and 2016 Chandra light curves makes this scenario unlikely because flares are usually much shorter (see Figure 6.2b). However, the variations seen in the optical spectrum (Figure 6.5) are similar to those observed in the tMSP XSS J12270–4859, which switches from emission to no emission on hour timescales (de Martino et al., 2014).

In the accreting state, the known tMSPs are more radio-bright than other neutron star X-ray binaries at similar X-ray luminosities, and they were proposed to follow a similar radio–X-ray correlation as black hole X-ray binaries, albeit a factor of five fainter in the radio band (Deller et al., 2015). On short time scales, the radio and X-ray emission of the tMSP J1023+0038 are anticorrelated, with higher radio emission during X-ray low modes (Bogdanov et al., 2018). During flaring episodes, J1023+0038 can become indistinguishable from black holes. Some AMXPs can reach similar radio luminosities to the mean luminosities of tMSPs for brief periods of time (Chapter 4). In the accreting state, the tMSP XSS J12270–4859 has an X-ray luminosity close to that of NGC 6652 B, and one confirmed tMSP in a globular cluster, M28I, has a very hard X-ray spectrum ($\Gamma = 1.41 \pm 0.01$; Papitto et al., 2013), similar to NGC 6652 B ($\Gamma = 1.3 \pm 0.1$).

Two of the three confirmed tMSPs show strong associations with Fermi sources. The third, M28I, is in a globular cluster which has been detected by Fermi, but for which some or all of the γ-rays may come from other objects in the cluster. NGC 6652 is also one of the globular clusters identified as a bright γ-ray source, but with few known MSPs; $\sim$ 50 MSPs are thought to exist in this cluster (Abdo et al., 2010), although only one (DeCesar et al., 2015) has been discovered to date. If placed at the distance of NGC 6652, the tMSP J1023+0038 in the accreting state would account for $\approx$ 20% of the γ-ray flux of NGC 6652. If NGC 6652 B is a tMSP, it might account for a large fraction of the γ-ray flux of the cluster, possibly explaining the discrepancy between the expected number of pulsars and their actual detections.

With only three confirmed tMSPs, the full parameter space spanned by these systems is uncertain; further discoveries are required to constrain their X-ray power spectra, to explain mode-switching and radio loudness, and to find any radio–X-ray correlations within individual tMSPs and within the population as a whole.

To summarise, we found that NGC 6652 B is like to be an X-ray binary with a neutron star or black hole primary, and a $\sim 1 M_{\odot}$ donor. Radial velocity measurements

would be needed to confirm its nature.

6.2 NGC 6388

A faint radio source at the detection threshold in the 5.5 GHz image (~4.5σ) was found to be coincident with the X-ray source CX4 (Figure 6.6; Maxwell et al., 2012). It was originally identified as a cataclysmic variable from its X-ray properties (a very hard spectrum, with photon index $\Gamma = 0.9 \pm 0.4$ at 90% confidence, consistent with a partial covering model; Maxwell et al., 2012), but the radio emission is too bright for a cataclysmic variable. At an X-ray luminosity of 10^{33} erg s^{-1}, the source lies on the black hole radio/X-ray correlation (Figure 6.11), making it a candidate to host a quiescent black hole. We constrained the radio spectrum of this source to $\alpha < -0.3 \pm 0.4$).

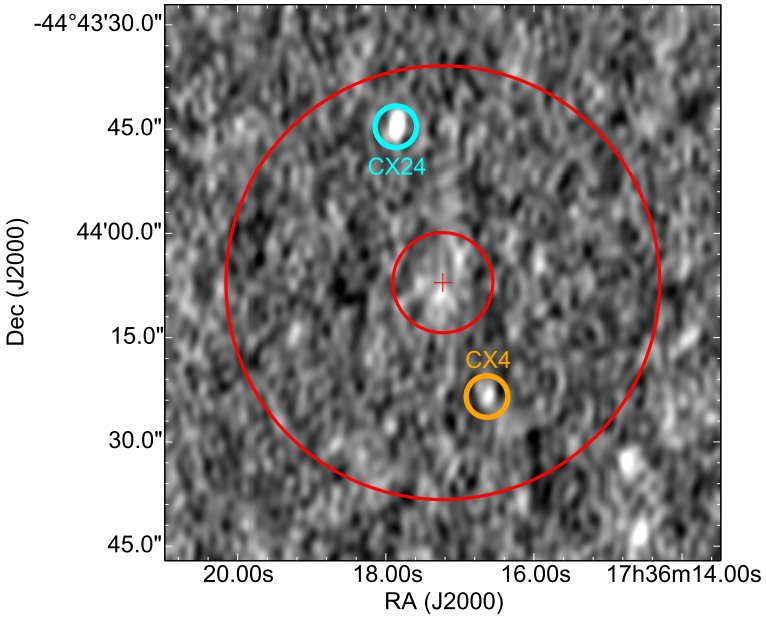

Figure 6.6: 5.5-GHz ATCA image of the core regions of NGC 6388 (rms noise level 3.8 μJy bm^{-1}). The red cross marks the cluster centre, and the inner and outer red circles denote the core and half-mass radii, respectively. Radio detections within the half-mass radius are coincident with the X-ray sources CX4 and CX24 (from Maxwell et al. (2012)).

Having aligned the Chandra and *HST* astrometry using four objects detected in both bands, we detected a match in archival *HST* data in the WFC3 275W image, although it was not detected in the WFC F606W or F814W images, implying a relatively blue, hot source ($T = 11000 - 13000$ K; Figures 6.7, 6.8). From the sparse available data, this source therefore appears to be very similar to 47 Tuc X9; a very blue object, with a hard X-ray spectrum, a relatively high quiescent X-ray luminosity, and a comparable radio-to-X-ray luminosity ratio.

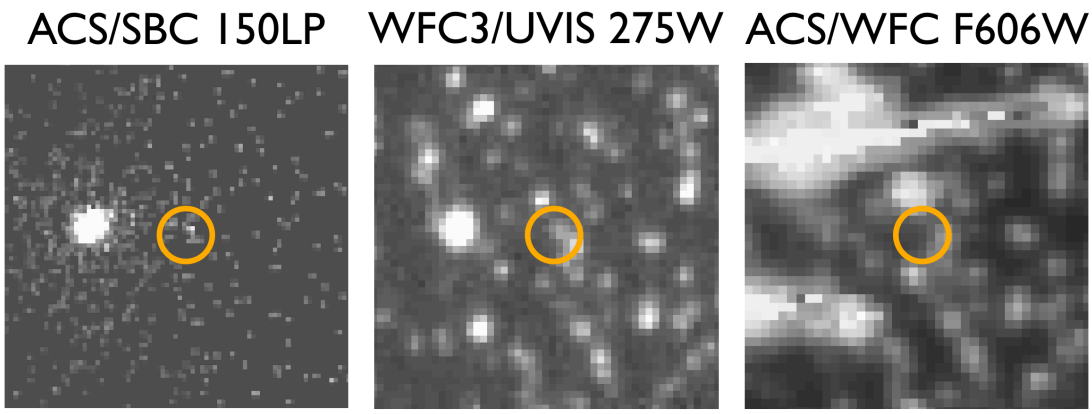

Figure 6.7: HST images of the region surrounding NGC 6388 CX4. The colored Chandra error circles are of radius 0.15″, as inferred from cross-matching four optical–X-ray matches within the cluster. CX4 has a 3–4σ detection in the ACS/SBC 150LP image, a clear counterpart in the WFC3 275W image, but no match in the WFC F606W image. It was also not detected in a WFC F814W image. The optical counterpart to CX4 is very blue; bright in the UV and not detected in redder bands.

The other (brighter) radio source within the cluster half-mass radius is the counterpart to source CX24 (Figure 6.6), with a radio flux density of 47 μJy and a radio spectrum consistent with being flat or inverted ($\alpha = 0.3 \pm 0.2$). At the distance of NGC 6388, this source would fall above the radio–X-ray correlation for black holes (Figure 6.11). However, we note that several candidate black hole X-ray binaries lie above this correlation, including a candidate black hole X-ray binary, M15 S2, which was recently found (in radio and optical data) in the foreground towards the globular cluster M15 (Tetarenko et al., 2016c). CX24 has a possible (but not definitive) optical counterpart. It is unclear if CX24 is an analog to M15 S2 in the Galactic field, or a background galaxy.

6.3 Terzan 1

The globular cluster Terzan 1, located 5.2 kpc away towards the Galactic bulge, contains one neutron star X-ray binary that underwent a persistent outburst from 1987 to 1999 (X1732–304; Cackett et al., 2006). Observations carried out with the VLA when the source was active identified a possible radio counterpart (Marti et al., 1998). Later, Cackett et al. (2006) identified a possible quiescent X-ray counterpart to X1732–304, although its position was offset by $\approx 2\sigma$ from the proposed radio counterpart.

In 2015, we carried out radio observations of Terzan 1 with ATCA and VLA, spanning 1–10 GHz. We detected the source discovered by Marti et al. (1998), at a similar flux density, and a spectral index $\alpha = -1.94 \pm 0.04$ ($S_\nu \propto \nu^\alpha$; Figure 6.9b). Owing to the extended array configurations of our observations (6A with ATCA,

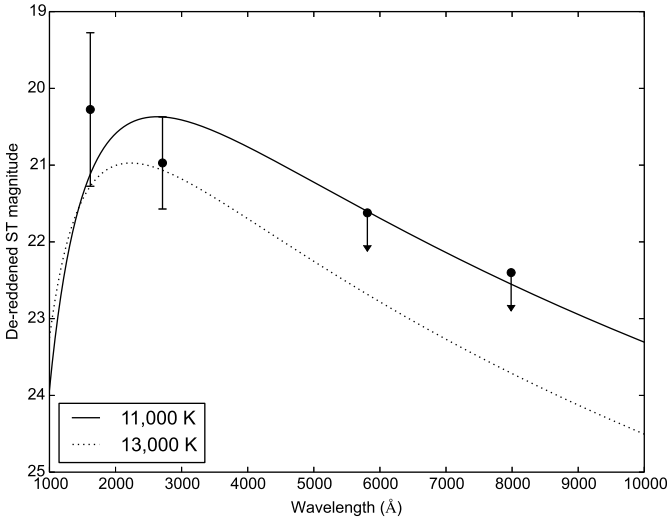

Figure 6.8: Optical broadband spectrum of NGC 6388 CX4, and two representative black body models (full line, 11000 K; dotted line, 13000 K). The characteristic temperature of this X-ray binary is likely to be in this range.

BnA with VLA), the source appears slightly extended to both arrays above 5 GHz (Figure 6.9a), which gives us confidence the extension is not a spurious effect. In addition, subtracting a point-source model from the ATCA 9 GHz image leaves a significant (3σ) residual component. Due to source crowding and high extinction towards Terzan 1, the optical counterparts of the radio or X-ray sources have not yet been identified, which makes their nature uncertain.

6.3.1 Possible interpretations

The radio source in Terzan 1 could be coincident with the core of the cluster, which makes it likely it is part of it. Its ultra-steep spectrum ($\alpha \approx -2$) makes it even less likely it is a galaxy, as only ≈3% extragalactic sources have $\alpha < -1.2$ (e.g., Huynh et al., 2012). We therefore find it unlikely that the radio source towards Terzan 1 has an extragalactic origin.

Next, we reconsider the possibility this radio source is associated with the nearby X-ray source CX2 (possibly X1732–304). First, we need to align the positions of the X-ray sources to the absolute reference frame. We cross-match the X-ray catalogue of Cackett et al. (2006) with the *Gaia* (Perryman et al., 2001) source catalogue (data release 2) by using a 0.6″ matching radius. Ignoring any matches within 0.7′ from the cluster centre to avoid mismatches due to clustering, we find eight x-ray/optical matches. We find the X-ray positions of Cackett et al. (2006) need to be shifted by -0.03″±0.2″ in right ascension, and -0.13″±0.14″ in declination. Unfortunately, we could not lock in the X-ray and radio frames due to a lack of cross-matching sources

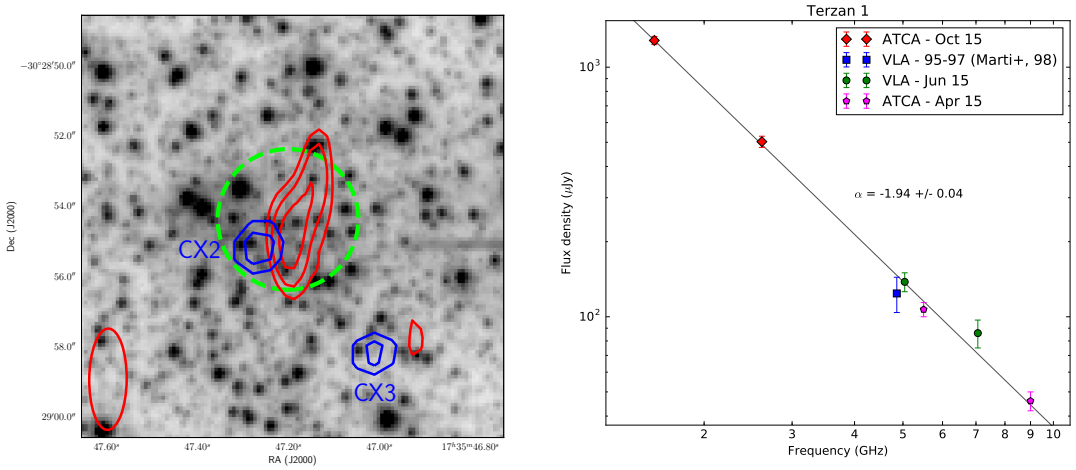

(a) (b)

Figure 6.9: (a) Optical image (*HST*, F814W; PI: Ortolani) of the central region of Terzan 1, overlaid with radio (ATCA, 9 GHz) and X-ray (*Chandra*; PI: Wijnands) contours in red and blue respectively. The radio contours are drawn at levels $\sqrt{2}^{n} \times$rms, where $n = -2, 2, 3, \ldots$, and rms $= 4\,\mu$Jy. *CX2* and *CX3* are X-ray sources identified by Cackett et al. (2006). The synthesised beam of the radio observations is displayed in the lower left corner. The cluster core is displayed with a dashed green circle. The radio source appears resolved, lies at the core of Terzan 1, and could be associated with *CX2*, the possible quiescent counterpart of the neutron star X-ray binary X1732–304. (b) The radio spectrum of the source, using the integrated flux density at each frequency. All observations are consistent with a non-variable ultra-steep spectrum, including our reanalysis of the data from Marti et al. (1998), carried out in 1995 and 1997 when X1732–304 was active.

in these bands. However, the absolute astrometry of ATCA is expected to be better than 0.3″. The offset between the X-ray position and the position of the radio peak (1″ away) is then significant at the >3σ level.

This slight astrometric offset, the ultra-steep spectral index, and the constant radio flux between observations in the X-ray active and quiescent states of X1732–304 (Figure 6.9b) point strongly against synchrotron emission from a compact jet from this source. Alternatively, the jets could interact with the surrounding medium, giving rise to a visible radio lobe or hotspots (see Fig 6.9a), similar to the black hole X-ray binary 1E1740.7–2942 in the Galactic bulge, whose radio lobes extend up to 30″ from the core (Mirabel et al., 1992). This scenario could be compatible with the constant source flux density between the active and quiescent states of X1732–304, as the radio lobes would only be indirectly related to the X-ray state of the system. Radio lobes would also have a steep radio spectrum ($\alpha \approx -0.8$), as opposed to the expected flat spectrum of the core (Mirabel et al., 1992), although a spectral index $\alpha \approx -2$ would be exceptional. The greatest problem with producing radio lobes, however, is the requirement of a dense interstellar medium, which globular clusters are very poor in (Freire et al., 2001). The

proximity of Terzan 1 to the Galactic plane ($l = 357.6$, $b = 1.0$), however, might lead to capture of gas by the cluster as it orbits the Galactic centre. Indeed, Li et al. (2016) found that the multiple stellar populations observed in globular clusters could be explained by the accretion of gas from the Galactic disc early in their evolution. There is no observational evidence of current gas accretion in Galactic globular clusters, however. Therefore, we consider that the Terzan 1 source is unlikely to be a radio lobe produced by the jets of either the quiescent X1732–304 or another X-ray binary.

Even though timing searches have not yet found any MSPs in Terzan 1 [1](Manchester et al., 2005), it could contain as-yet undiscovered MSPs. Some MSPs hidden to timing searches could still be visible to continuum observations as sources with spectral indices $\alpha = -1.7$, with half found to fill the $-2.0 \leq \alpha \leq -1.5$ range (Kramer et al., 1998). The resolved radio emission in Terzan 1 could therefore be two close-by MSPs. However, pulsars are often seen to scintillate, but our radio source does not show any evidence for inter- or intra-observation variability. Based on a two-component fit in the image plane, on the lack of spectral curvature, and the lack of evidence for an offset of its centre with frequency, we estimate that the two putative pulsars would have a similar spectral index, one being half as bright as the other. This scenario could be tested by VLBI observations that confirm the presence of two point-sources with the proper motion of Terzan 1 ($\mu \approx 1$ mas yr^{-1}; Rossi et al., 2015).

6.4 NGC 6397

Within 16 core radii of NGC 6397, we detected six radio sources, of which we estimated around five (and at least one) are part of the cluster. Cross-matching our radio catalogue with the *Chandra* source catalogue of Cohn et al. (2010), we find matches for the X-ray sources U12, U18 and U97 and possibly for U24. U12 is a known MSP, first found in radio timing searches (D'Amico et al., 2001; Cohn et al., 2010). We measure its spectral index to be $\alpha < -0.8 \pm 0.5$.

U18 was suggested to be an MSP based on its optical and X-ray properties, which has up to now remained undetected in the radio band (Bogdanov et al., 2010; Cohn et al., 2010). The MAVERIC detection of its radio counterpart with spectral index $\alpha = -1.9 \pm 0.4$ is consistent with the MSP interpretation.

The nature of U97 could not be pinpointed by Cohn et al. (2010), but they suggest it could be an active binary, with a blue optical counterpart and no evidence for $H\alpha$ emission. Its radio counterpart has a spectral index $\alpha = -1.2 \pm 0.6$, and a radio luminosity of 10^{27} erg s^{-1}. This luminosity is similar in value to the most extreme flares observed from RS CVn systems (Mutel et al., 1987), which makes it possible we have observed such a system.

[1] `http://www.atnf.csiro.au/people/pulsar/psrcat/`

The model that best describes the X-ray spectrum of U24 is that of a neutron star surface, heated by past accretion onto its surface, making it an X-ray binary candidate (Grindlay et al., 2001b). U24 remains undetected in the optical band (Cohn et al., 2010). Next to the X-ray source, $1.1'' \pm 0.4''$ away, we found a radio source with $\alpha = -0.6 \pm 0.6$. If the two objects are related (they might not be, given the astrometric shift), the neutron star could be active as a radio pulsar if accretion stopped. This is consistent with the non-variable X-ray emission and lack of a power-law component in its X-ray spectrum, indicating no active (or insignificant) accretion at present (Grindlay et al., 2001b). Otherwise, the radio emission could come from a jet. In either case, U24 is likely to be a tMSP system. We do not attempt to place this source on the radio–X-ray plane because its X-ray spectrum is dominated by the neutron star surface rather than by accretion.

6.5 Terzan 6

In Chapter 3, we found the one source within the core of Terzan 6 is significantly above the background. We measured its spectral index to be $\alpha = -0.4 \pm 0.1$. The core of this cluster contains one neutron star X-ray binary, GRS 1747–312, which goes into outburst once every ~6 months (in't Zand et al., 2003). The *Swift*/BAT transient monitor[2] shows GRS 1747–312 was not in outburst at the time of our radio observations. In addition, there is a small astrometric shift of $0.7'' \pm 0.2''$ from the nominal X-ray position measured in a *Chandra* image astrometrically-aligned to the absolute frame of reference (in't Zand et al., 2003). For these reasons, we may not have detected direct core emission from GRS 1747–312, but if associated, the radio emission may nonetheless be related to its frequent outbursts.

6.6 NGC 6352

In Chapter 3, within half a core radius of NGC 6352, we found that three radio sources, of which we have estimated 0^{+1}_{-0}, and up to three (at 3σ confidence) are not associated with the cluster. Optical imaging data can be used to determine if an object is extragalactic based on its morphology. Cross-matching these three sources with a broadband *HST* image taken with the F814W filter of the ACS/WFC camera (PI: Sarajedini), we find two of them are coincident with spiral or elliptical galaxies. This number of radio galaxies in the cluster core is consistent with our estimate for the rate of background sources within 2σ. We do not identify an optical counterpart for the remaining source, and we estimate the lower limit on its de-reddened magnitudes (taking $E(B-V) = 0.22$;

[2] https://swift.gsfc.nasa.gov/results/transients/

Harris, 1996) to be $m > 23$. This magnitude is much fainter than the main-sequence turn-off (Pulone et al., 2003). The only magnetically-active stars that could reach high enough radio luminosities to be detected in our imaging data are RS CVn binaries and FK Com stars (Benz and Guedel, 1994). These require at least one giant or sub-giant component (Berdyugina, 2005), which we rule out from the *HST* data. If it resides within the cluster, it must be associated with low-level accretion in an X-ray binary with a low mass donor ($< 0.5 M_{\odot}$), or a pulsar. To further determine what its nature might be, we study its X-ray properties.

For this, we retrieved a 19.8 ks *Chandra* observation (PI: Kong). None of the radio sources within the core are detected in the X-ray band. Taking a 1″ aperture (which encloses ∼ 85% of the total energy of the point-spread-function; Allen et al., 2004), the 3σ upper limit on the count rate $CR = 3.3 \times 10^{-4}\,\mathrm{s}^{-1}$ (Gehrels, 1986) corresponds to an infinite-aperture count rate $CR = 3.9 \times 10^{-4}\,\mathrm{s}^{-1}$. Using WebPIMMS[3] and assuming a column density $N_{\mathrm{H}} = 2 \times 10^{21}\,\mathrm{cm}^{-2}$ (Kalberla et al., 2005), a power-law spectrum with $\Gamma = 2$, and a distance of 5.6 kpc (Harris, 1996), the upper limit on the unabsorbed 1–10 keV X-ray luminosity is $L_{\mathrm{X}} \lesssim 2 \times 10^{31}\,\mathrm{erg\,s}^{-1}$.

The radio luminosity of the source without an optical counterpart is $L_{\mathrm{R}} \approx 3 \times 10^{27}\,\mathrm{erg\,s}^{-1}$ (at 5 GHz). The only sources which can reach such high radio luminosities relative to their X-ray luminosities are black holes and pulsars. The spectral index we have measured for this source is $\alpha < 0.0 \pm 0.3$. This spectral index is consistent with either an X-ray binary or pulsar. Otherwise, it can still be a background galaxy, which is consistent with the measured source counts at 3σ.

6.7 ω Centauri

Based on its morphology, we classify one extended source in the core of ω Centauri as a planetary nebula candidate (Figure 6.10). It has an integrated flux density of $290 \pm 23\,\mu$Jy at 5.5 GHz. This source is ∼8″ across, which at a distance of 6.4 kpc, corresponds to a size of 0.25 pc. This is similar to the other four known planetary nebulae in globular clusters, which have sizes of 0.1–0.3 pc (Jacoby et al., 1997). To investigate the possibility of optical line emission from this putative nebula, we obtained an H α difference image based on a F656N (acquired 18/11/2011) and a F606W (acquired 24/11/2011) image (*HST*/WFC3/UVIS, PI: E. Sabbi). No extended H α emission was found at the position of the radio emission, with a limit on the surface brightness of ∼22 mag arcsec^{-2} (Vega system). Deeper observations would be needed to confirm or refute this scenario.

[3]https://heasarc.gsfc.nasa.gov/cgi-bin/Tools/w3pimms/w3pimms.pl

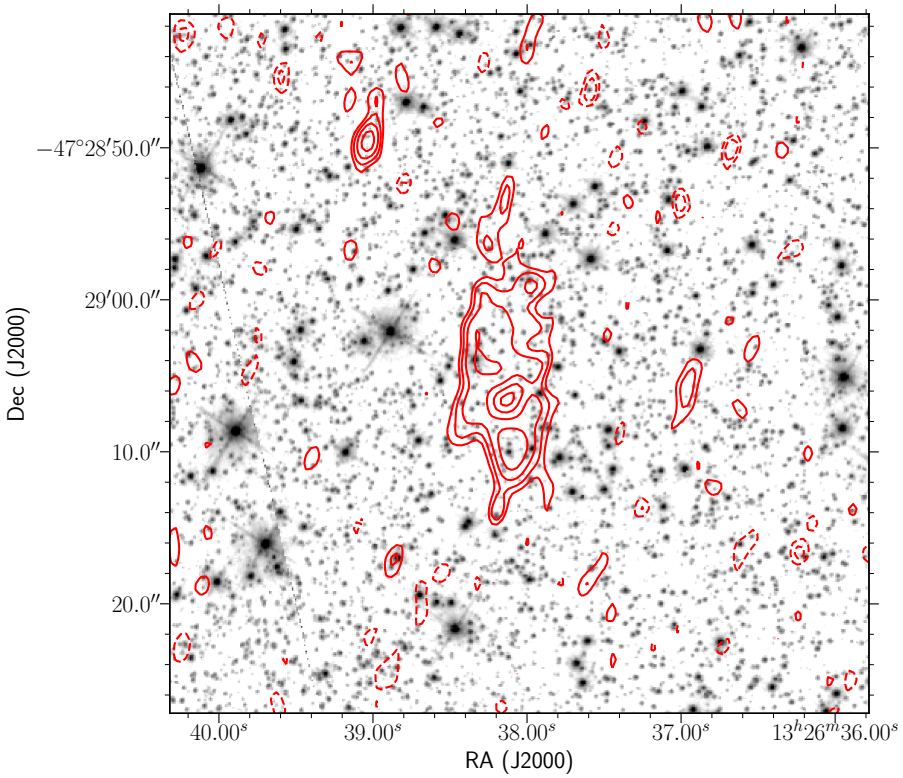

Figure 6.10: Planetary nebula candidate in ω Cen. The background image (*HST*/WFPC2, F555W, PI: Ferraro) is overlaid with radio contours at 5.5 GHz (red, at levels $\sqrt{2}^{n} \times$ rms, where $n = -2, 2, 3, \ldots$, and rms = 4.1 μJy).

6.8 Summary

This chapter highlights the importance of multi-wavelength observations in identifying the nature of radio (and X-ray) sources. So far, we have only investigated a few clusters with large and/or significant excesses. The globular clusters NGC 6652, NGC 6388, Terzan 1, Terzan 6 and NGC 6397 contain radio sources which are likely associated with neutron star or black hole X-ray binaries. In Figure 6.11 we show the radio and X-ray luminosities of those sources discussed in this chapter, which have been detected in the radio and X-ray bands and are consistent with having flat or inverted radio spectra. Future studies should perform similar cross-matching studies for all detected radio sources. To ascertain the nature of radio sources with stellar optical counterparts, optical spectroscopy is needed, provided field crowding does not impede the acquisition of such spectra.

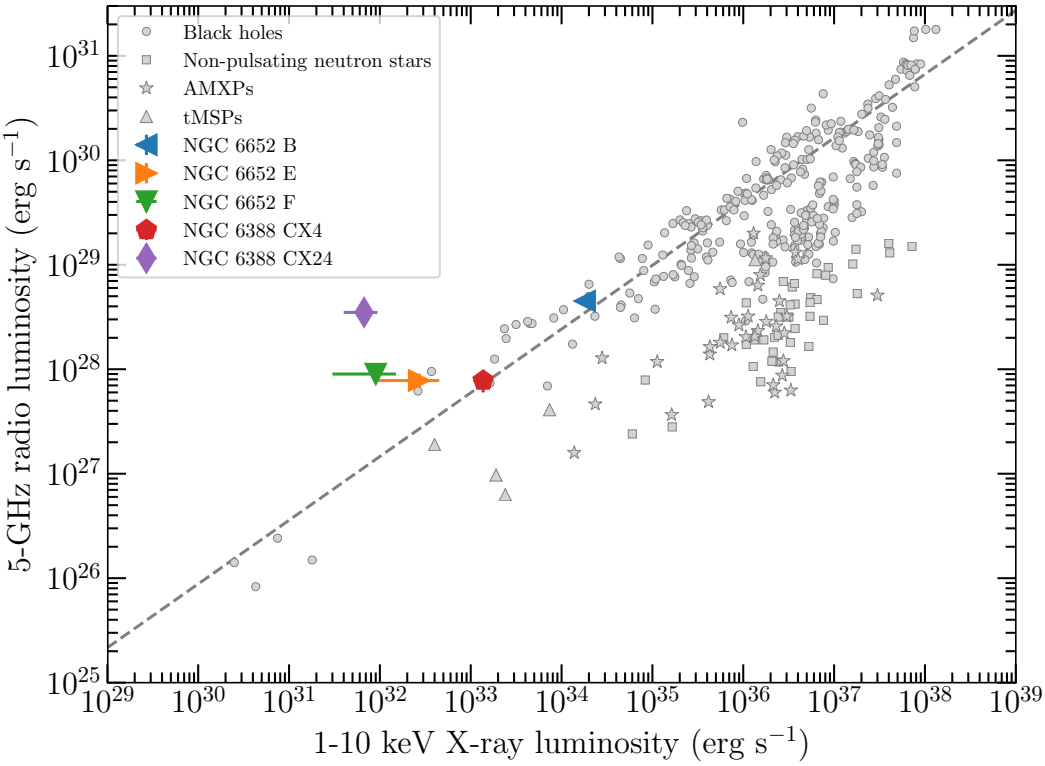

Figure 6.11: The radio and X-ray luminosities of four sources with flat radio spectra within the half-light radii of two clusters – NGC 6652 and NGC 6388. These sources could be neutron star or black hole X-ray binaries. Data collated by Bahramian et al. (2018).

Chapter 7

Discussion and conclusion

All known radio sources in globular clusters are either pulsars, neutron star LMXBs, or planetary nebulae. However, other classes of astrophysical sources with potentially detectable radio emission exist in globular clusters: black hole LMXBs, cataclysmic variables, and magnetic stars. These have not yet been detected in the radio band, probably owing to the sensitivity of previous radio surveys of globular clusters. As strong gravitational wave sources, black holes are of special interest. This is especially true as most of what is assumed about their presence in globular clusters comes from numerical simulations, with scarce observational constraints.

To uncover the faint ($> 20\ \mu$Jy) population of radio sources within globular clusters, we carried out a comprehensive survey of Galactic clusters under the MAVERIC survey. In Chapter 3, I presented the results from the ATCA survey of 26 Galactic globular clusters. We found that at most ~70 from a total of ~1300 detected sources could be associated with the globular clusters we observed. Some clusters contain on the order of 1–5 sources, while the majority of clusters may not host any at all. In the case studies we explored in Chapter 6, X-ray and optical data were used to constrain the nature of some of these radio sources. Most of the radio sources were either associated with pulsars or X-ray binaries (neutron stars or black holes). In this chapter, we compare these results with other estimates of the occurrence rate of radio-loud objects in globular clusters. We then highlight different ways in which MAVERIC data can be used, and finalise with a look towards the future.

7.1 Nature of the radio source population

In this section, we explore the types of sources which might be seen as radio emitters in globular clusters. First, we consider the well known sources: planetary nebulae, pulsars and neutron star X-ray binaries. Second, we investigate other potential sources of radio emission: magnetically-active stars, white dwarfs and black holes. I provide

rough estimates for the number of detectable radio sources for each of these classes by considering their occurrence rates in globular clusters, and their typical or extreme radio luminosities.

7.1.1 Planetary nebulae

In an optical survey of 133 globular clusters, Jacoby et al. (1997) detected four planetary nebulae. These four planetary nebulae have physical sizes of 0.1–0.3 pc, which at a distance of 8 kpc correspond to angular sizes of a 2″–8″ across, which may either appear resolved or unresolved in our observations. One of the above planetary nebulae is located in one of the targets in our survey, NGC 6441, and we detected it in the radio band as an extended source. Therefore, it is possible that we detected some previously unknown planetary nebulae. Such an object may be found in ω Cen (Chapter 6). The radio identification of planetary nebulae in globular clusters may be more efficient than optical identification, as this band does not suffer from the same crowding issues as optical observations.

7.1.2 Pulsars

For a typical globular cluster, Ivanova et al. (2008) estimated the number of observable pulsars is on the order of five, while Turk and Lorimer (2013) predict that a cluster contains a number of $\ln N_{\rm PSR} = -1.1 + 1.5 \log \Gamma$, where Γ is the stellar encounter rate. For a typical globular cluster with $\Gamma = 100$, this equation predicts seven pulsars, similar to the predictions of Ivanova et al. (2008). Over our sample of 26 globular clusters, we predict a total number ∼550 pulsars, most located in high-interaction clusters (∼100 pulsars in Terzan 5). Based on the fraction of confirmed pulsars with known positions in our globular cluster sample, which we detected in the ATCA MAVERIC data (7–10%; Chapter 3), we can naively estimate we may have detected on the order of ∼50 pulsars out of the total pulsar population in our sample, most of which have previously been unknown to timing searches. Pulsars that are visible in continuum images but have not yet been detected in timing searches could be particularly interesting. Highly accelerated pulsars (in close orbits with other compact objects), or gas in their immediate vicinity (gas accreted or ablated from their companions) can smear out pulsations without loss of flux. One such object would be NGC 6397 U18, which has been proposed to be a pulsar based on its optical and X-ray properties, but never seen to pulsate in the radio band (Chapter 6). Only the brighter end of the pulsar population is likely to have been detected in timing searches. This means the detection probability of any given pulsar in the MAVERIC data could be much lower than 10%, and the estimate of ∼50 pulsars represents an upper limit only.

7.1.3 Accreting neutron stars

The radio–X-ray correlation for black holes has been investigated over eight decades of X-ray luminosity in a variety of objects. In contrast, the radio/X-ray luminosity behaviour of neutron star X-ray binaries is more poorly known, owing to their less powerful jets. Most radio detections of neutron star LMXBs were made above $L_X \gtrsim 10^{36}\,\mathrm{erg\,s^{-1}}$. We therefore set out to constrain neutron star behaviour below this luminosity by observing three systems in outburst as they decayed towards quiescence, and one quiescent system. We detailed this campaign in Chapter 4. We found that our neutron star sample have fainter radio jets than black holes at the same X-ray luminosities. During radio flares, we observed one AMXP to reach radio luminosities five times lower than expected for a black hole, similar to the tMSPs.

The most radio-loud (relative to its X-ray luminosity) low-luminosity neutron star X-ray binary known is PSR J1023+0038, which can reach $L_R \sim 10^{27}\,\mathrm{erg\,s^{-1}}$ during brief (∼1 h) flaring episodes and X-ray low modes (Bogdanov et al., 2018), making it indistinguishable from black hole systems. On average, however, it is similar to the other tMSPs (five times more radio-faint than black holes). Using all the available black hole and neutron star data, Gallo et al. (2018) found that taken as a whole, the neutron star population is a factor of ∼22 more radio-faint than the black hole population. At low luminosities, however, there is an overlap of their respective confidence intervals, owing to the few detections in this range.

The ATCA survey covered the location of three known persistent neutron star X-ray binaries, with $L_X > 10^{35}\,\mathrm{erg\,s^{-1}}$(Bahramian et al., 2014)[1]: 4U 1820–30 in NGC 6624, XB 1832–330 in NGC 6652, and 4U 1746–37 in NGC 6441. Of these, we only detected 4U 1820–30. With luminosities of $L_X = 10^{36} - 10^{37}\,\mathrm{erg\,s^{-1}}$ (Heinke et al., 2001; Bałucińska-Church et al., 2004), the other two sources could be just below the delectability limit in the radio band. Out of the neutron star transients, we detected EXO 1745–248 in Terzan 5 (the MAVERIC observations were scheduled to coincide with its outburst in 2015; Tetarenko et al., 2016b), and possibly the recurrent transient GRS 1747–312 in Terzan 6, and the quiescent system XB 1732–304 in Terzan 1 (Chapter 6). These four radio sources do not constitute a large fraction of the total population of sources we detected. Instead, quiescent neutron star systems that have never gone into outburst may contribute more to the radio source population. In addition, the potential radio counterparts of GRS 1747–312 and XB 1732–304 were identified when these sources were in quiescence. However, they have much larger radio luminosities than expected in quiescence, steep spectral indices ($\alpha = -0.4$ and $\alpha = -2$), are slightly shifted from the position of the X-ray sources, and (in the case of XB 1732–304 only) is extended. These properties suggest that if these are indeed the counterparts of the

[1] `https://bersavosh.github.io/research/gc_lmxbs.html`

two X-ray binaries, they are likely to have arisen from the interaction of the jet with the intra-cluster gas during their last outbursts. In this case, neutron stars which have never been observed to go into outburst may not produce similar outputs in the radio band.

Quiescent neutron star X-ray binaries in globular clusters typically have X-ray luminosities ranging from $\sim 10^{32}$ erg s^{-1} up to a few $\times 10^{33}$ erg s^{-1} (Heinke et al., 2003). At these X-ray luminosities, most neutron stars are expected to have radio luminosities up to a few $\times 10^{26}$ erg s^{-1}, but some tMSPs could reach a few $\times 10^{27}$ erg s^{-1}.

Ivanova et al. (2008) estimated the number of neutron star X-ray binaries in a typical globular cluster is around two. Similarly, Pooley et al. (2003) predict a number of $N_{\rm XRB} = \Gamma/100$ neutron star X-ray binaries per globular cluster (where Γ is the stellar encounter rate, as before). This equation predicts about one neutron star X-ray binary in a typical globular cluster with $\Gamma = 100$, and a total of ~220 across our whole sample, mostly found in high-interaction clusters (~70 neutron star LMXBs in Terzan 5).

Out of the 18 transient or persistent known X-ray binaries in globular clusters with confirmed neutron stars, only one is a known tMSP (M28I; Papitto et al., 2013). The estimates of one tMSP every 18 neutron star systems, and a total of 220 neutron star systems naively translate to ~12 radio-loud quiescent neutron star X-ray binaries across our sample. We therefore estimate a conservative upper limit of ~60 neutron stars (~50 pulsars and ~12 X-ray binaries) detected across the survey. Even if this estimate is highly uncertain and may be subject to large systematics, it is consistent with the number of sources we estimated to be part of the clusters in our survey.

7.1.4 Active binaries

Magnetically-active binaries can have radio luminosities of up to 10^{26} erg s^{-1} in quiescence (Morris and Mutel, 1988), with extreme flaring events of up to 10^{27} erg s^{-1} in the case of RS CVn binaries (Mutel et al., 1987). Such sources may be common in globular clusters. In Chapter 6, we identified radio emission from the active binary candidate NGC 6397 U97 at the level of $\sim 10^{27}$ erg s^{-1}. However, NGC 6397 is the most nearby globular cluster in our survey, at a distance of 2.3 kpc. If U97 were to be placed at the distance of the next-nearest globular cluster in our sample (NGC 6752 at 4 kpc), it would lie below the detection threshold. The rarity of potential flares exceeding the sensitivity of our survey suggests that active binaries may not contribute significantly to the radio source population.

7.1.5 Accreting white dwarfs

Given the large numbers of white dwarfs in each globular cluster (Monelli et al., 2005 detected over 2000 white dwarfs in ω Cen), it is possible that at least some of the radio sources within globular clusters are white dwarfs. Cataclysmic variables are thought to

occur at a rate of ∼200 per typical globular cluster (Ivanova et al., 2006). Non-magnetic cataclysmic variables can reach radio luminosities of up to 10^{26} erg s^{-1} during short outbursts (Coppejans et al., 2016). In globular clusters, however, the duty cycles of cataclysmic variables is very low ($\lesssim$0.1 per cent; Belloni et al., 2017). These two factors make it unlikely that we have observed radio emission from any non-magnetic cataclysmic variable. A survey of nine quiescent magnetic cataclysmic variables within 100 pc has revealed emission at $\sim 10^{26}$ erg s^{-1} for just one of them (AE Aqr; Mason and Gray, 2007), and the rest are fainter. Barrett et al. (2017) conducted a survey of 121 magnetic cataclysmic variables (without distance information) with the VLA, detecting 18 of them. While flares from magnetic cataclysmic variables can reach a few $\times 10^{27}$ erg s^{-1} (Pavelin et al., 1994), such flares have short durations (∼1 h). The mean radio luminosity from any magnetic cataclysmic variable might not be high enough to be picked up in our radio survey.

AM CVn objects, which are mass-transferring white dwarf–white dwarf binaries, may also have significant radio emission. The theoretical work of Willes et al. (2004) suggests the best frequency for observing AM CVn binaries is around 5 GHz (included in the MAVERIC spectral coverage), at which they could reach radio luminosities of up to $\sim 10^{29}$ erg s^{-1}, depending on their orbital period.

For an orbital period of 1000 s, they found AM CVn systems can reach radio luminosities of up to $L_{\rm R} \lesssim 10^{28}$ erg s^{-1}. For the same orbital period, Nelemans et al. (2004b) predict an X-ray luminosity in the range $L_{\rm X} = 10^{29} - 10^{34}$ erg s^{-1} and an absolute V-band magnitude in the range $M_{\rm V} = 6 - 8$, corresponding to an apparent magnitude in the range $m_{\rm v} = 20 - 22$ (ignoring extinction effects) at a distance of 6 kpc. This shows that in certain instances AM CVn systems may be visible in the radio band, but not in the X-ray or optical bands. Ramsay et al. (2007) carried out radio observations of three candidate quiescent AM CVn systems. Of these, one (RX J0806 +15) was detected at a flux density of 100 μJy. At a distance of ∼0.9 kpc, its radio luminosity is similar to that of other cataclysmic variables in outburst, at $\sim 10^{27}$ erg s^{-1} (Esposito et al., 2014). With an estimated ∼200 AM CVn binaries in each typical globular cluster (Ivanova et al., 2006), these sources could form a significant part of the low-luminosity radio source population of globular clusters.

Symbiotic stars, which are white dwarfs fed by the winds of red giants, can be much brighter in the radio band. We detected the symbiotic star H 1–36 in the same field as NGC 6441 (but not in the cluster), at a flux density of ∼64 mJy at 5.5 GHz. Because it lies 5.2′ away from NGC 6441, it fell outside of the primary beam at 9 GHz and thus we could not measure its spectral index. However, Taylor and Seaquist (1984), who measured a similar flux density of ∼50 mJy at 6 GHz for H 1–36, also measured an inverted spectrum with $\alpha \approx 0.6$ at these frequencies. At a distance of ∼4.5 kpc, its radio luminosity is $\sim 10^{30}$ erg s^{-1}. We have not identified any such luminous radio sources

with inverted spectra within one half-light radius of any cluster. Even though AM CVn binaries and symbiotic stars have been predicted to exist in globular clusters, none have yet been confirmed. Zurek et al. (2016) have identified one candidate AM CVn in the globular cluster NGC 1851 (which could also be a symbiotic star). The only known white dwarf pulsar AR Sco has a persistent radio luminosity of $10^{27}\,\mathrm{erg\,s^{-1}}$ (Marsh et al., 2016). Little is known about such objects, including their occurrence in globular clusters. As AR Sco is only 100 pc away (Marsh et al., 2016), such objects could be abundant.

7.1.6 Accreting black holes

Based on numerical simulations, Kremer et al. (2018) found that only 0–3 mass-transferring binaries with a black hole may be found in a given globular cluster at a given time. This result is independent of the total number of black holes in the cluster, and is consistent with the estimate we have provided in Chapter 5 (one per cluster) based on the number of ultraluminous X-ray sources with black hole accretors in extragalactic globular clusters.

At a given orbital period, black hole LMXBs are fainter in the X-ray band by $\sim$ two orders of magnitude than their neutron star counterparts (Menou et al., 1999; Reynolds and Miller, 2011; Armas Padilla et al., 2014). Assuming that in globular clusters, black hole LMXBs have the same orbital period distribution as neutron star LMXBs, the quiescent X-ray luminosity of neutron stars in the range of $10^{32} - 10^{34}\,\mathrm{erg\,s^{-1}}$ (Section 7.1.3) translates to quiescent luminosities for black holes in the range of $10^{30} - 10^{31}\,\mathrm{erg\,s^{-1}}$. The radio–X-ray correlation for black holes would then predict radio luminosities in the range $10^{26} - 10^{27}\,\mathrm{erg\,s^{-1}}$ for quiescent black holes. Persistent systems which do not undergo outbursts could exceed that luminosity.

In Chapter 6, we took black hole candidates to be those sources which lie within the scatter of the radio–X-ray correlation for accreting black holes, have a radio spectral index consistent with $\alpha \geq 0$, and are consistent with having a point-source optical counterpart. We preliminarily found six black hole candidates: 47 Tuc X9, NGC 6652 B, E and F, NGC 6388 CX4 and CX24. With the exception of symbiotic stars and AM CVn binaries (which have not been yet been confirmed to exist in globular clusters), these sources are more radio luminous than any known cataclysmic variable system. However, CX24 may be a background galaxy, and the other sources could be neutron stars.

X9 was initially identified as a black hole candidate by Miller-Jones et al. (2015) based on the same criteria listed above, and was suggested to be ultracompact based on its relatively high X-ray luminosity. Later, Bahramian et al. (2017) found an orbital period of 28.2 min from the X-ray light curve, and line emission in the soft X-ray spectrum from oxygen-rich gas, strengthening the ultracompact classification. In

Chapter 5, we acquired an optical spectrum of X9, finding no emission or absorption features. The lack of H α emission, which dominates the spectra of typical X-ray binaries, suggests a lack of hydrogen in the composition of the donor, consistent with the ultracompact nature suggested previously. However, the nature of the accreting object remains elusive, as both a neutron star and a black hole can explain most of the observables of X9. The high-amplitude 7-day superorbital period is hard to reconcile with a black hole, and the very hard X-ray spectrum ($\Gamma = 1.1$) is unexpected for a neutron star. However, the detection of a 7-day period in X9 was due to the exceptional 3-week monitoring program of 47 Tuc undertaken by *Chandra*. Detecting similar variability time scales in other systems has been very difficult.

Intermediate-mass black holes are expected to be found at the centres of globular clusters (Miller and Hamilton, 2002), and to be emitting in the radio band, similar to AGN at the galaxy centres. However, we have not found any radio source associated with such a black hole in our globular cluster sample or in a stack of all clusters (Tremou et al., 2018). This suggests that either they do not exist, or their radiative efficiency is lower than predicted based on our current understanding of low-level accretion processes.

7.1.7 Summary

The radio sensitivity we reached in our survey is at the level of $\sim 10^{27}\,\mathrm{erg\,s^{-1}}$. We therefore find it likely the population of radio sources is mainly composed of neutron stars (radio pulsars and X-ray binaries), with a few planetary nebulae and active binaries. Some radio sources may also be black holes and white dwarfs (as white dwarf pulsars and AM CVn binaries). Some of these double-degenerate systems are potentially detectable by the future gravitational wave detector *LISA* (Amaro-Seoane et al., 2017). In the crowded fields of globular clusters, the radio band may provide the best available way of identifying an electromagnetic counterpart to some *LISA* sources.

7.2 Secondary science

Images from the MAVERIC survey can be used as a baseline of comparison for studies of transient and variable sources. So far, we used MAVERIC data for this purpose in Tetarenko et al. (2016b), Homan et al. (2016b) and Díaz Trigo et al. (2017). In Tetarenko et al. (2016b), the MAVERIC observations of Terzan 5 were acquired contemporaneously with *Swift*/XRT observations to study disc/jet coupling in the neutron star X-ray binary EXO 1745–248. We found this source to have a very steep radio/X-ray correlation relative to other neutron stars. In Homan et al. (2016b), we used our radio observations of the globular cluster NGC 2808 to astrometrically align an archival *HST*

image of the cluster to the absolute frame of reference. We performed this to determine the absolute position, and hence to identify the putative quiescent optical counterpart, of the X-ray transient MAXI J0911–635, which we did not detect in the radio band (Tudor et al., 2016). In Díaz Trigo et al. (2017), we estimated the radio flux density of the variable neutron star 4U 1820–30 in the globular cluster NGC 6624 using MAVERIC data, during observations acquired at a later date. These more recent observations had a shorter integration time, and used only four out of six ATCA antennas in a more compact configuration. For these reasons, the sensitivity of these observations was poorer, and the PSF was much larger relative to the MAVERIC data. With the assumption that all radio sources in the field, with the exception of 4U 1820–30, were non-variable, we used the field model calculated from the MAVERIC data to estimate the flux density of 4U 1820–30. This enabled a calculation of the jet break frequency in a neutron star jet.

7.3 Conclusion

The stellar dynamics in the dense environments of globular clusters drive the formation of close, mass-transferring binaries, many of which remain undiscovered. Those systems containing compact objects may launch strong jets detectable with radio telescopes. Radio observations can thus be an important tool to uncover some of the neutron star and black hole population of globular clusters. Coupling X-ray, optical and radio observations can efficiently identify black hole candidates, which have proven elusive until recently.

The MAVERIC survey was designed to explore the population of compact objects (black holes in particular) through radio observations. Part of the survey was carried out with ATCA, which observed 26 globular clusters in the southern sky. To maximise the chances of finding sources that reside in clusters (rather than just background galaxies), the most nearby and massive globular clusters were prioritised. We found that some globular clusters host a few radio sources, most of which are likely to be pulsars and X-ray binaries, but some may also be planetary nebulae and active binaries.

7.4 Future work

To further refine the number and nature of radio sources within globular clusters, the radio source catalogue has to systematically be cross-matched with optical and X-ray catalogues. In Chapter 6, we have carried out an ad-hoc cross-matching method, using only the published *Chandra* source catalogues. Some globular clusters in the MAVERIC sample do not yet have *Chandra* source catalogues available, either because the X-ray observations have not been published, or because some of the observations

have only been carried out recently (some under the MAVERIC collaboration). The uniform processing and analysis of all *Chandra* observations of MAVERIC globular clusters (southern and northern) is currently being conducted (A. Bahramian, in preparation).

The optical morphology and variability can be used as a tool to classify a source as extragalactic (extended, non-variable) or stellar (point-source, variable). A point source does not necessarily imply a source within the cluster (especially in the case of low SNR), as background AGN can also appear stellar. Planetary nebulae in clusters can also be extended.

Colour-magnitude diagrams can be used to identify the source of the optical emission in accreting sources. The magnitude of the optical counterpart can constrain whether the donor star is a giant (brighter than the main-sequence turn-off, with $M \gtrsim 1 M_{\odot}$), or a main sequence dwarf ($M \lesssim 1 M_{\odot}$) or white dwarf (fainter than the main-sequence turn-off). In general, the disc has a substantial contribution to the optical light of accreting systems. Otherwise, a position on the CMD of the cluster indicates most of the optical emission is dominated by the donor star (but a combination of the accretion disc and jet can also coincidentally appear as stellar light). An optical counterpart that is redder than the CMD of the cluster can be a sign of a stripped donor (Ivanova et al., 2017) or large jet contribution. A blue counterpart is generally taken as evidence of an accretion disc.

The information gained on the nature of radio sources based on their spectral indices may be enhanced with follow-up observations at lower (< 2 GHz) and higher ($>$ 15 GHz) frequencies than those covered by the MAVERIC survey. AGN or star-forming galaxies can be identified based on their X-ray–to–optical flux ratios (Mushotzky and Wandel, 1989; Anderson et al., 2003; Akiyama et al., 2003), and to a lesser extent, the radio–to–optical ratio (Afonso et al., 2005). The optical/X-ray (Russell et al., 2006; Bernardini et al., 2016) and radio/X-ray correlations for neutron stars and black holes (see Chapter 4) can similarly be used to find new X-ray binary candidates.

Confirming cluster membership of individual sources is only possible for bright (in the radio or optical bands) sources using VLBI, optical spectroscopy or optical astrometry with *Gaia*. Such studies can be used to measure the proper motion or radial velocity of a radio or optical source, and compare them to the motion of the globular cluster around the Galaxy, combined with the motion of stars within the cluster (described by the central velocity dispersion). Confirming the nature of cluster members can be achieved via mass estimation, or the detection of radio or X-ray pulsations in the case of pulsars. Minimum masses can be estimated using radial velocity measurements from the absorption spectra of companion stars, acquired over at least one full orbit. In our preliminary work, we identify NGC 6652 B as a source bright enough for future dynamical mass measurements. Deep, high-time resolution

acceleration searches, which can account for orbital accelerations in tight binaries (Ransom et al., 2002), can be used to confirm steep-spectrum radio sources as pulsars. Without these multi-wavelength studies, some indication of the nature of these radio sources may be obtained from their radial distribution and radio luminosity functions.

The MAVERIC data can also be used for variability studies. Our radio source analysis presented in Chapter 3 was performed on the stacked data on each cluster. Most clusters, however, have been observed over two or three days. Imaging each day separately can be used to constrain the variability of sources on such time scales, with the potential of finding scintillating pulsars, flaring stars, or outbursting compact objects. Highly variable sources might require simultaneous radio and X-ray observations to measure the power of the jet relative to the radiative output of the disc.

The current MAVERIC survey has a typical sensitivity of $L_{\rm R} \approx 10^{27}$ erg s^{-1}. At this luminosity, we have only detected the most luminous accreting systems. Most of these are likely to either have degenerate ($P_{\rm orb} \lesssim 1$ hr) or (sub-)giant donors ($P_{\rm orb} \gtrsim 1$ d), and have high mass transfer rates driven either by gravitational radiation or stellar evolution. However, globular cluster systems with orbital periods between 1 hr and 1 d are likely to be much too faint to be detected in quiescence in the radio band with current facilities. The detection in the radio band of such systems, possibly powered by magnetic braking, will require next-generation radio telescopes, such as the planned Square Kilometre Array (SKA) and Next Generation VLA (ngVLA) (Selina et al., 2018). These facilities may also be able to detect coronal emission from magnetic stars, and place tighter constraints on the presence of IMBHs in globular clusters (Wrobel et al., 2018).

Publications

Publications directly related to this thesis include:

- **Tudor, V.**; Miller-Jones,J. C. A.; Knigge, C.; Maccarone, T. J.; Tauris, T. M.; Bahramian, A.; Chomiuk, L.; Heinke, C. O.; Sivakoff, G. R.; Strader, J.; Plotkin, R. M.; Soria, R.; Albrow, M. D.; Anderson, G. E.; van den Berg, M.; Bernardini, F.; Bogdanov, S.; Britt, C. T.; Russell, D. M.; Zurek, D. R. (2018), "HST spectrum and timing of the ultra-compact X-ray binary candidate 47 Tuc X9", *Monthly Notices of the Royal Astronomical Society*, 476, 1889

  This work is reproduced in Chapter 5.

- **Tudor, V.**; Miller-Jones, J. C. A.; Patruno, A.; D'Angelo, C. R.; Jonker, P. G.; Russell, D. M.; Russell, T. D.; Bernardini, F.; Lewis, F.; Deller, A. T.; Hessels, J. W. T.; Migliari, S.; Plotkin, R. M.; Soria, R.; Wijnands, R. (2017), "Disc-jet coupling in low-luminosity accreting neutron stars", *Monthly Notices of the Royal Astronomical Society*, 470, 324

  This work is reproduced in Chapter 4.

- Tremou, E.; Strader, J.; Chomiuk, L.; Shishkovsky, L.; Maccarone, T. J.; Miller-Jones, J. C. A.; **Tudor, V.**; Heinke, C. O.; Sivakoff, G. R.; Seth, A. C.; Noyola, E. (2018), "The MAVERIC Survey: Still No Evidence for Accreting Intermediate-mass Black Holes in Globular Clusters", *The Astrophysical Journal*, 862, 16

  In Tremou et al., 2018, we searched for evidence of IMBHs at the centre of globular clusters in the full MAVERIC (ATCA and VLA) survey. No such evidence was found. I provided the images for those clusters observed with ATCA.

- Shishkovsky, L.; Strader, J.; Chomiuk, L.; Bahramian, A.; Tremou, E.; Li, K.-L.; Salinas, R.; **Tudor, V.**; Miller-Jones, J. C. A.; Maccarone, T. J.; Heinke, C. O.; Sivakoff, G. R. (2018), "The MAVERIC Survey: A Red Straggler Binary with an Invisible Companion in the Galactic Globular Cluster M10", *The Astrophysical Journal*, 855, 55

This work reports on the discovery of radio emission from a binary in the globular cluster M10, observed as part of the MAVERIC survey with the VLA. This system is either a face-on black hole or a flaring RS CVn binary. I contributed to the discussion.

- Bahramian, A.; Heinke, C. O.; **Tudor, V.**; Miller-Jones, James C. A.; Bogdanov, S.; Maccarone, T. J.; Knigge, C.; Sivakoff, G. R.; Chomiuk, L.; Strader, J.; Garcia, J. A.; Kallman, T. (2017), "The ultracompact nature of the black hole candidate X-ray binary 47 Tuc X9", *Monthly Notices of the Royal Astronomical Society*, 467, 2199

  As a follow-up to the discovery of a radio counterpart to 47 Tuc X9 by Miller-Jones et al., 2015, Bahramian et al. 2017 investigated the X-ray spectrum and timing properties, as well as the simultaneous radio and X-ray luminosity of the source. My contribution was the calibration and analysis of the radio data.

- Díaz Trigo, M.; Migliari, S.; Miller-Jones, J. C. A.; Rahoui, F.; Russell, D. M.; **Tudor, V.** (2017), "ALMA observations of 4U 1728–34 and 4U 1820–30: first detection of neutron star X-ray binaries at 300 GHz", *Astronomy & Astrophysics*, 600, 8

  Díaz Trigo et al., 2017 report on the first detections of mm emission with the Atacama Large Millimeter/submillimeter Array (ALMA) from neutron star LMXBs (4U 1728–34 and 4U 1820–30). These observations were carried out quasi-simultaneously with radio, infrared and X-ray observations to confirm the presence of a jet. For 4U 1820–30, located in the globular cluster NGC 6624, observed as part of our radio survey, I provided a model for the radio sources located in its vicinity. I also characterised the properties of the possible optical counterparts to two unrelated mm sources in the same field of 4U 1820–30.

- Tetarenko, A. J.; Bahramian, A.; Sivakoff, G. R.; Tremou, E.; Linares, M.; **Tudor, V.**; Miller-Jones, J. C. A.; Heinke, C. O.; Chomiuk, L.; Strader, J.; Altamirano, D.; Degenaar, N.; Maccarone, T.; Patruno, A.; Sanna, A.; Wijnands, R. (2016), "Disc-jet coupling in the Terzan 5 neutron star X-ray binary EXO 1745–248", *Monthly Notices of the Royal Astronomical Society*, 460, 345

  This paper investigates the radio and X-ray correlation in the 2016 neutron star transient EXO 1745–248 in the globular cluster Terzan 5. My contribution was to provide three of the five measurements of the radio flux, which were acquired as part of our globular cluster survey.

Astronomer's Telegrams:

- Bahramian, A.; Tetarenko, A.; Sivakoff, G.; Strader, J.; Chomiuk, L.; Heinke, C.; Miller-Jones, J.; Tremou, E.; **Tudor, V.** (2018), "VLA & Swift Observations of Liller 1 Indicate CXOU J173324.6–332321 is Likely a Neutron Star X-Ray Binary", *The Astronomer's Telegram*, No. 11646

- Tetarenko, A. J.; Bahramian, A.; Sivakoff, G. R.; Heinke, C. O.; Shaw, A. W.; Wijnands, R.; Degenaar, N.; Russell, T. D.; Miller-Jones, J. C. A.; Plotkin, R. M.; **Tudor, V.**; Homan, J.; Kuulkers, E.; Chakrabarty, D.; Chomiuk, L.; Strader, J.; Tremou, E.; Kennea, J. A.; Altamirano, D.; in't Zand, J. J. M.; Deller, A.; Maccarone, T. J.; Rivera-Sandoval, L. (2017), "Radio localization of IGR J16597-3704, a candidate neutron star X-ray binary undergoing an outburst in NGC 6256", *The Astronomer's Telegram*, No. 10894

- Russell, T.; Degenaar, N.; Miller-Jones, J.; **Tudor, V.** (2017), "Radio luminosity upper limits of the transient neutron star low-mass X-ray binary GRO J1744-28", *The Astronomer's Telegram*, No. 10106

- Homan, J.; Sivakoff, G.; Pooley, D.; Heinke, C.; Strader, J.; **Tudor, V.**; Miller-Jones, J. (2016), *Chandra identification of the X-ray transient MAXI J0911–635/Swift J0911.9–6452 in NGC 2808*, *The Astronomer's Telegram*, No. 8971

- **Tudor, V.**; Bahramian, A.; Sivakoff, G.; Chomiuk, L.; Heinke, C.; Li, R.; Maccarone, T.; Miller-Jones, J.; Plotkin, R.; Russell, T.; Strader, J.; Tetarenko, A.; Tremou, E. (2016), "Radio non-detection during nearly-simultaneous Swift/XRT observations of MAXI J0911–635/Swift J0911.9–6452 in NGC 2808", *The Astronomer's Telegram*, No. 8914

Bibliography

Abada-Simon, M., Lecacheux, A., Bastian, T. S., Bookbinder, J. A., and Dulk, G. A. (1993). The spectrum and variability of radio emission from AE Aquarii. *ApJ*, 406:692–700.

Abbott, B. P., Abbott, R., Abbott, T. D., Abernathy, M. R., Acernese, F., Ackley, K., Adams, C., Adams, T., Addesso, P., Adhikari, R. X., Adya, V. B., Affeldt, C., Agathos, M., Agatsuma, K., Aggarwal, N., Aguiar, O. D., Aiello, L., Ain, A., Ajith, P., Allen, B., Allocca, A., Altin, P. A., Anderson, S. B., Anderson, W. G., Arai, K., Arain, M. A., Araya, M. C., Arceneaux, C. C., Areeda, J. S., Arnaud, Collaboration, L. S., and Collaboration, V. (2016). Observation of gravitational waves from a binary black hole merger. *Phys. Rev. Lett.*, 116:061102.

Abbott, B. P., Abbott, R., Abbott, T. D., Acernese, F., Ackley, K., Adams, C., Adams, T., Addesso, P., Adhikari, R. X., Adya, V. B., and et al. (2017). Gravitational Waves and Gamma-Rays from a Binary Neutron Star Merger: GW170817 and GRB 170817A. *ApJ*, 848:L13.

Abdo, A. A., Ackermann, M., Ajello, M., Baldini, L., Ballet, J., Barbiellini, G., Bastieri, D., Bellazzini, R., Blandford, R. D., Bloom, E. D., Bonamente, E., Borgland, A. W., Bouvier, A., Brandt, T. J., Bregeon, J., Brigida, M., Bruel, P., Buehler, R., Buson, S., Caliandro, G. A., Cameron, R. A., Caraveo, P. A., Carrigan, S., Casandjian, J. M., Charles, E., Chaty, S., Chekhtman, A., Cheung, C. C., Chiang, J., Ciprini, S., Claus, R., Cohen-Tanugi, J., Conrad, J., Decesar, M. E., Dermer, C. D., de Palma, F., Digel, S. W., Silva, E. D. C. E., Drell, P. S., Dubois, R., Dumora, D., Favuzzi, C., Fortin, P., Frailis, M., Fukazawa, Y., Fusco, P., Gargano, F., Gasparrini, D., Gehrels, N., Germani, S., Giglietto, N., Giordano, F., Glanzman, T., Godfrey, G., Grenier, I., Grondin, M.-H., Grove, J. E., Guillemot, L., Guiriec, S., Hadasch, D., Harding, A. K., Hays, E., Jean, P., Jóhannesson, G., Johnson, T. J., Johnson, W. N., Kamae, T., Katagiri, H., Kataoka, J., Kerr, M., Knödlseder, J., Kuss, M., Lande, J., Latronico, L., Lee, S.-H., Lemoine-Goumard, M., Llena Garde, M., Longo, F., Loparco, F., Lovellette, M. N., Lubrano, P., Makeev, A., Mazziotta, M. N., Michelson, P. F., Mitthumsiri, W., Mizuno, T., Monte, C., Monzani, M. E., Morselli, A., Moskalenko,

I. V., Murgia, S., Naumann-Godo, M., Nolan, P. L., Norris, J. P., Nuss, E., Ohsugi, T., Omodei, N., Orlando, E., Ormes, J. F., Pancrazi, B., Parent, D., Pepe, M., Pesce-Rollins, M., Piron, F., Porter, T. A., Rainò, S., Rando, R., Reimer, A., Reimer, O., Reposeur, T., Ripken, J., Romani, R. W., Roth, M., Sadrozinski, H. F.-W., Saz Parkinson, P. M., Sgrò, C., Siskind, E. J., Smith, D. A., Spinelli, P., Strickman, M. S., Suson, D. J., Takahashi, H., Takahashi, T., Tanaka, T., Thayer, J. B., Thayer, J. G., Tibaldo, L., Torres, D. F., Tosti, G., Tramacere, A., Uchiyama, Y., Usher, T. L., Vasileiou, V., Venter, C., Vilchez, N., Vitale, V., Waite, A. P., Wang, P., Webb, N., Winer, B. L., Yang, Z., Ylinen, T., Ziegler, M., and Fermi LAT Collaboration (2010). A population of gamma-ray emitting globular clusters seen with the Fermi Large Area Telescope. *A&A*, 524:A75.

Afonso, J., Georgakakis, A., Almeida, C., Hopkins, A. M., Cram, L. E., Mobasher, B., and Sullivan, M. (2005). The Phoenix Deep Survey: Spectroscopic Catalog. *ApJ*, 624:135–154.

Agol, E. and Kamionkowski, M. (2002). X-rays from isolated black holes in the Milky Way. *MNRAS*, 334:553–562.

Akiyama, M., Ueda, Y., Ohta, K., Takahashi, T., and Yamada, T. (2003). Optical Identification of the ASCA Medium Sensitivity Survey in the Northern Sky: Nature of Hard X-Ray-Selected Luminous Active Galactic Nuclei. *ApJS*, 148:275–315.

Albrow, M. D., Gilliland, R. L., Brown, T. M., Edmonds, P. D., Guhathakurta, P., and Sarajedini, A. (2001). The Frequency of Binary Stars in the Core of 47 Tucanae. *ApJ*, 559:1060–1081.

Allard, F., Homeier, D., and Freytag, B. (2012). Models of very-low-mass stars, brown dwarfs and exoplanets. *Philosophical Transactions of the Royal Society of London Series A*, 370:2765–2777.

Allen, C., Jerius, D. H., and Gaetz, T. J. (2004). Parameterization of the Chandra point spread function. In Flanagan, K. A. and Siegmund, O. H. W., editors, *X-Ray and Gamma-Ray Instrumentation for Astronomy XIII*, volume 5165 of *Procspie*, pages 423–432.

Altamirano, D., Watts, A., Linares, M., Markwardt, C. B., Strohmayer, T., and Patruno, A. (2010). Type I X-ray bursts and burst oscillations in the accreting millisecond X-ray pulsar IGR J17511-3057. *MNRAS*, 409:1136–1145.

Amaro-Seoane, P., Audley, H., Babak, S., Baker, J., Barausse, E., Bender, P., Berti, E., Binetruy, P., Born, M., Bortoluzzi, D., Camp, J., Caprini, C., Cardoso, V., Colpi, M., Conklin, J., Cornish, N., Cutler, C., Danzmann, K., Dolesi, R., Ferraioli, L.,

Ferroni, V., Fitzsimons, E., Gair, J., Gesa Bote, L., Giardini, D., Gibert, F., Grimani, C., Halloin, H., Heinzel, G., Hertog, T., Hewitson, M., Holley-Bockelmann, K., Hollington, D., Hueller, M., Inchauspe, H., Jetzer, P., Karnesis, N., Killow, C., Klein, A., Klipstein, B., Korsakova, N., Larson, S. L., Livas, J., Lloro, I., Man, N., Mance, D., Martino, J., Mateos, I., McKenzie, K., McWilliams, S. T., Miller, C., Mueller, G., Nardini, G., Nelemans, G., Nofrarias, M., Petiteau, A., Pivato, P., Plagnol, E., Porter, E., Reiche, J., Robertson, D., Robertson, N., Rossi, E., Russano, G., Schutz, B., Sesana, A., Shoemaker, D., Slutsky, J., Sopuerta, C. F., Sumner, T., Tamanini, N., Thorpe, I., Troebs, M., Vallisneri, M., Vecchio, A., Vetrugno, D., Vitale, S., Volonteri, M., Wanner, G., Ward, H., Wass, P., Weber, W., Ziemer, J., and Zweifel, P. (2017). Laser Interferometer Space Antenna. *ArXiv e-prints*.

Anderson, S. F., Margon, B., Deutsch, E. W., Downes, R. A., and Allen, R. G. (1997). Time-Resolved Ultraviolet Observations of the Globular Cluster X-Ray Source in NGC 6624: The Shortest Known Period Binary System. *ApJ*, 482:L69–L72.

Anderson, S. F., Voges, W., Margon, B., Trümper, J., Agüeros, M. A., Boller, T., Collinge, M. J., Homer, L., Stinson, G., Strauss, M. A., Annis, J., Gómez, P., Hall, P. B., Nichol, R. C., Richards, G. T., Schneider, D. P., Vanden Berk, D. E., Fan, X., Ivezić, Ž., Munn, J. A., Newberg, H. J., Richmond, M. W., Weinberg, D. H., Yanny, B., Bahcall, N. A., Brinkmann, J., Fukugita, M., and York, D. G. (2003). A Large, Uniform Sample of X-Ray-Emitting AGNs: Selection Approach and an Initial Catalog from the ROSAT All-Sky and Sloan Digital Sky Surveys. *AJ*, 126:2209–2229.

Anglada, G., Estalella, R., Mauersberger, R., Torrelles, J. M., Rodriguez, L. F., Canto, J., Ho, P. T. P., and D'Alessio, P. (1995). The molecular environment of the HH 34 system. *ApJ*, 443:682–697.

Armas Padilla, M., Wijnands, R., Degenaar, N., Muñoz-Darias, T., Casares, J., and Fender, R. P. (2014). Swift J1357.2-0933: the faintest black hole? *MNRAS*, 444:902–905.

Armitage, P. J. and Livio, M. (1996). Accretion Disks in Interacting Binaries: Simulations of the Stream-Disk Impact. *ApJ*, 470:1024.

Arnaud, K., Smith, R., and Siemiginowska, A. (2011). *Handbook of X-ray Astronomy*. Cambridge University Press.

Arnaud, K. A. (1996). XSPEC: The First Ten Years. In Jacoby, G. H. and Barnes, J., editors, *Astronomical Data Analysis Software and Systems V*, volume 101 of *Astronomical Society of the Pacific Conference Series*, page 17.

Arnett, W. D., Schramm, D. N., and Truran, J. W. (1989). On relative supernova rates and nucleosynthesis roles. *ApJ*, 339:L25–L27.

Astraatmadja, T. L. and Bailer-Jones, C. A. L. (2016). Estimating Distances from Parallaxes. III. Distances of Two Million Stars in the Gaia DR1 Catalogue. *ApJ*, 833:119.

Atwood, W. B., Abdo, A. A., Ackermann, M., Althouse, W., Anderson, B., Axelsson, M., Baldini, L., Ballet, J., Band, D. L., Barbiellini, G., and et al. (2009). The Large Area Telescope on the Fermi Gamma-Ray Space Telescope Mission. *ApJ*, 697:1071–1102.

Bachetti, M., Harrison, F. A., Walton, D. J., Grefenstette, B. W., Chakrabarty, D., Fürst, F., Barret, D., Beloborodov, A., Boggs, S. E., Christensen, F. E., Craig, W. W., Fabian, A. C., Hailey, C. J., Hornschemeier, A., Kaspi, V., Kulkarni, S. R., Maccarone, T., Miller, J. M., Rana, V., Stern, D., Tendulkar, S. P., Tomsick, J., Webb, N. A., and Zhang, W. W. (2014). An ultraluminous X-ray source powered by an accreting neutron star. *Nature*, 514:202–204.

Baglio, M. C., D'Avanzo, P., Muñoz-Darias, T., Breton, R. P., and Campana, S. (2013). The long-term evolution of the X-ray pulsar XTE J1814-338: A receding jet contribution to the quiescent optical emission? *A&A*, 559:A42.

Bahramian, A., Heinke, C. O., Sivakoff, G. R., Altamirano, D., Wijnands, R., Homan, J., Linares, M., Pooley, D., Degenaar, N., and Gladstone, J. C. (2014). Discovery of the Third Transient X-Ray Binary in the Galactic Globular Cluster Terzan 5. *ApJ*, 780:127.

Bahramian, A., Heinke, C. O., Sivakoff, G. R., and Gladstone, J. C. (2013). Stellar Encounter Rate in Galactic Globular Clusters. *ApJ*, 766:136.

Bahramian, A., Heinke, C. O., Tudor, V., Miller-Jones, J. C. A., Bogdanov, S., Maccarone, T. J., Knigge, C., Sivakoff, G. R., Chomiuk, L., Strader, J., Garcia, J. A., and Kallman, T. (2017). The ultracompact nature of the black hole candidate X-ray binary 47 Tuc X9. *MNRAS*, 467:2199–2216.

Bahramian, A., Miller-Jones, J., Strader, J., Tetarenko, A., Plotkin, R., Rushton, A., Tudor, V., Motta, S., and Shishkovsky, L. (2018). Radio/X-ray correlation database for X-ray binaries.

Bailer-Jones, C. A. L. (2015). Estimating Distances from Parallaxes. *PASP*, 127:994.

Baldovin, C., Kuulkers, E., Ferrigno, C., Bozzo, E., Chenevez, J., Brandt, S., Beckmann, V., Bird, A., Domingo, A., Ebisawa, K., Jonker, P., Kretschmar, P., Markwardt,

C., Oosterbroek, T., Paizis, A., Risquez, D., Sanchez-Fernandez, C., Shaw, S., and Wijnands, R. (2009). INTEGRAL discovered a new hard X-ray source: IGRJ17511-3057. *The Astronomer's Telegram*, 2196.

Ballantyne, D. R. and Strohmayer, T. E. (2004). The Evolution of the Accretion Disk around 4U 1820-30 during a Superburst. *ApJ*, 602:L105–L108.

Bałucińska-Church, M., Church, M. J., and Smale, A. P. (2004). The orbital period of the dipping, bursting, globular cluster X-ray source XB 1746-371 from Rossi X-ray Timing Explorer observations. *MNRAS*, 347:334–338.

Bardeen, J. M. and Petterson, J. A. (1975). The Lense-Thirring Effect and Accretion Disks around Kerr Black Holes. *ApJ*, 195:L65.

Barkana, R. and Loeb, A. (2001). In the beginning: the first sources of light and the reionization of the universe. *PhR*, 349:125–238.

Barrett, P. E., Dieck, C., Beasley, A. J., Singh, K. P., and Mason, P. A. (2017). A Jansky VLA Survey of Magnetic Cataclysmic Variable Stars. I. The Data. *AJ*, 154:252.

Barthelmy, S. D., Barbier, L. M., Cummings, J. R., Fenimore, E. E., Gehrels, N., Hullinger, D., Krimm, H. A., Markwardt, C. B., Palmer, D. M., Parsons, A., Sato, G., Suzuki, M., Takahashi, T., Tashiro, M., and Tueller, J. (2005). The Burst Alert Telescope (BAT) on the SWIFT Midex Mission. *SSR*, 120:143–164.

Bassa, C. G., Patruno, A., Hessels, J. W. T., Keane, E. F., Monard, B., Mahony, E. K., Bogdanov, S., Corbel, S., Edwards, P. G., Archibald, A. M., Janssen, G. H., Stappers, B. W., and Tendulkar, S. (2014). A state change in the low-mass X-ray binary XSS J12270-4859. *MNRAS*, 441:1825–1830.

Bates, S. D., Lorimer, D. R., and Verbiest, J. P. W. (2013). The pulsar spectral index distribution. *MNRAS*, 431:1352–1358.

Baumgardt, H. (2017). N -body modelling of globular clusters: masses, mass-to-light ratios and intermediate-mass black holes. *MNRAS*, 464:2174–2202.

Baumgardt, H. and Hilker, M. (2018). A catalogue of masses, structural parameters, and velocity dispersion profiles of 112 Milky Way globular clusters. *MNRAS*, 478:1520–1557.

Baumgardt, H., Makino, J., and Hut, P. (2005). Which Globular Clusters Contain Intermediate-Mass Black Holes? *ApJ*, 620:238–243.

Begelman, M. C. (2010). Evolution of supermassive stars as a pathway to black hole formation. *MNRAS*, 402:673–681.

Begelman, M. C., McKee, C. F., and Shields, G. A. (1983). Compton heated winds and coronae above accretion disks. I Dynamics. *ApJ*, 271:70–88.

Bekki, K. and Freeman, K. C. (2003). Formation of ω Centauri from an ancient nucleated dwarf galaxy in the young Galactic disc. *MNRAS*, 346:L11–L15.

Belczynski, K., Bulik, T., Fryer, C. L., Ruiter, A., Valsecchi, F., Vink, J. S., and Hurley, J. R. (2010). On the Maximum Mass of Stellar Black Holes. *ApJ*, 714:1217–1226.

Bellazzini, M., Pasquali, A., Federici, L., Ferraro, F. R., and Pecci, F. F. (1995). Low-mass X-ray binaries in globular clusters: A new metallicity effect. *ApJ*, 439:687–694.

Belloni, D., Zorotovic, M., Schreiber, M. R., Leigh, N. W. C., Giersz, M., and Askar, A. (2017). mocca-SURVEY database I. Accreting white dwarf binary systems in globular clusters - III. Cataclysmic variables - implications of model assumptions. *MNRAS*, 468:2429–2446.

Benz, A. O. and Guedel, M. (1994). X-ray/microwave ratio of flares and coronae. *A&A*, 285:621–630.

Berdyugina, S. V. (2005). Starspots: A Key to the Stellar Dynamo. *Living Reviews in Solar Physics*, 2:8.

Bergeron, P., Saffer, R. A., and Liebert, J. (1992). A spectroscopic determination of the mass distribution of DA white dwarfs. *ApJ*, 394:228–247.

Bernardini, F., Cackett, E. M., Brown, E. F., D'Angelo, C., Degenaar, N., Miller, J. M., Reynolds, M., and Wijnands, R. (2013). Daily multiwavelength Swift monitoring of the neutron star low-mass X-ray binary Cen X-4: evidence for accretion and reprocessing during quiescence. *MNRAS*, 436:2465–2483.

Bernardini, F., Russell, D. M., Kolojonen, K. I. I., Stella, L., Hynes, R. I., and Corbel, S. (2016). On the Optical-X-Ray Correlation from Outburst to Quiescence in Low-mass X-Ray Binaries: The Representative Cases of V404 Cyg and Cen X-4. *ApJ*, 826:149.

Best, P. N., van Dokkum, P. G., Franx, M., and Röttgering, H. J. A. (2002). μJy radio sources in the cluster MS1054-03. *MNRAS*, 330:17–34.

Bildsten, L. (2002). Hot White Dwarf Donors in Ultracompact X-Ray Binaries. *ApJ*, 577:L27–L30.

Blandford, R. D. and Konigl, A. (1978). Relativistic Jets as Compact Radio Sources. In *Bulletin of the American Astronomical Society*, volume 10 of *BAAS*, page 629.

Blandford, R. D. and Payne, D. G. (1982). Hydromagnetic flows from accretion discs and the production of radio jets. *MNRAS*, 199:883–903.

Blandford, R. D. and Znajek, R. L. (1977). Electromagnetic extraction of energy from Kerr black holes. *MNRAS*, 179:433–456.

Blundell, K. M. and Hirst, P. (2011). Jet Propulsion of Wind Ejecta from a Major Flare in the Black Hole Microquasar SS433. *ApJ*, 735:L7.

Bogdanov, S., Archibald, A. M., Bassa, C., Deller, A. T., Halpern, J. P., Heald, G., Hessels, J. W. T., Janssen, G. H., Lyne, A. G., Moldón, J., Paragi, Z., Patruno, A., Perera, B. B. P., Stappers, B. W., Tendulkar, S. P., D'Angelo, C. R., and Wijnands, R. (2015). Coordinated X-Ray, Ultraviolet, Optical, and Radio Observations of the PSR J1023+0038 System in a Low-mass X-Ray Binary State. *ApJ*, 806:148.

Bogdanov, S., Deller, A. T., Miller-Jones, J. C. A., Archibald, A. M., Hessels, J. W. T., Jaodand, A., Patruno, A., Bassa, C., and D'Angelo, C. (2018). Simultaneous Chandra and VLA Observations of the Transitional Millisecond Pulsar PSR J1023+0038: Anti-correlated X-Ray and Radio Variability. *ApJ*, 856:54.

Bogdanov, S. and Halpern, J. P. (2015). Identification of the High-energy Gamma-Ray Source 3FGL J1544.6–1125 as a Transitional Millisecond Pulsar Binary in an Accreting State. *ApJ*, 803:L27.

Bogdanov, S., Heinke, C. O., Özel, F., and Güver, T. (2016). Neutron Star Mass-Radius Constraints of the Quiescent Low-mass X-Ray Binaries X7 and X5 in the Globular Cluster 47 Tuc. *ApJ*, 831:184.

Bogdanov, S., van den Berg, M., Heinke, C. O., Cohn, H. N., Lugger, P. M., and Grindlay, J. E. (2010). A Chandra X-ray Observatory Study of PSR J1740-5340 and Candidate Millisecond Pulsars in the Globular Cluster NGC 6397. *ApJ*, 709:241–250.

Bolton, C. T. (1972). Identification of Cygnus X-1 with HDE 226868. *Nature*, 235:271–273.

Bondi, H. (1952). On spherically symmetrical accretion. *MNRAS*, 112:195.

Bondi, H. and Hoyle, F. (1944). On the mechanism of accretion by stars. *MNRAS*, 104:273.

Bower, G. C., Roberts, D. A., Yusef-Zadeh, F., Backer, D. C., Cotton, W. D., Goss, W. M., Lang, C. C., and Lithwick, Y. (2005). A Radio Transient 0.1 Parsecs from Sagittarius A*. *ApJ*, 633:218–227.

Boyles, J., Lorimer, D. R., Turk, P. J., Mnatsakanov, R., Lynch, R. S., Ransom, S. M., Freire, P. C., and Belczynski, K. (2011). Young Radio Pulsars in Galactic Globular Clusters. *ApJ*, 742:51.

Bozzo, E., Kuulkers, E., Bazzano, A., Beckmann, V., Bird, T., Bodaghee, A., Chenevez, J., Del Santo, M., Domingo, A., Jonker, P., Kretschmar, P., Markwardt, C., Paizis, A., Pottschmidt, K., Sanchez-Fernandez, C., Wijnands, R., Ferrigno, C., and Tuerler, M. (2015a). INTEGRAL detects a new outburst from the millisecond X-ray pulsar IGR J17511-3057. *The Astronomer's Telegram*, 7275:1.

Bozzo, E., Papitto, A., Sanna, A., Falanga, M., Campana, S., Salvo, T. d., Iaria, R., Pintore, F., Riggio, A., and Egron, E. (2015b). The first thermonuclear X-ray burst from IGR J00291+5934. *The Astronomer's Telegram*, 7852.

Brassington, N. J., Fabbiano, G., Blake, S., Zezas, A., Angelini, L., Davies, R. L., Gallagher, J., Kalogera, V., Kim, D.-W., King, A. R., Kundu, A., Trinchieri, G., and Zepf, S. (2010). The X-ray Spectra of the Luminous LMXBs in NGC 3379: Field and Globular Cluster Sources. *ApJ*, 725:1805–1823.

Braun, H. (1997). PhD thesis, , Ludwig-Maximilians-Univ. München, (1997).

Breen, P. G. and Heggie, D. C. (2013). On black hole subsystems in idealized nuclear star clusters. *MNRAS*, 436:584–589.

Breivik, K., Chatterjee, S., and Larson, S. L. (2017). Revealing Black Holes with Gaia. *ApJ*, 850:L13.

Briggs, D. S. (1995). PhD thesis, New Mexico Institute of Mining and Technology.

Bult, P. and van der Klis, M. (2014). Discovery of 1-5 Hz Flaring at High Luminosity in SAX J1808.4-3658. *ApJ*, 789:99.

Burderi, L., Di Salvo, T., D'Antona, F., Robba, N. R., and Testa, V. (2003). The optical counterpart to SAX J1808.4-3658 in quiescence: Evidence of an active radio pulsar? *A&A*, 404:L43–L46.

Burgay, M., Burderi, L., Possenti, A., D'Amico, N., Manchester, R. N., Lyne, A. G., Camilo, F., and Campana, S. (2003). A Search for Pulsars in Quiescent Soft X-Ray Transients. I. *ApJ*, 589:902–910.

Burrows, D. N., Hill, J. E., Nousek, J. A., Kennea, J. A., Wells, A., Osborne, J. P., Abbey, A. F., Beardmore, A., Mukerjee, K., Short, A. D. T., Chincarini, G., Campana, S., Citterio, O., Moretti, A., Pagani, C., Tagliaferri, G., Giommi, P., Capalbi, M., Tamburelli, F., Angelini, L., Cusumano, G., Bräuninger, H. W., Burkert, W., and Hartner, G. D. (2005). The Swift X-Ray Telescope. *SSR*, 120:165–195.

Butt, Y. M., Maccarone, T. J., and Prantzos, N. (2003). Jet-induced Nucleosynthesis in Misaligned Microquasars. *ApJ*, 587:748–753.

Cackett, E. M., Brown, E. F., Miller, J. M., and Wijnands, R. (2010). Quiescent X-ray Emission From Cen X-4: A Variable Thermal Component. *ApJ*, 720:1325–1332.

Cackett, E. M., Wijnands, R., Heinke, C. O., Pooley, D., Lewin, W. H. G., Grindlay, J. E., Edmonds, P. D., Jonker, P. G., and Miller, J. M. (2006). A Chandra X-ray observation of the globular cluster Terzan 1. *MNRAS*, 369:407–415.

Camilo, F. and Rasio, F. A. (2005). Pulsars in Globular Clusters. In Rasio, F. A. and Stairs, I. H., editors, *Binary Radio Pulsars*, volume 328 of *Astronomical Society of the Pacific Conference Series*, page 147.

Campana, S., D'Avanzo, P., Casares, J., Covino, S., Israel, G., Marconi, G., Hynes, R., Charles, P., and Stella, L. (2004a). Indirect Evidence of an Active Radio Pulsar in the Quiescent State of the Transient Millisecond Pulsar SAX J1808.4-3658. *ApJ*, 614:L49–L52.

Campana, S., Israel, G. L., Stella, L., Gastaldello, F., and Mereghetti, S. (2004b). The Variable Quiescence of Centaurus X-4. *ApJ*, 601:474–478.

Campana, S. and Stella, L. (2000). On the Bolometric Quiescent Luminosity and Luminosity Swing of Black Hole Candidate and Neutron Star Low-Mass X-Ray Transients. *ApJ*, 541:849–859.

Campana, S., Stella, L., Gastaldello, F., Mereghetti, S., Colpi, M., Israel, G. L., Burderi, L., Di Salvo, T., and Robba, R. N. (2002). An XMM-Newton Study of the 401 Hz Accreting Pulsar SAX J1808.4-3658 in Quiescence. *ApJ*, 575:L15–L19.

Campana, S., Stella, L., Mereghetti, S., and Cremonesi, D. (2000). BeppoSAX observation of Cen X-4 in quiescence. *A&A*, 358:583–586.

Cantrell, A. G., Bailyn, C. D., McClintock, J. E., and Orosz, J. A. (2008). Optical State Changes in the X-Ray-quiescent Black Hole A0620-00. *ApJ*, 673:L159.

Cappellaro, E., Turatto, M., Tsvetkov, D. Y., Bartunov, O. S., Pollas, C., Evans, R., and Hamuy, M. (1997). The rate of supernovae from the combined sample of five searches. *A&A*, 322:431–441.

Casares, J. (2015). A FWHM-K_2 Correlation in Black Hole Transients. *ApJ*, 808:80.

Casares, J. (2016). Mass Ratio Determination from H_α Lines in Black Hole X-Ray Transients. *ApJ*, 822:99.

Casares, J. (2018). Hibernating black holes revealed by photometric mass functions. *Monthly Notices of the Royal Astronomical Society*, 473(4):5195–5209.

Casella, P., Maccarone, T. J., O'Brien, K., Fender, R. P., Russell, D. M., van der Klis, M., Pe'Er, A., Maitra, D., Altamirano, D., Belloni, T., Kanbach, G., Klein-Wolt, M., Mason, E., Soleri, P., Stefanescu, A., Wiersema, K., and Wijnands, R. (2010). Fast infrared variability from a relativistic jet in GX 339-4. *MNRAS*, 404:L21–L25.

Castor, J. I., Abbott, D. C., and Klein, R. I. (1975). Radiation-driven winds in Of stars. *ApJ*, 195:157–174.

Caswell, J. L. (2009). Precise Positions of Methanol Masers. *PASA*, 26:454–467.

Chakrabarty, D. (1998). High-Speed Optical Photometry of the Ultracompact X-Ray Binary 4U 1626-67. *ApJ*, 492:342–351.

Chakrabarty, D. and Morgan, E. H. (1998). The two-hour orbit of a binary millisecond X-ray pulsar. *Nature*, 394:346–348.

Chevalier, C., Ilovaisky, S. A., van Paradijs, J., Pedersen, H., and van der Klis, M. (1989). Optical studies of transient low-mass X-ray binaries in quiescence. I - Centaurus X-4: Orbital period, light curve, spectrum and models for the system. *A&A*, 210:114–126.

Chomiuk, L., Linford, J. D., Yang, J., O'Brien, T. J., Paragi, Z., Mioduszewski, A. J., Beswick, R. J., Cheung, C. C., Mukai, K., Nelson, T., Ribeiro, V. A. R. M., Rupen, M. P., Sokoloski, J. L., Weston, J., Zheng, Y., Bode, M. F., Eyres, S., Roy, N., and Taylor, G. B. (2014). Binary orbits as the driver of γ-ray emission and mass ejection in classical novae. *Nature*, 514:339–342.

Chomiuk, L., Strader, J., Maccarone, T. J., Miller-Jones, J. C. A., Heinke, C., Noyola, E., Seth, A. C., and Ransom, S. (2013). A Radio-selected Black Hole X-Ray Binary Candidate in the Milky Way Globular Cluster M62. *ApJ*, 777:69.

Chou, Y., Grindlay, J. E., and Bloser, P. F. (2001). Timing Analysis of the Light Curve of the Dipping-Bursting X-Ray Binary X1916-053. *ApJ*, 549:1135–1144.

Church, R. P., Strader, J., Davies, M. B., and Bobrick, A. (2017). Formation Constraints Indicate a Black Hole Accretor in 47 Tuc X9. *The Astrophysical Journal Letters*, 851(1):L4.

Clark, B. G. (1980). An efficient implementation of the algorithm 'CLEAN'. *A&A*, 89:377.

Clark, G. W. (1975). X-ray binaries in globular clusters. *ApJ*, 199:L143–L145.

Clarke, J. T., Capel, D., and Bowyer, S. (1984). The evolution of the optical spectrum of the dwarf nova SS Cygni over one complete outburst cycle. *ApJ*, 287:845–855.

Clausen, D., Sigurdsson, S., and Chernoff, D. F. (2014). Dynamically formed black hole+millisecond pulsar binaries in globular clusters. *MNRAS*, 442:207–219.

Clemens, J. C., Crain, J. A., and Anderson, R. (2004). The Goodman spectrograph. In Moorwood, A. F. M. and Iye, M., editors, *Ground-based Instrumentation for Astronomy*, volume 5492 of *Procspie*, pages 331–340.

Cohn, H. N., Lugger, P. M., Couch, S. M., Anderson, J., Cool, A. M., van den Berg, M., Bogdanov, S., Heinke, C. O., and Grindlay, J. E. (2010). Identification of Faint Chandra X-ray Sources in the Core-collapsed Globular Cluster NGC 6397: Evidence for a Bimodal Cataclysmic Variable Population. *ApJ*, 722:20–32.

Colpi, M., Mapelli, M., and Possenti, A. (2003). Probing the Presence of a Single or Binary Black Hole in the Globular Cluster NGC 6752 with Pulsar Dynamics. *ApJ*, 599:1260–1271.

Condon, J. J. (1984). Cosmological evolution of radio sources. *ApJ*, 287:461–474.

Condon, J. J. (2007). Deep Radio Surveys. In Afonso, J., Ferguson, H. C., Mobasher, B., and Norris, R., editors, *Deepest Astronomical Surveys*, volume 380 of *Astronomical Society of the Pacific Conference Series*, page 189.

Condon, J. J., Cotton, W. D., Fomalont, E. B., Kellermann, K. I., Miller, N., Perley, R. A., Scott, D., Vernstrom, T., and Wall, J. V. (2012). Resolving the Radio Source Background: Deeper Understanding through Confusion. *ApJ*, 758:23.

Conner, J. P., Evans, W. D., and Belian, R. D. (1969). The Recent Appearance of a New X-Ray Source in the Southern Sky. *ApJ*, 157:L157.

Coomber, G., Heinke, C. O., Cohn, H. N., Lugger, P. M., and Grindlay, J. E. (2011). The Unusual X-Ray Binaries of the Globular Cluster NGC 6652. *ApJ*, 735:95.

Coppejans, D. L., Körding, E. G., Miller-Jones, J. C. A., Rupen, M. P., Knigge, C., Sivakoff, G. R., and Groot, P. J. (2015). Novalike cataclysmic variables are significant radio emitters. *MNRAS*, 451:3801–3813.

Coppejans, D. L., Körding, E. G., Miller-Jones, J. C. A., Rupen, M. P., Sivakoff, G. R., Knigge, C., Groot, P. J., Woudt, P. A., Waagen, E. O., and Templeton, M. (2016). Dwarf nova-type cataclysmic variable stars are significant radio emitters. *MNRAS*, 463:2229–2241.

Corbel, S., Coriat, M., Brocksopp, C., Tzioumis, A. K., Fender, R. P., Tomsick, J. A., Buxton, M. M., and Bailyn, C. D. (2013). The 'universal' radio/X-ray flux correlation: the case study of the black hole GX 339-4. *MNRAS*, 428:2500–2515.

Corbel, S., Koerding, E., and Kaaret, P. (2008). Revisiting the radio/X-ray flux correlation in the black hole V404 Cyg: from outburst to quiescence. *MNRAS*, 389:1697–1702.

Corbel, S., Tomsick, J. A., and Kaaret, P. (2006). On the Origin of Black Hole X-Ray Emission in Quiescence: Chandra Observations of XTE J1550-564 and H1743-322. *ApJ*, 636:971–978.

Coriat, M., Corbel, S., Prat, L., Miller-Jones, J. C. A., Cseh, D., Tzioumis, A. K., Brocksopp, C., Rodriguez, J., Fender, R. P., and Sivakoff, G. R. (2011). Accretion-outflow connection in the outliers of the "universal" radio/X-ray correlation. In Romero, G. E., Sunyaev, R. A., and Belloni, T., editors, *Jets at All Scales*, volume 275 of *IAU Symposium*, pages 255–259.

Coriat, M., Fender, R. P., and Dubus, G. (2012). Revisiting a fundamental test of the disc instability model for X-ray binaries. *MNRAS*, 424:1991–2001.

Corral-Santana, J. M., Casares, J., Muñoz-Darias, T., Rodríguez-Gil, P., Shahbaz, T., Torres, M. A. P., Zurita, C., and Tyndall, A. A. (2013). A Black Hole Nova Obscured by an Inner Disk Torus. *Science*, 339:1048–1051.

Crawford, D. F., Jauncey, D. L., and Murdoch, H. S. (1970). Maximum-Likelihood Estimation of the Slope from Number-Flux Counts of Radio Sources. *ApJ*, 162:405.

Cseh, D., Kaaret, P., Corbel, S., Krding, E., Coriat, M., Tzioumis, A., and Lanzoni, B. (2010). Radio observations of NGC 6388: an upper limit on the mass of its central black hole. *MNRAS*, 406:1049–1054.

Cummings, J. R., Page, K. L., Palmer, D. M., Racusin, J. L., and Siegel, M. H. (2015). Trigger 650140: Swift detection of IGR J00291+5934. *GRB Coordinates Network*, 18051.

Curtis, H. D. (1918). Descriptions of 762 Nebulae and Clusters Photographed with the Crossley Reflector. *Publications of Lick Observatory*, 13:9–42.

Da Costa, G. S. and Armandroff, T. E. (1995). Abundances and Kinematics of the Globular Cluster Systems of the Galaxy and of the Sagittarius Dwarf. *AJ*, 109:2533.

Dage, K. C., Zepf, S. E., Bahramian, A., Kundu, A., Maccarone, T. J., and Peacock, M. B. (2018). X-ray Variability from the Ultraluminous Black Hole Candidate X-ray Binary in the Globular Cluster RZ 2109. *ArXiv e-prints*.

D'Amico, N., Possenti, A., Manchester, R. N., Sarkissian, J., Lyne, A. G., and Camilo, F. (2001). An Eclipsing Millisecond Pulsar with a Possible Main-Sequence Companion in NGC 6397. *ApJ*, 561:L89–L92.

D'Angelo, C. R., Fridriksson, J. K., Messenger, C., and Patruno, A. (2015). The radiative efficiency of a radiatively inefficient accretion flow. *MNRAS*, 449:2803–2817.

De Falco, V., Kuiper, L., Bozzo, E., Galloway, D. K., Poutanen, J., Ferrigno, C., Stella, L., and Falanga, M. (2017). The 2015 outburst of the accretion-powered pulsar IGR J00291+5934: INTEGRAL and Swift observations. *A&A*, 599:A88.

de Jong, J. A., van Paradijs, J., and Augusteijn, T. (1996). Reprocessing of X rays in low-mass X-ray binaries. *A&A*, 314:484–490.

de Martino, D., Casares, J., Mason, E., Buckley, D. A. H., Kotze, M. M., Bonnet-Bidaud, J.-M., Mouchet, M., Coppejans, R., and Gulbis, A. A. S. (2014). Unveiling the redback nature of the low-mass X-ray binary XSS J1227.0-4859 through optical observations. *MNRAS*, 444:3004–3014.

de Val-Borro, M., Karovska, M., and Sasselov, D. (2009). Numerical Simulations of Wind Accretion in Symbiotic Binaries. *ApJ*, 700:1148–1160.

de Zotti, G., Massardi, M., Negrello, M., and Wall, J. (2010). Radio and millimeter continuum surveys and their astrophysical implications. *AAPR*, 18:1–65.

DeCesar, M. E., Ransom, S. M., Kaplan, D. L., Ray, P. S., and Geller, A. M. (2015). A Highly Eccentric 3.9 Millisecond Binary Pulsar in the Globular Cluster NGC 6652. *ApJ*, 807:L23.

Del Santo, M., Nucita, A. A., Lodato, G., Manni, L., De Paolis, F., Farihi, J., De Cesare, G., and Segreto, A. (2014). The puzzling source IGR J17361-4441 in NGC 6388: a possible planetary tidal disruption event. *MNRAS*, 444:93–101.

Deller, A. T., Moldon, J., Miller-Jones, J. C. A., Patruno, A., Hessels, J. W. T., Archibald, A. M., Paragi, Z., Heald, G., and Vilchez, N. (2015). Radio Imaging Observations of PSR J1023+0038 in an LMXB State. *ApJ*, 809:13.

Deloye, C. J. and Bildsten, L. (2003). White Dwarf Donors in Ultracompact Binaries: The Stellar Structure of Finite-Entropy Objects. *ApJ*, 598:1217–1228.

Deutsch, E. W., Margon, B., and Anderson, S. F. (2000). Ultracompact X-Ray Binaries in Globular Clusters: Variability of the Optical Counterpart of X1832-330 in NGC 6652. *ApJ*, 530:L21–L24.

Dewdney, P. E., Hall, P. J., Schilizzi, R. T., and Lazio, T. J. L. W. (2009). The Square Kilometre Array. *IEEE Proceedings*, 97:1482–1496.

Dewi, J. D. M., Pols, O. R., Savonije, G. J., and van den Heuvel, E. P. J. (2002). The evolution of naked helium stars with a neutron star companion in close binary systems. *MNRAS*, 331:1027–1040.

Díaz Trigo, M., Migliari, S., Miller-Jones, J. C. A., Rahoui, F., Russell, D. M., and Tudor, V. (2017). ALMA observations of 4U 1728-34 and 4U 1820-30: first detection of neutron star X-ray binaries at 300 GHz. *A&A*, 600:A8.

Drappeau, S., Malzac, J., Coriat, M., Rodriguez, J., Belloni, T. M., Belmont, R., Clavel, M., Chakravorty, S., Corbel, S., Ferreira, J., Gandhi, P., Henri, G., and Petrucci, P.-O. (2017). Dark jets in the soft X-ray state of black hole binaries? *MNRAS*, 466:4272–4278.

Dufour, P., Fontaine, G., Liebert, J., Schmidt, G. D., and Behara, N. (2008). Hot DQ White Dwarfs: Something Different. *ApJ*, 683:978–989.

Dunkel, J., Chluba, J., and Sunyaev, R. A. (2006). Accretion of helium and metal-rich gas onto neutron stars and black holes at high luminosities. *Astronomy Letters*, 32:257–262.

Eastman, J., Siverd, R., and Gaudi, B. S. (2010). Achieving Better Than 1 Minute Accuracy in the Heliocentric and Barycentric Julian Dates. *PASP*, 122:935.

Ebisuzaki, T., Makino, J., Tsuru, T. G., Funato, Y., Portegies Zwart, S., Hut, P., McMillan, S., Matsushita, S., Matsumoto, H., and Kawabe, R. (2001). Missing Link Found? The "Runaway" Path to Supermassive Black Holes. *ApJ*, 562:L19–L22.

Eckert, D., Walter, R., Kretschmar, P., Mas-Hesse, M., Palumbo, G. G. C., Roques, J.-P., Ubertini, P., and Winkler, C. (2004). IGR J00291+5934, a new X-ray transient discovered with INTEGRAL. *The Astronomer's Telegram*, 352.

Eddington, A. S. (1913). On a formula for correcting statistics for the effects of a known error of observation. *MNRAS*, 73:359–360.

Edmonds, P. D., Gilliland, R. L., Heinke, C. O., and Grindlay, J. E. (2003). An Extensive Census of Hubble Space Telescope Counterparts to Chandra X-Ray Sources in the Globular Cluster 47 Tucanae. II. Time Series and Analysis. *ApJ*, 596:1197–1219.

Eggleton, P. P. (1983). Approximations to the radii of Roche lobes. *ApJ*, 268:368.

Eggleton, P. P. and Kisseleva-Eggleton, L. (2006). A Mechanism for Producing Short-Period Binaries. *Ap&SS*, 304:75–79.

Ehlert, S., Allen, S. W., Brandt, W. N., Xue, Y. Q., Luo, B., von der Linden, A., Mantz, A., and Morris, R. G. (2013). X-ray bright active galactic nuclei in massive galaxy clusters - I. Number counts and spatial distribution. *MNRAS*, 428:3509–3525.

Einstein, A. (1916). Die Grundlage der allgemeinen Relativitätstheorie. *Annalen der Physik*, 354:769–822.

Ekşi, K. Y., Andaç, İ. C., Çıkıntoğlu, S., Gençali, A. A., Güngör, C., and Öztekin, F. (2015). The ultraluminous X-ray source NuSTAR J095551+6940.8: a magnetar in a high-mass X-ray binary. *MNRAS*, 448:L40–L42.

Elbert, O. D., Bullock, J. S., and Kaplinghat, M. (2018). Counting black holes: The cosmic stellar remnant population and implications for LIGO. *MNRAS*, 473:1186–1194.

Elebert, P., Reynolds, M. T., Callanan, P. J., Hurley, D. J., Ramsay, G., Lewis, F., Russell, D. M., Nord, B., Kane, S. R., Depoy, D. L., and Hakala, P. (2009). Optical spectroscopy and photometry of SAX J1808.4-3658 in outburst. *MNRAS*, 395:884–894.

Engel, M. C., Heinke, C. O., Sivakoff, G. R., Elshamouty, K. G., and Edmonds, P. D. (2012). A 2.15 hr Orbital Period for the Low-mass X-Ray Binary XB 1832-330 in the Globular Cluster NGC 6652. *ApJ*, 747:119.

Espinasse, M. and Fender, R. (2018). Spectral differences between the jets in 'radio-loud' and 'radio-quiet' hard-state black hole binaries. *MNRAS*, 473:4122–4129.

Esposito, P., Israel, G. L., Dall'Osso, S., and Covino, S. (2014). Swift X-ray and ultraviolet observations of the shortest orbital period double-degenerate system RX J0806.3+1527 (HM Cnc). *A&A*, 561:A117.

Evans, W. D., Belian, R. D., and Conner, J. P. (1970). Observations of the Development and Disappearance of the X-Ray Source Centaurus XR-4. *ApJ*, 159:L57.

Fabian, A. C. (2012). Observational Evidence of Active Galactic Nuclei Feedback. *ARA&A*, 50:455–489.

Fabian, A. C., Pringle, J. E., and Rees, M. J. (1975). Tidal capture formation of binary systems and X-ray sources in globular clusters. *MNRAS*, 172:15p–18p.

Falcke, H. and Biermann, P. L. (1995). The jet-disk symbiosis. I. Radio to X-ray emission models for quasars. *A&A*, 293.

Falcke, H., Körding, E., and Markoff, S. (2004). A scheme to unify low-power accreting black holes. Jet-dominated accretion flows and the radio/X-ray correlation. *A&A*, 414:895–903.

Fan, X., Narayanan, V. K., Lupton, R. H., Strauss, M. A., Knapp, G. R., Becker, R. H., White, R. L., Pentericci, L., Leggett, S. K., Haiman, Z., Gunn, J. E., Ivezić, Ž., Schneider, D. P., Anderson, S. F., Brinkmann, J., Bahcall, N. A., Connolly, A. J., Csabai, I., Doi, M., Fukugita, M., Geballe, T., Grebel, E. K., Harbeck, D., Hennessy, G., Lamb, D. Q., Miknaitis, G., Munn, J. A., Nichol, R., Okamura, S., Pier, J. R., Prada, F., Richards, G. T., Szalay, A., and York, D. G. (2001). A Survey of z>5.8 Quasars in the Sloan Digital Sky Survey. I. Discovery of Three New Quasars and the Spatial Density of Luminous Quasars at z˜6. *AJ*, 122:2833–2849.

Farr, W. M., Sravan, N., Cantrell, A., Kreidberg, L., Bailyn, C. D., Mandel, I., and Kalogera, V. (2011). The Mass Distribution of Stellar-mass Black Holes. *ApJ*, 741:103.

Farrell, S. A., Webb, N. A., Barret, D., Godet, O., and Rodrigues, J. M. (2009). An intermediate-mass black hole of over 500 solar masses in the galaxy ESO243-49. *Nature*, 460:73–75.

Feigelson, E. D. and Nelson, P. I. (1985). Statistical methods for astronomical data with upper limits. I - Univariate distributions. *ApJ*, 293:192–206.

Fender, R., De Bruyn, G., Pooley, G., and Stappers, B. (2004a). The radio counterpart of IGR J00291+5934. *The Astronomer's Telegram*, 361.

Fender, R., Wu, K., Johnston, H., Tzioumis, T., Jonker, P., Spencer, R., and van der Klis, M. (2004b). An ultra-relativistic outflow from a neutron star accreting gas from a companion. *Nature*, 427:222–224.

Fender, R. P. (2001). Powerful jets from black hole X-ray binaries in low/hard X-ray states. *MNRAS*, 322:31–42.

Fender, R. P., Belloni, T. M., and Gallo, E. (2004c). Towards a unified model for black hole X-ray binary jets. *MNRAS*, 355:1105–1118.

Fender, R. P., Gallo, E., and Jonker, P. G. (2003). Jet-dominated states: an alternative to advection across black hole event horizons in 'quiescent' X-ray binaries. *MNRAS*, 343:L99–L103.

Fender, R. P., Garrington, S. T., McKay, D. J., Muxlow, T. W. B., Pooley, G. G., Spencer, R. E., Stirling, A. M., and Waltman, E. B. (1999). MERLIN observations of relativistic ejections from GRS 1915+105. *MNRAS*, 304:865–876.

Fender, R. P. and Hendry, M. A. (2000). The radio luminosity of persistent X-ray binaries. *MNRAS*, 317:1–8.

Fender, R. P., Russell, D. M., Knigge, C., Soria, R., Hynes, R. I., and Goad, M. (2009). An anticorrelation between X-ray luminosity and Hα equivalent width in X-ray binaries. *MNRAS*, 393:1608–1616.

Ferrarese, L. and Merritt, D. (2000). A Fundamental Relation between Supermassive Black Holes and Their Host Galaxies. *ApJ*, 539:L9–L12.

Fiacconi, D. and Rossi, E. M. (2017). Light or heavy supermassive black hole seeds: the role of internal rotation in the fate of supermassive stars. *MNRAS*, 464:2259–2269.

Flower, D. R., Penn, C. J., and Seaton, M. J. (1982). Ultraviolet spectra of planetary nebulae. IX - High-dispersion observations of NGC 7662. *MNRAS*, 201:39P–43P.

Fomalont, E. B., Geldzahler, B. J., and Bradshaw, C. F. (2001). Scorpius X-1: Energy Transfer from the Core to the Radio Lobes. *ApJ*, 553:L27–L30.

Ford, E. B., Kozinsky, B., and Rasio, F. A. (2000). Secular Evolution of Hierarchical Triple Star Systems. *ApJ*, 535:385–401.

Fragile, P. C., Blaes, O. M., Anninos, P., and Salmonson, J. D. (2007). Global General Relativistic Magnetohydrodynamic Simulation of a Tilted Black Hole Accretion Disk. *ApJ*, 668:417–429.

Fragile, P. C., Mathews, G. J., and Wilson, J. R. (2001). Bardeen-Petterson Effect and Quasi-periodic Oscillations in X-Ray Binaries. *ApJ*, 553:955–959.

Fragos, T., Lehmer, B. D., Naoz, S., Zezas, A., and Basu-Zych, A. (2013). Energy Feedback from X-Ray Binaries in the Early Universe. *ApJ*, 776:L31.

Frank, J., King, A., and Raine, D. J. (2002). *Accretion Power in Astrophysics: Third Edition*. Cambridge University Press.

Frank, J., King, A. R., and Lasota, J.-P. (1987). The light curves of low-mass X-ray binaries. *A&A*, 178:137–142.

Freire, P. C., Kramer, M., Lyne, A. G., Camilo, F., Manchester, R. N., and D'Amico, N. (2001). Detection of Ionized Gas in the Globular Cluster 47 Tucanae. *ApJ*, 557:L105–L108.

Freire, P. C. C., Ridolfi, A., Kramer, M., Jordan, C., Manchester, R. N., Torne, P., Sarkissian, J., Heinke, C. O., D'Amico, N., Camilo, F., Lorimer, D. R., and Lyne, A. G. (2017). Long-term observations of the pulsars in 47 Tucanae - II. Proper motions, accelerations and jerks. *MNRAS*, 471:857–876.

Froning, C. S., Cantrell, A. G., Maccarone, T. J., France, K., Khargharia, J., Winter, L. M., Robinson, E. L., Hynes, R. I., Broderick, J. W., Markoff, S., Torres, M. A. P., Garcia, M., Bailyn, C. D., Prochaska, J. X., Werk, J., Thom, C., Béland, S., Danforth, C. W., Keeney, B., and Green, J. C. (2011). Multiwavelength Observations of A0620-00 in Quiescence. *ApJ*, 743:26.

Gaensler, B. M., Stappers, B. W., and Getts, T. J. (1999). Transient Radio Emission from SAX J1808.4-3658. *ApJ*, 522:L117–L119.

Gaia Collaboration, Prusti, T., de Bruijne, J. H. J., Brown, A. G. A., Vallenari, A., Babusiaux, C., Bailer-Jones, C. A. L., Bastian, U., Biermann, M., Evans, D. W., and et al. (2016). The Gaia mission. *A&A*, 595:A1.

Galleti, S., Federici, L., Bellazzini, M., Fusi Pecci, F., and Macrina, S. (2004). 2MASS NIR photometry for 693 candidate globular clusters in M 31 and the Revised Bologna Catalogue. *A&A*, 416:917–924.

Gallo, E., Degenaar, N., and van den Eijnden, J. (2018). Hard state neutron star and black hole X-ray binaries in the radio:X-ray luminosity plane. *MNRAS*, 478:L132–L136.

Gallo, E., Fender, R., Kaiser, C., Russell, D., Morganti, R., Oosterloo, T., and Heinz, S. (2005). A dark jet dominates the power output of the stellar black hole Cygnus X-1. *Nature*, 436:819–821.

Gallo, E., Fender, R. P., Miller-Jones, J. C. A., Merloni, A., Jonker, P. G., Heinz, S., Maccarone, T. J., and van der Klis, M. (2006). A radio-emitting outflow in the quiescent state of A0620-00: implications for modelling low-luminosity black hole binaries. *MNRAS*, 370:1351–1360.

Gallo, E., Fender, R. P., and Pooley, G. G. (2003). A universal radio-X-ray correlation in low/hard state black hole binaries. *MNRAS*, 344:60–72.

Gallo, E., Homan, J., Jonker, P. G., and Tomsick, J. A. (2008a). Chandra Detection of XTE J1650-500 in Quiescence and the Minimum Luminosity of Black Hole X-Ray Binaries. *ApJ*, 683:L51–L54.

Gallo, E., Migliari, S., Markoff, S., Tomsick, J. A., Bailyn, C. D., Berta, S., Fender, R., and Miller-Jones, J. C. A. (2007). The Spectral Energy Distribution of Quiescent Black Hole X-Ray Binaries: New Constraints from Spitzer. *ApJ*, 670:600–609.

Gallo, E., Miller, B. P., and Fender, R. (2012). Assessing luminosity correlations via cluster analysis: evidence for dual tracks in the radio/X-ray domain of black hole X-ray binaries. *MNRAS*, 423:590–599.

Gallo, E., Miller-Jones, J. C. A., Russell, D. M., Jonker, P. G., Homan, J., Plotkin, R. M., Markoff, S., Miller, B. P., Corbel, S., and Fender, R. P. (2014). The radio/X-ray domain of black hole X-ray binaries at the lowest radio luminosities. *MNRAS*, 445:290–300.

Gallo, E., Treu, T., Jacob, J., Woo, J.-H., Marshall, P. J., and Antonucci, R. (2008b). AMUSE-Virgo. I. Supermassive Black Holes in Low-Mass Spheroids. *ApJ*, 680:154–168.

Galloway, D. K. and Cumming, A. (2006). Helium-rich Thermonuclear Bursts and the Distance to the Accretion-powered Millisecond Pulsar SAX J1808.4-3658. *ApJ*, 652:559–568.

Galloway, D. K., Markwardt, C. B., Morgan, E. H., Chakrabarty, D., and Strohmayer, T. E. (2005). Discovery of the Accretion-powered Millisecond X-Ray Pulsar IGR J00291+5934. *ApJ*, 622:L45–L48.

Garcia, M. R., McClintock, J. E., Narayan, R., Callanan, P., Barret, D., and Murray, S. S. (2001). New Evidence for Black Hole Event Horizons from Chandra. *ApJ*, 553:L47–L50.

Gebhardt, K., Rich, R. M., and Ho, L. C. (2005). An Intermediate-Mass Black Hole in the Globular Cluster G1: Improved Significance from New Keck and Hubble Space Telescope Observations. *ApJ*, 634:1093–1102.

Gehrels, N. (1986). Confidence limits for small numbers of events in astrophysical data. *ApJ*, 303:336–346.

Gehrels, N., Chincarini, G., Giommi, P., Mason, K. O., Nousek, J. A., Wells, A. A., White, N. E., Barthelmy, S. D., Burrows, D. N., Cominsky, L. R., Hurley, K. C., Marshall, F. E., Mészáros, P., Roming, P. W. A., Angelini, L., Barbier, L. M., Belloni, T., Campana, S., Caraveo, P. A., Chester, M. M., Citterio, O., Cline, T. L., Cropper, M. S., Cummings, J. R., Dean, A. J., Feigelson, E. D., Fenimore, E. E., Frail, D. A., Fruchter, A. S., Garmire, G. P., Gendreau, K., Ghisellini, G., Greiner, J., Hill, J. E., Hunsberger, S. D., Krimm, H. A., Kulkarni, S. R., Kumar, P., Lebrun, F., Lloyd-Ronning, N. M., Markwardt, C. B., Mattson, B. J., Mushotzky, R. F., Norris, J. P., Osborne, J., Paczynski, B., Palmer, D. M., Park, H.-S., Parsons, A. M., Paul, J., Rees, M. J., Reynolds, C. S., Rhoads, J. E., Sasseen, T. P., Schaefer, B. E., Short, A. T., Smale, A. P., Smith, I. A., Stella, L., Tagliaferri, G., Takahashi, T., Tashiro, M., Townsley, L. K., Tueller, J., Turner, M. J. L., Vietri, M., Voges, W., Ward, M. J., Willingale, R., Zerbi, F. M., and Zhang, W. W. (2004). The Swift Gamma-Ray Burst Mission. *ApJ*, 611:1005–1020.

Gendre, B., Barret, D., and Webb, N. A. (2003). An XMM-Newton observation of the globular cluster Omega Centauri. *A&A*, 400:521–531.

Giacconi, R., Gursky, H., Paolini, F. R., and Rossi, B. B. (1962). Evidence for x Rays From Sources Outside the Solar System. *Physical Review Letters*, 9:439–443.

Gierliński, M., Done, C., and Page, K. (2008). X-ray irradiation in XTE J1817-330 and the inner radius of the truncated disc in the hard state. *MNRAS*, 388:753–760.

Giersz, M. and Heggie, D. C. (2011). Monte Carlo simulations of star clusters - VII. The globular cluster 47 Tuc. *MNRAS*, 410:2698–2713.

Gies, D. R. and Bolton, C. T. (1986). The Optical Spectrum of HDE 226868 = Cygnus X-1. III. A Focused Stellar Wind Model for He II lambda 4686 Emission. *ApJ*, 304:389.

Giesers, B., Dreizler, S., Husser, T.-O., Kamann, S., Anglada Escudé, G., Brinchmann, J., Carollo, C. M., Roth, M. M., Weilbacher, P. M., and Wisotzki, L. (2018). A detached stellar-mass black hole candidate in the globular cluster NGC 3201. *MNRAS*, 475:L15–L19.

Giles, A. B., Hill, K. M., and Greenhill, J. G. (1999). The optical counterpart of SAX J1808.4 - 3658, the transient bursting millisecond X-ray pulsar. *MNRAS*, 304:47–51.

Gilfanov, M., Revnivtsev, M., Sunyaev, R., and Churazov, E. (1998). The millisecond X-ray pulsar/burster SAX J1808.4-3658: the outburst light curve and the power law spectrum. *A&A*, 338:L83–L86.

Gilliland, R. L., Brown, T. M., Guhathakurta, P., Sarajedini, A., Milone, E. F., Albrow, M. D., Baliber, N. R., Bruntt, H., Burrows, A., Charbonneau, D., Choi, P., Cochran, W. D., Edmonds, P. D., Frandsen, S., Howell, J. H., Lin, D. N. C., Marcy, G. W., Mayor, M., Naef, D., Sigurdsson, S., Stagg, C. R., Vandenberg, D. A., Vogt, S. S., and Williams, M. D. (2000). A Lack of Planets in 47 Tucanae from a Hubble Space Telescope Search. *ApJ*, 545:L47–L51.

González Hernández, J. I., Rebolo, R., Peñarrubia, J., Casares, J., and Israelian, G. (2005). On the kinematics of the neutron star low mass X-ray binary Cen X-4. *A&A*, 435:1185–1190.

Gratton, R. G., Bragaglia, A., Carretta, E., Clementini, G., Desidera, S., Grundahl, F., and Lucatello, S. (2003). Distances and ages of NGC 6397, NGC 6752 and 47 Tuc. *A&A*, 408:529–543.

Greenhill, J. G., Giles, A. B., and Coutures, C. (2006). A transient I-band excess in the optical spectrum of the accreting millisecond pulsar SAX J1808.4-3658. *MNRAS*, 370:1303–1308.

Grindlay, J. E. (1987). On the origin of neutron stars in globular clusters. In Helfand, D. J. and Huang, J.-H., editors, *The Origin and Evolution of Neutron Stars*, volume 125 of *IAU Symposium*, pages 173–184.

Grindlay, J. E., Bailyn, C. D., Cohn, H., Lugger, P. M., Thorstensen, J. R., and Wegner, G. (1988). Discovery of a possible X-ray triple - 4U 1915-05. *ApJ*, 334:L25–L29.

Grindlay, J. E., Heinke, C., Edmonds, P. D., and Murray, S. S. (2001a). High-Resolution X-ray Imaging of a Globular Cluster Core: Compact Binaries in 47Tuc. *Science*, 292:2290–2295.

Grindlay, J. E., Heinke, C. O., Edmonds, P. D., Murray, S. S., and Cool, A. M. (2001b). Chandra Exposes the Core-collapsed Globular Cluster NGC 6397. *ApJ*, 563:L53–L56.

Grindlay, J. E. and Seaquist, E. R. (1986). Radio observations of galactic bulge and globular cluster X-ray sources. *ApJ*, 310:172–175.

Gusinskaia, N. V., Deller, A. T., Hessels, J. W. T., Degenaar, N., Miller-Jones, J. C. A., Wijnands, R., Parikh, A. S., Russell, T. D., and Altamirano, D. (2017). Jet quenching in the neutron star low-mass X-ray binary 1RXS J180408.9-342058. *MNRAS*, 470:1871–1880.

Hammerstein, E. K., Cackett, E. M., Reynolds, M. T., and Miller, J. M. (2018). Constraining the inclination of the Low-Mass X-ray Binary Cen X-4. *MNRAS*.

Harris, W. E. (1996). A Catalog of Parameters for Globular Clusters in the Milky Way. *AJ*, 112:1487.

Hartman, J. M., Galloway, D. K., and Chakrabarty, D. (2011). A Double Outburst from IGR J00291+5934: Implications for Accretion Disk Instability Theory. *ApJ*, 726:26.

Hartman, J. M., Patruno, A., Chakrabarty, D., Kaplan, D. L., Markwardt, C. B., Morgan, E. H., Ray, P. S., van der Klis, M., and Wijnands, R. (2008). The Long-Term Evolution of the Spin, Pulse Shape, and Orbit of the Accretion-powered Millisecond Pulsar SAX J1808.4-3658. *ApJ*, 675:1468–1486.

Heggie, D. C. (1975). Binary evolution in stellar dynamics. *MNRAS*, 173:729–787.

Heggie, D. C., Hut, P., and McMillan, S. L. W. (1996). Binary–Single-Star Scattering. VII. Hard Binary Exchange Cross Sections for Arbitrary Mass Ratios: Numerical Results and Semianalytic FITS. *ApJ*, 467:359.

Heinke, C. O., Edmonds, P. D., and Grindlay, J. E. (2001). Identification of the Low-Mass X-Ray Binary and Faint X-Ray Sources in NGC 6652. *ApJ*, 562:363–367.

Heinke, C. O., Grindlay, J. E., Edmonds, P. D., Cohn, H. N., Lugger, P. M., Camilo, F., Bogdanov, S., and Freire, P. C. (2005). A Deep Chandra Survey of the Globular Cluster 47 Tucanae: Catalog of Point Sources. *ApJ*, 625:796–824.

Heinke, C. O., Grindlay, J. E., Lugger, P. M., Cohn, H. N., Edmonds, P. D., Lloyd, D. A., and Cool, A. M. (2003). Analysis of the Quiescent Low-Mass X-Ray Binary Population in Galactic Globular Clusters. *ApJ*, 598:501–515.

Heinke, C. O., Ivanova, N., Engel, M. C., Pavlovskii, K., Sivakoff, G. R., Cartwright, T. F., and Gladstone, J. C. (2013). Galactic Ultracompact X-Ray Binaries: Disk Stability and Evolution. *ApJ*, 768:184.

Heinz, S. and Grimm, H. J. (2005). Estimating the Kinetic Luminosity Function of Jets from Galactic X-Ray Binaries. *ApJ*, 633:384–391.

Heinz, S. and Sunyaev, R. A. (2003). The non-linear dependence of flux on black hole mass and accretion rate in core-dominated jets. *MNRAS*, 343:L59–L64.

Hewish, A., Bell, S. J., Pilkington, J. D. H., Scott, P. F., and Collins, R. A. (1968). Observation of a Rapidly Pulsating Radio Source. *Nature*, 217:709–713.

Heywood, I., Jarvis, M. J., and Condon, J. J. (2013). Sample variance, source clustering and their influence on the counts of faint radio sources. *MNRAS*, 432:2625–2631.

Hills, J. G. (1976). The formation of binaries containing black holes by the exchange of companions and the X-ray sources in globular clusters. *MNRAS*, 175:1P–4P.

Hills, J. G. (1984). Did the binary stars in globular clusters come to an early end by being too eccentric? *AJ*, 89:1811–1815.

Hirose, M. and Osaki, Y. (1990). Hydrodynamic simulations of accretion disks in cataclysmic variables - Superhump phenomenon in SU UMa stars. *PASJ*, 42:135–163.

Hjellming, R. M. (1979). Novalike Object in Centaurus. *IAU Circular*, 3369.

Hjellming, R. M., Calovini, T. A., Han, X. H., and Cordova, F. A. (1988). Transient radio emission from the X-ray nova ASM 2000+25. *ApJ*, 335:L75–L78.

Hjellming, R. M., Han, X. H., Cordova, F. A., and Hasinger, G. (1990). Radio observations of the X-ray binary Cygnus X-2. *A&A*, 235:147–155.

Holt, S. S. (1976). Temporal X-ray astronomy with a pinhole camera. *Ap&SS*, 42:123–141.

Homan, J., Neilsen, J., Allen, J. L., Chakrabarty, D., Fender, R., Fridriksson, J. K., Remillard, R. A., and Schulz, N. (2016a). Evidence for Simultaneous Jets and Disk Winds in Luminous Low-mass X-Ray Binaries. *ApJ*, 830:L5.

Homan, J., Sivakoff, G., Pooley, D., Heinke, C., Strader, J., Tudor, V., and Miller-Jones, J. (2016b). Chandra identification of the X-ray transient MAXI J0911-635/Swift J0911.9-6452 in NGC 2808. *The Astronomer's Telegram*, 8971.

Homer, L., Anderson, S. F., Wachter, S., and Margon, B. (2002). The Ultraviolet Spectrum of the Ultracompact X-Ray Binary 4U 1626-67. *AJ*, 124:3348–3357.

Honeycutt, R. K., Kaitchuck, R. H., and Schlegel, E. M. (1987). Atlas of time-resolved spectrophotometry of cataclysmic variables. *ApJS*, 65:451–458.

Hong, J., Vesperini, E., Belloni, D., and Giersz, M. (2017). Dynamical formation of cataclysmic variables in globular clusters. *MNRAS*, 464:2511–2516.

Hooper, D. and Linden, T. (2016). The gamma-ray pulsar population of globular clusters: implications for the GeV excess. *JCAP*, 8:018.

Howell, S. B. (2006). *Handbook of CCD Astronomy*. Cambridge University Press.

Hoyle, F. and Lyttleton, R. A. (1939). The effect of interstellar matter on climatic variation. *Proceedings of the Cambridge Philosophical Society*, 35:405.

Hulse, R. A. and Taylor, J. H. (1975). Discovery of a pulsar in a binary system. *ApJ*, 195:L51–L53.

Huynh, M. T., Hopkins, A. M., Lenc, E., Mao, M. Y., Middelberg, E., Norris, R. P., and Randall, K. E. (2012). The ATLAS 5.5 GHz survey of the extended Chandra Deep Field South: catalogue, source counts and spectral indices. *MNRAS*, 426:2342–2358.

Hynes, R. I., Bradley, C. K., Rupen, M., Gallo, E., Fender, R. P., Casares, J., and Zurita, C. (2009). The quiescent spectral energy distribution of V404 Cyg. *MNRAS*, 399:2239–2248.

Hynes, R. I., Charles, P. A., Garcia, M. R., Robinson, E. L., Casares, J., Haswell, C. A., Kong, A. K. H., Rupen, M., Fender, R. P., Wagner, R. M., Gallo, E., Eves, B. A. C., Shahbaz, T., and Zurita, C. (2004). Correlated X-Ray and Optical Variability in V404 Cygni in Quiescence. *ApJ*, 611:L125–L128.

Iacolina, M. N., Burgay, M., Burderi, L., Possenti, A., and di Salvo, T. (2010). Search for pulsations at high radio frequencies from accreting millisecond X-ray pulsars in quiescence. *A&A*, 519:A13.

Illarionov, A. F. and Sunyaev, R. A. (1975). Why the Number of Galactic X-ray Stars Is so Small? *A&A*, 39:185.

in 't Zand, J. J. M., Heise, J., Muller, J. M., Bazzano, A., Cocchi, M., Natalucci, L., and Ubertini, P. (1998). Discovery of the X-ray transient SAX J1808.4-3658, a likely low-mass X-ray binary. *A&A*, 331:L25–L28.

in't Zand, J. J. M., Cumming, A., van der Sluys, M. V., Verbunt, F., and Pols, O. R. (2005). On the possibility of a helium white dwarf donor in the presumed ultracompact binary 2S 0918-549. *A&A*, 441:675–684.

in't Zand, J. J. M., Hulleman, F., Markwardt, C. B., Méndez, M., Kuulkers, E., Cornelisse, R., Heise, J., Strohmayer, T. E., and Verbunt, F. (2003). Bursts, eclipses, dips and a refined position for the luminous low-mass X-ray binary in the globular cluster Terzan 6. *A&A*, 406:233–243.

in't Zand, J. J. M., Jonker, P. G., and Markwardt, C. B. (2007). Six new candidate ultracompact X-ray binaries. *A&A*, 465:953–963.

Irwin, J. A., Brink, T. G., Bregman, J. N., and Roberts, T. P. (2010). Evidence for a Stellar Disruption by an Intermediate-mass Black Hole in an Extragalactic Globular Cluster. *ApJ*, 712:L1–L4.

Isobe, T., Feigelson, E. D., and Nelson, P. I. (1986). Statistical methods for astronomical data with upper limits. II - Correlation and regression. *ApJ*, 306:490–507.

Israel, G. L., Belfiore, A., Stella, L., Esposito, P., Casella, P., De Luca, A., Marelli, M., Papitto, A., Perri, M., Puccetti, S., Castillo, G. A. R., Salvetti, D., Tiengo, A., Zampieri, L., D'Agostino, D., Greiner, J., Haberl, F., Novara, G., Salvaterra, R., Turolla, R., Watson, M., Wilms, J., and Wolter, A. (2017a). An accreting pulsar with extreme properties drives an ultraluminous x-ray source in NGC 5907. *Science*, 355:817–819.

Israel, G. L., Papitto, A., Esposito, P., Stella, L., Zampieri, L., Belfiore, A., Rodríguez Castillo, G. A., De Luca, A., Tiengo, A., Haberl, F., Greiner, J., Salvaterra, R., Sandrelli, S., and Lisini, G. (2017b). Discovery of a 0.42-s pulsar in the ultraluminous X-ray source NGC 7793 P13. *MNRAS*, 466:L48–L52.

Istrate, A. G., Tauris, T. M., and Langer, N. (2014). The formation of low-mass helium white dwarfs orbiting pulsars . Evolution of low-mass X-ray binaries below the bifurcation period. *A&A*, 571:A45.

Ivanova, N. (2006). Low-Mass X-Ray Binaries and Metallicity Dependence: Story of Failures. *ApJ*, 636:979–984.

Ivanova, N. (2008). Population of Dynamically Formed Triples in Dense Stellar Systems. In Hubrig, S., Petr-Gotzens, M., and Tokovinin, A., editors, *Multiple Stars Across the H-R Diagram*, page 101.

Ivanova, N., Chaichenets, S., Fregeau, J., Heinke, C. O., Lombardi, Jr., J. C., and Woods, T. E. (2010). Formation of Black Hole X-ray Binaries in Globular Clusters. *ApJ*, 717:948–957.

Ivanova, N., da Rocha, C. A., Van, K. X., and Nandez, J. L. A. (2017). Formation of Black Hole X-Ray Binaries with Non-degenerate Donors in Globular Clusters. *ApJ*, 843:L30.

Ivanova, N., Fragos, T., Kim, D.-W., Fabbiano, G., Avendano Nandez, J. L., Lombardi, J. C., Sivakoff, G. R., Voss, R., and Jordán, A. (2012). On the Origin of the Metallicity Dependence in Dynamically formed Extragalactic Low-mass X-Ray Binaries. *ApJ*, 760:L24.

Ivanova, N., Heinke, C. O., Rasio, F. A., Belczynski, K., and Fregeau, J. M. (2008). Formation and evolution of compact binaries in globular clusters - II. Binaries with neutron stars. *MNRAS*, 386:553–576.

Ivanova, N., Heinke, C. O., Rasio, F. A., Taam, R. E., Belczynski, K., and Fregeau, J. (2006). Formation and evolution of compact binaries in globular clusters - I. Binaries with white dwarfs. *MNRAS*, 372:1043–1059.

Jacoby, G. H., Morse, J. A., Fullton, L. K., Kwitter, K. B., and Henry, R. B. C. (1997). Planetary Nebulae in the Globular Cluster PAL 6 and NGC 6441. *AJ*, 114:2611.

Jahoda, K., Swank, J. H., Giles, A. B., Stark, M. J., Strohmayer, T., Zhang, W., and Morgan, E. H. (1996). In-orbit performance and calibration of the Rossi X-ray Timing Explorer (RXTE) Proportional Counter Array (PCA). In Siegmund, O. H. and Gummin, M. A., editors, *EUV, X-Ray, and Gamma-Ray Instrumentation for Astronomy VII*, volume 2808 of *Proc. SPIE*, pages 59–70.

Jamil, O., Fender, R. P., and Kaiser, C. R. (2010). iShocks: X-ray binary jets with an internal shocks model. *MNRAS*, 401:394–404.

Johnson, H. M. (1976). Radio sources in the field of globular clusters. *ApJ*, 208:706–708.

Johnston, H. M. and Kulkarni, S. R. (1992). Deep VLA images of globular clusters - NGC 6624. *ApJ*, 393:L17–L19.

Johnston, H. M., Kulkarni, S. R., and Goss, W. M. (1991). Deep VLA images of globular clusters. *ApJ*, 382:L89–L92.

Jonas, J. L. (2009). MeerKAT - The South African Array With Composite Dishes and Wide-Band Single Pixel Feeds. *IEEE Proceedings*, 97:1522–1530.

Jonker, P. G., Bassa, C. G., Nelemans, G., Steeghs, D., Torres, M. A. P., Maccarone, T. J., Hynes, R. I., Greiss, S., Clem, J., Dieball, A., Mikles, V. J., Britt, C. T., Gossen, L., Collazzi, A. C., Wijnands, R., In't Zand, J. J. M., Méndez, M., Rea, N., Kuulkers, E., Ratti, E. M., van Haaften, L. M., Heinke, C., Özel, F., Groot, P. J., and Verbunt, F. (2011). The Galactic Bulge Survey: Outline and X-ray Observations. *ApJS*, 194:18.

Jonker, P. G., Campana, S., Steeghs, D., Torres, M. A. P., Galloway, D. K., Markwardt, C. B., Chakrabarty, D., and Swank, J. (2005). Chandra observations of the millisecond X-ray pulsar IGR J00291+5934 in quiescence. *MNRAS*, 361:511–516.

Jonker, P. G., Gallo, E., Dhawan, V., Rupen, M., Fender, R. P., and Dubus, G. (2004). Radio and X-ray observations during the outburst decay of the black hole candidate XTE J1908+094. *MNRAS*, 351:1359–1364.

Jonker, P. G., Miller-Jones, J., Homan, J., Gallo, E., Rupen, M., Tomsick, J., Fender, R. P., Kaaret, P., Steeghs, D. T. H., Torres, M. A. P., Wijnands, R., Markoff, S., and Lewin, W. H. G. (2010). Following the 2008 outburst decay of the black hole candidate H 1743-322in X-ray and radio. *MNRAS*, 401:1255–1263.

Jonker, P. G., Miller-Jones, J. C. A., Homan, J., Tomsick, J., Fender, R. P., Kaaret, P., Markoff, S., and Gallo, E. (2012). The black hole candidate MAXI J1659-152 in and towards quiescence in X-ray and radio. *MNRAS*, 423:3308–3315.

Jonker, P. G., Torres, M. A. P., and Steeghs, D. (2008). Optical and X-Ray Observations of IGR J00291+5934 in Quiescence. *ApJ*, 680:615–619.

Jordán, A., Côté, P., Blakeslee, J. P., Ferrarese, L., McLaughlin, D. E., Mei, S., Peng, E. W., Tonry, J. L., Merritt, D., Milosavljević, M., Sarazin, C. L., Sivakoff, G. R., and West, M. J. (2005). The ACS Virgo Cluster Survey. X. Half-Light Radii of Globular Clusters in Early-Type Galaxies: Environmental Dependencies and a Standard Ruler for Distance Estimation. *ApJ*, 634:1002–1019.

Jordán, A., Peng, E. W., Blakeslee, J. P., Côté, P., Eyheramendy, S., and Ferrarese, L. (2015). The ACS Fornax Cluster Survey. XI. Catalog of Globular Cluster Candidates. *ApJS*, 221:13.

Jordán, A., Peng, E. W., Blakeslee, J. P., Côté, P., Eyheramendy, S., Ferrarese, L., Mei, S., Tonry, J. L., and West, M. J. (2009). The ACS Virgo Cluster Survey XVI. Selection Procedure and Catalogs of Globular Cluster Candidates. *ApJS*, 180:54–66.

Jordi, K., Grebel, E. K., and Ammon, K. (2006). Empirical color transformations between SDSS photometry and other photometric systems. *A&A*, 460:339–347.

Joss, P. C. and Li, F. K. (1980). Helium-burning flashes on accreting neutron stars - Effects of stellar mass, radius, and magnetic field. *ApJ*, 238:287–295.

Kaaret, P., Feng, H., and Roberts, T. P. (2017). Ultraluminous X-Ray Sources. *ARA&A*, 55:303–341.

Kaiser, C. R., Sunyaev, R., and Spruit, H. C. (2000). Internal shock model for micro-quasars. *A&A*, 356:975–988.

Kalberla, P. M. W., Burton, W. B., Hartmann, D., Arnal, E. M., Bajaja, E., Morras, R., and Pöppel, W. G. L. (2005). The Leiden/Argentine/Bonn (LAB) Survey of Galactic HI. Final data release of the combined LDS and IAR surveys with improved stray-radiation corrections. *A&A*, 440:775–782.

Kalemci, E., Dinçer, T., Tomsick, J. A., Buxton, M. M., Bailyn, C. D., and Chun, Y. Y. (2013). Complete Multiwavelength Evolution of Galactic Black Hole Transients during Outburst Decay. I. Conditions for "Compact" Jet Formation. *ApJ*, 779:95.

Kalogera, V., King, A. R., and Rasio, F. A. (2004). Could Black Hole X-Ray Binaries Be Detected in Globular Clusters? *ApJ*, 601:L171–L174.

Kalogera, V. and Webbink, R. F. (1996). Formation of Low-Mass X-Ray Binaries. I. Constraints on Hydrogen-rich Donors at the Onset of the X-Ray Phase. *ApJ*, 458:301.

Kalogera, V. and Webbink, R. F. (1998). Formation of Low-Mass X-Ray Binaries. II. Common Envelope Evolution of Primordial Binaries with Extreme Mass Ratios. *ApJ*, 493:351–367.

Kaluzienski, L. J., Holt, S. S., and Swank, J. H. (1980). The 1979 X-ray outburst of Centaurus X-4. *ApJ*, 241:779–786.

Katz, J. I. (1975). Two kinds of stellar collapse. *Nature*, 253:698.

Kaur, R., Kaper, L., Ellerbroek, L. E., Russell, D. M., Altamirano, D., Wijnands, R., Yang, Y.-J., D'Avanzo, P., de Ugarte Postigo, A., Flores, H., Fynbo, J. P. U., Goldoni, P., Thöne, C. C., van der Horst, A., van der Klis, M., Kouveliotou, C., Wiersema, K., and Kuulkers, E. (2012). Very Large Telescope/X-shooter Spectroscopy of the Candidate Black Hole X-Ray Binary MAXI J1659-152 in Outburst. *ApJ*, 746:L23.

Kawaguchi, K., Kyutoku, K., Nakano, H., Okawa, H., Shibata, M., and Taniguchi, K. (2015). Black hole-neutron star binary merger: Dependence on black hole spin orientation and equation of state. *PRD*, 92(2):024014.

Khargharia, J., Froning, C. S., and Robinson, E. L. (2010). Near-infrared Spectroscopy of Low-mass X-ray Binaries: Accretion Disk Contamination and Compact Object Mass Determination in V404 Cyg and Cen X-4. *ApJ*, 716:1105–1117.

Kim, D.-W., Fabbiano, G., Ivanova, N., Fragos, T., Jordán, A., Sivakoff, G. R., and Voss, R. (2013). Metallicity Effect on Low-mass X-Ray Binary Formation in Globular Clusters. *ApJ*, 764:98.

Kimmig, B., Seth, A., Ivans, I. I., Strader, J., Caldwell, N., Anderton, T., and Gregersen, D. (2015). Measuring Consistent Masses for 25 Milky Way Globular Clusters. *AJ*, 149:53.

King, A. and Lasota, J.-P. (2016). ULXs: Neutron stars versus black holes. *MNRAS*, 458:L10–L13.

Kippenhahn, R. and Weigert, A. (1990). *Stellar Structure and Evolution*.

Kızıltan, B., Baumgardt, H., and Loeb, A. (2017). An intermediate-mass black hole in the centre of the globular cluster 47 Tucanae. *Nature*, 542:203–205.

Klencki, J., Wiktorowicz, G., Gładysz, W., and Belczynski, K. (2017). Dynamical formation of black hole low-mass X-ray binaries in the field: an alternative to the common envelope. *MNRAS*, 469:3088–3101.

Knevitt, G., Wynn, G. A., Vaughan, S., and Watson, M. G. (2014). Black holes in short period X-ray binaries and the transition to radiatively inefficient accretion. *MNRAS*, 437:3087–3102.

Knigge, C., Dieball, A., Maíz Apellániz, J., Long, K. S., Zurek, D. R., and Shara, M. M. (2008). Stellar Exotica in 47 Tucanae. *ApJ*, 683:1006–1030.

Körding, E., Rupen, M., Knigge, C., Fender, R., Dhawan, V., Templeton, M., and Muxlow, T. (2008). A Transient Radio Jet in an Erupting Dwarf Nova. *Science*, 320:1318.

Körding, E. G., Knigge, C., Tzioumis, T., and Fender, R. (2011). Detection of radio emission from a nova-like cataclysmic variable: evidence of jets? *MNRAS*, 418:L129–L132.

Kotze, M. M. and Charles, P. A. (2012). Characterizing X-ray binary long-term variability. *MNRAS*, 420:1575–1589.

Koushiappas, S. M., Bullock, J. S., and Dekel, A. (2004). Massive black hole seeds from low angular momentum material. *MNRAS*, 354:292–304.

Kozai, Y. (1962). Secular perturbations of asteroids with high inclination and eccentricity. *AJ*, 67:591.

Kraft, R. P., Burrows, D. N., and Nousek, J. A. (1991). Determination of confidence limits for experiments with low numbers of counts. *ApJ*, 374:344–355.

Kramer, M., Xilouris, K. M., Lorimer, D. R., Doroshenko, O., Jessner, A., Wielebinski, R., Wolszczan, A., and Camilo, F. (1998). The Characteristics of Millisecond Pulsar Emission. I. Spectra, Pulse Shapes, and the Beaming Fraction. *ApJ*, 501:270–285.

Krauss, M. I., Schulz, N. S., Chakrabarty, D., Juett, A. M., and Cottam, J. (2007). High-Resolution X-Ray Spectroscopy of the Ultracompact LMXB Pulsar 4U 1626-67. *ApJ*, 660:605–614.

Kreidberg, L., Bailyn, C. D., Farr, W. M., and Kalogera, V. (2012). Mass Measurements of Black Holes in X-Ray Transients: Is There a Mass Gap? *ApJ*, 757:36.

Kremer, K., Chatterjee, S., Rodriguez, C. L., and Rasio, F. A. (2018). Accreting Black Hole Binaries in Globular Clusters. *ApJ*, 852:29.

Krimm, H. A., Holland, S. T., Corbet, R. H. D., Pearlman, A. B., Romano, P., Kennea, J. A., Bloom, J. S., Barthelmy, S. D., Baumgartner, W. H., Cummings, J. R., Gehrels, N., Lien, A. Y., Markwardt, C. B., Palmer, D. M., Sakamoto, T., Stamatikos, M., and Ukwatta, T. N. (2013). The Swift/BAT Hard X-Ray Transient Monitor. *ApJS*, 209:14.

Kulkarni, S. R., Hut, P., and McMillan, S. (1993). Stellar black holes in globular clusters. *Nature*, 364:421–423.

Kulkarni, S. R., Navarro, J., Vasisht, G., Tanaka, Y., and Nagase, F. (1992). Millisecond pulsars and quiescent LMXBs. In *X-Ray Binaries and the Formation of Binary and Millisecond Radio Pulsars*, pages 99–104.

Kundu, A., Maccarone, T. J., and Zepf, S. E. (2002). The Low-Mass X-Ray Binary-Globular Cluster Connection in NGC 4472. *ApJ*, 574:L5–L9.

Landau, L. D. and Lifshitz, E. M. (1975). *The classical theory of fields*.

Langer, N. (1998). Coupled mass and angular momentum loss of massive main sequence stars. *A&A*, 329:551–558.

Larwood, J. (1998). On the precession of accretion discs in X-ray binaries. *MNRAS*, 299:L32–l36.

Latta, R. B. (1981). A monte carlo study of some two-sample rank tests with censored data. *Journal of the American Statistical Association*, 76(375):713–719.

Latyshev, I. N. (1978). Star density in the solar neighborhood. *SvA*, 22:186–188.

Lavalley, M., Isobe, T., and Feigelson, E. (1992). ASURV: Astronomy Survival Analysis Package. In Worrall, D. M., Biemesderfer, C., and Barnes, J., editors, *Astronomical Data Analysis Software and Systems I*, volume 25 of *Astronomical Society of the Pacific Conference Series*, page 245.

Lense, J. and Thirring, H. (1918). *Phys. Z.*, 156:19.

Lewis, F., Roche, P., Russell, D. M., and Fender, R. P. (2008). Monitoring LMXBs with the Faulkes Telescopes. In Bandyopadhyay, R. M., Wachter, S., Gelino, D., and Gelino, C. R., editors, *A Population Explosion: The Nature & Evolution of X-ray Binaries in Diverse Environments*, volume 1010 of *American Institute of Physics Conference Series*, pages 204–206.

Lewis, F., Russell, D. M., Jonker, P. G., Linares, M., Tudose, V., Roche, P., Clark, J. S., Torres, M. A. P., Maitra, D., Bassa, C. G., Steeghs, D., Patruno, A., Migliari, S., Wijnands, R., Nelemans, G., Kewley, L. J., Stroud, V. E., Modjaz, M., Bloom, J. S., Blake, C. H., and Starr, D. (2010). The double-peaked 2008 outburst of the accreting milli-second X-ray pulsar, IGR J00291+5934. *A&A*, 517:A72.

Li, C., de Grijs, R., Deng, L., Geller, A. M., Xin, Y., Hu, Y., and Faucher-Giguère, C.-A. (2016). Formation of new stellar populations from gas accreted by massive young star clusters. *Nature*, 529:502–504.

Li, X.-D., Bombaci, I., Dey, M., Dey, J., and van den Heuvel, E. P. J. (1999). Is SAX J1808.4-3658 a Strange Star? *Physical Review Letters*, 83:3776–3779.

Lii, P. S., Romanova, M. M., Ustyugova, G. V., Koldoba, A. V., and Lovelace, R. V. E. (2014). Propeller-driven outflows from an MRI disc. *MNRAS*, 441:86–100.

Linares, M., Shahbaz, T., and Casares, J. (2018). Peering into the Dark Side: Magnesium Lines Establish a Massive Neutron Star in PSR J2215+5135. *ApJ*, 859:54.

Linares, M., Tudose, V., and Migliari, S. (2008). A WSRT radio observation of IGR J00291+5934 in outburst. *The Astronomer's Telegram*, 1667.

Lindegren, L., Hernández, J., Bombrun, A., Klioner, S., Bastian, U., Ramos-Lerate, M., de Torres, A., Steidelmüller, H., Stephenson, C., Hobbs, D., Lammers, U., Biermann, M., Geyer, R., Hilger, T., Michalik, D., Stampa, U., McMillan, P. J., Castañeda, J., Clotet, M., Comoretto, G., Davidson, M., Fabricius, C., Gracia, G., Hambly, N. C., Hutton, A., Mora, A., Portell, J., van Leeuwen, F., Abbas, U., Abreu, A., Altmann, M., Andrei, A., Anglada, E., Balaguer-Núñez, L., Barache, C., Becciani, U., Bertone, S., Bianchi, L., Bouquillon, S., Bourda, G., Brüsemeister, T., Bucciarelli, B., Busonero, D., Buzzi, R., Cancelliere, R., Carlucci, T., Charlot, P., Cheek, N., Crosta, M., Crowley, C., de Bruijne, J., de Felice, F., Drimmel, R., Esquej, P., Fienga, A., Fraile, E., Gai, M., Garralda, N., González-Vidal, J. J., Guerra, R., Hauser, M., Hofmann, W., Holl, B., Jordan, S., Lattanzi, M. G., Lenhardt, H., Liao, S., Licata, E., Lister, T., Löffler, W., Marchant, J., Martin-Fleitas, J.-M., Messineo, R., Mignard, F., Morbidelli, R., Poggio, E., Riva, A., Rowell, N., Salguero, E., Sarasso, M., Sciacca, E., Siddiqui, H., Smart, R. L., Spagna, A., Steele, I., Taris, F., Torra, J., van Elteren, A., van Reeven, W., and Vecchiato, A. (2018). Gaia Data Release 2. The astrometric solution. *A&A*, 616:A2.

Liu, K., Eatough, R. P., Wex, N., and Kramer, M. (2014). Pulsar-black hole binaries: prospects for new gravity tests with future radio telescopes. *MNRAS*, 445:3115–3132.

Liu, Q. Z., van Paradijs, J., and van den Heuvel, E. P. J. (2006). Catalogue of high-mass X-ray binaries in the Galaxy (4th edition). *A&A*, 455:1165–1168.

Liu, Q. Z., van Paradijs, J., and van den Heuvel, E. P. J. (2007). A catalogue of low-mass X-ray binaries in the Galaxy, LMC, and SMC (Fourth edition). *A&A*, 469:807–810.

Longair, M. S. (1966). On the interpretation of radio source counts. *MNRAS*, 133:421.

Lu, T.-N. and Kong, A. K. H. (2011). Radio Continuum Observations of 47 Tucanae and ω Centauri: Hints for Intermediate-mass Black Holes? *ApJ*, 729:L25.

Luri, X., Brown, A. G. A., Sarro, L. M., Arenou, F., Bailer-Jones, C. A. L., Castro-Ginard, A., de Bruijne, J., Prusti, T., Babusiaux, C., and Delgado, H. E. (2018). Gaia Data Release 2. Using Gaia parallaxes. *A&A*, 616:A9.

Lutz, T. E. and Kelker, D. H. (1973). On the Use of Trigonometric Parallaxes for the Calibration of Luminosity Systems: Theory. *PASP*, 85:573.

Lützgendorf, N., Kissler-Patig, M., Noyola, E., Jalali, B., de Zeeuw, P. T., Gebhardt, K., and Baumgardt, H. (2011). Kinematic signature of an intermediate-mass black hole in the globular cluster NGC 6388. *A&A*, 533:A36.

Lyne, A. G., Brinklow, A., Middleditch, J., Kulkarni, S. R., and Backer, D. C. (1987). The discovery of a millisecond pulsar in the globular cluster M28. *Nature*, 328:399–401.

Ma, C., Arias, E. F., Bianco, G., Boboltz, D. A., Bolotin, S. L., Charlot, P., Engelhardt, G., Fey, A. L., Gaume, R. A., Gontier, A.-M., Heinkelmann, R., Jacobs, C. S., Kurdubov, S., Lambert, S. B., Malkin, Z. M., Nothnagel, A., Petrov, L., Skurikhina, E., Sokolova, J. R., Souchay, J., Sovers, O. J., Tesmer, V., Titov, O. A., Wang, G., Zharov, V. E., Barache, C., Boeckmann, S., Collioud, A., Gipson, J. M., Gordon, D., Lytvyn, S. O., MacMillan, D. S., and Ojha, R. (2009). The Second Realization of the International Celestial Reference Frame by Very Long Baseline Interferometry. *IERS Technical Note*, 35.

Maccarone, T. J. (2002). On the misalignment of jets in microquasars. *MNRAS*, 336:1371–1376.

Maccarone, T. J. (2003). Do X-ray binary spectral state transition luminosities vary? *A&A*, 409:697–706.

Maccarone, T. J. (2004). Radio emission as a test of the existence of intermediate-mass black holes in globular clusters and dwarf spheroidal galaxies. *MNRAS*, 351:1049–1053.

Maccarone, T. J. (2005). Using radio emission to detect isolated and quiescent accreting black holes. *MNRAS*, 360:L30–L34.

Maccarone, T. J., Kundu, A., Zepf, S. E., and Rhode, K. L. (2007). A black hole in a globular cluster. *Nature*, 445:183–185.

Maccarone, T. J., Kundu, A., Zepf, S. E., and Rhode, K. L. (2010). Fading of the X-ray flux from the black hole in the NGC 4472 globular cluster RZ 2109. *MNRAS*, 409:L84–L88.

Maccarone, T. J., Kundu, A., Zepf, S. E., and Rhode, K. L. (2011). A new globular cluster black hole in NGC 4472. *MNRAS*, 410:1655–1659.

MacDonald, R. K. D., Bailyn, C. D., Buxton, M., Cantrell, A. G., Chatterjee, R., Kennedy-Shaffer, R., Orosz, J. A., Markwardt, C. B., and Swank, J. H. (2014). The Black Hole Binary V4641 Sagitarii: Activity in Quiescence and Improved Mass Determinations. *ApJ*, 784:2.

Machin, G., Lehto, H. J., McHardy, I. M., Callanan, P. J., and Charles, P. A. (1990). VLA Observations of Four Bright Globular Cluster X-Ray Sources. *MNRAS*, 246:237.

Madau, P. and Haardt, F. (2015). Cosmic Reionization after Planck: Could Quasars Do It All? *ApJ*, 813:L8.

Madau, P. and Rees, M. J. (2001). Massive Black Holes as Population III Remnants. *ApJ*, 551:L27–L30.

Malumuth, E. M., Hill, R. S., Gull, T., Woodgate, B. E., Bowers, C. W., Kimble, R. A., Lindler, D., Plait, P., and Blouke, M. (2003). Removing the Fringes from Space Telescope Imaging Spectrograph Slitless Spectra. *PASP*, 115:218–234.

Malzac, J. (2013). Internal shocks at the origin of the flat spectral energy distribution of compact jets. *MNRAS*, 429:L20–L24.

Manchester, R. N., Hobbs, G. B., Teoh, A., and Hobbs, M. (2005). The Australia Telescope National Facility Pulsar Catalogue. *AJ*, 129:1993–2006.

Mann, C., Richer, H., Heyl, J., Anderson, J., Kalirai, J., Caiazzo, I., Möhle, S., Knee, A., and Baumgardt, H. (2018). A Multi-Mass Velocity Dispersion Model of 47 Tucanae Indicates No Evidence for an Intermediate Mass Black Hole. *ArXiv e-prints*.

Margalit, B. and Metzger, B. D. (2017). Constraining the Maximum Mass of Neutron Stars from Multi-messenger Observations of GW170817. *ApJ*, 850:L19.

Markoff, S., Nowak, M., Corbel, S., Fender, R., and Falcke, H. (2003). Exploring the role of jets in the radio/X-ray correlations of GX 339-4. *A&A*, 397:645–658.

Markoff, S., Nowak, M. A., and Wilms, J. (2005). Going with the Flow: Can the Base of Jets Subsume the Role of Compact Accretion Disk Coronae? *ApJ*, 635:1203–1216.

Markwardt, C. B., Altamirano, D., Swank, J. H., Strohmayer, T. E., Linares, M., and Pereira, D. (2009). RXTE Detects 245 Hz X-ray Pulsations from IGR J17511-305. *The Astronomer's Telegram*, 2197.

Marsh, T. R., Gänsicke, B. T., Hümmerich, S., Hambsch, F.-J., Bernhard, K., Lloyd, C., Breedt, E., Stanway, E. R., Steeghs, D. T., Parsons, S. G., Toloza, O., Schreiber, M. R., Jonker, P. G., van Roestel, J., Kupfer, T., Pala, A. F., Dhillon, V. S., Hardy, L. K., Littlefair, S. P., Aungwerojwit, A., Arjyotha, S., Koester, D., Bochinski, J. J., Haswell, C. A., Frank, P., and Wheatley, P. J. (2016). A radio-pulsing white dwarf binary star. *Nature*, 537:374–377.

Marsh, T. R., Robinson, E. L., and Wood, J. H. (1994). Spectroscopy of A0620-00 - the Mass of the Black-Hole and an Image of its Accretion Disc. *MNRAS*, 266:137.

Marti, J., Mirabel, I. F., Rodriguez, L. F., and Chaty, S. (1998). The radio counterparts of GX 354-0 and Terzan 1. *A&A*, 332:L45–L48.

Mashian, N. and Loeb, A. (2017). Hunting black holes with Gaia. *MNRAS*, 470:2611–2616.

Mason, P. A. and Gray, C. L. (2007). AR Ursae Majoris Discovered to Be a Persistent Radio Polar: Results from a VLA Survey of Magnetic Cataclysmic Variables. *ApJ*, 660:662–668.

Mattila, S., Pérez-Torres, M., Efstathiou, A., Mimica, P., Fraser, M., Kankare, E., Alberdi, A., Aloy, M. Á., Heikkilä, T., Jonker, P. G., Lundqvist, P., Martí-Vidal, I., Meikle, W. P. S., Romero-Cañizales, C., Smartt, S. J., Tsygankov, S., Varenius, E., Alonso-Herrero, A., Bondi, M., Fransson, C., Herrero-Illana, R., Kangas, T., Kotak, R., Ramírez-Olivencia, N., Väisänen, P., Beswick, R. J., Clements, D. L., Greimel, R., Harmanen, J., Kotilainen, J., Nandra, K., Reynolds, T., Ryder, S., Walton, N. A., Wiik, K., and Östlin, G. (2018). A dust-enshrouded tidal disruption event with a resolved radio jet in a galaxy merger. *ArXiv e-prints*.

Maxwell, J. E., Lugger, P. M., Cohn, H. N., Heinke, C. O., Grindlay, J. E., Budac, S. A., Drukier, G. A., and Bailyn, C. D. (2012). X-Ray Binaries in the Ultrahigh Encounter Rate Globular Cluster NGC 6388. *ApJ*, 756:147.

Mazeh, T. and Shaham, J. (1979). The orbital evolution of close triple systems - The binary eccentricity. *A&A*, 77:145–151.

McClure, R. D., Vandenberg, D. A., Smith, G. H., Fahlman, G. G., Richer, H. B., Hesser, J. E., Harris, W. E., Stetson, P. B., and Bell, R. A. (1986). Mass functions for globular cluster main sequences based on CCD photometry and stellar models. *ApJ*, 307:L49–L53.

McConnell, D. and Ables, J. G. (2000). Radio sources near the core of the globular cluster 47 Tucanae. *MNRAS*, 311:841–845.

McConnell, D., Deacon, R., and Ables, J. G. (2001). Radio Images of the Globular Cluster 47 Tucanae. *PASA*, 18:136–139.

McHardy, I. M., Gunn, K. F., Newsam, A. M., Mason, K. O., Page, M. J., Takata, T., Sekiguchi, K., Sasseen, T., Cordova, F., Jones, L. R., and Loaring, N. (2003). A medium-deep Chandra and Subaru survey of the 13-h XMM/ROSAT deep survey area. *MNRAS*, 342:802–822.

McHardy, I. M., Koerding, E., Knigge, C., Uttley, P., and Fender, R. P. (2006). Active galactic nuclei as scaled-up Galactic black holes. *Nature*, 444:730–732.

McLaughlin, D. E., Harris, W. E., and Hanes, D. A. (1994). The spatial structure of the M87 globular cluster system. *ApJ*, 422:486–507.

McLaughlin, D. E. and van der Marel, R. P. (2005). Resolved Massive Star Clusters in the Milky Way and Its Satellites: Brightness Profiles and a Catalog of Fundamental Parameters. *ApJS*, 161:304–360.

McMullin, J. P., Waters, B., Schiebel, D., Young, W., and Golap, K. (2007). CASA Architecture and Applications. In Shaw, R. A., Hill, F., and Bell, D. J., editors, *Astronomical Data Analysis Software and Systems XVI*, volume 376 of *Astronomical Society of the Pacific Conference Series*, page 127.

Menou, K., Esin, A. A., Narayan, R., Garcia, M. R., Lasota, J.-P., and McClintock, J. E. (1999). Black Hole and Neutron Star Transients in Quiescence. *ApJ*, 520:276–291.

Menou, K. and McClintock, J. E. (2001). The Quiescent Emission Spectrum of Centaurus X-4 and Other X-Ray Transients Containing Neutron Stars. *ApJ*, 557:304–310.

Merloni, A., Heinz, S., and di Matteo, T. (2003). A Fundamental Plane of black hole activity. *MNRAS*, 345:1057–1076.

Middleditch, J., Mason, K. O., Nelson, J. E., and White, N. E. (1981). 4U 1626-67 - A prograde spinning X-ray pulsar in a 2500 S binary system. *ApJ*, 244:1001–1021.

Migliari, S. (2011). Jets from neutron star X-ray binaries: towards a unified scheme. In Romero, G. E., Sunyaev, R. A., and Belloni, T., editors, *IAU Symposium*, volume 275 of *IAU Symposium*, pages 233–241.

Migliari, S. and Fender, R. P. (2006). Jets in neutron star X-ray binaries: a comparison with black holes. *MNRAS*, 366:79–91.

Migliari, S., Fender, R. P., Rupen, M., Jonker, P. G., Klein-Wolt, M., Hjellming, R. M., and van der Klis, M. (2003). Disc-jet coupling in an atoll-type neutron star X-ray binary: 4U 1728-34 (GX 354-0). *MNRAS*, 342:L67–L71.

Migliari, S., Fender, R. P., Rupen, M., Wachter, S., Jonker, P. G., Homan, J., and van der Klis, M. (2004). Radio detections of the neutron star X-ray binaries 4U 1820 - 30 and Ser X-1 in soft X-ray states. *MNRAS*, 351:186–192.

Migliari, S., Ghisellini, G., Miller-Jones, J., and Russell, D. (2012). Jet Models for Neutron Star X-Ray Binaries. *International Journal of Modern Physics Conference Series*, 8:108–113.

Migliari, S., Miller-Jones, J. C. A., and Russell, D. M. (2011). The influence of spin on jet power in neutron star X-ray binaries. *MNRAS*, 415:2407–2416.

Migliari, S., Tomsick, J. A., Miller-Jones, J. C. A., Heinz, S., Hynes, R. I., Fender, R. P., Gallo, E., Jonker, P. G., and Maccarone, T. J. (2010). The Complete Spectrum of the Neutron Star X-ray Binary 4U 0614+091. *ApJ*, 710:117–124.

Miller, M. C. and Hamilton, D. P. (2002). Production of intermediate-mass black holes in globular clusters. *MNRAS*, 330:232–240.

Miller-Jones, J. C. A., Gallo, E., Rupen, M. P., Mioduszewski, A. J., Brisken, W., Fender, R. P., Jonker, P. G., and Maccarone, T. J. (2008). Zooming in on a sleeping giant: milliarcsecond High Sensitivity Array imaging of the black hole binary V404 Cyg in quiescence. *MNRAS*, 388:1751–1758.

Miller-Jones, J. C. A., Russell, D. M., and Migliari, S. (2009). Radio upper limits for the accreting millisecond X-ray pulsar IGR J17511-3057. *The Astronomer's Telegram*, 2232.

Miller-Jones, J. C. A., Sivakoff, G. R., Altamirano, D., Tudose, V., Migliari, S., Dhawan, V., Fender, R. P., Garrett, M. A., Heinz, S., Körding, E. G., Krimm, H. A., Linares, M., Maitra, D., Markoff, S., Paragi, Z., Remillard, R. A., Rupen, M. P., Rushton, A., Russell, D. M., Sarazin, C. L., and Spencer, R. E. (2010). Evolution of the Radio-X-ray Coupling Throughout an Entire Outburst of Aquila X-1. *ApJ*, 716:L109–L114.

Miller-Jones, J. C. A., Strader, J., Heinke, C. O., Maccarone, T. J., van den Berg, M., Knigge, C., Chomiuk, L., Noyola, E., Russell, T. D., Seth, A. C., and Sivakoff, G. R. (2015). Deep radio imaging of 47 Tuc identifies the peculiar X-ray source X9 as a new black hole candidate. *MNRAS*, 453:3918–3931.

Miller-Jones, J. C. A., Wrobel, J. M., Sivakoff, G. R., Heinke, C. O., Miller, R. E., Plotkin, R. M., Di Stefano, R., Greene, J. E., Ho, L. C., Joseph, T. D., Kong, A. K. H., and Maccarone, T. J. (2012). The Absence of Radio Emission from the Globular Cluster G1. *ApJ*, 755:L1.

Mirabel, I. F., Dhawan, V., Chaty, S., Rodriguez, L. F., Marti, J., Robinson, C. R., Swank, J., and Geballe, T. (1998). Accretion instabilities and jet formation in GRS 1915+105. *A&A*, 330:L9–L12.

Mirabel, I. F., Dijkstra, M., Laurent, P., Loeb, A., and Pritchard, J. R. (2011). Stellar black holes at the dawn of the universe. *A&A*, 528:A149.

Mirabel, I. F. and Rodríguez, L. F. (1994). A superluminal source in the Galaxy. *Nature*, 371:46–48.

Mirabel, I. F., Rodriguez, L. F., Cordier, B., Paul, J., and Lebrun, F. (1992). A double-sided radio jet from the compact Galactic Centre annihilator 1E1740.7-2942. *Nature*, 358:215–217.

Mohan, N. and Rafferty, D. (2015). PyBDSF: Python Blob Detection and Source Finder. Astrophysics Source Code Library.

Monelli, M., Corsi, C. E., Castellani, V., Ferraro, I., Iannicola, G., Prada Moroni, P. G., Bono, G., Buonanno, R., Calamida, A., Freyhammer, L. M., Pulone, L., and Stetson, P. B. (2005). The Discovery of More than 2000 White Dwarfs in the Globular Cluster ω Centauri. *ApJ*, 621:L117–L120.

Moody, K. and Sigurdsson, S. (2009). Modeling the Retention Probability of Black Holes in Globular Clusters: Kicks and Rates. *ApJ*, 690:1370–1377.

Morris, D. H. and Mutel, R. L. (1988). Radio emission from RS CVn binaries. III - A VLA survey of 103 systems. *AJ*, 95:204–214.

Morscher, M., Pattabiraman, B., Rodriguez, C., Rasio, F. A., and Umbreit, S. (2015). The Dynamical Evolution of Stellar Black Holes in Globular Clusters. *ApJ*, 800:9.

Motta, S. E., Casella, P., and Fender, R. (2018). Radio-loudness in black hole transients: evidence for an inclination effect. *MNRAS*.

Mukai, K. (1993). PIMMS and Viewing: proposal preparation tools. *Legacy, vol. 3, p.21-31*, 3:21–31.

Mukherjee, D., Bult, P., van der Klis, M., and Bhattacharya, D. (2015). The magnetic-field strengths of accreting millisecond pulsars. *MNRAS*, 452:3994–4012.

Mushotzky, R. F. and Wandel, A. (1989). On the ratio of the infrared-to-ultraviolet continuum to the X-rays in quasars and active galaxies. *ApJ*, 339:674–688.

Mutel, R. L., Morris, D. H., Doiron, D. J., and Lestrade, J. F. (1987). Radio emission from RS CVn binaries. II - Polarization and spectral properties. *AJ*, 93:1220–1228.

Narayan, R., Mahadevan, R., Grindlay, J. E., Popham, R. G., and Gammie, C. (1998). Advection-dominated accretion model of Sagittarius A*: evidence for a black hole at the Galactic center. *ApJ*, 492:554–568.

Narayan, R. and McClintock, J. E. (2008). Advection-dominated accretion and the black hole event horizon. *NAR*, 51:733–751.

Narayan, R., McClintock, J. E., and Yi, I. (1996). A New Model for Black Hole Soft X-Ray Transients in Quiescence. *ApJ*, 457:821.

Narayan, R. and Ostriker, J. P. (1990). Pulsar populations and their evolution. *ApJ*, 352:222–246.

Narayan, R., Piran, T., and Shemi, A. (1991). Neutron star and black hole binaries in the Galaxy. *ApJ*, 379:L17–L20.

Narayan, R. and Yi, I. (1994). Advection-dominated accretion: A self-similar solution. *ApJ*, 428:L13–L16.

Narayan, R. and Yi, I. (1995). Advection-dominated Accretion: Underfed Black Holes and Neutron Stars. *ApJ*, 452:710.

Nelemans, G. and Jonker, P. G. (2010). Ultra-compact (X-ray) binaries. *NAR*, 54:87–92.

Nelemans, G., Jonker, P. G., Marsh, T. R., and van der Klis, M. (2004a). Optical spectra of the carbon-oxygen accretion discs in the ultra-compact X-ray binaries 4U 0614+09, 4U 1543-624 and 2S 0918-549. *MNRAS*, 348:L7–L11.

Nelemans, G., Jonker, P. G., and Steeghs, D. (2006). Optical spectroscopy of (candidate) ultracompact X-ray binaries: constraints on the composition of the donor stars. *MNRAS*, 370:255–262.

Nelemans, G., Yungelson, L. R., and Portegies Zwart, S. F. (2004b). Short-period AM CVn systems as optical, X-ray and gravitational-wave sources. *MNRAS*, 349:181–192.

Nelson, L. A. and Rappaport, S. (2003). Theoretical Considerations on the Properties of Accreting Millisecond Pulsars. *ApJ*, 598:431–445.

Nelson, R. P. and Papaloizou, J. C. B. (2000). Hydrodynamic simulations of the Bardeen-Petterson effect. *MNRAS*, 315:570–586.

Noyola, E., Gebhardt, K., and Bergmann, M. (2008). Gemini and Hubble Space Telescope Evidence for an Intermediate-Mass Black Hole in ω Centauri. *ApJ*, 676:1008–1015.

Nucita, A. A., De Paolis, F., Ingrosso, G., Elia, D., de Plaa, J., and Kaastra, J. S. (2006). An XMM-Newton Search for X-Ray Emission from the Microlensing Event MACHO-96-BLG-5. *ApJ*, 651:1092–1097.

Ogilvie, G. I. and Dubus, G. (2001). Precessing warped accretion discs in X-ray binaries. *MNRAS*, 320:485–503.

Oka, T., Mizuno, R., Miura, K., and Takekawa, S. (2016). Signature of an Intermediate-mass Black Hole in the Central Molecular Zone of Our Galaxy. *ApJ*, 816:L7.

Oka, T., Tsujimoto, S., Iwata, Y., Nomura, M., and Takekawa, S. (2017). Millimetre-wave emission from an intermediate-mass black hole candidate in the Milky Way. *Nature Astronomy*, 1:709–712.

Olech, A., Rutkowski, A., and Schwarzenberg-Czerny, A. (2009). Curious Variables Experiment: SDSS J210014.12+004446.0 - dwarf nova with negative and positive superhumps. *MNRAS*, 399:465–473.

Orosz, J. A., Bailyn, C. D., Remillard, R. A., McClintock, J. E., and Foltz, C. B. (1994). Quiescent accretion disks in black hole X-ray novae. *ApJ*, 436:848–858.

Osaki, Y. (1985). Irradiation-induced mass-overflow instability as a possible cause of superoutbursts in SU UMa stars. *A&A*, 144:369–380.

Özel, F., Psaltis, D., Güver, T., Baym, G., Heinke, C., and Guillot, S. (2016). The Dense Matter Equation of State from Neutron Star Radius and Mass Measurements. *ApJ*, 820:28.

Özel, F., Psaltis, D., Narayan, R., and McClintock, J. E. (2010). The Black Hole Mass Distribution in the Galaxy. *ApJ*, 725:1918–1927.

Özel, F., Psaltis, D., Narayan, R., and Santos Villarreal, A. (2012). On the Mass Distribution and Birth Masses of Neutron Stars. *ApJ*, 757:55.

Paczynski, B. (1977). A model of accretion disks in close binaries. *ApJ*, 216:822–826.

Paczynski, B. and Trimble, V. (1979). Galactic center pulsar as a test of black hole existence and properties. In Burton, W. B., editor, *The Large-Scale Characteristics of the Galaxy*, volume 84 of *IAU Symposium*, pages 401–403.

Paizis, A., Nowak, M. A., Wilms, J., Courvoisier, T. J.-L., Ebisawa, K., Rodriguez, J., and Ubertini, P. (2005). Chandra and RXTE spectroscopy of the accreting msec pulsar IGR J00291+5934. *A&A*, 444:357–363.

Papaloizou, J. and Pringle, J. E. (1977). Tidal torques on accretion discs in close binary systems. *MNRAS*, 181:441–454.

Papitto, A., Bozzo, E., Sanchez-Fernandez, C., Romano, P., Torres, D. F., Ferrigno, C., Kajava, J. J. E., and Kuulkers, E. (2016). The 2015 outburst of the accreting millisecond pulsar IGR J17511-3057 as seen by INTEGRAL, Swift, and XMM-Newton. *A&A*, 596:A71.

Papitto, A., Ferrigno, C., Bozzo, E., Rea, N., Pavan, L., Burderi, L., Burgay, M., Campana, S., di Salvo, T., Falanga, M., Filipović, M. D., Freire, P. C. C., Hessels, J. W. T., Possenti, A., Ransom, S. M., Riggio, A., Romano, P., Sarkissian, J. M.,

Stairs, I. H., Stella, L., Torres, D. F., Wieringa, M. H., and Wong, G. F. (2013). Swings between rotation and accretion power in a binary millisecond pulsar. *Nature*, 501:517–520.

Papitto, A., Riggio, A., di Salvo, T., Burderi, L., D'Aì, A., Iaria, R., Bozzo, E., and Menna, M. T. (2010). The X-ray spectrum of the newly discovered accreting millisecond pulsar IGR J17511-3057. *MNRAS*, 407:2575–2588.

Papitto, A. and Torres, D. F. (2015). A Propeller Model for the Sub-luminous State of the Transitional Millisecond Pulsar PSR J1023+0038. *ApJ*, 807:33.

Paresce, F., de Marchi, G., and Ferraro, F. R. (1992). Possible cataclysmic variable in the core of the globular cluster 47 Tucanae. *Nature*, 360:46–48.

Parikh, A. S., Wijnands, R., Degenaar, N., Altamirano, D., Patruno, A., Gusinskaia, N. V., and Hessels, J. W. T. (2017). Very hard states in neutron star low-mass X-ray binaries. *MNRAS*, 468:3979–3984.

Patruno, A., Bult, P., Gopakumar, A., Hartman, J. M., Wijnands, R., van der Klis, M., and Chakrabarty, D. (2012). Accelerated Orbital Expansion and Secular Spin-down of the Accreting Millisecond Pulsar SAX J1808.4-3658. *ApJ*, 746:L27.

Patruno, A., Jaodand, A., Kuiper, L., Bult, P., Hessels, J., Knigge, C., King, A. R., Wijnands, R., and van der Klis, M. (2016a). Radio pulse search and X-Ray monitoring of SAX J1808.4-3658: What Causes its Orbital Evolution? *ArXiv e-prints*.

Patruno, A., Maitra, D., Curran, P. A., D'Angelo, C., Fridriksson, J. K., Russell, D. M., Middleton, M., and Wijnands, R. (2016b). The Reflares and Outburst Evolution in the Accreting Millisecond Pulsar SAX J1808.4-3658: A Disk Truncated Near Co-Rotation? *ApJ*, 817:100.

Patruno, A., Watts, A., Klein Wolt, M., Wijnands, R., and van der Klis, M. (2009). 1 Hz Flaring in SAX J1808.4-3658: Flow Instabilities near the Propeller Stage. *ApJ*, 707:1296–1309.

Patruno, A. and Watts, A. L. (2012). Accreting Millisecond X-Ray Pulsars. *ArXiv e-prints, 1206.2727*.

Patterson, J., Kemp, J., Harvey, D. A., Fried, R. E., Rea, R., Monard, B., Cook, L. M., Skillman, D. R., Vanmunster, T., Bolt, G., Armstrong, E., McCormick, J., Krajci, T., Jensen, L., Gunn, J., Butterworth, N., Foote, J., Bos, M., Masi, G., and Warhurst, P. (2005). Superhumps in Cataclysmic Binaries. XXV. q_{crit}, $\epsilon(q)$, and Mass-Radius. *PASP*, 117:1204–1222.

Pavelin, P. E., Spencer, R. E., and Davis, R. J. (1994). A 5-GHZ Radio Survey of Magnetic Cataclysmic Variables. *MNRAS*, 269:779.

Peacock, M. B., Zepf, S. E., and Maccarone, T. J. (2012). Limits on [O III] 5007 Emission from NGC 4472's Globular Clusters: Constraints on Planetary Nebulae and Ultraluminous Black Hole X-Ray Binaries in Globular Clusters. *ApJ*, 752:90.

Pearson, K. J. (2003). Superhumps, magnetic fields and the mass ratio in AM Canum Venaticorum. *MNRAS*, 346:L21–L25.

Pearson, T. J. and Readhead, A. C. S. (1984). Image formation by self-calibration in radio astronomy. *Annual Review of Astronomy and Astrophysics*, 22(1):97–130.

Penninx, W., Lewin, W. H. G., Zijlstra, A. A., Mitsuda, K., and van Paradijs, J. (1988). A connection between the X-ray spectral branches and the radio brightness in GX17+2. *Nature*, 336:146–148.

Penrose, R. and Floyd, R. M. (1971). Extraction of Rotational Energy from a Black Hole. *Nature Physical Science*, 229:177–179.

Perera, B. B. P., Stappers, B. W., Lyne, A. G., Bassa, C. G., Cognard, I., Guillemot, L., Kramer, M., Theureau, G., and Desvignes, G. (2017). Evidence for an intermediate-mass black hole in the globular cluster NGC 6624. *MNRAS*, 468:2114–2127.

Perley, R. A., Chandler, C. J., Butler, B. J., and Wrobel, J. M. (2011). The Expanded Very Large Array: A New Telescope for New Science. *ApJ*, 739:L1.

Perryman, M. A. C., de Boer, K. S., Gilmore, G., Høg, E., Lattanzi, M. G., Lindegren, L., Luri, X., Mignard, F., Pace, O., and de Zeeuw, P. T. (2001). GAIA: Composition, formation and evolution of the Galaxy. *A&A*, 369:339–363.

Peters, P. C. (1964). Gravitational Radiation and the Motion of Two Point Masses. *Physical Review*, 136:1224–1232.

Peterson, B. M., Wanders, I., Horne, K., Collier, S., Alexander, T., Kaspi, S., and Maoz, D. (1998). On Uncertainties in Cross-Correlation Lags and the Reality of Wavelength-dependent Continuum Lags in Active Galactic Nuclei. *Publications of the Astronomical Society of the Pacific*, 110:660–670.

Peuten, M., Zocchi, A., Gieles, M., Gualandris, A., and Hénault-Brunet, V. (2016). A stellar-mass black hole population in the globular cluster NGC 6101? *MNRAS*, 462:2333–2342.

Pinto, C., Costantini, E., Fabian, A. C., Kaastra, J. S., and in't Zand, J. J. M. (2014). Unveiling the environment surrounding low-mass X-ray binary SAX J1808.4-3658. *A&A*, 563:A115.

Pinto, C., Kaastra, J. S., Costantini, E., and de Vries, C. (2013). Interstellar medium composition through X-ray spectroscopy of low-mass X-ray binaries. *A&A*, 551:A25.

Plotkin, R. M., Gallo, E., and Jonker, P. G. (2013). The X-Ray Spectral Evolution of Galactic Black Hole X-Ray Binaries toward Quiescence. *ApJ*, 773:59.

Plotkin, R. M., Gallo, E., Markoff, S., Homan, J., Jonker, P. G., Miller-Jones, J. C. A., Russell, D. M., and Drappeau, S. (2015). Constraints on relativistic jets in quiescent black hole X-ray binaries from broad-band spectral modelling. *MNRAS*, 446:4098–4111.

Plotkin, R. M., Miller-Jones, J. C. A., Gallo, E., Jonker, P. G., Homan, J., Tomsick, J. A., Kaaret, P., Russell, D. M., Heinz, S., Hodges-Kluck, E. J., Markoff, S., Sivakoff, G. R., Altamirano, D., and Neilsen, J. (2017). The 2015 Decay of the Black Hole X-Ray Binary V404 Cygni: Robust Disk-jet Coupling and a Sharp Transition into Quiescence. *ApJ*, 834:104.

Podsiadlowski, P. and Rappaport, S. (2000). Cygnus X-2: The Descendant of an Intermediate-Mass X-Ray Binary. *ApJ*, 529:946–951.

Podsiadlowski, P., Rappaport, S., and Pfahl, E. D. (2002). Evolutionary Sequences for Low- and Intermediate-Mass X-Ray Binaries. *ApJ*, 565:1107–1133.

Poindexter, S., Afonso, C., Bennett, D. P., Glicenstein, J.-F., Gould, A., Szymański, M. K., and Udalski, A. (2005). Systematic Analysis of 22 Microlensing Parallax Candidates. *ApJ*, 633:914–930.

Pooley, D., Lewin, W. H. G., Anderson, S. F., Baumgardt, H., Filippenko, A. V., Gaensler, B. M., Homer, L., Hut, P., Kaspi, V. M., Makino, J., Margon, B., McMillan, S., Portegies Zwart, S., van der Klis, M., and Verbunt, F. (2003). Dynamical Formation of Close Binary Systems in Globular Clusters. *ApJ*, 591:L131–L134.

Pooley, G. (2004). IGR J00291+5934 - radio observation. *The Astronomer's Telegram*, 355.

Possenti, A., Cerutti, R., Colpi, M., and Mereghetti, S. (2002). Re-examining the X-ray versus spin-down luminosity correlation of rotation powered pulsars. *A&A*, 387:993–1002.

Poutanen, J., Krolik, J. H., and Ryde, F. (1997). The nature of spectral transitions in accreting black holes - The case of CYG X-1. *MNRAS*, 292:L21–L25.

Pradel, N., Charlot, P., and Lestrade, J.-F. (2006). Astrometric accuracy of phase-referenced observations with the VLBA and EVN. *A&A*, 452:1099–1106.

Prager, B. J., Ransom, S. M., Freire, P. C. C., Hessels, J. W. T., Stairs, I. H., Arras, P., and Cadelano, M. (2017). Using Long-term Millisecond Pulsar Timing to Obtain Physical Characteristics of the Bulge Globular Cluster Terzan 5. *ApJ*, 845:148.

Prentice, R. L. and Marek, P. (1979). A qualitative discrepancy between censored data rank tests. *Biometrics*, 35(4):861–867.

Priedhorsky, W. C. and Verbunt, F. (1988). Tidal forces and mass transfer instabilities in low-mass X-ray binaries. *ApJ*, 333:895–905.

Pulone, L., De Marchi, G., Covino, S., and Paresce, F. (2003). HST observations of the metal rich globular clusters NGC 6496 and NGC 6352. *A&A*, 399:121–131.

Quataert, E. and Narayan, R. (1999). Spectral Models of Advection-dominated Accretion Flows with Winds. *ApJ*, 520:298–315.

Ramsay, G., Brocksopp, C., Wu, K., Slee, B., and Saxton, C. J. (2007). A search for electron cyclotron maser emission from compact binaries. *MNRAS*, 382:461–465.

Ransom, S. M., Eikenberry, S. S., and Middleditch, J. (2002). Fourier Techniques for Very Long Astrophysical Time-Series Analysis. *AJ*, 124:1788–1809.

Ratti, E. M., Jonker, P. G., Miller-Jones, J. C. A., Torres, M. A. P., Homan, J., Markoff, S., Tomsick, J. A., Kaaret, P., Wijnands, R., Gallo, E., Özel, F., Steeghs, D. T. H., and Fender, R. P. (2012). The black hole candidate XTE J1752-223 towards and in quiescence: optical and simultaneous X-ray-radio observations. *MNRAS*, 423:2656–2667.

Ray, A., Kembhavi, A. K., and Antia, H. M. (1987). Evolution of stellar binaries formed by tidal capture. *A&A*, 184:164–172.

Reines, A. E., Sivakoff, G. R., Johnson, K. E., and Brogan, C. L. (2011). An actively accreting massive black hole in the dwarf starburst galaxy Henize2-10. *Nature*, 470:66–68.

Remillard, R. A. and McClintock, J. E. (2006). X-Ray Properties of Black-Hole Binaries. *ARA&A*, 44:49–92.

Retter, A., Chou, Y., Bedding, T. R., and Naylor, T. (2002). Detection of negative superhumps in a low-mass X-ray binary - an end to the long debate on the nature of V1405 Aql (X1916-053). *MNRAS*, 330:L37–L42.

Revnivtsev, M. G. and Sunyaev, R. A. (2002). An Upper Limit on the X-ray Luminosity of the Microlensing Black Hole OGLE-1999-BUL-32. *Astronomy Letters*, 28:69–72.

Reynolds, M. T. and Miller, J. M. (2011). An Anomalous Quiescent Stellar Mass Black Hole. *ApJ*, 734:L17.

Rhode, K. L. and Zepf, S. E. (2001). The Globular Cluster System in the Outer Regions of NGC 4472. *AJ*, 121:210–224.

Ribó, M., Munar-Adrover, P., Paredes, J. M., Marcote, B., Iwasawa, K., Moldón, J., Casares, J., Migliari, S., and Paredes-Fortuny, X. (2017). The First Simultaneous X-Ray/Radio Detection of the First Be/BH System MWC 656. *ApJ*, 835:L33.

Richer, H. B., Fahlman, G. G., Buonanno, R., Fusi Pecci, F., Searle, L., and Thompson, I. B. (1991). Globular cluster mass functions. *ApJ*, 381:147–159.

Riggio, A., Papitto, A., Burderi, L., di Salvo, T., Bachetti, M., Iaria, R., D'Aì, A., and Menna, M. T. (2011). Timing of the accreting millisecond pulsar IGR J17511-3057. *A&A*, 526:A95.

Rivera Sandoval, L. E., van den Berg, M., Heinke, C. O., Cohn, H. N., Lugger, P. M., Anderson, J., Cool, A. M., Edmonds, P. D., Wijnands, R., Ivanova, N., and Grindlay, J. E. (2018). New cataclysmic variables and other exotic binaries in the globular cluster 47 Tucanae*. *MNRAS*, 475:4841–4867.

Rodriguez, C. L., Morscher, M., Wang, L., Chatterjee, S., Rasio, F. A., and Spurzem, R. (2016). Million-body star cluster simulations: comparisons between Monte Carlo and direct N-body. *MNRAS*, 463:2109–2118.

Romanova, M. M., Ustyugova, G. V., Koldoba, A. V., and Lovelace, R. V. E. (2009). Launching of conical winds and axial jets from the disc-magnetosphere boundary: axisymmetric and 3D simulations. *MNRAS*, 399:1802–1828.

Rossi, L. J., Ortolani, S., Barbuy, B., Bica, E., and Bonfanti, A. (2015). Proper motions and kinematics of selected bulge globular clusters. *MNRAS*, 450:3270–3288.

Rupen, M. P., Dhawan, V., and Mioduszewski, A. J. (2004). Further radio observations of IGR J00291+5934. *The Astronomer's Telegram*, 364.

Rupen, M. P., Dhawan, V., and Mioduszewski, A. J. (2005). Radio detections of SAX J1808.4-3658. *The Astronomer's Telegram*, 524.

Rupen, M. P., Dhawan, V., Mioduszewski, A. J., Stappers, B. W., and Gaensler, B. M. (2002). Sax J1808.4-3658. *IAU Circular*, 7997.

Russell, D. M., Fender, R. P., Hynes, R. I., Brocksopp, C., Homan, J., Jonker, P. G., and Buxton, M. M. (2006). Global optical/infrared-X-ray correlations in X-ray binaries: quantifying disc and jet contributions. *MNRAS*, 371:1334–1350.

Russell, D. M., Fender, R. P., and Jonker, P. G. (2007). Evidence for a jet contribution to the optical/infrared light of neutron star X-ray binaries. *MNRAS*, 379:1108–1116.

Russell, D. M., Markoff, S., Casella, P., Cantrell, A. G., Chatterjee, R., Fender, R. P., Gallo, E., Gandhi, P., Homan, J., Maitra, D., Miller-Jones, J. C. A., O'Brien, K., and Shahbaz, T. (2013). Jet spectral breaks in black hole X-ray binaries. *MNRAS*, 429:815–832.

Russell, D. M., Miller-Jones, J. C. A., Maccarone, T. J., Yang, Y. J., Fender, R. P., and Lewis, F. (2011). Testing the Jet Quenching Paradigm with an Ultradeep Observation of a Steadily Soft State Black Hole. *ApJ*, 739:L19.

Russell, T. D., Miller-Jones, J. C. A., Curran, P. A., Soria, R., Altamirano, D., Corbel, S., Coriat, M., Moin, A., Russell, D. M., Sivakoff, G. R., Slaven-Blair, T. J., Belloni, T. M., Fender, R. P., Heinz, S., Jonker, P. G., Krimm, H. A., Körding, E. G., Maitra, D., Markoff, S., Middleton, M., Migliari, S., Remillard, R. A., Rupen, M. P., Sarazin, C. L., Tetarenko, A. J., Torres, M. A. P., Tudose, V., and Tzioumis, A. K. (2015). Radio monitoring of the hard state jets in the 2011 outburst of MAXI J1836-194. *MNRAS*, 450:1745–1759.

Rutledge, R., Moore, C., Fox, D., Lewin, W., and van Paradijs, J. (1998). Possible Radio Counterpart of MXB 1730-335. *The Astronomer's Telegram*, 8.

Rybicki, G. B. and Lightman, A. P. (1979). *Radiative processes in astrophysics*. WILEY-VCH Verlag GmbH & Co. KGaA, Weinheim.

Ryon, J. E. (2018). *Advanced Camera for Surveys Instrument Handbook for Cycle 26 v. 17.0*. STScI.

Salaris, M. and Cassisi, S. (2005). *Evolution of Stars and Stellar Populations*. Wiley-VCH.

Salaris, M., Held, E. V., Ortolani, S., Gullieuszik, M., and Momany, Y. (2007). Deep near-infrared photometry of the globular cluster 47 Tucanae. Reconciling theory and observations. *A&A*, 476:243–253.

Samland, M. (1998). Modeling the Evolution of Disk Galaxies. II. Yields of Massive Stars. *ApJ*, 496:155–171.

Sanna, A., Riggio, A., Pintore, F., D'Ai, A., Di Salvo, T., Burderi, L., Iaria, R., Scarano, F., and Segreto, A. (2015). Swift/BAT detected a possible new outburst of the X-ray transient SAX J1808.4-3658. *The Astronomer's Telegram*, 7364:1.

Saracino, S., Dalessandro, E., Ferraro, F. R., Geisler, D., Mauro, F., and Lanzoni, B. (2016). GEMINI/GeMS observations of globular clusters in the Galactic bulge. *MmSAI*, 87:697.

Sarazin, C. L., Kundu, A., Irwin, J. A., Sivakoff, G. R., Blanton, E. L., and Randall, S. W. (2003). Low-Mass X-Ray Binaries and Globular Clusters in Early-Type Galaxies. *ApJ*, 595:743–759.

Sari, R., Piran, T., and Halpern, J. P. (1999). Jets in Gamma-Ray Bursts. *ApJ*, 519:L17–L20.

Sault, R. J., Teuben, P. J., and Wright, M. C. H. (1995). A Retrospective View of MIRIAD. In Shaw, R. A., Payne, H. E., and Hayes, J. J. E., editors, *Astronomical Data Analysis Software and Systems IV*, volume 77 of *Astronomical Society of the Pacific Conference Series*, page 433.

Sault, R. J. and Wieringa, M. H. (1994). Multi-frequency synthesis techniques in radio interferometric imaging. *A&AS*, 108.

Schachter, J., Filippenko, A. V., and Kahn, S. M. (1989). Bowen fluorescence in Scorpius X-1. *ApJ*, 340:1049–1063.

Schlafly, E. F., Meisner, A. M., Stutz, A. M., Kainulainen, J., Peek, J. E. G., Tchernyshyov, K., Rix, H.-W., Finkbeiner, D. P., Covey, K. R., Green, G. M., Bell, E. F., Burgett, W. S., Chambers, K. C., Draper, P. W., Flewelling, H., Hodapp, K. W., Kaiser, N., Magnier, E. A., Martin, N. F., Metcalfe, N., Wainscoat, R. J., and Waters, C. (2016). The Optical-infrared Extinction Curve and Its Variation in the Milky Way. *ApJ*, 821:78.

Selina, R. J., Murphy, E. J., McKinnon, M., Beasley, A., Butler, B., Carilli, C., Clark, B., Erickson, A., Grammer, W., Jackson, J., Kent, B., Mason, B., Morgan, M., Ojeda, O., Shillue, W., Sturgis, S., and Urbain, D. (2018). The Next Generation Very Large Array: A Technical Overview. *ArXiv e-prints*.

Sengar, R., Tauris, T. M., Langer, N., and Istrate, A. G. (2017). Novel modelling of ultracompact X-ray binary evolution - stable mass transfer from white dwarfs to neutron stars. *MNRAS*, 470:L6–L10.

Seward, F. D. and Charles, P. A. (2010). *Exploring the X-ray Universe*. Cambridge University Press.

Seymour, N., Dwelly, T., Moss, D., McHardy, I., Zoghbi, A., Rieke, G., Page, M., Hopkins, A., and Loaring, N. (2008). The star formation history of the Universe as revealed by deep radio observations. *MNRAS*, 386:1695–1708.

Shahbaz, T., Linares, M., Nevado, S. P., Rodríguez-Gil, P., Casares, J., Dhillon, V. S., Marsh, T. R., Littlefair, S., Leckngam, A., and Poshyachinda, S. (2015). The binary millisecond pulsar PSR J1023+0038 during its accretion state - I. Optical variability. *MNRAS*, 453:3461–3473.

Shahbaz, T., Smale, A. P., Naylor, T., Charles, P. A., van Paradijs, J., Hassall, B. J. M., and Callanan, P. (1996). An atlas of optical continuum and line emission from low-mass X-ray binaries. *MNRAS*, 282:1437–1453.

Shahbaz, T., Watson, C. A., and Dhillon, V. S. (2014). The spotty donor star in the X-ray transient Cen X-4. *MNRAS*, 440:504–513.

Shakura, N. I. and Sunyaev, R. A. (1973). Black holes in binary systems. Observational appearance. *A&A*, 24:337–355.

Shaposhnikov, N. and Titarchuk, L. (2006). Comprehensive Analysis of RXTE Data from Cygnus X-1: Spectral Index-Quasi-Periodic Oscillation Frequency-Luminosity Correlations. *ApJ*, 643:1098–1113.

Shih, I. C., Kundu, A., Maccarone, T. J., Zepf, S. E., and Joseph, T. D. (2010). A Variable Black Hole X-ray Source in an NGC 1399 Globular Cluster. *ApJ*, 721:323–328.

Shishkovsky, L., Strader, J., Chomiuk, L., Bahramian, A., Tremou, E., Li, K.-L., Salinas, R., Tudor, V., Miller-Jones, J. C. A., Maccarone, T. J., Heinke, C. O., and Sivakoff, G. R. (2018). The Maveric Survey: a Red Straggler Binary with an Invisible Companion in the Galactic Globular Cluster M10. *ArXiv e-prints*.

Shlosman, I., Vitello, P. A., and Shaviv, G. (1985). Active galactic nuclei - Internal dynamics and formation of emission clouds. *ApJ*, 294:96–105.

Sigurdsson, S. and Hernquist, L. (1993). Primordial black holes in globular clusters. *Nature*, 364:423–425.

Silk, J. (2013). Unleashing Positive Feedback: Linking the Rates of Star Formation, Supermassive Black Hole Accretion, and Outflows in Distant Galaxies. *ApJ*, 772:112.

Sion, E. M., Holberg, J. B., Oswalt, T. D., McCook, G. P., and Wasatonic, R. (2009). The White Dwarfs Within 20 Parsecs of the Sun: Kinematics and Statistics. *AJ*, 138:1681–1689.

Sippel, A. C. and Hurley, J. R. (2013). Multiple stellar-mass black holes in globular clusters: theoretical confirmation. *MNRAS*, 430:L30–L34.

Skottfelt, J., Bramich, D. M., Figuera Jaimes, R., Jørgensen, U. G., Kains, N., Arellano Ferro, A., Alsubai, K. A., Bozza, V., Calchi Novati, S., Ciceri, S., D'Ago, G., Dominik, M., Galianni, P., Gu, S.-H., Harpsøe, K. B. W., Haugbølle, T., Hinse, T. C., Hundertmark, M., Juncher, D., Korhonen, H., Liebig, C., Mancini, L., Popovas, A., Rabus, M., Rahvar, S., Scarpetta, G., Schmidt, R. W., Snodgrass, C., Southworth, J., Starkey, D., Street, R. A., Surdej, J., Wang, X.-B., and Wertz (The Mindstep Consortium), O. (2015). Searching for variable stars in the cores of five metal-rich globular clusters using EMCCD observations. *A&A*, 573:A103.

Skrutskie, M. F., Cutri, R. M., Stiening, R., Weinberg, M. D., Schneider, S., Carpenter, J. M., Beichman, C., Capps, R., Chester, T., Elias, J., Huchra, J., Liebert, J., Lonsdale, C., Monet, D. G., Price, S., Seitzer, P., Jarrett, T., Kirkpatrick, J. D., Gizis, J. E., Howard, E., Evans, T., Fowler, J., Fullmer, L., Hurt, R., Light, R., Kopan, E. L., Marsh, K. A., McCallon, H. L., Tam, R., Van Dyk, S., and Wheelock, S. (2006). The Two Micron All Sky Survey (2MASS). *AJ*, 131:1163–1183.

Smak, J. (1971). Eruptive Binaries. II. U Geminorum. *AcA*, 21:15.

Smits, M., Maccarone, T. J., Kundu, A., and Zepf, S. E. (2006). The globular cluster mass/low mass X-ray binary correlation: implications for kick velocity distributions from supernovae. *A&A*, 458:477–484.

Smolčić, V., Delhaize, J., Huynh, M., Bondi, M., Ciliegi, P., Novak, M., Baran, N., Birkinshaw, M., Bremer, M. N., Chiappetti, L., Ferrari, C., Fotopoulou, S., Horellou, C., McGee, S. L., Pacaud, F., Pierre, M., Raychaudhury, S., Röttgering, H., and Vignali, C. (2016). The XXL Survey. XI. ATCA 2.1 GHz continuum observations. *A&A*, 592:A10.

Soleri, P. and Fender, R. (2011). On the nature of the 'radio-quiet' black hole binaries. *MNRAS*, 413:2269–2280.

Solheim, J.-E. (2010). AM CVn Stars: Status and Challenges. *PASP*, 122:1133.

Soria, R., Musaeva, A., Wu, K., Zampieri, L., Federle, S., Urquhart, R., van der Helm, E., and Farrell, S. (2017). Outbursts of the intermediate-mass black hole HLX-1: a wind-instability scenario. *MNRAS*, 469:886–905.

Spitzer, Jr., L. (1969). Equipartition and the Formation of Compact Nuclei in Spherical Stellar Systems. *ApJ*, 158:L139.

Spruit, H. C. and Taam, R. E. (1993). An instability associated with a magnetosphere-disk interaction. *ApJ*, 402:593–604.

Stacey, W. S., Heinke, C. O., Cohn, H. N., Lugger, P. M., and Bahramian, A. (2012). An Examination of the X-Ray Sources in the Globular Cluster NGC 6652. *ApJ*, 751:62.

Stacey, W. S., Heinke, C. O., Elsner, R. F., Edmonds, P. D., Weisskopf, M. C., and Grindlay, J. E. (2011). Transient Extremely Soft X-ray Emission from the Unusually Bright Cataclysmic Variable in the Globular Cluster M3: A New CV X-ray Luminosity Record? *ApJ*, 732:46.

Steeghs, D. and Casares, J. (2002). The Mass Donor of Scorpius X-1 Revealed. *ApJ*, 568:273–278.

Steele, M. M., Zepf, S. E., Maccarone, T. J., Kundu, A., Rhode, K. L., and Salzer, J. J. (2014). Composition of an Emission Line System in Black Hole Host Globular Cluster RZ2109. *ApJ*, 785:147.

Stella, L., Priedhorsky, W., and White, N. E. (1987). The discovery of a 685 second orbital period from the X-ray source 4U 1820 - 30 in the globular cluster NGC 6624. *ApJ*, 312:L17–L21.

Strader, J., Chomiuk, L., Maccarone, T. J., Miller-Jones, J. C. A., and Seth, A. C. (2012a). Two stellar-mass black holes in the globular cluster M22. *Nature*, 490:71–73.

Strader, J., Chomiuk, L., Maccarone, T. J., Miller-Jones, J. C. A., Seth, A. C., Heinke, C. O., and Sivakoff, G. R. (2012b). No Evidence for Intermediate-mass Black Holes in Globular Clusters: Strong Constraints from the JVLA. *ApJ*, 750:L27.

Sukhbold, T., Ertl, T., Woosley, S. E., Brown, J. M., and Janka, H.-T. (2016). Core-collapse Supernovae from 9 to 120 Solar Masses Based on Neutrino-powered Explosions. *ApJ*, 821:38.

Sun, M., Grier, C. J., and Peterson, B. M. (2018). PyCCF: Python Cross Correlation Function for reverberation mapping studies. Astrophysics Source Code Library.

Sutantyo, W. (1975). The formation of globular cluster X-ray sources through neutron star-giant collisions. *A&A*, 44:227–230.

Taam, R. E. and Spruit, H. C. (2001). The Evolution of Cataclysmic Variable Binary Systems with Circumbinary Disks. *ApJ*, 561:329–336.

Tanaka, K. (2018). ALMA Images of the Host Cloud of the Intermediate-mass Black Hole Candidate CO-0.40-0.22*: No Evidence for Cloud-Black Hole Interaction, but Evidence for a Cloud-Cloud Collision. *ApJ*, 859:86.

Taniguchi, Y., Shioya, Y., Tsuru, T. G., and Ikeuchi, S. (2000). Formation of Intermediate-Mass Black Holes in Circumnuclear Regions of Galaxies. *PASJ*, 52:533–537.

Tauris, T. M., Langer, N., and Kramer, M. (2012). Formation of millisecond pulsars with CO white dwarf companions - II. Accretion, spin-up, true ages and comparison to MSPs with He white dwarf companions. *MNRAS*, 425:1601–1627.

Tauris, T. M., Langer, N., and Podsiadlowski, P. (2015). Ultra-stripped supernovae: progenitors and fate. *MNRAS*, 451:2123–2144.

Tauris, T. M. and van den Heuvel, E. P. J. (2006). *Formation and evolution of compact stellar X-ray sources*, pages 623–665. Cambridge University Press.

Taylor, A. R. and Seaquist, E. R. (1984). Radio emission from symbiotic stars - A binary model. *ApJ*, 286:263–268.

Taylor, G. B., Carilli, C. L., and Perley, R. A., editors (1999). *Synthesis Imaging in Radio Astronomy II*, volume 180 of *Astronomical Society of the Pacific Conference Series*.

Tendulkar, S. P., Yang, C., An, H., Kaspi, V. M., Archibald, A. M., Bassa, C., Bellm, E., Bogdanov, S., Harrison, F. A., Hessels, J. W. T., Janssen, G. H., Lyne, A. G., Patruno, A., Stappers, B., Stern, D., Tomsick, J. A., Boggs, S. E., Chakrabarty, D., Christensen, F. E., Craig, W. W., Hailey, C. A., and Zhang, W. (2014). NuSTAR Observations of the State Transition of Millisecond Pulsar Binary PSR J1023+0038. *ApJ*, 791:77.

Tetarenko, A. J., Bahramian, A., Sivakoff, G. R., Tremou, E., Linares, M., Tudor, V., Miller-Jones, J. C. A., Heinke, C. O., Chomiuk, L., Strader, J., Altamirano, D., Degenaar, N., Maccarone, T., Patruno, A., Sanna, A., and Wijnands, R. (2016a). Disc-Jet Coupling in the Terzan 5 Neutron Star X-ray Binary EXO 1745-248. *MNRAS*.

Tetarenko, A. J., Bahramian, A., Sivakoff, G. R., Tremou, E., Linares, M., Tudor, V., Miller-Jones, J. C. A., Heinke, C. O., Chomiuk, L., Strader, J., Altamirano, D., Degenaar, N., Maccarone, T., Patruno, A., Sanna, A., and Wijnands, R. (2016b). Disc-jet coupling in the Terzan 5 neutron star X-ray binary EXO 1745-248. *MNRAS*, 460:345–355.

Tetarenko, B. E., Bahramian, A., Arnason, R. M., Miller-Jones, J. C. A., Repetto, S., Heinke, C. O., Maccarone, T. J., Chomiuk, L., Sivakoff, G. R., Strader, J., Kirsten, F., and Vlemmings, W. (2016c). The First Low-mass Black Hole X-Ray Binary Identified in Quiescence Outside of a Globular Cluster. *ApJ*, 825:10.

Thompson, A. R., Moran, J. M., and Swenson, Jr., G. W. (2017). *Interferometry and Synthesis in Radio Astronomy, 3rd Edition*. Springer.

Thompson, T. A., Kochanek, C. S., Stanek, K. Z., Badenes, C., Post, R. S., Jayasinghe, T., Latham, D. W., Bieryla, A., Esquerdo, G. A., Berlind, P., Calkins, M. L., Tayar, J., Johnson, J. A., Holoien, T. W.-S., Auchettl, K., and Covey, K. (2018). Discovery of an Extraordinary Binary System. *ArXiv e-prints*.

Timmes, F. X., Woosley, S. E., and Weaver, T. A. (1996). The Neutron Star and Black Hole Initial Mass Function. *ApJ*, 457:834.

Tody, D. (1993). IRAF in the Nineties. In Hanisch, R. J., Brissenden, R. J. V., and Barnes, J., editors, *Astronomical Data Analysis Software and Systems II*, volume 52 of *Astronomical Society of the Pacific Conference Series*, page 173.

Torres, M. A. P., Jonker, P. G., Steeghs, D., Roelofs, G. H. A., Bloom, J. S., Casares, J., Falco, E. E., Garcia, M. R., Marsh, T. R., Mendez, M., Miller, J. M., Nelemans, G., and Rodríguez-Gil, P. (2008). Observations of the 599 Hz Accreting X-Ray Pulsar IGR J00291+5934 during the 2004 Outburst and in Quiescence. *ApJ*, 672:1079–1090.

Tremou, E., Strader, J., Chomiuk, L., Shishkovsky, L., Maccarone, T. J., Miller-Jones, J. C. A., Tudor, V., Heinke, C. O., Sivakoff, G. R., Seth, A. C., and Noyola, E. (2018). The MAVERIC Survey: Still No Evidence for Accreting Intermediate-mass Black Holes in Globular Clusters. *ApJ*, 862:16.

Treves, A., Turolla, R., Zane, S., and Colpi, M. (2000). Isolated Neutron Stars: Accretors and Coolers. *PASP*, 112:297–314.

Truss, M. and Done, C. (2006). The decline and fall of GRS 1915+105: the end is nigh? *MNRAS*, 368:L25–L29.

Tsygankov, S. S., Mushtukov, A. A., Suleimanov, V. F., and Poutanen, J. (2016). Propeller effect in action in the ultraluminous accreting magnetar M82 X-2. *MNRAS*, 457:1101–1106.

Tudor, V., Bahramian, A., Sivakoff, G., Chomiuk, L., Heinke, C., Li, R., Maccarone, T., Miller-Jones, J., Plotkin, R., Russell, T., Strader, J., Tetarenko, A., and Tremou, E. (2016). Radio non-detection during nearly-simultaneous Swift/XRT observations

of MAXI J0911-635/Swift J0911.9-6452 in NGC 2808. *The Astronomer's Telegram*, 8914.

Tudor, V., Miller-Jones, J. C. A., Patruno, A., D'Angelo, C. R., Jonker, P. G., Russell, D. M., Russell, T. D., Bernardini, F., Lewis, F., Deller, A. T., Hessels, J. W. T., Migliari, S., Plotkin, R. M., Soria, R., and Wijnands, R. (2017). Disc-jet coupling in low-luminosity accreting neutron stars. *MNRAS*, 470:324–339.

Tudose, V., Fender, R. P., Linares, M., Maitra, D., and van der Klis, M. (2009). The disc-jet coupling in the neutron star X-ray binary Aquila X-1. *MNRAS*, 400:2111–2121.

Turk, P. J. and Lorimer, D. R. (2013). An empirical Bayesian analysis applied to the globular cluster pulsar population. *MNRAS*, 436:3720–3726.

Ustyugova, G. V., Koldoba, A. V., Romanova, M. M., and Lovelace, R. V. E. (2006). "Propeller" Regime of Disk Accretion to Rapidly Rotating Stars. *ApJ*, 646:304–318.

van den Heuvel, E. P. J. (1975). Modes of mass transfer and classes of binary X-ray sources. *ApJ*, 198:L109–L112.

van Haaften, L. M., Nelemans, G., Voss, R., Toonen, S., Portegies Zwart, S. F., Yungelson, L. R., and van der Sluys, M. V. (2013). Population synthesis of ultracompact X-ray binaries in the Galactic bulge. *A&A*, 552:A69.

van Haaften, L. M., Nelemans, G., Voss, R., Wood, M. A., and Kuijpers, J. (2012). The evolution of ultracompact X-ray binaries. *A&A*, 537:A104.

van Paradijs, J. and McClintock, J. E. (1994). Absolute visual magnitudes of low-mass X-ray binaries. *A&A*, 290:133–136.

Vanderlinde, K. W., Levine, A. M., and Rappaport, S. A. (2003). Rossi X-Ray Timing Explorer All-Sky Monitor Detection of the Orbital Period of Scorpius X-1. *PASP*, 115:739–747.

Vanderplas, J., Connolly, A., Ivezić, Ž., and Gray, A. (2012). Introduction to astroml: Machine learning for astrophysics. In *Conference on Intelligent Data Understanding (CIDU)*, pages 47 –54.

Verbunt, F. (1993). Origin and evolution of X-ray binaries and binary radio pulsars. *ARA&A*, 31:93–127.

Verbunt, F. and Rappaport, S. (1988). Mass transfer instabilities due to angular momentum flows in close binaries. *ApJ*, 332:193–198.

Verbunt, F., Wijers, R. A. M. J., and Burm, H. M. G. (1990). Evolutionary scenarios for the X-ray binary pulsars 4U 1626-67 and Hercules X-1, and their implications for the decay of neutron star magnetic fields. *A&A*, 234:195–202.

Volonteri, M., Haardt, F., and Madau, P. (2003). The Assembly and Merging History of Supermassive Black Holes in Hierarchical Models of Galaxy Formation. *ApJ*, 582:559–573.

Volonteri, M. and Rees, M. J. (2005). Rapid Growth of High-Redshift Black Holes. *ApJ*, 633:624–629.

Vrtilek, S. D., Raymond, J. C., Garcia, M. R., Verbunt, F., Hasinger, G., and Kurster, M. (1990). Observations of Cygnus X-2 with IUE - Ultraviolet results from a multiwavelength campaign. *A&A*, 235:162–173.

Wang, Z., Archibald, A. M., Thorstensen, J. R., Kaspi, V. M., Lorimer, D. R., Stairs, I., and Ransom, S. M. (2009). SDSS J102347.6+003841: A Millisecond Radio Pulsar Binary That Had a Hot Disk During 2000-2001. *ApJ*, 703:2017–2023.

Wang, Z., Breton, R. P., Heinke, C. O., Deloye, C. J., and Zhong, J. (2013). Multiband Studies of the Optical Periodic Modulation in the X-Ray Binary SAX J1808.4-3658 during Its Quiescence and 2008 Outburst. *ApJ*, 765:151.

Wang, Z. and Chakrabarty, D. (2010). Discovery of a 693.5 s Period in the X-Ray Binary 4U 1820 - 30: A Superhump Interpretation. *ApJ*, 712:653–657.

Weisskopf, M. C., Brinkman, B., Canizares, C., Garmire, G., Murray, S., and Van Speybroeck, L. P. (2002). An Overview of the Performance and Scientific Results from the Chandra X-Ray Observatory. *PASP*, 114:1–24.

Wex, N. and Kopeikin, S. M. (1999). Frame Dragging and Other Precessional Effects in Black Hole Pulsar Binaries. *ApJ*, 514:388–401.

White, N. E. and Holt, S. S. (1982). Accretion disk coronae. *ApJ*, 257:318–337.

White, N. E. and Swank, J. H. (1982). The discovery of 50 minute periodic absorption events from 4U 1915-05. *ApJ*, 253:L61–L66.

Whitehurst, R. (1988). Numerical simulations of accretion disks. I - Superhumps - A tidal phenomenon of accretion disks. *MNRAS*, 232:35–51.

Whitehurst, R. and King, A. (1991). Superhumps, resonances and accretion discs. *MNRAS*, 249:25–35.

Wijers, R. A. M. J. and Pringle, J. E. (1999). Warped accretion discs and the long periods in X-ray binaries. *MNRAS*, 308:207–220.

Wijers, R. A. M. J. and van Paradijs, J. (1991). An upper limit to the number of pulsars in globular clusters. *A&A*, 241:L37–L40.

Wijnands, R. (2006). Accretion-Driven Millisecond X-ray Pulsars. In Lowry, J. A., editor, *Trends in Pulsar Research*, page 53.

Wijnands, R., Degenaar, N., Armas Padilla, M., Altamirano, D., Cavecchi, Y., Linares, M., Bahramian, A., and Heinke, C. O. (2015). Low-level accretion in neutron star X-ray binaries. *MNRAS*, 454:1371–1386.

Wijnands, R., Méndez, M., Markwardt, C., van der Klis, M., Chakrabarty, D., and Morgan, E. (2001). The Erratic Luminosity Behavior of SAX J1808.4-3658 during Its 2000 Outburst. *ApJ*, 560:892–896.

Wijnands, R. and van der Klis, M. (1998). A millisecond pulsar in an X-ray binary system. *Nature*, 394:344–346.

Willes, A. J., Wu, K., and Kuncic, Z. (2004). Radio Emission from Ultrashort-Period Double Degenerate Binaries. *PASA*, 21:248–251.

Wilman, R. J., Miller, L., Jarvis, M. J., Mauch, T., Levrier, F., Abdalla, F. B., Rawlings, S., Klöckner, H.-R., Obreschkow, D., Olteanu, D., and Young, S. (2008). A semi-empirical simulation of the extragalactic radio continuum sky for next generation radio telescopes. *MNRAS*, 388:1335–1348.

Wilson, W. E., Ferris, R. H., Axtens, P., Brown, A., Davis, E., Hampson, G., Leach, M., Roberts, P., Saunders, S., Koribalski, B. S., Caswell, J. L., Lenc, E., Stevens, J., Voronkov, M. A., Wieringa, M. H., Brooks, K., Edwards, P. G., Ekers, R. D., Emonts, B., Hindson, L., Johnston, S., Maddison, S. T., Mahony, E. K., Malu, S. S., Massardi, M., Mao, M. Y., McConnell, D., Norris, R. P., Schnitzeler, D., Subrahmanyan, R., Urquhart, J. S., Thompson, M. A., and Wark, R. M. (2011). The Australia Telescope Compact Array Broad-band Backend: description and first results. *MNRAS*, 416:832–856.

Windhorst, R. A., van Heerde, G. M., and Katgert, P. (1984). A deep Westerbork survey of areas with multicolor Mayall 4 M plates. I - The 1412 MHz catalogue, source counts and angular size statistics. *A&AS*, 58:1–37.

Wood, M. A., Thomas, D. M., and Simpson, J. C. (2009). SPH simulations of negative (nodal) superhumps: a parametric study. *MNRAS*, 398:2110–2121.

Woodgate, B. E., Kimble, R. A., Bowers, C. W., Kraemer, S., Kaiser, M. E., Danks, A. C., Grady, J. F., Loiacono, J. J., Brumfield, M., Feinberg, L., Gull, T. R., Heap, S. R., Maran, S. P., Lindler, D., Hood, D., Meyer, W., Vanhouten, C., Argabright, V., Franka, S., Bybee, R., Dorn, D., Bottema, M., Woodruff, R., Michika, D., Sullivan, J., Hetlinger, J., Ludtke, C., Stocker, R., Delamere, A., Rose, D., Becker, I., Garner, H., Timothy, J. G., Blouke, M., Joseph, C. L., Hartig, G., Green, R. F., Jenkins, E. B., Linsky, J. L., Hutchings, J. B., Moos, H. W., Boggess, A., Roesler, F., and Weistrop, D. (1998). The Space Telescope Imaging Spectrograph Design. *PASP*, 110:1183–1204.

Wrobel, J. M., Miller-Jones, J. C. A., Nyland, K. E., and Maccarone, T. J. (2018). Intermediate-Mass Black Holes in Globular Cluster Systems. *ArXiv e-prints*.

Wu, Q. and Gu, M. (2008). The X-Ray Spectral Evolution in X-Ray Binaries and Its Application to Constrain the Black Hole Mass of Ultraluminous X-Ray Sources. *ApJ*, 682:212–217.

Wyrzykowski, Ł., Kostrzewa-Rutkowska, Z., and Rybicki, K. (2016). Microlensing by single black holes in the Galaxy. In Różańska, A. and Bejger, M., editors, *37th Meeting of the Polish Astronomical Society*, volume 3, pages 121–124.

Zabalza, V. (2015). Naima: a Python package for inference of particle distribution properties from nonthermal spectra. In *34th International Cosmic Ray Conference (ICRC2015)*, volume 34 of *International Cosmic Ray Conference*, page 922.

Zdziarski, A. A., Kawabata, R., and Mineshige, S. (2009). Viscous propagation of mass flow variability in accretion discs. *MNRAS*, 399:1633–1640.

Zdziarski, A. A., Wen, L., and Gierliński, M. (2007). The superorbital variability and triple nature of the X-ray source 4U 1820-303. *MNRAS*, 377:1006–1016.

Zechmeister, M. and Kürster, M. (2009). The generalised Lomb-Scargle periodogram. A new formalism for the floating-mean and Keplerian periodograms. *A&A*, 496:577–584.

Zepf, S. E., Maccarone, T. J., Bergond, G., Kundu, A., Rhode, K. L., and Salzer, J. J. (2007). [O III] λ5007 Emission from the Black Hole X-Ray Binary in an NGC 4472 Globular Cluster. *ApJ*, 669:L69–L72.

Zepf, S. E., Stern, D., Maccarone, T. J., Kundu, A., Kamionkowski, M., Rhode, K. L., Salzer, J. J., Ciardullo, R., and Gronwall, C. (2008). Very Broad [O III] $\lambda\lambda$4959, 5007 Emission from the NGC 4472 Globular Cluster RZ 2109 and Implications for the Mass of Its Black Hole X-Ray Source. *ApJ*, 683:L139.

Zinn, R. (1980). The globular cluster system of the Galaxy. II - The spatial and metallicity distributions, the second parameter phenomenon, and the formation of the cluster system. *ApJ*, 241:602–617.

Zurek, D. R., Knigge, C., Maccarone, T. J., Pooley, D., Dieball, A., Long, K. S., Shara, M., and Sarajedini, A. (2016). A far-ultraviolet variable with an 18-minute period in the globular cluster NGC 1851. *MNRAS*, 460:3660–3668.

Signed contribution statements

To Whom It May Concern,

I, Vlad Tudor, have outlined my contributions to each publication (“Radio survey of globular clusters”, “Disk-jet coupling in low-luminosity accreting neutron stars” and “HST spectrum and timing of the ultra-compact X-ray binary candidate 47 Tuc X9”) at the beginning of its respective thesis chapter.

(Signature of Candidate)

I, as a Co-Author, endorse that the level of contribution indicated by the candidate at the beginning of each chapter is appropriate.

(Full Name of Co-Author) (Signature of Co-Author)